CENTRAL INSTITUTE OF PHYSICS

LASERS AND APPLICATIONS

A VOLUME DEDICATED TO ALL THOSE WHO INVENTED THE

LASER

AND MADE POSSIBLE

ITS APPLICATION

IN SCIENCE AND TECHNOLOGY

BUCHAREST 1985

CONTENTS

FOREWORD

THE LASER AT ITS 25th ANNIVERSARY

I. Ursu
The Central Institute of Physics

The invention of Laser, one of the most exciting scientific breakthroughs of the century, has been the outcome of an interdisciplinary effort involving contributions of many singular minds and teams throughout the world. The way to this discovery was paved by a host of significant results in various fields such as optics, gas discharges, spectroscopy, solid state physics, quantum mechanics, thin film depositing technology, electronics and fine mechanics.

The advent, 25 years ago, of the first born - J.M.Maiman's ruby laser - followed shortly by other solid state devices such as the CaF_2:U and CaF_2:Sm ones, and by the first gas laser - on Helium-Neon - initiated an almost explosive development of lasers of various kinds (gas-, liquid-, solid state-, and plasma-lasers), working in various regimes, from c.w. to very short pulses (femtosecond range), with peak powers up to terawatts and covering almost all the optical range from vacuum ultraviolet up to the milimeter region. Laser has greatly influenced the subsequent advancement of technology, including several areas with problems that have not been given a final solution as yet (e.g., communications on laser carriers, triggering and control of nuclear fusion reactions, etc.). At the same time, lasers have opened new prospects for basic research, and particularly for the interdisciplinary investigations.

Romania's first He-Ne laser, that was first operated on October the 20th, 1962, was the achievement of a research group led by our late colleague, professor Ion Agarbiceanu, at the time head of the Laboratory for Optical Methods in Nuclear Physics at the Institute of Atomic Physics in Bucharest - Magurele.

I believe we in Romania are entitled to take pride in the fact that such a remarkable result was obtained within less than a year from the first news on Laser worldwide.

Romanian physical research was already relying on a sound expertise and experience, and was increasingly gaining recognition for several outstanding results, in such laser-relevant fields, as e.g. gas discharges, optics/spectroscopy (particularly hyperfine structures), dielectric multilayer thin films research and technology, solid state physics, magnetooptical resonance, theoretical physics. A well-established school in electronics and mechanics was also available. Such assets made possible the prompt setting up of a complex research group that proved itself as soon able to give Romanian physics the access to a highly sophisticated instrument.

About the same time dynamic developments in quantum electronics (paramagnetic resonance absorption and stimulated emission of microwaves by transition ions in crystals) were

"ALMOST" 25 YEARS OF LASERS IN ROMANIA

M.Ivascu
The Central Institute of Physics, Bucharest

The laser - as its very name states - is a device for amplifying light by means of the stimulated emission of radiation. Its discovery came shortly after that of the maser which does the same thing in the microwave range. They both lie at the origin of a new branch of contemporary science: quantum electronics. Furthermore, it is only too fair to acknowledge their tremendous impact on virtually all fields of modern science and technology. Among these I shall mention at random the production of energy in fusion reactions, the onset and control of complex physico-chemical processes, the development of high purity and other special materials advanced tools (with special characteristics such as a very high accuracy), the transmission, processing and storage of information to say nothing of a wealth of domains in fundamental research, ranging from nuclear and atomic physics to chemistry and biology.

There are two ways to approach the problem of quantum amplifiers of radiation. One of them is the extension of traditional optics research (absorption, spontaneous emission) to the investigation of stimulated emission. The other one concerns the use of quantum electronics methods in the optical domain. According to their own tradition and specific goals of research, different countries have decided to follow either of these ways or both of them, in parallel. The latter choice was taken among others by Romania.

The optical approach has been adopted by the group at the Institute of Atomic Physics in Bucharest, lead by Professor Ion Agarbiceanu, and it resulted in the operation of the first Romanian laser in 1962, shortly after the discovery of the laser effect. Romania thus ranges among the world's first nations to obtain - in a practically independent way - original results in this brand new domain of research. I shall not enter any further details concerning this type of research since our achievements are presented in the introductory survey by Professor Ursu.

I shall stop a bit more at the second way - the quantum electronics approach - another major field of interest for our Institute. This approach is entirely due to the initiative of Professor Ioan Ursu, who is the founder of the Romanian School of quantum electronics. These studies originate in Professor Ursu's own investigations on electron spin resonance and maser processes in crystals doped with transitional ions.

Soon came the first high performance lasers, solid state lasers, as a result of the research initiated by Professor Ursu and his group, using active media which were, as I would like to stress, prepared at the National Center of Physics.

From the very beginning, a wide R & D programme was devised, which was aimed at correlating the Institute's efforts with the specific needs, not only of our own research, but also, and even more important, with the needs of Romania's economy and social life.

New types of lasers were thus developed of higher efficiency and reliability, tunable over a wide spectral range, along with large laser installations such as those designed for the production and investigation of dense hot plasmas or the development of new enrichment methods and isotope separation. Besides, one should not overlook the nonlinear optics studies which led to obtaining new wavelengths in the laser output, as well as the spectroscopy devices using lasers tunable in the visible and ultraviolet, the laser automatic data processing, parametric lasers allowing a high accuracy interferometry, and scores of other impressive achievements.

To conclude this short presentation of what might be called the "contemporary history" of lasers in Romania, I will go back to reemphasize the benefits of a policy "tuning" physics research to the needs of national economy.

We take much pride from our having succeeded to balance fundamental and applicative research - and this does not confine to only laser research (currently developed at the Institute for Physics and Technology of Radiation). We are costantly open to every scientific challenge as much as to the needs of our colleagues working in industry, agriculture or medicine (the latter being obviously of a fundamental social impact).

It is in this direction too that we have followed the advice and suggestions and, which is the most important, the personal example of Professor Ursu.

PHYSICS RESEARCH AND APPLICATIONS WITH THE FIRST ROMANIAN LASER

A.Agafitei, V.Vasiliu
Central Institute of Physics, Bucharest, ROMANIA

The first Romanian He/Ne laser that became operational on Octomber 20, 1962, had a resonant cavity whose metallic structure consisted of four thermocompensating rods providing a good mechanical stability of the laser mirrors over a long operation period. A photograph of the device is given in Fig.1.

Each thermocompensating rod was made of several different metals to minimise the thermal dilatation caused by variation in temperature during laser operation. The metallic assembly had a thermal dilatation coefficient of about $5\cdot10^{-8}$ degree^{-1}.

The resonant cavity consisted of a razotherm or quartz tube of 85 cm in length ans 12 mm in inner diameter, with or without inner electrodes. Adjoining either there was a metallic chamber including the mirrors with high reflection coefficient within the relevant spectral range. Mirror position could be accurately adjusted by twisting, from outside the chambers, two micrometric screws for the vertical and horizontal planes respectively, with respect to the discharge tube axis. The mirrors (of 1 m in length) could be adjusted from the outside for their holders where mounted in silphons that allowed minute mechanical shifts.

Parallelism adjustment for the resonant cavity mirrors was achieved through an original method using an optical system with multiple reflection on the laser mirrors. The method provided an adjustment accuracy of ± 1.5 arc seconds, which sufficed to assure mirror parallelism and perfect normality on the optical axis of the discharge tube, hence appropriate conditions were created for the laser effect to be obtained . Thi final adjustment was carried out in service by maximizing the value of the emitted signal.

The electric discharge in the active medium was provided by either a high frequency (39 MHz) generation or the direct application to the discharge tube electrodes of a direct or alternating voltage..

For the spectroscopic analysis of the radiation emitted by the active medium, the research group developed out of standard laboratory apparata a direct-reading spectrometer that, used a cooled photomultiplier and served as either emission spectra recorder or photon counter. The diagram of this device is given in Fig.2 . The instrument enabled fast recording over a wide spectral range in order not to exceed the time interval for which emission conditions of the investigated source were virtually unchanged. A medium-resolution monochromatorwas used, followed by a liquid nitrogen-cooled photomultiplier, whose spectral sensitivity ranged from 0.35 to 1.2 µm. Supply came from a stabilized (10^{-4}) direct voltage source, which was adjustable within the range of 500-2000 V, and the photocurrent was amplified using an electrometric amplifier, then let to recording potentiometer via a decade resistance devider to reduce the sensitivity of the recorder (with a dynamic range of 40 db for photocurrent measurement).

Using the thermocompensating rod-equipped resonator, laser oscillation was obtained on the 1152.3 nm, 1118 nm and 1160 nm transitions, the former of which was also the strongest. The most intense laser emission occured at high frequency, high direct voltage supply, These results were among others reported at the 3rd International Congress in Quantum Electronics held in Paris on February 11-15, 1963. The abstract of this our report presented at the Congress is shown in Fig.3.

A 3 m long, external mirror He-Ne laser (Fig.4) was build in December 1962. The tubes employed to build it were sealed by either optical contact, welding or epoxy resin of the aralidite type such windows may be seen in Fig.5.

This device helped evidence laser oscillation on six new near infrared transitions, previously unreported in literature: 1049.8 ($2s_3$ -- $2p_7$); 1084.4 ($2s_2$ -- $2p_6$); 1114.3 ($2s_4$ -- $2p_8$); 1139 ($2s_5$ -- $2p_8$); 1176.7 ($2s_2$ -- $2p_2$); and 1523.1 ($2s_2$ -- $2p_1$).

From the first laser which had been equipped with thermo-compensating rods, we subsequently moved on to the system using external mirrors which was found to provide better opportunities for both laboratory studies and many applications.

Rasotherm glass tubes and melted quartz tubes of 3 to 15 mm in inner diameter and 20 to 300 cm in length were used in the different construction variants. Some of the tubes employed had their slits sticked up by either optical contact on epoxy resin of the araldite type; others had welded slits. Different manufacturing technologies were worked out for each type of slit.

The discharge tube and the mirrors were both fixed by means of special mechanical holders to optical benches of high mechanical stability. To support the external mirrors, a mechanical system was used which allowed for the independent rotation of each mirror around two perpendicular axes, so that window parallelism was much more easily obtained. The plane and spherical mirrors with curvature radii from 60 to 400 cm and fine optical processing up to /80, were alternatively coated, in vacuum, with 13 succesive deposits of zinc sulphide and cryolite, and had a reflexion coefficient r = 99.2%. Other research dealed with the mode of the He-Ne laser emission on infrared radiation and its quantum efficiency.

FIGURE CAPTIONS

Fig. 1 Photograph of the first He-Ne laser made in Romania

Fig. 2 Diagram of the spectrophotometer with direct reading for laser spectroscopic research

Fig. 3 Summary of the paper presented at the third International Congress of Quantum Electronics

Fig. 4 Photograph of the 3 m He-Ne laser

Fig. 5 Photograph of the laser windows used in 1963

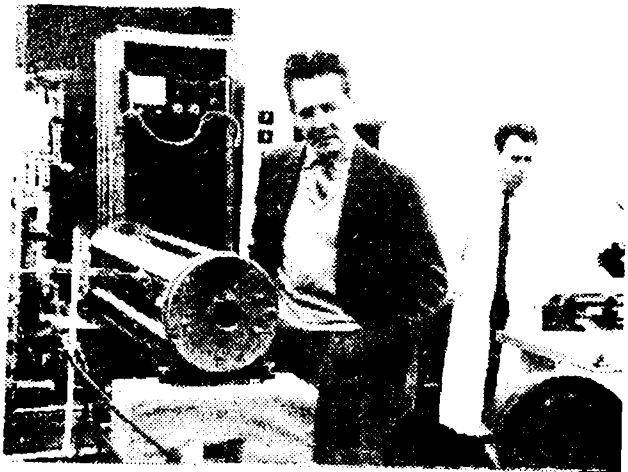

Fig. 1a

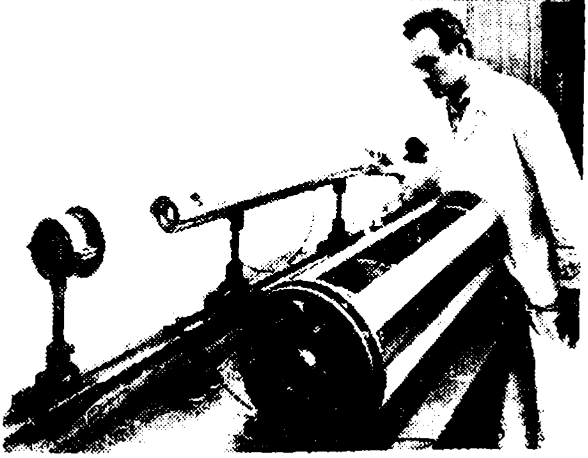

Fig. 1b

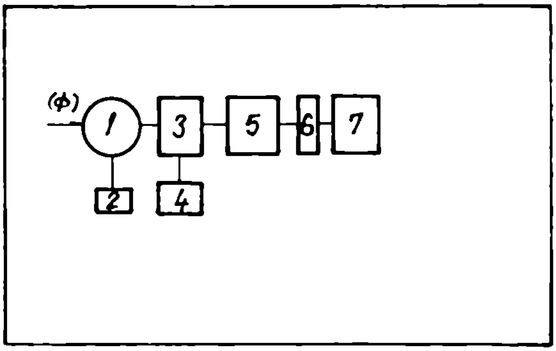

Fig. 2

1-Monochromator
2-Sincron motor
3-Photomultiplier
4-Photomultiplier supply source.
5-Electronic amplifier EMU-3
6-Decadic resistive divider
7-Recording potentiometer

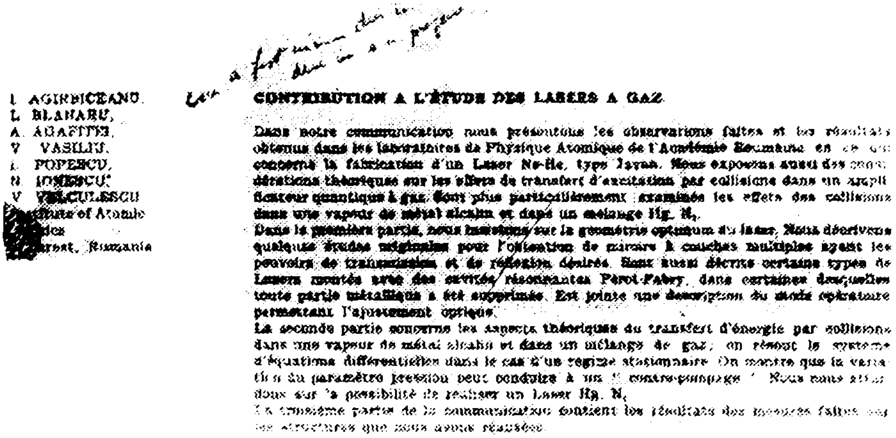

[illegible]

I. AGIRBICEANU,
L. BLANARU,
A. AGAFITEI,
V. VASILIU,
I. POPESCU,
N. IONESCU,
V. VELCULESCU
[illegible]stitute of Atomic
[illegible]sics
[illegible]arest, Rumania

CONTRIBUTION A L'ÉTUDE DES LASERS A GAZ

Dans notre communication nous présentons les observations faites et les résultats obtenus dans les laboratoires de Physique Atomique de l'Académie Roumaine en ce qui concerne la fabrication d'un Laser Ne-He, type Javan. Nous exposons aussi des considérations théoriques sur les effets de transfert d'excitation par collisions dans un amplificateur quantique à gaz. Sont plus particulièrement examinés les effets des collisions dans une vapeur de métal alcalin et dans un mélange Hg. N_2.

Dans la première partie, nous insistons sur la géométrie optimum du laser. Nous décrivons quelques études originales pour l'obtention de miroirs à couches multiples ayant les pouvoirs de transmission et de réflexion désirés. Sont aussi décrits certains types de Lasers montés avec des cavités résonnantes Pérot-Fabry, dans certaines desquelles toute partie métallique a été supprimée. Est jointe une description du mode opératoire permettant l'ajustement optique.

La seconde partie concerne les aspects théoriques du transfert d'énergie par collisions dans une vapeur de métal alcalin et dans un mélange de gaz; on résout le système d'équations différentielles dans le cas d'un régime stationnaire. On montre que la variation du paramètre pression peut conduire à un « contre-pompage ». Nous nous arrêtons sur la possibilité de réaliser un Laser Hg. N_2

La troisième partie de la communication contient les résultats des mesures faites sur les structures que nous avons réalisées.

Fig. 3

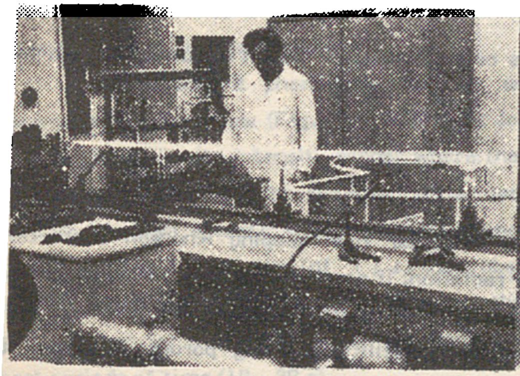

Fig. 4

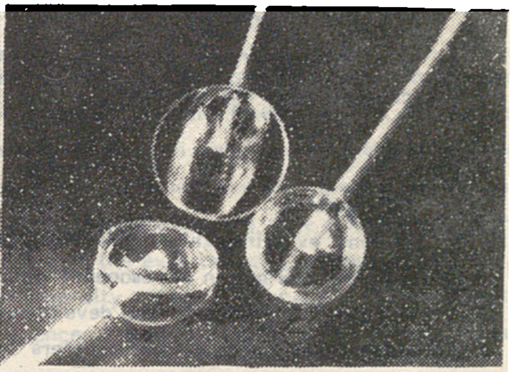

Fig. 5a

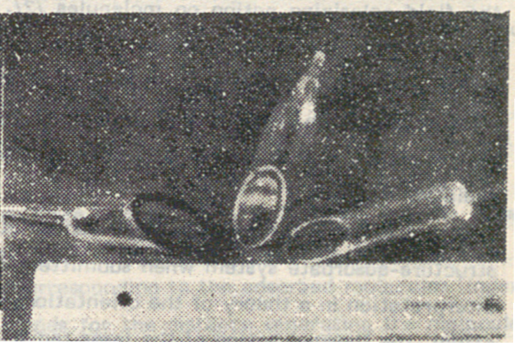

Fig. 5b

Fig. 5c

LASER CONTROL OF MOLECULAR FLOWS THROUGH POROUS MEDIA AND METAL CAPILLARIES

I.Ursu, R.Alexandrescu, V.Draganescu, D.Dragulinescu, C.Grigoriu,
I.N.Mihailescu, I.Morjan
Central Institute of Physics, Bucharest, Romania
A.M.Prokhorov, N.V.Karlov, V.A.Krevchenko, A.S.Laguchev,
N.A.Orlov, Yu.N.Petrov
Institute of General Physics, Moscow, Academy of Sciences, U.S.S.R.

Effects of resonance laser radiation on molecular flows through porous structures are discussed with particular reference to the dependence of the permeability of a fine-pored membrane on the variation in the incident laser intensity. A theoretical interpretation of these phenomena are given which accounts for the orientational action of the radiation field.

Preliminary experimental results concerning laser driven diffusion through metal capillaries are also reported.

Introduction

It was experimentally shown that a molecular flow keeping Knudsen character is diminished under the action of resonance laser radiation, if passing through a porous or capillary structure /1,3/. The interest in the development of these experimental techniques has not only a fundamental character but it also refers to the possibility of using porous structures and capillaries for laser controlling gas flows and component separation from gaseous mixtures.

The theoretical explanation of these phenomena shows that the specific features of molecules' behaviour on the surface in a resonant electromagnetic field are mainly determined by the field polarizing action on molecules /2/. A variation of the adsorption potential further causes a decrease of the molecular diffusion coefficient on the surface and, accordingly, of the diffusion velocity. Besides the interaction of field polarized molecules and surface ones, an interaction of the induced molecular dipole with its reflection into the wall takes place which may explain the modifications of the diffused flow, corresponding to changes in the incident radiation intensity.

Experimental results are presented concerning the behaviour of the transparent porous structure-adsorbate system when submitted to the resonance laser radiation, together with the interpretation in a theory of the orientational action of the radiation field. Besides the resonant effect, the thermal action of the laser radiation on both resonant and non resonant molecules is also analysed. Finaly, some experimental results concerning laser driven diffusion through metal capillaries are reported.

Effects of resonance laser radiation on molecular flows through porous structures

The molecular transit of small toluene flows (0.1-1 mg/h) through samples of fine-pored mica (filter diameter and thickness of 1 mm and 40 μm respectively, pore size ≈ 50 Å) was investigated when submitted to the resonant c.w. CO laser radiation of 0.1-10 W/cm^2 ($\lambda \approx 5.4$ μm). The gas pressure was (1-3) torr when admitted into pores and (10^{-4}-10^{-3}) torr at the sample exit. The laser irradiated the porous sample at the exit of the gas flow. The gas flows were detected and recorded by a quadrupole mass spectrometer KM-2. Mention should be made that in these experiments the Knudsen character of the flow was carefully checked up. The experiments were carried on at room temperature.

As mentioned before, in a rather wide range of flows (from 0.1 to 100 mg/h) and for many different substances, the flow locking degree rises with the incident laser radiation. In these experiments, a much more intricate dependence of the sample permeability on the radiation intensity was found. Thus, as one may notice from Fig.1, high permeability spikes were evidenced in this case, for which the molecular flow through the sample grows larger than it does in the absence of the laser radiation.

These transient phenomena may be analysed from the temporal evolution of the transmitted toluene flow (Fig. 2) at different levels of the incident laser intensity. We notice that, corresponding to intensity ranges where the laser irradiation results in diminishing the flow of resonance molecules, the radiation action induces a fast flow decrease followed by a slow increase (thermal effect), while after switching off the radiation, the flow slowly falls down again (Fig. 2b). Sharp spikes (of ∿ 1 s) were observed in the evolution of the transmitted flow, when switching on/off the laser radiation in other intensity ranges (Fig.2,c,d,e). Mention should be made that for minimizing thermal effects influence, the laser was switched on for rather short periods of time (10 - 20 s).

The theory of the orientational action of the radiation field, which accounts for the evolution of the tramsitted flow, starts from the adsorption potential for the laser polarized molecules. Using the general expression that was given in /2/ one may write the variation of the adsorption potential caused by the interaction of a polarized molecule with its image induced into the wall material as:

$$\Delta U^{\perp} = \alpha^2 \frac{d^4 E^2 \cos^2\theta (1+\cos^2\theta)(\delta_1\delta_2+\gamma_1\gamma_2)}{16h^2R^3(\delta_1^2+\gamma_1^2)(\delta_2^2+\gamma_2^2)} \tag{1}$$

if the laser field is perpedicular to the surface. Here, $\delta_j = \omega_j - \omega_\ell$ stands for the laser frequency detuning out of the center of the resonance line of the two molecules, δ_1 , δ_2 , γ_1 , γ_2 are the detunings and molecular line widths corresponding to the adsorbed molecules (index 1) and their images (index 2) respectively, R_0 stands for the distance separating the molecule from the surface, while α is the radiation reflection coefficient out of the surface. If $\vec{d}$ is the matrix element of the transition, then Θ is the angle between $\vec{E}$ and $\vec{d}$.

A similar expression may be derived for the interaction between polarized and unpolarized molecules, in the gaseous phase and on the surface, respectively /3/.

For an R_0 of the order of the molecular size, one has to consider the interaction with the molecules of the nearest surroundings, which can be accounted for by summing the pair wise interactions, $\Delta U^{\perp}$. This summation greatly depends on molecular location and orientation. If $\gamma_2 > \delta_2$, $\gamma_1 > \delta_1$, the surface projections of the induced molecular moments are equiprobably directed along and across the field and $\Delta U^{\perp} = 0$ for an arbitrary momentum distribution of the molecules diffused from the gaseous phase. If $\delta_2 \gg \gamma_2$, $\delta_1 \gg \gamma_1$, the projections of the induced molecular dipole moment on surface and in the gaseous phase are parallel when δ_1 , δ_2 have identical signs and antiparallel if their signs are different. Then, if the molecule is placed over the center of a square with diagonals of 2a, whose angles are occupied by adsorbed molecules, $\Delta U^{\perp}$ is given by

$$\Delta U^{\perp} = 4 \, \frac{(a^2 - R_0^2)\, d^2}{(a^2 + R_0^2)^{5/2}} \cdot A ; \tag{2}$$

$$A = \left[(\vec{E}_0 , \vec{d}_1)(\vec{E}_0 , \vec{d}_2) / 4\hbar^2 \right] \left\{ \left(\left[\exp i \left(\frac{\omega_1 R}{c} - \vec{k}\,\vec{R} \right) \right] / \left[(\delta_1 + i\gamma_1)(\delta_2 - i\gamma_2) \right] \right) + \text{c.c.} \right\}$$

where $\vec{k}$ is the wave vector, $\vec{r}$ is the molecular radius vector and $\vec{R} = \vec{r}_2 - \vec{r}_1$.

One notices that when averaging the potential (2) over the coordinates of a diffused molecule, $\Delta U^{\perp}$ does not vanish.

For $\vec{E}$ directed along the surface, we have $\delta_1 = \delta_2 = 0$, and corresponding expressions for $\Delta U_0^{\parallel}$ may be deduced.

The important conclusion derived from eqs. 1,2 is the strong dependence of ΔU_0 on the molecular orientation, which is of particular significance. Also, we note that one gets a variation of the adsorption potential for laser polarized molecules which is always $\leqslant 0$, i.e. under the action of the resonant field the adsorption potential deepens.

When the potential $\Delta U^{\perp}$ is greater than kT, the diffused molecules will be placed at definite locations on the surface and oriented. The value $\Delta U / kT$ is therefore characterizing the molecular orientability degree along the laser field $\vec{E}$. So, if the absolute values of the adsorption potential are increasing, this will result in further increased molecular orientability. However, depending on molecular orientation on the porous surface, the adsorption potential of molecules grows lower, and consequently, the diffusion coefficient rises. This was the case when a certain degree of molecular filling was attained /3/ or when flows of nonspherical symmetrical molecules were used (like toluene) which positions and orientations are shifted relatively to the adsorption potential maximum in laser radiation field. This is the very case also for certain values of the radiation intensity, where the filter heating causes the molecules' de-orientation, i.e. a slow fall of the diffused flow (Fig.2e). For comparison, in the case of chaotic molecule arrangement the thermal effect will be reversed (Fig.2b). Finally, we consider that the first spike on Figs.2 c,d,e can be accounted for by the thermal evaporation of the molecules from the sample surface, while the second and third spikes can be accounted for by the molecular orientation processes. The duration of these spikes is determined by the characteristic times in which the molecules fill up the surface and diffuse through the porous sample, respectively.

Thermal effect

From the experimental evidence previously exposed, one may observe the importance of the thermal action of laser radiation on both resonant and nonresonant molecules. The investigation of superficial diffusion processes under laser heating was performed on porous polymeric films having a metal covered surface /4/. On laser irradiation of such films, the radiation is practically not penetrating into the pore's volume, while the field, even that surrounding the metallic surface, remains low and has no significant polarizing action on the adsorbed molecules. The heating of the reflecting metal-covered surface is the primary effect, while the temperature below the shielded surface is slowly changing, due to the poor thermal conductivity of the film.

The study of molecular transit in the case of benzene (resonant to the CO laser radiation), sulphure hexafluoride (resonant to the CO_2 laser radiation) and nitrogen, through a fine-porous polymer film which was metal-covered on one face (pore diameter $\sim$ 1500 Å, porousity $\sim$ 2%, film diameter $\approx$ 4 mm) under irradiation with c.w. CO and CO_2 lasers has shown that the flows of resonant and nonresonant gases are similarly modified under the action of laser radiation. The dependence of the relative increase of the C_6H_6 molecular flow on the CO laser radiation intensity was shown in Fig.3. The strong exponential evolution reveals, as mainly responsible for the flow increase, the evaporation of the molecules which are diffusing through the outlet surface under the laser action.

Our experiments pointed out that, in laser irradiated porous structures, many processes may contribute to the different aspects of flow changes, like molecules' adsorption on the external surface and volume diffusion of molecules in pores and molecules' evaporation at a surface heating. On the ability to control the simultaneous influence of these processes depends the correct interpretation of laser driven effects on resonant molecular flow through porous media.

Laser driven resonant gas flows through metal capillaries

The surface polarisation action of the electromagnetic wave on resonant molecules also takes place at the diffusion of molecular flows through metal capillaries /5/.

In comparison to capillaries which are transparent to laser radiation /1/, metal capillaries have the advantage of extending the range of laser wavelengths and corresponding resonant gases. Also, due to the important values of the induced dipole reflection coefficient at a metal surface, polarization effects at resonant molecular flows through metal capillaries may be expected.

We performed preliminary experiments with nickel capillary of 0.5 mm in diameter, placed with one end in a high vacuum system provided with a ionic pump (FAN-SPI-2) and with the other end connected to a preliminary vacuum system, through which the gas flow entered at pressures between 0.5 and 12 torr. The gases used in the experiment were SF_6 and N_2. The molecular mass spectra were recorded by a quadrupole mass spectrometer Balzers QMG 111. The focalised c.w. CO_2 laser radiation was introduced in the capillary at the gas exit.

Under laser irradiation and for pressure ranges 1-2 torr, our investigations showed a diminishing of the resonant molecular flow Q (keeping the laser power constant and ≈ 7 Watt). The radiation influence on nonresonant N_2 flow results in a slow increase, due to thermal effect. If the flow enters the capillary at pressures situated around 10-15 torr, the effect of relative flow decrease Q/Q_0 attains a value of ∿ 0.5 at the same radiation intensity. Further improvements must be performed to allow the system to work at such pressure ranges.

With increased laser intensity, the capillary permeability to SF_6 flow decreases. With a capillary of 155 mm length the greatest attenuation of Q/Q_0 was of ∿ 0.3-0.4 at a radiation intensity at the capillary exit of 32 Watt/cm^2 /5/.

The interest in developing the metal capillary technique in order to laser control gaseous flows and component separation is further sustained by investigations of the different processes involved (like temperature and pressure dependence irradiation geometry, etc.) together with theoretical interpretation of these phenomena.

Figure Captions

Fig. 1 - The dependence of the relative toluene molecule flow through a fine-pored mica membrane on CO laser radiation intensity.
a) - a molecular flow of 3 mg/h; b) - of 0.5 mg/h; c) - of 0.1 mg/h.

Fig. 2 - Time dependent radiation influence on the molecular flow through a fine-pored membrane.
a) - laser radiation; b) - molecular flow changing (molecules on the porous surface are not oriented); c), d), e) - molecular flow changing (the orientation effect grows from c) to e)).

Fig. 3 - Dependence of the relative flow change of benzene on the incident CO laser radiation intensity.
a) - in the case of a ∿ 0.4 mg/h flow; b) - for a ∿ 1 mg/h flow.

References

/1/ N.V.Karlov, A.N.Orlov, Yu.N.Petrov, A.M.Prokhorov, A.A.Surkov, M.A.Yakubova, JETP Letters, 9, 269 (1983)

/2/ N.V.Karlov, A.M.Orlov, Yu.N.Petrov, A.M.Prokhorov, JETP Letters, 8, 426 (1982)

/3/ I.Ursu, R.Alexandrescu, V.Draganescu, I.N.Mihailescu, I.Morjan, A.M.Prokhorov, N.V.Karlov, V.A.Kravchenko, A.N.Orlov, Yu.N.Petrov, Journal de Physique, May (1985), to be published

/4/ I.Ursu, R.Alexandrescu, N.Comaniciu, I.N.Mihailescu, I.Morjan, A.M.Prokhorov, N.V.Karlov, V.A.Kravchenko, N.A.Orlov, Yu.N.Petrov, Journ.of Molec.Structure, 114, 317 (1984)

/5/ N.V.Karlov, A.S.Lagutchev, A.N.Orlov, Yu.N.Petrov, JETP Letters, 9, 10, 598 (1983)

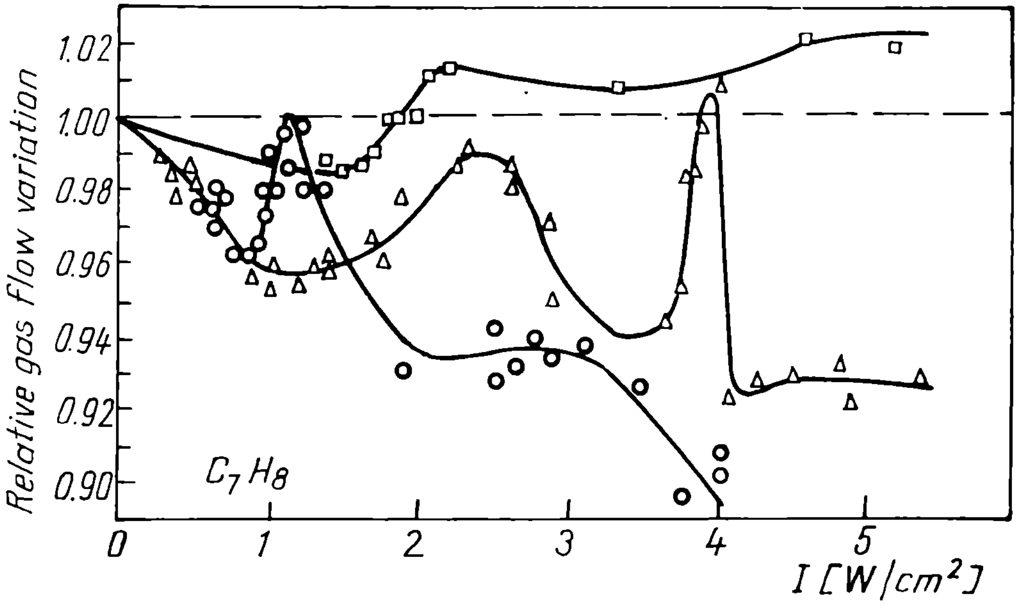

Fig. 1

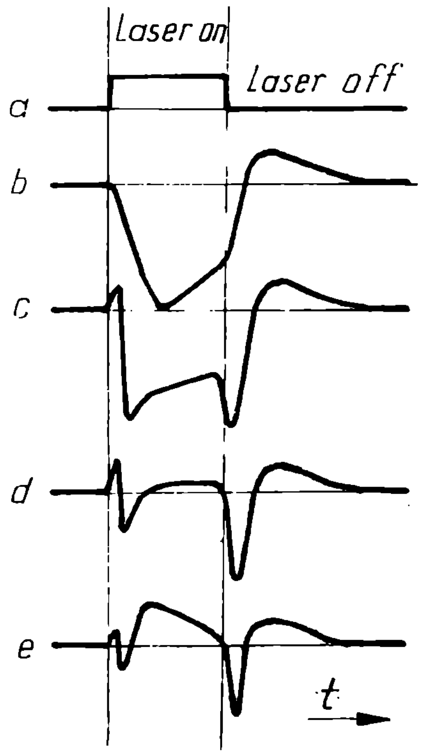
Laser on
Laser off
a
b
c
d
e
t

Fig. 2

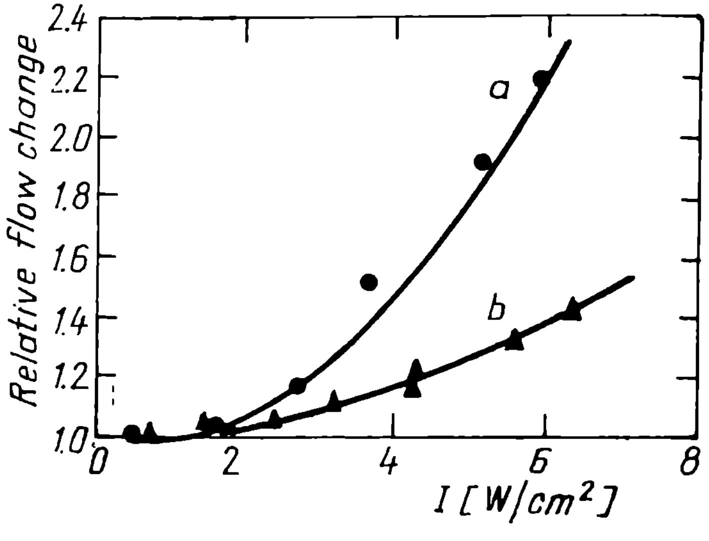
Relative flow change
2.4
2.2
2.0
1.8
1.6
1.4
1.2
1.0
0
2
4
6
8
I [W/cm²]
a
b

Fig. 3

INFLUENCE OF THE TARGET QUALITY AND STATE ON THE EVOLUTION OF THE INTERACTION PROCESS OF HIGH POWER LASER RADIATION WITH SOLID TARGETS

I.Ursu, Ileana Apostol, Doina Craciun, Maria Dinescu, I.N.Mihailescu
L.Nanu, Leona Nistor, A.Popa, V.S.Teodorescu
Central Institute of Physics, Bucharest, ROMANIA
A.M.Prokhorov, N.I.Chapliev, V.I.Konov
Institute of General Physics, Moscow, URSS

A systematic analysis is presented on the influence of the target surface quality and state on the evolution process of high power laser radiation with solid targets.

A systematic electron-microscopy is performed on the metallic surfaces, either preexsitent or induced by processing or as a result of power laser irradiation. Metallic and nonmetallic defects were revealed with a vaporization thresholds lower than that of an ideal plane metallic surface, which might lead to a lowering of the breakdown threshold of a gas in the neighbourhood of the metalic target.

The specification of threshold conditions for the breakdown plasma initiation in gases, as an effect of enough powerful laser irradiation of solid target is significant both for scientific and practical reasons:

(i) to receive a proper physical explanation on the well-known experimental evidence of the dramatic lowering of the plasma ignition threshold in a gas in the neighbourhood of solid surfaces as compared to pure gas breakdown [1-6];

(ii) as the target surface is involved as an initiator in the breakdown ignition, a particular attention has to be paid to the physico-chemical state of the surface and especially to its influence on the plasma threshold;

(iii) the rather dense and hot plasma appearing as a result of the gas breakdown, leads to the energy redistribution inside the interaction zone and lies at the origin of a supplementary thermal [7] and mechanical [1] action upon the target, which proves to be of special importance when using powerful lasers for material processing [8];

(iv) plasma formation on metallic components which are to be used in laser resonators as in other optical setups involving powerful laser radiation is strongly limiting the handled output energy density [9-10];

On th other hand, the breakdown plasma generation in a gas in the neighbourhood of solid target under the action of powerful laser radiation occurs as a result of the superficial vaporization of the target and the development of an avalanche in the vapour [2]. There is a significant difference between the phenomena underlying this process in the case of non-metallic and metallic targets:

(i) Because the typical nonmetallic targets (graphite, glass, plastics) strongly absorb laser light and/or have low heat conductivities, the threshold level of the incident laser radiation intensity that is able to induce target vaporization, I_v, lies below that corresponding to gas breakdown ignition I_{br}, i.e.

$$I_{br} > I_v \tag{1}$$

That is why when the incident intensity of the laser radiation tends to I_r, the intense vaporization of a nonmetallic taget surface supplies the original centers for the development of the avalanche ionisation process.

The defects and impurities of all kinds therefore seem not to be significantly involved in the breakdown ignition in the neighbourhood of nonmetallic targets.

(ii) For metals we usually have

$$I_v > I_{br} \tag{2}$$

The defects and impurities on metallic surfaces were therefore proposed as the source of centers from which the avalanche ionisation is initiated [2,4].

A large experimental effort was therefore focused during last year to the investigation of real metallic surfaces, both prior and after the powerful laser irradiation, with the aim of highlighting the defects and impurities that could be implied in the laser radiation-metallic target interaction process [11-15]. We shall further refer to some recent data obtained by electron microscopy methods on the defects and impurities covering the metallic surfaces and which could be either:

- pre-existent;
- introduced by the metallic surface processing;
- a result of the powerful laser irradiation.

1. Previous to laser irradiation

1.1. Metallic targets whose surface was only subjected to alcohol cleaning

Al, Cu and Ti samples were subjected to elemental analysis in which oxygen was identified but no traces of carbon on nitrogen were evidenced [15].

The following surface defects were observed, to which the lowering of the breakdown threshold can be ascribed:

(i) Dielectric centres, appearing lighter on the scanning images (fig.1).

The dimensions of these nonmetallic centres are in the range of several μm and their density reaches 10^6 cm^{-2}. The centres can be seen in more detail in figs 2,3.

The microanalysis of these regions showed strong metal and oxygen lines while carbon and nitrogen were missing. The dimensions and concentration of these centers are both diminished as a result of surface cleaning with alcohol.

(ii) Defects in the target material itself in the form of a thin layer of flakes, grooves, pores etc. [16,17]. Typical images of such defects, with a concentration (1-2) orders of magnitude lower than the concentration of the nonmetallic centres are given in figs. 4,5.

The thickness l of these defects was of the order of several μm. The vaporisation threshold value of a thin superficial layer of a thickness l, termally insulated from the metallic support, can be estimated as

$$I_v \simeq \frac{c \rho_s T_v \ell}{A \tau_l}, \qquad (3)$$

where

$c \simeq 0.9$ $Jg^{-1}\ {}^{o}C^{-1}$, $\rho_s \simeq 2.7\ g.cm^{-3}$ are the metal's specific heat and density respectively, while τ_l is the absorption time (taken to be for instance the FWHN of the first peak in a TEA-CO_2 laser pulse, during which the breakdown plasma initiation takes place or not). For $T_v \simeq 2600$ K, $l \simeq 3\times10^{-5}$ cm one gets $I_v \simeq 2\times10^{7}$ Wcm^{-2}, i.e. $I_v \sim I_{br}$ as predicted before and in very good concordance with the experimental evidence [1-6,15].

1.2. Metalic targets whose surface was subjected to working operations

It was shown that the surface working procedure has an essential influence on the surface and concentration of defects [11-15].

For illustration we selected some of our recent results [15], when the metallic (Cu) samples were submitted to the following working procedures:

(i) the surfaces had been polished first with a diamond paste, containing abrazive particles with minimum dimensions $\lesssim$ 1 μm (further referred mechanical polishing);

(ii) some of the samples were then subjected to a high-temperature annealing (up to 100°C), in a furnance evacuated to $\lesssim 10^{-4}$ Torr for 5 min (thermal treatment);

(iii) other samples were subjected to polishing with an orthophosphoric acid solution (electrochemical polishing);

The samples absorptivity (within an accurcy of + 15%) was determinated, before and after laser irradiation, by means of calorimetric method, using the heating curve of the target (and its derivative), which was probed with cw CO_2 laser radiation [18-19].

From fig.6, one can see that on mechanically polished surfaces scratches were left by the abrasive metarial. The average distance between scratches was ~ 0.5 μm, while their width was ~ 0.1 μm. Also, a great number (10^7-10^8 cm^{-2}) of abrasive particles (the white dots), with typical dimensions of 0.1-0.5 μm, remained attached to the metallic blade.

Scratches were much less pronounced on samples that had been subjected to either high-temperature annealing (fig.7) or electrochemical polishing (fig.8). The high-temperature annealing and the electrochemical polishing also significantly lowered the concentration of alien inclusions.

Defects were also identified in the target material itself in form of growing steps, grooves (fig.9), flakes (fig.10), and pores (fig.11). They were less frequent, as their concentration was only 10^4-10^5 cm^2. Flake- and pore-type defects grow much more pronounced as a result of electro-chemical polishing of high temperature annealing. High-temperature annealing also results in the advent of numerous growing steps (fig.12), probably by recrystallization in superficial layer.

We shall further introduce some quantitative elements.

In figs.13, 14 the behaviour of the delay time, t_d, between the beginning of the laser pulse and the appearance of the plasma light was represented, for different irradiation spots in the case of some monocrystalline copper targets which were subjected to a higher quality polishing (A) and to polishing of lower quality (B) respectively.

One notices:

(1) For a given irradiation spot area, A_s, the delay time showed a strong decrease tendency as a function of the focused energy density, ρ , when $\rho \gtrsim \rho_{br}$ while for $\rho \gtrsim \rho_{br}$ the delay time kept approximately constant;

(2) The minimum delay to the plasma light appearance was of (30-50) ns while the maximum delay typically does not exceed 250 ns, and in any case, keeps lower than the duration of the initial peak;

(3) The essential difference due to the surface state was found in the corresponding threshold energy density values; thus for $A_s \simeq 0.43$ mm^2 in the case of targets A, I_{br} (15-20) J/cm^2, while for $A_s \simeq 0.45$ mm^2, $I_{br} \simeq 10.5$ J/cm^2 was evidenced in the case of the targets B; for larger spots, of 2.81 and 2.9 mm^2, the difference is not evident, (3-5) versus (4.6-5.2) J/cm^2 (such a behaviour is obviously pointed out to the breakdown initiation on the account of the surface defects and impurities, whose density depends on the surface processing degree; indeed, for the radiation surface large enough, rather numerous initiation centres are acting within the irradiation spots, even for relatively clean surfaces and the breakdown threshold appear to be comparable [20]);

The lowering of the irradiation spot leads to the increase of the threshold energy density (the so-called "dimensional effect"). The dimensional dependence of the breakdown threshold can be two possible causes:

(i) the losses by electron diffusion out of the interaction zone;

(ii) the stochastic character of the breakdown initiation centers within the irradiation zone.

It appears rather hard to distinguish between two mechanisms so far. Thus (fig.15), a case for the stochastic mechanism might be found in the increase of the scattering of the experimentally determined values of the threshold energy density when decreasing the irradiation spot area while the threshold energy density keeps constant for $A_s \geqslant 0.8$ mm^2.

On the other hand, the coefficient of electrons free diffusion in vapours evaluated as

$$D = \frac{kT_v}{m_e n_e \tau} \leq 7 \times 10^4 \text{ cm}^2/\text{s} \qquad (4a)$$

(where k is the Boltzmann constant, $n_e \simeq (2\text{-}3) \times 10^{18}$ cm^{-3} the electron density, $\tau \simeq 10^{-12}$ cm^2 the effective electron-neutral particles collision cross-section and $T_v \simeq 3110$ K) is congruent with the value of $\simeq 4.2 \times 10^4$ cm^2/s inferred from

$$d^2 = Dt_d \qquad (4b)$$

where d is the laser spot diameter. This result is therefore supporting the first of the afore mentioned mechanisms.

dimensional effect based on the introduction of periodical structures as a result of powerful laser irradiation of metallic surface.

In table I a number of data were collected on the concentration of alien including, n, absorptivity A_0, and the threshold energy density required to induce the air breakdown plasma in front of the metallic target, ρ_{br}, in the case of the three afore mentioned working procedures.

Table I

	Mechanical polishing	Thermal annealing	Chemical polishing
n cm^{-2} ,	1×10^{8}	6×10^{7}	3×10^{7}
A_o (%)	1.23	1.42	0,85
ρ_{br} ($J.cm^{-2}$)	9.5	5.4	13.5

It is to be pointed out that

(1) the initial absorptivity of all samples was relatively small, in spite of the high degree of contamination by abrazive material;

(2) a direct interdependence exists between the initial absorptivity and the initiation threshold of air breakdown in front of these targets;

(3) there is no evidence of a clear link between the density of the abrasive particles and the target absorptivity, but the latter seems somewhat dependent on the defects in material (i.e. flakes, pores, growing steps).

In conclusion, there is always a considerable number of defects and impurities that cover real metalic surfaces, to whose presence can be attributed the lowering of the vaporization Initiation threshold, resulting in low-threshold gas breakdown in the neighbourhood of metallic target.

2. After laser irradiation

2.1. The targets were submitted to a large number of pulses (up to several thousands) at intensity levels inferior to the monopulse breakdown ignition threshold.

The irradiations [15] were performed with pulsed CO_2 laser systems delivering $\leqslant$ 10 J in monopulse and $\leqslant$ 0.4 J at a high repetition rate ($f \leqslant 1$ k Hz) at average duration of several µs, that were focused in spots approximately 2.2×10^{-2} cm^2. The incident laser beam attenuation was obtained through an arrangement of calibrated polyethylene filters.

The breakdown threshold was established either visually or from fast streak camera recording .

We observed that after a certain irradiation time, a plasma accompanies every incident laser pulse. Two mechanisms can be made responsible for this experimental evidence:

2.2. Laser activated metal oxidation

In fig.16 we give a typical photographic image of copper target which was heated under the action of powerful CO_2 laser radiation in the above mentioned conditions [15]. The following features are to be mentioned:

(i) we emphasize the presence of oxide layers which turn out to be thermally insulated from the metallic substrate;

(ii) cracks are induced into the oxide (which accounts in our opinion for the increased oxidation reaction rate in the case of laser irradiation in comparison with the isothermic oxidation conditions in "clasical" oxidation).

The oxide films (the specific presence of the CuO and Cu_2O was identified) are then more easily vaporised by the laser radiation and the gas breakdown is induced by lower intensities.

This assertion gets further weight as:

- the oxides can be regarded as thermally insulated from the metallic substance when

(5a) $\tau < x^2/\chi$

in this case (χ of Cu_2O $\tau = \tau_1 \sim 10^{-7}$), one gets $x \lesssim 1$ µm, in good keeping with the experimental observation;

- if interference phenomena are taken into account, the temperature at the oxide air interface rises with x until

(5b) $x \lesssim \lambda/4n$

one finds again $x \lesssim 1$ µm, so the oxide layer is consequently underlying the low threshold vaporization.

2.3. Development and accumulation of remanent plastic deformations [14, 20-23]

Repeated action of the laser radiation results in significant morphological of the surface. In fig.17 one observs the photograph of the border of an irradiation zone together with an unirradiated fragment.

The border of irradiation zone presents a strongly pronounced bright character, while in the irradiation zone a granular structure shows up (fig.18). The typical grain diameter is d (20-50)m. The depth of the border between grains is rising when both the total number of laser pulses and the incident energy density are rising. The width of the border between grains can reach values of ~ (6-10) µm while the border depth reaches ~ (1-2) µm (fig.19).

Inside the irradiation zone, local defects were identified (flakes with melted borders, separated drops of frozen fusion (fig.20); the incidence of such defects is relatively small, $n < 10^4$ cm^{-2}.

Accurate etching with fluorine hydride showed that the initial structure of the unirradiated material is characterized by larger grains as compared to the irradiation zone.

To help in analysing the results, a simple mode was used.

The maximum variation of the mirror surface temperature induced under the action of such a laser pulse can be obtained from

$$T_{max} = \frac{2A\rho}{(\pi k \rho_s c \tau)^{1/2}} \qquad (6)$$

where k, ρ, c are target thermal conductivity, density and specific heat respectively. As a result of this fast temperature increase, the surface layer tends to expand. Inertial forces, originating in the neighbouring cold regions withstand this expansion. Mechanical strains are then induced in the zone surrounding the heated portion. As the depth of the heated layer is rather small ($\sim 10^{-3}$ cm), the axial stress falls to zero in characteristic times of $\sim 10^{-8}$ s, while the radial stresses last for $\sim 10^{-5}$ s, corresponding to the irradiation spot diameter of 1 cm. The relation between the radial stresses and the surface layer temperature is given by

$$\sigma_{yy} = \sigma_{zz} = \frac{\alpha E}{1-\nu} \Delta T \qquad (7)$$

Here α, E, ν are the dilatation coefficient, the Young modulus and the Poisson coefficient of the metal respectively. The minimum temperature which causes plastic deformation is equal to

$$T_{min} = \frac{(1-\nu)\,\sigma}{\alpha} \qquad (8)$$

Here σ is the elasticity of the material. Taking into account the eq.(6) one gets an estimate of the minimum energy density for which the plastic deformation threshold is reached

$$\rho_{min} = \frac{(1-\nu)\,(\pi k \rho_s c \tau)^{1/2}}{2A\alpha E}\,\sigma \qquad (9)$$

By repeated temperature cycles following periodical laser irradiation the plastic deformations accumulates if

$$\rho \sim \rho_d = 2\rho_{min} = \frac{(1-\nu)\,(\pi k \rho_s c \tau)^{1/2}}{A\alpha E} \qquad (10)$$

The plastic deformations emerge on the surface as deformations where the sliding bands the free border overlap. Then, as a result of repeated laser irradiation a gradual damage of the surface (mainly cracking) is initiated, which, in its turn leads to metallic surface defects underlying the lowering of the vaporization threshold. By the vaporization of these defects, the conditions are met for air plasma ignition at a reduced energy density while the hot zone of the ignited plasma underlies the significant increase of the mechanical and thermal stress of the target surface thus causing its dramatic damage.

Let us further introduce the corresponding calculation. The minimum temperature which leads to the plastic deformations advent in the case of aluminium is $\Delta T_{min} \simeq 25^{\circ}$C which correspond to an energy density of $\rho_{min} \simeq 2{,}5$ J cm^{-2}. The threshold for the plastic deformations correspond consequently to $\rho_d \geqslant 5$ J cm^{-2}, in very good according with the afore-mentioned experimental evidence.

We want to point out here the large potential application of this effect (for example in optical recording) as well as its important consequence for the development of high performance metallic optics to be used in connection with very high power laser system [23, 24]. As a matter of fact we consider already necessary that every laser component for very powerful laser system to be characterized from now on by the monopulse damage threshold and the threshold of damage cumulation.

2.3. Powerful pulsed laser irradiation ($I>I_{br}$)

The absorptivity, A_1, and the threshold energy density for including air breackdown, , subsequent to powerful laser irradiation behaves as the specified in Table II.

Table II

	Mechanical polishing	Thermal annealing	Chemical polishing
A (%)	1.13	1.29	0.8
ρ^{1}_{br} (J.cm^{-2})	13.7	13.3	9.5

The point to note first is the lower absorptivity ($A_1 > A_0$) following the powerful laser irradiation. It seems that the cleaning effect [19] prevails in this case over the oxidation process.

However, the competition between the cleaning effect and the induction of new defects appears to be rather critical. Thus, while the breakdown threshold energy density was increased in the first two cases it was lowered for the electrochemically worked surfaces (these targets turn out to be more subject to the new defects induction due to the absence of the amorphous layer removed by this type of working).

The same situation was evidenced in fig.13 (target of better processing) where no significant differences are to be noticed in the $t_d(\rho)$ evolution in the case of the first shot (∇) and the next one (*) directed to a same location, of $\simeq 2.18$ mm^2, on the copper target surface.

Finally, we must point out that the analysis of the $\rho_{br}(A)$ evolution has to be correlated with information on the specific surface state, lest misinterpretation of the experimental results should arise. For instance, from tables I and II one sees that for electrochemically and mechanically polished copper target before and after laser irradiation for $A_0 \simeq 0.83\%$ and A_1 1.13% the respective threshold energy densities are rather closed of $13.3 \simeq 13.7$ J/cm^2.

In the fig. 21 we represented the behaviour of the energy spent for plasma initiation, computed as

$$\rho'_{th} = \int_0^{t_d} I(t)dt \tag{11}$$

where the integral was performed over the real temporal shape of the laser pulse, as a function of the irradiation spot area. We note the similarity between the evolution of $\rho'_{th}(A_s)$ and $\rho_{th}(A_s)$ evolutions.

On the other hand, it is obvious that if the probability of the breakdown ignition is defined as related to the development of the ionization avalanche, the most significant parameter characterizing the breakdown appearance is the incident laser intensity (I criterion). However, if most of the adsorbed laser energy is consumed for defects heating (up to their vaporization), as we evidenced the situation stays in the case of the powerful CO_2 laser irradiation of metals, the breakdown threshold will be properly characterized by the ρ'_{th} quantity (ρ criterion).

As a very important concluding remark we emphasize therefore that in order to describe adequately the breakdown threshold condition in front of metallic targets, in the general case, it is therefore necessary to specify the values of I, ρ_{th}, ρ'_{th}, t_d, A_0, A, as well as the real temporal shape of the laser pulse.

Finally we point out that pulsed irradiation of metallic targets in the ambient gases, whether in the presence or absence of breakdown plasma, can result in the controlled modification of the target surface condition and physico-chemical properties at the irradiation sites.

REFERENCE

1/ A.I.Barchukov, F.V.Bunkin, V.I.Konov, A.M.Prokhorov, JETP Letters 17, 194 (1973)

2/ A.I.Barchukov, F.V.Bunkin, V.I.Konov, A.A.Lubin, JETP Letters 39, 469 (1974)

3/ W.E.Maher, R.B.Hall, R.R.Johnson, J.Appl.Phys. 45, 2138 (1974)

4/ D.C.Smith, J.Appl.Phys. 48, 2217 (1977)

5/ I.Apostol, D.Dragulinescu, C.Grigoriu, I.N.Mihailescu, I.Morgan, Al.Nitoi. I.M. Popescu, M.V.Udrea, V.I.Konov, Proc.XIIth ICPIG (Eindhoven, 1975), part A (North-Holland, Amsterdam-Oxford, 1975), p.337

6/ I.Apostol, D.Dragulinescu, C.Grigoriu, I.N.Mihailescu, I.Morgan, Al.Nitoi. I.M.Popescu, M.V.Udrea, V.I.Konov, Rev.Roum.Phys. 19, 895 (1974)

7/ S.Marcus, J.E.Lowder, D.L.Mooney, J.Appl.Phys. 47, 2966 (1976)

8/ J.A.McKay, J.T.Schriempf, IEEE J.Quant.Electron. QE-17, 2008 (1981)

9/ H.M.Musal: (in) "Laser Induced Damage in Optical Materials", NBS Spec.Publ. NG-20 (1980), p.227

10/ S.G.Burgin, I.N.Goncharov, V.I.Konov, A.M.Prokhorov, Yu.A.Skvortsov, N.I.Chapliev, Izvestia AN SSSR, Phys.Series 46, 1943 (1982)

11/ J.O.Portens, D.L.Decker, J.L.Jernigan, W.N.Faith, M.Bass, IEEE J.Quant.lectron., QE-14, 776 (1978)

12/ S.C.Seitel, J.O.Portens, D.L.Decker, W.N.Faith, D.J.Grandjean, IEEE J.Quant.Electron. QE-17, 2072 (1981)

13/ J.O.Portens, D.L.Decker, W.N.Faith, D.J.Grandjean, S.C.Seitel, M.J.Soileau, IEEE J.Quant.Electron. QE-17, 2078 (1981)

14/ S.J.Thomas, R.F.Harrison, F.J.Figueira, Appl.Phys.Lett. 40, 200 (1982)

15/ N.Koumvakalis, C.S.Lee, M.Bass, IEEE J.Quant.Electron. QE-19, 1482 (1983)

16/ I.Ursu, I.Apostol, D.Craciun, M.Dinescu, I.N.Mihailescu, L.C.Nistor, Al.Popa, V.S.Teodorescu, A.M.Prokhorov, I.N.Chapliev, V.I.Konov, J.Phys.D.: Appl.Phys. 17, 717 (1984)

17/ C.T.Walters, R.H.Barnes, R.E.Beverly III, J.Appl.Phys. 49, 2937 (1978)

18/ M.I.Arzuov, M.E.Karasev, V.I.Konov, V.V.Kostin, S.M.Metev, A.S.Silenko, N.I.Chapliev, Kvantovaya Elektronyka 8, 392 (1978)

19/ I.Ursu, I.Apostol, I.N.Mihailescu, L.C.Nistor, V.S.Teodorescu, E.Turcu, A.M.Prokhorov, N.I.Chapliev, V.I.Konov, V.G.Ralchenko, V.N.Tokarev, Appl.Phys. A29, 209 (1982)

20/ C.S.Lee, N.Koumvakalis, M.Bass, Appl.Phys.Lett. 41, 625 (1982)

21/ H.M.Musal Jr., NBS Special Publ. 568 (1979), p.159

22/ J.F.Figuera, S.J.Thomas, IEEE J.Quant.Electron. QE-18, 1380 (1982)

23/ I.Ursu, I.Apostol, M.Dinescu, I.N.Mihailescu, Al.Popa, A.M.Prokhorov, V.I.Konov, I.N.Chapliev, Appl.Phys. A34, 133 (1984)

24/ H.E.Bennett, A.H.Guenther, D.Milam, B.E.Newnam, Appl.Optics 22, 3276 (1983).

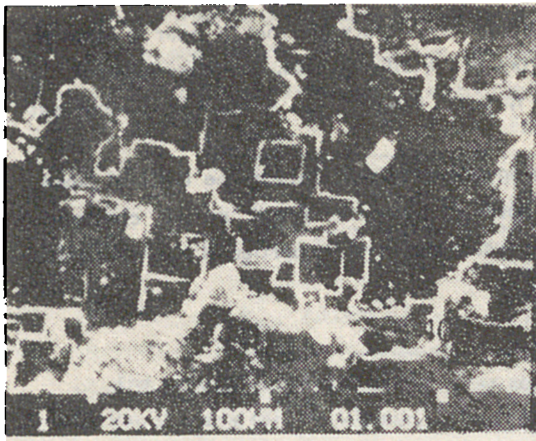

Fig. 1

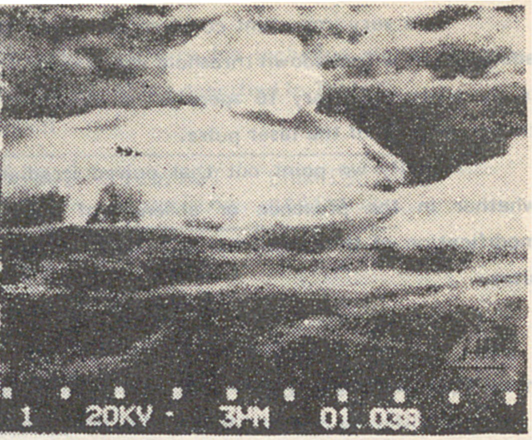

Fig. 2

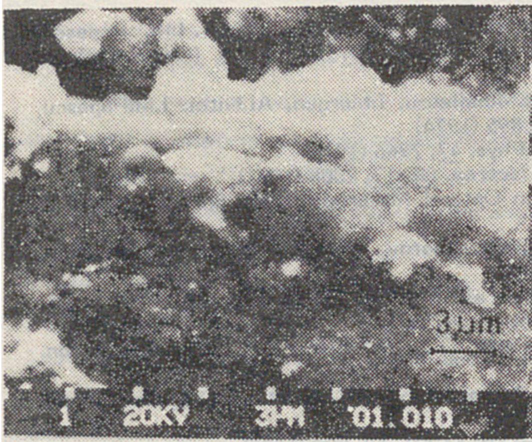

Fig. 3

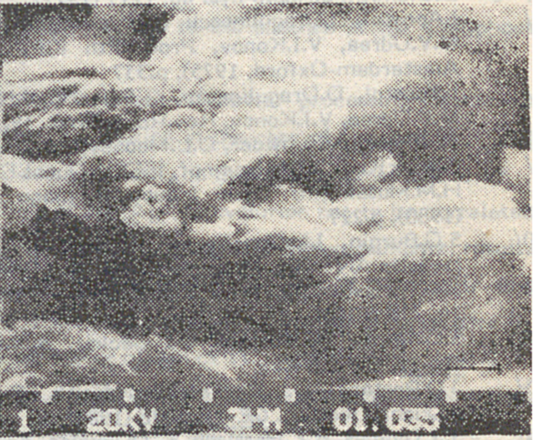

Fig 4

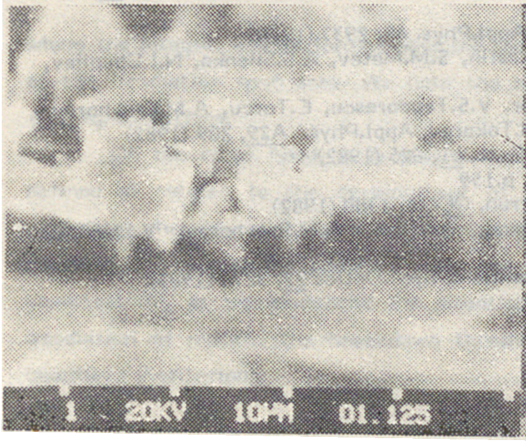

Fig. 5

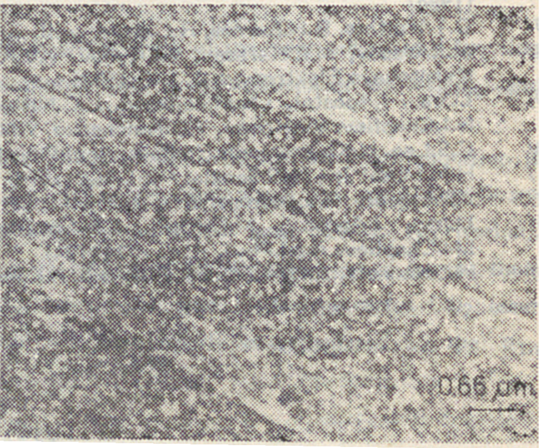

Fig. 6

Fig. 7

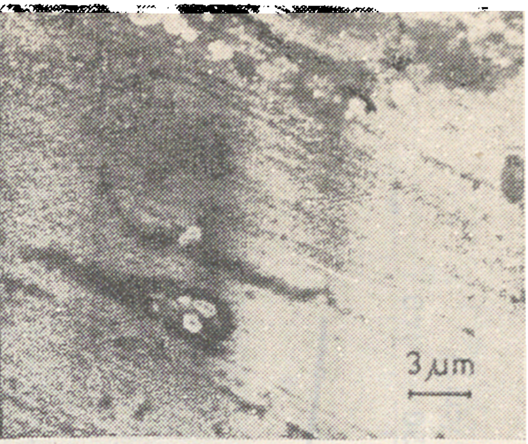

Fig. 8

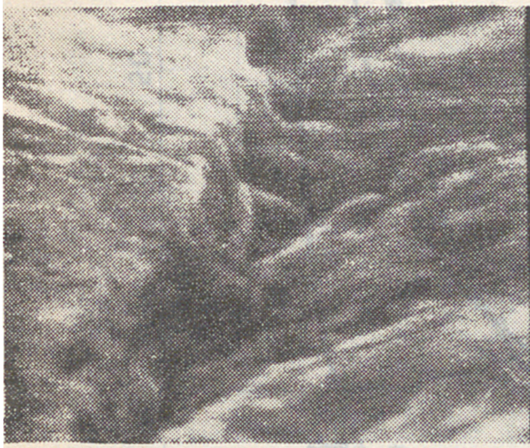

Fig. 9

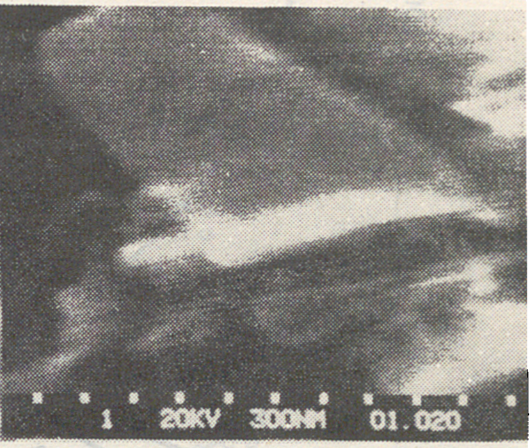

Fig. 10

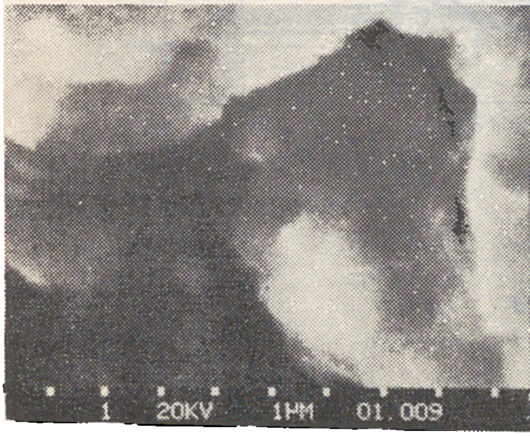

Fig. 11

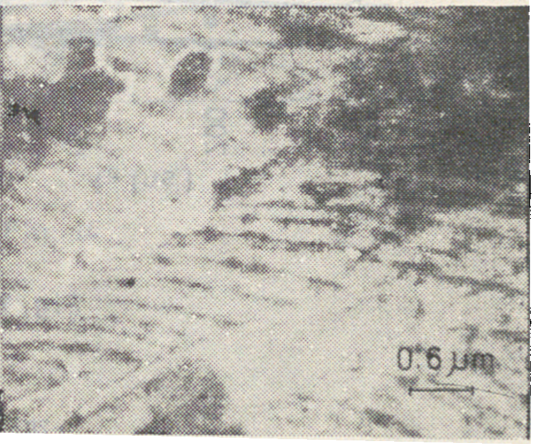

Fig. 12

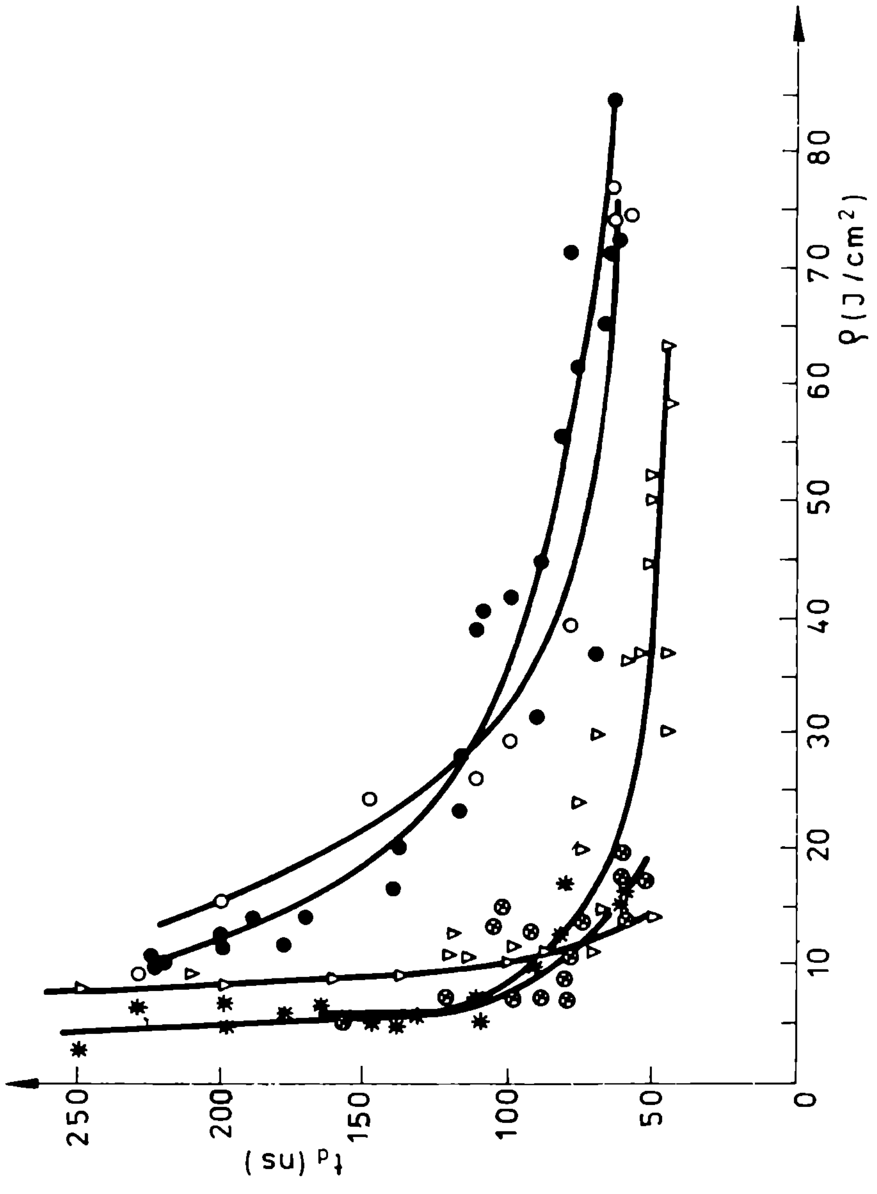

Fig. 13

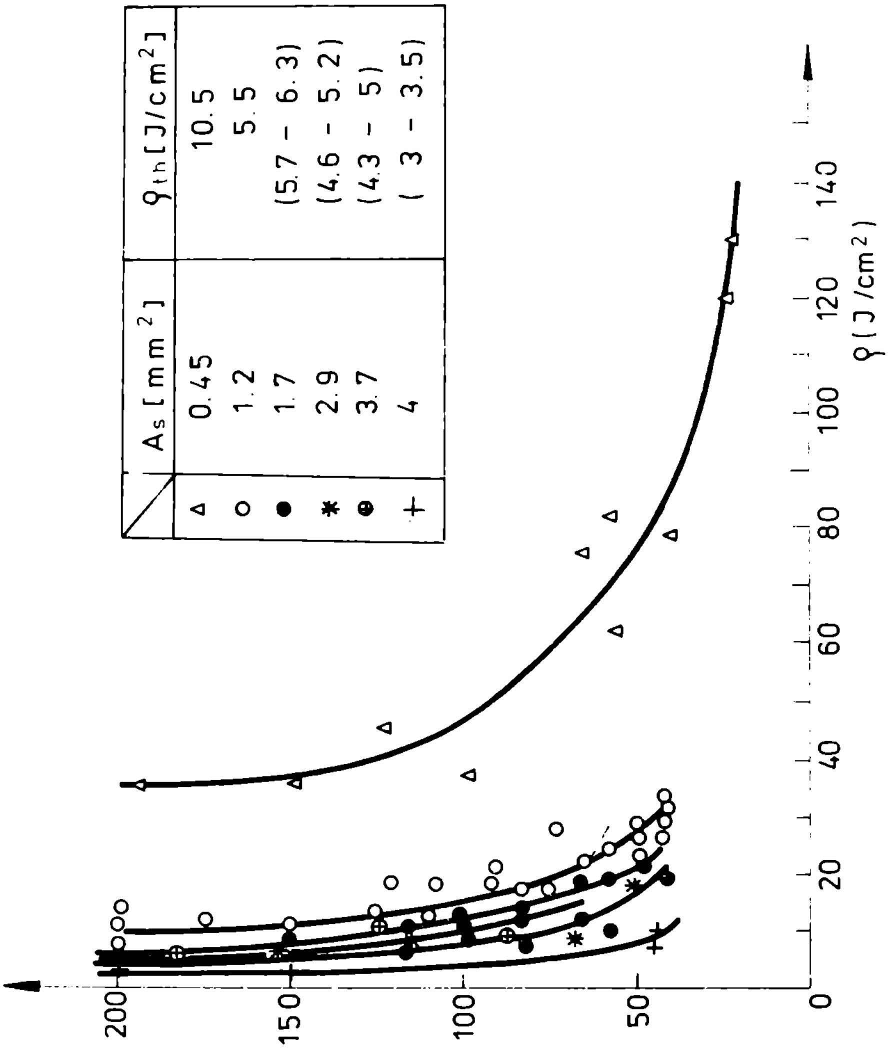

A_s [mm^2]
ϱ_{th} [J/cm^2]
△ 0.45 10.5
○ 1.2 5.5
● 1.7 (5.7 - 6.3)
✱ 2.9 (4.6 - 5.2)
⊕ 3.7 (4.3 - 5)
+ 4 (3 - 3.5)
t_d (ns)
200
150
100
50
0
20
40
60
80
100
120
140
ϱ (J/cm^2)

Fig. 14

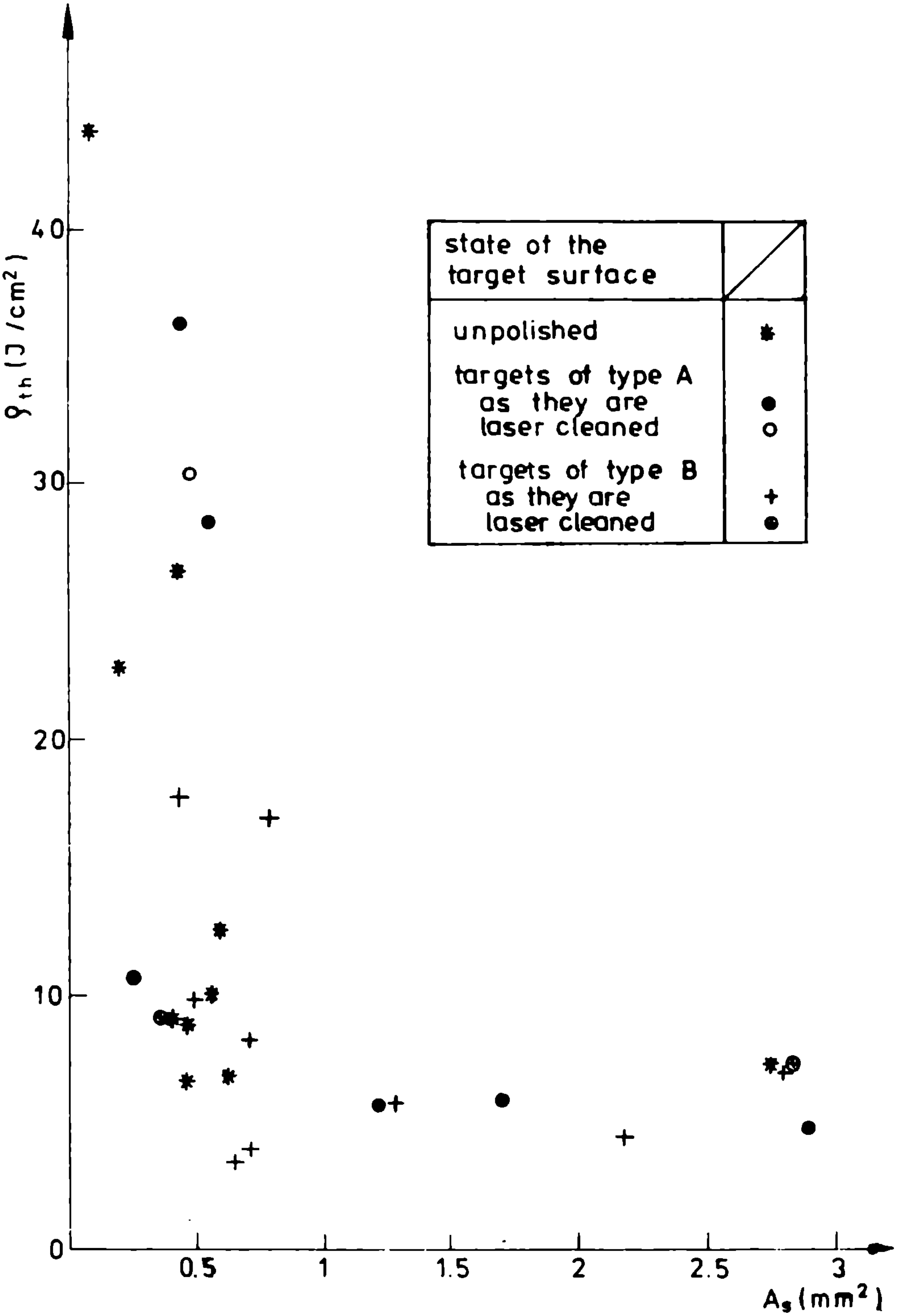

ρ_{th} (J/cm^2)
40
30
20
10
0
0.5
1
1.5
2
2.5
3
A_s (mm^2)
state of the target surface
unpolished ✱
targets of type A
as they are ●
laser cleaned ○
targets of type B
as they are +
laser cleaned ⊙

Fig. 15

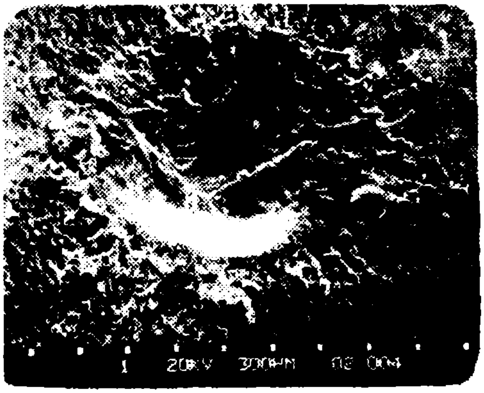

Fig. 16

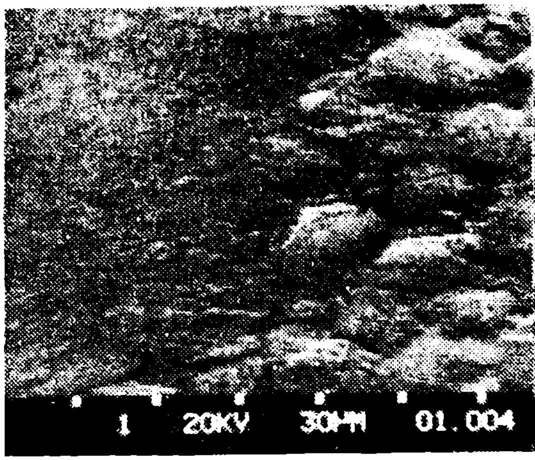

Fig. 17

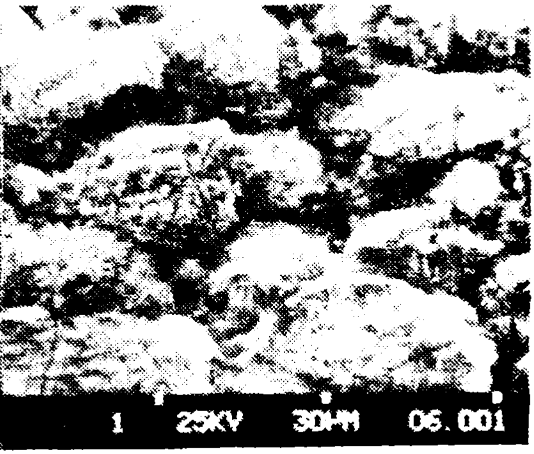

Fig. 18

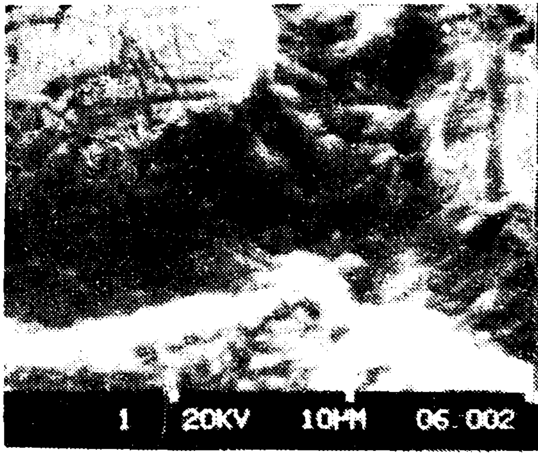

Fig. 19

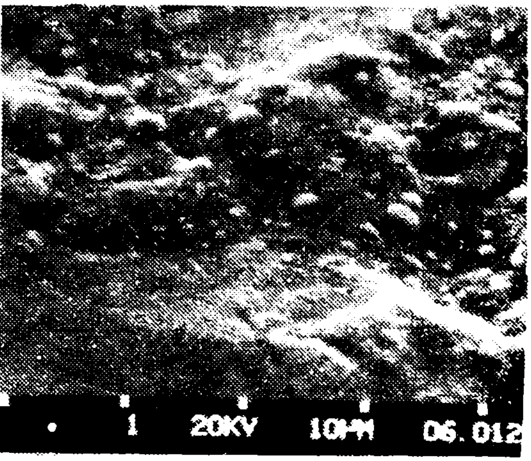

Fig. 20

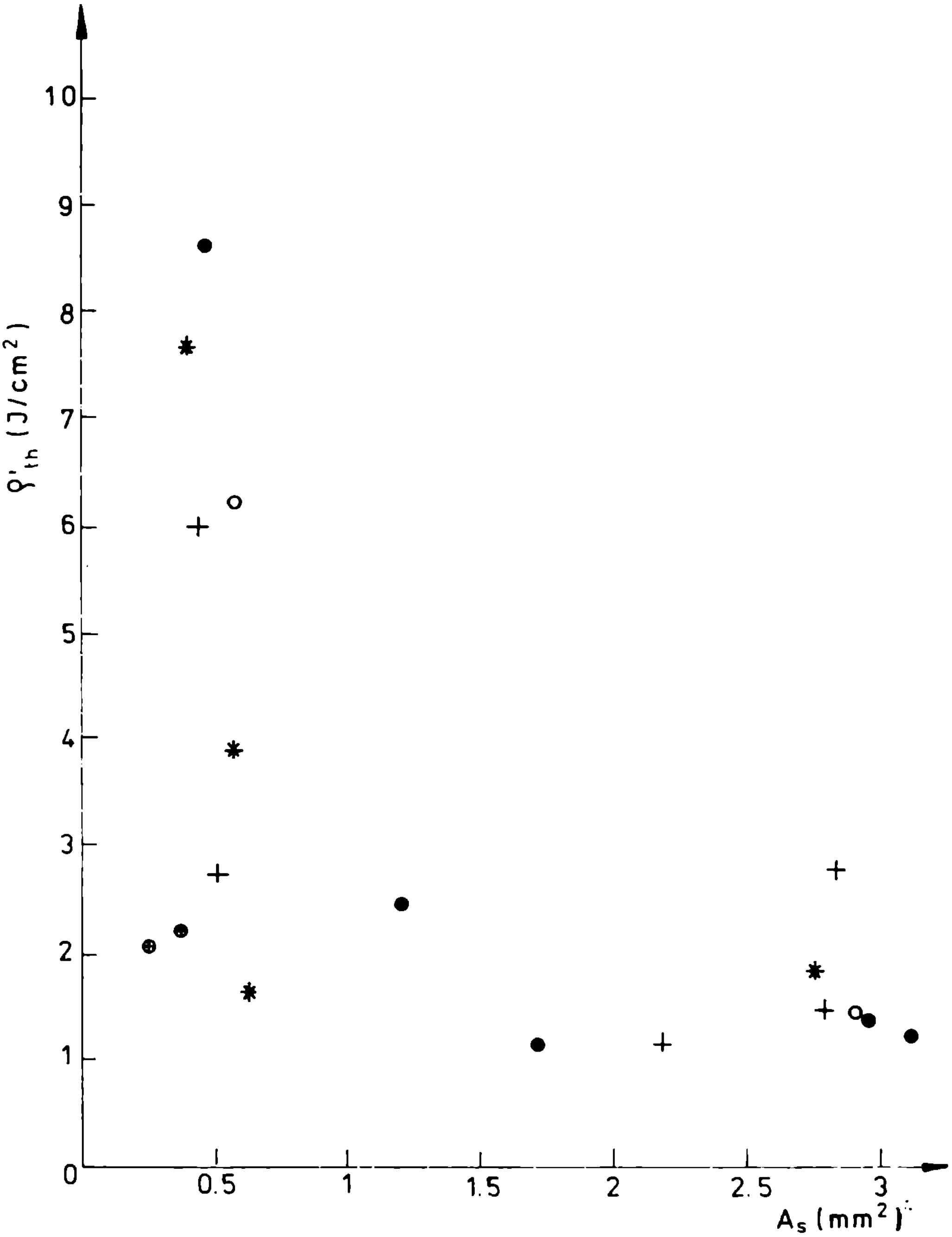

Fig. 21

RECENT ADVANCES IN THE STUDY OF THE Nd: GLASS LASER WITH PLASMA MIRROR

V. Draganescu, M. Isbasescu, E. Udrea, I. Ursu, V.G. Velculescu
Central Institute of Physics, Bucharest, Romania
V.F. Fedorov, I.V. Fomenkov, A.N. Malkov, A.M. Prokhorov, V.A. Spiridonov
Institute of General Physics, Academy of Sciences, Moscow, URSS

A Nd:glass laser with plasma mirror generates smooth output or single/multiple giant pulses, strongly depending on the pumping level. The smooth generation can be explained by taking into account the experimental values of the reflection and absorption of the plasma in front of the target.. A sudden heating of the plasma is followed by an increase of the reflection which gives rise to the giant pulse. A numerical simulation of this model is in agreement with the experimental data.

1. Introduction

As it is well known, the plasma mirror laser (PML) is able to generate very short, powerful laser pulses and a hot, dense plasma near the target surface. Many papers /1-10/ have reported investigations on this laser, both with superradiant and with unstable oscillator triggering. The understanding of the dynamics of the laser-plasma system is in a continuous development.

The PML with oscillator-amplifier configuration requires lower energy pumping and yields more powerful pulses than the superradiantly triggered PML. We shall further refer to this type of PML, although the physical mechanism seems to be the same in the both cases.

Three distinct types of temporal emission of this laser were observed, depending mainly on the pumping of the oscillator. For low pumping, the laser yiels typical spikes, which change insignificantly if one removes the target. At a well defined value of the pumping - the threshold of the PML - one obtains a quasi-continuous generation (smooth profile of the temporal emission). At this point, normal spikes are generated again if the target is removed. A little increase of the pumping, over PML - threshold, causes simultaneously Q-switched and mode - locked pulses, due to the strong nonlinearity of the resonator plasma.

In the following, we shall present the temporal behaviour of the emission of a Nd:glass laser with plasma mirror and propose a model for the smooth profile and the giant pulse mode of this laser. Section 2 presents the experimental set-up and the main experimental data of our PML. Section 3 offers an explanation of the smooth profile and giant pulse regime based on the analysis of the rate equations.

2. Laser system and experimental results

A typical experimental set-up /7,8/ is shown in Fig.1. The rods have a 4.5 cm diameter and 68 cm length, with faces cut at 5° angle. A Cassegrain telescope with magnification close to 2 is used as unstable confocal resonator. The dielectric mirrors, with reflectivities over 99% and curvature radii of 478 cm and 254 cm are separated by 112 cm. The diameter of the convex mirror is half of the rod diameter. Each rod is water cooled and pumped by four flashlamps in a quasi-elliptical stainless steel cavity. The lamps are simultaneously triggered by a high voltage pulse applied on the cavities. The laser beam is focused on a graphite target in air by means of a 52 cm focal length lens.

The known types of PML temporal emission, depending mainly on the pumping of the oscillator, were observed. The pumping of each amplifier is about 34 kJ and corresponding free running gain is close to 4.

Normal relaxation spikes are generated for low pumping of the oscillator. The laser threshold of the telescope oscillator is = 16 kJ. The spike emission lasts about 0.6 ms of the 1.5 ms long flashlamp pulse and starts about 0.6 ms after the lamp triggering. The spikes change insignificantly if one removes the target. Typical overall energy is 120 J for 18 kJ, 34 kJ and 34 kJ pumping of the oscillator and respectively the two amplifiers.

Near the 21 kJ pump level of the oscillator, the emission becomes smooth. Like the previous spikes, the smooth emission lasts 0.6 ms and starts 0.6 ms after trigger. It disappears if the target is removed or if it is moved out of focus by more than ± 1 cm. The overall energy output is typically 140 J. According to the above definition, the pumping required by the smooth generation is the PML threshold.

Giant pulses are generated over the PML threshold. They overtop the smooth profile and contain a significant part of the output energy. For example, at = 23 KJ oscillator pumping, a single giant pulse is observed, with an energy of 40 J, while the total output is 150 J. Multiple giant pulses are generated at higher pumping, e.g. 4 pulses, 360 J total energy, at 24 kJ pumping level of the oscillator.

The fast photodiode shows mode locking structure of the giant pulses, consisting of 1-3 trains of about 10 ultrashort pulses with the repetition rate of 10 ns and the interval between trains of about 100 ns. The mode-locking of this PML will be treated elsewhere.

3. Model of the smooth and giant pulse generation

As we have seen, at a certain pump level - the PML threshold - the spike emission turns into smooth generation and, above this level, giant pulses raise from the quasicontinuous profile. To explain this process, we must correlate the evolution of the plasma absorption and reflection, with the laser dynamics /2, 9/. The strong plasma - laser coupling determines the operation mode of the laser i.e., smooth generation, giant pulse and mode locking /10/. Except the mode locking, the working regimes of the PML may be derived from the appropriate rate equations.

The rate equations system of the 4-level Nd:glass laser is written as follows:

$$\frac{dq}{dt} = \xi(N_3-N_2)q - \eta q \tag{1}$$

$$\frac{dN_2}{dt} = \xi(N_3-N_2)q - \frac{N_2}{\tau_2} \tag{2}$$

$$\frac{dN_3}{dt} = W(t) - \xi(N_3-N_2)q - \frac{N_3}{\tau_3} \tag{3}$$

with

$$\xi = \frac{\sigma\ell}{\tau_p} \quad ; \quad \eta = -\frac{1}{\tau_p}\ln\left[R_1R_2(1-A)\right] = \frac{1}{\tau_c} \tag{4}$$

where

q - is the photon density, N_2, N_3 - are the population densities and τ_2,τ_3 - the lifetimes of the lower and upper laser levels, respectively; W(t) is the pumping rate due to the flashlamp; σ is the effective cross-section of the stimulated emission in the Nd:glassrod; ℓ is the length of the active medium; $\tau_p = 2L/c$; L is the optical length of the PML resonator; c is the speed of light in vacuum; τ_c is the decay time of the photons in the resonator; R_1, R_2 are the reflectivities of the mirrors and A is the overall absorption in front of the target. $N_{2,3}$ and q are given for a volume unit and, in order to obtain the laser output, q must be multiplied by the volume of the active medium.

For a more correct modelling of the PML, we should write, besides the equations (1-4), a system of hydrodynamic equations describing the evolution of the plasma and an expression for the radiation absorption in this plasma. The elaboration of these partial differential equations becomes a very difficult task due to the presence of air and to the long evaluation time of the plasma.

However, we shall try to obtain the main features of the PML, starting from some well known physical considerations, correlated with the available experimental data. Firstly, we may consider that the energy measured before the starting of the PML emission corresponds to a laser beam, intense enough to produce 10^7-10^8 W/cm^2 in the lens focus. At these intensities, a plasma layer that is sufficiently reflecting is obtained, which is able to start the PML. From this moment, we do not have on oscillator followed by amplifiers any more, but the whole system acts as an oscillator between the concave dielectric mirror and the plasma mirror. On the other hand, in order to reach these power densities, a suitable initial radiation intensity together with the corresponding population inversion must be assumed. That means that the initial conditions of the equations (1-4) at the start of the PML are not $q(0) = 0$, $n_i(0) = 0$ any more, which give rise to the well known spikes but $q(0) = q^{th}$ and $n_i(0) = n_i^{th}$, where n_i is the population inversion, and all the threshold values correspond to the pumping at the start of the PML, namely W(0). The overall shape of the output shown in Fig. 2 b and c is a quasicontinuous profile, modulated by slowly damping ripples which derive from more or less blunted spikes. The actual form of the output depends on how near to q^{th} are taken the $q(0)$ values.

Secondly, we want to point out that all the information about the plasma and the absorbing layer in front of the target is contained in the reflectivity R_2 and the absorption A of the plasma. In spite of the fact that the target plasma reflectivity R_2 may be rather high, the quantity which enters into the system and which is experimentally measured is R_2 (1-A). Of course, this expression takes account of all possible absorptions: of the plasma, of the hot flare and eventually of the powder cloud ejected from the target. Experimentally it was found that, during the smooth profile generation R_2 (1-A) takes a rather constant value of about 3×10^{-4}, which gives $\eta = 7.4 \times 10^7 s^{-1}$.

Thus, by choosing initial conditions near threshold and a correct value for η, the system (1-3) gives the PML output shown in fig.2 b, c. While in b we started with the thresold conditions, in c we used $q(0) = 0.8\ q^{th}$; we see that the further the initial conditions from threshold, the more resembling to the spikes is the output profile. The other constants are: $\zeta = 2\times10^{-16} m^3 s^{-1}$; $W(0) = 5.6\times10^{26} m^{-3} s^{-1}$; $R_1 = 0.99$; $\tau = 10^{-7} s$; $\tau = 4\times10^{-4} s$; $6\times10^{-8} s$ /11/. A further smoothing of the profile could be obtained by considering an even weaker dependence of R_2 (1-A) upon q, as it was pointed out in /10/. Obviously, the absorption may be influenced by the plasma temperature, and therefore, by the incident flux, but until now such a dependence was not established experimentally.

Now, let us consider the mechanism of the generation of the giant pulses. This process leads to a new value of η, corresponding to the measured $R_2(1-A) \simeq 5\times10^{-3}$. It follows that the giant pulse generation is due just to the switching of η form $7.4\times10^7 s^{-1}$ to, say, $3.8.\times10^7 s^{-1}$, i.e. $R_2(1-A) = 2.4\times10^{-2}$. It is very likely that this sudden change of the reflectivity is due to a self focusing process in the target plasma, which may occurat a certain photon density. A rough calculation shows that the population inversion in the Q-switch regime is about 1.25 times grater than that in the smooth profile. It gives a pulse of about 400 ns width and 50 J energy, which is in good agreement with the experimental data. Fig. 2d shows the output found by integrating the system (1-3) and supposing that the switching of η occurs when the photon density reaches $q_g \sim 10^{19}$ In our case, this means a reasonable value of 10^{12} - $10^{13} W/cm^2$ in the focus, when self-focusing is expected. The integrated energy is shown in Fig. 2e, in good agreement with the experimental data /12/. For higher pumping, the $q_g$level may be reached many times, each time accompanied by a switch of η, and this explain the observed train of giant pulses.

4. Concluding remarks

Summarising, we emphasize the progress in the understanding of the plasma mirror laser.

The above presented Nd:glass PML is in many aspects similar to the previous ones /1-3/. It switches from smooth generation to giant pulse mode by increasing the pumping.

The model assigns the smooth profile to the change of the quality factor of the resonator with suitable chosen initial conditions. The quality factor contains all the informations on the plasma, namely its reflectivity and absorption. A steep increase of the reflectivity due probably to a self-focusing process of the laser radiation, leads to giant pulse formation.

An exact analysis would require more detailed calculations concerning the processes during the irradiation of the target, based upon careful diagnostic of the plasma. For the moment, a satisfactory fitting of the theory with the experimental data was obtained in the frame of a rather simple physical model.

References

/1/ V.A.Batanov, K.S.Gotcholashvily, B.V.Ershov, A.N.Malkov, P.O.Kolesnitchenko, A.M.Prokhorov, V.B.Fedorov, Pis'ma v JETF 19, 411 (1974).

/2/ V.A.Batanov, D.A.Dementiev, A.N.Malkov, A.M.Prokhorov, V.B.Fedorov, JETF 77, 2186 (1979).

/3/ A.N.Malkov, A.M.Prokhorov, V.B.Fedorov, V.I.Fomenkov, Pis'ma v JETF 33, 630 (1971).

/4/ S.I.Anisimov, V.A.Batanov, V.P.Gorkovsky, I.N.Djukov, V.P.Kopilov, JETF 83, 1747 (1982).

/5/ P.Hribek, V.Kubecek, M.Vrbova, Appl.Phys., B29, 177 (1982).

/6/ Idem, Kvant.electr. 10, 2341 (1983).

/7/ A.Agafitei, D.Apostol, G.Bajeu, V.Draganescu, A.Farcas, C.Fenic, M.Isbasescu, R.Medianu, A.Stratan, Rev.Roum.Phys. 27, 365 (1982).

/8/ V.Draganescu, A.Agafitei, D.Apostol, G.Bajeu, A.Farcas, C.Fenic, N.Heresanu, M.Isbasescu, R.Medianu, A.Stratan, Rev.Roum.Phys. 27, 629 (1982).

/9/ V.Draganescu, M.Isbasescu, E.Udrea, V.G.Velculescu, Rev.Roum.Phys. 26, 573 (1981).

/10/ M.Isbasescu, E.Udrea, V.G.Velculescu, "Laser and Applications" (Proceedings of the Int.Conf. and School, Bucharest, Part 2, 597 (1982).

/11/ M.Isbasescu, V.G.Velculescu, Optoelectronics, 6,483 (1974).

/12/ V.Draganescu, M.Isbasescu, E.Udrea, I.Ursu, V.G.Velculescu, V.B.Fedorov, I.V.Fomenkov, A.N.Malkov, A.M.Prokhorov, V.A.Spiridonov, presented at the National Conf. "Progress in Physics", Sibiu, oct. 1984.

FIGURE-CAPTIONS

Fig. 1 Schematic diagram of the experimental set-up LR- laser rods; M - dielectric mirrors; S - beam splitters; L - lenses; T - target; P - photodiode; O - oscilloscope; C - calorimeter.

Fig. 2 Typical time-evolution of the pumping and of the calculated functions: a - pumping function W; b,c - smooth profile (b starts at the threshold, c takes $q(o) = 0.8\ q^{th}$; P is the output power; d - single giant pulse; e - integral of the output power of fig. 2d (E is the output energy, reversed for the sake of comparison with experimental data /12/).

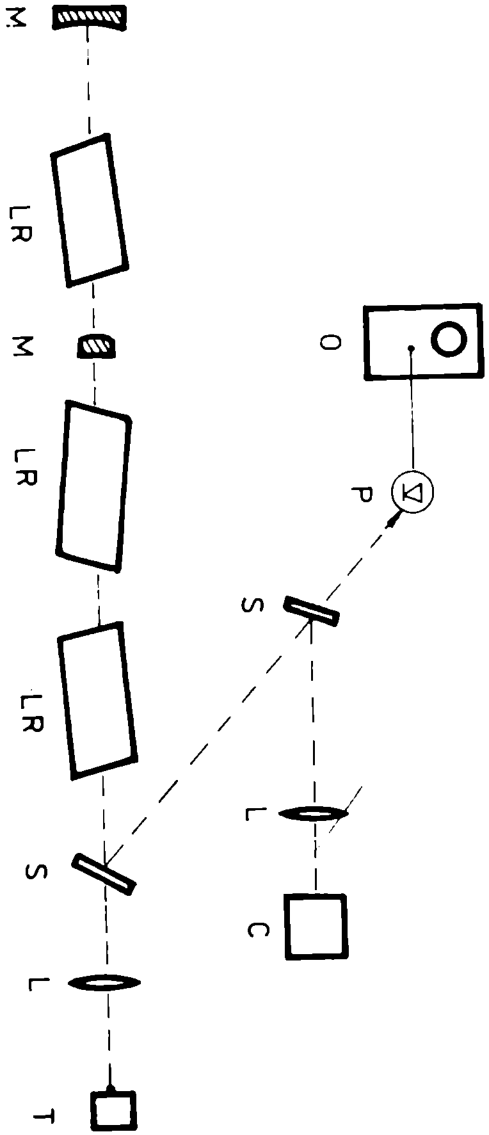

Fig.1

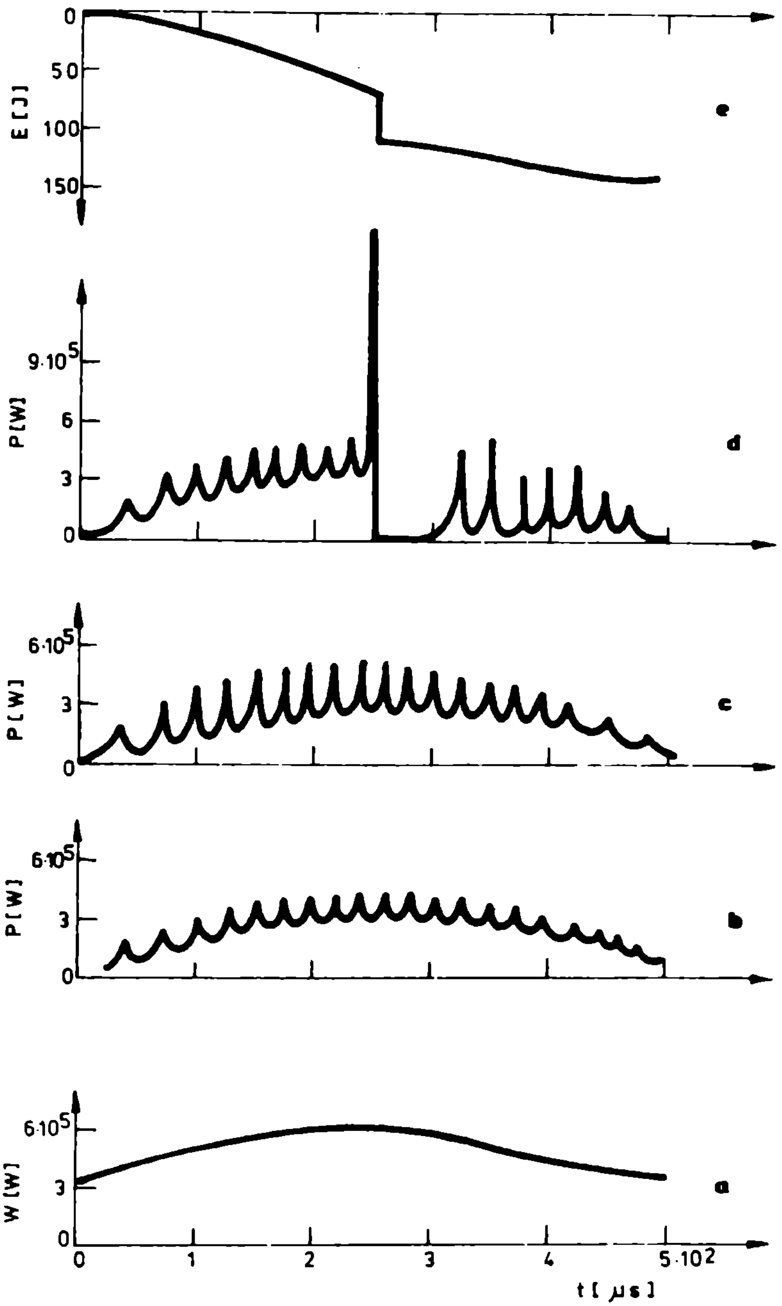
0
50
100
150
E [J]
e
9·10⁵
6
3
0
P [W]
d
6·10⁵
3
0
P [W]
c
6·10⁵
3
0
P [W]
b
6·10⁵
3
0
W [W]
a
0
1
2
3
4
5·10²
t [µs]

Fig. 2

TEMPERATURE DETERMINATION IN CW CO_2 LASER HEATED MOLECULAR GASES

I.Ursu, R.Alexandrescu, C.Grigoriu, I.N.Mihailescu, I.Morjan
Central Institute of Physics, ROMANIA

A.M.Prokhorov, F.V.Bunkin, B.S.Luk'yanchuk, E.A.Morozova. G.A.Shaf
Institute of General Physics, Moscow, U.S.S.R.

Temperature determinations of gas mixtures as heated by a CW CO_2 laser radiation were performed inside the action zone of laser radiation. The method is based on information derived from the radiation spectra of gas mixtures, and also allows for the determination of some thermophysical parameters of the molecular gases.

Introduction

We investigated thermal radiation spectra of molecular gases for which the light radiated on different lines is in a thermodynamic equilibrium with the substance /1/. When laser heating the gaseous mixture up to temperatures of ~ 1000 K, the recorded spectrum appears as a superposition of the thermal radiation spectrum and the luminescence spectrum of the gas. The radiation spectrum appears as a system of narrow lines, whose envelope is determined by a Plank function of the temperature T.

We further present experimentally recorded radiation spectra proceeding from the SF_6 mixtures with molecular gases (e.g. ammonia, xenon, helium, air), under the action of a CW CO_2 laser radiation. It is known that SF_6 presents strong absorption bond in the generation range of the CO_2 laser. The buffer gas pressure increase for a constant SF_6 pressure results in an increase in the sample heat capacity, while the total absorbed laser energy keeps constant. Thus, by selecting the buffer gas properly one can modify the temperature within the laser heated zone by changing the pressure of the buffer gas.

Experimental

Thermal radiation emitted spectra were studied by heating a molecular gas with a CW laser source stabilized on the P(16) ($\lambda = 948\ cm^{-1}$) line. The incident power was varied in the (11 - 25) W range and the beam diameter was (5 - 7) mm. The laser radiation was focussed (with the aid of a NaCl lens, ≈ 40 cm focal length) inside a cross-shaped gas cell, containing the gas mixture. The input window was made of ZnSe, while the output and the two lateral windows were made of KBr. The internal diameter of the cell was of 25 mm, the distance between the input and the output windows was of 60 mm; the lateral windows were at 30 mm from the input window and at 50 mm from each other. The radiation emitted at 90° relatively to the incident laser beam by the gas in the center of the cell was recorded with a IKS-29 spectrophotometer. Spectra for both pure SF_6 and SF_6 mixtures with air, ammonia, helium and xenon were recorded /2/.

In order to estimate the rising time τ_0 of the thermal radiation until a stationary state is reached, the radiation collected through a lateral window of the cell was focused onto a nitrogen cooled GeAu detector and the amplified signal was visualised on an oscilloscope.

Results

The recorded radiation spectra in the (400 - 1400) cm^{-1} range are shown in Fig. 1.

One notices that the radiation spectra of the gas mixture consist of three components corresponding to the three strong absorption lines of the SF_6 molecule (the ν_3 (= 947 cm^{-1}), ν (≈ 605 cm^{-1}) and $\nu_2 + \nu_4$ (≈ 1280 cm^{-1}) transitions, respectively).

The intensity distribution in the radiation spectrum is modified when changing the gas contents (i.e. the partial pressures of SF_6 and buffer gas). In Figs. 2, 3 we have thus shown the SF_6 pressure dependence of the $I(\nu_4)/I(\nu_3)$ and $I(\nu_2 + \nu_4)/I(\nu_3)$ ratios, for a given pressure of a certain buffer gas (ammonia, helium, xenon) and a fixed level of the incident laser power (∿ 20 W). Here $I(\nu_3)$, $I(\nu_4)$, $I(\nu_2 + \nu_4)$ stand for the intensity radiated on the maximum of the respective transitions.

On the other hand, with the SF_6 pressure increase, the laser radiation absorption and, correspondingly, the gas mixture temperature also increase. The maximum of the emitted intensity arround the ν_3 transition is then shifted to "red". It was shown that absorption maximum of the ν_3 transition is shifted by 13 to 37 cm^{-1} relatively to the radiation maximum, corresponding to pressures of SF_6 from 1 to 50 torr. The maximum value of the radiation intensity is therefore not influenced by the absorption on the ν_3 transition (see Fig. 1). In the case of the ν_4 transition, the maxima of the radiation and absorption lines coincide for low pressures of SF_6 ($\lesssim$ 20 torr) and so this transition is strongly self-absorbed. However, when increasing the SF_6 pressure up to 50 torr, the shape of the absorption profile is shifted by ∿ 10 cm^{-1}, but if the buffer gass pressure increases, the absorption profile shift is significant only for lower pressures of SF_6 .

Analysis

The radiation intensity for a gas mixture uniformly heated may be expressed as /3/

$$I = I_p(1-e^{-\chi' l}) \qquad (1)$$

where $\chi' = \chi(1 - e^{-h\nu/kT})$ stands for the absorption index of the gas mixture when the stimulated emission is taken into account. I_p is the spectral intensity of the Plank equilibrium radiation /3/, l the thickness of the layer heated to a temperature T and h, k the Plank and Boltzmann constants respectively. So, the radiation intensity of the thermal radiation at a given frequency incident onto a photodetector is given by

$$I(\nu) = \frac{2h\nu^3}{c^2}\left[1 - e^{\chi(1-e^{-\frac{h\nu}{kT}})\ell}\right](e^{\frac{h\nu}{kT}} - 1)^{-1} \tag{2}$$

The temperature evolution of $\chi(T)$ for the laser wavelength-tuned on the P(16) line can be obtained from /4/ as

$$\chi(T) = \beta T^{-1} \tag{3}$$

where β = const.

Knowing that at a constant volume, the pressure dependence on temperature is /3/

$$p(T) = AT^2$$

one gets

$$\chi(T) \sim 1/\sqrt{p} \tag{5}$$

By an appropriate normation of the pressure from (2), (5) we obtain

$$I(\nu) \sim (e^{\frac{1}{\sqrt{p}}} - 1)^{-1}\cdot\left[1 - e^{-\frac{\beta}{\sqrt{p}}(1-e^{-\frac{1}{\sqrt{p}}})\ell}\right] \tag{6}$$

and, for $\chi(T) \approx$ const.

$$I(\nu) \sim (e^{\frac{1}{\sqrt{p}}} - 1)^{-1}\left[1 - e^{-\gamma(1-e^{-\frac{1}{\sqrt{p}}})\ell}\right] \tag{7}$$

where $\gamma \approx$ const.

Using data for the temperature dependence of the radiation maximum in the case of the ν_3 transition which were derived in /5/, and knowing the evolution of the maximum when increasing the SF_6 pressure, the dependence of the gas mixture temperature on the SF_6 pressure was found in a very good concordance with the predictions of eq. 4 /2/.

The computed value of $1/I(\nu_3)$ (eq.6), in which $\nu = \nu_3$, $\beta \simeq 1$, $l \simeq 1$) gave the curve 4 in Fig. 2. In Fig. 3 we have shown (curve 4) the computed evolution of the ratio between the intensity radiated on the $\nu_2 + \nu_4$ and ν_3 lines respectively (with $\beta \approx 1$, $\gamma = 1$, $l \simeq 1$ and $\chi(T) \approx$ const. for the transition $\nu_2 + \nu_4$ which has a small absorption of the corresponding frequency).

Figs. 2, 3 illustrate that the approximations given by the eqs. (6), (7) are in good agreement with the experimental investigations.

A direct experimental information which avoids the difficulties related to the nonlinear equation of thermal conduction in gas mixtures with significant thermodiffusive effects, is the rising time of the thermal radiation until a stationary state is reached. The establishing temperature time may be written for two cases /6/: either by a thermal conduction process along the cell radius, when

$$\tau_0 \sim \frac{R^2}{a} \tag{8}$$

or via the convective heat exchange through the cell walls, when

$$\tau_0 = \frac{1}{2}\,\frac{R\rho c}{\mu} \tag{9}$$

Here, a stands for the temperature conduction coefficient, R is the cell radius, ρ , c are the gas density and specific heat, respectively, and μ stands for the constant of convective thermal exchange.

Using the temperature dependence of the temperature conduction coefficient

$$a(T) \approx a_0 + \frac{da}{dT}T \tag{10}$$

and defining τ_0 as the time for which the thermal radiation signal increase by e times, i.e. to a value of $I_{max}(1 - e^{-1})$, we obtain from (8)

$$\tau_0 = \frac{R^2}{a_0 + \frac{da}{dT}(1-e^{-1})\,T_{stat}} \tag{11}$$

The values of the establishing time of the thermal radiation τ_0, obtained for different mixtures of SF_6 with xenon, helium, air and ammonia, are given in Table 1.

Table 1

P_{SF_6} (torr)	Buffer gas	$P_{Buffer\ gas}$ (torr)	τ_0(s)	$\lambda = ac\rho$ ($W.m^{-1}.grd^{-1}$)	$a = \frac{R^2}{\tau_0}$ ($m^2.s^{-1}$)	T,K
6	Xe	70	0.06	0.196	$4.17.10^{-4}$	625
6		125	0.075	0.0188	$3.33.10^{-4}$	592
6		180	0.085	0.016	$2.94.10^{-4}$	547
6	He	45	0.26			321
10	air	0	0.04	0.0534	$6.25.10^{-4}$	1210*
10		660	0.07	0.0288	$3.57.10^{-4}$	640
10		750	0.082	0.0229	$3.05.10^{-4}$	520
6	NH_3	65	0.07	0.0443	$3.57.10^{-4}$	585

* According to /1/, the temperature value at this point is = 1275.

The columns 5, 6 contain the estimated heat conduction and temperature conduction coefficients for the gas mixtures. The temperature values listed in the column 7 were obtained with the aid of eq. (11) excepting for the SF_6 - helium mixture. For this latter case, it was shown /2/ tnat the convective thermal exchange through the lateral wall is prevailing and eq. (9) is then valid.

The experimental results reported here show that when heating mixtures of molecular gases under the action of a laser radiation, spectra of thermal radiation are emitted. Proceeding from these spectra, one can establish the temperature inside the action zone of the laser radiation as well as some parameters of the mixtures, such as heat conduction and temperature conduction coefficients. The thermal spectra also contain information on the nonequilibrium thermo-dynamical processes which develop in gaseous phase /2/ and which allow, among others, to identify the intermediate reaction products.

FIGURE CAPTIONS

Fig. 1 Intensity distribution in the spectrum of SF_6 and xenon mixture ($P_{Xe} \approx$ 70 torr)

a - $P_{SF_6} \approx$ 5 torr
b - $P_{SF_6} \approx$ 15 torr
c - $P_{SF_6} \approx$ 35 torr

Fig. 2 Dependence of the ratio between the intensities emitted on the ν_4 and ν_3 lines on the SF_6 pressure for different mixtures

1) - $P_{NH_3} \approx$ 30 torr   2) - $P_{Xe} \approx$ 70 torr
3) - $P_{He} \approx$ 80 torr   4) - theoretical estimation

Fig. 3 Dependence of the ratio between the intensities emitted on the ($\nu_2 + \nu_4$) and ν_3 lines on the SF_6 pressure for different mixtures

1) - $P_{NH_3} \approx$ 30 torr   2) - $P_{Xe} \approx$ 70 torr
3) - $P_{He} \approx$ 80 torr   4) - theoretical estimation

REFERENCES

/1/ I.Ursu, R.Alexandrescu, C.Grigoriu, I.N.Mihailescu, I.Morjan, A.M.Prokhorov, F.V.Bunkin, B.S.Luk'yanchuk, E.A.Morozova, G.A.Shefeev, Proceedings of the 3rd International Conference on Infrared Physics, Edit. F.K.Kneubühl, Zürich, July, 1984

/2/ R.Alexandrescu, F.V.Bunkin, B.S.Luk'yanchuk, I.N.Mihailescu, E.A.Morozova, G.A.Shafeev, Preprint IOFAN No. 223 Moscow, 1984

/3/ Ya.B.Zeldovich, Yu.P.Raizer, "Physics of Shock Waves and High Temperature Hydrodynamical Processes", Nauka, Moscow, 1966

/4/ F.Bochmenn, Max-Plank Institut für Quantum Optik, MPQ-57, Dec. 1981

/5/ A.V.Novak, J.L.Lyman, J.Quant.Spectr.Radiat.Transfer, 15, 945 (1975)

/6/ N.A.Kirichenko, A.G.Korepanov, B.S.Luk'yanchuk, Preprint FIAN No.23, Moscow, 1981

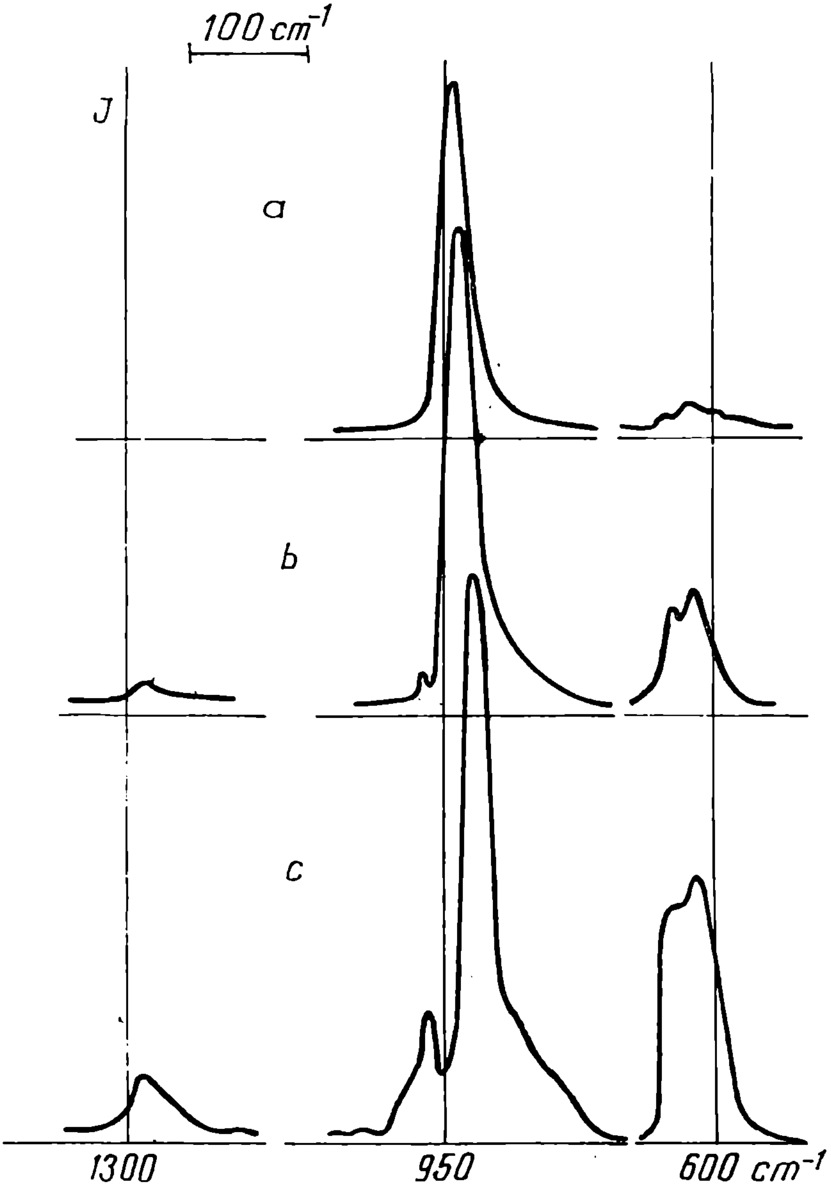

Fig. 1

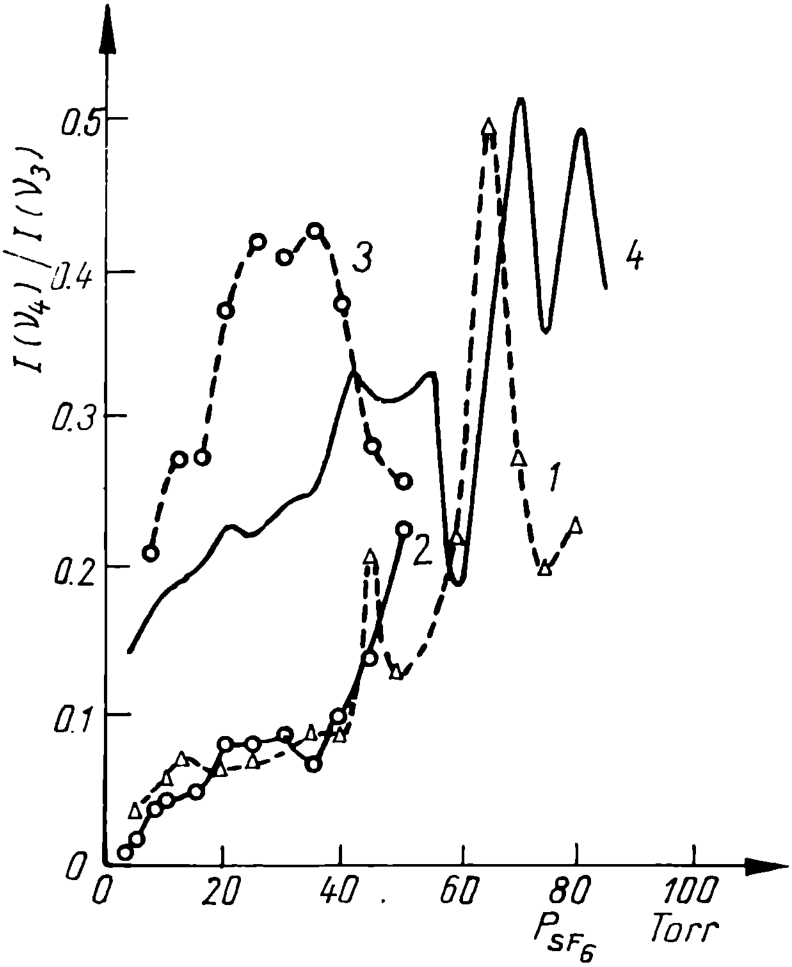

Fig. 2

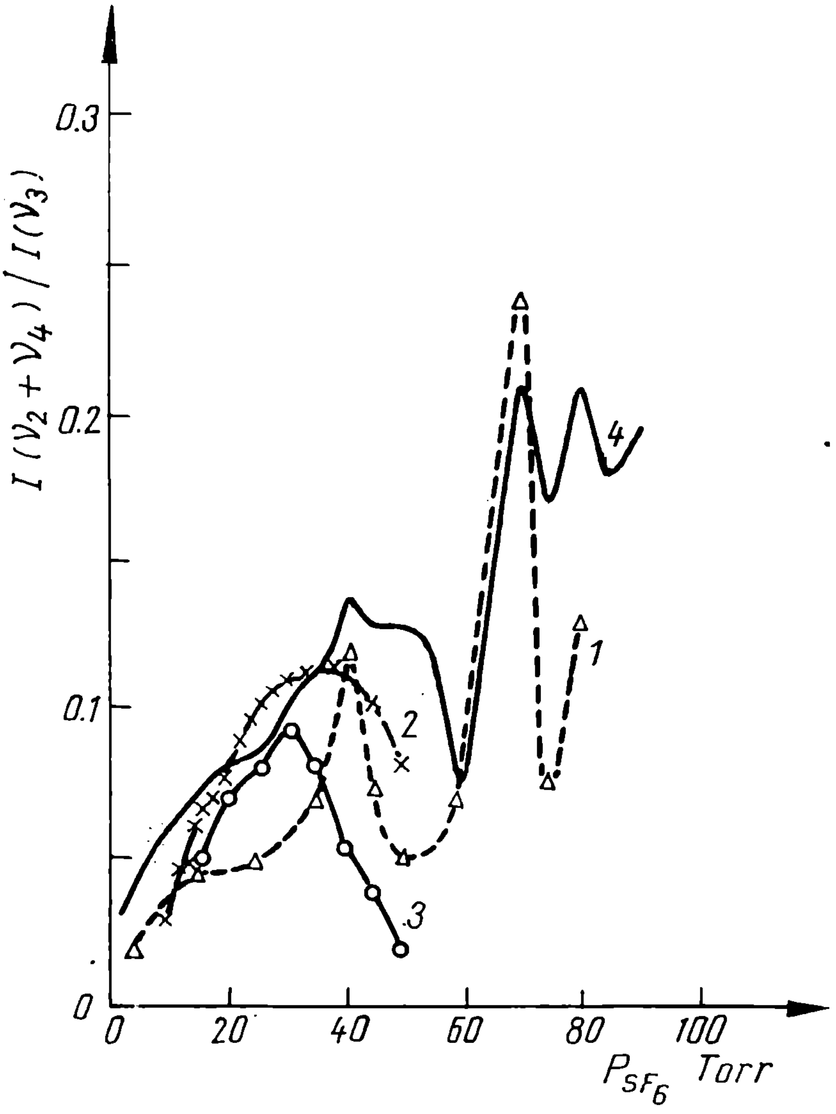

Fig. 3

COLOR CENTER PASSIVE Q-SWITCHING OF YAG:Nd LASERS

I.Ursu, A.Lupei, V.Lupei, C.Stoicescu, F.Domsa, V.I.Manzatu, S.Georgescu
Central Institute of Physics, Bucharest

1. Introduction

Giant pulse laser emission with a high repetition rate is of great practical interest. Electrooptical Q-switches could solve the problem, but their use is sometimes inconvenient due to their complexity and fairly high price. The most simple and cheap are passive Q-switches using saturable absorption of some organic dyes. However, in this case the obtained peak powers are rather small, present high instabilities and large losses.

In the last years a new type of passive Q-switch based on saturable absorption in crystals with color centers become the subject of increased interest. The most suitable system for neodymium lasers is a LiF crystal with F_2^- color centers /1-5/. These centers present at room temperature a saturable absorption band, peaked at about ~ 960 nm, with a linewidth of ~ 1.62 x 10^3 cm^{-1}, thus the 1.06 μ emission of neodymium lasers falls inside this band. The good thermal properties of LiF lead to the possibility of using these Q-switches in high repetition regime.

Using such a Q-switch larger single pulse energies than with dye-absorbers can be obtained. However, they have the same disadvantage, multiple pulse lasing at high pumping. A method to overcome this difficulty has been proposed by us /6/ by using a combined system consisting of a mechanical and color center LiF:F_2^- Q-switch.

Two directions have been followed in our research: a technological approach to improve the LiF:F_2^- Q-switch qualities (F_2^- centers concentration, losses, thermal stability, damage threshold etc.) and an experimental and theoretical study of the generation characteristics of a YAG:Nd laser using such Q-switches. Results connected to both directions of investigation shall be briefly presented.

2. Results and discussion

Lithium fluoride single crystals have been grown by Czochralski method using resistance or induction heating. Growth has been done in vacuum or different atmospheres. Attention has been paid to optical quality of the crystals. Proper heat treatments have been found to improve optical characteristics of the crystals. Optical testing including scattering, stresses birefringence, interference fringes etc. has been done with the KP-74 complex.
F_2^- centers have been obtained by irradiation with a Co^{60} source.

Studies to find technological conditions to increase F_2^- centers concentration in LiF at a lower level of losses include dependences on: γ - irradiation conditions, raw material and growth conditions. Absorption coefficients are determined at room temperature by using a Cary 17 spectrometer. Values up to 0.4 cm^{-1} at 1.06 μ have been obtained.

Data about residual absorption (losses) in Q-switch have been obtained from the transmission through it of a YAG:Nd laser. An experimental set-up consisting of a YAG:Nd laser (Spectra Physics) with a pulse width of 10 nsec and output energy that can be continuously varied, a powermeter and some simple optics have been used. At large energies, a linear dependence between the energy transmitted through $LiF:F_2^-$ absorber and incident energy is obtained. Residual absorption coefficient is estimated from the slope of this curve. Values between 0.04 and 0.09 cm^{-1}, function of technological conditions, have been determined.

Laser characteristics of such a Q-switch have been tested in several configurations using different YAG:Nd rods grown and processed in our laboratory. Experimental set-up consists of a plane-plane configuration resonator with a cilindrical reflector and a Xenon flash lamp. Repetition rate of the pumping source is up to 10 Hz.

Emission characteristics can be characterized by a diagram as in Fig. 1 where output energy function of pumping is presented. A 5x70 mm YAG:Nd rod, a Q-switch with initial transmission of 30%, output mirror with R = 8 % have been used. Free generation emission (o) passive $LiF:F_2^-$ Q-switching (△) and combined system mechanical and $LiF:F_2^-$ Q-switch (●) are presented. The multiple pulsing in the case of using $LiF:F_2^-$ alone is observed. Pulse width is less than 10 nsec. By the combined system multiple pulsing is overcome, pulse width is shorter (larger peak powers) and an increase of the single pulse energy with pumping is obtained.

A theoretical analysis to find the proper conditions for a given laser configuration has been done by solving rate equations, including those connected to passive Q-switch. Dependences on: Q-switch characteristics (initial and final transmission), output mirror reflectivity, pumping pulse width, laser rod characteristics, etc., have been numerically obtained. It has been found that output power is essentially determined by Q-switch characteristics and laser rod cross section. A rather monotonous dependence on extraction mirror reflectivity (R) is obtained. In Fig.2 the output energy (single pulse) by using three different Q-switches as function of R is presented. Low reflectivities are favourable for larger extraction energies, at a higher threshold.

The theoretical analysis shows that the observed strong dependence of the output on the particular laser rods used in our experiment could be explained solely by the differences in laser rods and we have to admit variations in stimulated emission cross-section and efficiency. Such variations in YAG:Nd laser rods with the same nominal concentration of neodymium have been recently connected with the existence of several non-equivalent positions of Nd^{3+}, and this was, in turn explained as an effect of impurities or defects /7/. A systematic study of these effects by laser spectroscopy with an attempt to connect the properties of the rods with the conditions of the crystal growth is in progress.

REFERENCES

/1/ Yu.L.Gusef, S.I.Marennikov, S.Yu.Novajlov, Kv.Electr. 5, 1685 (1978)

/2/ A.A.Tarasov, Kv.Electr., 9, 1727 (1982)

/3/ T.T.Basiev, I.Yu.Itskhaki, B.G.Lysoi, S.V.Mirov, O.B.Cherednichenko, Kv.Electr. 10, 619 (1983)

/4/ A.Lupei, V.Lupei, V.I.Manzatu, S.Georgescu, F.Domsa, Rev.Roum.Phys., 28, 529 (1983)

/5/ V.P.Chebotayev, S.I.Marenniko, V.A.Smirnov, Appl.Phys. B.31, 193 (1983)

/6/ V.Lupei, A.Lupei, V.Ionita Manzatu, S.Georgescu, F.Domsa, Opt.Comm., 48, 3, 203 (1983)

/7/ D.P.Devor, L.G. De Shazer, Opt.Comm., vol.46, 2, 97 (1983)

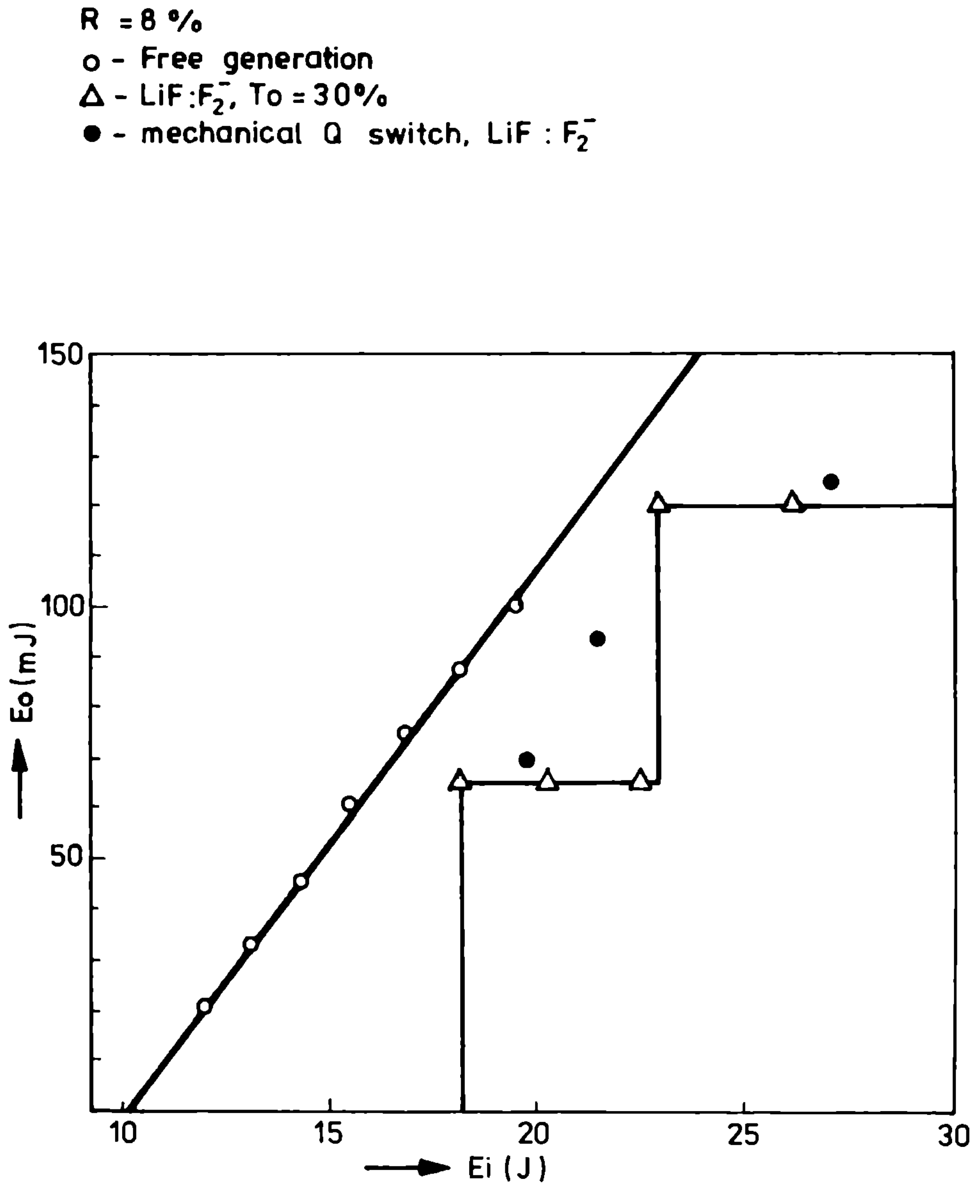
R = 8 %
o - Free generation
Δ - LiF:F_2^-, To = 30%
● - mechanical Q switch, LiF : F_2^-
150
100
50
Eo (mJ)
10
15
20
25
30
Ei (J)

Fig.1.

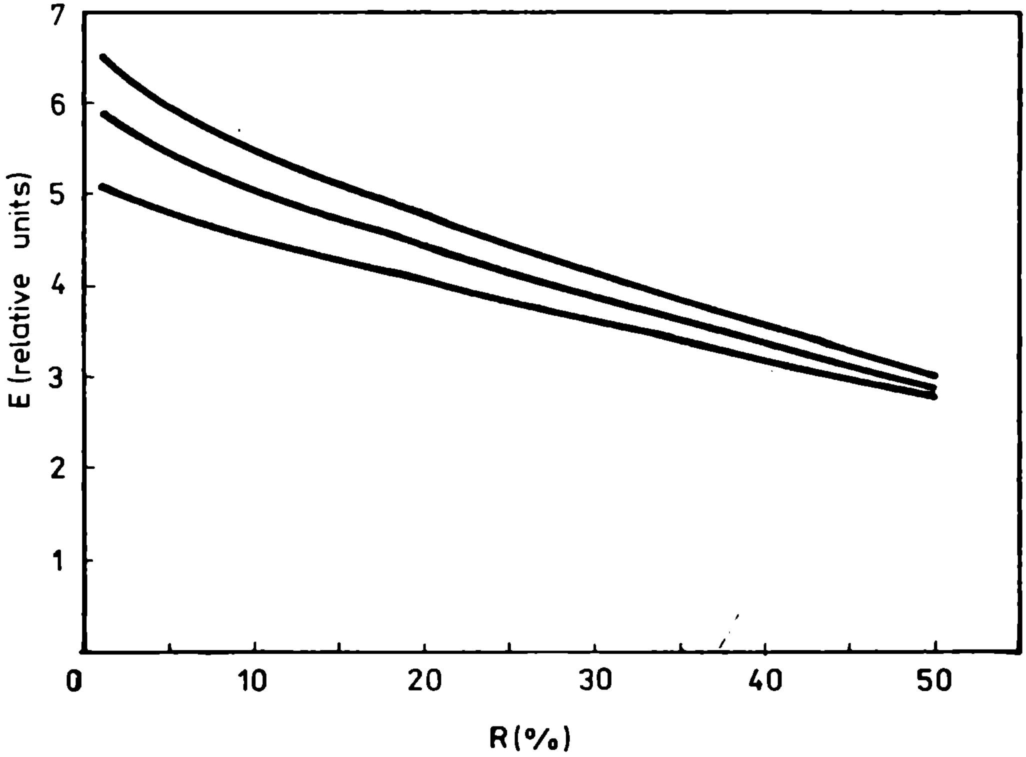

Fig.2.

ANALYSIS OF GRATING RESONATORS BY MEANS OF MATRIX TECHNIQUES

A.Belea, I.Iovitz Popescu
Faculty of Physics, University of Bucharest, P.O.Box 5211

This paper introduces an optical transfer matrix for the arrangement known as Littrow mounting of a diffraction grating. The results thus obtained are applied to the analysis of the usual grating resonator used for pulsed dye lasers. Several new designs (of stable and astable type) are also investigated.

I. Introduction

A classical design of the pulsed dye laser resonator is based upon the use of a diffraction grating in Littrow mounting. Although frequently employed, this configuration lacks a comprehensive investigation in terms of optical resonators' theory so that usually, its design parameters are chosen in a somewhat arbitrary manner. This state of the art is in some sort a consequence of the fact that the properties of a diffraction grating are not suitable for an integral equation approach, while the alternate, optical transfer matrix tehnique may not account for pure diffractive phenomena.

However, in practice, apart from the spectral discrimination, the actual behaviour of a diffraction grating in Littrow mounting resembles that of a conventional optical system. In fact, we shall show that this similarity is not merely conjectural but can be supported by means of a simple optical transfer matrix. This result provides us with the necessary preliminaries for a standard analysis of grating resonators.

II. The optical transfer matrix for a Littrow mounting of a diffraction grating

Let us consider the configuration shown in fig.1, where Π_1 and Π_2 represent respectively the imput and output reference planes, while Π_G specify the plane of the grating. The same figure also indicates the choise of various coordinate systems and the meaning of different symbols apperating in the subsequent equations.

A successive use of Kirchhoff's diffration integral emphasizes the correlation between the optical fields in Π_1 and Π_2 with due consideration of fields in Π_R. Thus we find

$$u_{\pi_2}(x_3,y_3) = \frac{\exp[ik(L+L')]}{(2i\lambda)^2 L\cdot L'} \iint \chi(y_2)\, u(x_1,y_1)\,[1+\cos(\vec{n},\vec{r}_{12})]\,[1+\cos(-\vec{n}_2,\vec{r}_{23})]\exp ik\Delta \, dx_1\,dy_1\,dx_2\,dy_2 \tag{1}$$

where

$$\Delta \quad \frac{x_1^2+y_1^2}{2L} + \frac{x_3^2+y_3^2}{2L'} + \left(\frac{1}{2L} + \frac{1}{2L'}\right)(x_2^2+y_2^2) - \left(\frac{x_1}{L} + \frac{x_3}{L'}\right)x_2 - \left(\frac{y_1}{L} + \frac{y_3}{L'}\right)y_2 \sin\alpha$$

$$\text{and}\quad \chi(y_2) = \begin{cases} 1 & \text{if } y_2 \text{ is the ordinate of an edge of the grating} \\ 0 & \text{otherwise} \end{cases}$$

If Littrow's condition $2a.\cos\alpha = k\lambda$ is fulfilled (where α is the angle $y_2 0_2 z_2$, fig.1) then the angular distribution of the diffrared field has a maximum value along the incidence direction, which thus represents a natural optical axis for the system. As usual, we shall assume that for all fields propagating along directions close to the optical axis the paraxial approximations are valid so that, $1+\cos(\vec{n}_1,\vec{r}_{12}) \simeq 2; 1+\cos(\vec{n}_2,\vec{r}_{23}) \simeq 2$.

The elements A, B, C, D of the optical transfer matrix /1/ can be obtained by a rearangement of (1) so as to assume the form:

$$u_{\pi_2} = \frac{\exp[ik(L+L')]}{i\lambda B} \int u_{\pi_1} \exp \frac{ik}{2B}\left[A(x_1^2+y_1^2) + D(x_3^2+y_3^2) - 2(x_1x_3+y_1y_3)\right] dx_1 dy_1 \tag{2}$$

A convenient change of variables from x_2, y_2 to u,w leads to

$$u_{\pi_2} = \frac{\exp[ik(L+L')]}{i\lambda} \cdot 4 \cdot \frac{\int_{-\infty}^{\infty} e^{iu^2} du \int_{-\infty}^{\infty} \chi(w) e^{iw^2} dw}{4\pi i(L+L')} \int u_{\pi_1} e^{ik\Delta_1} dx_1 dy_1 \tag{a}$$

where

$$\Delta_1 = \frac{x_1^2}{2(L+L')} + \frac{L+L'\cos^2\alpha}{2L(L+L')} y_1^2 + \frac{x_3^2}{2(L+L')} + \frac{L'+L\cos^2\alpha}{2L'(L+L')} y_3^2 \tag{3}$$

$$- \frac{x_1x_3}{L+L'} - \frac{\sin^2\alpha}{L+L'} y_1y_3 \tag{b}$$

A new change of variables through

$$x_1 = a\tilde{x}_1 \qquad y_1 = b\tilde{y}_1 \qquad x_3 = c\tilde{x}_3 \qquad y_3 = d\tilde{y}_3 \tag{4}$$

performs the required matching of coefficients appearing in (3.b) if

$$a^2 = b^2 \frac{L+L'\cos^2\alpha}{L} \qquad c^2 = d^2 \frac{L'+L\cos^2\alpha}{L'} \qquad \frac{ac}{L+L'} = ? = bd\frac{\sin^2\alpha}{2(L+L')} \tag{5}$$

Using these results in (3) and making a final identification with (2) we find

$$B = (L+L')\frac{c}{b^2}\sqrt{\frac{L}{L+L'\cos^2\alpha}} \qquad A = c\sqrt{\frac{L+L'\cos^2\alpha}{L}}$$

$$D = \frac{d^2}{b^2}\,\frac{L'+L\cos^2\alpha}{L'}\sqrt{\frac{L}{L+L'\cos^2\alpha}} \cdot c \tag{6}$$

$$C = \frac{A \cdot D - 1}{B}$$

where
$$C = \frac{\pi i}{\int_{-\infty}^{\infty} e^{iu^2}\,du \int_{-\infty}^{\infty} X(w)\,e^{iw^2}\,dw} \tag{7}$$

while b and d may take arbitrary values.

By simple algebraical operations it may be shown that (5) implies L+L'=0 so that the above expressions of A, B and D are simplified to

$$A = C\cdot\sin\alpha \qquad D = \frac{1}{C\cdot\sin\alpha} \qquad B = 0 \tag{8}$$

where the necessary condition AD-BC=1 has also been used.

Considerations presented elsewhere /2/ enable us to find C=0, so that the optical transfer matrix for a diffraction grating in Littrow mounting assumes the following final form

$$M_G = \begin{pmatrix} C\sin\alpha & 0 \\ 0 & \frac{1}{C\sin\alpha} \end{pmatrix} \tag{9}$$

A simple check of (9) may be done for the case of a continous diffraction grating in Littrow mounting (i.e. plane mirror). Then $X(\omega) = 1$ and $\alpha\ \frac{\pi}{2}$ so that it is easy to see that we get the well known result.

From a practical point of view the development of subsequent sections is greatly simplified by the assumption that we are dealing with an "ideal" grating for which $C = 1$. From (7) we see that our assumption fits in as the number of grooves per millimeter increases.

III. Analysis of the usual design of grating resonators

The design shown in fig.2 represents the usual arrangement for a pulsed dye laser resonator. Although in practice $\phi = 0$ (i.e. the optical power of the plane mirror), it will prove valuable to assume first that ϕ may take any value.

Calculating the transfer matrix for a complete roundtrip of the resonator we find the following values for its elements

$$\begin{aligned} \mathcal{A} &= A - 3(A+D)\left[1 - \frac{t_4}{m\cdot\Sigma} - \frac{t_5}{m^2\Sigma}\right] \\ \mathcal{B} &= -(A+D)\,\Sigma\left[1 - \frac{t_4}{m\Sigma} - \frac{t_5}{m^2\Sigma}\right] \\ \mathcal{C} &= -D\psi \\ \mathcal{D} &= D \end{aligned} \tag{10}$$

where $\psi = \phi\,\Sigma$ while all other symbols must be refered to fig.2.

The trace of the matrix generated by (10) is

$$A+\mathcal{D} = (A+D)\left[1 - 5\left(1 - \frac{t_4}{m\Sigma} - \frac{t_5}{m^2\Sigma}\right)\right] \tag{11}$$

and this result indicates the important influence of the grating matrix elements up on the general behaviour of the resonator.

If $\phi = 0$ (as commonly used), since A+D>2, then also $\mathcal{A} + \mathcal{D} > 2$, which means that the arrangement illustrated in fig.2 is of astable type. This situation involves an appropriate output design for the laser beam and a corresponding value for the gain of the resonator given by

$$M = \frac{1}{2}\left[\mathcal{A}+\mathcal{D} + \sqrt{(\mathcal{A}+\mathcal{D})^2-4}\right] \tag{12}$$

In our case, as the tuning of the laser requires different Littrow angles, the gain of the resonator is variable over the spectral band of interest.

Another problem connected with the usual " $\varphi = 0$" resonator arises from the fact that, although variable, A+D takes values very close to 2. From (11)we see that any mechanical perturbation of the output mirror may lead to $\mathcal{A} + \mathcal{D} < 2$ (through $\neq 0$), and thus induces a change from astable to stable type resonator. From the proceding arguments it becomes clear that $= 0$ does mot make the best choise.

IV. Stable and astable grating resonators with controlled parameters

It is known that a stable resonator is described by a roundtrip matrix whose trace takes values in the interval (-2,2). In the opposite case, the resonator is astable.

Out of a variety of possible designs, we shall investigate just three arrangements which may be obtained from the usual one by minor modifications (see fig.3).

The trace for the first arrangement (fig.3.a) is given by (11), while for the other two (fig.3.b,c) we find respectively

$$\begin{gathered} \mathcal{A}+\mathcal{D} = [A+D]\left[1- \Phi_{sist} \cdot \Sigma\left(1 - \frac{t_4}{m} + \frac{t_5}{m^2}\right) - \tau \frac{A\varphi + D\varphi_L}{A+D}\right] \\ \Phi_{sist} = \psi + \varphi_L - \tau\psi\varphi_L \end{gathered} \tag{13}$$

and

$$\mathcal{A}+\mathcal{D} = (A+D)\left[1 - m'^2\epsilon\left(1 - \frac{mAt_4' + m't_4D}{m \cdot m'\Sigma} + \frac{At_1 + Dt_5}{A+D\ m^2}\right)\right] \qquad \epsilon = \psi\Sigma \tag{14}$$

As we may note, (11) contains 5 parameters (t_4, t_5, m, Σ , ψ) which permit an effective control of the resonator behaviour in the selected band of operation. To the same end, (13) and (14) offer respectively 7 and 8 ajustable parameters.

When typical values are introduced in the above relations, so as to identify the type of operation at the ends of the spectral band of interest, one obtains the diagrams illustrated in fig.4. The validity of these diagrams for all the configurations discussed is a consequence of the fact that in order to improve the spectral resolution of the grating, one must employ a rather strong magnifying telescope ($m \sim 10 \div 20$). However, ξ in fig.4 means $\psi\Sigma$ for an arrangement as in fig.3.a, $\phi_{1st}\Sigma$ for the resonator shown in fig.3.b, and $\tan\phi\,\Sigma$ for the arrangement shown in fig.3.c.

As a general rule, fig.4 indicates that all configurations disscussed may be adjusted to operate as well as stable or astable resonators. The resonator in fig.3.a generates a narrow cross section laser beam, while the other two geometries may be designed such as to produce a light beam of given cross section.

In the specific case of astable operation one must ensure a constant gain of the resonator over the entire spectral range of the dye. This may be accomplished by means of numerical techniques which allow the identification of simultaneous solutions of (12), when specialized at the ends of the spectral band of interest.

V. Conclusions

We have shown that the Littrow mounting of a diffraction grating may be described in terms of a conventional optical transfer matrix. The results thus obtained were applied to the analysis of several grating resonators. It was shown that each arrangement offers a set of design parameters through which one may completely control the behaviour of stable or astable resonators.

Acknowledgement

One of us (A.B.) wants to express his gratitude to dr. Denisa Popescu for many illuminating discussions which made possible this work.

REFERENCE

1. H.Kogelnik, T.Li, Appl.Opt., 5, 1550 (1966)
2. A.Belea, I.I.Popescu, (to be published).

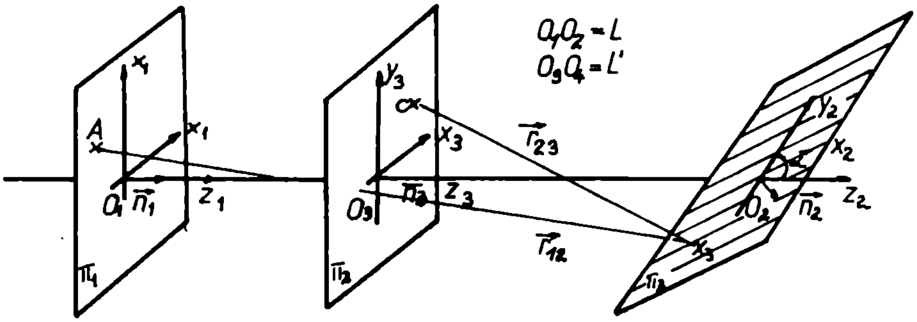

O1O2 = L
O3O4 = L'
y1
A
x1
O1
n1
z1
π1
y3
α
x3
O3
n3
z3
π3
r23
r12
y2
x2
O2
n2
z2
π2

Fig. 1

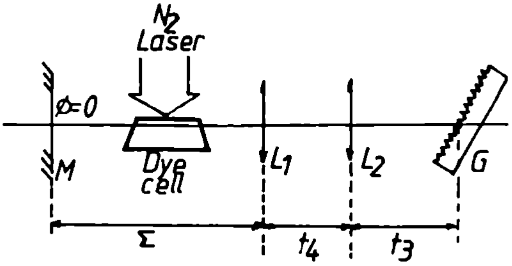

N2
Laser
ϕ=0
M
Dye
cell
L1
L2
G
Σ
t4
t3

Fig.2

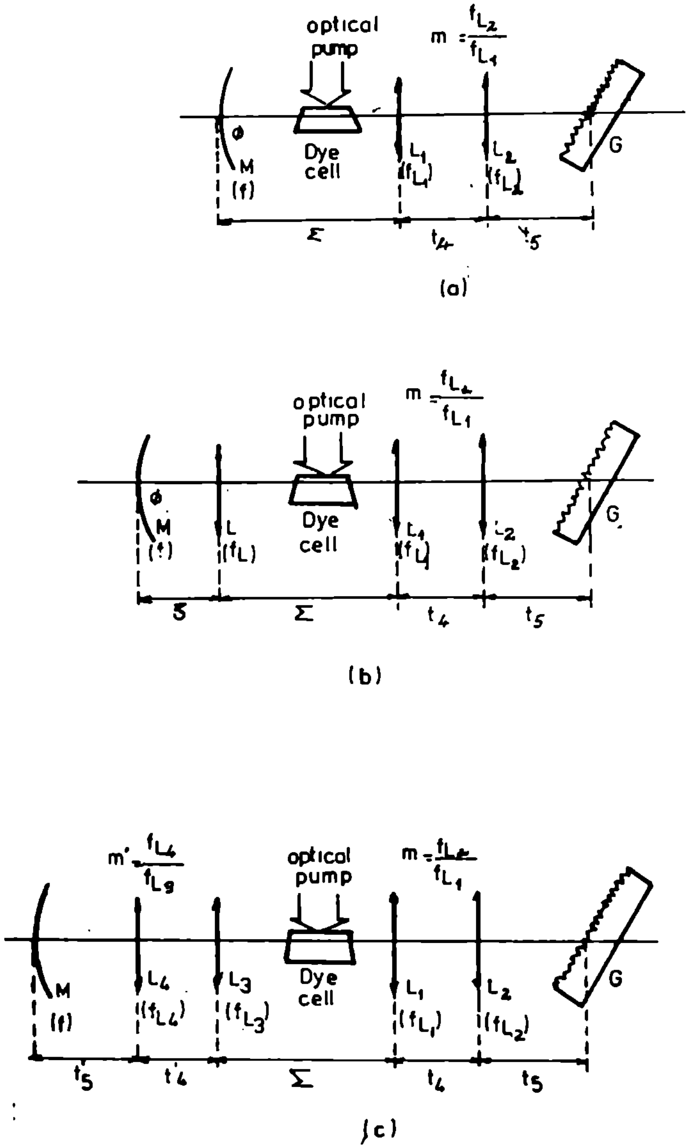
optical pump
$m = \frac{f_{L_2}}{f_{L_1}}$
$m' = \frac{f_{L_4}}{f_{L_3}}$
Dye cell
ϕ
M
(f)
L
(f_L)
L_1
(f_{L_1})
L_2
(f_{L_2})
L_3
(f_{L_3})
L_4
(f_{L_4})
G
δ
Σ
t_4
t_5
t'_4
t'_5

(a)

(b)

(c)

Fig.3

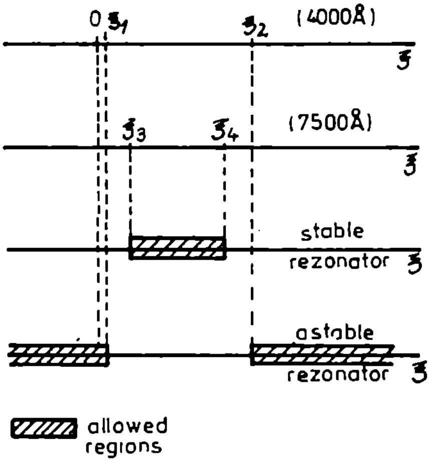
0
ξ_1
ξ_2
(4000Å)
ξ
ξ_3
ξ_4
(7500Å)
ξ
stable
rezonator
ξ
astable
rezonator
ξ
allowed regions

Fig. 4

HOLLOW CATHODE METAL VAPOUR LASERS

I.M.Popescu, M.I.Cilea, A.M.Preda, C.P.Cristescu
The Physics Department of
the Polytechnic Institute of Bucharest

The paper presents the results of the study of three different types of hollow cathode metal vapour lasers made up in our laboratory: the He-Cd-Zn laser, the laser with two active plasmas and the He-Zn laser with brass cathode. The characteristics of each system are presented.

1. Introduction

The metal vapour lasers are interesting from both the scientific and the technologic points of view. The laser oscillation can be obtained on transition either of the metal ion or of the metal atom.

The metal vapour lasers working on ionic transitions can generate a great variety of oscillations in the range between the ultraviolet and the near infrared, with reasonable efficiency. Most of them are characterized by low threshold current and relatively high gain /1/.

Usually a buffer gas is necessary. In most systems the helium plays this role, but Ne and Ar are also used ocasionally /2,3/.

The partial pressure of the metal vapour necessary is in the range 10^{-2} - 10^{-1} Torr.

In the metal vapour ionic lasers, besides the direct electron collisions, two excitation mechanisms play an important role:

a) Charge transfer in thermal energy collisions between ground state helium ions (He^+) and metal atoms in the atomic ground state (M). As a result, a certain ionic level of the metal atom is prefferentially populated. The reaction can be written:

$$He^+ + M \text{ --- } (M^+)^* + He$$

b) Penning reaction

$$He(2^3S) + M \text{ --- } (M^+)^* + He + e$$

where the metal ion population is seated by energy transfer from the helium metastables (2^3S) to the ground state metal atoms.

The homogeneity of the metal vapour buffer gas mixture in the discharge space is a stringent condition for the proper working of a metal vapour laser. An important step in solving this problem was the introduction of the hollow cathode discharge.

The rest of the paper is dedicated to the recent results obtained by the authors in the study of hollow - cathode metal vapour lasers.

2. Hollow cathode He-Cd-Zn laser

It is well known /4/ that the temperature which insures the necessary metal vapour partial pressure (10^{-2} - 10^{-1} Torr) in the case of Zn is some 100 degrees higher than for Cd. While the working temperature of the He-Cd system is in the neighbourhood of 200°C, the He-Zn system oscillates when the wall temperature is in excess 280°C. The oscillation of the He-Cd laser ceases at a temperature lower than the threshold temperature for the He-Zn laser. These results have led to the general belief that the He-Zn and He-Cd plasmas are incompatible for simultaneous laser operation. However, making use of the relation between the evaporation rate E and the absolute temperature T which, in the case of Cd /5/, has the form $\log E = A - 5050\ \emptyset T^{-1}$, with A and $\emptyset$ constants, one can show /6/ that, on condition that the cadmium amount present in the discharge zone is small enough, the optimum partial pressure can be preserved for a wide range of temperatures. In fact, the appropriate Cd pressure can be maintained up to temperatures well in the range characteristic for the He-Zn laser so that simultaneous oscillation on Cd^+ and Zn^+ lines appears possible.

Using this observation, a laser discharge tube was constructed in which a carefully chosen small amount of Cd was introduced besides the usual amount of Zn. The cathode is a 60 cm stainless steel tube with 4 mm i.d. and the anode is a metal cylinder set coaxially with the cathode. Helium is used as buffer gas at a pressure of 10 Torr. The discharge current is 0.9 A.

Figure 1 shows tha laser output at λ = 537.8 nm (CdII) and λ = 492.4 nm (ZnII) versus the temperature of the tube wall.

In the range 265 - 285°C the two lines oscillate simultaneously with no influence on one another.

The possibility of simultaneous oscillation on transitions of different metal atoms (ions) is very attractive because of the large number of oscillations which can be generated by a single laser in a wide spectrum.

3. The He-Zn laser with two active plasmas

The metal vapour discharges used laser devices are usually sustained by d.c. voltages. In the following we present a discharge tube working on a.c. voltage which provides laser oscillation on both alternances of the applied voltage. It consists of two cylindrical electrodes set parallel to the discharge tube axis as shown in figure 2.

Each cylinder can play the rôle either of hollow cathode or of anode, depending upon the direction of the applied voltage. Thus conditions for laser operation exist in each of the two hollow electrodes during one half of the cycle of the a.c. voltage. The characteristics of the two laser beams depend upon the two resonators, so that "simultaneous" oscillation can be obtained on two different transitions of the Zn ion.

Also, by introducing a small amount of cadmium in the discharge zone, one of the laser beams can be a CdII line and the other a ZnII line.

The output dependence upon the buffer gas pression and the wall temperature is similar to the usual hollow cathode laser.

The output at 492.4 nm versus the effective discharge current is that shown in figure 3 for a wide range of helium pressure.

4. He-Zn laser with brass hollow-cathode

The active atoms (metal atoms) are usually obtained by evaporation of small metal pieces placed somewhere in the discharge zone or in its immediate neighbourhood. The heat generated by the discharge is usually sufficient for the generation of a metal vapour partial pressure of 10^{-2} - 10^{-1} Torr necessary in most metal vapour lasers.

It was already mentioned that the uniform distribution of the active atoms along the discharge is a very important condition.

Usually, the hollow cathodes are made out of refractory metals such as stainless steel, kovar etc. These materials, due to their relatively low thermal conduction, generate strong nonuniformity of the temperature along the discharge and consequently of the active atoms distribution.

The result is discharge instabilities which usually terminate the life of the laser tube.

We managed to avoid these difficulties by making the hollow cathode out of rich Zn brass /8/. The discharge tube consists of a 60 cm brass tube with 4-6 mm i.d., which plays the role of hollow cathode, and another tube of the same material with 15 mm i.d. which is the anode. The discharge is taking place inside the cathode through 4 mm diameter holes perforated 4 cm apart, along a generator of the cathode cylinder.

The discharge is fed on two voltages: a low half rectified voltage which serves for the heating up of the discharge tube and a high, pulsed voltage which excite the active species. The coupling of the two circuits is shown in figure 4.

The helium pressure is around 8 Torr and the average current of the heating up discharge is 750 mA.

The current pulses, obtained by use of a TGU-1-35/3 thiraton, have a duration of 1 µs and frequency of 400 Hz.

In these conditions simultaneous oscillation have been obtained on 491.1 and 492.4 nm ZnII lines and 533.7 and 537.8 nm CdII lines. Cadmium was present as impurity in the brass. The laser output at 492.4 nm versus the discharge current is shown in figure 5 for three values of the buffer gas pressure.

Laser oscillation was also obtained when the discharge was fed on the half rectified voltage.

The use of brass as cathode material brings in considerable improvement in He-Zn hollow cathode lasers in the following respects:

a) The discharge is very stable and the temperature is uniformalong the length of the discharge.

b) In so far as the metal of interest - zinc - is embedded in the cathode material, the distribution of the active atoms in the discharge zone obtained by evaporation is remarkably uniform.

c) The lifetime of such a laser is much longer than for a refractory metal hollow cathode laser. A brass cathode device constructed in our laboratory have been in use for more than 500 hours without any alterations of the output characteristics.

REFERENCES

/ 1/ T.Iijima, Y.Sugawara, Jap.J.Appl.Phys. vol.20, nr.6 (1981)

/ 2/ G.R.Fowles, W.T.Silfvast, IEEE J.Quant.Electron. vol. QE-1, nr.3 (1965)

/ 3/ K.Rozsa, M.Janossy, L.Csillag, J.Bergou, Phys.Lett. vol. 63A, p. 231 (1977)

/ 4/ G.I.Collins, J.Appl.Phys., vol.44, nr.10 (1973)

/ 5/ K.G.Hernqvist, IEEE J.Quant.Electron vol. QE-14, nr.2 (1978)

/ 6/ M.I.Cilea, A.M.Preda, I.M.Popescu, C.P.Cristescu, Rev.Roum.Phys., vol. 19, nr.6 (1984)

/ 7/ M.I.Cilea, A.M.Preda, C.P.Cristescu, The 5th National Conference "Plasma Physics and Technology" Iaşi (1983)

/ 8/ M.I.Cilea, A.M.Preda, I.M.Popescu, Rev.Roum.Phys. (to be published)

/ 9/ M.I.Cilea, A.M.Preda, I.M.Popescu, Rev.Roum.Phys. (to be published)

/10/ W.Sasaki, H.Ueda, T.Ohta, IEEE J.Quant.Electron. vol.QE-19, nr.8 (1983)

/11/ T.Iijima, Jap.J.Appl.Phys., vol.15, nr.7 (1976)

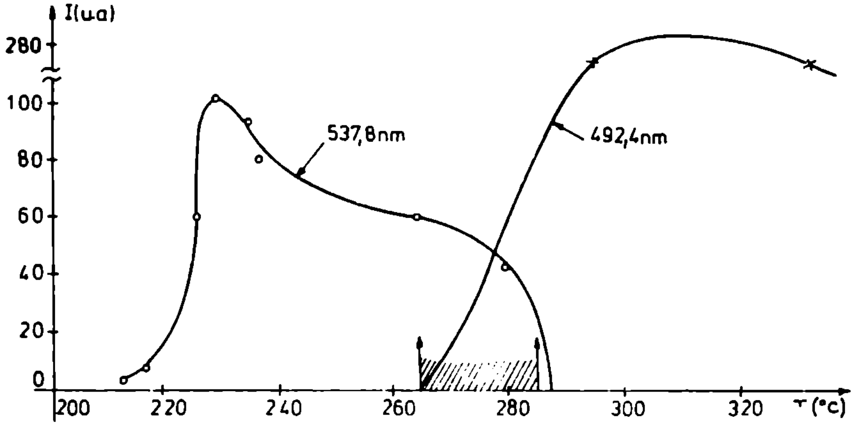

Fig. 1

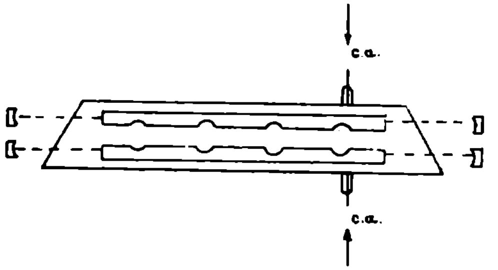

Fig. 2

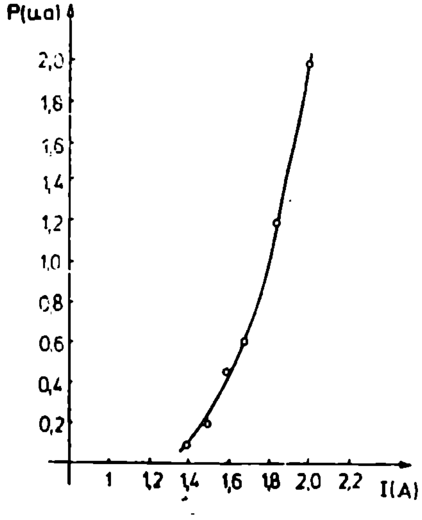

Fig 3

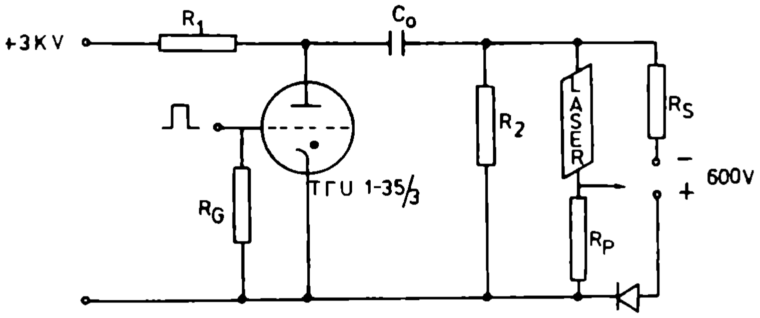
+3KV
R1
C0
R2
LASER
RS
RG
RP
TГU 1-35/3
600V
−
+

Fig. 4

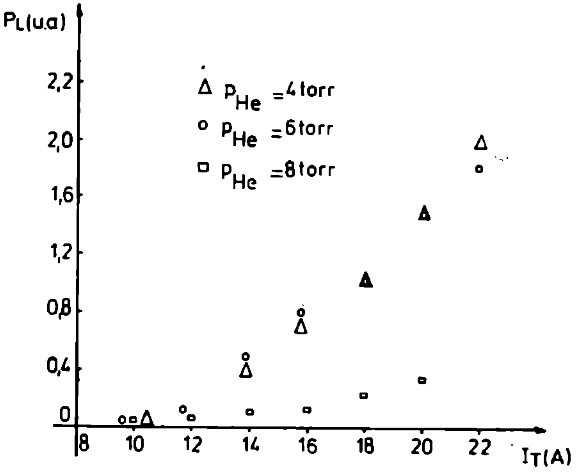
PL(u.a)
2,2
2,0
1,6
1,2
0,8
0,4
0
Δ pHe =4torr
○ pHe =6torr
□ pHe =8torr
8
10
12
14
16
18
20
22
IT(A)

Fig. 5

ACCURATE MATHEMATICAL METHODS FOR SMOOTHING OUT EMPIRICAL FUNCTIONS AND PERFORMING DIRECT AND INVERSE ABEL TRANSFORMS

Nicholas Ionescu-Pallas
Central Institute of Physics, IPTRD,
Laser Division, Bucharest, Romania

The problem of evaluating direct and inverse Abel transforms (used in optics and plasma physics) is considered in view of elaborating improved calculation method as compared with the existing ones. A smoothing out method, based on orthogonal polynomials, is proposed on this occasion. The method has the advantage that leads to polynomials in $\sqrt{1-x^2}$ and , accordingly, the inverse Abel transform of a certain function (given as a set of empirical data) becomes a quite simple operation (almost a consequence of the specific manner of smoothing). The problem of mechanical integration on the range (0,1) is also examinated (as being directly connected to the Abel transform or to the coefficient determination of smoothing out polynomial) and some new improved formulas are proposed. Finally, the problem of polynomial oscillations (introduced during the smoothing process) is analysed and suggestions are made how to reduce their amplitude.

Using Abel transform for plasma diagnosis

Let us consider a certain material medium filling a cylinder of infinite length and circular cross section of radius R. A monochromatic light wave

$$\psi = a\cos(\omega t - kx) \quad /, \quad k = \frac{2\pi}{\lambda} \quad , \quad \omega = 2\pi\nu \quad , \quad \lambda\nu = v = \frac{c}{n} \ ,$$

travelling in a direction perpendicular on the cylinder generatrice, intercepts the cylinder surface in a point A, has a path inside the cylinder, in a transverse section, and leaves the cylinder surface in another point B. The phase shift underwent by the wave is

$$\Delta\varphi_{\overline{AB}} = \frac{\omega}{c}\int_A^B (n-1)\,ds \approx 2\,\frac{\omega}{c}\int_0^{\sqrt{R^2-\rho^2}} \left\{ n\left(\sqrt{\rho^2+x^2}\right) - 1 \right\} dx \tag{1}$$

where the deviation of wave direction inside the cylinder, as a result of the refraction, was neglected and the refractive index of the material was assumed as depending solely on the distance from the axis to a given point in a transverse plane. ρ 's the y coordinate in this plane of either A or B points. Now, let us adopt the following denotations (implying a variable changing).

$$\sqrt{\rho^2+x^2} = r, \quad \frac{\rho}{R} = \zeta, \quad \frac{r}{R} = \tau, \quad \Delta\phi(\rho) = f(\zeta), \quad 2\frac{\omega}{c}R[n(r)-1] = g(\tau) \tag{2}$$

with the aid of which the integral (1) becomes

$$f(\zeta) = \int_{\zeta}^{1} g(\tau)\frac{\tau d\tau}{\sqrt{\tau^2-\zeta^2}} \quad . \tag{3}$$

It is of practical interest to estimate g(τ) (the refractive index distribution) when f(ζ) is given (the phase change distribution). The solution is exactly known (inverse Abel transform)

$$g(\zeta) = -\frac{2}{\pi}\int_{\zeta}^{1}\frac{f'(\tau)d\tau}{\sqrt{\tau^2-\zeta^2}} \tag{4}$$

Nevertheless, owing to the fact that what is really known is only the values (altered by experimental errors) of the function f(ζ) in few points (which, in addition, may be non equidistant) and owing to the subsequent difficulties, coming from the necessity of performing the derivation of an experimental function, and, thereafter, of evaluating a singular integral, the estimation of inverse Abel transform, proceeding from empirical data, is a highly intricate problem. Such problems pertain to the class of ill conditioned problems (instability in the Hadamard's sense). The solutions, so far proposed, for evaluating the function g(ζ), are to a great extent empirical, and cannot ensure a high level of confidence and accurateness together with a rapid convergence of the mathematical algorithms used for processing the empirical data. The best approximation recommended in the literature is based on a previous smoothing of empirical data, on a going over from few non-equidistant to many equidistant integration points, on a discretizing of the (direct) Abel integral

$$f(\tfrac{s}{N}) = \frac{1}{N}\sum_{sj}^{N-1}\int_{j}^{j+1} g(\tfrac{\xi}{N})\frac{\xi d\xi}{\sqrt{\xi^2-s^2}} \quad , \quad s = 0,\ 1,\ 2,\ \dots\ N-1, \tag{5}$$

on an approximation of the unknown function g by a finite difference expansion

$$g(\tfrac{\xi}{N}) = (1+\Delta)^{\xi-j}g(\tfrac{j}{N}) = g(\tfrac{j}{N}) + \frac{(\xi-j)}{1!}\Delta g(\tfrac{j}{N}) + \frac{1}{2!}(\xi-j)(\xi-j-1)\Delta^2 g(\tfrac{j}{N})$$
$$+ \frac{1}{3!}(\xi-j)(\xi-j-1)(\xi-j-2)\Delta^3 g(\tfrac{j}{N}) + \dots , \tag{6}$$

on a certain option about the degree of approximation (for instance, to discard differences higher then second ones), on performing the integration on every strip $j \le \xi \le j+1$ and finally, on inversing the problem in order to find $g_k \equiv g(\frac{k}{N})$ in terms of $f_s \equiv f(\frac{s}{N})$ by inversing a certain matrix with known elements. In the case of second difference approximation (the most elaborate case of this method, to be found in literature - but not treated in full rigor), we obtain

$$f_s = \frac{1}{N}\sum_{sj}^{N-2}\left\{g_j\alpha_j^{(s)} + (g_{j+1}-g_j)\beta_j^{(s)} + \frac{1}{2}(g_{j+2}-2g_{j+1}+g_j)\gamma_j^{(s)}\right\} \tag{7}$$

$$+ \frac{1}{N}\left\{g_{N-1}\alpha_{N-1}^{(s)} + (g_N - g_{N-1})\beta_{N-1}^{(s)} + \frac{1}{2}(g_N - 2g_{N-1} + g_{N-2})\gamma_{N-1}^{(s)}\right\}$$

$$(s = 0,\ 1,\ 2,\ \dots\ N-2)$$

$$f_{N-1} = \frac{1}{N}\left\{g_{N-1}\alpha_{N-1}^{(N-1)} + (g_N - g_{N-1})\beta_{N-1}^{(N-1)} + \frac{1}{2}(g_N - 2g_{N-1} + g_{N-2})\gamma_{N-1}^{(N-1)}\right\}$$

where

$$\alpha_j^{(s)} = \int_j^{j+1} \frac{\xi d\xi}{\sqrt{\xi^2 - s^2}} = \sqrt{(j+1)^2 - s^2} - \sqrt{j^2 - s^2} \tag{8}$$

$$\beta_j^{(s)} = \int_j^{j+1} (\xi - j)\frac{\xi d\xi}{\sqrt{\xi^2 - s^2}} = \frac{1}{2}\left[j\sqrt{j^2 - s^2} - (j-1)\sqrt{(j+1)^2 - s^2}\right] + \frac{1}{2} s^2 \ln \frac{(j+1) + \sqrt{(j+1)^2 - s^2}}{j + \sqrt{j^2 - s^2}}$$

$$\gamma_j^{(s)} = \int_j^{j+1} (\xi - j)(\xi - j - 1)\frac{\xi d\xi}{\sqrt{\xi^2 - s^2}} = \left[\frac{1}{3}(j+1)(j - \frac{1}{2}) + \frac{2}{3} s^2\right]\sqrt{(j+1)^2 - s^2} -$$

$$- \left[\frac{1}{3}(j + \frac{3}{2}) j + \frac{2}{3} s^2\right]\sqrt{j^2 - s^2} - (2j+1)\frac{1}{2} s^2 \ln \frac{(j+1) + \sqrt{(j+1)^2 - s^2}}{j + \sqrt{j^2 - s^2}}$$

For $s = 0$ we have $\alpha_j = 1$, $\beta_j = \frac{1}{2}$, $\gamma_j = -\frac{1}{6}$ and obtain

$$f_0 = \int_0^1 g(\tau)d\tau = \frac{1}{N}\sum_0^{N-2}{}_j\left\{g_j + \frac{1}{2}(g_{j+1} - g_j) - \frac{1}{12}(g_{j+2} - 2g_{j+1} + g_j)\right\} \tag{9}$$

$$+ \frac{1}{N}\left\{g_{N-1} + \frac{1}{2}(g_N - g_{N-1}) - \frac{1}{12}(g_N - 2g_{N-1} + g_{N-2})\right\}$$

$$= \frac{1}{N}\left\{\sum_0^{N-1}{}_j\, g_j + \frac{7}{12}(g_{N-1} - g_0) - \frac{1}{12}(g_N - g_1) + \frac{1}{2}(g_N - g_{N-1}) - \frac{1}{12}(g_N - 2g_{N-1} + g_{N-2})\right\}$$

For arbitrary s we obtain, after adequate reordering of the terms

$$f_s = \frac{1}{N}\left\{\sum_{s+2}^{N-2}{}_j\, g_j\left|(\alpha_j^{(s)} - \beta_j^{(s)} + \frac{1}{2}\gamma_j^{(s)}) + (\beta_{j-1}^{(s)} - \gamma_{j-1}^{(s)}) + \frac{1}{2}\gamma_{j-2}^{(s)}\right| + \Omega\right\} \tag{10}$$

$$\Omega \equiv \left[g_N(\beta_{N-1}^{(s)} - \frac{1}{2}\gamma_{N-1}^{(s)} + \frac{1}{2}\gamma_{N-2}^{(s)}) + g_{N-1}(\alpha_{N-1}^{(s)} - \beta_{N-1}^{(s)} - \gamma_{N-1}^{(s)} + \beta_{N-2}^{(s)}\right.$$

$$\left. - \gamma_{N-2}^{(s)} + \frac{1}{2}\gamma_{N-3}^{(s)}) + \frac{1}{2} g_{N-2}\gamma_{N-1}^{(s)}\right] + \left[g_s(\alpha_s^{(s)} - \beta_s^{(s)} + \frac{1}{2}\gamma_s^{(s)})\right.$$

$$\left. + g_{s+1}(\beta_s^{(s)} - \gamma_s^{(s)} + \alpha_{s+1}^{(s)} - \beta_{s+1}^{(s)} + \frac{1}{2}\gamma_{s+1}^{(s)})\right],\quad s = 0,\ 1,\ 2,\ \dots\ N-4$$

$$f_{N-1} = \frac{1}{N}\Big\{g_N(\beta_{N-1}^{(N-1)} + \frac{1}{2}\gamma_{N-1}^{(N-1)}) + g_{N-1}(\alpha_{N-1}^{(N-1)} - \beta_{N-1}^{(N-1)} - \gamma_{N-1}^{(N-1)})$$

$$+ \frac{1}{2} g_{N-2}\gamma_{N-1}^{(N-1)}\Big\}$$

$$f_{N-2} = \frac{1}{N}\Big\{g_N(\beta_{N-1}^{(N-2)} + \frac{1}{2}\gamma_{N-1}^{(N-2)} + \frac{1}{2}\gamma_{N-2}^{(N-2)}) + g_{N-1}(\alpha_{N-1}^{(N-2)} - \beta_{N-1}^{(N-2)} - \gamma_{N-1}^{(N-2)}$$

$$+ \beta_{N-2}^{(N-2)} - \gamma_{N-2}^{(N-2)}) + g_{N-2}(\frac{1}{2}\gamma_{N-1}^{(N-2)} + \alpha_{N-2}^{(N-2)} - \beta_{N-2}^{(N-2)} + \frac{1}{2}\gamma_{N-2}^{(N-2)})\Big\}$$

$$f_{N-3} = \frac{1}{N}\Big\{g_N(\beta_{N-1}^{(N-3)} + \frac{1}{2}\gamma_{N-1}^{(N-3)} + \frac{1}{2}\gamma_{N-2}^{(N-3)}) +$$

$$+ g_{N-1}(\alpha_{N-1}^{(N-3)} - \beta_{N-1}^{(N-3)} - \gamma_{N-1}^{(N-3)} + \beta_{N-2}^{(N-3)} - \gamma_{N-2}^{(N-3)} + \frac{1}{2}\gamma_{N-3}^{(N-3)}) +$$

$$+ g_{N-2}(\frac{1}{2}\gamma_{N-1}^{(N-3)} + \alpha_{N-2}^{(N-3)} - \beta_{N-2}^{(N-3)} + \frac{1}{2}\gamma_{N-2}^{(N-3)} + \beta_{N-3}^{(N-3)} - \gamma_{N-3}^{(N-3)}) +$$

$$+ g_{N-3}(\alpha_{N-3}^{(N-3)} - \beta_{N-3}^{(N-3)} + \frac{1}{2}\gamma_{N-3}^{(N-3)})$$

This is an algebraic system of N equations for the quantities $(g_0, g_1, g_2, \ldots, g_N)$ which may be solved (provided that g_0 is given) by reverting the matrix of the system. There are here two kinds of difficulties preventing us to reach a high level of precision: first) the ill conditioning of the system of equations due to the tendency of the coeficients (α_j, β_j, γ_j) to accomplish more and more an indetermination of the form $\infty - \infty$ at the expense of increasing the number N of integration points. The tendency is so much more stressed as we increase the order of approximation (β_j is more divergent than α_j, γ_j is more divergent than β_j, a.s.o.); second) to increase the convergence of the procedure for $N \to \infty$ it is necessary to increase the order of approximations, id est to include higher order finite differences (at least third order in view of accounting for the inflexion points). This entails, however, to previously perform a very accurate smoothing out. All in all, the method turns out to be very tedious and not able to ensure a reasonable accuracy. An improving of the method may still be achieved by partially taking apart the divergent parts of the coefficients α_j, β_j, γ_j. We obtain

$$\alpha_j^{(s)} = \frac{(2j+1)}{\sqrt{(j+1)^2-s^2} + \sqrt{j^2-s^2}} \tag{11}$$

$$\beta_j^{(s)} = \frac{1}{2}\left\{\frac{(2j^2-1) - s^2(2j-1)}{j\sqrt{j^2-s^2} + (j-1)\sqrt{(j+1)^2-s^2}} + s^2 \ln\frac{(j+1) + \sqrt{(j+1)^2-s^2}}{j + \sqrt{j^2-s^2}}\right\}$$

$$\gamma_j^{(s)} = -\frac{1}{6}\cdot\frac{\left\{[2j^2(2j+3)-1] - 3s^2(2j+1)[8s^2+4j(j+1)-3]\right\}}{[4s^2+(j+1)(2j-1)]\sqrt{(j+1)^2-s^2} + [4s^2+j(2j+3)]\sqrt{j^2-s^2}} -$$

$$-(j+\frac{1}{2})s^2 \ln\frac{(j+1) + \sqrt{(j+1)^2-s^2}}{j + \sqrt{j^2-s^2}}, \qquad s \le j \le N-1, \quad 0 \le s \le N-$$

In this way, the method may be applied at least for performing the direct Abel transform. (There is however a slow divergence of the coefficients $\alpha_{N-1}^{(N-1)}$, $\beta_{N-1}^{(N-1}$, $\gamma_{N-1}^{(N-1)}$ even in the case of completely avoiding the indetermination

$$\alpha_{N-1}^{(N-1)} \sim \sqrt{2}(N-1)^{1/4} \ , \ \beta_{N-1}^{(N-1)} \sim \frac{1}{3}\sqrt{2}(N-1)^{1/4} \ , \ \gamma_{N-1}^{(N-1)} \sim -\frac{2}{3.5}\sqrt{2}(N-1)^{1/4} \tag{12}$$

but it brings no serious difficulty. More difficult is a residual $\infty-\infty$ indetermination still persisting in the expressions of $\beta_j^{(s)}$ and $\gamma_j^{(s)}$. For instance, three digits are lost due to this situation in the case N = 20.)

Some accurate formulas for performing direct and inverse Abel transforms

Owing to the lack of accurate methods in the literature of this subject, we have undertaken a study in view of filling up the respective gap. Once the smoothing out of empirical data is accepted as a necessary stage towards the final evaluation of an Abel integral, we are in a position to calculate the value of the smoothed out empirical function at any point in the range $(0 < x < 1)$ and, as a matter of fact, it is of little interest to still confine ourselves to equidistant integration points.But, if non-equidistant integration points may be used, then adequate variable transformation may avoid the (integrable) singularity of the integrant, converting the integral in a conventional one, whereof we are already acquainted how to be approximated.

Using the transformation $\tau = \sqrt{x^2+(1-x^2)\zeta^2}$, the direct Abel transform becomes

$$f(\zeta) = \sqrt{1-\zeta^2}\int_0^1 g\left(\sqrt{x^2+(1-x^2)\zeta^2}\right)dx \tag{13}$$

Now, it is opportune to write

$$f(\zeta) = \frac{1}{2}\sqrt{1-\zeta^2}\int_{-1}^{+1} g\left(\sqrt{x^2+(1-x^2)\zeta^2}\right)dx \tag{13'}$$

or

$$f(\zeta) = \frac{1}{2}\sqrt{1-\zeta^2}\int_{-1}^{+1}\left\{\sqrt{1-x^2}\, g\left(\sqrt{x^2+(1-x^2)\zeta^2}\right)\right\}\frac{dx}{\sqrt{1-x^2}}$$

and, accordingly, to apply the Legendre or the Tohebisheff integration formulas. The second case exhibits the advantage of an increased accurateness, because the integration points are given analytically and, accordingly, the number of points may be taken arbitrarily large

$$f(\zeta) = \sqrt{1-\zeta^2}\,\frac{\pi}{2n}\sum_{k=1}^{n}\left(\sin\frac{2k-1}{2n}\pi\right) g\left(\sqrt{\cos^2\frac{2k-1}{2n}\pi+\zeta^2\sin^2\frac{2k-1}{2n}\pi}\right) \tag{14}$$

For odd n, the respective formula acquires a symmetrical form

$$f(\zeta) = \frac{1}{2}\sqrt{1-\zeta^2}\,\frac{\pi}{2m+1}\sum_{k=-m}^{+m}\cos\frac{k\pi}{2m+1}\, g\left(\sqrt{\sin^2\frac{k\pi}{2m+1}+\zeta^2\cos^2\frac{k\pi}{2m+1}}\right) \tag{14'}$$

and is particularly suitable to be used in conjuction with a minicomputer. The convergence for

$m \to \infty$ of this formula is not, however, too rapid because in the case $g(\tau) = 1$ one obtains

$$f(\zeta) = \sqrt{1-\zeta^2}\,\frac{[\pi/2(2m+1)]}{\sin[\pi/2(2m+1)]} = \sqrt{1-\zeta^2}\left[1 + \frac{\pi^2}{24}\,\frac{1}{(2m+1)^2} + O(2m+1)^{-4}\right]$$

It is also possible to apply a modified version of the simple Tchebysheff formula

$$\int_0^1 f(x)\,dx = \frac{1}{N}\sum_{1}^{N}{}_k f(x_k) \tag{15}$$

Such a formula has real integration points even for $N > 9$ if, instead of requiring an exact result when $f(x)$ is a N-th degree polynomial, we ask only to have a given superior limit of error when $f(x)$ has the respective form. Applying this approximation principle to the case of direct Abel transform, we obtained the following formulas (having a relative error $\lesssim 10^{-5}$)

$$\begin{aligned} f(\zeta) &= \sqrt{1-\zeta^2}\,\frac{1}{27}\sum_{1}^{27}{}_k\, g\left(\sqrt{\sin^2\psi_k + \zeta^2\cos^2\psi_k}\right) \\ f(\zeta) &= \sqrt{1-\zeta^2}\,\frac{1}{63}\sum_{1}^{63}{}_k\, g\left(\sqrt{x_k^2 + (1-x_k^2)\,\zeta^2}\right) \end{aligned} \tag{16}$$

The angles ψ_k $(k = 1,2,3,\ldots,27)$ and the roots x_k $(k = 1,2,3,\ldots,63)$ are given in the addenda. For the same number of integration points $(2m + 1 = N = 27)$ the first formula (16) gives a precision definitely higher than formula (14').

Similar treatment may be applied to the inverse Abel transform, provided that $f'(0) = 0$. One obtains

$$g(\zeta) = \frac{2}{\pi}(1-\zeta^2)^{-1/2}\left\{f(\zeta) - \int_0^1 [f(R)-f(\zeta)]\frac{dx}{x^2}\right\}$$

where

$$R \equiv \sqrt{x^2 + (1-x^2)\,\zeta^2} = \sqrt{\zeta^2 + (1-\zeta^2)\,x^2} \tag{17}$$

Taking formula (17) as a starting point, we may derive an analytical expression of the inverse transform, based on derivatives of $f(\zeta)$, namely

$$\begin{aligned} g(\zeta) = \frac{2}{\pi}\Big\{ & (1-\zeta^2)^{-1/2} f(\zeta) - \frac{1}{2}\,\frac{(1-\zeta^2)^{1/2}}{\zeta}\,f'(\zeta) + \frac{1}{24}\,\frac{(1-\zeta^2)^{3/2}}{\zeta^3}[f'(\zeta)-\zeta f''(\zeta)] - \\ & - \frac{1}{80}\,\frac{(1-\zeta^2)^{5/2}}{\zeta^5}\left[f'(\zeta) - \zeta f''(\zeta) + \frac{1}{3}\,\zeta^2 f'''(\zeta)\right] + \\ & + \frac{5}{896}\,\frac{(1-\zeta^2)^{7/2}}{\zeta^7}\left[f'(\zeta) - \zeta f''(\zeta) + \frac{2}{5}\,\zeta^2 f'''(\zeta) - \frac{1}{15}\,\zeta^3 f^{IV}(\zeta)\right] - \ldots\Big\} \end{aligned} \tag{18}$$

$\zeta \neq 0$, $\zeta \neq 1$

$$g(0) = \frac{2}{\pi}\left\{f(0) - \frac{1}{1.2!}\,f''(0) - \frac{1}{2.3!}\,f'''(0) - \frac{1}{3.4!}\,f^{IV}(0) - \ldots\right\}$$

When $f(\zeta) = \sqrt{1-\zeta^2}$ one obtains

$$g(\zeta) = g(0) = \frac{2}{\pi}\left(1 + \frac{1}{2} + \frac{1}{24} + \frac{1}{80} + \frac{5}{896} + \frac{7}{2304} + \dots\right) \simeq 1 .$$

The most efficient result to be derived from the integral (13) is the following one. If

$$g(\tau) = \sum_{0}^{n}{}_{j}\, b_j (1-\tau^2)^{\lambda_j}, \tag{19}$$

where b_j and λ_j are 2n arbitrary parameters, then

$$f(\zeta) = \sum_{0}^{n}{}_{j}\, a_j (1-\zeta^2)^{\lambda_j + \frac{1}{2}} \quad , \qquad a_j = b_j \mu_j \quad ; \quad \mu_j = \frac{\sqrt{\pi}}{2} \cdot \frac{\Gamma(\lambda_j + 1)}{\Gamma(\lambda_j + \frac{3}{2})} \tag{20}$$

Conversely, if $f(\zeta)$ is given under the form (20) then $g(\tau)$ is obtained under the form (19), the coefficients b_j being $b_j = a_j/\mu_j$. This suggestsa powerful method of performing the inverse Abel transform on the following line of reasoning: the smoothing out of empirical data should be globally and analytically performed in such a way as for delivering us an expression of the form (20). The coefficients A_j are obtained as a result of the smoothing out process all over the range $(0 < x < 1)$. For the sake of simpliness we adopt the following expression of λ_j

$$\lambda_j = \lambda - \frac{1}{2} + j \tag{21}$$

Thus

$$f(\zeta) = \sum_{0}^{n}{}_{j}\, a_j (1-\zeta^2)^{\lambda + j}$$

$$= q^{\lambda}\left[a_0 + a_1 q + a_2 q^2 + a_3 q^3 + a_4 q^4 + a_5 q^5 + \dots\right] \qquad q \equiv (1-\zeta^2) \tag{22}$$

$$g(\tau) = \sum_{0}^{n}{}_{j}\, \frac{2}{\sqrt{\pi}} \cdot \frac{\Gamma(\lambda + j + 1)}{\Gamma(\lambda + j + \frac{1}{2})}\, a_j (1-\tau^2)^{\lambda + j - \frac{1}{2}}$$

For $\lambda = 0$, $g(\tau)$ acquires the simple expression

$$g(\tau) = \frac{2}{\pi} a_0 \eta^{-\frac{1}{2}} + \frac{4}{\pi} a_1 \eta^{+\frac{1}{2}} + \frac{16}{3\pi} a_2 \eta^{3/2} + \frac{32}{5\pi} a_3 \eta^{5/2}$$
$$+ \frac{256}{35\pi} a_4 \eta^{7/2} + \frac{512}{63\pi} a_5 \eta^{9/2} + \dots \qquad \eta \equiv (1-\tau^2) \tag{23}$$

For $\lambda = \frac{1}{2}$ one obtains

$$g(\tau) = a_0 + \frac{3}{2} a_1 \eta + \frac{15}{8} a_2 \eta^2 + \frac{35}{16} a_3 \eta^3 + \frac{315}{128} a_4 \eta^4 + \frac{693}{256} a_5 \eta^5 + \dots$$

In this way, the problem of evaluating the inverse Abel transform is reduced to the problem of performing a global analytical smoothing out. There are, in principle, two possible ways to work out a smoothing problem - either by applying the Gauss least square method, which leads to calculation of high order determinants and (for this reason) to an ill conditioned problem, or by resorting to the orthogonal function method (in principle, equivalent to the first one), which exhibits the main difficulty of non-existence, in the literature of applied mathematics, of a set of orthogonal polynomials, defined on the domain (0,1) and having definite mathematical properties. Facing these difficulties, we however chose the second alternative and gave an almost ideal solution as may be seen in the sequel. We succeeded to reach the following outstanding result: being given a certain analytical and bounded function defined on the domain (0,1), it is always possible to find a polynomial approximation optimizing the integral of the function on the respective interval (polynomization). The approximation is obtained by applying a standard mathematical formula and is equivalent - under given restrictions - to the homologous approximation coming from the least square method.

Smoothing out by means of orthogonal polynomials

Let us consider an analytical and bounded function f(x), defined on the domain $-1 \le x \le +1$, and whose parity (under reflection $x \to -x$) is not specified. We may write

$$f(x) \equiv \frac{1}{2}[f(+x)+f(-x)] + \frac{1}{2}[f(+x)-f(-x)] \tag{24}$$

It may be expanded (as an accepted approximation) in a finite series of Legendre polynomials

$$f(x) = \sum_{r=1}^{N} A_r \bar{P}_r(x) + \sum_{s=0}^{N} B_s \bar{P}_{2s+1}(x), \tag{25}$$

where

$$\begin{gathered}\bar{P}_n(x) = \sqrt{n+\frac{1}{2}}\,P_n(x), \qquad P_n(x) = \frac{1}{2^n \cdot n!}\,\frac{d^n(1-x^2)^n}{dx^n} \\ \int_{-1}^{+1} \bar{P}_n(x)\bar{P}_m(x) = \delta_{nm}, \quad \bar{P}_n(-x) = (-1)^m \bar{P}_n(+x)\end{gathered} \tag{26}$$

The coefficients A_r and B_s may be determined by resorting to the orthogonality of Legendre polynomials. We first obtain

$$\frac{1}{2}\int_{-1}^{+1}[f(+x)+f(-x)]\bar{P}_l(x)dx + \frac{1}{2}\int_{-1}^{+1}[f(+x)-f(-x)]\bar{P}_l(x)dx =$$

$$\sum_{r=0}^{N} A_r \delta_{2r,l} + \sum_{s=0}^{N} B_s \delta_{2s+1,l}$$

whence, by specifying $l = 2\nu$, or $l = 2\nu+1$, respectively

$$A_\nu = \frac{1}{2}\int_{-1}^{+1}[f(+x)+f(-x)]\bar{P}_{2\nu}(x)dx = \int_{0}^{1}[f(+x)+f(-x)]\bar{P}_{2\nu}(x)dx$$

$$B_\nu = \frac{1}{2}\int_{-1}^{+1}[f(+x)-f(-x)]\bar{P}_{2\nu+1}(x)dx = \int_{0}^{1}[f(+x)-f(-x)]\bar{P}_{2\nu+1}(x)dx$$

Further on, we need information about the parity of f(x). In absence of any information of this kind (which often happens to be the case for empirical functions) we put forward two plausible conjectures

$$\begin{array}{llll} \text{1-st:} & f(x) = f'(0)x + F(x), & F(-x) = +F(+x) & \text{(case a)} \\ \text{2-nd:} & f(x) = f(0) + G(x), & G(-x) = -G(+x) & \text{(case b)} \end{array} \tag{28}$$

Now, the coefficients of the Legendre expansions may be easily evaluated and, accordingly, we may write

(case a)

$$A_\nu = 2\int_0^1 [f(x)-f'(0)x]\bar{P}_{2\nu}(x)dx, \quad B_0 = 2f'(0)\int_0^1 x\bar{P}_1(x)dx$$

$$= \sqrt{\tfrac{2}{3}}\, f'(0), \quad B_\nu = 0, \quad (\nu > 0)$$

$$f(x) = xf'(0) + \sum_{0}^{N}{}_r\, \bar{P}_{2r}(x)2\int_0^1 [f(x)-f'(0)x]\bar{P}_{2r}(x)dx \tag{29a}$$

(case b)

$$A_0 = 2f(0)\int_0^1 \bar{P}_0(x)dx = \sqrt{2}\, f(0), \quad A_\nu = 0, \quad (\nu > 0)$$

$$B_\nu = 2\int_0^1 [f(x)-f(0)]\bar{P}_{2\nu+1}(x)dx$$

$$f(x) = f(0) + \sum_{0}^{N}{}_s\, \bar{P}_{2s+1}(x)2\int_0^1 [f(x)-f(0)]\bar{P}_{2s+1}(x)dx \tag{29b}$$

The approximations in the two cases (a,b) ensure the continuity of the function and of its first derivative at x = 0.

It may be demonstrated that Legendre (polynomial) expansion is equivalent with Gauss (least square) method.

If we want to perform the inverse Abel transform, then, the case (a) is to be preferred rather than the case (b) and the condition f(1) = 0 must be adopted. Let us assume that $f(x) \propto (1-x)^\lambda$ in the proximity of x = 1. Then, we adopt the alternative conjectures

$$\left.\begin{array}{lll} f(x) = (1-x^2)^\lambda [f'(0)x+F(x)], & F(-x) = F(+x) & \text{(case a')} \\ f(x) = (1-x^2)^\lambda [f(0)+G(x)], & G(-x) = -G(+x) & \text{(case b')} \end{array}\right\} \lambda > 0 \tag{30}$$

The parameter λ may be determined only by knowing again some additional information about f(x). When no such information is available, the value $\lambda = \frac{1}{2}$ is to be preferred instead of the value $\lambda = 0$ (unconditioned optimizing) which leads to excessive distortion of the inverse Abel transform at the edge x = 1. Now, the approximation formulas become

$$f(x) = (1-x^2)^\lambda \left\{ f'(0)x + \sum_{0}^{N}{}_r\, \bar{P}_{2r}(x)2\int_0^1 \left[\frac{f(x)}{(1-x^2)^\lambda} - f'(0)x\right]\bar{P}_{2r}(x)dx \right\}$$

$$f(x) = (1-x^2)^\lambda \left\{ f(0) + \sum_{0}^{N}{}_s \bar{P}_{2s+1}(x) 2\int_0^1 \left[\frac{f(x)}{(1-x^2)^\lambda} - f(0)\right]\bar{P}_{2s+1}(x)dx \right\} \tag{31}$$

The continuity conditions (for f(x) and f'(x)) at x = 0 are, in the cases (a',b') too, preserved. (Moreover, the second derivative at x = 0 acquires a correct value in the case of even approximation.)

For even approximation, the function f(x) is obtained under the form

$$f(x) = f'(0)\,x\cdot(1-x^2)^\lambda + \sum_{0}^{N}{}_r a_r (1-x^2)^{r+\lambda} \tag{32}$$

and the inverse Abel transform may be easily obtained for f'(0) = 0. Our first task is to obtain an analytical expression for a_r. In this purpose, we introduce new polynomials $Z_l(\lambda)$ related to even Legendre polynomials

$$Z_l(\lambda) = P_{2l}(x) \quad , \quad \lambda = x^2 \tag{33}$$

and obeying a certain differential equation which may be derived from the differential equation of Legendre polynomials by operating there the necessary changes of index and argument

$$\lambda(1-\lambda)\frac{d^2 Z_l(\lambda)}{d\lambda^2} + \left(\frac{1}{2} - \frac{3}{2}\lambda\right)\frac{dZ_l(\lambda)}{d\lambda} + l\left(l + \frac{1}{2}\right)Z_l(\lambda) = 0 \tag{34}$$

The solution of this equation turns out to be

$$Z_l(\lambda) = \sum_{0}^{l}{}_j (-1)^{l-j} 2^{-2l} \frac{[2(l+j)]!}{(l-j)!(l+j)!(2j)!}\lambda^j \equiv \sum_{0}^{l}{}_j (-1)^{l-j} \gamma_j^l \lambda^j \tag{35}$$

It is now opportune to define a new variable (suggested by formula (32)) and, acccordingly, new polynomials, namely

$$\Omega_l(q) = Z_l(\lambda) \quad , \quad q = 1-\lambda \tag{36}$$

The new polynomials satisfy the differential equation

$$q(1-q)\frac{d^2\Omega_l(q)}{dq^2} + \left(1 - \frac{3}{2}q\right)\frac{d\Omega_l(q)}{dq} + l\left(l + \frac{1}{2}\right)\Omega_l(q) = 0 \tag{37}$$

whose solution is

$$\Omega_l(q) = \sum_{0}^{l}{}_j (-1)^j \frac{l!}{j!(l-j)!}\frac{\Gamma(l + j + \frac{1}{2})}{j!\,\Gamma(l + \frac{1}{2})} q^j \equiv \sum_{0}^{l}{}_j (-1)^j \alpha_j^l q^j$$

$$= 1 - \frac{1}{(1!)^2} l\cdot\left(l + \frac{1}{2}\right)q + \frac{1}{(2!)^2} l(l-1)\cdot\left(l + \frac{1}{2}\right)\left(l + \frac{3}{2}\right)q^2 - \frac{1}{(3!)^2} l(l-1)(l-2) \tag{38}$$

$$\cdot\left(l + \frac{1}{2}\right)\left(l + \frac{3}{2}\right)\left(l + \frac{5}{2}\right)q^3 + \ldots + \frac{(-1)^l}{l!}\left(l + \frac{1}{2}\right)\left(l + \frac{3}{2}\right)\left(l + \frac{5}{2}\right)\ldots\left(2l - \frac{1}{2}\right)q^l$$

Now, let us consider a function $\tilde{\phi}(q)$. It may be approximated by a finite series of $\{\Omega_l\}$ polynomials

$$\Phi(q) \quad \sum_{0}^{N}{}_{l}\, C_l \Omega_l(q) \quad , \quad C_l = (4l+1)\int_{0}^{1} \varphi(x) Z_l(x^2)\,dx \quad , \quad \varphi(x) \equiv \Phi(1-x^2) \tag{39}$$

But, by the very process of this approximation, $\Omega_l(q)$ became a polynomial of N-th degree of the argument q, and we need to determine the coefficients of this polynomial

$$\Phi(q) = \sum_{0}^{N}{}_{l}\, C_l \left\{ \sum_{0}^{l}{}_{j} (-1)^j \alpha_j^l q^j \right\} \equiv \sum_{0}^{N}{}_{s}\, \beta_s q^s \quad , \quad \beta_s = (-1)^s \sum_{0}^{N-s}{}_{k}\, C_{s+k} \alpha_s^{s+k} \tag{40}$$

Keeping in mind that the C-coefficients are related - through the intermediary of Z-polynomials -to the γ -coefficients, we may equally write

$$\beta_s = (-1)^s \int_{0}^{1} P_N^{(s)}(x^2)\, \varphi(x)\,dx$$

$$P_N^{(s)}(x^2) = \sum_{s}^{N}{}_{k} \sum_{0}^{k}{}_{j} (-1)^{k+j} (4k+1)\, \alpha_s^k \gamma_j^k x^{2j} \equiv \sum_{0}^{N}{}_{l}\, \Gamma_{Ns}^{l} x^{2l} \tag{41}$$

$$\Phi(q) = \sum_{0}^{N}{}_{s} (-1)^s q^s \int_{0}^{1} P_N^{(s)}(x^2)\, \varphi(x)\,dx$$

It remained to us to determine the Γ -coefficients of the P-polynomials. The technique used in this purpose is the same as for the β -coefficients (although a little more complicated) - i.e. to calculate the coefficient of a given power of the argument. One obtains

$$\Gamma_{Ns}^{l} = \begin{cases} (-1)^{s+1} \sum\limits_{0}^{N-s}{}_{j} (-1)^j [4(s+j)+1]\, \alpha_s^{s+j} \gamma_l^{s+j} \quad , & l \leq s \\ \sum\limits_{0}^{N-s}{}_{j} (-1)^j [4(l+j)+1]\, \alpha_s^{l+j} \gamma_l^{l+j} \quad , & l \geq s \end{cases} \tag{42}$$

In our case

$$\varphi(x) = \left\{ \frac{f(x)}{(1-x^2)^{\lambda}} - f'(0)x \right\} \tag{43}$$

and, accordingly,

$$a_r = (-1)^r \int_{0}^{1} P_N^{(r)}(x^2) \left\{ \frac{f(x)}{(1-x^2)^{\lambda}} - f'(0)x \right\} dx \tag{44}$$

The smoothing out problem is thus reduced to the problem of evaluating the integrals in (44). The final optimization formula is

$$f(x) = f'(0)x(1-x^2)^{\lambda} + \sum_{0}^{N} r(-1)^{r}(1-x^2)^{r+\lambda} \int_{0}^{1} P_N^{(r)}(x^2)\left\{\frac{f(x)}{(1-x^2)^{\lambda}} - f'(0)x\right\}dx \tag{45}$$

The first polynomials $Z_l(\lambda)$, [illegible]$_l(q)$ and $P_N(\lambda)$ are given in addenda.

In practical applications, the (inverse) Abel transform is connected to some physical quantities, as for Instance the refractive index distribution, which must be everywhere finite. This entails the additional condition

$$f'(0) = 0 \tag{46}$$

Polynomial oscillations

The most serious difficulty, we come across when we apply least square method or (equivalently) the orthogonal polynomial method is the occurence of polynomial oscillations. No general method exists at present to avoid these undesired oscillations, although some indications, to be respected in view of minimizing them, may be formulated. Let us, for instance, consider the function $f(x) = x$. If we want to approximate it by even Lagrange polynomials, then we have to interpret it as the right branch $(0 < x < 1)$ of the even function $F(x) = \sqrt{x^2}$, defined on the domain $(-1 < x < 1)$. What is really approximated in this case is the function $F(x)$, whose derivative is not continuous at $x = 0$. Indeed, $\lim_{x\to 0}\{F'(+x) - F'(-x)\} = 2\frac{x}{|x|} = 2 \neq 0$. As a consequence, the approximant

$$\begin{aligned} f(x) = x \approx{} & +1.020508 - 1.187012\, q + 5.201904\, q^2 - 15.727905\, q^3 \\ & + 19.381674\, q^4 - 8.633655\, q^5 = +0.055514 + 3.608498\, x^2 \\ & - 12.028317\, x^4 + 24.537759\, x^6 - 23.786601\, x^8 + 8.633655\, x^{10} \equiv \tilde{f}(x) \end{aligned} \tag{47}$$

where $q = 1 - x^2$, exhibits large polynomial oscillations (especially in the proximity of zero). The increase of the approximation order gives no significant improvement, the convergence process being slow. Indeed, the next approximation

$$\begin{aligned} f(x) = x \approx{} & \frac{14,105}{14,336} + \frac{247}{1,024}\, q - \frac{134,147}{16,384}\, q^2 + \frac{71,383}{2,048}\, q^3 - \frac{18,538,585}{262,144}\, q^4 \\ & + \frac{8,788,507}{131,072}\, q^5 - \frac{50,702,925}{2,097,152}\, q^6 \end{aligned} \tag{47'}$$

only slightly changes the maximal departures ascertained in the previous approximation ($f(0) = 0.047254$ instead of $f(0) = 0.055514$). Nevertheless, such an approximation is not altogether destituted of certain practical virtues - these actually depending on the destination assigned to the respective approximant. If we want to use expression (47) for calculating the inverse Abel transform, we will obtain very wrong results, for the Abel transform is a typical operation amplifying the polynomial oscillations (a kind of undesired "mathematical laser"). Contrarily, the respective approximant is quite adequate for calculating the integral of f(x), for the integral is a typical operation damping the polynomial oscillations (a kind of welcome "mathematical anti-laser"). Indeed, proceeding from (47) we may derive the useful and "accurate" formula

$$x^2 \approx +0.111\,028\,x + 2.405\,666\,x^3 - 4.811\,326\,x^5 + 7.010\,788\,x^7 - 5.285\,912\,x^9 + 1.569\,756\,x^{11} \quad (48)$$

Another useful example is the approximation of the circle. Let us ignore the true value of the parameter λ ($\lambda = \frac{1}{2}$) (which would lead to the tautologic expression $F(x) = \sqrt{1-x^2}$) and assume $\lambda = 0$. This leads to the "polynomization" of the circle

$$F(x) = \pm\sqrt{1-x^2} \approx \pm\{0.087203 + 2.834104\,q - 7.085261\,q^2 + 12.044944\,q^3 - 10.216693\,q^4 + 3.337453\,q^5\} = \pm\{1.001750 - 0.618907\,x^2 + 1.123943\,x^4 - 4.552702\,x^6 + 6.470572\,x^8 - 3.337453\,x^{10}\} \quad (49)$$

Proceeding from (49), we may calculate the inverse Abel transform of $\sqrt{1-x^2}$. The rigorous result must be 1. One obtains

$$g(x) = 1 \approx 0.055515\,q^{-1/2} + 3.608493\,q^{+1/2} - 12.028313\,q^{3/2} + 24.537758\,q^{5/2} - 23.786601\,q^{7/2} + 8.633655\,q^{9/2} \equiv \tilde{g}(x) \quad (50)$$

Now, let us compare (47) to (50). We ascertain the fulfilment of the relationship

$$x\tilde{g}(\sqrt{1-x^2}) = \tilde{f}(x) \quad (51)$$

which is the same connection between the approximants of the functions g(x) and f(x) as between these (exact) functions. The polynomial oscillations of F(x) in (49) (defined as oscillations of the approximated radius of the circle) do not exceed, in their amplitude, about 3×10^{-3}, while the polynomial oscillations of g(x) in (50) have an amplitude up to 2×10^{-2} in the interval $0 < x < 0.96$ and up to 9×10^{-2} in the interval $0 < x < 0.98$. The divergence of g(x) for $x \to 1$ is a consequence of ignoring the true value of the λ parameter. (This divergence, however, is not too dramatic - the amplitude of oscillations amounting to 13×10^{-7} in the interval $0 < x < 0.998$.)

When all the analyticity conditions at x = 0 and x = 1 are fulfilled, we expect to have a minimizing of the polynomial oscillations. Such an example may be prepared as follows. Let us consider the function $y(x) = 1 - x^2$. By adopting for λ the value $\lambda = \frac{1}{2}$, we obtain the approximant

$$f(x) = 1-x^2 \approx 0.087203\,q^{1/2} + 2.834104\,q^{3/2} - 7.085261\,q^{5/2} + 12.044944\,q^{7/2} - 10.216693\,q^{9/2} + 3.337453\,q^{11/2} \quad (52)$$

which satisfies the conditions: $y(1) = 0$, $y'(0) = 0$. The inverse Abel transform of y(x) is $g(x) = \frac{4}{\pi}\sqrt{1-x^2}$, whence we obtain a new approximation of the circle

$$\sqrt{1-x^2} \approx 0.068489 + 3.338850\, q - 10.433908\, q^2 + 20.693918\, q^3 - 19.746985\, q^4 + 7.095750\, q^5 \tag{53}$$

On the other hand, formula (52) may be regarded as a new approximation of the function $y(x) = x$

$$y(x) = x \approx 0.087203\, x^{1/2} + 2.834104\, x^{3/2} - 7.085261\, x^{5/2} + 12.044944\, x^{7/2} - 10.216693\, x^{9/2} + 3.337453\, x^{11/2} \tag{54}$$

whose polynomial oscillations are much decreased as compared to the oscillations of the approximants (47) or (47'). At the same time, the approximant (53) for the circle is almost comparable to the approximant (49). The pair of functions (52), (53), connected one to another through an Abel transform, is an example of how polynomial oscillations may be decreased (but not suppressed) by correctly establishing the limiting conditions.

Working out an empirical example

When we go over from the problem of "polynomizing" and Abel transform of a certain analytical function to the problem of Abel transform of a certain empirical function, known (with a certain error) only in few (eventually non-equidistant) points we come across specific aspects preventing us from the confortable applying of a standard method. We illustrate the situation on an experimental set of data kindly delivered by Dr. Ileana Apostol.

x	f(x)	x	f(x)	x	f(x)
0.0000	(-1.94)	0.5204	- 0.39	0.8777	+ 0.71
0.1607	- 0.81	0.6187	0.00	0.9113	+ 0.71
0.3189	- 0.77	0.6787	+ 0.65	0.9592	+ 0.48
0.4005	- 0.71	0.7986	+ 1.03	1.0000	0

(The data represent the shifts of the 16-th frange in an experiment aiming at evaluating the electron density in a laser produced plasma.) We first made a diagram of the data and concluded that the value f(0) = -1.94 is, presumably, much altered by uncontrolled errors. According to the convention about to unprobable events, we eliminated this value and replaced it by f(0) = -0.85 as suggested by the diagram. Thereafter, we ascertain that the conditions f'(0) = 0, f(1) = 0 are fulfilled. In principle, we may now apply the standard optimizing method (either in the least square version or in the orthogonal polynomial one) having in mind the following difficulties: 1) owing to the small number of experimental points, polynomial oscillations of undesired amplitude will be introduced during the smoothing out process; 2) the artificial increasing of the number of points may introduce unrealistic variations in the curvature with the same undesired consequences for the Abel transform. Under the given circumstances, the most reasonable attitude seems to be that of a global examination of the diagram, out of which we may obtain the additional information: 1) The function f(x) has a high order contact at x = 0; 2) In the interval 0 < x < 1, f(x) has a single maximum whose coordinate and abscissa may be graphically estimated. Accordingly, we adopt the trial expression

$$f(x) = a_1(x^{2n+2}-1) + a_2(x^{2n+4}-1) + a_3(x^{2n+6}-1) \tag{55a}$$

The coefficients (a_1, a_2, a_3) are determined by the conditions $f(0) = f_0$, $f'(x_1) = 0$, $f(x_1) = f_1$, while the parameter n stands for ensuring the high contact at $x = 0$ and, at the same time a general fitting of the curve. Taking $n = 1,2,3$ we conclude that the best fitting is obtained for $n = 2$, namely

$$a_1 = 47.30360 \quad , \quad a_2 = -91.35796 \quad , \quad a_3 = +44.90436 \tag{55b}$$

In view of performing the Abel transform, we have to go from x to q variable ($q = 1 - x^2$)

$$\begin{aligned} f(x) = {} & -1.00076\ q + 42.80664\ q^2 - 130.91536\ q^3 \\ & + 133.16334\ q^4 - 44.90436\ q^5 \end{aligned} \tag{56}$$

The Abel transform is now easily to perform by applying formula (23) ($\lambda = 0$, $a_0 = 0$)

$$\begin{aligned} g(x) = {} & -1.27421\ q^{1/2} + 72.67081\ q^{3/2} - 266.69858\ q^{5/2} \\ & + 310.03331\ q^{7/2} - 116.16306\ q^{9/2} \end{aligned} \tag{57}$$

The physical meaning of g(x) is delivered by the relation

$$g(x) = 2\left[n(x)-1\right]\frac{R}{\lambda} \quad , \quad x = \frac{r}{R} \tag{58}$$

where R is the radius of the cylindrical plasma, n - the refractive index of the plasma, λ the laser wave length (used for obtaining the interferometric pattern) and r the distance from the plasma axis in a perpendicular plane. As the polynomial oscillations are completely avoided and the smoothed out curve systematically reproduces the trend of empirical data, the results (56 - 57) are the best ones obtained with a quite small number of parameters. To use more parameters (this implying necessarily the increase of time spent for mathematical processing of data) becomes opportune only when (by specifying the errors of all the empirical data) we decide to consider as relevant other details of the experimental curve.

Concerning the mechanism of avoiding the polynomial oscillations, we observe that expression (56) of f(x), which has the form (40) and, in principle, contains 6 coefficients (β_0, β_1, β_2,..., β_5) to be determined, was actually evaluated only by using the three coefficients (a_1, a_2, a_3) in (55b). Accordingly, $\beta_0 = 0$ and $\beta_k = \beta_k(a_1, a_2, a_3)$ $k = 1,2,...,5$. We may formulate the following conjecture. Avoiding the polynomial oscillations is equivalent to establishing certain constraints among the coefficients of smoothed out approximant, which may take the form of some parametric dependences.

Determining the coefficients β_k

When no additional information may be obtained in view of avoiding the polynomial oscillations, it remains to us only to evaluate, using mechanical quadrature methods, the integrals in (45). If the function f(x) is given for equidistant values of its argument, then it is recommended to use Gregory-type formulas (modified for suppressing high order finite differences which may accumulate errors)

$$\frac{1}{b-a}\int_a^b F(x)dx = \frac{1}{N}\Big\{\sum_{0}^{N}{}_j\, F\Big(a+j\,\frac{b-a}{N}\Big) - \sum_{0}^{n}{}_l\,(-1)^l C_l^{(n)}\Big[F\Big(a+l\,\frac{b-a}{N}\Big) + F\Big(b-l\,\frac{b-a}{N}\Big)\Big] \tag{59a}$$

The values of the coefficients $C_\ell^{(n)}$ are given as rational numbers

(59b)

$n = 2$

$C_0^{(2)} = \frac{5}{8}$, $C_1^{(2)} = \frac{1}{6}$, $C_2^{(2)} = \frac{1}{24}$

$n = 4$

$C_0^{(4)} = \frac{965}{1440}$, $C_1^{(4)} = \frac{462}{1440}$, $C_2^{(4)} = \frac{336}{1440}$, $C_3^{(4)} = \frac{146}{1440}$, $C_4^{(4)} = \frac{27}{1440}$

$n = 6$

$C_0^{(6)} = \frac{84161}{120960}$, $C_1^{(6)} = \frac{55688}{120960}$, $C_2^{(6)} = \frac{66109}{120960}$, $C_3^{(6)} = \frac{57024}{120960}$,

$C_4^{(6)} = \frac{31523}{120960}$, $C_5^{(6)} = \frac{9976}{120960}$, $C_6^{(6)} = \frac{1375}{120960}$

If the function f(x) is given for non-equidistant abscissas no longer we have at our disposal very accurate estimation methods. However, good results are obtained by using Simpson parabolic rule for arbitrary intervals.

$$\int_{x_1}^{x_N} y(x)dx = \sum_{1}^{N-2}{}_k \int_{x_k}^{x_{k+1}} y(x)dx + \int_{x_{N-1}}^{x_N} y(x)dx \approx \sum_{1}^{N-2}{}_k \Big\{\frac{1}{2}(y_k+y_{k+1})\Delta x_k - \frac{1}{6}\cdot\frac{\Delta\big(\frac{\Delta y_k}{\Delta x_k}\big)}{\Delta x_k+\Delta x_{k+1}}\cdot(\Delta x_k)^3\Big\} + y_{N-1}\Delta x_{N-1} + \frac{1}{2}\frac{\Delta y_{N-2}}{\Delta x_{N-2}}(\Delta x_{N-1})^2 + \frac{1}{6}(3\Delta x_{N-2}+2\Delta x_{N-1})\cdot\frac{\Delta\big(\frac{\Delta y_{N-2}}{\Delta x_{N-2}}\big)}{\Delta x_{x-2}+\Delta x_{N-1}}\cdot(\Delta x_{N-1})^2 \tag{60}$$

where $\Delta x_k = x_{k+1} - x_k$, $\Delta y_k = y_{k+1} - y_k = y(x_{k+1}) - y(x_k)$. Formula (60) is quite efficient when the differences Δx_k do not differ too much from one to another and the number N of integration points is sufficiently large. It is also possible to increase (by interpolation) the number of points with the aid of formulas

$$y_{k+\frac{1}{2}} \approx \frac{1}{2}(y_{k+1}+y_k) - \frac{1}{4}\,\frac{(\Delta x_k)^2}{\Delta x_k+\Delta x_{k+1}}\,\Delta\left(\frac{\Delta y_k}{\Delta x_k}\right) \qquad k = 1, \dots N-2$$

$$y_{N-\frac{1}{2}} \approx y_{N-2} + \frac{1}{2}(x_N+x_{N-1}-2x_{N-2})\frac{\Delta y_{N-2}}{\Delta x_{N-2}} + \frac{1}{4}(x_N+x_{N-1}-2x_{N-2})\frac{\Delta x_{N-1}}{\Delta x_{N-2}+\Delta x_{N-1}}\,\Delta\left(\frac{\Delta y_{N-2}}{\Delta x_{N-2}}\right) \tag{61}$$

in view of improving the graphical representation of experimental data (and, eventually, of observing additional features of the curve useful for avoiding polynomial oscillations). After the increase of number of experimental points by using formula (61) (if necessary even many times) the integrals of the form

$$\int_0^1 P_N^{(r)}(x^2)\,y(x)\,dx$$

are evaluated by using formula (60) for $Y(x) = P_N^{(r)}(x)y(x)$. During this evaluation process the random experimental errors of $y(x)$ are automatically avoided.

A D D E N D A

I. Equivalence between least square method and the orthogonal polynomial method

We proceed from the functionals

$$\int_0^1 [f(\zeta) - \sum_0^r{}_l\; C_l\Omega_l(q)]^2 d\zeta = F(r;C_k) \quad , \quad (k = 0, 1, 2, \dots r) \tag{1,a}$$

$$\int_0^1 [f(\zeta) - \sum_0^r{}_l\; a_l q^l\,]^2 d\zeta = (r;a_k) \quad , \quad (k = 0, 1, 2, \dots r) \tag{1,b}$$

and require their optimization

$$\frac{\partial F}{\partial C_k} = 0 \quad , \quad \frac{\partial \Phi}{\partial a_k} = 0 \quad , \quad (k = 0, 1, 2, \dots r) \tag{2}$$

whence

$$C_k = (4k+1)\int_0^1 f(\zeta)\Omega_k(q)\,d\zeta \quad , \quad \int_0^1 f(\zeta)q^k d\zeta = \sum_0^r{}_l\; a_l\int_0^1 q^{l+k}d\zeta \tag{3}$$

But, because $f(\zeta) = \sum_0^r{}_l\; C_l\Omega_l(q)$ we obtain in the particular case $f(\zeta) = q^k$

$$q^k = \sum_0^k{}_l\left\{(4l+1)\int_0^1 q^k\Omega_l(q)\,d\zeta\right\}\Omega_l(q) \equiv \sum_0^k{}_l\; \tilde{C}_l\Omega_l \tag{4}$$

The second formula in (3) may now be written

$$\sum_{0}^{r} {}_{l}\, a_r \int_0^1 q^{l+k} d\zeta = \sum_{0}^{k} {}_{l} \left\{ \int_0^1 q^k \Omega_l(q)\, d\zeta \right\} \left\{ (4l+1) \int_0^1 f(\zeta)\Omega_l(q)\, d\zeta \right\} = \sum_{0}^{k} {}_{l}\, C_l \int_0^1 q^k \Omega_l(q)\, d\zeta \qquad (5)$$

Therefore, (from (5) and (3)) we have

$$\int_0^1 f(\zeta) q^k d\zeta = \int_0^1 q^k \sum_{0}^{k} {}_{l} C_l \Omega_l(q)\, d\zeta \qquad (6)$$

At the same time, expanding f(ζ) in Ω -series we have as well

$$\int_0^1 f(\zeta) q^k d\zeta = \int_0^1 q^k \sum_{0}^{r} {}_{l}\, C_l \Omega_l(q)\, d\zeta \qquad (6')$$

Formula (6) is a consequence of (1,b) combined with (1,a), while formula (6') is a consequence exclusively of (1,a). If the methods (1,a) and (1,b) are equivalent, then the formulas (6) and (6') must be equivalent as well. Subtracting, part by part, (6') from (6) we obtain

$$\int_0^1 q^k \sum_{k+1}^{r} {}_{l}\; C_l \Omega_l(q)\, d\zeta = 0$$

But this expression is indeed zero, because q^k may replaced by its expansion in (4)

$$\sum_{0}^{k} {}_{l'} \sum_{k+1}^{r} {}_{l}\; \tilde{C}_{l'} C_l \int_0^1 \Omega_{l'} \Omega_l\, d\zeta = \sum_{0}^{k} {}_{l'} \sum_{k+1}^{r} {}_{l}\; \tilde{C}_{l'} C_l \; \frac{\delta_{l'l}}{(4l+1)} \equiv 0$$

(To notice that the expression of q^k in (4) cannot contain Ω -polynomials of order higher than k, because always it is possible to express q^k as a linear combination of (whatsoever) polynomials of degree ranging from 0 to k (but not exceeding k !)) Q.E.D.

II. Generating function for Ω -polynomials and the first Ω -polynomials

$$\frac{1}{2}\left[(1 - 2z\sqrt{1-q} + z^2)^{-\frac{1}{2}} + (1 + 2z\sqrt{1-q} + z^2)^{-\frac{1}{2}} \right] = \sum_{0}^{\infty} {}_{j}\; \Omega_j(q) z^{2j}$$

$$\Omega_0(q) = 1 \,,\; \Omega_1(q) = 1 - \frac{3}{2}q \,,\; \Omega_2(q) = 1 - 5q + \frac{35}{8}q^2 ,$$

$$\Omega_3(q) = 1 - \frac{21}{2}q + \frac{189}{8}q^2 - \frac{231}{16}q^3 \,,\; \Omega_4(q) = 1 - 18q + \frac{297}{4}q^2 - \frac{429}{4}q^3 + \frac{6435}{128}q^4 \,,\; \Omega_5(q) = 1 - \frac{55}{2}q + \frac{715}{4}q^2 - \frac{3575}{8}q^3 + \frac{60775}{128}q^4 - \frac{46189}{256}q^5 \,,\; \Omega_6(q) = 1 - 39q + \frac{2925}{8}q^2 - \frac{5525}{4}q^3 + \frac{314925}{128}q^4 - \frac{529074}{256}q^5 + \frac{676039}{1024}q^6 ;$$

III. Generating function for Z-polynomials and the first Z-polynomials

$$\frac{1}{2}\left[(1 - 2z\sqrt{\lambda} + z^2)^{-\frac{1}{2}} + (1 + 2z\sqrt{\lambda} + z^2)^{-\frac{1}{2}}\right] = \sum_{0}^{\infty}{}_{j}\ Z_j(\lambda) z^{2j}$$

$$Z_0(\lambda) = 1 \ , \quad Z_1(\lambda) = \frac{3}{2}\lambda - \frac{1}{2} \ , \qquad Z_2(\lambda) = \frac{35}{8}\lambda^2 - \frac{15}{4}\lambda + \frac{3}{8}$$

$$Z_3(\lambda) = \frac{231}{16}\lambda^3 - \frac{315}{16}\lambda^2 + \frac{105}{16}\lambda - \frac{5}{16}$$

$$Z_4(\lambda) = \frac{6435}{128}\lambda^4 - \frac{12012}{128}\lambda^3 + \frac{6930}{128}\lambda^2 - \frac{1260}{128}\lambda + \frac{35}{128}$$

$$Z_5(\lambda) = \frac{46189}{256}\lambda^5 - \frac{109395}{256}\lambda^4 + \frac{90090}{256}\lambda^3 - \frac{30030}{256}\lambda^2 + \frac{3465}{256}\lambda - \frac{63}{256}$$

$$Z_6(\lambda) = \frac{676039}{1024}\lambda^6 - \frac{969969}{512}\lambda^5 + \frac{2078505}{1024}\lambda^4 - \frac{255255}{256}\lambda^3$$

$$+ \frac{225225}{1024}\lambda^2 - \frac{9009}{512}\lambda + \frac{231}{1024}$$

IV. The polynomials $P_n^{(r)}(x^2)$

N = 0

$$P_0^{(0)}(x^2) = 1$$

N = 1

$$P_1^{(0)}(x^2) = \frac{3}{2}(5x^2-1) \ ,$$

$$P_1^{(1)}(x^2) = \frac{15}{4}(3x^2-1)$$

N = 2

$$P_2^{(0)}(x^2) = \frac{15}{8}(21x^4-14x^2+1) \ ,$$

$$P_2^{(1)}(x^2) = \frac{105}{8}(15x^4-12x^2+1) \ ,$$

$$P_2^{(2)}(x^2) = \frac{315}{64}(35x^4-30x^2+3)$$

N = 3

$$P_3^{(0)}(x^2) = \frac{7}{16}(429x^6-495x^4+135x^2-5) \quad ,$$

$$P_3^{(1)}(x^2) = \frac{63}{32}(1001x^6-1265x^4+375x^2-15) ,$$

$$P_3^{(2)}(x^2) = \frac{63}{128}(9009x^6-11935x^4+3795x^2-165) \quad ,$$

$$P_3^{(3)}(x^2) = \frac{3003}{256}(231x^6-315x^4+105x^2-5)$$

N = 4

$$P_4^{(0)}(x^2) = \frac{45}{128}(2431x^8-4004x^6+2002x^4-308x^2+7)$$

$$P_4^{(1)}(x^2) = \frac{45}{64}(21879x^8-38038x^6+20020x^4-3234x^2+77)$$

$$P_4^{(2)}(x^2) = \frac{6435}{512}(5049x^8-9072x^6+4970x^4-840x^2+21)$$

$$P_4^{(3)}(x^2) = \frac{495}{512}(94809x^8-174174x^6+98280x^4-17290x^2+455)$$

$$P_4^{(4)}(x^2) = \frac{109395}{16384}(6435x^8-12012x^6+6930x^4-1260x^2+35)$$

N = 5

$$P_5^{(0)}(x^2) = \frac{33}{256}(29393x^{10}-62985x^8+46410x^6-13650x^4+1365x^2-21)$$

$$P_5^{(1)}(x^2) = \frac{2145}{512}(24871x^{10}-55233x^8+42126x^6-12810x^4+1323x^2-21)$$

$$P_5^{(2)}(x^2) = \frac{4290}{2048}(323323x^{10}-735471x^8+576198x^6-180390x^4+19215x^2-315)$$

$$P_5^{(3)}(x^2) = \frac{36465}{2048}(95095x^{10}-220077x^8+176022x^6-56490x^4+6195x^2-105)$$

$$P_5^{(4)}(x^2) = \frac{692835}{32768}(85085x^{10}-199485x^8+162162x^6-53130x^4+5985x^2-105)$$

$$P_5^{(5)}(x^2) = \frac{969969}{65536}(46189x^{10}-109395x^8+90090x^6-30030x^4+3465x^2-63)$$

N = 6

$$P_6^{(0)}(x^2) = \frac{91}{1024}(185725x^{12}-490314x^{10}+479655x^8-213180x^6 +42075x^4-2970x^2+33)$$

$$P_6^{(1)}(x^2) = \frac{105}{1024}(6277505x^{12}-16997552x^{10}+17043741x^8-7759752x^6 +1567995x^4-113256x^2+1287)$$

$$P_6^{(2)}(x^2) = \frac{23205}{8192}(2130375x^{12}-5874154x^{10}+6006033x^8-2791404x^6 +576345x^4-42570x^2+495)$$

$$P_6^{(3)}(x^2) = \frac{146965}{4096}(635375x^{12}-1776060x^{10}+1844271x^8-872256x^6 +183645x^4-13860x^2+165)$$

$$P_6^{(4)}(x^2) = \frac{440895}{131072}(12072125x^{12}-34106930x^{10}+35862255x^8-17213196x^6 +3687915x^4-284130x^2+3465)$$

$$P_6^{(5)}(x^2) = \frac{88179}{131072}(50702925x^{12}-144479192x^{10}+153481185x^8-74594520x^6 +16231215x^4-1275120x^2+15939)$$

$$P_6^{(6)}(x^2) = \frac{16900975}{1048576}(676039x^{12}-1939938x^{10}+2078505x^8-1021020x^6 +225225x^4-18018x^2+231)$$

V. Roots for the Tchebisheff-like integration formula

x_k (N = 63)

6.315049450(-3)	0.1491721923	0.2920293352	0.4348864780	0.5777436209	0.7206007637	0.8634579066
2.849866747(-2)	0.1713558103	0.3142129532	0.4570700960	0.5999272389	0.7427843818	0.8856415246
3.365987264(-2)	0.1765170155	0.3193741584	0.4622313012	0.6050884441	0.7479455869	0.8908027298
5.943527256(-2)	0.2022924154	0.3451495583	0.4880067011	0.6308638440	0.7737209868	0.9165781297
7.142857143(-2)	0.2142857143	0.3571428571	0.5000000000	0.6428571429	0.7857142857	0.9285714286
8.342187030(-2)	0.2262790132	0.3691361560	0.5119932989	0.6548504417	0.7977075846	0.9405647274
0.1091972702	0.2520544131	0.3949115559	0.5377686988	0.6806258416	0.8234829845	0.9663401274
0.1143584754	0.2572156182	0.4000727611	0.5429299040	0.6857870468	0.8286441897	0.9715013325
0.1365420934	0.2793992363	0.4222563791	0.5651135220	0.7079706648	0.8508278077	0.9936849505

VI. Angles for the Tchebisheff-like integration formula

1. 00°50'39".443
2. 03°48'46".099
3. 04°30'16".677
4. 07°58'17".774
5. 09°35'38".653
6. 11°13'27".610
7. 14°45'40".878
8. 15°28'33".960
9. 18°34'41".416
10. 20°22'09".174
11. 23°34'03".230
12. 24°19'21".173
13. 28°09'54".767
14. 30°00'00".000
15. 31°52'09".732
16. 36°01'27".145
17. 36°52'55".416
18. 40°41'14".622
19. 42°57'11".815
20. 47°09'08".168
21. 48°10'36".588
22. 53°38'38".303
23. 56°26'33".670
24. 59°27'53".485
25. 67°08'25".836
26. 68°59'15".504
27. 80°09'07".128

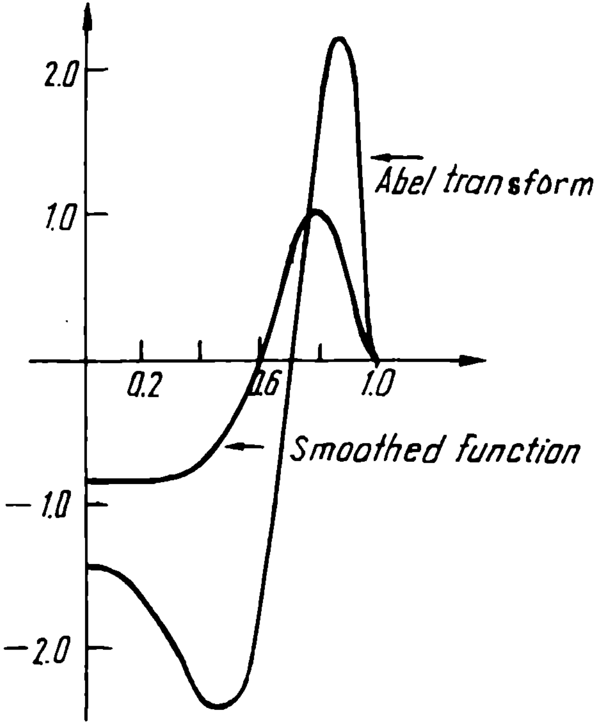

An empirical example

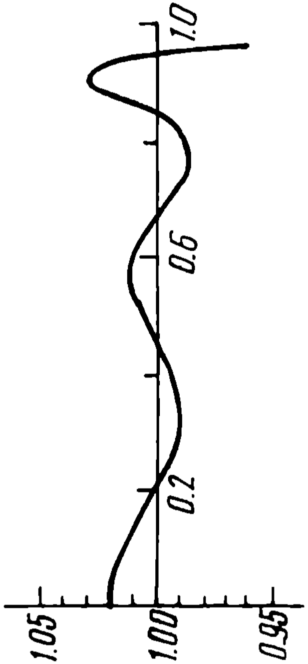

Polynomial oscillations in the Abel transf. of polynomized circle

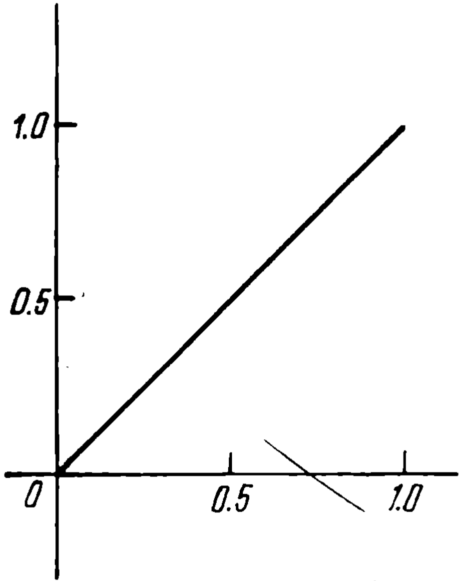

Polynomizing the line $y=x$ with an odd polynomial in $\sqrt{x}$

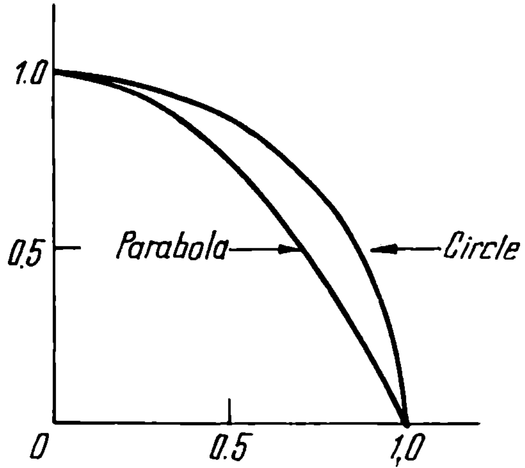

Approximating the parabola $y=1-x^2$ by an odd polynomial in $\sqrt{1-x^2}$ and performing its Abel transform

THE ROLE OF THE CROSS-RELAXATION MECHANISMS IN THE QUASISTATIONARY GENERATION REGIME OF THE YAG:Er LASER

S.Georgescu, V.Lupei, I.Ursu
Central Institute of Physics, Bucharest, ROMANIA
V.I.Zhekov, V.A.Lobachev, T.M.Murina, A.M.Prokhorov
Institute of General Physics, Academy of Sciences of the USSR, Moscow

1. Introduction

Erbium-doped YAG is an effective medium for generation in the 3 μm region. First laser oscillation was reported in 1974 (transition $^4I_{11/2} \rightarrow {}^4I_{13/2}$, λ = 2.94 μm, 300 K /1/). The YAG:Er is also the first laser medium for which the generation can be obtained for 100% activator concentration with flash lamp pumping /2/.

Even though the terminal level has a longer lifetime (2 ÷ 6 ms, depending on the Erbium concentration) than the initial one (80 ÷ 110 μs), the quasicontinuous generation regime was obtained /3/. The cross-relaxation mechanism $^4I_{13/2} \rightarrow {}^4I_{15/2}$; $^4I_{13/2} \rightarrow {}^4I_{9/2}$ (Fig. 1) followed by a rapid multiphonon relaxation to $^4I_{11/2}$, can explain this effect /3/. The influence of this cross-relaxation process on the decay of the initial laser level ($^4I_{11/2}$) has been revealed in /4/ using a tunable dye laser and in /5/ using a modulated argone laser.

The anti-Stokes luminiscence of the $^4S_{3/2}$ level (when pumped in red through $^4I_{15/2} \rightarrow {}^4F_{9/2}$ transition) using a krypton laser (λ = 6471 Å) has been reported in /6/ and attributed to a new cross-relaxation mechanisms, $^4I_{11/2} \rightarrow {}^4I_{15/2}$; $^4I_{11/2} \rightarrow {}^4F_{7/2}$ (followed by rapid relaxations to $^4S_{3/2}$ (see Fig. 1)). In /6/ is also discussed the role of a third cross-relaxation mechanism (proposed by Van Uitert and Johnson /7/) $^4S_{3/2}$ ($^2H_{11/2}$) $\rightarrow {}^4I_{9/2}$ (followed by $^4I_{9/2} \rightarrow {}^4I_{11/2}$); $^4I_{15/2} \rightarrow {}^4I_{13/2}$ (Fig. 1) in producing a population inversion.

The influence of the cross-relaxation from the $^4I_{11/2}$ level on the decay curve of $^4I_{11/2}$ and the direct proof that the anti-Stokes luminiscence of $^4S_{3/2}$ is due to this process were obtained using a tunable dye laser, the pumping transition being $^4I_{15/2} \rightarrow {}^4F_{9/2}$ /8/.

In this paper an analysis of the role of the cross-relaxation processes on the quasistationary generation regime of YAG:Er laser is performed by solving the rate equations.

2. Rate equations

The rate equations used to describe the kinetics of $^4S_{3/2}$, $^4F_{9/2}$, $^4I_{11/2}$ and $^4I_{13/2}$ levels, including the three cross-relaxation processes /8/ are connected here to the laser terms as follows:

$$\frac{dN_*}{dt} = - \frac{N_*}{T_*} - W_* N_0 N_* + N_2 N_2^2 + Rp \qquad (1)$$

$$\frac{dN_3}{dt} = -\frac{N_3}{T_3} + \frac{N_4}{T_4} \quad ; \qquad \frac{d\phi}{dt} = \phi v[\sigma(\alpha N_2 - \beta N_1) - \rho] \tag{1}$$

$$\frac{dN_2}{dt} = -\frac{N_2}{T_2} - 2W_2N_2^2 + \frac{N_3}{T_3} + W_4N_0N_4 + W_1N_1^2 - \sigma\phi(\alpha N_2 - \beta N_1)$$

$$\frac{dN_1}{dt} = -\frac{N_1}{T_1} + \frac{N_2}{T_2} - 2W_1N_1^2 + W_4N_0N_4 + \sigma\phi(\alpha N_2 - \beta N_1)$$

where R_p is the pumping rate, σ - emission cross section, ϕ - photon flux density in the laser cavity, ρ - the total lasses in the cavity, v - the propagation speed of the light in the active medium, and α, β are the Boltzmann coefficients for the Stark sublevels between which the laser transition takes place. N_1 to N_4 are the populations of the levels $^4I_{13/2}$, $^4I_{11/2}$, $^4F_{9/2}$, $^4S_{3/2}$, respectively, T_1, T_2, T_3, T_4 being their lifetimes. W_i are the rate constants for the cross relaxation processes: W_1 for $^4I_{13/2} \rightarrow {^4I_{15/2}}$; $^4I_{13/2} \rightarrow {^4I_{9/2}}$; W_2 for $^4I_{11/2} \rightarrow {^4I_{15/2}}$, $^4I_{11/2} \rightarrow {^4I_{7/2}}$ and W_4 for $^4S_{3/2}$ ($^2H_{11/2}$) $\rightarrow {^4I_{9/2}}$, $^4I_{15/2} \rightarrow {^4I_{13/2}}$ process. N_0 is the population of the ground level. In our conditions $N_0 \simeq N_t$ - the total number of Er^{3+} ions per cm^3.

The $^4I_{9/2}$ was not included in the rate equations (1) due to its very short lifetime (under our experimental possibilities). From this level on excitationrelaxes very rapidly to $^4I_{11/2}$.

The computer solutions of the rate equations (1) were obtained with the following numerical values (for 50% Er^{3+} concentration): $\sigma_p = 3 \times 10^{-20}$ cm^2, $\alpha = 0.2$, $\beta = 0.04$, $\rho = 0.02$ cm^{-1} /5/, $T_1 = 2$ ms, $T_2 = 100$ µs, $T_3 = 1.2$ µs, $T_4 = 15$ µs /8/. For 50% Er^{3+} concentration $W_1 = 2.5 \times 10^{-16}$ cm^3s^{-1} /5/. The analysis of the available data concerning the concentration dependence of W_1 (Table I) suggests $W_1 \sim Co^2$ where Co is the Er^{3+} concentration (in % at.) in YAG. The only available data on W_2 are given in ref. /8/: $W_2 = 5.1 \times 15^{-17}$ cm^3s^{-1} for 10% Er concentration. Supposing the same type of concentration

TABLE I.

The cross-relaxation constants W_1, W_2 for different Er^{3+} concentrations

Er^{3+}% at.	10	15	50
W_1 (10^{-17} cm^3s^{-1})	1.8	2.5	25
W_2 (10^{-17} cm^3s^{-1})	5.1	n.a.	n.a.
Reference	/8/	/5/	/5/

dependece, $W_2 \sim Co^2$, a value of 7×10^{-16} cm^3s^{-1} can be obtained for 50% Er^{3+}. The value of W_4N_0 was obtained from the expression $1/T_{4m} = 1/T_4 + W_4N_0$ /8/ where T_{4m} is the fluorescent lifetime of $^4S_{3/2}$ level for different concentrations. For a 50% Er concentration, our estimation is $W_4N_0 = 5 \times 10^6$ s^{-1}. The pumping was assumed to be in $^4S_{3/2}$ because in the usual flash lamp excitation the main absorption bands are above $^4S_{3/2}$ and the excitation goes rapidly to this level.

The analysis of the radiative lifetimes of the levels implied in the rate equations (1) obtained with a modified Indd-Ofelt analysis /9/ shows that for these levels (except for $^4I_{13/2}$) the nonradiative ways of desactivation prevail: multiphonon or cross-relaxation. In Fig. 1, the multiphonon transitions are noted with dashed arrows. The $^4I_{13/2} \rightarrow {}^4I_{15/2}$ transition is radiative and denoted in Fig. 1 by a full arrow.

The role of the cross-relaxation process described by W_4 on inducing the population inversion was discussed elsewhere /10/. For high Er^{3+} concentration this process prevail over the radiative and multiphonon ways of $^4S_{3/2}$ desactivation. Our calculations show that immediately after switching on the pumping,. the populations of the $^4I_{11/2}$ (via $^4S_{3/2} \rightarrow {}^4I_{9/2}$, $^4I_{9/2} \rightarrow {}^4I_{11/2}$) and $^4I_{13/2}$ (via $^4I_{15/2} \rightarrow {}^4I_{13/2}$) are equal. However, a population inversion takes place between the second Stark sublevel of $^4I_{11/2}$ and the seventh Stark sublevel of $^4I_{13/2}$ (transition $x_2 \rightarrow y_7$ /10/)..In all our present calculations, W_4N_0 is maintained constant (5×10^6 s^{-1}).

To evidence the role of the cross-relaxation processes W_1 and W_2, we discuss below the solutions of the system of equations (1) in three cases. In all three cases we use the same pumping conditions: the pumping is switched on at t = 0 at the value $R_p = 10^{23}$ $cm^{-3}s^{-1}$ and maintained constant.

a) $W_1 = W_2 = 0$. In this case only some spikes are obtained (Fig. 2). To explain this, is shown in Fig.3, the time dependence of the gain $\sigma(\alpha N_2 - \beta N_1)$. After about 110 µs, the gain decreases under the losses because $T_2 < T_1$ (selfsaturation regime).

b) $W_1 \neq 0$, $W_2 = 0$ (in our example $W_1 = 2.5 \times 10^{-16}$ cm^3s^{-1}). The situation is changed substantially and the stationary regime is obtained (Fig.4).

c) $W_1 \neq 0$, $W_2 \neq 0$ (we have taken $W_1 = 2.5 \times 10^{-16}$ cm^3s^{-1}, $W_2 = 7 \times 10^{-16}$ cm^3s^{-1}). In this case the situation does not differ dramatically from case b) (Fig.5).

Thus, the first cross-relaxation mechanism ($W_1 \neq 0$) causes the stationary regim and the second one ($W_2 \neq 0$) has a minor effect: the begining of the emission is delayed (73 µs instead of 60 µs) and the efficiency is a little lowered.

A pulse duration longer then 1 ms for the YAG:Er laser has been reported /11/. Since after ~ 300 µs the stationary regime is established (Figs. 4, 5), it is interesting to analyse the stationary case, i.e., dNi/dt = 0, $d\phi/dt = 0$. Thus, the system (1) becomes:

$$-\frac{N_4}{T_4} - W_4N_0N_4 + W_2N_2^2 + R_p = 0 \quad ; \quad \frac{N_3}{T_3} = \frac{N_4}{T_4} \qquad (2)$$

$$-\frac{N_2}{T_2} - 2W_2N_2^2 + \frac{N_3}{T_3} + W_4N_0N_4 + W_1N_1^2 - \rho\phi = 0$$

$$-\frac{N_1}{T_1} + \frac{N_2}{T_2} - 2W_1N_1^2 + W_4N_0N_4 + \rho\phi \quad ; \qquad \sigma(\alpha N_2 - \beta N_1) = \gamma \tag{2}$$

This system was numerically solved by the Newton method. The first interesting results are presented in Fig.6. This shows the flux density ϕ in the stationary regime as a function of pumping rate Rp for different W_2. No limitation of the ϕ with Rp is observed, the dependence going to a straight line (as long as No $\simeq$ Nt, Nt $\sim 5 \times 10^{21}$ cm^{-3}) - Fig.7 shows the disactivation rate of the $^4I_{11/2}$ level through the laser channel in pumping rate units, $\rho\phi$ /Rp, function of Rp. This unit, $\rho\phi$ /Rp, can be interpreted as a number of laser quanta generated in the laser cavity by a pumping quantum. For W_2=0, this number tends to 3, as expected in /6/. When $W_2 \neq 0$ the efficiency is reduced but even for very high values of W_2 (e.g. 3×10^{-15} cm^{3}s^{-1}) $\rho\phi$ /Rp > 1.

Figs. 8 and 9 show the rates of different mechanisms of the desactivation of the level in units of pumping rate Rp for two cases: for the threshold conditions (Fig.8) and far from threshold (Fig.9). In the latter case the laser rate becomes important.

3. Conclusions

Our calculations, based on a realistic model including cross-relaxation mechanisms, explain the many characteristics of the YAG:Er laser. These calculations also shows a quite large efficiency of transformation of the pumping energy into laser radiation which practically compensates the Stokes losses of the pumping radiation.

REFERENCES

/1/ E.V.Zharikov, V.I.Zhekov, L.A.Kulevskii, T.M.Murina, V.V.Osiko, A.M.Prokhorov, A.D.Saveliev, V.V. Smirnov, B.P.Starikov, M.I.Tismoshechkin, Kvant.Elektr. 1(8), 1867 (1974).

/2/ A.M.Prokhorov, A.A.Kaminskii, V.V.Osiko, M.I.Tismoshechkin, E.V.Zharikov, T.I.Butaeva, S.E.Sarkisov, A.G.Petrosyan, V.A.Fedorov, Phys.Stat.Sol.(a) 40, K69 (1977).

/3/ H.S.Bagdasarov, V.I.Zhekov, V.A.Lobachev, T.M.Murina, A.M.Prokhorov, Kvant.Elektr. 10(2) 452 (1983).

/4/ I.Ursu, V.Lupei, S.Georgescu, C.Ionescu, I.Voicu, Symp. "Progrese in Fizica", Sibiu, 1984.

/5/ V.I.Zhekov, V.A.Lobachev, T.M.Murina, A.M.Prokhorov, Kvant. Elektr. 11(1) 189 (1984).

/6/ H.S.Bagdasarov, V.I.Zhekov, V.A.Lobachev, A.A.Manenkov, T.M.Murina, A.M.Prokhorov, Izv. ANSSSR, ser.fiz. 48(9), 1765 (1984).

/7/ Van Uitert, L.F.Johnson, J.Chem.Phys. 44, 3514 (1966).

/8/ V.I.Zhekov, T.M.Murina, A.M.Prokhorov, M.I.Studenikin, S.Georgescu, V.Lupei, I.Ursu, to be published in Kvant.Elektr. (1985).

/9/ S.Georgescu, C.Ionescu, I.Voicu, V.I.Zhekov, to be published in Rev.Roum.Phys. (1985).

/10/ V.I.Zhekov, V.A.Lobachev, T.M.Murina, A.M.Prokhorov, Kvant.Elektr. 8 (2) 451 (1981).

/11/ V.I.Zhekov, V.A.Lobachev, T.M.Murina, A.M.Prokhorov, Kvant.Elektr. 10 (9) 1871 (1983)

FIGURE CAPTIONS

Fig.1 Energy level scheme of Er^{3+} in YAG and mechanisms of relaxation of excitation

Fig.2 Photon flux density in the laser cavity versus time when $W_1 = W_2 = 0$ (case a)

Fig.3 Gain ($N_2 - N_1$) versus time when $W_1 = W_2 = 0$

Fig.4 Photon flux density in the laser cavity versus time for $W_1 = 2.5 \times 10^{-16}$ cm^3s^{-1}, $W_2 = 0$ (case b)

Fig.5 Photon flux density in the laser cavity versus time for $W_1 = 2.5 \times 10^{-16}$ cm^3s^{-1}, $W_2 = 7 \times 10^{-16}$ cm^3S^{-1} (case c)

Fig.6 Photon flux density versus pumping rate R_p in the stationary regime

Fig.7 Efficiency of laser quanta generation,for different value W_2,function of pumping rate Rp

Fig.8 The rates (in units of pumping rate Rp) of different transitions taking place in the laser generation of YAG:Er at threshold in stationary regime; the width of the arrows are proportional to the rates

Fig.9 The same as in Fig.8, but far from threshold

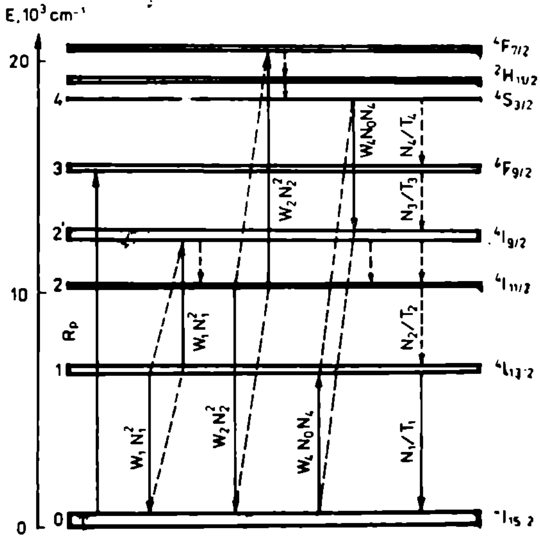

FIG. 1.

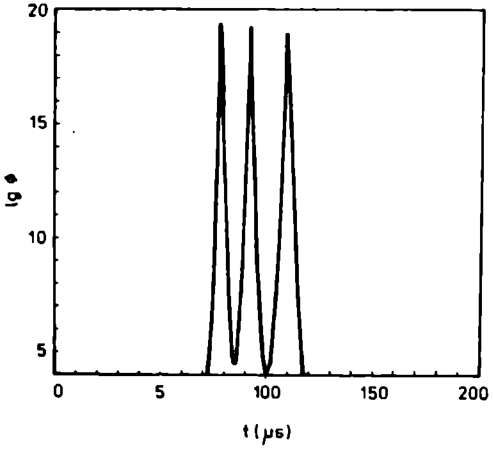
20
15
10
5
lg Φ
0
5
100
150
200
t (μs)

FIG. 2.

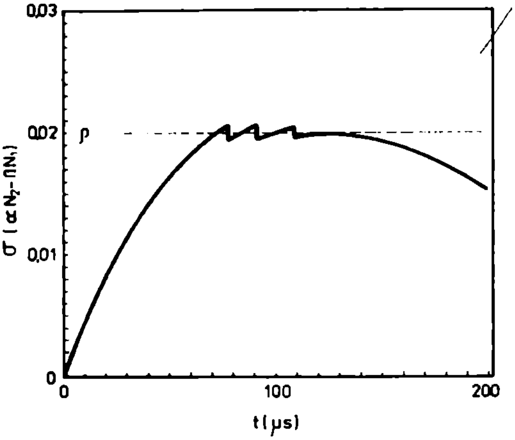
0,03
0,02
0,01
0
ρ
σ (αN₂-βN₁)
0
100
200
t (μs)

FIG. 3.

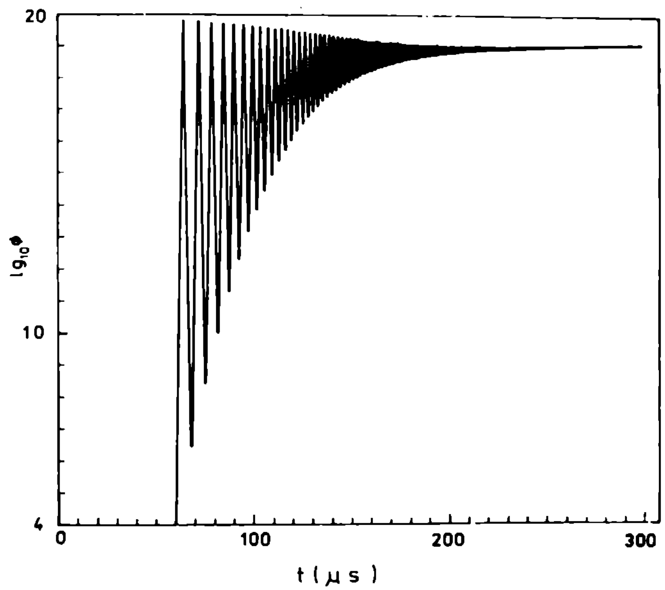

FIG. 4.

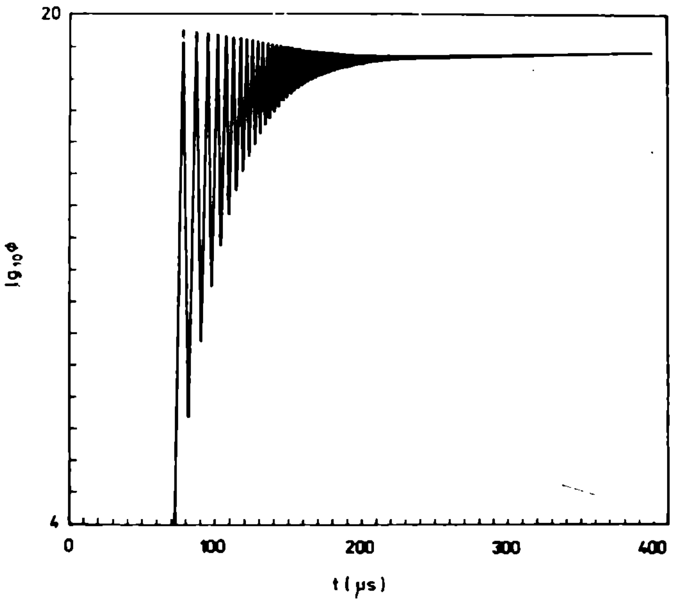

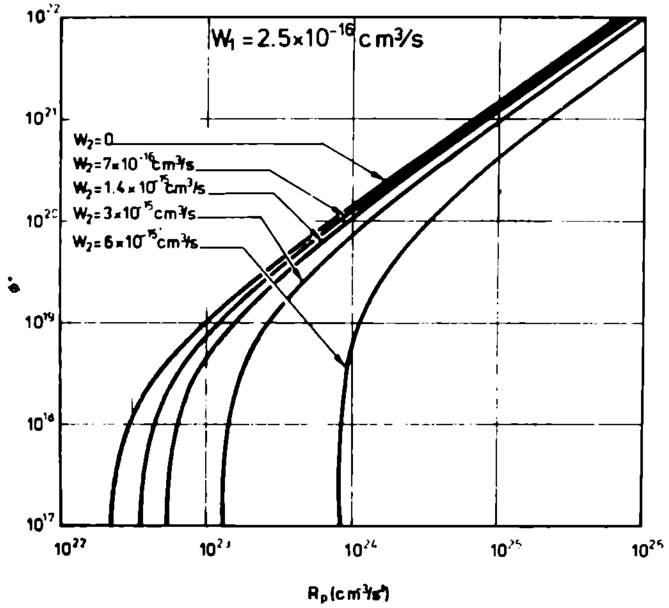
$W_1 = 2.5\times10^{-16}$ cm³/s
$W_2 = 0$
$W_2 = 7\times10^{-16}$ cm³/s
$W_2 = 1.4\times10^{-15}$ cm³/s
$W_2 = 3\times10^{-15}$ cm³/s
$W_2 = 6\times10^{-15}$ cm³/s
Φ
10^{22}
10^{21}
10^{20}
10^{19}
10^{18}
10^{17}
10^{22}
10^{23}
10^{24}
10^{25}
10^{26}
R_p (cm^{-3}s^{-1})

FIG. 6.

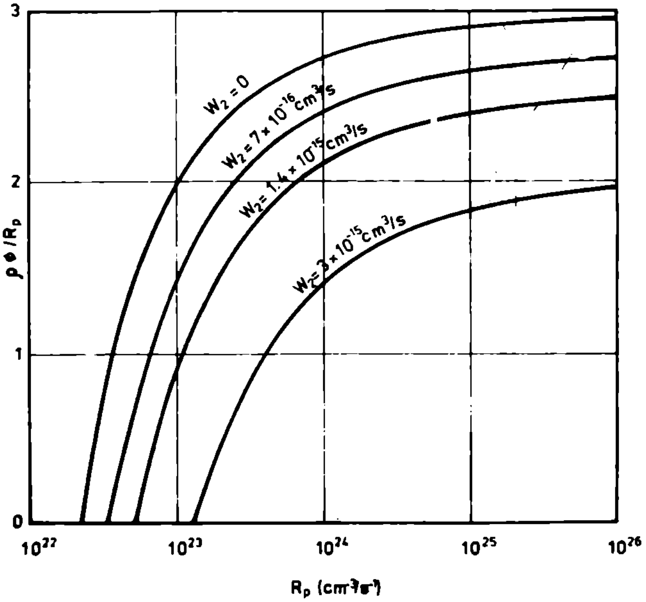
$W_2 = 0$
$W_2 = 7\times10^{-16}$ cm³/s
$W_2 = 1.4\times10^{-15}$ cm³/s
$W_2 = 3\times10^{-15}$ cm³/s
3
2
1
0
$\rho\Phi/R_p$
10^{22}
10^{23}
10^{24}
10^{25}
10^{26}
R_p (cm^{-3}s^{-1})

FIG. 7.

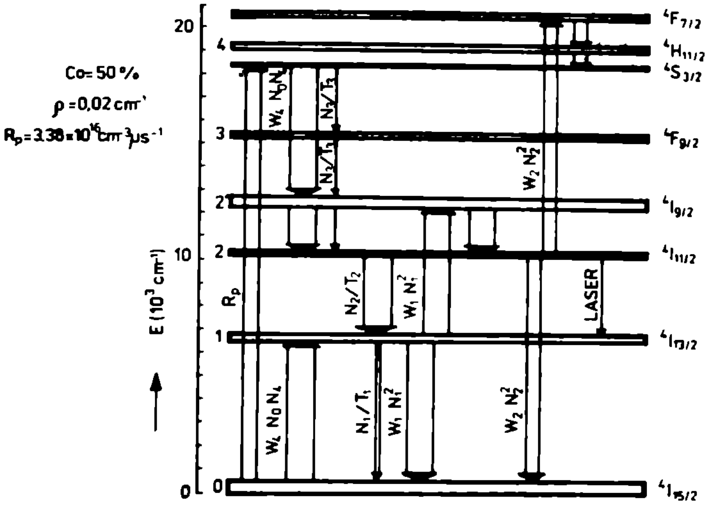
Co= 50 %
ρ =0,02 cm⁻¹
Rp=3.38×10¹⁶cm⁻³µs⁻¹
20
10
0
E (10³ cm⁻¹)
4
3
2'
2
1
0
⁴F7/2
⁴H11/2
⁴S3/2
⁴F9/2
⁴I9/2
⁴I11/2
⁴I13/2
⁴I15/2
W4 N0N4
N3/T3
N2/T1
Rp
N2/T2
W1 N1²
LASER
W4 N0 N4
N1/T1
W1 N1²
W2 N2²
W2 N2²

FIG. 8.

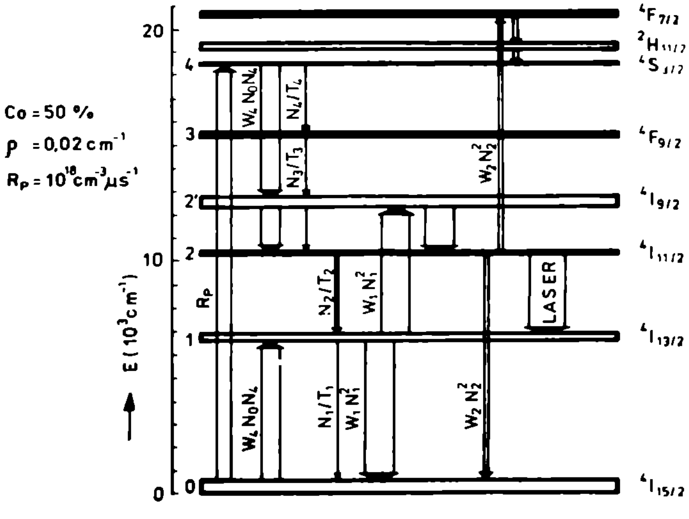
Co = 50 %
ρ = 0,02 cm⁻¹
Rp = 10¹⁸cm⁻³µs⁻¹
20
10
0
E (10³cm⁻¹)
4
3
2'
2
1
0
⁴F7/2
²H11/2
⁴S3/2
⁴F9/2
⁴I9/2
⁴I11/2
⁴I13/2
⁴I15/2
W4 N0N4
N4/T4
N3/T3
W2 N2²
Rp
N2/T2
W1 N1²
LASER
W4 N0N4
N1/T1
W1 N1²
W2 N2²

FIG. 9.

He-Ne LASER EQUIPMENT FOR ALIGNMENT, ORIENTATION AND GUIDING

V.Vasiliu, M.Ristici
Laser Department
Institute for Physics and Technology of Radiation Apparata

The paper describes some of the He-Ne laser equipment for alignment, orientation and guiding purposes having been produced in Romania. Such equipment allows for the laser beam to define a sense of direction, a reference plane or a part of it and is used in industrial constructions, in the construction of water power galleries, tunnels, in land redamation, for the proper alignment of rolled steel in front of the shearing machine, or of the terra-cotta cahles, etc. The Romanian made alignment-guiding laser equipment includes the following models: LGA-2, LGA-3, LGA-4, ALGOCS, ELAC-1, ELAC-2, ELOF-CT, Laser Goniometer, RTP-01, RTP-02; METROLAS, ELICF.

The manufacture of He-Ne laser equipment for alignment, orientation and guiding in Romania is the result of the research activities carried out in the He-Ne laser field since 1962 by a group of researchers headed by professor Ion Agarbiceanu. Therefore, it is an honour for us to dedicate the results of the work we performed in this field to the memory of our scientific leader directing our efforts during the early stages in our research.

We shall always remember with great pleasure of professor Agarbicenau's advice on any research problems and experiments that finally turned into scientific papers or equipment for the benefit of our people, of mankind in general and for the steady increase of the prestige of science. Professor Agarbiceanu's image lingers on as on ever lasting memory stimulating us in all of our research activities.

The alignment orientation and guiding He/Ne laser equipment incorporates a low output power (1-3 mW) He-He laser, a non-focussed optical system for applying corrections to the emitted beam divergence (angle), a mechanical assembly ensuring the stable spatial orientation of the laser beam reference direction and a supply voltage unit.

The features of the equipment differ from one type to another, depending on the required operating conditions and on the equipment the motion of which should be guided or aligned.

He-Ne laser equipment for alignment and guiding purposes have been extensively applied in various departments of the national economy.

As the emitted radiation beam provided to display special properties as related to its monochromatic feature, its coherence, directionality and light intensity, the use of the He-Ne lasers largely extended the application field of the alignment and guiding optical methods and in many cases, their use has been simplified.

The alignment methods can be generally described as being of two types, i.e. the alignment of a group of points along a straight line (the reference line represented by the laser beam) and the alignment of fixed point belonging to a machine, the trajectory of which should go along a straight line (this is also represented by the He-Ne laser emitted bright beam).

The first method is applied for assemblying the components of a tool-machine with a very high accuracy, for travel crane stiding rail laying, for laying railways for high-speed trains, for errecting supporting pillars of large industrial bays, for the installation of large petrol, natural gas or water pipes, drainage systems, etc.

The second method is applied for the alignment of tool-machines designed to perform rock drilling for hydro-power station approach tunneles, drilling of railroad or underground tunnels, of drainage ploughs, of floating cranes, of excavation or concreting performing installations, of other equipment needed to perform drainage ditches, or to provide the required bed of concrete or asphalt coating roads, of landing or taking off strips, etc.

We may distinguish between 3 types of alignment-guiding laser equipment, depending on the geometry of the laser emitted beam. In the first case, the light beam representing a direction path produces a punctiform light spot. In the second case, the light beams describes a plane by its several times a second rotation in the given plane. The spatial orientation of the direction or reference plane represented by the laser beam can be selected according to the user's requirements. In the third case, the light spot produced by the alignment equipment is represented by a reference line obtained by means of an optical system based on cylindrical lenses instead of the collimator telescope.

As in the case of highly accurate optical measurements for long distances, the highly accurate laser alignment following a long path across the atmosphere is limited to a great extent by the cloudiness and variations in the air reflection (optical) index. Under special circumstances, the alignment accuracy reached the value of 10^{-8} along a distance of about 4 Km, using laser alignment /1, 2/.

The use of He-Ne laser alignment system does not only depend on the accuracy that can be attained but also on the measurement reproducibility along larger distances and during longer periods of time.

The He-Ne laser alignment equipment is based on the fact that emitted radiation takes the shape of an extremely narrow light beam described by a very low divergence factor, irrespective of the distance covered, and a high light intensity, pointing along a single direction and being similar to a straight and narrow ray.

At present, alignment equipment is mainly used for linearity and dip control /3/.

We have developed a series of alignment, orientation and guiding He-Ne laser equipment that can be operated under different environmental conditions. The Romanian made equipment designed for such purposes includes the following devices: LGA-2; LGA-3; LGA-4; ALGOCS; ELOF-CT; ELAC-1; ELAC-2; RTP-01; RTP-02; RTO-03; METROLAS; ELICF; Laser Goniometer.

Out of this series, we shall only present our latest devices which actually represent the second generation of such Romanian-made alignment and guiding equipment.

The largest range of applications of such alignment-guiding He-Ne laser equipment is in the excavation or drilling galleries and tunnels.

For such purpose, the ALGOCS equipment has been designed which is a highly specialized and complex device emitting a light beam of a good divergence factor (5×10^{-5} rad). /4, 5/

The ALGOCS underground alignment and direction control equipment is properly sealed off as to be operated under the hostile underground conditions (dampy and dusty). It incorporates a 2 mW output power He-Ne laser, a collimator telescope, a pointing (sighting) telescope, a laser power supply unit and the mechanical assemblies ensuring the spatial orientation of the laser emitted beam.

The primary supply voltage is of 12 V (d.c.). The accesories of this equipment are represented by rods provided with plexiglass-made diaphragms and gridded panels (boards).

The equipment indicates the excavation direction by means of the emitted beam along a 500 m distance (for visual detection) and up to 1000 m (for photoelectrical detection).

The models cited above ensure the alignment and lead direction control of the Romanian-made horizontal drilling rigs, on large diameter full cross sections, operated on hydro power station sites.

The ALGOCS equipment has been widely used in Romania due to its performance features, small size and a good mechanical stability.

The ALGOCS equipment can be mounted on a metal tripod so that it may be used on any construction site where a reference direction is required and is consequently provided by the laser beam. The reference space direction can be wherever wanted, since the equipment can be horizontally or vertically rotated and also vertically shifted for a few tens of centimeters.

The schematic diagram of the equipment is given in Fig.1 and its general view is illustrated in Fig.2.

We have also developed the ELAC-1 equipment (see picture of Fig.3) for providing reference direction by means of the laser beam in coal mine excavations. The equipment incorporates a 1-3 mW output power He-Ne laser, a collimator telescope (magnification = 15), a mechanical assembly for laser beam spatial positioning to provide the reference direction and a power supply unit for the laser (primary supply voltage: 380V; 50 Hz). It is a solid state construction, reliable and well-sealed off for the mining special conditions. The equipment housing is made up of cast silumin. The equipment also allows to perform alignment/guiding up to 500 m (observation made visually) and up to 1 km (detection is made photoelectrically). /6-8/

ELAC-2 belongs to the same category of equipment including an in-line symmetry He-Ne laser and is incorporated into a welded housing. It is less heavy and can be operated under the mining firedamp conditions.

Its schematic diagram is given in Fig.4.

All of the equipment described above can ensure alignment and guiding for rock excavation or correcting machines along curved direction. In this case, ciphers obtained on the basis of computer programmes are used; the parameters of the curve pathway stands for the input data and the output data are represented by the parameters to be measured by means of the alignment and guiding equipment for obtained the required sense of direction. /9/.

In order to improve the accuracy of guiding measurements for drilling equipment in describing curved pathways, we have produced the METROLAS alignment equipment which allows to obtain direction control by means of the two laser beams that should continuously fall upon two fixed points on the drilling installation. /10/

Another type of such equipment can describe a circular sector (by means of the beam light) whose projected image is a straight line. The LGA-4 equipment was consequently developed including a 3 mW output power, in-line He-Ne laser, a system of cylindrical lenses, the power supply unit and the mechanical assemblies for spatial positioning. /11/

The equipment allows to obtain a straight line in relation to which a material or a mechanical component can be aligned. It is mainly used in the ferrous metallurgy industry, where the reference line, most adequately aligned to the cutting shears, allows for the rolled steel to be properly lined up in front of the cutting shears in order to perfectly and most economically cut their edges.

A general view of the equipment is illustrated in Fig.5.

Another equipment model producing two reference lines displaced at 90° angle to each other is the ELOF-CT equipment designed to be used in the building material industry for guiding terra-cotta cable cutting machines. It is designed to be operated under the very dusty conditions to be found in the building material industry. /12/

We have also developed a class of He-Ne laser equipment which provides a reference plane by means of the laser radiation /13, 14/. They are destined to be used in guiding work carried out in the fields of land reclamation, road construction, large scale foundation footing, landing and taking-off strips, etc.

This equipment incorporated a He-Ne laser emitting system, a collimating optical system, a tripod, a pentaprism, and the electromechanical assembly allowing it to rotate in a plane; the power supply unit for the laser, the reception system mounted on the levelling assembly plate (blade) and a device indicating the position of the reference plane which is installed inside the operator's room.

The class of this equipment includes the RTP-01, RTP-02 and RTP-03 apparata and their use determined an increase of the efficiency and the quality of the work performed.

The general picture of the RTP-02 equipment is illustrated in Fig.6.

In order to ensure equipment alignment for highly errected building., a **Laser Goniometer** /15/ providing alignment services on vertically errected buildings was produced; it is equipped with a special optical system helping to detect any twisting (laying) or drifting (shifting) motion in a horizontal plane of the sliding panels and to measure and prevent them /2, 16/. A general view of this equipment is presented in Fig. 7. It is used for building-up draft chimneys and cooling towers of steam power plants, TV relay towers, granaries, and also for testing tower building cranes of the portal type etc.

The equipment incorporates a 2 mW output power He-Ne laser, a non-focussed telescope (mangnifying power: 25), a goniometer-type mechanical assembly allowing a highly accurate spatial alignment of the reference direction provided by He-Ne laser beam.

FIGURE CAPTIONS

Fig. 1 ALGOCS Equipment Schematic Diagram
Fig. 2 General view of the ALGOCS Alignment-Guidance Equipment
Fig. 3 General view of the ELAC-1 Equipment Providing alignment and guiding in mining drilling
Fig. 4 ELAC-2 Equipment Schematic Diagram
Fig. 5 General view of the LGA-4 Equipment
Fig. 6 General view of the RTP-02 Equipment
Fig. 7 General view of the He-Ne Laser Goniometer

REFERENCES

/1/ V.Vasiliu, V.Draganescu, "Echipamente cu laser He-Ne pentru orientare, directionare, ghidare si aliniere", LOP-29-1982, CIP Press

/2/ V.Vasiliu, "Utilizarea echipamentelor cu laseri He-Ne in economia nationala", LOP-42-1983, CIP Press

/3/ V.Draganescu, D.Apostol, D.Dumitras, V.Vasiliu, V.Vlad, "Noi rezultate in fizica si ingineria laserilor", St.Cer.Fiz., 37, (1985)

/4/ V.Vasiliu, P.Bachmann, M.Ristici, R.Medianu, R.Constantinescu, St.Cerc.Fiz., 35, 484 (1983

/5/ V.Vasiliu, P.Bachmann, P.Ghilac, M.Ristici, R.Medianu, S.Georgescu, "Echipament cu laser He-Ne pentru orientarea si directionarea utilajelor de forat orizontal in sectiune plina", Progrese in fizica, Craiova, 29 sept.- 1 oct. 1983

/6/ V.Vasiliu, Z.Maris, P.Bachmann, M.Ristici, "Ghidarea excavarii mecanice in conditii mine de carbune cu ajutorul echipamentelor cu laser He-Ne", Progrese in fizica, Sibiu, 1984

/7/ V.Vasiliu, P.Bachmann, Z.Maris, M.Ristici, St.Cerc.Fiz., 37 (1985)

/8/ V.Vasiliu, Z.Maris, P.Bachmann, R.Constantinescu, M.Ristici, "Echipament cu laser He-Ne pentru orientare, ghidare, aliniere pentru conditii mine de carbune", LOP-48-1984, CIP Press

/9/ V.Vasiliu, N.Ionescu-Pallas, Z.Maris, V.G.Velculescu, "Urmarirea operatiilor de excavatie pe trasee curbe si utilizarea dispozitivelor de control cu laser", LOP-51-1984, CIP Press

/10/ V.Vasiliu, P.Bachmann, Z.Maris, M.Ristici, N.Ionescu-Pallas, St.Cerc.Fiz., 35, 489 (1983)

/11/ V.Vasiliu, M.Ristici, I.Serban, St.Cerc.Fiz., 37, (1985)

/12/ V.Vasiliu, P.Bachmann, N.Iancu, St.Cerc.Fiz., 37, (1985)

/13/ P.Bachmann, I.Chis, A.I.Ciura, C.Grigoriu, M.V.Udrea, V.Vasiliu, "Instalatii cu laser He-Ne pentru descrierea unui plan", Progrese in fizica, 29 sept.- 1 oct. 1983, Craiova

/14/ P.Bachmann, I.Chis, A.I.Ciura, C.Grigoriu, M.V.Udrea, V.Vasiliu, "Echipament cu laser He-Ne pentru descrierea unui plan de referinta", LOP-48-1984, CIP Press

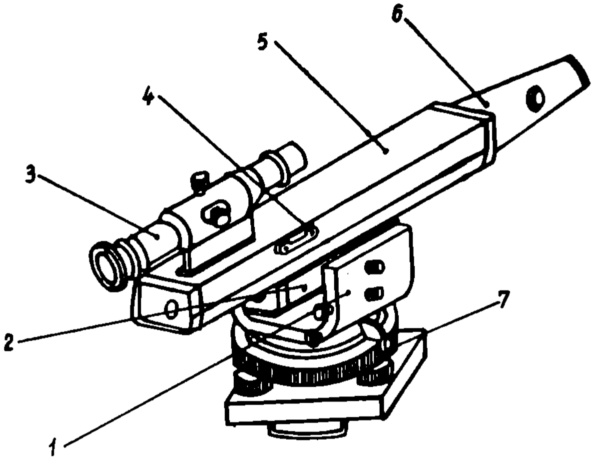

Fig.1

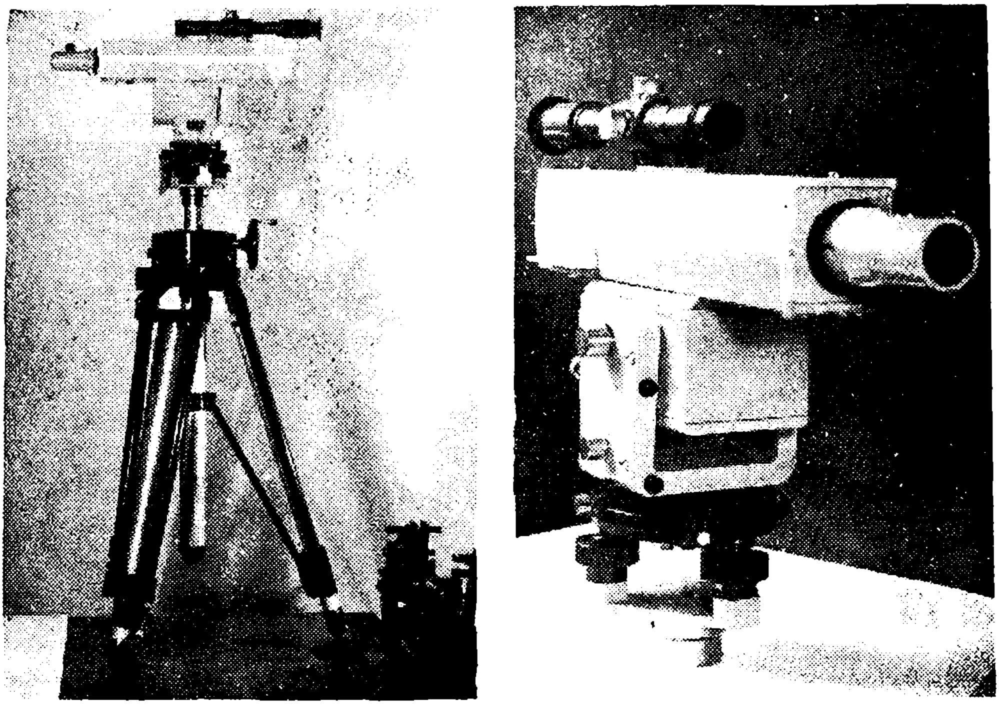

Fig. 2

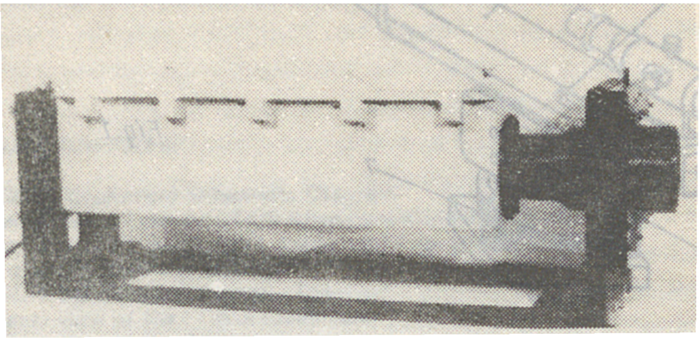

Fig 3

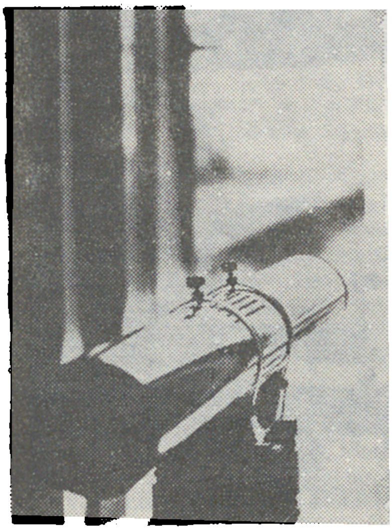

Fig.4

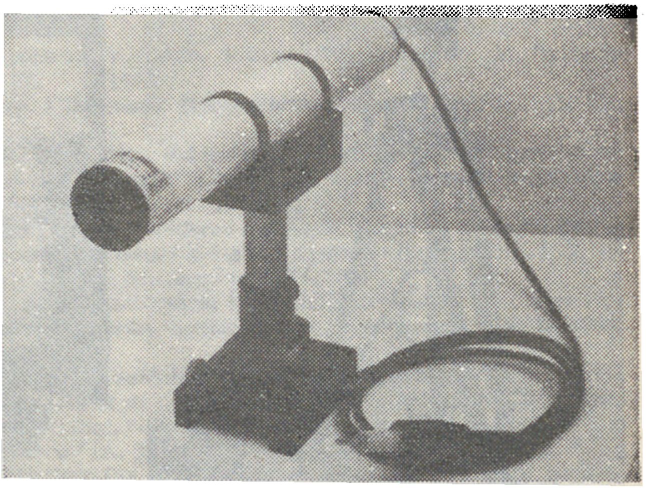

Fig 5

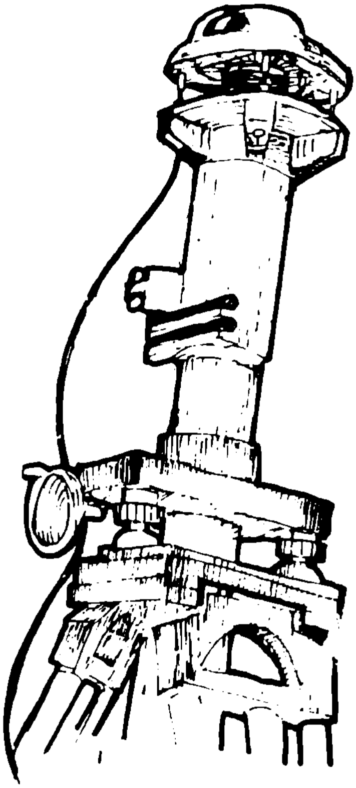

Fig. 6

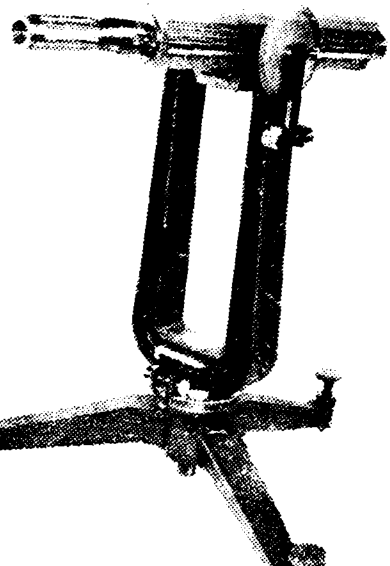

Fig. 7

CONTRIBUTIONS TO THE DEVELOPMENT OF HELICAL TEA-CO_2 LASERS

V.S.Tatu, V.Draganescu, C.Grigoriu, I.N.Mihailescu
Central Institute of Physics, Bucharest-Magurele, MG-6

"We put in operation various configurations of helical TEA-CO_2 lasers. The electrode system consisted of a helical anode and an 180°-opposite helical cathode, made-up of the same number of resistively-loaded (1 kΩ ± 10%; 2x220 Ω ± 10%)-pins, or capacitively-loaded (500 pF)-pins. In the late case, the electrode system consisted of a double helical anode, and an 180°-opposite double helical cathode, remoted by 20°, respectively. The discharge length was 23.8 mm, and 20 mm, respectively. In the first system, an input energy in the range (28 ÷ 163) J was applied on the laser tube; a maximum output energy of 2.2 J was obtained for the optimum CO_2:N_2:He = 2 : 3 : 10 active mixture. We also obtained very stable and uniform discharges by enriching the active mixture with xylene vapours. The output laser performances were then considerably improved. The second system is in course of experiment."

1. Introduction

The helical electrode configuration was first introduced for transversely excited atmospheric pressure (TEA) CO_2 lasers, by Beaulieu, /1/. Extensive studies /2 ÷ 12/ of the behaviour of helical TEA-CO_2 lasers revealed that the helical electrode structure causes a circular symmetrization of the active volume with a gain distribution which, at atmospheric pressure, is tightly confined to the vicinity of the laser axis. The radial gain profile naturally favoures TEM_{00} mode excitation, that determined a great interest for helical TEA-CO_2 lasers as master oscillators within large double-discharge amplifier systems; also, the helical geometry has been found appropriate for TEA-CO_2 laser axial mode-locking operation.

2. The helical electrode structure and the laser building-up

In our first works /12,14/, we used 2 ÷ 4 jointed sticrylic glass tubes of 70 mm external diameter. The electrode system consisted of a helical anode and an 180°-opposite helical cathode, each made of iron pin electrodes, of 2.5 mm diameter, distributed along the tube with 36 pairs per turn. The electrode gap and the helix pitch were chosen to be 23.8 mm and 180 mm, respectively. The cathode row outer resistors are soldered together by means of a copper wire, whereas the anode row consists solely of a copper wire which joints the successive electrodes.

Initially, the values of cathode resistors where chosen to be (1 ± 10%) kΩ. Due to the damaging of these resistors during the laser discharge working at high pressures of the active medium, we proceeded to a series of resistors, diminishing at the same time their total value until (2 x 220 ± 10%) Ω, which also exercised a favourable influence over the laser output. In this manner, we obtained a satisfactorily operation of laser, even at higher voltage supplies, and repetition rates, till to the active mixture pressures of the order of an atmosphere. The laser built-up by us was operated without gas flow.

The laser resonator consisted of a chromium-gold-coated glass mirror, of total reflectivity, given curvature radius R, and a plane-plane uncoated germanium window of about 50% reflectivity. In our experiments, R-values were taken to be 20 m and 10.5 m, respectively.

Electrical input energy of the discharge was in the range (28 ÷ 163) J, resulting in an overall efficiency of about 1%, under our conditions. High voltage transverse pulses of (24 ÷ 52) KV, with a rise-time of about 50 ns and a duration of about 1 µs, from a Marx generator of a 100 nF low-inductance capacity, were applied on the laser tube.

3. Experimental results. Discussions

The investigations are referred to the optimal function conditions of the built-up laser, as well as to the dependence of the laser output on the composition, the total pressure of the active gaseous medium and the charging voltage, respectively. The research dealt with the geometrical parameters of the resonant cavity, too, details of the performed research being reported in /14/.

The shape of the generated laser beam is a typical one, with a primary pulse width maximum (FWHM) up to 200 ns, and a "tail" of some µs duration.

The laser energy output was measured by means of a plane calorimeter with a plexiglass absorber, its outlet being coupled by a digital microvoltmeter Takeda-Riken TR 6515/6018. Power peaks of about 1.1 MW have been obtained with energies up to 2.2 J per shot.

We notices here, that our research was undertaken in a stationary active gaseous mixture, for various families of active mixtures of CO_2:N_2:He, in proportion of 1:1:n, 1:2:n, 2:1:n, 3:2:n, and 2:3:n, respectively, with the corresponding values of n-ranging from 4 to 18 for the first family, from 3 to 10 for the last family, and from 3 to 14 for the rest of the families. In this way, some mixtures n_1:n_2:n_3, with the ratio n_1:n_2 greater than 0 and smaller than or equal to 1, and $n_3 = 2(n_1+n_2)$, were investigated.

Two experimental situations were chosen as typical: (1) - for a constant pressure of the active mixture, and for various charging voltages, measurements over all the active mixtures of each family were performed (Fig. 1); (2) - the most energetic mixture of each family was investigated for a constant charging voltage, but for various values of the total pressure (Fig. 2). In Fig. 3 the laser energy output dependence on the relative composition CO_2:N_2, (n_1:n_2), is presented.

By analysing the experimental data, some practical conclusions are derived, as follows:

a. - For a given pressure of the active mixture, the laser energy output depends critically on the total pressure of the investigated mixture (Fig. 2). When the ratio P_{CO_2}:P_{N_2} is greater than or equal to 1, the laser operates most favourable at relatively higher pressures of the active mixture: (380 ÷ 465) Torr. When the ratio P_{CO_2}:P_{N_2} is smaller than 1, the laser operates best at smaller pressures of the stationary mixture: (152 ÷ 304) Torr.

b. - A general improvement of the laser performances, particularly concerning the reproducibility and the fiability of its operation, was obtained by enriching the active gaseous mixture with xylene vapours, /13/. Thus, the laser operated very stable even at atmospheric pressure of the active mixture, without appearing a rapidly damaging of the cathode resistors. However, the maximum energies were obtained even in that case for pressures smaller than the atmospheric ones (Fig.2).

The laser beam divergence was measured through the intensity distributions in the focus of some long-focal-distance lenses, resulting in a value of about 2.40 ÷ 2.90 mrad.

4. Recent studies

At present, a helical TEA laser with a modified structure of the electrode system, consisting in the preservation of the helix pitch of 180 mm, but changing the inner distance, cathode-anode, at 20 mm, is devised and built-up being now in course of experimentation.

The detailed electrode system is made of two helical anodes and two 180°-opposite helical cathodes, the two helices of the same kind being separated by 20° (Fig.4), /15/. The cathode-electrode-pins, as well as the anode-electrode-pins, are soldered together capacitively: instead of previous cathode resistors, we utilized, in this case, capacitors (500 pF), distributed on regular groups of electrodes. We intend to perform researches about N_2, and about CO_2:N_2:He mixtures, too.

REFERENCES

/1/ A.J.Beaulieu, D.R.E.V., M-2005/70 (Januar 1970); Laser Focus, 6, 14(1970); Appl.Phys.Lett., 16, 504 (1970)

/2/ K.Büchl, Laser, 2, 45 (1970)

/3/ J.Gilbert, Bull.American Phys.Soc., 15, ser. II, 808 (1970)

/4/ K.A.Laurie, M.M.Hale, I.E.E.E. J. Quantum Electron., QE-6, 8, 530 (1970)

/5/ R.Fortin, M.Gravel, J.L.Lachambre, R.Tremblay, Bull.American Phys.Soc., 15, ser.II, 808 (1970)

/6/ C.Yamabe, M.Nakatsuka, M.Yokoyama, Progress Report VI, Lab. for Plasma & Quantum Electronics, Fac. of Engineering, Osaha University, p.21 (August 1970)

/7/ J.Gilbert, J.L.Lachambre, Appl.Phys.Lett., 18, 187 (1971)

/8/ R.Fortin, M.Gravel, R.Tremblay, Canadian J.Phys., 49, 1783 (1971)

/9/ D.T.Rampton, D.P.Gandhi, Appl.Phys.Lett., 21, 457 (1972)

/10/ A.Giraud, H.Pepin, J.G.Vallee, Canadian J.Phys., 51, 1705 (1973)

/11/ G.P.Kuzmin, Radiotekhnika i Elektronika, U.S.S.R., 18, 8, 1553 (1973)

/12/ I.N.Mihailescu, I.Neda-Apostol, I.M.Popescu, V.S.Tatu, Rev.Roum.Phys., 18, 1, 137 (1973)

/13/ I.Apostol, D.Dragulinescu, C.Grigoriu, I.N.Mihailescu, Al.Nitoi, I.M.Popescu, Rev.Roum.Phys., 18, 10, 1185 (1973)

/14/ I.Apostol, Gh.Dragulescu, D.Dragulinescu, C.Grigoriu, I.N.Mihailescu, I.Morjan, Al.Nitoi, I.M.Popescu, V.S.Tatu, St.Cerc.Fiz., 28, 1, 3 (1976)

/15/ V.S.Tatu, Brevet de inventie, OSIM-R.S.Romania, nr. 61348 (27 iunie 1975)

FIGURE CAPTIONS

Fig. 1 The laser energy output dependence for various charging voltages, and for a constant pressure (p = 304 Torr). Typical curves for the investigated families of the active mixtures CO_2:N_2:He: a) o-1:1:4; x-1:1:8; o-1:1:18. b) o-1:2:3; x-1:2:10; o-1:2:14. c) o-2:1:3; x-2:1:10; o-2:1:14. d) o-3:2:3; x-3:2:10; o-3:2:14. e) o-2:3:6; x-2:3:6; o-2:3:10.

Fig. 2 The laser energy output dependence on total pressure, for U(kV) = ct = 51 kV, and for various active mixtures CO_2:N_2:He : o-1:1:8; x-1:2:14; o-2:1:14; ;-2:3:10; -3:2:14; -1:1:8:xylene.

Fig.3 The laser energy output dependence on active mixtures CO_2:N_2:He = n_1:n_2:n_3, with $0<n_1:n_2\leq 1$, and $n_3 = 2(n_1 + n_2)$, for a constant pressure (304 Torr), and for various charging voltages: o - 39 kV; x - 42 kV; o - 45 kV; + - 48 kV; - 51 kV.

Fig. 4 a) Laser image in a longitudinal plane.

b) Laser image in a transverse plane.

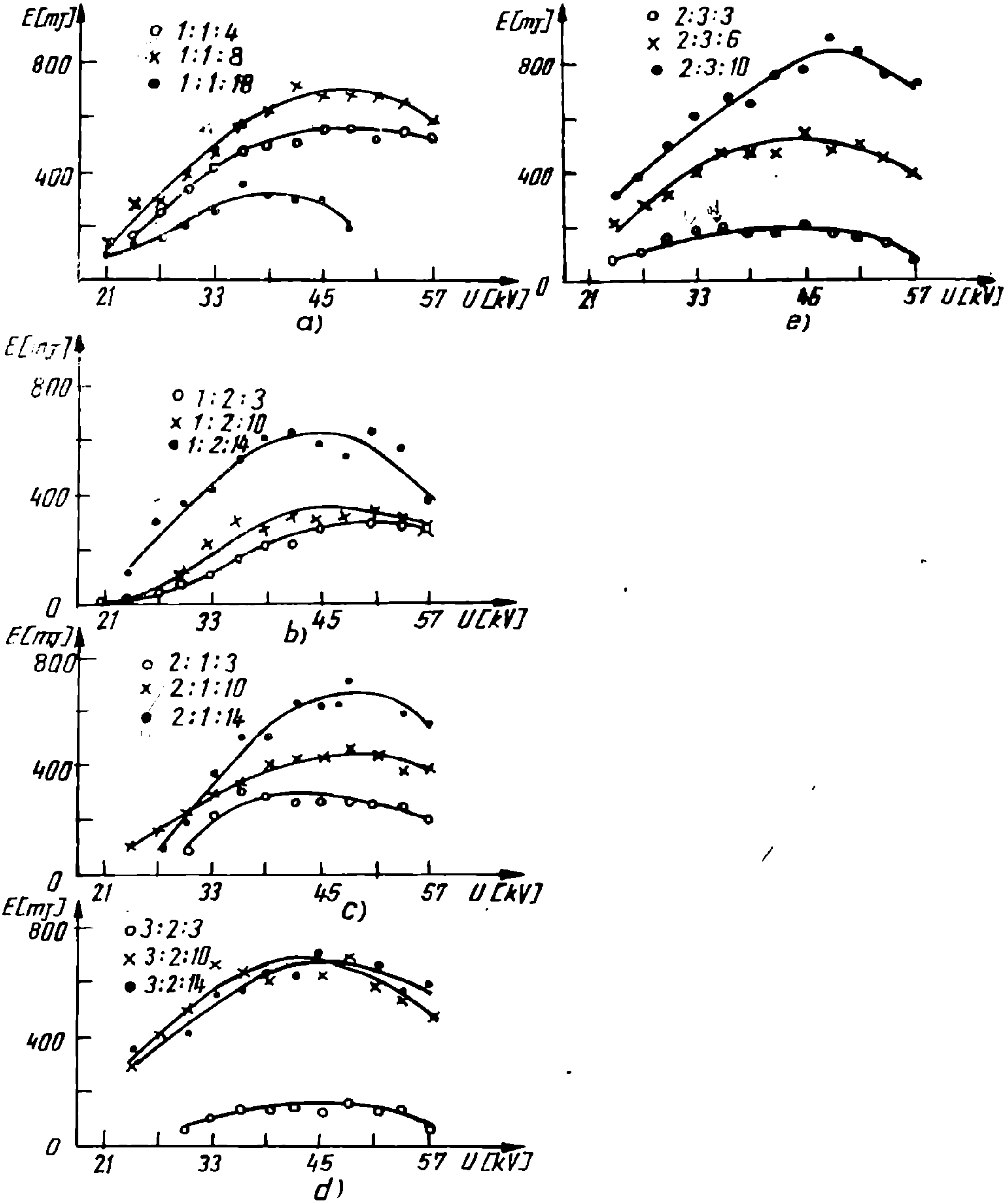
E[mJ]
800
400
o 1:1:4
x 1:1:8
● 1:1:18
21
33
45
57
U[kV]
a)
E[mJ]
800
400
0
o 2:3:3
x 2:3:6
● 2:3:10
21
33
45
57
U[kV]
e)
E[mJ]
800
400
0
o 1:2:3
x 1:2:10
● 1:2:14
21
33
45
57
U[kV]
b)
E[mJ]
800
400
0
o 2:1:3
x 2:1:10
● 2:1:14
21
33
45
57
U[kV]
c)
E[mJ]
800
400
0
o 3:2:3
x 3:2:10
● 3:2:14
21
33
45
57
U[kV]
d)

Fig.1

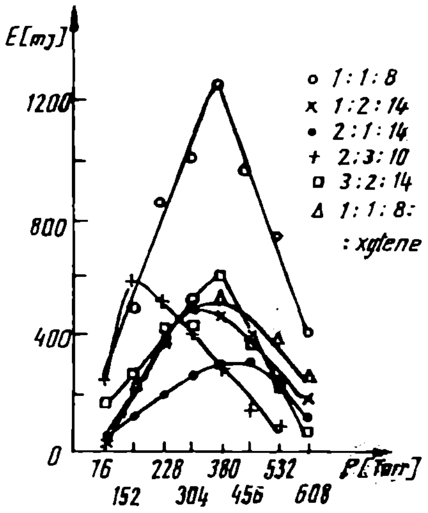
E[mJ]
1200
800
400
0
76
152
228
304
380
456
532
608
P[Torr]
o 1:1:8
x 1:2:14
• 2:1:14
+ 2:3:10
□ 3:2:14
Δ 1:1:8:
: xylene

Fig. 2

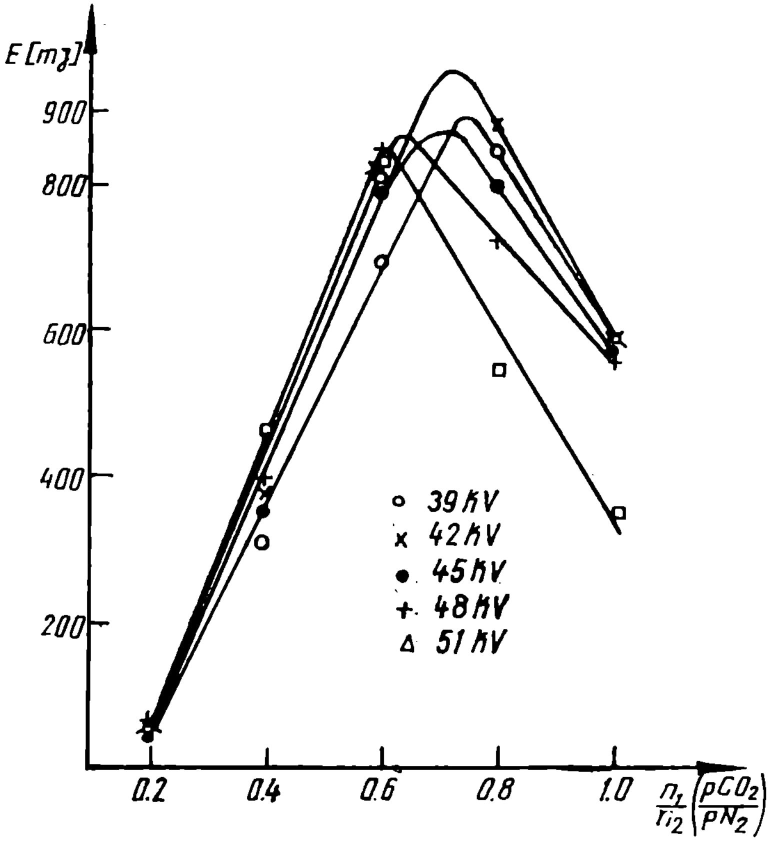
E[mJ]
900
800
600
400
200
0.2
0.4
0.6
0.8
1.0
$\frac{n_1}{n_2}\left(\frac{pCO_2}{pN_2}\right)$
o 39 kV
x 42 kV
• 45 kV
+ 48 kV
Δ 51 kV

Fig. 3

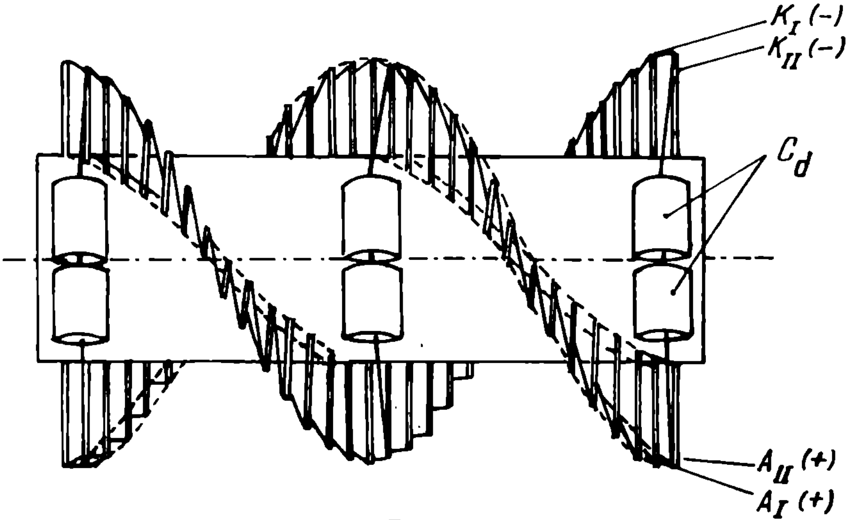

Fig. 4,a

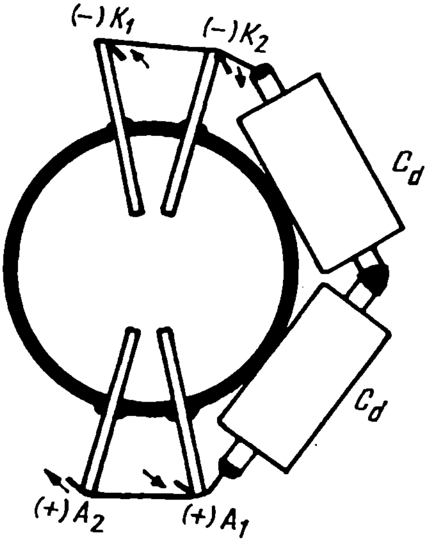

Fig. 4,b

OPTICAL BISTABILITY RESEARCHES

I.M.Popescu, P.E.Sterian, E.N.Stefanescu, A.Gh.Podoleanu, Mihaela A.Dumitru
Department of Physics, Bucharest Polytechnical Institute

The results presented in the paper represent contributions - both theoretical and experimental - to the intrinsic or hybrid optical bistability. These results are mainly related to: the theoretical approach of intrinsic bistability in a general fashion and elaboration of an adequate semiclassical analysis model, the study of the amplification capabilities of the bistable devices, the analysis of some hybrid bistable devices, some experiments performed on new types of magneto-optic and liquid crystal devices etc.

1. Introduction

After the first studies of bistability predicted by Szöke et al. /1/, some years later McCall /2/treated absorptive optical bistability in a Fabry-Perot cavity using Maxwell-Bloch equations. Subsequently, Gibbs et al. /3/ first observed bistability using the D lines of Na vapour.

These results stimulated theoretical and experimental works on the intrinsic absorptive bistability.

We can see especially theoretical references: Bonifacio and Lugiato /8/, Meystre /7/, Carmichael and Herman /9/, Agrawal et al. /10/ and also the experiments performed by Sandle and Gallagher et al. /11/.

The first proposal for a hybrid bistable device was by Kastalskii /4/ and the first hybrid device was constructed by Smith and Turner /5,6/, and of about the same time by Garmire et al. /13/.

Our studies on bistability are concerned with both intrinsic and hybrid bistability /14-25/.

The main results presented in this paper are: the theoretical approach of intrinsic bistability in a general fashion, and elaboration of an adequate semiclassical analysis model /19/21/, the study of the amplification capabilities of the opto-electronics devices based on the optical bistability effect /16/, the theoretical analysis of some hybrid bistable devices /15/, the experiments performed on the magneto-optic and liquid crystal bistable devices /18,23/ etc.

2. Semiclassical model of the optical intrinsic bistability

In our studies, largely presented in papers /19,21/ we give up the first order differential field equation generally used in different optical bistability models.

In fact, Maxwell equations lead to a second order differential equation which gives the effective distribution of the electric field amplitudes ("rapidly varying amplitudes"). In this equation we just introduce the polarization obtained from Bloch equations in order to obtain an equation containing all the information about the field propagation in the cavity. Now, if in this equation we consider the approximation of "slowly varying amplitudes" generally used in all well known theories of optical bistability, a first order differential field equation is obtained again, but this time, the information about propagation effects is fully spared, because in this case, the neglected terms are small in all regions of operation.

The obtained second order differential field equation is

$$\frac{d^2E}{d\zeta^2} + \left[\kappa^2 + \kappa\left(\frac{i\alpha_0 - \beta_0}{1+|E|^2} + i\alpha'\right)l\right]E = 0 \tag{1}$$

where E is the rapidly varying amplitude of the internal field divided to the saturation field,

$$\kappa = k\ell \qquad \zeta = \frac{z}{\ell}$$

$$\alpha_0 = \frac{2}{\hbar c} g\eta\kappa p \frac{\gamma_\perp}{\Delta\omega^2 + \gamma_\perp^2}, \quad \beta_0 = \frac{\Delta\omega}{\gamma_\perp}\alpha_0 \equiv \alpha_0\delta \tag{2}$$

$g = \omega p/2\varepsilon$, α' being the absorption coefficient, p - the matrix element of the dipolar electric moment, η - the refractive index, $k = \omega\eta/c$, $\Delta\omega = \omega_0 - \omega$, ω_0 - the transition frequency, ω - the radiation frequency, l - the length of the Fabry-Perot cavity and c, h, ε having their usual meaning.

The phenomenon of optical bistability is determined by the multiplicative factor B of the solution of the equation (1)

$$B = \left|1 - Re^{-2\kappa_1''}e^{i2\kappa_1'}\right| \tag{3}$$

$$\kappa_1 = \kappa_1' + i\kappa_1'' = \kappa - \frac{\beta l}{2} + \frac{i(\alpha+\alpha')}{2} \tag{4}$$

where

$$\alpha = \frac{\alpha_0}{1+|E|^2}, \quad \beta = \frac{\beta_0}{1+|E|^2} \tag{5}$$

When the bistability is determined by the real part κ_1' it is dispersive and when it is determined by the imaginary part κ_1'' it is of absorptive type (R is the cavity mirror reflectivity). Particularly in the mean-field limit ($\alpha_0\ell \ll 1$, $\delta\alpha_0\ell \ll 1$) the bistability characteristic depends only on Bonifacio's cooperativity $C = \alpha_0\ell/4T$ or on $C\delta$ (T is the cavity mirror transmissivity).

Subsequently, the Maxwell-Bloch equations are solved in the "slowly varying amplitudes" approximation to obtain analytical expressions of the transmission characteristic. The obtained transmission characteristic of a Fabry-Perot resonator is

$$y^2 = x^2\left[\frac{1+R^2-2R\cos(2\theta-2\Phi)}{T^2} + \frac{4(1+R)C}{1+(1+R)x^2} + \frac{1+3R^2}{4}\left(\frac{4C}{1+(1+R)x^2}\right)^2\right] \tag{6}$$

with

$$\phi = \frac{\alpha_0 l/2}{1 + (1+R)x^2}\,\delta\,, \quad \text{where } \phi \text{ is cavity detuning.} \tag{7}$$

The expression (6) can be compared with similar expressions obtained with the "truncated Bloch hierarchy".

It results that our expression gives switch-on power higher as a result of fully taking into account the standing wave effects. This theoretical result presented in fig. 1 has been expected from the experimental works /11/. Also, from expression (6) results the conditions of pure absorptive and pure dispersive optical bistability. Figure 2 shows the influence of the cavity detuning on the bistability characteristics.

3. Amplification capabilities of the optical bistable devices

Bonifacio's theoretical model of bistability /8/ provides a basis for the definition and analytical computation of the most important amplification parameters of these devices: small signal amplification, pulse amplification and time response.

For steady state operation the bistability characteristic is

$$y = x + 2C\,\frac{x}{1+x^2} \tag{8}$$

Small signal amplification is defined by the expression

$$A_\delta = \frac{\delta x}{\delta y} \tag{9}$$

where $\delta\,x$ and $\delta\,y$ are small variations around steady state x_0 and y_0 values. Using the definition (9) and the differential equations for polarization, population difference and field which describe the system evolution result:

$$A_\delta(\omega) = \left\{ 1 + i\,\frac{\omega}{K} - 2C\,\frac{x_0^2 - (1 + i\,\frac{\omega}{2qK})}{(x_0^2+1)\left[x_0^2 + (1+i\,\frac{\omega}{qK})(1+i\,\frac{\omega}{2kq})\right]} \right\}^{-1} \tag{10}$$

where $K = \frac{CT}{2\ell}$ and $q = \frac{\gamma_\perp}{K} = \frac{\gamma_\parallel}{2K}$.

Similarly, the maximum pulse amplification for a specific operation regime of the device has the expression:

$$A_p = \frac{\dfrac{1 + \dfrac{2C}{C-\sqrt{C^2-4C}}}{(C-1-\sqrt{C^2-4C})^{1/2}} - \dfrac{1 + \dfrac{2C}{C + \dfrac{2C}{C+\sqrt{C^2-4C}}}}{(C-1+\sqrt{C^2-4C})^{1/2}}}{\left(1 + \dfrac{2C}{C-\sqrt{C^2-4C}}\right)(C-1-\sqrt{C^2-4C})^{1/2} - \left(1 + \dfrac{2C}{C+\sqrt{C^2-4C}}\right)(C-1+\sqrt{C^2-4C})^{1/2}}.$$

where C is the cooperativity.

The time response of the device is also calculated in paper /16/ by integration the differential equation of the device for a unity pulse applied at the entrance at t = 0.

4. Analysis of the electro-optic bistable devices

Several electro-optical bistable devices are developed in bulk or integrated optics. In paper /15/ we analyzed two representative types of such devices: a bistable Fabry-Perot resonator containing an electro-optic phase modulator and an integrated two arm interferometer, the elaborated model being general. The bistability characteristic is obtained using the transfer functions for both the device and feedback loop. The main results are: the differential equations of bistable and multistable operation of the devices, the bistability characteristics, the critical points of the hysteresis cycle, the amplification parameters etc.

For example, the obtained bistability characteristic of the bistable Fabry-Perot resonator are:

$$\frac{y}{x} = \frac{1}{1+C'\cos^2 \Phi} \tag{12}$$

where Φ is the phase difference induced by the feedback voltage and parameter

$$C' = \frac{4R}{(1-R)^2} \tag{13}$$

is defined by analogy with cooperativity C.

The bistability and multistability characteristics of the device are presented in fig. 3, where z is equal with every member of the equation

$$x = \frac{1+C'\cos^2 x}{C'\sin 2x} \tag{14}$$

which determine the limits of the stability regions of operation.

The electro-optic bistable devices with a delayed one or two feedback voltage are also discussed theoretical using Lyapounov method for stability analysis /20/.

5. Experiments on the liquid crystal bistable devices

We experimented two types of liquid crystal bistable devices: in separate configuration or non-resonant type and with passive resonator type /23,25/. a) Block diagram of the non-resonant bistable liquid crystal device is presented in fig. 4. In the low state (i) the liquid crystal is biased such as his transmission T is minimal and the exit power is

$$P_o^i = T_m P_e \tag{15}$$

where P_e is the incident power. When V_A rises, T also rises to T_M and the exit power in the high state(s) is

$$P_0^S = T_M P_e \tag{16}$$

the thresholf power being P_e^+. Similarly when P_e is reduced, there exists a value $P_e^{-e} \neq P_e^+$ which the device to tip into the low state. The values P_e^+ and P_e^- are determined by expressions:

$$P_e^+ = \frac{P_1}{KT_m}$$
$$P_e^- = \frac{P_2}{KT_M} \tag{17}$$

where P_1 and P_2 are the photodetector incident signals which determine the linear operation region of the amplifier AC and K is a constant factor. From fig. 5 we get the expression of the hysteresis cycle area:

$$A_H = \frac{\Delta T}{K' T_m T_M}(P_1 T_M - P_2 T_m)(P_1 T_M + P_2 T_m) \tag{18}$$

b) Block diagram of the liquid crystal bistable device in the passive resonator is presented in fig. 6.

The nematic liquid crystal cell situated in the passive cavity O_2O_3 coupled at the active O_1O_2 cavity of the HeNe laser is excited by an electronic feedback loop.

Dependance of the amplifier voltage V_A on the P_F signal at the photodetector for the values between P_F^+ and P_F^-, is essential for the bistable operation of the device.

The experimental cycle is presented in fig. 7.

6. Experiments on the magneto-optic bistable devices

In paper /18/ we present a new type of bistable "magneto-optic" device, developed from the active laser cavity by applying an axial magnetic field, the field being driven electronically by means of a feedback loop.

The block diagram of the device is presented in fig. 8. The two levels "high" and "low" of the laser signal P_0^+ and P_0^- respectively, which characterize the bistable behaviour of the device are situated in the quasilinear region of the curve which express the dependance of the laser intensity versus the B coil current. These levels are determined by the nonlinearities of the amplification stage. The hysteresis cycle of the device presented in fig. 9 can be controlled so that the device can be used as a magneto-optic circuit element, for example, as a pulse oscillator.

7. Other results

Other bistability studies presented in the references refered to: behaviour and operation conditions of the nonlinear bistable interfaces /23/ optical bistability in the stratified anizotropic media /22/, theoretical analysis of the bistability-selffocusing limit /23/ etc.

8. Conclusions

The results presented in this paper represent contributions both theoretical and experimental to the optical bistability. Our method of integrating the field equation is more precise in comparison with the "truncated Bloch hierarchy", where important terms for the saturation region, which is essential for the optical bistability, have been neglected. At the same time, our model reflects in an analytical form the effect of standing waves and is in accordance with experiments.

The expression established for the small signal amplification, pulse amplification and time response of the Fabry-Perot bistable device show the interdependence of different parameters of the field-cavity coupled system and can be used for the analysis of the dynamic behaviour of optical bistable devices as circuit elements. The conclusions obtained on the analysis of the electro-optic bistable device are general for the study of all devices with phase induced nonlinearities. At the same time, the systemic treatment of this kind of devices is important for their characterization like opto-electronic circuit elements.

Our experimental works concerning hybrid bistable devices reveal a new type of bistable behaviour, with a view to using them in applications.

FIGURE CAPTIONS

Fig. 1 Bistability characteristics after developed model. The incident y versus the transmitted field x for T = 0.01: (1) $\alpha_0 \ell = 0.1$; (2) $\alpha_0 \ell = 0.2$; (3) $\alpha_0 \ell = 0.4$

Fig. 2 The influence of the cavity detuning on the bistability characteristics: (1) $\emptyset = 0.01$ rad; (2) $\emptyset = 0.03$ rad; (3) $\emptyset = 0.1$ rad; (4) $\emptyset = 0.3$ rad.

Fig. 3 The bistability and multistability characteristics of the device

Fig. 4 Block diagram of the nonresonant bistable liquid crystal device: LCD-liquid crystal device; β: beam-splitter; POL: polarizer; PD: photodetector; A.C.: amplifier; S_1, S_2: power supplies; P_0, P_e: output respective input powers; V_A: output amplifier voltage; V_S - liquid crystal device bias voltage

Fig. 5 The hysteresis cycle of the device

Fig. 6 Block diagram of the liquid crystal bistable device in the passive resonator. M_1, M_2: the laser mirrors; M_3: high reflectivity mirror; LCD: liquid crystal device; POL: polarizer ; P.S.: power supply; A.C.: amplifier; PD: photodetector; Σ : optical addition stage; r: resistor; S, R: set and reset inputs; P_0: optical output signal; P_e: input optical signal; P_r: feedback signal; P_p: signal on the photodetector; V_A: output amplifier voltage; A_V:liquid crystal device bias voltage

Fig. 7 The experimental cycle

Fig. 8 Block diagram of the bistable magneto-optic device; Σ : addition stage; PD$_1$, PD$_2$: photodetectors; A.S.: amplifier stage; P.A.: power stage; L: coil around the laser tube; CO: optical switch; LED: light emitting diode; TG: triangle generator; O: oscilloscope; S, R: set and reset inputs; P$_o$: optical output signal; P$_p$: signal on the photodetector; P$_r$: feedback signal; P$_e$: input optical signal; V: reference voltage

Fig. 9 The hysteresis cycle of the magneto-optic bistable device

REFERENCES

/ 1/ A.Szőke, V.Daneu, J.Goldhar, N.A.Kurnit, Appl.Phys.Lett. 15, 376 (1969); E.Spiller, J.Appl.Phys., 43, 1673 (1972), H.Seidel, US Patent 3 610 731 (1971)

/ 2/ S.L.McCall, Phys.Rev. A9, 1515 (1974)

/ 3/ H.M.Gibbs, S.L.McCall, T.N.C.Venkatesen, Phys.Rev.Lett., 36, 113 (1976)

/ 4/ A.A.Kastalskií, Sov.Phys.Semicond., 7, 635 (1973)

/ 5/ P.W.Smith, E.H.Turner, Appl.Phys.Lett., 30, 282 (1977)

/ 6/ A.Schnapper, M.Papuchon, C.Puech, Opt.Comm., 29, 364 (1979)

/ 7/ P.Meystre, Opt.Commun., 26, 277 (1978)

/ 8/ R.Bonifacio, L.A.Lugiato, Phys.Rev. A, 18, 1129 (1978)

/ 9/ H.J.Carmichael, J.A.Herman, Z.Physiks B, 38, 365 (1980)

/10/ G.P.Agrawal, H.J.Carmichael, Phys.Rev. A, 19, 2074 (1979)

/11/ W.J.Sandle, A.Gallagher, Phys.Rev. A, 24, 2017 (1981)

/12/ I.M.Popescu,P.E.Sterian,E.N.Stefanescu, Proc.Int.Sch. "LAICS", Romania, 328-329 (1982)

/13/ E.Garmire, J.H.Marburger, S.D.Alen, Appl.Phys.Lett., 32, 320 (1978)

/14/ E.N.Stefanescu, P.E.Sterian, I.M.Popescu, Lucr.2 Simp.Nat.Tehn.Micr. 30-31 oct, Bucharest 1981, p. 443

/15/ P.E.Sterian, I.M.Popescu, E.N.Stefanescu, Lucr.2 Simp.Nat.Tehn.Micr. 30-31 oct, Bucharest 1981, p. 459

/16/ I.M.Popescu, P.E.Sterian, E.N.Stefanescu, Stud.Cerc.Fiz., Tom 34, No.10, Bucharest, 1982, p.905

/17/ I.M.Popescu, E.N.Stefanescu, P.E.Sterian, Bul.Inst.Pol.,Bucuresti,Tom XLIV,3, 1982, p.29

/18/ I.M.Popescu, A.Gh.Podoleanu, P.E.Sterian, Rev.Phys.Appl., 18, 313 (1983)

/19/ I.M.Popescu, E.N.Stefanescu, P.E.Sterian, Rev.Roum.Phys., Tom 19, No.2,Buc.,183 (1984)

/20/ P.E.Sterian, I.M.Popescu, E.N.Stefanescu, 3 Simp.Nat.Tehn.Micr.,18-19 nov. 1983 Buc.

/21/ I.M.Popescu, E.N.Stefanescu, P.E.Sterian, Rev.Roum.Phys., (in print)

/22/ E.N.Stefanescu, P.E.Sterian, I.M.Popescu, Lucr.Ses.An.ICEFIZ, 4-5 oct.1984, Sibiu, p.456

/23/ I.M.Popescu, M.A.Dumitru, P.E.Sterian, Bul.Inst.Pol. Bucuresti (in print)

/24/ I.M.Popescu, M.A.Dumitru, P.E.Sterian, Rev.Roum.Phys. (in print)

/25/ A.Gh.Podoleanu, Ph.D. Thesis, Inst.Pol.Bucharest, 1984

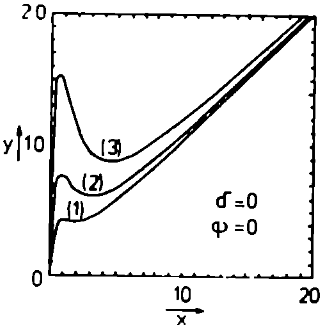

Fig. 1

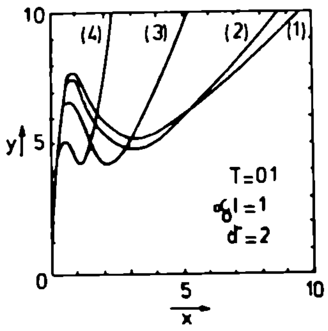

Fig. 2

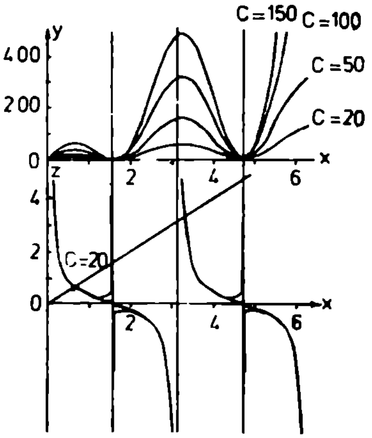

Fig. 3

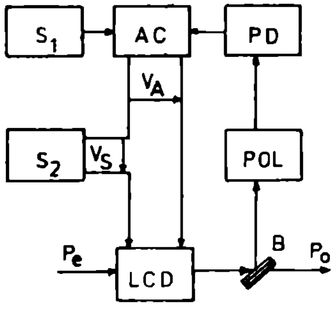

Fig. 4

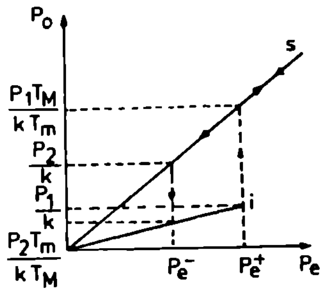

Fig. 5

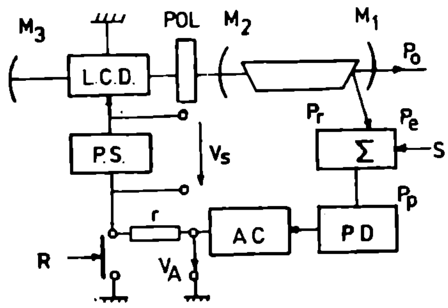

Fig. 6

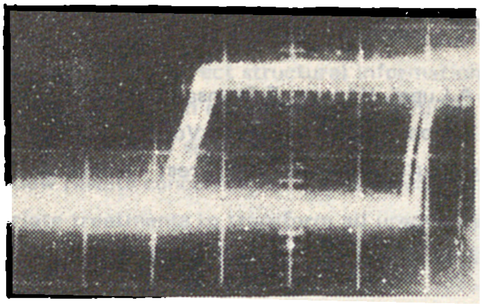

Fig. 7

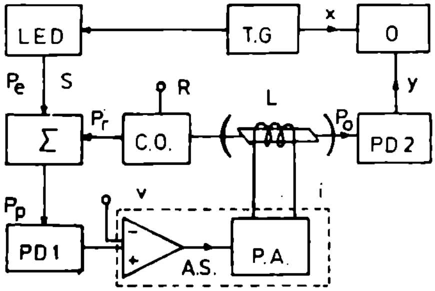

Fig. 8

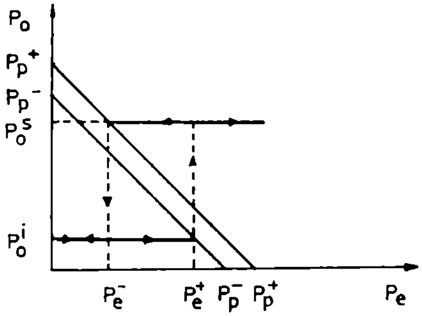

Fig. 9

DETECTION OF URANIUM TRACES IN WATER BY LASER EXCITED FLUORESENCE*

I.Ursu, A.Lupei, V.Lupei, F.Domsa, C.Ionescu,
A.Ponta, O.Radulescu, L.Voicu
Central Institute of Physics, Bucharest - Romania

1. Introduction

The detection of very small quantities of uranium from water is important from several points of view: hydrogeochemical exploration of uranium, migration of uranium material through soils and mineral deposites (especially around nuclear waste repositories), geophysical research etc. Many of the methods for uranium detection, reported in the literature, involve either enrichment (or separation) or have rather poor sensitivity or are destructive.

Several of the uranium ions (especially U^{6+}) present strong luminescence in solid matrices (such as alkali or alkaline earths fluorides). This fluorescence can be used in an analytical method for concentration determinations. The selectivity and sensitivity of such a method can be improved by laser excitation.

Thus, if uranium from the aqueous solution could be controllably incorporated in a suitable valency state in a solid matrix, its luminescence emission under laser excitation can be, in principle, used in order to measure the uranium concentration. Quantitative measurements by laser induced fluorescence imply some requirements on the samples: incorporation of uranium should be as large as possible; all uranium should be incorporated in the same valency and structural center; sharp excitation and fluorescent lines, for selectivity; the chosen center should be stable in time and under laser excitation, etc. These requirements could be satisfied by U^{6+} in CaF_2 single crystals, where sharp luminiscent lines are observed at 77 K and lower temperatures /2-4/. However, single crystal is not a fassible form for everyday analytical work. A more appropriate form is that of microcrystals created by precipitation from solution and calcination. CaF_2 proved to be a promising matrix in this respect since it can be easily handled and polycrystalline form presents sharp U^{6+} luminiscent lines /1,5,6/. By careful choice of the experimental conditions, amounts as low as 4×10^{-14} Mol (10^{-5} parts per billion) could be detected by laser excited luminiscence /5,6/.

As was outlined before, in CaF_2 single crystals /2,4/ and polycrystalline form /1,5-7/ U^{6+} can form various centers. Besides, our EPR studies /3,4/ indicated that in the same crystals U^{5+} valency form too. Since from the technological point of view it is essential to have all of the uranium in the same center (and valency), the ellucidation of the structure of these center

---

*) Work performed under a contract with IAEA

is important.

Luminiscence studies, including those under laser excitation can give information on the variety of uranium centers, but not direct structural information. EPR on U^{5+}, transformed from U^{6+} by different methods (irradiation or heating) could provide structural information. For such purposes only the crystalline form is appropriate.

In this paper new results concerning U^{6+} luminiscent centers in CaF_2 single crystals shall be presented. Appropriate treatments to transform all uranium in a given valency and center are also studied. The second part of the paper is dedicated to similar studies on the polycrystalline CaF_2-U form.

2. Experiment

Single crystals of CaF_2 doped with U_3O_8 (or UO_2) were grown by the Czochralski or the Bridgman method. Oxygen deficit in the growth process leads to uranium valency states other than +6. The crystal with larger oxygen content presents a slight oxidation, has a white cloudy color but also contains some quantities of U^{5+}. The kinetics of U^{6+} and U^{5+} transformations were studied by γ-irradiation or heat treatments.

Microcrystallite form of CaF_2 containing uranium has been prepared by precipitation from solution and subsequent calcination. Fluorescence measurements on U^{6+} have been performed at 300 K or 77 K by using the third harmonic of a YAG:Nd laser (Quanta-Ray-DCR). The detection system consists mainly of a monochromator (GDM-1000) and box car integrator (PARC-162). Studies concerning U^{5+} centers have been performed at 77 K, using a Varian E-12 EPR spectrometer.

3. Results and discussion

3.A. Spectroscopy of U^{6+} and U^{5+} in CaF_2 single crystals

Our previous studies /3,4/ using classical luminiscence revealed in white clouly CaF_2-U samples, green luminescence under u.v. excitation. Low temperature spectra are dominated by a line at 5212.5 Å (C_1-center) and other smaller sharp lines at longer wavelengths Fig. 2b. Since by an improved phase sensitive technique (chronospectroscopy) no other centers could be separated and no sample dependence of the lines was obvious, it has been assumed that longer wavelengths lines are vibronics connected to the 5212.5 Å transition /3/. However, in the same samples, EPR measurements revealed the presence of several U^{5+} centers. The most intense U^{5+} centers observed in our samples are: a) a trigonal center (Tr) without any superhyperfine structure, also observed in green CaF_2 samples /8/ and assigned to a U^{5+} substitutional ion surrounded by six O^{2-} and two fluorine vacancies; b) a rhombic (Rh_1) center /9/ with a similar structure, except that only five O^{2-} replace F^- and c) a low symmetry center (Rh_3) with no superhyperfine structure and having a slightly different structure from Tr center /3/. All U^{5+} centers in CaF_2 are uranate structures and it is expected that U^{6+} are also such centers.

In order to select a model for the U^{6+}-C_1 center, a study of the $U^{6+} \rightleftharpoons U^{5+}$

transformations by γ-irradiation was performed /3/. The most obvious effect of irradiation is a U^{6+}-C_1 center decrease and a U^{5+}-Tr center increase. The irradiation process can provide electrons, captured by U^{6+} to transform it into U^{5+}. Therefore, the model for the C_1-U^{6+} center is very likely to be a UO^{6-} trigonally distorted octahedron, Fig. 1 /3/. U^{6+} is completely compensated in this case and local symmetry is trigonal with inversion, as previous Zeeman studies have shown /2/.

Following the irradiation, another U^{6+} center (C_2) emitting at 5468.5 Å (77 K) was evidenced. Using the chronospectroscopy technique we have been able to separate the lines belonging to C_1 and C_2 luminiscent centers, but no structure for the later has been proposed. The elucidation of the C_2-U^{6+} center structure is important from the technological point of view, since it is the most disturbing center for concentration determinations /5/. For this purpose, combined laser spectroscopy on U^{6+} and EPR on U^{5+} centers were used to follow the kinetics of $U^{6+} \rightleftharpoons U^{5+}$ transformations by γ-irradiation and heating.

If our as-grown single crystal CaF_2-U samples contain practically only the C_1 center, irradiation produces the 5468 Å (C_2 center). Time resolved spectroscopy can be used to separate lines belonging to different centers. Fig. 3 presents luminiscence spectra at 77 K detected at different time delays following the laser pulse. Lifetimes of the two lines at 77 K are rather different: 410 μsec for 5212.5 A and 20 μsec for 5468 Å lines. A two exponential fitting was necessary, since some of the vibronics associated to 5212.5 Å line are overlapping with the 5468 Å line. Room temperature lifetimes for the two centers are 170 μsec for C_1 and ∿ 30 μsec for C_2.

A signifiant increase of the U^{5+}(Tr) center and decrease of the rhombic Rh_3-U^{5+} center was observed after irradiation. EPR characteristics are very similar for the two centers: g_{111} = 0.19, $g_{\perp}$ = 1.048 for TrU^{5+} and $g_z = 0.2$, $g_x = 1.019$, $g_y = 1.054$ for Rh_3, where Z, X and Y are slightly rotated from the <111>, <110> and <112> axes. No superhyperfine structure is resolved in either cases. For this reason, it has been assumed that the Rh_3 center has a similar structure with Tr, an UO_6 complex like in Fig. 1. The - 1 excharge in the case of Tr U^{5+} is very likely to be far away compensated; whereas in the case of the Rh_3-U^{5+} center a close compensator, very likely a fluorine vacancy, can be assumed.

The most probable structure for C_2-U^{6+} is a similar one with Rh_3: U^{6+} substitutional for Ca^{2+}, six O^{2-} and two fluorine vacancies replacing the nearest F^- (like in Fig. 1) and a fluorine vacancy in the neighbourhod of this complex. Lower lifetimes connected to this center suggest a lower symmetry for it. Heating effects sustain this assumption. A several minute heating at 600°C has the reverse effect of irradiation: the U^{5+} - Rh_3 center increases and the U^{6+} - C_2 is destroyed. By heating at 1000°C in air the Rh_3 center is also destroyed. A fluorine vacancy migration, activated by heating can explain such effects. All these centers: $C_2(U^{6+})$, $Tr(U^{5+})$ could be transformed into $C_1(U^{6+})$ by heating. The most heating-resistant is the U^{5+} - Rh_1 center whose structure involves one F^-, therefore O^{2-} is necessary to replace F^- to transform this center into a U^{6+} - C_1 center.

3.B. Spectroscopy of uranium in pollycristalline CaF_2

Luminiscence studies on CaF_2-U precipitated from solution and calcinated in air in different conditions have resolved four major classes of U^{6+} luminiscent centers /6/. The relative intensity of these centers is function of the concentration and calcination process. At low uranium content (< 10^{-2}%), two centers: C_1 and C_2 are the most intensive. A variation of the of the C_2-center concentration from sample to sample was observed, even though the conditions for preparation had been the same. High temperature calcination (over 600°C) determines its disappearance. Single crystals studies are in agreement with this observation, indicating also the reason: the C_2-U^{6+} center can be transformed by heating a C_1-U^{6+} or Rh_3-U^{5+} center.

Samples with concentrations of 6.10^{-5} to 6×10^{-11}. Molar uranium, calcinated at 1000°C, present strong green luminiscence. Even at average power of the third harmonic of YAG:Nd laser (Quanta Ray) a very good signal to noise ratio has been obtained for luminiscent spectra. Detection limits of our experimental set-up can be easily increased by laser power or appropriate optics. Therefore, actual determinations of the uranium content in water ($\sim 10^{-10}$ Molar in usual ground waters) can be performed. Problems connected to precipitation efficiency, impurities interferences, etc. have to be solved. Low temperature measurements are more selective as concerning impurities interferences or laser scattering.

Our studies on single CaF_2:U crystals have shown that main U^{6+} centers, C_1 and C_2, are essentially connected to the O^{2-} presence in the sample. The proposed structure, based on luminiscence and EPR data, for the C_1 center is presented in Fig. 1. Kinetics of the $U^{5+} \rightleftharpoons U^{6+}$ transformation during irradiation and heating suggest a similar structure for the C_2 center, with an extrafluorine vacancy in the neighbourhood. Heating can easily activate this vacancy and transform C_2 into C_1 center.

Other U^{6+} centers observed by M.V.Johnston and J.C.Wright /6,7/ could be connected to impurities (such as cations). Since such impurities are likely to be found in ground waters and can affect uranium concentration determinations, a study concerning other centers structures is in progress.

REFERENCES

/1/ J.V.Nichols, Phys.Rev. 155, 151 (1967)

/2/ N.B.Manson, G.A.Shah, W.A.Runciman, Sol.St.Coum. 16, 645 (1975)

/3/ A.Lupei, V.Lupei, J.Phys. C.Sol.St.Phys., 12, 1123 (1979)

/4/ I.Ursu, V.Lupei, A.Lupei, Rev.Roum.Phys., 23, 673(1978)

/5/ D.Parry, S.M.Kleiner, H.R.Bowman, F.P.Milanovich, T.Hirschfels, S.Miller, Anal.Chem. 53, 1048 (1981)

/6/ M.V.Johnston, Y.C.Wright, Anal.Chem. 53, 1050 (1981)

/7/ M.V.Johnston, J.C.Wright, J.Chem.Phys. 73, 1250 (1981)

/8/ V.Lupei, A.Lupei, I.Ursu, J.Phys. C.10, 4587 (1977)

/9/ A.Lupei, V.Lupei, J.Phys. C.11, 2861 (1978)

FIGURE CAPTIONS

Fig. 1 Proposed model for O_1-U^{6+} center in CaF_2.

Fig. 2 Luminiscence spectra of CaF_2:U^{6+} at 77 K, λ_{exc} = 355 nm:
a) recorded after laser pulse; b) recorded at 100 μsec after laser pulse.

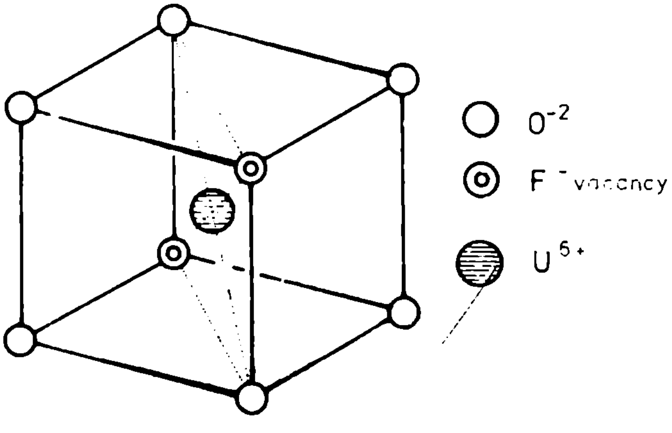

Fig.1

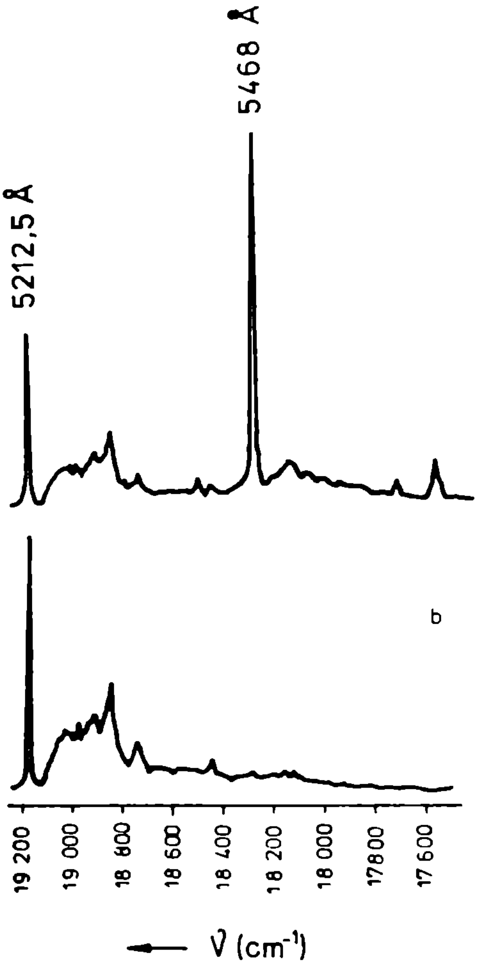
5212,5 Å
5468 Å
b
19 200
19 000
18 800
18 600
18 400
18 200
18 000
17800
17 600
ν̃ (cm⁻¹)

Fig.2.

LASER CRYSTALS AND THEIR APPLICATIONS

I.Ursu and V.Lupei

Central Institute of Physics, 76900 Bucharest, Romania

1. INTRODUCTION

Solid state lasers are now extensively used due to some unparalleled qualities: small size, good efficiency, a wide range of wavelengths available, from UV to middle infrared, a variety of working regims, from cw to very short pulses with extremely high peak power and so on. Of central importance in a solid state laser is the active medium, a transparent solid, usually a single crystal, containing a fairly large concentration of identical active centers. Such active centers are characterized by discrete energy levels or bands that, on interaction with an external excitation, can produce stimulated emission.

The static and dynamic properties of the electronic energy levels of the active centers determine the wavelength of the stimulated emission; they also direct the choice of the means of excitation, and the regime of generation. Other important parts of a laser such as the pump system and the optical resonator are subordinated to the active medium; they must provide the necessary environment for, in a given active medium, the threshold for stimulated emission be reached and exceeded.

This remark holds also in the case of nonlinear devices, where the performance of the system is mainly determined by that of the nonlinear element.

On such grounds, the research on laser crystals in Romania is integrated in a R and D programme which bears upon the active medium, the laser as a whole and, in some cases, on technological applications of lasers. Work is mainly concentrated in the Laboratory for Laser Active Media and Interaction of Radiation with Matter at the National Centre of Physics, Bucharest. The programme relies largely on the expertise acquired by this group in quantum optics, microwave physics and technology, and in the investigation of electronic structure of ions of transition elements in crystals by electron paramagnetic resonance and optical spectroscopy methods.

The present report updates a previous review, presented at the International Conference and School "Laser and Applications" (Laics '82), held in Bucharest, September 1982 [1].

Our programme on laser crystals and applications involves basic, applied and technological research, as well as a laboratory-scale production. The main objectives are [1,2]:

- crystal growth and processing; passive and active testing of laser active media; electrooptic, nonlinear and pyroelectric crystals and materials for UV and IR optics;
- new laser crystals and laser designs;
- engineering of solid state lasers;
- practical use of solid state lasers, especially for material processing and thermal treatment.

The main sections of the programme are:

1. Research on physics of laser active centers.
2. Growth and processing of laser active media; nonlinear, electrooptic and pyroelectric crystals and crystals for UV and IR optics.
3. Research on the properties of laser crystals, and their passive and active testing.
4. Construction of devices based on the above-mentioned crystals (lasers, electrooptic and nonlinear devices, detectors).

5. Research for technological applications of solid state lasers. Manufacture of laser-based equipment for materials processing.

6. Related studies and other applications of the systems used, or investigated, as laser crystals.

In the following we shall review some of the main results obtained along these lines.

2. RESEARCH ON PHYSICS OF LASER-ACTIVE CENTERS

Work is aimed at obtaining basic data that are necessary in order to characterize a laser-active center and its interaction with the host crystal.

2.1. Methods used in the study of laser-active centers

A large variety of physical methods is used for the investigation of laser-active centers: UV-, visible-, and IR-, optical spectroscopy; luminescence spectroscopy; excitation spectra; lifetime measurements; amplitude and phase chronospectroscopy; laser spectroscopy (with dye lasers continuously tunable from 217 nm to 2 micrometers or on the 2nd, 3rd or 4th harmonic of a YAG:Nd laser); thermoluminescence; electron paramagnetic resonance (9 and 35 GH microwave bands), and so on. Measurements under the influence of external factors such as temperature (from liquid helium up to the range of hundred degrees) can be performed for most of these methods. Influence of X or gamma irradiation of these centers with a cobalt source can also be investigated.

Some of these methods are computer- or microprocessor-controlled. Desk-top or cabinet computers are used for data acquisition and processing and for computing various parameters of the experiment.

A considerable effort was devoted to improving experimental techniques. A typical example in this respect is chronospectroscopy. If in a luminescence experiment the excitation light is modulated, this would induce a phase-shifted, modulated, emission; the phase shift is due to the finite lifetime of the pump and emitting level. If the sample under investigation contains several luminescent centers with different lifetimes, the resolution of the spectra can be increased by cancelling out some of the luminescent spectra, by a suitable choice of phase in the detecting system [3]. In these experiments the connection between phase shift and lifetime has been established in a simple model of an equivalent LC circuit for a two-level system. We extended these studies to real three-level systems by using rate equations [4] -- a method that gives the lifetimes for the emitting and pump levels. Using phase spectra versus wavelength the optimum modulation frequency for the best resolution of the spectra can be estimated. Analytical expresions for line intensities as functions of modulation frequency given by this model [5] indicate again the lifetimes of the pump and emitting levels

2.2. Research topics, on laser-active centers in crystals

2.2.1. Nature and structure of the active centers in crystals

A. Ions under study: 3rd group, lanthanides, actinides.

B. Problems of study: identification of the valence states, crystal field symmetry, structure of the centers, charge compensation mechanisms, distribution of the active ions among various possible centers and so on.

C. Typical examples

a) the study of a diversity of Nd^{3+} centers in YAG. A systematic investigation of a large number of YAG:Nd crystals, performed in various laboratories [6,7], including ours, shows a large fan of performances, among them the capacity of stimulated emission. As a possible source of these qualities, perturbations of the crystal field acting on Nd^{3+} ion due to lattice defects or impurities have been assumed. Thus by using selective laser spectroscopy we detected several non-equivalent sites in some of our YAG:Nd samples in the luminescence line $R_1 \rightarrow Z_1$ of the transition $^4F_{3/2} \rightarrow {}^4I_{9/2}$ at liquid nitrogen temperature. The distribution of the Nd^{3+} ions among these sites depends essentially on the crystal growth conditions and, sometimes, on the position in crystal wherefrom the sample under study has been cut.

Such centers have different lifetimes and show a non-exponential decay. The YAG crystals with 1 to 3 at % Nd with the largest number of centers show the shortest life-time in a normal, non-selective, measurement at room temperature;

b) the distribution of Nd^{3+} among various centers in calcium tungstate crystals with different charge compensation means has been studied;

c) the elucidation of the nature and structure of luminescent uranium centers in alkali- or alkaline-earth fluorides grown in presence of oxygen; for alkali fluoride these centers consist of uranate groups embedded in the lattice: U^{6+} substitutes for the host alkali cation and the charge compensation is achieved by substituting five (for the prevailing center) or six F^- nearest neighbours by O^{2-} ions [8,9]. In the last case the negative extracharge is compensated by cationic impurities localized near this complex, so that a large variety of centers results [10,11]. In case of calcium fluoride the main luminescent center consists of a substitutional U^{6+} ion surrounded by six substituted O^{2-} ions and two fluorine vacancies on the same body-diagonal [12,13];

d) new U^{3+} centers with cubic, tetragonal or orthorombic symmetry have been observed in alkaline-earth fluorides, and a correlation of the occurence of these centers with crystal growth conditions proved possible [14-17].

2.2.2. Research on the electronic structure of the active centers

In order to determine the electron energy levels of ions in crystals and their dynamic properties a large variety of studies have been performed, e.g.: Nd^{3+} in YAG, YAP, $CaWO_4$, NdPP, LaF_3, CaF_2 and so on, Er^{3+} in YAG, GdAG, GGG, ErAG, LaF_3, (Er,La)PP, Pr^{3+} in LaF_3, CaF_2, U^{3+} in CaF_2, SrF_2, Cr^{3+} in ruby, YAG, Ti^{3+} in Al_2O_3 etc.

Typical examples are:

a) The energy spectrum of the various centers of Nd^{3+} in YAG, by site-selective laser spectroscopy. Luminescence, excitation, and life-time, measurements were used in order to determine the electronic structure of various centers, the interactions between centers and their effect upon the laser-performance of crystals.

b) Determination of electronic structure of Nd^{3+} in $YAlO_3$. The Stark components of the energy levels have been measured by optical absorption and luminescence and the electrostatic, spin-orbit, and configuration, parameters have been estimated [18].

c) A low-temperature spectroscopic investigation of Ti^{3+}-doped Al_2O_3 reveals, besides the well-known broad absorption band, a very sharp line at 617.7 nm followed by a progression of lines with a spacing of about 200 cm^{-1}. This line was attributed to a zero-phonon transition between the lowest level of the ground state and the lowest level of the Jahn-Teller split ^2E excited state [19].

d) A study of the kinetics of population and decay of Er^{3+} luminescence in LaF_3 (transition $^4S_{3/2} \rightarrow {}^4I_{15/2}$) by chronospectroscopic method and selective pumping in various upper levels shows that the decay lifetime from the immediately adjacent $^4H_{11/2}$ level on $^4S_{3/2}$ is about 1 microsecond whereas that corresponding to the decay from the farther away situated $^4G_{11/2}$ level is about 100 microseconds. This difference is explained by the cascade behaviour of the decay in the latter case [20].

e) Details of the energy level diagram for the main luminescent centers of U^{6+} in LiF, NaF and CaF_2 have been determined and correlated with the physical structure and symmetry of the centers.

2.2.3. Crystal field effects

A. Problems:

- measurements of crystal field parameters
- wavefunctions of the Stark levels of the transition ions in crystals
- intensity of transitions
- crystal field models: role of covalency and overlap for 3d, lanthanide and actinide ions in crystals.

B. Typical examples:

a) Analitical wavefunctions for the representations which enter more than once in the cubic crystal field decomposition of the electronic energy levels. These wavefunctions depend on the composition parameter x of the crystal field potential, i.e. on the ratio of the sixth- to the fourth order parameters of this potential. Usually this dependence is computed numerically and tables of functions calculated for a given increment of x are available. By making a complete use of the transformation properties of the wavefunctions under the cubic point group operators (especially the rotations $R_z(\pi/2)$ and $R_y(\pi/2)$, analytical expressions of these functions versus x have been obtained. The matrix elements of a given operator between such wavefunctions are dependent on x, and this parameter can thus be easily estimated from experiments which involve the measurement of these matrix elements [21].

b) Crystal field effects and the Judd-Ofelt theory for Er^{3+} in YAG. The crystal field levels of the ground $^4I_{15/2}$ level of Er^{3+} in YAG are grouped into two distinct groups of four closely packed levels with quite a large gap between groups. Thus a basic assumption of the Judd-Ofelt theory (equal population of the crystal-field components of the ground level) is no longer valid. A calculation which approximates the population of the crystal field levels inside each group as equal, but different from that corresponding to the other groups was performed. For some transitions such a calculation gives results above those yielded by the usual Judd-Ofelt theory, whereas for other, figures fall beyond [21].

c) Crystal field models for Nd^{3+} and U^{3+} cubic crystal fields. Since the ground crystal field level of these ions in the cubic crystal field of CaF_2 is one of the two Γ_8 representations, its wavefunctions depend upon the composition parameter x and thus this parameter can be estimated simply from EPR experiments. The measurements performed in our laboratory for U^{3+} [23] gave for the composition parameters a value in excellent agreement with earlier calculations [24] based upon an overlap and covalency model, while in case of Nd^{3+} the agrement is poor and other contributions (such as point charge) must be taken into account. This conclusion is in agrement with the orbital reduction factor for g_J for the two ions in question and with the superhyperfine interaction measurements.

2.2.4. Hyperfine structure investigations

Problems:

- measurements of hyperfine structure parameters;
- use of hyperfine structure data in order to check the validity of electron structure and crystal field calculations;
- relativistic effects;
- estimation of nuclear moments [25].

2.2.5. Research on interactions between ions in crystals

Problems:

- exchange and multipole interactions between ions in crystals;
- pairs and larger assemblies of ions in crystals;
- energy transfer and migration;
- cross-relaxation processes;
- up-conversion of radiation.

Typical examples:

a) Energy transfer from actinide to lanthanide ions in crystals. U^{6+} complexes transfer very effectively the energy to the trivalent lanthanide energy levels located 16,000 to 1900 cm^{-1} above the ground state, while the U^{3+} ones transfer the energy to the lower (below 4000 cm^{-1}) energy levels of the lanthanide ions.

b) Up-conversion, energy transfer and cross-relaxation in crystals with high-concentrations of rare-earths. Violet and blue emissions were observed from crystals of YAG heavily doped with Er^{3+} when excited either in red (6475 Å) or green (second harmonic of the YAG:Nd laser). From the time-evolution of emission and dependence of intensity on concentration of Erbium it was concluded that various energy transfer and cross-relaxation processes contribute to this up-conversion [26].

c) Up-conversion and energy transfer from Yb^{3+} to Er^{3+}, Ho^{3+}, Tm^{3+} in matrices such as YF_3 or CaF_2 were investigated.

2.2.6. Channeling of charged particles in crystals

Problems:

- electromagnetic radiation of channeld particles;
- channeling in doped crystals;

- energy transfer from channeled particles to ions in crystals as a method for pumping the very high energy levels of the transition ions.

2.2.7. Characterization of the transition ions in crystals as laser-active centers

A. Problems:

- characterization of the energy levels of the ions in crystals as pump, metastable and terminal laser levels;
- new laser schemes;
- new laser-active media;
- active media for tunable solid state lasers.

Examples:

a) YAG:Er as a laser-active crystal. Though the lifetime of the terminal level of the 3 micron transition $^4I_{11/2} \rightarrow {}^4I_{13/2}$ of YAG:Er is considerably larger than that of the initial laser level (a fact which usually prevents an effective laser emission), a quasistationary regime of laser emission was achieved in this crystal at large concentrations of Erbium. This was explained by the fact that the energy level diagram of Er^{3+} in YAG alows that several cross-relaxation processes take place, some of them being very effective in depopulating the terminal laser level and re-pumping the initial level of the laser transition. Such cross-relaxations can easily be put into evidence by their effect upon the evolution of the level populations under short-pulse excitation [27].

b) Uranium ions as laser-active centers. A systematic investigation of the properties of various centers in crystals shows that they possess some very interesting properties as laser-active centers [28]. Thus, various U^{6+}, U^{5+}, U^{4+} or U^{3+} centers have very strong and effective pump bands in UV and visible. However, due to the strong electron-phonon coupling or to some peculiarities of the energy level diagram, these centers may be used at room temperature mostly as three-level laser systems: in some cases the absorption in excited states precludes even this. Uranium ions can, however, transfer very effectively the energy to other ions, for instance, to the trivalent lanthanide ions. Thus, hexavalent uranium could be used as a sensitizer for the $^4F_{3/2}$ level of Nd^{3+} on which the 1.06 and 1.32 micrometer radiation is generated. On the other hand, trivalent uranium could be used to sensitize (from the $^4I_{11/2}$ level) levels for middle-infrared generation; the $^4I_{13/2}$ of Nd^{3+} (which could lase at 5.5 micrometers to the $^4I_{11/2}$ level) $^7F_4$ level of Tb^{3+} (which could lase at about 8 micrometers to $^7F_5$), $^7F_5$ of Eu^{3+}, $^5I_6$ of Pm^{3+}, $^6H_{13/2}$ of Dy^{3+}, $^6H_{11/2}$ of Sm^{3+}, and so on.

3. GROWTH AND PROCESSING OF LASER-ACTIVE MEDIA; NONLINEAR, ELECTROOPTIC AND DETECTOR CRYSTALS; UV AND IR MEDIA

3.1. Main topics

The main lines of work in this field are:

- high sensitivity analysis by chemical methods, atomic absorption spectroscopy, emission spectroscopy, X-ray microprobing, neutron activation;
- purification of some raw materials;
- research on thermal effects in crystal growth; design and construction of the thermal set-up (thermal insulation, screens, afterheaters and so on);
- crystal growth;

- correlation of the crystal growth parameters with data obtained from testing;

- studies on the effects on the quality of crystals of instabilities or irregularities;

- preliminary quality testing;

- heat treatment;

- high-precision processing of laser components;

- anti-reflex coating.

3.2. Crystal growth methods

Crystal growth is performed with commercially available, or with home-made, equipment. This activity is restricted to crystals grown from melt. The methods currently used are:

- flame fusion;
- pulling from melt;
- temperature gradient method;
- zone melting;
- edge-defined film-fed growth (EFG).

Of these, the most used is pulling from melt (Czochralski) method, under manual or automatic control.

Research on crystal growth in unusual conditions was also performed, e.g. growth of crystals with a given profile in low gravity conditions [29]: in a closed crucible containing the raw material a capillary die (made of a wetting material) is inserted. In microgravity conditions (on an orbital station) the capillary forces produce a fast flow of melted material through capillary and the shape of the melt drop at the end of it cannot be controlled as in an usual EFG method. Because of this on top of the wetting die a non-wetting die is placed, which controls the shape of the melt drop and inside of which the crystalization occurs on a seed, or simply, by crossing a region with temperature suitable for solidification. The experiment performed with germanium during the cosmic fly of the first Romanian astronaut in May 1981 showed that the wetting capillary has a very strong pump indeed (about all of the material is pumped out of the crucible) and the capillary diffusion mechanism contributes essentially to a perfect mixing and a uniform doping for the germanium-gallium system. Besides other spectacular applications (such as growth of silicon plates for producing solar cells directly on an orbital station) this method could be used to grow laser crystals of pre-determined shape and composition or with an uniform impurity distribution.

3.3. Main results obtained in the field of laser crystals and components

A large variety of crystals have been grown, most of them for the first time in our country: Calcium fluoride (1972), strontium fluoride (1973), sodium fluoride (1972), cadmium fluoride (1973), sapphire (1973), ruby (1973), calcium tungstate (1974), calcium molibdate (1975), lanthanide-sodium hexachlorides (1975), neodymium pentaphosphate (1975), silver chloride (1975), lithium tantalate (1976), lanthanum trifluoride (1976) and so on.

3.3.1. Laser active media

Some of the main results in this field are:

A. High-quality YAG:Nd crystals for pulsed or cw laser operation. Typical features of the YAG:Nd rods are:

Shape: right circular cylinders with flat or spherical (with various curvatures) ends.

Average concentration of neodymium:

- for pulsed lasers: 1.1 to 1.3 at %
- for cw lasers: 0.7 to 1 at %.

Maximum variation of the Nd concentration along the rod: 10% of the average value.

Size of the rod (diameter x lenght, mm):

- for pulsed laseres: up to 5 x 70
- for cw lasers: up to 6 x 90.

Number of bubbles or inclusions: none

Attenuation: typical 30 dB at 50 mm length.

Number of fringes (Mach-Zender): 0.5 per inch.

Flatness of ends: $\lambda/10$.

Perpendicularity of faces to the rod axis: better than 5'.

Parallelism of faces: better than 4".

Orientation of rod axis < 111 > : ± 4^{o}.

Hard antireflection coating.

The threshold for pulsed operation is of a few joules and the shape efficiency is up to 1.6%.

B. Czochralsky ruby, rods up to 10 x 120 mm.

C. Calcium tungstate doped with neodymium.

D. Calcium molibdate doped with neodymium.

E. Yttrium aluminate doped with neodymium.

F. Highly concentrated YAG:Er.

G. Mixed garnets doped with neodymium or erbium.

H. Alkaline-earth (Ca,Sr,Ba) fluorides doped with lanthanides or uranium.

I. Lanthanum trifluoride doped with lanthanides.

J. Mixed fluorides.

K. Neodymium pentaphosphate.

L. Halide crystals with color centers for tunable emission.

3.3.2. Non-linear and electrooptic crystals

A. High-homogeneity lithium niobate crystals for Q-switches, modulators, frequency doubling, parametric generation.

B. Lithium tantalate for modulators.

C. Barium sodium niobate.

D. Crystals with color centers for passive shutters.

3.3.3. Crystals for infrared detection

A. Pyroelectric crystals: lithium tantalate, strontium barium niobate.

B. Quantum counter systems: CdF_2, trihalides.

3.3.4. Crystals for UV and IR optics

A. Potassium, sodium and silver chloride.

B. Lithium or sodium fluoride.

C. Calcium fluoride.

D. Sapphire.

Attention was also given to some transparent polycristalline materials produced by hot pressing.

4. RESEARCH ON PROPERTIES OF ACTIVE MEDIA AND THEIR PASSIVE AND ACTIVE TESTING

An essential segment of our activity is devoted to the study of the properties of active media and to the development of significant tests which give an as comprehensive as possible characterization of the laser active media [30].

Both the passive parameters (in various stages: crystal, component, before or after thermal treatment and so on) and the active ones are measured. The passive parameters are measured in normal passive (non-pumped) situation by usual laboratory physical methods, while the active ones are measured under pumping conditions. Thus the active parameters are common to the rod and to the laser set-up used for measurement.

The aim of measuring these parameters is to get a close prediction of the rod performance in lasers and to get meaningful data in order to control the crystal growth and the complementary technologies so as to confer to the rod the desired parameters [31]. At the same time, the active testing gives essential data that are required in the construction of lasers with optimum performances for a given rod.

Depending on the particular case in question, some or all of the parameters given below are measured.

1. Passive parameters

4.1.1. Spectroscopic parameters

- emission lines;
- pump levels;
- lifetimes;
- cross-sections;
- linewidths;
- branching ratios;
- fluorescence quantum yield.

Methods; optical absorption spectroscopy, luminescence, lifetime measurements, amplitude and phase chronospectroscopy, excitation spectroscopy, laser spectroscopy.

4.1.2. Optical parameters

- refraction index and its variations;
- scattering of light on bubbles, inclusions and other defects;
- number of interface fringes;
- extinction ratio;
- passive divergence.

Methods: interferometry, transmission between crossed polarizers, scattering of light (total, radial and longitudinal), shadow projection, far field intensity distribution, near field image.

4.1.3. Structural parameters

- degree of microcristallinity;
- orientation;
- twinning;
- mosaic structure;
- dislocations;
- facets;
- number of structural centers of the active ion;
- local symmetry of the center;
- structure of the centers;
- distribution of the activator ions among the possible centers;
- charge compensation mechanisms;
- clustering, and so on.

Methods: X-ray structural methods, electron paramagnetic resonance, optical spectroscopy, laser site-selective spectroscopy, optical microscopy, scanning electron microscopy, termoluminescence and so on.

4.1.4. Chemical parameters

- composition;
- concentration of the active ion and its variation along and across the crystal;
- valency states of the activator ions;
- concentration of accidental impurities (or of charge compensators) and its variation along and across the crystal;
- composition of bubbles and inclusions;
- chemical stability;
- photochemical processes;
- thermochemical processes;

Methods: atomic absorption spectroscopy, emission spectroscopy, laser microspectroscopy, X-ray microprobe analysis, activation analysis, laser induced fluorescence, infrared, visible and ultraviolet absorption, magnetic resonances, chemical analysis, and so on.

4.1.5. Mechanical and geometrical parameters

- hardness;
- cleavage;
- elastic moduli;
- flatness of end faces (for flat-ended rods);
- rugosity;
- number of scratches or other surface defects on unit area;
- orientation of the rod axis with respect to the crystallographic axes;
- perpendicularity of the end faces on the rod axis;
- parallelism of faces;
- radius of curvature of faces (for spherical-ended faces).

4.1.6. Thermal parameters

- thermal conduction;
- thermal expansion;
- thermochemical and thermomechanical stability.

4.2. Active parameters

4.2.1. Emission thereshold;

4.2.2. Slope efficiency;

4.2.3. Gain spectroscopy;

4.2.4. Losses;

4.2.5. Emission wavelength;

4.2.6. Beam divergence;

4.2.7. Structure of modes;

4.2.8. Polarization;

4.2.9. Thermal effects;

4.2.10. Damage;

4.2.11. Colourability.

Similar specialized tests have been developed for other crystals (nonlinear, electrooptic, detectors and so on).

5. CONSTRUCTION OF DEVICES

A large variety of devices (lasers, Q-switches, modulators, detectors) have been manufactured in our laboratory, on the variety of crystals described above; among them is the first Romanian YAG:Nd laser.

A comprehensive work is carried out in research, design and construction of various mechanical, optical and electronic parts for lasers: laser heads, mirror mounts, mirrors of various curvatures and reflectivities, reflectors for the pump radiation, optical focussing systems, closed-loop cooling systems for lasers (with liquid-liquid or liquid-air heat exchange), power supplies and so on. A permanent interest is devoted to the research on laser generation in various regimes, as for instance, cw generation, Q-switching, short pulse generation, selection of modes and so on. As a typical example let us mention the work on passive Q-switches for pulsed YAG:Nd lasers, based on LiF crystals with F_2^- centers. Research on the properties of such Q-switches, coupled with the properties of the laser-active rod leads to a simple, inexpensive and reliable way to obtain Q-switched pulses from YAG:Nd lasers [32,33]. By combining the passive LiF:F_2^- switch with a slow switch (a spinning prism switch) we obtained giant, monopulse generation even under pump regimes where each of these switches gives multipole-pulse lasing. Moreover, in this case pulse energy varies almost linearly with the pump pulse, duration of the pulse is reduced and thus peak power is dramatically enhanced [34].

Among the main results obtained in device manufacturing let us mention:

5.1. Lasers

5.1.1. Pulsed ruby lasers (relaxed or in a Q-switch regime) with energies up to 10 J.

5.1.2. Various types of pulsed YAG:Nd lasers, with an energy in free-generation regime up to 400 mJ and, in a Q-switch regime, up to 120 mJ (peak powers up to 20 MW), and a repetition frequency up to 10 Hz.

5.1.3. Various types of cw YAG:Nd lasers with tungsten halogen pumping, with powers up to 60 W [35] (in construction up to 100 W).

5.1.4. Frequency-doubled pulsed or cw YAG:Nd lasers.

5.1.5. Pulsed $CaWO_4$:Nd lasers (energies up to 1J per pulse).

5.1.6. Research on construction of 3-micron erbium lasers and of tunable lasers with 3d-ions is under way.

5.2. Non-liniar and electrooptic devices

5.2.1. Frequency-doubling lithium niobate elements for pulsed YAG:Nd lasers.

5.2.2. Frequency doubling barium sodium niobate cells for cw YAG:Nd lasers.

5.2.3. Q-switches and modulators with lithium niobate (apertures up to 6 mm, contrast ratio better than 1000:1, length of the active element 25 mm).

5.2.4. Modulators with lithium tantalate (apertures up to 2.5 mm, two-crystal modulators with 40 mm of length).

5.2.5. Passive Q-switches with $LiF:F_2^-$ crystals.

5.2.6. Combined active-passive Q-switches for YAG:Nd lasers.

5.2.7. Research on acusto-optical modulators and Q-switches is under way.

5.3. Pyroelectric detectors and radiometers

5.3.1. Pyroelectric detectors with lithium tantalate (apertures up to 5 mm and sensitivity up to 1.8 µA/mW).

5.3.2. Infrared radiometers for non-contact temperature measurements up to 1600°C.

6. PRACTICAL APPLICATIONS OF SOLID STATE LASERS

Systematic research on the action of pulsed or cw solid state lasers on various materials has been undertaken in order to use these lasers in various fields such as:

6.1. Technological applications

6.1.1. Thermal treatments

- surface hardening of grey cast iron or of allied alloys [36];
- annealing of semiconductors.

6.1.2. Processing of metals or of other hard materials

- drilling
- welding
- cutting
- material removal

6.1.3. Microprocessing of electronic components

- trimming of resistors;
- cutting of silicon plates

6.1.4. Marking or engraving of metallic parts or electronic components

Special equipment was deisgned and constructed, with high precision mechanical positioning of the part to be processed and with microprocessor or computer control of the laser processing.

6.2. Medical applications, such as endoscopic surgery and coagulation, liver or brain surgery and so on.

6.3. Other applications, such as non-linear optics, pumping with lasers, telemetry and so on.

7. RELATED STUDIES AND OTHER APPLICATIONS OF THE SYSTEMS INVESTIGATED AS LASER-ACTIVE MEDIA

A large variety of doped crystals was investigated as laser- active media or for other laser applications. A considerable volume of very interesting data on properties of interest for applications other than in lasers has been obtained. Some of these are briefly reviewed in the following:

7.1. Use of rare-earth or uranium-doped crystals as thermoluminescent systems for nuclear or X-ray dosimetry.

Very promising properties in this respect are recorded with the system LiF:U^{6+}: following an X or gamma irradiation U^{6+} traps an electron (produced by the irradiation of the crystal) and changes the valency state to U^{5+}. By heating the crystals, one electron from U^{5+} is released, and uranium returns to its original valency, U^{6+}, but this time in an excited state from which it emits a bright green luminescence. This emission has great potential for thermoluminescent dosimetry, provided some technological problems such as reproductibility from batch would be satisfactorily solved.

7.2. Use of hyperfine structure of some uranium-doped crystals for measurements of uranium isotopic abundance

The U^{6+} ion from NaF:U crystals grown in air can be converted to U^{5+} by X or gamma irradiation. This latter ion is paramagnetic and can be detected by EPR at liquid nitrogen temperature. The odd isotopes of uranium have nuclear spins and show hyperfine structure in the spectra, while the even isotopes, which do not possess a nuclear spin, do not show such a structure. Thus by comparing the relative total intensities from the spectra of each isotope, which appear simultaneously, a very accurate method for measuring the uranium isotopic abundances can be obtained. This appears to be very useful for measuring non-volatile compounds of uranium which can be used as dopants for the NaF crystals.

7.3. Use of laser-induced luminescence for detection of ultratrace levels of lanthanide and actinides

By precipitation of the lanthanides or actinides from aqueous solutions with properly chosen hosts or by melting their compounds with suitable hosts, some systems which show very strong luminescence could be obtained. By using laser selective excitation, luminescence signals of an intensity proportional to that of the lanthanide or actinide element in the batch could be obtained; such a method may be used in order to detect ultratrace levels of these elements.

Some of the crystals or crystal growth methods investigated for laser uses could find application in other fields. Such an example is the profilled saphire, with a wide range of applications in fine mechanics.

8. PRESENT AND FUTURE TRENDS

At present research work is mainly directed toward the following objectives: improving quality and increasing sizes of laser crystals and components; finding new laser schemes; new wavelength ranges; tunable solid state lasers; concentrated laser crystals; construction of high-power, and high-brightness, lasers; lasers with large repetition frequency; very short pulse generation; non-linear, electrooptic and acustooptic devices; optical bistable devices, etc. Attention will be given to specific applications of solid state lasers, manufacturing of customized equipment based on lasers and active media, designed in view of a maximum efficiency.

REFERENCES

1. V.Lupei, I.Ursu, Proc.Int.Conf. and School "Lasers and Applications" Bucharest 1982, CIP-Press (1983), p.155.
2. V.Lupei, I.Voicu, O.Radulescu, I.Ursu, Proc.Int.Conf. on Lasers, Guangznou-China-1983, p.348.
3. H.Engstrom, L.F.Mollenauer, Phys.Rev. 87, 1616 (1973).
4. S.Georgescu, H.Totia, F.Domsa, V.Lupei, J.Phys. E, 12, 473 (1979).
5. A.Lupei, V.Lupei, J.Phys. C, 12, 1123 (1979).
6. L.D.Merkle, R.C.Powell, Phys.Rev. B, 20, 75 (1979).
7. D.P.Devor, L.G. Deshazer, Opt.Commun. 46, 97 (1983).
8. V.Lupei, I.Ursu, Proc.XVIIIth Congress AMPERE, Nottingham 1974, publ.by Univ.of Nottingham (1974), vol.I, p.177.
9. V.Lupei, A.Lupei, S.Georgescu, I.Ursu, J.Phys. C, 9, 1619 (1976).
10. A.Lupei, V.Lupei, I.Ursu, J.Phys. C, 15, 5489 (1982).
11. V.Lupei, A.Lupei, Phys.St.Sol. (b) 94, 301 (1979).
12. V.Lupei, A.Lupei, I.Ursu, J.Phys. C, 10, 4587 (1977).
13. I.Ursu, V.Lupei, A.Lupei, Rev.Roum.Phys. 23, 673 (1978).
14. V.Lupei, C.Stoicescu, Proc.XIXth Congress AMPERE, Heidelberg 1976, p.243.
15. V.Lupei, C.Stoicescu, I.Ursu, J.Phys. C, 9, L317 (1976).
16. V.Lupei, C.Stoicescu, I.Ursu, Rev.Roum.Phys. 22, 549 (1977).
17. V.Lupei, J.Phys. C, 16, 6623 (1983).
18. C.Ciucu, S.Georgescu, V.Lupei, Rev.Roum.Phys. 26, 169 (1981).
19. A.Lupei, V.Lupei, C.Ionescu, H.C.Tang, M.L.Chen (to be published).
20. A.Lupei, H.Totia, C.Lupu, Rev.Roum.Phys. 26, 93 (1981).
21. V.Lupei, C.Stoicescu (to be published).
22. S.Georgescu, C.Ionescu, I.Voicu, V.I.Zhekov (to be published).
23. V.Lupei, C.Stoicescu, Rev.Roum.Phys. 23, 673 (1978).
24. D.Sengupta, J.O.Artman, J.Chem.Phys. 54, 1010 (1981).

25. V.Lupei, J.Phys. C, 16, 6627 (1983).

26. S.Georgescu, V.Lupei, I.Ursu (to be published).

27. V.I.Jekov, T.M.Murina, A.M.Prokhorov, M.I.Studenkin, S.Georgescu, V.Lupei, I.Ursu, Kvantovaya Electronika (in press).

28. V.Lupei, I.Ursu (to be published).

29. V.Lupei, D.Toma et al, "Salyut 6-Soyuz. Material Science and Technology", Moscow, Ed.Nauka 1985 (in Rusian), p.133.

30. I.Ursu, V.Lupei, Int.Conf.and School "Laser and Applications", Bucharest 1982, CIP-AP, vol.1, p.63.

31. V.Lupei, E.Ristici, I.Voicu, S.Georgescu, O.Radulescu, Proc.Int.Conf.on Lasers, Guangzhou-China 1983, p.369.

32. A.Lupei, V.Lupei et al, Rev.Roum.Phys. 28, 6 (1983).

33. A.Lupei, V.Lupei, F.Domsa, S.Georgescu, V.Ionita-Manzatu, I.Ursu, Proc.Int.Conf.on Lasers, Guangzhou-China 1983, p.377.

34. V.Lupei, A.Lupei, V.I.Manzatu, S.Georgescu, F.Domsa, Opt.Commun.48, 203 (1983).

35. I.Ursu, V.Lupei, V.Ionita-Manzatu, Int.Conf.and School "Lasers and Applications", Bucharest 1982, CIP-AP, vol.2, p.393.

36. I.Ursu, V.Lupei, C.Lupu, Int.Conf.and School "Lasers and Applications", Bucharest 1982, CIP-AP, vol.2, p.394.

OPTOVOLTAIC EFFECT AND LASER FREQUENCY STABILIZATION

D.C. Dumitras, D.C.A. Dutu, V. Draganescu, N. Comaniciu
Central Institute of Physics
Institute of Physics and Technology for Radiation Devices
Bucharest, P.O.Box MG-6, Romania

1. Introduction

The gas laser frequency stabilization has numerous applications in the fields of spectroscopy, interferometry, metrology, optical communications, geophysics etc. The new stabilization methods developed during the past years have produced improvements in the stability of gas lasers, which have enabled the realization of an optical frequency standard superior to the krypton 86 standard.

The carbon dioxide molecular lasers offer several advantages over the other known lasers /1/. The most important features characterizing the CO_2 laser output beam which account for the wide range of their applications are as follows:

a) An efficient conversion of the pumping energy into a high output energy. It varies with the type of laser, i.e. 8 - 15 per cent for medium power sealed-off lasers and up to 30 per cent for e-beam pumped CO_2 lasers.

b) A small atmospheric attenuation of the CO_2 laser radiation. The CO_2 lasers operate in the 9-11 µm region, within the atmospheric transmission "window" with reduced attenuation, which extends from 9.5 to 13 µm. Under favourable atmospheric conditions, the attenuation has an extremely low value (0.1 dB/km).

c) A wide oscillation bandwidth available for optical frequencies. For low pressure CO_2 lasers, the oscillation bandwidth varies in the range of 100-200 MHz and/can reach high values of over 1 GHz under high operating pressures (for example in the case of waveguide lasers /2/).

This paper is dealing with the frequency stabilization of single mode, medium power, sealed-off CO_2 lasers. The term "medium" designates the geometrical dimensions of CO_2 lasers, namely tube length less than 80 cm and bore diameters 10 mm or less; the output power varies between 3 and 20 Watts.

The sealed-off CO_2 lasers use a static gas mixture, which means that no bulky gas tanks and vacuum pumps will be needed and there will be substantial savings in the consumption of working gases, particularly helium, which is quite expensive. Consequently, the sealed-off CO_2 lasers can be easily handled, mounted and operated.

The method of frequency stabilization is based on the optovoltaic effect in CO_2 laser plasma, which is superior to other methods, because it is simple, doesn't need a supplementary detection element and the output beam could be entirely used.

After the discussion of the frequency stabilization on the top of the gain curve, the work focusses on plasma impedance changes and the dependence of the optovoltaic signal on the discharge current and on the laser vibrational-rotational lines, which give valuable information about the mechanisms and kinetics of CO_2 laser systems, useful in laser frequency stabilization. The last two chapters present the automatic laser frequency servo-control system used in frequency stabilized CO_2 lasers and the evaluation of CO_2 laser frequency stability by measuring the error signal in the feedback loop.

2. Stabilization scheme

A free-running or unstabilized laser is subject to many perturbations of its frequency and the single axial mode output while necessary, is not sufficient to reduce the frequency oscillation range. There are basically two reasons for this, both arising from variations in the length of the cavity. First, the varying cavity length causes the position of the axial mode to move and so the frequency of the output varies correspondingly. Secondly, this variation in frequency takes place under the gain curve and so the output will also vary in intensity. If the frequency separation of the axial modes is sufficiently large, then even under high gain conditions the output could fall to zero.

The effect of these factors can (in principle) be eliminated by using a thermally compensated mechanical structure and by keeping the atmosphere out of the laser cavity. There is, of course, a limit on the stability that can be achieved in this way, which is named passive stabilization. In practice, this limit is usually set by vibration. In order to increase the stability beyond this limit, it is necessary to employ some type of feedback mechanism which will correct for vibrational effects (and residual deficiencies in the thermal stability).

The principle of the active stabilization schemes is based on a comparison between the frequency of a single frequency laser (single-mode, single-line) and some stable reference. If the laser frequency is different from that of the reference, an error-sensing discriminant is used to derive a signal proportional to the deviation. This error signal is used to control the laser frequency and re-tune it to that of the reference. Such a servo-loop locks the laser frequency to that of the reference.

The basic requirement for a suitable error signal is /1/ that it has a magnitude proportional to the amount of length correction required and /2/ that it indicates the direction of the required length correction.

For moderate stability, the CO_2 laser line profile can be used as the discriminating curve /3/. This method is more appropriate for the CO_2 laser than for He-Ne laser because the CO_2 rotational line profile is narrow and has much steeper slopes than that of the neon line in a He-Ne laser. The error signal is produced by allowing the laser cavity resonance to "ride" around the steep part of the line profile slope and its amplitude is dependent on the change in mirror separation. This scheme requires internal frequency modulation (jittering) of the laser in order to sense the sign of the derived error signal. Stabilization is then obtained by re-establishing the required separation with a servo-control system.

This scheme has the disadvantage, of course, that the output beam from the laser is frequency modulated, but the amount of modulation needed to derive the errror signal is small and, in many applications, the presence of the frequency modulation is of no consequence.

The cavity length is controlled by a piezoelectrically driven mirror along the cavity axis, which responds to the sum of a DC control voltage, plus a small jitter signal at some convenient frequency (~500 Hz). As it can be seen in Fig.1, where a laser line versus frequency curve is drawn, the small cavity jitter induces a sinusoidal variation in laser intensity as the cavity mode scans across the transition line gain profile, which is compared in phase to the jitter signal. The error signal developed by the phase detector can serve to drive the cavity resonance to the centre of the laser gain curve. In this way, the electronic feedback loop seeks the centre of the lasing gain profile, the lock-in point being the zero crossing of the phase detector response. In case the mean mode frequency is lower than the line centre frequency, the phase of the observed laser intensity variation in opposite to that when the mode frequency is higher than the line centre frequency. The amplitude of the intensity variation increases with the frequency offset from the line centre.

A system for stabilizing to the top of the gain curve at the frequncy ν_0 is illustrated in Fig.2. The position of the coupling mirror is sinusoidally modulated (with an amplitude that is a small fraction of $\lambda/2$) thereby modulating the optical resonator length and optical resonator mode frequency. The laser output power is thereby sinusoidally modulated at the chosen modulation frequency (for small modulation amplitude). The modulation index is zero when the mode frequency is ν_0 since the slope of the laser power output versus ν is zero for $\nu=\nu_0$. The phase of modulated component of the laser power relative to the modulation voltage applied to the piezoelectric transducer is opposite for $\nu>\nu_0$ as compared to the phase when $\nu<\nu_0$. The modulated component of the laser power is measured, preamplified and phase sensitively detected. The phase sensitively detected signal after filtering provides a discriminator signal that is zero for the resonator length L_0, where a resonator mode frequency is at ν_0 and is positive on one side of ν_0 and negative on the other side. This discriminator signal is DC amplified and is applied to the piezoelectric transducer through a high voltage amplifier, with proper phase to constitute stable negative feedback. The result is to stabilize the resonator length so that oscillation occurs at ν_0.

In lieu of using an IR detector to sense the laser intensity variation, the cavity length could be adjusted using the optovoltaic effect, a method discovered by Skolnick /4/. As the internal laser radiation field intensity is altered by changing the resonant cavity alignment, the discharge impedance, which is proportional to the slope of the output power versus frequency curve of the laser, is also modulated. The impedance variation is measured by exciting the plasma tube with a high speed current regulated power supply and measuring the resulting variation in the voltage drop across the plasma tube (the optovoltaic signal). An intensity variation of 1% is sufficient to significantly (~ 0.1%) change the discharge impedance /5/. This impedance change can be detected as current fluctuation (optogalvanic), or as voltage variation (optovoltaic).

Using a current-regulated power supply, the discharge impedance fluctuation is detected as an AC component of the voltage drop across the plasma tube. The block diagram is modified as in Fig.2 (dashed lines). The optovoltaic signal, being large enough, can be directly introduced in the tuned amplifier, the rest of the circuits being unchanged. Therefore, the method of frequency stabilization using the optovoltaic effect in CO_2 lasers is simple and doesn't need a supplementary detector with its associated power supply.

3. Optovoltaic effect

The CO_2 laser radiation field intensity is large enough and when is varied it introduces significant changes in the laser plasma microscopic parameters such as sidelight intensity plasma impedance and gas temperature. From among these parameters, a distinct interest is given to plasma impedance, because it is possible to establish a direct correspondance between laser radiation field intensity changes and some electrical characteristics (current, voltage), which can be detected and used in electronic feedback systems, so avoiding special transducers such as optical, acousto-optical or pressure transducers.

The impedance changes depend on the power flow within the cavity and are probably due to direct or indirect connection between the population of various energy levels and the ionization process in the laser gas mixture. Experimentally, such measurements are easily made by modulating the laser radiation field, either by a mechanical chopper or by applying a repetitive voltage to a piezoelectric transducer.

Our experimental investigation presented in this section are directed to the evaluation of the optovoltaic signal and its dependence on discharge current and on laser vibtrational-rotational lines, aiming at the frequency stabilization of CO_2 lasers /6/.

The experimental arrangement includes a sealed-off CO_2 laser model LIR-21 SF (maximum output power 20W) /3/ and a constant current high voltage power supply model SIT-8025 C/D, with sufficiently rapid response feedback circuit /7/. The laser was tuned on different vibrational-rotational lines in the bands $00^{\circ}1-(10^{\circ}0,02^{\circ}0)_I$ and $00^{\circ}1-(10^{\circ}0,02^{\circ}0)_{II}$ of a CO_2 molecule using a selective resonant cavity formed by a flat diffraction grating and a curved coupling mirror of 10 m in radius.

We have measured the voltage changes on the discharge tubes for different values of the discharge current and different intensities of three laser lines: P(10) and P(20) in the band $00^{\circ}1-(10^{\circ}0,02^{\circ}0)_I$ and P(30) in the band $00^{\circ}1-(10^{\circ}0,02^{\circ}0)_{II}$. The discharge current was changed in the range of 13-27 mA and the power of the laser lines was adjusted for four different values: $P_1 = P_{max}$, $P_2 = 10W$, $P_3 = 5W$ and $P_4 = 3W$ for P(20) and P(10) lines and $P_1 = P_{max}$, $P_2 = 4W$, $P_3 = 3W$ and $P_4 = 1W$ for P(30) line.

Parameters were determined for every discharge current I_k as follows:

- the voltage across the discharge tube U_{Ai} (anode voltage) for the values P_i (i = 0,1 2, 3, 4) of the power of laser lines (i = 0 means $P_0 = 0$, obtained by introducing a screen in the laser cavity);

- the anode voltage change in respect with P = 0:

$$\Delta U_{Ai} = U_{Ai} - U_{Ao}$$

for i = 1, 2, 3, 4;

- the optovoltaic signal - the voltage change on unit laser power:

$$\frac{\Delta U_{Ai}}{\Delta P} = \frac{U_{Ai} - U_{Ao}}{P_i - P_o}$$

for i = 1, 2, 3, 4;

- the average optovoltaic signal:

$$\overline{\frac{\Delta U_A}{\Delta P}} = \frac{\sum_{i=1}^{n} \frac{\Delta U_{Ai}}{n}}{n} \quad , \qquad n = 4 \quad ;$$

- the static plasma impedance for P = 0:

$$Z_o = \frac{U_{Ao}}{I_k} \quad ,$$

- the average plasma impedance change on unit laser power:

$$\overline{\frac{\Delta Z}{\Delta P}} = \frac{1}{I_k} \overline{\frac{\Delta U_A}{\Delta P}} \quad ;$$

- the average percentage plasma impedance change on unit laser power:

$$\overline{\frac{\Delta Z/Z_o}{\Delta P}} = \frac{1}{U_{Ao}} \overline{\frac{\Delta U_A}{\Delta P}}$$

Fig.3 shows these parameters which characterize the optovoltaic effect in CO_2 lasers, the discharge current and the vibrational-rotational lines being parameters.

One can draw the following conclusions:

(i) The optovoltaic signal decreases when the discharge current increases, having large values at smaller currents than the optimum current for maximum power (Iopt). This observation suggests that the optovoltaic signal presents a current dependence closer to the population inversion or to the small-signal gain than the current dependence of the output power.

(ii)The average percentage plasma impedance change on unit laser power shows a reduced dependence on discharge current for values smaller then Iopt and is maximum for the P(20) line. Making a comparison between this parameter measured at the same discharge current and different vibrational-rotational lines with the computed normalized small-signal gain function on rotational quantum number, one can remark again that there is a proportional dependence between the optovoltaic signal and the small-signal gain.

(iii) The large values of the average optovoltaic signal ($\overline{\Delta U_A}/\Delta P \approx 20$ V/W) makes it possible to use the optovoltaic effect to the detection of output power changes owing to the modification of cavity length or the frequency of laser radiation. It has to be mentioned that the signal obtained in this way is higher than the signal given by most infrared detectors.

(iv) Using a variable frequency mechanical chopper inside the laser cavity, the optovoltaic signal amplitude and phase dependence on the modulation frequency and phase of the laser field has been determinated. In the frequency range of 20-200 Hz, the optovoltaic signal is in phase with the laser field modulation and its amplitude decreases when the modulation frequency is increased.

These observations and conclusions could explain the physical mechanism which is responsible for plasma impedance change in CO_2 lasers. The explanation is based on the competition between the de-excitation of the upper laser level by stimulated emission or by V-V and V-T collisional processes described by

$$CO_2\,(00^\circ1) + M \rightarrow CO_2\,(n,m^1,o) + M + \Delta E,$$

where M is a possible collision partner (CO_2, CO, O_2, N_2, He, Xe, H_2) and ΔE is the energy exchanged between the excited molecules and the translation mode.

For a constant pumping rate, an increased laser radiation determines the grawing of the stimulated emission process and a decrease of the number of molecules which transfers their energy to translation mode (and then, a decrease of the gas temperature). A lower temperature means an increased collision rate between molecules and electrons, so the plasma impedance will be higher. For a constant excitation current, the voltage on the laser tube is larger, the same tendency being observed experimetally too in Fig. 3.

The significant magnitude of the optovoltaic signal allows conveniently to use the optovoltaic effect for discrimination characteristic (phase sensitive detection of optovoltaic signal) in frequency stabilized CO_2 lasers.

4. Automatic laser frequency servo-control system

The laser stabilization at the top of a line profile entails the search of an extremum, which is done using a small amplitude, sinusoidal modulation signal. The correction signal is generated by a quasilinear discriminant characteristic obtained in the output of a phase sensitive detector.

The block diagram of the functional modules used in the frequency stabilized CW CO_2 lasers is shown in Fig. 4. The fifteen functional modules denoted in the block diagram by a three letters code can be grouped in three main blocks in accordance with the specific function played in the operation of the frequency stabilized CO_2 laser:

1 - a high speed regulated current power supply, which excites the CW CO_2 laser tube;

2 - a servo-control system (lock-in amplifier), which controls the length of the resonant cavity;

3 - a logic electronic system which allows an efficient and operative control and monitoring of the frequency stabilized CO_2 laser operation.

This chapter will only deal with the automatic laser frequency servo-control system.

The piezoelectric transducer built in our institute has a sensitivity of 9.6×10^{-3} µm/V in the displacement section (in its linear range between 500 V and 1700 V) and 1.26×10^{-3} µm/V in the modulation section.

The modulation signal, with a frequency of 520 Hz is generated by a pilot oscillator and applied to the piezoelectric transducer through a modulation amplifier. The modulation signal amplitude can be varied between 0 and 150 V peak-to-peak. Both circuits are placed on the same functional module (OMA). The signal from the pilot oscillator is also applied to the phase sensitive detector (PSD) electronic module as reference frequency.

For CW CO_2 lasers excited by regulated current power supplies, the modulation signal which appears in the emitted radiation can be measured according to the optovoltaic effect using a simple band-pass filter like that denoted with OVP (optovoltaic probe) in Fig. 4.

The optovoltaic signal is amplified through a two-stage tuned AC amplifier (ACA). The gain of the tuned amplifier can be adjusted from 40 dB to more than 100 dB and the input impedance is larger than 100 kΩ . The bandwidth of the amplifier is very narrow (3.6 Hz at 3 dB), since the quality factor for every stage is about 40. The high gain and the very narrow bandwidth of the tuned amplifier ensure a signal-to-noise ratio better than 1000.

The amplified optovoltaic signal is introduced in the phase sensitive detector (PSD) module, based on a four-pole analogue commutator. The fine phase adjustment is achieved with a phase locked loop (PLL) circuit. The phase in the reference channel can be either continuously adjusted from -45° to +135° using a RC phase shifter and the capture band of the PLL circuit β E 565 or reversed by 180° with a phase switch.

The error signal is obtained in the output of the special electronic module DCA (DC amplifier) by processing the output signal of the phase sensitive detector. The DCA module has two modes of operation, namely:

- gain of ten amplifier with integrating time constant of 1 second;
- high gain integrator with output slewing rate of about 6 V/s per volt of input.

The first mode allows the observation of the smoothed output of the demodulator (stabilization discriminant), while the second mode is used in closed-loop stabilization to observe the error signal.

The high voltage amplifier (HVA) module works on the principle of a switching high voltage power supply. The output voltage is controlled between zero and - 1700 V through a DC supply voltage proportional to the error signal given by an integrator and/or to a bias voltage selected by an operator. The feedback loops of the high voltage amplifier ensure a linear output characteristic for this circuit and its over-current protection.

To prevent the interruption of lock-in stabilization if the amplitude and the sense of the error signal requires a correction voltage over the preset limits of the HVA circuit (imposed by the piezoelectric transducer characteristics), a mode-jump circuit (MJC) module has been incorporated in the automatic frequency servo-control system. The input-output conditions are fulfilled through an optimized design using only a quad Norton amplifier type βM 3900. The mode-jump circuit has the function to introduce a preset voltage step equivalent to a mirror translation given by an integer number of λ /2 (by the piezoelectric transducer) whenever the correction voltage exceeds the preset limits near 0 and - 1.7 kV. Such a jump to an equivalent point within the normal range of operation of the piezoelectric transducer causes a mirror translation of $\pm n\ \lambda/2$, so as a new longitudinal mode to fall on the top of the laser gain curve.

The mode jump circuit has two modes of operation: "calibrate" and "auto", which can be selected with a mode-jump selector switch. The "calibrate" mode of operation is used only for the adjustment of the step size of the jump, while the "auto" mode is normally used in frequency stabilized operation for automatic initiation of the mode jump at any of the preset limits. By its operation between adjustable preset limits, the MJC module also provides an efficient protection of the piezoelectric transducer from excessive bias voltage.

The modular design of the electronic circuits belonging to the automatic servo-control system allows a compact and versatile construction for a large range of applications, not only in the frequency stabilization of gas lasers, but also for piezoelectric transducer characterization, signal processing and so on.

5. Evaluation of laser frequency stability

To measure the laser frequency stability, several methods can be used. The most direct method is optical heterodyne measurement, in which the beams from two similar lasers are mixed and the frequency difference is monitored.

We have developed a new method to evaluate the CO_2 laser frequency stability /8/. The error signal in the feedback loop was found to be proportional to laser frequency deviation against the top of the gain curve. To measure the laser frequency stability, the amplitude of error signal is calibrated in frequency units.

Based on mode pulling effects, a transcedental equation relating the laser frequency ν to the cavity length L is derived. The various factors are conveniently normalized to give the following expression

$$\delta L = -\left[\delta\nu + \frac{G}{2}\,\mathrm{arctg}(2Q\delta\nu)\right],$$

where

$$\delta L = (L-L_0)/L_0,$$

$$\delta\nu = (\nu-\nu_0)/\nu_0,$$

$$G = \lambda_0\alpha_0$$

and

$$Q = \nu_0/2\Delta\nu_L.$$

Here, ν_0 and λ_0 are the frequency and wavelength respectively at line centre, which correspond to a cavity length L_0; α_0 is the small signal gain at line centre; and $\Delta\nu_L$ is the Lorentz line halfwidth.

These particular parameters were chosen because their magnitudes describe the macroscopic process of index tuning. G, the effective gain per wavelength, is a measure of the unsaturated gain. The quality factor Q, which is used frequently in amplifier characterization, indicates the width of the gain $\alpha(\nu)$. It is easily seen that the product G.Q is just the peak value of the mode pulling term $c\alpha(\nu)/2\Delta\nu_L$

In our experimental measurements, the LIR-15SF frequency stabilized CO_2 laser was used, which was tuned on P(20) 00^01-$(10^00, 02^00)_I$ line ($\nu_o = 2.8306 \times 10^{13}$ Hz, $\lambda_o = 10.591$ µm). The experimental set-up includes the laser tube (inner diameter 5 mm, discharge length 25 cm), the automatic servo-control system, a powermeter and a X-Y recorder. A discharge current of 11.5 mA was maintained through the tube.

Using the calculated value of $\Delta\nu_L$ (82.39 MHz) and the measured value of small-signal gain α_o (0.0108 cm^{-1}), the quality factor Q and the effective gain per wavelength G are determined:

$$Q = 1.7178 \times 10^4$$

$$G = 1.1438 \times 10^{-5}$$

In a separate measurement, the displacement characteristic of the piezoelectric transducer was determined. From the linear portion of the curve displacement function on applied voltage, a sensitivity of $K = \Delta L/\Delta V = 9.6 \times 10^{-3}$ µm/V is deduced for the piezoelectric transducer.

As it can be remarked in Fig.5, the following measurement were also made:

- the voltage range applied to the piezoelectric transducer to scan the oscillation bandwidth of P(20) line, selected from laser signature:

$$V_{PZT} = 700 - 550 = 150 \text{ V};$$

- the error signal deviation U_ε corresponding to the oscillation bandwidth of the P(20) line (the phase sensitive detector output signal);
- the laser power variation for the P(20) line, selected from laser signature;
- the error signal fluctuation ΔU_ε when the CO_2 laser is active frequency stabilized on the top of gain curve of the P(20) line.

Now we are able to estimate the frequency stability of the CO_2 laser. The P(20) line is frequency scanned for a voltage of 150 V applied to the piezoelectric transducer, which means a 1.44 µm displacement. This value corresponds to $\delta L = 2.4 \times 10^{-6}$ and from the equation which relates the laser frequency to cavity length it results $\delta\nu = 1.525 \times 10^{-6}$.

The frequency excursion of the P(20) line is

$$\Delta\nu = \delta\nu \cdot \nu_o = 43.167 \text{ MHz}$$

value which corresponds to 139 divisions of a peak to peak excursion of the error signal. So,

$$\frac{\Delta\nu}{U_{\varepsilon_{pp}}} = 0.31 \text{ MHz/div.}$$

When the laser is active frequency stabilized, the error signal variation is 2 divisions, that is a frequency instability of

$$\Delta\nu = \Delta U_\varepsilon \frac{\Delta\nu}{U_{\varepsilon_{pp}}} = 0.62 \text{ MHz}$$

results for our laser.

Finally, the laser frequency stability of

$$\frac{\Delta\nu}{\nu_0} = 2.2\times10^{-8}$$

is determined.

Using the experimental set-up previously described, the error signal variation ΔU_ε was measured with active frequency stabilization or passive frequency stabilization (open feedback loop) on a period of 150 s (Fig.6). Curves a and e are traced with active frequency stabilization, while curves b, c and d correspond to the error signal variation without active frequency stabilization, when the operating frequency is on the left side, on the centre or on the right side of gain curve, respectively. The frequency stability is ten times worse when the laser is only passive frequency stabilized .

The error signal variation measurement also allows a rapid evaluation of response time of the electronic servo-control system, which automatically adjust the laser cavity length. As it can be remarked in Fig.7, the error signal transient response time is of approximately 1,2 s, when an axially step function deformation is applied to the laser cavity. This value is in good agreement with the response time of feedback loop (1.1 s) computed by using the Evans method.

6. Conclusions

This paper reviews some theoretical and experimental results regarding the frequency stabilization of sealed-off CO_2 lasers. These lasers, owing to their efficient conversion of pumping energy, small atmospheric attenuation, large oscillation bandwidth and constructive simplicity have found numerous applications in physics, chemistry and technology.

The laser plasma tubes designed by us have to fulfil the following requirements: the shortest overall length possible for a given discharge length; operation in the lowest transversal mode TEMoo; a significant reservoir volume to discharge volume ratio to ensure long life operation; and a large single pass gain to obtain the tunability of the CO_2 laser in an increased spectral range. Applying these criteria, we have designed, constructed and tested sealed-off CO_2 lasers with output power between 4 W (LIR-15 SF) and 20 W (LIR-21 SF).

The method of frequency stabilization applied by us, namely the frequency stabilization on the top of the gain curve is discussed especially as related to the optovoltaic effect, which is used to derive the error signal. Studying the influence of the discharge parameters on the optovoltaic effect, large values of the averge optovoltaic signal (20 V/W) were revealed, which makes it possible to use the optovoltaic effect for the detection of output power changes owing to the modification of cavity length or the frequency of laser radiation.

The automatic laser frequency servo-control systems developed in our department have a modular design of the electronic circuits, allowing a compact and versatile construction. Using integrated circuits on a large scale, our high-performance frequency servo-control systems are reliable and can be used not only for laser frequency stabilization, but also for piezoelectric transducer characterization, signal processing and so on.

The new method for the evaluation of CO_2 laser frequency stability is based on the calibration of the amplitude of the error signal in frequency units. So, we have obtained a frequency stability of 2.2×10^{-8} and a response time of the electronic servo-control system of 1.2 s.

REFERENCES

/1/ D.C. Dumitras: "Gas lasers", Ed.Academiei RSR, Bucharest, 1982

/2/ D.C.Dumitras: "Waveguide lasers", Proceedings of the International Conference and School "Lasers and Application", Bucharest, 1982, Part I, p. 483-544

/3/ D.C. Dumitras, D.C. Dutu, N. Comaniciu, V. Draganescu, R. Alexandrescu, I. Morjan, Rev. Roum. Phys., 26, 485 (1981)

/4/ M.L.Skolnick, IEEE J.Quant. Electr., QE-6, 139 (1970)

/5/ A.L.S.Smith, S.Moffatt, Opt. Comm., 30, 213 (1979)

/6/ D.C.A.Dutu, V.Draganescu, N.Comaniciu, D.C.Dumitras, Rev.Roum.Phys., 30, 127 (1985)

/7/ D.C.A. Dutu, D.C. Dumitras, Rev.Roum.Phys., 27, 647 (1982)

/8/ D.C.A.Dutu, D.C.Dumitras, V. Draganescu, N. Comaniciu, Rev.Roum.Phys., 30, 47 (1985)

FIGURE CAPTIONS

Fig. 1 Generation of the error-frequency signal

Fig. 2 Block diagram for frequency stabilization on the top of gain curve using either an IR detector or the optovoltaic effect

Fig. 3 The characteristic parameters of optovoltaic effect in sealed-off CO_2 laser plasma

Fig. 4 Block diagram of the functional modules used in the frequency-stabilized CO_2 laser model LIR-25SF

Fig. 5 The power variation and the error signal for the frequency stabilized CO_2 laser LIR-15SF

Fig. 6 The error signal variation ΔU_ε with active frequency stabilization (curves a and e) or with passive frequency stabilization (curves b, c and d)

Fig. 7 The transient response of error signal ΔU_ε when an axially step function deformation is applied to the laser cavity

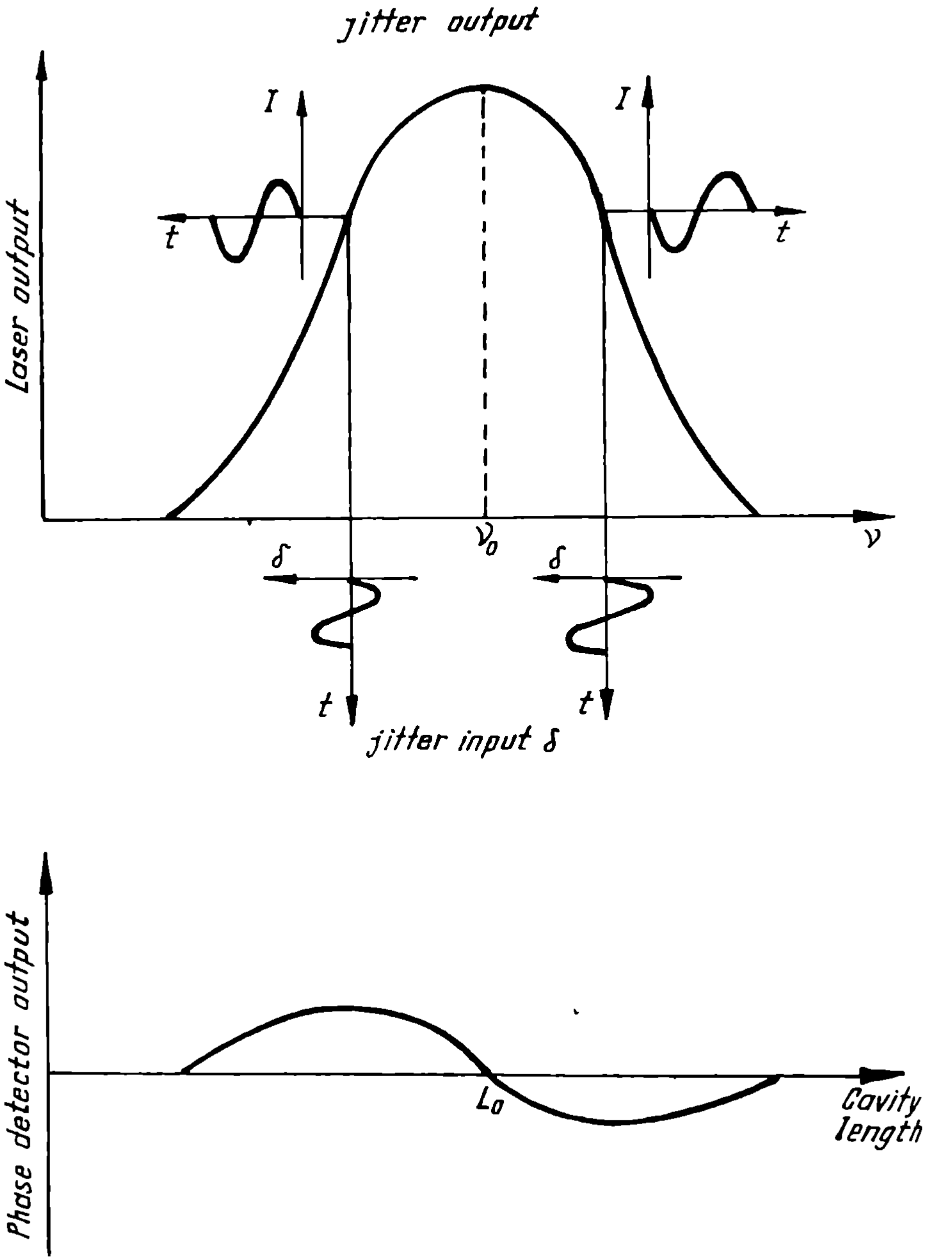
jitter output
I
t
I
t
Laser output
ν_0
ν
δ
δ
t
t
jitter input δ
Phase detector output
L_0
Cavity length

Fig.1

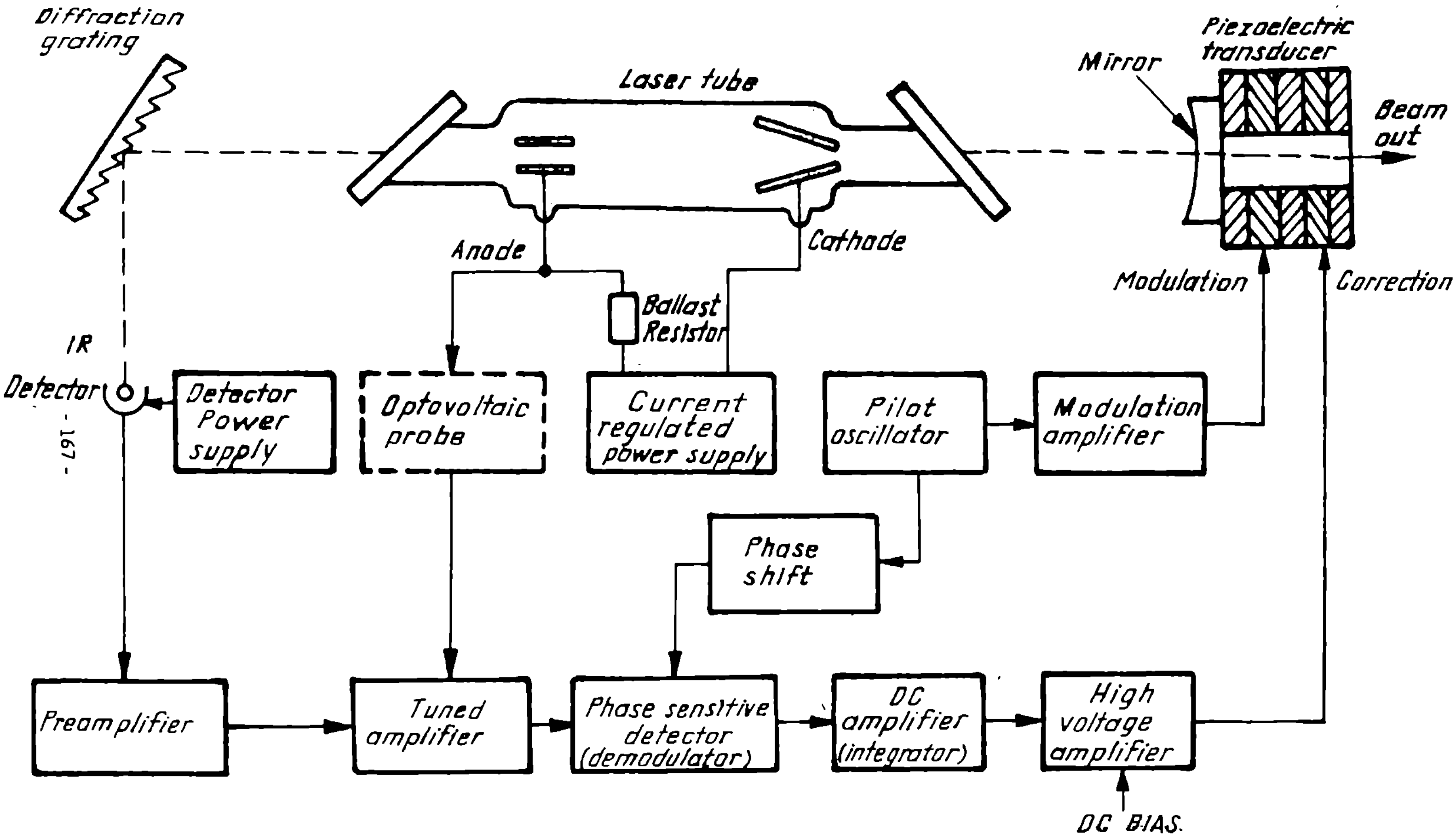
Diffraction grating
Laser tube
Mirror
Piezoelectric transducer
Beam out
Anode
Cathode
Modulation
Correction
Ballast Resistor
IR Detector
Detector Power supply
Optovoltaic probe
Current regulated power supply
Pilot oscillator
Modulation amplifier
Phase shift
Preamplifier
Tuned amplifier
Phase sensitive detector (demodulator)
DC amplifier (integrator)
High voltage amplifier
DC BIAS.

Fig.2

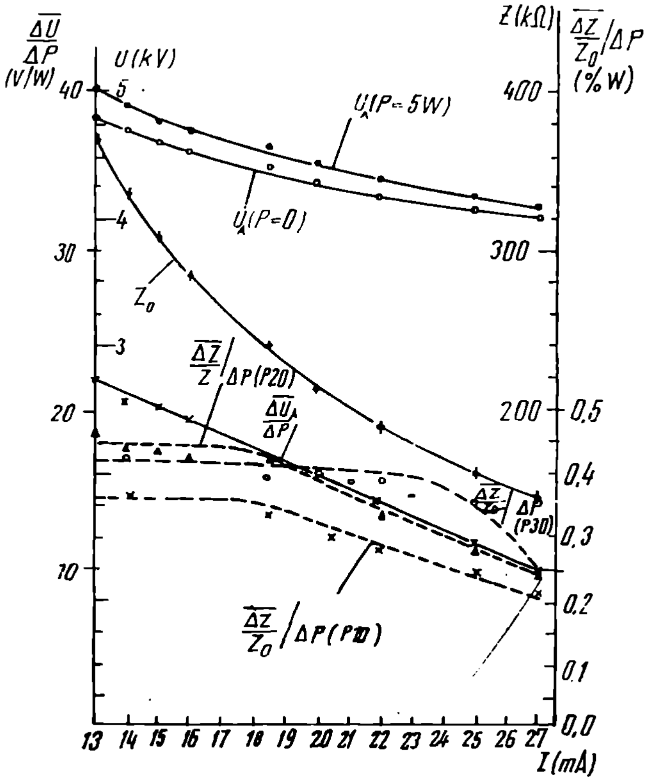

ΔU/ΔP (V/W)
U(kV)
Z(kΩ)
ΔZ/Z0/ΔP (%W)
40
30
20
10
5
4
3
400
300
200
0.5
0.4
0.3
0.2
0.1
0.0
U_A(P=5W)
U_A(P=0)
Z0
ΔZ/Z/ΔP(P20)
ΔU_A/ΔP
ΔZ/Z0/ΔP (P30)
ΔZ/Z0/ΔP(P10)
13
14
15
16
17
18
19
20
21
22
23
24
25
26
27
I(mA)

Fig.3

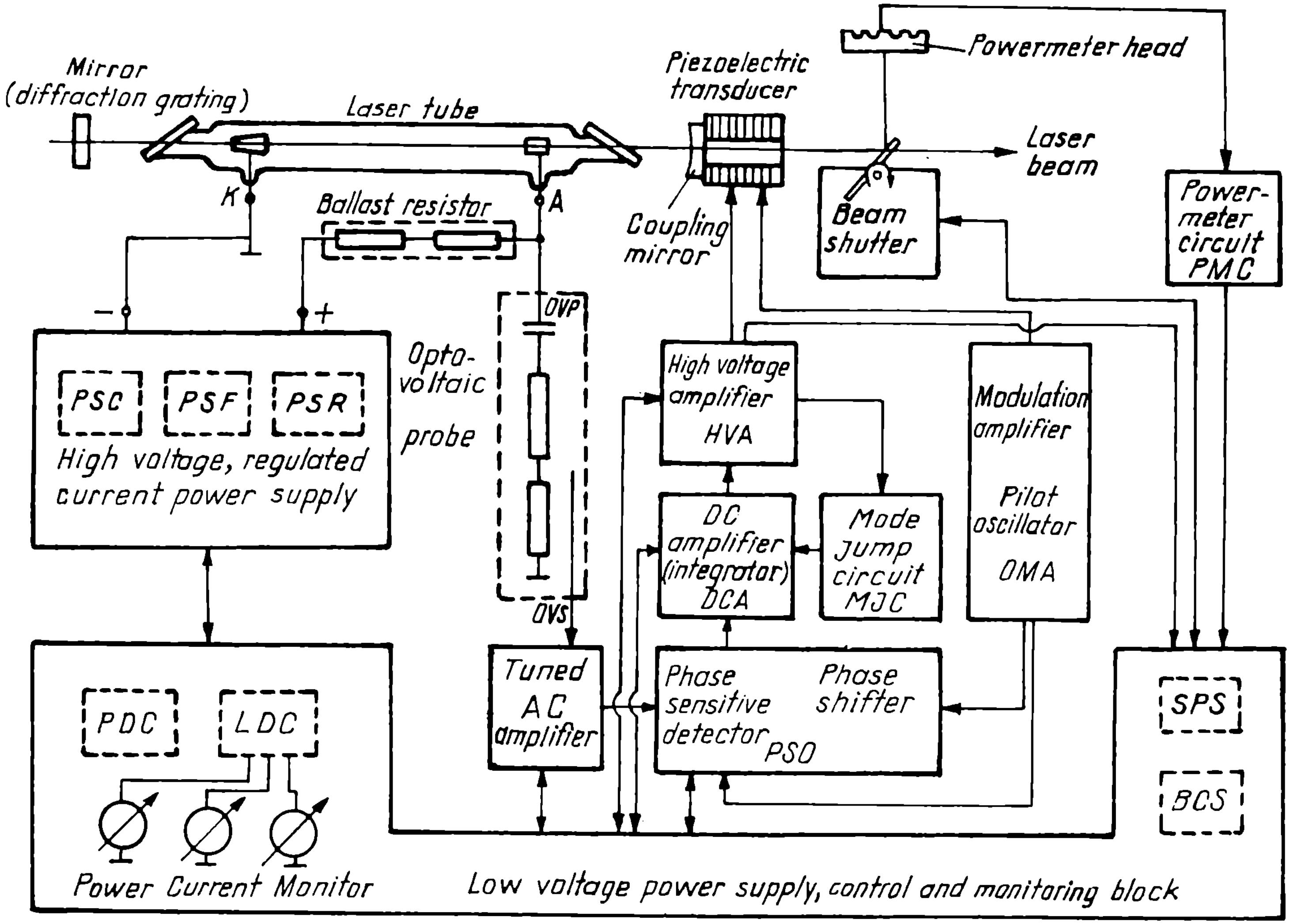
Mirror
(diffraction grating)
Laser tube
Piezoelectric transducer
Powermeter head
Laser beam
K
A
Ballast resistor
Coupling mirror
Beam shutter
Powermeter circuit PMC
OVP
Opto-voltaic probe
OVS
PSC
PSF
PSR
High voltage, regulated current power supply
High voltage amplifier HVA
DC amplifier (integrator) DCA
Mode Jump circuit MJC
Modulation amplifier
Pilot oscillator
OMA
Tuned AC amplifier
Phase sensitive detector
Phase shifter
PSO
SPS
BCS
PDC
LDC
Power Current Monitor
Low voltage power supply, control and monitoring block

Fig. 4

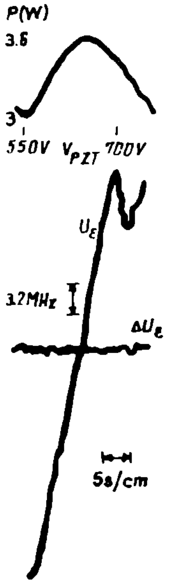

Fig. 5

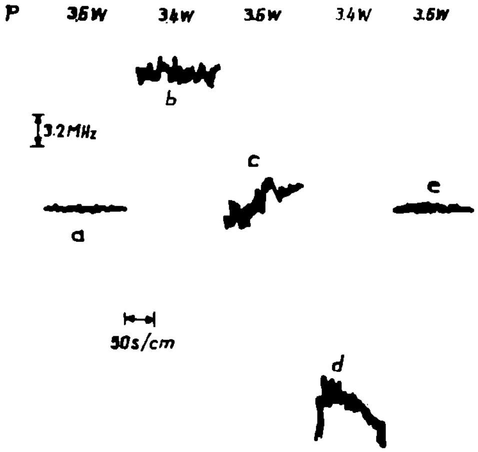

Fig. 6

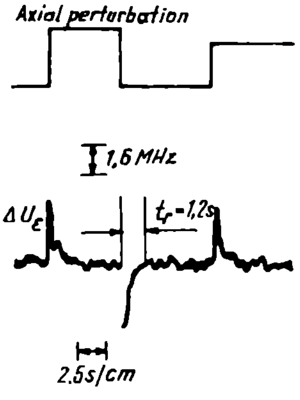

Fig. 7

INTERACTION PROCESS STUDIES FOR OPTICAL HARMONICS GENERATION

I.M.Popescu, N.N.Puscas, P.E.Sterian, D.Irimescu
Department of Physics, Bucharest Polytechnical Institute, Romania

The main results presented in the paper concerning the interaction process studies for optical harmonics generation are: a theoretical method for calculus of the different high order nonlinear susceptibilities, numerical evaluation of some of these susceptibilities in alkali metal vapours, the study of the seventh harmonic generation by nonresonant interaction processes and by two-photon resonant absorption.

1. Introduction

Different high order harmonics generation (five /1/. seven /2/, nine /3/), in alkali metal vapours and rare gases is one of the most promising methods for coherent light production in the V.U.V. and soft X ray region. The theoretical models for the analysis of the high order optical harmonics generation with the help of the coupled equations imply the knowledge of nonlinear susceptibilities /4,5,6/ of different orders for the numerical integration of these equations with a view to the theoretical evaluation of the possible conversion efficiencies of the interactions in different media.

This paper presents our contributions concerning the interaction processes for optical harmonic generation. The main results are: a theoretical method development for calculus of the different high order nonlinear susceptibilities (fifth /7,8/, seventh /9/ and ninth order /10/) and numerical evaluation of some of these susceptibilities in alkali metal vapours, the study of the seventh order harmonic generation by nonresonant interaction processes /11,12/ and by two-photon resonant absorption /13/.

2. Different high order nonlinear susceptibility calculus

In order to calculate the fifth order nonlinear susceptibility by taking into account the spin-orbit coupling and some damping effects Γ_{mn}, the following equations for the density matrix elements ρ , which describe the induced transitions between eigenstates of the nonlinear system, are considered:

$$i\hbar\left(\frac{\partial}{\partial t} + i\omega_{mn} + (1-\delta_{mn})\Gamma_{mn}\right)\rho_{mn} = \left[H'(t),\rho^{(n-1)}\right]_{mn} \qquad (1)$$

where H' = -μE represents the perturbation. The different order matrix elements of the density operator ρ may be written as:

$$\rho_{mn} = C_{mn}^{(k)} e^{-ik\omega t} + C_{mn}^{(k-2)} e^{-i(k-2)\omega t} + \ldots \text{ c.c.} \qquad (2)$$

These matrix elements occur in the calculation of the fifth-order polarization which has the form:

$$< P(5\omega t) > = N\sum_{mn} P_{nm} C_{nm}^{(5)} e^{-5i\omega t} + c.c. \qquad (3)$$

The fifth order susceptibility is the ratio between the average value of the polarization and the incident field. The effective calculus gives for the real part of the susceptibility an expression formed by terms having the general form:

$$\chi^{(5)}(-5\omega;\omega,\omega,\omega,\omega,\omega) = \frac{(ea_0)^6}{(\hbar c)^5} \cdot \frac{1}{2^5} \cdot \sum P_{ga}P_{ab}P_{bc}P_{cd}P_{de}P_{eg}$$

$$\frac{1}{[(\omega-\omega_{ag})^2+\Gamma^2][(2\omega-\omega_{bg})+\Gamma^2][(3\omega-\omega_{cg})^2+\Gamma^2][(4\omega-\omega_{dg})^2+\Gamma^2][(5\omega-\omega_{eg})^2+\Gamma^2]} \cdot$$

$$\Big\{(\omega-\omega_{ag})(2\omega-\omega_{bg})(3\omega-\omega_{cg})(4\omega-\omega_{dg})(5\omega-\omega_{eg}) - \Gamma^2[(\omega-\omega_{ag})\cdot(2\omega-\omega_{bg}) + \qquad (4)$$

$$+ (4\omega-\omega_{dg})(3\omega-\omega_{cg}) + (3\omega-(\omega_{ag}+\omega_{bg}))(7\omega-(\omega_{eg}+\omega_{dg})) + (\omega-\omega_{ag})(2\omega-\omega_{bg})$$

$$(3\omega-(\omega_{ag}+\omega_{bg})) + (3\omega-\omega_{cg})\cdot(4\omega-\omega_{dg})\cdot(7\omega-(\omega_{eg}+\omega_{dg}))]\Big\} + \ldots$$

In the expression (4) P_{ij} represents the elctric dipole moment between states i and j, a_0 is the Bohr radius, ω is the angular frequency, g refers to the fundamental state and a, b, ... refer to all excited states. We neglected the terms which contain powers of Γ greater than 2 as being insignificant.

The eigenstates of the alkali metal atoms involving spin-orbit coupling are specified by the ket vectors: $|n, l, s = \frac{1}{2}, J, m\rangle$. The dipole matrix elements have the form:

$$<n,l,s,j,m|P_z|n',l',s',j',m'> = -e<l,s,j,m|T_0^{(1)}|l',s',j',m'> \cdot \qquad (5)$$

$$\cdot <n,l||r||n',l'>.$$

where

$$<l,s,j,m|T_0^{(1)}|l',s',j',m'> = (-1)^{j-m}\begin{pmatrix} j & 1 & j' \\ -m & 0 & m' \end{pmatrix}<l,s,j||T^{(1)}||l',s',j'> \qquad (6)$$

$$<l,s,j||T^{(1)}||l',s',j'> = (-1)^{l+s+j'+1}(2j+1)^{\frac{1}{2}}(2j'+1)^{\frac{1}{2}} \cdot \begin{Bmatrix} j & 1 & j' \\ l & s & l' \end{Bmatrix} \cdot <l||T^{(1)}||l'> \qquad (7)$$

$$<l||T^{(1)}||l'> = (-1)(2l+1)^{\frac{1}{2}}(2l'+1)^{\frac{1}{2}}\begin{pmatrix} l & 1 & l' \\ 0 & 0 & 0 \end{pmatrix} \qquad (8)$$

The calculus of the fifth order susceptibility and the drawing of dispersion curves involve computer aid

Taking into account the values of the dipole matrix elements for the transitions ns ⟶ n'p, mp ⟶ m'd and kd ⟶ k'f calculated in papers /5,8/, such dispersion curve for iodine laser radiation situated around $\lambda = 1{,}3$ µm is presented for Na atoms in figure 1. The obtained value $\chi^{(5)}(-5\omega;\omega,\omega,\omega,\omega,\omega)$ = 1,34 x 10^{-44} ESU for a damping coefficient $\Gamma = 0.5\ \mathrm{cm}^{-1}$ is in accordance with other published results /14/.

Neglecting the fine structure of the energetic levels implied in transitions, for the seventh order nonlinear susceptibility (per atom) the following experssion is obtained /10/:

$$\chi^{(7)}(7\omega) = \frac{8}{64\hbar^7} \sum_{b_1\ldots b_7} [\langle a s o \tfrac{1}{2}|z|b_1 p o \tfrac{1}{2}\rangle\langle b_1 p o \tfrac{1}{2}|z|b_2 s o \tfrac{1}{2}\rangle$$

$$\langle b_2 s o \tfrac{1}{2}|z|b_3 p o \tfrac{1}{2}\rangle\langle b_3 p o \tfrac{1}{2}|z|b_4 s o \tfrac{1}{2}\rangle\langle b_4 s o \tfrac{1}{2}|z|b_5 p o \tfrac{1}{2}\rangle \cdot \qquad (9)$$

$$\langle b_5 p o \tfrac{1}{2}|z|b_6 s o \tfrac{1}{2}\rangle\langle b_6 s o \tfrac{1}{2}|z|b_7 p o \tfrac{1}{2}\rangle\langle b_7 p o \tfrac{1}{2}|z|a\ s o \tfrac{1}{2}\rangle \cdot$$

$$\cdot \frac{1}{(\omega_{ab_1}+7\omega)(\omega_{ab_2}+6\omega)\ldots(\omega_{ab_7}+\omega)} + \ldots$$ other therms describing the interaction between other states and continuum.

The frequency dependence of the seventh order nonlinear susceptibility for Na and Li atoms for λ = 1.06 µm is presented in figure 2 (a) for the frequency variation around the fundamental and (b) for the frequency variation around the seventh harmonic.

Since the fine structure of the levels and the damping effects are neglected, at resonance, the seventh order nonlinear susceptibility becomes infinite.

3. Nonresonant interaction process model for the seventh harmonic generation

The coupled amplitude equations that describe the interaction of four waves /15/ are used for the analysis of the seventh harmonic generation in an isotropic and nonlinear medium that presents third, fifth and seventh order nonlinearities.

Following the model presented in paper /16/, it can be considered that the seventh harmonic generation results from both the direct processes that involve seventh order nonlinearities

$$\omega + \omega + \omega + \omega + \omega + \omega + \omega \longrightarrow 7\omega \qquad (10)$$

and the four possible step processes that involve third and fifth order nonlinearities:

$$\begin{cases} \omega + \omega + \omega \longrightarrow 3\omega \\ \omega + 3\omega + 3\omega \longrightarrow 7\omega \end{cases} \qquad (11)$$

$$\begin{cases} \omega + \omega + \omega \longrightarrow 3\omega \\ \omega + \omega + \omega + \omega + 3\omega \longrightarrow 7\omega \end{cases} \tag{12}$$

$$\begin{cases} \omega + \omega + \omega + \omega + \omega \longrightarrow 5\omega \\ \omega + \omega + 5\omega \longrightarrow 7\omega \end{cases} \tag{13}$$

$$\begin{cases} \omega + \omega + \omega \longrightarrow 3\omega \\ 3\omega + \omega + \omega \longrightarrow 5\omega \\ \omega + \omega + 5\omega \longrightarrow 7\omega \end{cases} \tag{14}$$

For the processes (10) and (11) for instance the general conditions for the wave vector mismatch take the form:

$$k_1 + k_1 + k_1 + k_1 + k_1 + k_1 + k_1 = k_7 + \Delta_{17} \tag{15}$$

$$k_1 + k_1 + k_1 = k_3 + \Delta_{13} \tag{16}$$

$$k_1 + k_3 + k_3 = k_7 + \Delta_{137} \tag{17}$$

and

$$\Delta_{17} = \Delta_{13} + \Delta_{137} \tag{18}$$

In the wave plane approximation for the same direct (10) and step (11) processes one obtains the following coupled normalized amplitude equations

$$\frac{da_1}{d\tilde{z}} = -\sigma_{10} a_1^2 \cdot a_3 \sin\phi - \sigma'_{10} a_3^2 a_7 \sin(\psi - 2\phi) - \sigma''_{10} a_1^6 a_7 \sin\psi \tag{19}$$

$$\frac{da_3}{d\tilde{z}} = a_1^3 \sin\phi - \sigma_{30} a_1 a_3 a_7 \sin(\psi - 2\phi) \tag{20}$$

$$\frac{da_7}{d\tilde{z}} = \sigma_{70} a_1 a_3 \sin(\psi - 2\phi) - \sigma'_{70} a_7 \sin\psi \tag{21}$$

$$\begin{aligned} \frac{d\varphi}{d\tilde{z}} = & -\tilde{\Delta}_{13} + \left(\frac{a_1^3}{a_3} - 3\sigma_{10} a_1 a_3\right)\cos\varphi - 3\sigma''_{10} a_1^5 a_7 \cos\psi + \\ & + \left(\sigma_{30} a_1 a_7 - 3\sigma'_{10} \frac{a_3^2 a_7}{a_1}\right)\cos(\psi - 2\varphi) \end{aligned} \tag{22}$$

$$\frac{d\psi}{d\tilde{z}} = -\tilde{\Delta}_{17} - 7\sigma_{10}a_1a_3\cos\phi + \left(\sigma_{70}\frac{a_1a_3^2}{a_7} - 7\sigma_{10}\frac{a_3a_7}{a_1}\right) \tag{23}$$

$$\cdot\cos(\psi-2\phi) + \left(\sigma''_{70}\frac{a_1^7}{a_7} - 7\sigma''_{10}a_1^5a_7\right)\cos$$

where σ_{10}, σ'_{10},..., are nonlinear coefficients that depend on several order nonlinear susceptibilities.

In a Na:Xe ($\frac{N_{Xe}}{N_{Na}}$ = 3.55; N_{Na} = 10^{17} atoms/cm^3) mixture, without wave vector mismatch ($\tilde{\Delta}_{13} = \tilde{\Delta}_{17} = 0$), for a laser radiation of λ = 1.06 µm and power density ∿ 10^{11}W/cm^2, the dependence of the fundamental a_1 (with a factor scale x1), third harmonic a_3 (x4.8x10^{-1}) and seventh harmonic a_7 (x4.7x10^{-2}) on a normalized distance $\tilde{z}$ is presented in figure 3. The maximum of the seventh normalized amplitude is obtained for $\tilde{z}$ = 9.3.

For Gaussian beam parameters that define the experimental configuration of the interaction processes mentioned above, presented in figure 4, we obtained the seventh harmonic amplitude which is dependent on the integral I defined by:

$$I = \int_{-2d}^{2(1-d)} \frac{e^{-\frac{i\Delta_{17}L\eta}{2}}}{(1-iq\eta)^6}\,d\eta - iWL\int_{-2d}^{2(1-d)} \frac{e^{-\frac{i\Delta_{137}L\eta}{2}}}{(1-iq\eta)^2}\,d\eta \cdot \tag{24}$$

$$\int_{-2d}^{\eta} \frac{e^{-\frac{i\Delta_{13}L\tau}{2}}}{(1-iq\tau)^4}\,d\tau = I_d - iWLI_s \text{ and } W = \sigma_3\upsilon_7/2\sigma'_7$$

1°. For weak focusing q < 1, where the focusing parameter q is defined by $q = \frac{L}{b}$, the maximum of the seventh harmonic power is obtained for phase matching conditions $\Delta_{13} = \Delta'_{17} = 0$.

For $d = \frac{1}{2}$, where $d = \frac{\ell_0}{L}$ defines the maximum spot position, the integral I reaches its maximum and we thus obtain:

$$I = 2\left[1 - 2q^2 + \frac{1}{5}q^4 - iWL\frac{2(1+q^2)(1-\frac{1}{3}q^2)}{1+iq}\right]\frac{1}{(1+q^2)^5} \tag{25}$$

2°. With strong focusing q > 1, and if only direct processes are taken into account, it results:

$$I = I_d = \frac{2\pi}{5!}\left(-\frac{L\Delta_{17}}{2}\right)^5 e^{-\frac{1}{2}L\Delta_{17}} \quad (\text{for } d \to \infty) \tag{26}$$

which has a maximum value for $\Delta_{17} = \frac{10}{b}$.

The contribution of the step processes can be evaluated from the maximum of the expression

$$R_e I_s = \frac{1}{2} \int_{1}^{1} \frac{e^{-\frac{i\Delta_{137} L\eta}{2}}}{(1-iq\,\eta)^2}\, d\eta \int_{-1}^{1} \frac{e^{-\frac{i\Delta_{13} L\tau}{2}}}{(1-iq\tau)^4}\, d\tau \qquad (27)$$

This is fulfilled for $\Delta_{17} = \frac{4}{b}$.

The conditions for wave vector mismatch considered above may be accomplished experimentally by variation of the mixture density of the inert gases and the alkali vapour metals.

4. Two-photon resonant absorption model for the seventh harmonic generation

It may also be considered that the generation of the seventh harmonic is produced by the resonant absorption of the two photons that correspond to the dipole transitions between levels $|1\rangle$ and $|2\rangle$ using the intermediate state $|\ell\rangle$ which can be bound or free (fig.5) under a four wave process of the type : $\omega + 3\omega + 3\omega = 7\omega$.

Considering that the total electric field consists of the incident field E_1 and the fields E_3 and E_7 of the generated harmonics, which are considered much smaller than E_1:

$$E(z,t) = E_1(z,t)\, e^{i(\omega t - k_1 z)} + E_3(z,t)\, e^{i(3\omega t - k_7 z)} + E_7(z,t)\, e^{i(\omega t - k_7 z)} \qquad (28)$$

using the density matrix formalism for the two-photon resonant absorption and the model presented in paper /17/ one obtains the following coupled amplitude equations:

$$\frac{dA_1}{dz} = -\frac{\omega N}{2c\varepsilon_0}\Big[\big(\langle\alpha_1(\omega)\rangle\sigma_{11} + \langle\alpha_2(\omega)\rangle\sigma_{22}\big)A_1 + \langle 2\gamma_{12}/\hbar\rangle\sigma_{12}A_1\cos^2 2\theta_1 + \\ + \langle\xi_{21}/\hbar\rangle\sigma_{12}A_3\cos(\theta_3-\theta_1)\Big] \qquad (29)$$

$$\frac{dA_3}{dz} = -\frac{3\omega N}{2c\varepsilon_0}\Big[\big(\langle\alpha_1(3\omega)\rangle\sigma_{11} + \langle\alpha_2(3\omega)\rangle\sigma_{22}\big)A_3\sin\Delta k_3 z - \\ - \langle\xi_{21}/\hbar\rangle\sigma_{12}A_1\sin(\theta_1-\theta_3-\Delta k_3 z)\Big] \qquad (30)$$

$$A_3\frac{d\theta_3}{dz} - k_3A_3 + \frac{3\omega}{2c\varepsilon_0}A_3 = -\frac{3\omega N}{2c\varepsilon_0}\Big[\big(\langle\alpha_1(3\omega)\rangle\sigma_{11} + \langle\alpha_2(3\omega)\rangle\sigma_{22}\big)A_3\cos\Delta k_3 z + \\ + \langle\xi_{21}/\hbar\rangle\sigma_{12}A_1\cos(\theta_1-\theta_3-\Delta k_3 z)\Big] \qquad (31)$$

$$\frac{dA_z}{dz} = \frac{7\omega N}{2c\varepsilon_0}\Big[\big(\langle\alpha_1(7\omega)\rangle\sigma_{11} + \langle\alpha_2(7\omega)\rangle\sigma_{22}\big)A_7\sin\Delta k\, z + \\ + \langle\xi_{21}/\hbar\rangle\sigma_{12}A_3\sin(\theta_3-\theta_7-\Delta k_7 z)\Big] \qquad (32)$$

$$A_7 \frac{d\theta_7}{dz} + k_7 A_7 + \frac{7\omega}{c} A_7 = - \frac{7\omega N}{2c\epsilon_0}\left[\left(\langle\alpha_1(7\omega)\rangle\sigma_{11} + \langle\alpha_2(7\omega)\rangle\sigma_{22}\right)A_7 \cos \Delta k_7 z + \right.$$

$$\left. + \langle\zeta_{21}/\hbar\rangle\sigma_{12}A_3\cos(\theta_3-\theta_7-\Delta k_7 z)\right] \tag{33}$$

where

$$\Delta k_m = m\kappa - k_n = \frac{\omega_m N}{2c\epsilon_0}\left\{\left[\alpha_1'(\omega)-\alpha_1(\omega_m)\right]\sigma_{11} + \left[\alpha_2'(\omega)-\alpha_2'(\omega_m)\right]\sigma_{22} + \right.$$

$$\left. + \frac{2}{\hbar}\mathrm{Re}\left[\gamma_{12}e^{-i(m-1)\theta}\sigma_{12}\right]\right\} \tag{34}$$

represents the wave vector mismatch.

The model takes into account:

- Stark shifts of the levels

$$\delta\omega_{21} = \hbar^{-1}\left\{\left[\alpha_1'(\omega)+\alpha_2'(\omega)\right]|E_1|^2 + \alpha_1'(3\omega)|E_3|^2\right\} \tag{35}$$

- ionization processes corresponding to the levels $|1\rangle$ and $|2\rangle$ due to the incident radiation and the third harmonic respectively

$$\gamma_1 = \gamma_{11}^{3\omega} = \hbar^{-1}\alpha_1''(3\omega)|E_3|^2 \tag{36}$$

$$\gamma_2 = \gamma_2^{\omega} + \gamma_2^{3\omega} = \hbar^{-1}\left[\alpha_2''(\omega)|E_1|^2 + \alpha_2''(3\omega)|E_3|^2\right] \tag{37}$$

$$\alpha_j(m\omega) = \alpha_j'(m\omega) - i\alpha_j(m\omega) = \hbar^{-1}\sum_{\ell}\left(\frac{|\mu_{\ell j}|^2}{\omega_{\ell j}-m\omega} + \frac{|\mu_{\ell j}|^2}{\omega_{\ell j}+m\omega}\right) \tag{38}$$

- absorption or emission of two-photon

$$\gamma_{12} = \sum_{\ell}\frac{\mu_{1\ell}\cdot\mu_{\ell 2}}{\omega_{\ell 2}+\omega} \tag{39}$$

- stimulated Raman scattering

$$\zeta_{21} = \sum_{\ell}\left(\frac{\mu_{2\ell}\mu_{\ell 1}}{\omega_{\ell 1}-3\omega} + \frac{\mu_{2\ell}\cdot\mu_{\ell 1}}{\omega_{\ell 2}+3\omega}\right) \tag{40}$$

and Doppler width $\delta_D = \omega_{21}(2RT/Mc^2)^{\frac{1}{2}}$

$$\langle A\rangle = \frac{1}{\delta_D\sqrt{\pi}}\int_{-\infty}^{\infty} A e^{-(\delta/\delta_D)^2}\, d\delta \tag{41}$$

5. Conclusions

The models for the fifth and seventh order nonlinear susceptibility calculus made by either neglecting the fine structure of the levels or by taking it into account, can be used for the numerical evaluation of these susceptibilties.

The obtained coupled amplitude equations and the dependence of the normalized distance of the normalized different harmonics can be used for the improvement of the conversion efficiency and for the optimal condition study of the seventh harmonic generation by two-photon resonant absorption.

REFERENCES

/ 1/ V.S.Doitcheva et al., Opt. & Quantum Electron, 10, 131-138 (1978)

/ 2/ J.Reintjes et al., IEEE, J.Quantum Electron QE-14, 581-596 (1978)

/ 3/ M.G.Grozeva et al., Optics Comm. 23, 77-79 (1977)

/ 4/ R.B.Miles and S.E.Harris; IEEE J.Quantum Electron. QE-9, 470-484 (1973)

/ 5/ H.Eicher, IEEE J.Quantum Electron. QE-11, 121-130 (1975)

/ 6/ V.M.Miev et al., Opt. & Quantum Electron. 11, 229-236 (1979)

/ 7/ I.M.Popescu, P.E.Sterian, N.N.Pu’ca’: Bul. IPB, 4, 27-30 (1982)

/ 8/ I.M.Popescu, N.N.Puscas, P.E.Sterian, I.Baranovscki, Rev.Roum.Phys. 5, 383-388 (1983)

/ 9/ D.Irimescu, I.M.Popescu, N.N.Puscas, P.E.Sterian, Bul.IPB, Seria Energetic’, Tom XIV, 18 (1983)

/10/ I.M.Popescu, P.E.Sterian, N.N.Puscas, St.Cerc.Fiz., 2, 139-143 (1984)

/11/ I.M.Popescu, N.N.Puscas, P.E.Sterian, Rev.Transp.Telecom. 9, 84-87 (1982)

/12/ I.M.Popescu, N.N.Puscas, P.E.Sterian, Int.Conf.Sch. "Laics", 327-328 (1982)

/13/ I.M.Popescu, N.N.Puscas, P.E.Sterian, D.Irimescu, Rev.Roum.Phys., 9, 807-813 (1984)

/14/ H.Puell, C.R.Vidal, Optics Comm. 27, 165-197 (1978)

/15/ J.A.Armstrong et al., Phys.Rev. vol.127, 1918-1939 (1962)

/16/ I.V.Tomov, M.C.Richardson, IEEE, J.Quantum Electron. QE-12, 521-531 (1975)

/17/ A.T.Georges, P.Lambropoulos, J.H.Marburger, Phys.Rev.A, 15, 300-305 (1976)

/18/ I.M.Popescu, P.E.Sterian, N.N.Puscas, "Photov. Optoelectr.Proc." Proc.Inter.Conf., 4-7 July 1984, Bucharest, Romania p.13

/19/ I.M.Popescu, P.E.Sterian, N.N.Puscas, Sem.Optoelectr. May 1984, IPB

/20/ I.M.Popescu, P.E.Sterian, N.N.Puscas, D.Irimescu, Ses.An. ICEFIZ, Craiova, 29 sept.- 1 oct. 1983

/21/ I.M.Popescu, N.N.Puscas, P.E.Sterian, D.Irimescu, 3 Simp.Nat.Techn.Micr.Buc. 18-19 nov. 1983

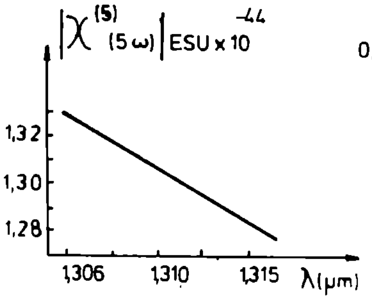
$|\chi^{(5)}_{(5\omega)}|$ ESU x 10^{-44}
1,32
1,30
1,28
1,306
1,310
1,315
λ(μm)

Fig.1

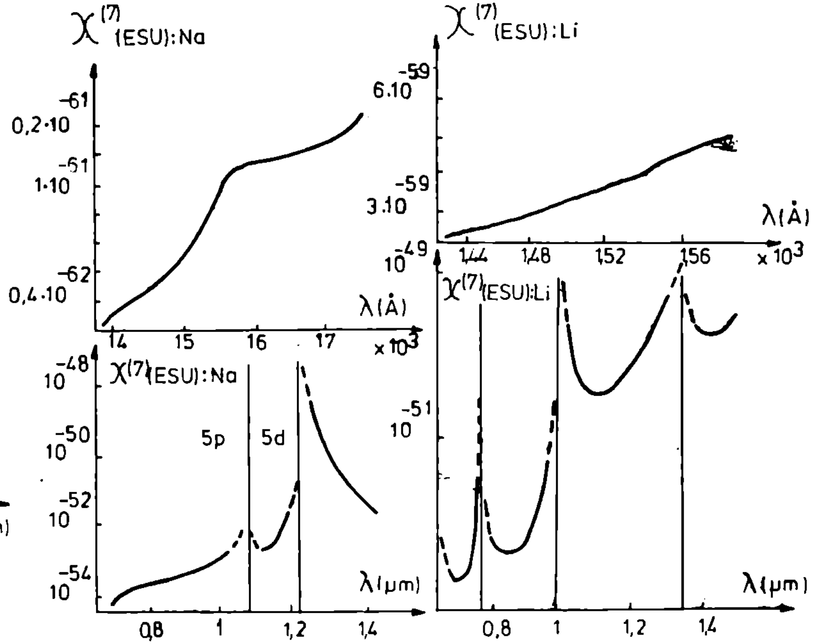
$\chi^{(7)}_{(ESU):Na}$
$0,2\cdot10^{-61}$
$1\cdot10^{-61}$
$0,4\cdot10^{-62}$
14
15
16
17
λ(Å)
x 10^3
$\chi^{(7)}_{(ESU):Na}$
10^{-48}
10^{-50}
10^{-52}
10^{-54}
5p
5d
0,8
1
1,2
1,4
λ(μm)
$\chi^{(7)}_{(ESU):Li}$
6.10^{-59}
3.10^{-59}
10^{-49}
1,44
1,48
1,52
1,56
λ(Å)
x 10^3
$\chi^{(7)}_{(ESU):Li}$
10^{-51}
0,8
1
1,2
1,4
λ(μm)

a

b

Fig 2

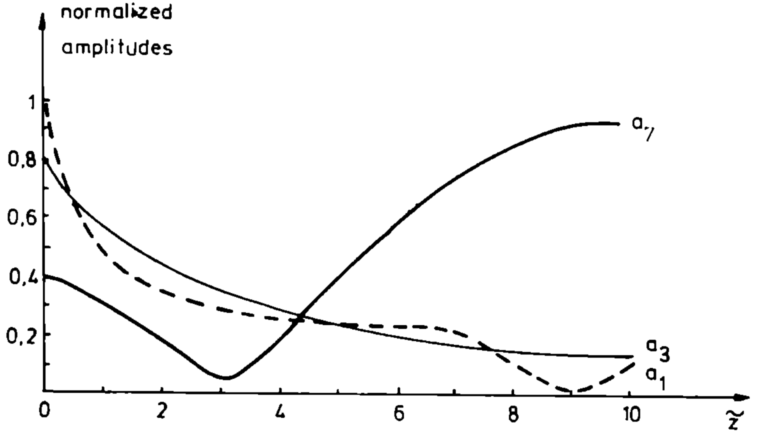

Fig.3

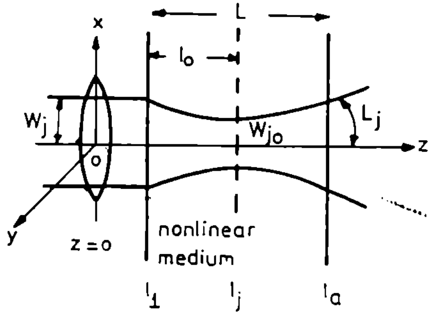

Fig.4

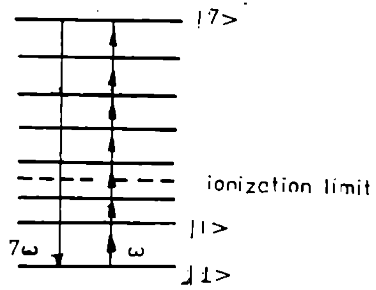

Fig.5

CONTROLLING THE REFRACTIVE INDEX DISTRIBUTION IN CYLINDRICAL BODIES THROUGH TRANSVERSALLY TRANSMITTED LIGHT MEASUREMENTS

Nicholas Ionescu-Pallas, Valentin Vlad,
Institute for Physics and Technology of Radiative Devices, Bucharest, Măgurele
Adriana Vlad, Valeriu Căpățînă
Polytechnic Institute of Bucharest
Ștefan Solomon
Institute for Nuclear Physics and Engineering
Mihai Jurbă
Faculty of Physics, Bucharest

A new method of evaluating the mathematical transform connecting the refractive index distribution in cylindrical bodies to the transversally transmitted light distribution, is presented. A computation program, based on this method, is devised, cummulating the following advantages: the characteristic singularity in the coordinate origin is avoided; a single numerical integration is used, instead of a double one, ensuring a rapid data processing; the algorithm takes into account an eventual index jump at the body edge; the refractive index profile is calculated with an error $< 1 \times 10^{-3}$. The method was checked by analytical simulations of some simple profiles and by using experimental data yielded by a cylindrical rod with a known index profile introduced in an optical set up directly connected to a computer. The processed data finally proved the mentioned advantages.

Statement of the problem

A transparent cylindrical body, having a circular transverse section, is horizontally lying in a transparent liquid whose refractive index is equal to the refractive index on the cylindrical surface of the body. A laser beam, passing in a horizontal plane, intercepts perpendicularly the cylinder, determining in a circular transverse section, a certain path inside the body, which is almost secant of the circle, parallel to the horizontal diameter. Let t be the distance from the interception point (incidence point) of the beam to the horizontal diameter of the transverse section and y the diameter coming from the spot of the emergence point on a vertical recording plane parallel to the cylinder, and perpendicularly ending on the same horizontal diameter. The recording plane is placed at a distance L from the center of the circular transverse section of the body, greater or equal to the radius R of the respective section. It is important that, at all events, L should be a little greater than R, in order to have a constant refractive index and a vanishing spatial gradient of the index in the radial transverse direction for any distance greater than L. The incident laser beam is displaced in parallels to itself so that the path inside the transverse section explores the circular surface beginning with the southern and ending with the northern pole (Figure 1). Accordingly, on the recording plane will appear a succession of bright points, being established a one-to-one correspondence between the laser beam incident on the cylindrical body at t and the measured light intensity at y.

If the cylindrical body under investigation would be altogether homogeneous and with a refractive index equal to the refractive index of the immersion bath, then the two perpendicular distances will be rigorously equal and the incident light intensity (at t) equal to the measured light intensity (at y) (this, however, implying that no absorption and no scattering of light takes place within the body). The energy of light is then conserved during the travelling through body and,moreover, its distribution against the height t is kept unchanged. If, instead of this ideal situation exhibiting no practical interest, the cylindrical body has a refractive index distribution depending on the distance r from the center of the transverse section to an arbitrary point of this section, then the light energy travelling through the body is still conserved, but the light intensity distribution in the recording plane is different from the distribution in a plane parallel to the recording one and tangent to the body surface in front of the laser beam.

Mathematical formulation

Let us adopt the location of the recording plane at $L = R + \varepsilon \cong \mathcal{R}$ in order to avoid eventual edge effects (due to the non-fulfilment of the conditions $n = n_{\infty}$, $dn/dr = 0$ at $r = R$) and introduces the notations

$$\frac{t}{\mathcal{R}} = \tau , \quad \frac{y}{\mathcal{R}} = \eta , \quad \frac{r}{\mathcal{R}} = \zeta \tag{1}$$

Thereafter, we divide the distance $\mathcal{R}$ in N equidistant intervals and consider the discrete values of (τ , η , ζ) corresponding to the equidistant division points. The conservation of light energy during the travelling through the cylindrical body delivers us the equation

$$\int_0^t I_0(t')\,dt' = \int_0^{y(t)} I(y')\,dy' \tag{2}$$

(which accounts for the energy balance of all the light beams passing in the band delimited by the horizontal diameter of the transverse circular section and a line parallel to this diameter and placed at a distance t of it). If we assume that I_0 is a constant quantity (steady irradiation) and, in addition, we take into account the obvious condition

$$y(\mathcal{R}) = \mathcal{R} \tag{3}$$

then, the incident intensity may be expressed as

$$I_0 = \frac{1}{\mathcal{R}} \int_0^{\mathcal{R}} I(y')\,dy' \tag{4}$$

Further on, it is opportune to introduce normalized intensities

$$\mathcal{I} = I(y)/I_0 = I(y) \times \frac{R}{\int_0^R I(y')\,dy'} \tag{5}$$

in terms of a dimensionless argument

$$\mathcal{I}(\eta) = \frac{J(\eta)}{\int_0^1 J(\eta')\,d\eta'} \tag{6}$$

where $I(y) \equiv J(\eta)$. It follows now that

$$\int_0^1 \mathcal{I}(\eta)\,d\eta = 1 \tag{7}$$

and the relations (4) and (2) become

$$I_0 = \int_0^1 J(\eta')\,d\eta' \tag{4'}$$

and

$$\tau = \frac{\int_0^\eta J(\eta')\,d\eta'}{\int_0^1 J(\eta'')\,d\eta''} = \int_0^{\eta(\tau)} \mathcal{I}(\eta')\,d\eta' \qquad \text{respectively.} \tag{2'}$$

As we already mentioned that between the quantities t and y a certain one-to-one relationship is established (as a result of energy conservation), we may, in principle, revert the function $\eta = \eta(\tau)$ to obtain $\tau = \tau(\eta)$. Then, by taking the derivative against η in (2') we come to a first noticeable equation

$$\mathcal{I}(\eta) = \frac{d\tau(\eta)}{d\eta} \tag{8}$$

Alternatively, resorting again to relation (2'), we may write

$$\mathcal{I}(\eta) = \frac{1}{\eta'(\tau)} \tag{8'}$$

The theory of the problem comes to a certain connection between the refractive index distribution in the transverse section of the cylindrical rod and the intensity distribution in the recording plane. We denote, first

$$F(r) = \frac{n(r)-n(R)}{n(R)} \cdot \pi \tag{9}$$

Thereafter, we introduce dimensionless variables

$$F(r) = f(\zeta) \quad , \quad n(r) = u(\zeta)$$
$$f(\zeta) = \pi \cdot \frac{u(\zeta)-u(1)}{u(1)} \tag{10}$$

The connection between the various dimensionless quantities is given by the transform (of the Abel's type) / /

$$f(\zeta) = \int_{\zeta}^{1} g(\tau) \frac{\tau d\tau}{\sqrt{\tau^2 - \zeta^2}} , \quad g(\tau) \equiv \left[1 - \frac{\eta(\tau)}{\tau}\right] \tag{11}$$

Taking in view that τ is connected to (normalized) intensity through relation (2'), $\tau\, g(\tau)$ may be written as

$$\tau g(\tau) = \int_{0}^{\eta(\tau)} [I(\eta') - 1] d\eta' \tag{12}$$

and, consequently, the functional (11) takes the form

$$f(\zeta) = \int_{\zeta}^{1} \frac{d\tau}{\sqrt{\tau^2 - \zeta^2}} \int_{0}^{\eta(\tau)} [I(\eta') - 1] d\eta' \tag{13}$$

After a partial integration, the double integral is reduced to a simple one

$$f(\zeta) = (\tau - \eta) \ln \frac{\tau + \sqrt{\tau^2 - \zeta^2}}{\zeta} \Bigg|_{\tau=\zeta}^{\tau=1} - \int_{\zeta}^{1} [I(\eta) - 1] \eta'(\tau) \times \ln \frac{\tau + \sqrt{\tau^2 - \zeta^2}}{\zeta} d\tau =$$

$$= - \int_{\zeta}^{1} \left[1 - \frac{1}{I(\eta)}\right] \ln \frac{\tau + \sqrt{\tau^2 - \zeta^2}}{\zeta} d\tau \tag{14}$$

Formula (14) is an accurate one and for its derivation the relations $\eta(1) = 1$ and $\eta'(\tau) = 1/I(\eta)$ were used. It is still possible to go over from the variable τ to the variable η (in the recording plane). In this case, one obtains

$$f(\zeta) = - \int_{\eta(\zeta)}^{1} [I(\eta) - 1] \ln \frac{\tau(\eta) + \sqrt{\tau^2(\eta) - \zeta^2}}{\zeta} d\eta \tag{15}$$

This formula is still an accurate one. To go further, it is necessary to make some useful approximations. If the quantity $f(0) = \pi \frac{u(0) - u(1)}{u(1)}$ is much smaller than 1, the following approximation does hold giving a good agreement with experimental data

$$\tau(\eta) \approx \eta \quad \Longrightarrow \quad \eta(\zeta) \approx \zeta \tag{16}$$

Physically, this is equivalent to the discarding of the effect of refraction inside the body (this not in any version of the functional $f \leftrightarrow I$, but only in formula (15), in which this effect is minimized). Thus, from (15) and (16), we obtain

$$f(\zeta) \approx - \int_{\zeta}^{1} [I(\eta) - 1] \ln\left(\frac{\eta + \sqrt{\eta^2 - \zeta^2}}{\zeta}\right) d\eta \tag{17}$$

The consequences of the approximation (16) were investigated in some practical cases when $\mathcal{I}(\eta)$ is bounded so that $|\mathcal{I}(\eta) - 1| \ll 1$. In such cases, the smallness of relative intensity entails the smallness of the refractive index contrast and the approximation is a fairly good one. For $\zeta = 0$, the integrant in (17) is logarithmically divergent (although the integral itself is convergent). It is therefore recommended to prevent the direct calculation of $f(\zeta)$ in the close vicinity of $\zeta = 0$ using formula (17). In such points $f(\zeta)$ may, for instance, be well evaluated by using finite difference method and proceeding from the points placed in their proximity, for which the respective formula still holds.

Numerical approximations

Let us divide the distance R in N equidistant intervals $R = N\delta$ and let the radial distance r ($0 \leqslant r \leqslant R$) be an integer number of δ, i.e. $r = s\delta$. It follows that $\zeta = \frac{r}{R} = \frac{s}{N}$. Further on, let us perform in (17) the variable change $\eta = \frac{\xi}{N}$. We thus obtain

$$f\left(\frac{s}{N}\right) \approx -\frac{1}{N}\int_{s}^{N}\left[\mathcal{I}\left(\frac{\xi}{N}\right)-1\right]\ln\left(\frac{\xi+\sqrt{\xi^2-s^2}}{s}\right)d\xi \tag{18}$$

Now, let us divide the interval (N - s) in equidistant interval of unit length. Thus, one reaches the formula

$$f\left(\frac{s}{N}\right) \approx -\frac{1}{N}\sum_{sj}^{N-1}\int_{j}^{j+1}\left[\mathcal{I}\left(\frac{\xi}{N}\right)-1\right]\ln\left(\frac{\xi+\sqrt{\xi^2-s^2}}{s}\right)d\xi \tag{19}$$

which is particularly suitable to be approximated with the aid of Gregory-type mechanical integration method. The quantities f(0) and $f\left(\frac{N-1}{N}\right)$ require a special treatment. An efficient computation program was elaborated and tested for known intensity distributions (derived by solving the inverse transform for simple refractive index distributions). In a second stage of numerical simulations, a white multiplicative noise, corresponding to a certain admitted band of error, was taken into account, and the stability of the integration method was checked.

Inverse functional transform

Formula (11) may be considered as a direct Abel transform between $g(\tau)$ and $f(\zeta)$, Accordingly, it may be reverted to give

$$g(\zeta) = \int_{\zeta}^{1}\left[-\frac{2}{\pi}\frac{1}{\tau}f'(\tau)\right]\frac{\tau\,d\tau}{\sqrt{\tau^2-\zeta^2}} \tag{20}$$

Thereafter, we change adequately the denomination of variables, introduce the expression of g in terms of $\mathcal{I}$ and, finally, by performing a certain derivative, we establish the inverse connection between $\mathcal{I}(\eta)$ and $f(\zeta)$ under the form

$$\left\{\frac{1}{\mathcal{I}(\eta)}\right\}_{\eta=\eta(\tau)} = 1 + \frac{2}{\pi}\left\{-\frac{f'(1)}{\sqrt{1-\tau^2}} + \int_{\tau}^{1}\left[\frac{d}{d\zeta}\left(\zeta\frac{df}{d\zeta}\right)\right]\frac{d\zeta}{\sqrt{\zeta^2-\tau^2}}\right\}. \tag{21}$$

To notice that this formula still holds for $\varepsilon \to 0$ ($R \to R$), when $f'(1)$ may be different from zero. We denote the right part of the equality (21) by $\Psi(\tau)$ and remember that the left side of the same equality is equal to $d\eta(\tau)/d\tau$. Thus, we obtain the integral equation

$$\eta(\tau) = \int_0^{\tau} \psi(\tau')\,d\tau' \qquad (22)$$

which is the starting point for simulating various cases of practical interest. Let us consider the function

$$f(\zeta) = \frac{2}{3}\,\alpha(1-\zeta^2)^{3/2}, \quad |\alpha| \ll 1 \qquad (23)$$

which is close to the real refractive index distribution, to be encountered in studying optical fibers (or cylindrical rods named "preforms", out of which the fibers are obtained through an axial pulling under certain thermal conditions). $f(\zeta)$ satisfies the condition $f'(1) = 0$. From (23) and (21) we obtain $\Psi(\tau) = 1 + \alpha(3\tau^2 - 1)$. Inserting this result in (22) we obtain the third degree algebraic equation

$$\eta(\tau) = \tau + \alpha(\tau^3-\tau) \qquad (24)$$

Reverting this equation, it results

$$\tau(\eta) = \eta - \alpha(\eta^3-\eta) + \alpha^2(3\eta^5-4\eta^3+\eta) - O(\alpha^3) \qquad (25)$$

The intensity may be now easily estimated as

$$I(\eta) = \frac{d\tau(\eta)}{d\eta} = 1 - \alpha(3\eta^2-1) + \alpha^2(15\eta^4-12\eta^2+1) - O(\alpha^3) \qquad (26)$$

If, instead of inverting the exact transform (15) we would invert the approximate transform (17), we will obtain $\Im(\eta) = 1 - \alpha(3\eta^2 - 1)$. In this way, we get an indication about the systematic error introduced together with the approximation going over from exact formula (15) to the approximate one (17). It is of the magitude order of the maximal refractive index contrast inside the body.

Another analytical case studied by us is the parabolic one

$$f(\zeta) = \frac{\pi}{4}\,\beta(1-\zeta^2), \quad |\beta| \ll 1, \qquad (27)$$

leading to the intensity distribution

$$I(\eta) = \left(1 + \beta\,\frac{2\tau^2-1}{\sqrt{1-\tau^2}}\right)^{-1}, \quad \tau(\eta) = \eta + O(\beta) \qquad (28)$$

Geometrical calculations

When the refractive index of the rod in the proximity of the cylindrical surface does not exactly coincide with the refractive index of the adaptation liquid (matching liquid whose role is to prevent the behaving of the rod as a cylindrical lens), then an additional signal is given, which combines with the signal coming from the refractive index distribution inside the body to give a total intensity distribution, measured in the recording plane. The pure non-adaptation effect may be calculated, for a rod with constant refractive index throughout its volume, by resorting to the refraction formula of a light ray (see the figures 2). In this way, we obtain the formulas

$$\eta(\tau) = [\tau-2f_1(\tau)] - \left\{\frac{L}{R} - \sqrt{1-[\tau-2f_1(\tau)]^2}\right\} \cdot \frac{2\zeta\sqrt{1-\zeta^2}}{1-2\zeta^2}$$

$$f_1(\tau) \equiv \zeta(\tau)\sqrt{1-K^2\tau^2}, \quad \zeta(\tau) \equiv \tau\left[\sqrt{1-K^2\tau^2} - K\sqrt{1-\tau^2}\right], \tag{29}$$

where $K = \frac{n_1}{n_2}$ is the ratio of refractive index in exterior medium to the refractive index in body. Formulas (29) do hold irrespective of the fact that $K > 1$ or $K < 1$ (although the ray path in the two cases is quite different). For $L = R + \varepsilon$ and $|K - 1| \ll 1$ the following relation between η and τ is derived

$$\eta(\tau) \approx \tau\left[1 - (1-K)\frac{L}{R}\frac{2}{\sqrt{1-\tau^2}}\right] \tag{30}$$

leading for f(ζ) to the expected result

$$f(\zeta) = \int_{\zeta}^{1} \frac{\tau-\eta(\tau)}{\sqrt{\tau^2-\zeta^2}}\,d\tau \approx (1-K)\,2\,\frac{L}{R}\int_{\zeta}^{1}\frac{\tau\,d\tau}{\sqrt{(1-\tau^2)(\tau^2-\zeta^2)}} = (1-K)\,\pi\,\frac{L}{R} \tag{31}$$

$$0 < \zeta < 1$$

More sofisticated calculations, undertaken by us, intended to make "analytical" the refractive index jump at the cylindrical surface. In this case, a composition law of intensities - coming from the two possible causes (intrinsic **refractive index** distribution in rod and non-adaptation jump of refractive index) was derived and used in practical applications.

Some analytical simulations

A smoothed out profile of refractive index distribution is given by the function

$$f_{\text{n.-ad.}}(\zeta) = \alpha(1-\zeta^2)^{7/2}\left(1 + \frac{7}{2}\zeta^2 + \frac{63}{8}\zeta^4 + \frac{231}{16}\zeta^6\right) \tag{32}$$

It ensures the fulfilment of the following analyticity conditions $f(1) = 0$, $f'(1) = 0$, $\mathfrak{J}(1) = 1$, $\mathfrak{J}'(1) = 0$. In addition, the respective function exhibits a high order contact at $\zeta = 0$ and has a single inflexion point at $\zeta = \sqrt{7/12} = 0.763765$. In conclusion, f(ζ) in (32) may be a reasonable choice for an "analytized" refractive index jump. It brings a contribution to light intensity distribution which may be assigned to non-perfect refractive index adaptation

$$\left(\frac{1}{I} - 1\right) = -\frac{3003}{16}\,\alpha(1-\tau^2)^2\left(\frac{5}{1024} + \frac{7}{256}\tau^2 + \frac{63}{512}\tau^4 + \frac{231}{256}\tau^6 - \frac{3003}{1024}\tau^8\right), \tag{33}$$

- The small parameter α may be either greater or smaller than zero, according to the fact that the refractive index on the inner cylindrical surface of the body is either greater or smaller than the refractive index of the adaptation liquid (in which the body is immersed). Concerning the intrinsic refractive index distribution of the investigated body, a reasonable function, obeying necessary boundary conditions would be

$$\eta(\tau) = \tau\left\{1 - \beta\sqrt{1-\tau^2}\,(1-\tau^4)^2\right\} \tag{34}$$

It brings a contribution to f(ζ) and $\mathfrak{I}$(η) according to formulas

$$f_{intr.}(\zeta) = 8\beta(1-\zeta^2)(1-\zeta^4)^2\left\{\frac{5}{32} + \frac{5}{128}\,\frac{1-\zeta^2}{1+\zeta^2} + \frac{3}{512}\left(\frac{1-\zeta^2}{1+\zeta^2}\right)^2\right\}$$

$$\left(\frac{1}{I} - 1\right)_{intr.} = \beta\left\{\frac{2\tau^2-1}{\sqrt{1-\tau^2}}(1-\tau^4) + 8\tau^4\sqrt{1-\tau^2}\right\}(1-\tau^4) \tag{35}$$

The small parameter β is a measure of the dopping process intensity, determining the axially symmetric refractive index distribution inside the body. For a good agreement it is necessary to have $\beta \gg |\alpha|$. The two causes of the total light intensity signal and the total refractive index distribution combine to give the total functions

$$f_{total}(\zeta) = f_{n\text{-}ad.}(\zeta') + f_{intr.}(\zeta)$$

$$\left\{\frac{1}{I(\eta)} - 1\right\}_{total} = \left\{\frac{1}{I(\eta)} - 1\right\}_{n\text{-}ad.} + \left\{\frac{1}{I(\eta)} - 1\right\}_{intr.} \tag{36}$$

In the final expression of $\mathfrak{I}(n)_{total}$, which is expressed in terms of τ , we may introduce the approximation $\tau \approx \eta$. Some numerical calculations for $n(0) - n(R - \varepsilon) = 5.03\times10^{-3}$ and $n(R - \varepsilon) - n(R + \varepsilon) = \pm\, 3.18\times10^{-3}$ led to total intensity distributions of recorded light having the expected experimental trend (Figure 3).

Exerimental setup and results

The experimental setup for controlling the refractive index distribution in cylindrical bodies through transversally transmitted light measurements is shown in Figure 1. The collimated light beam passes through the body, which is immersed in the matching liquid. The focusing objective images the observation plane onto the vidicon window inside the TV camera. An image analyzer digitizes and displays on the TV monitor the corresponding image together with the graph of the light intensity along a movable vertical line. The image analyzer is interfaced to a minicomputer, so that the algorithm from eq.(19) can be programmed in a high level language (FORTRAN) and the results displayed on the TTY terminal.

A typical light intensity distribution yielded by a gradient index cylindrical rod with a perfect parabolic index profile in our setup is shown in Figure 4a. Using this intensity distribution as input data for eq. (19), we have obtained the refractive index distribution from figure 4b, which fairly corresponds to the profile obtained by other (interferometric) methods. The dip from the origin is an artefact due to the sigularity in the integral relating refractive index to the intensity.

REFERENCES

/1/ H.M.Presby, D.Marcuse and H.W.Astle, Appl.Opt., 17, 2209 (1978)

/2/ D.Marcuse, Appl.Opt., 18, 9 (1979)

/3/ J.Auge, F.Gauthier et al., Mesure des profiles d'indice de refraction sur fibres et preforms", Rev.Tech. Thomson - C.S.F., Vol. 13, no. 4, 832 (1981)

/4/ J.Glasser, J.Chapelle, J.C.Boettner, Appl.Opt., Vol. 17, nr.23, 3750 (1978)

/5/ N.Ionescu-Pallas, V.Vlad, Şt.Solomon, A method for the control of the refractive index in optical fibers, Progress in Physics, Craiova, Oct. 1983 (communication)

/6/ N.Ionescu-Pallas, V.Vlad, M.Jurbă, Şt.Solomon, V.Căpăţînă, A.Vlad, Recording the refractive index profile in axially symmetric transparent cylindrical bodies, National Colloquium on Optics, Bucharest 1984 and Preprint LOP-48-1984, Central Institute of Physics, Bucharest

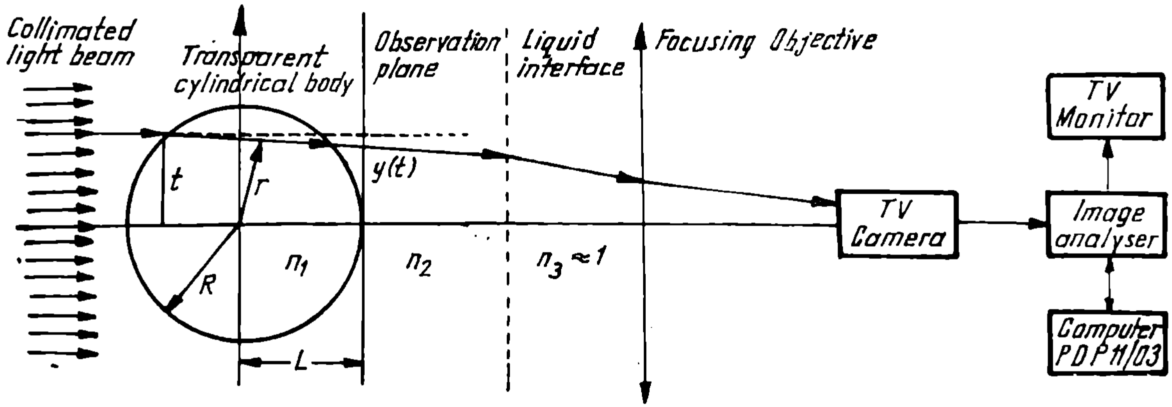
Collimated light beam
Transparent cylindrical body
Observation plane
Liquid interface
Focusing Objective
TV Monitor
TV Camera
Image analyser
Computer PDP 11/03
t
r
R
y(t)
n_1
n_2
$n_3 \approx 1$
L

Fig.1

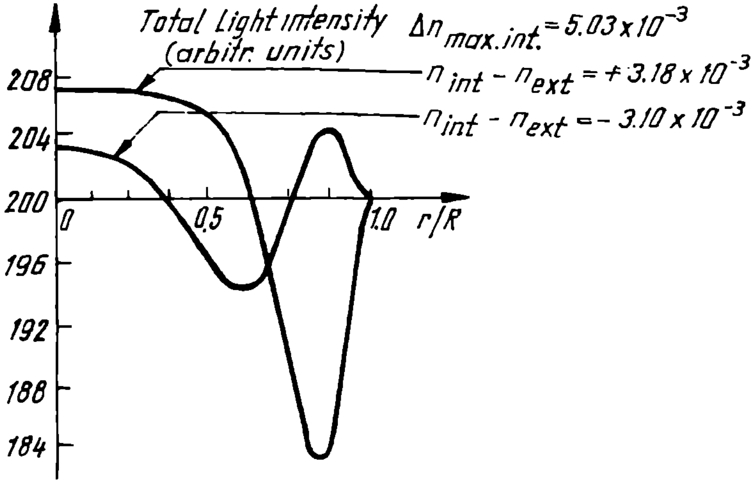
Total Light intensity (arbitr. units)
$\Delta n_{max.int.} = 5.03 \times 10^{-3}$
$n_{int} - n_{ext} = + 3.18 \times 10^{-3}$
$n_{int} - n_{ext} = - 3.10 \times 10^{-3}$
208
204
200
196
192
188
184
0
0.5
1.0
r/R

Fig.3

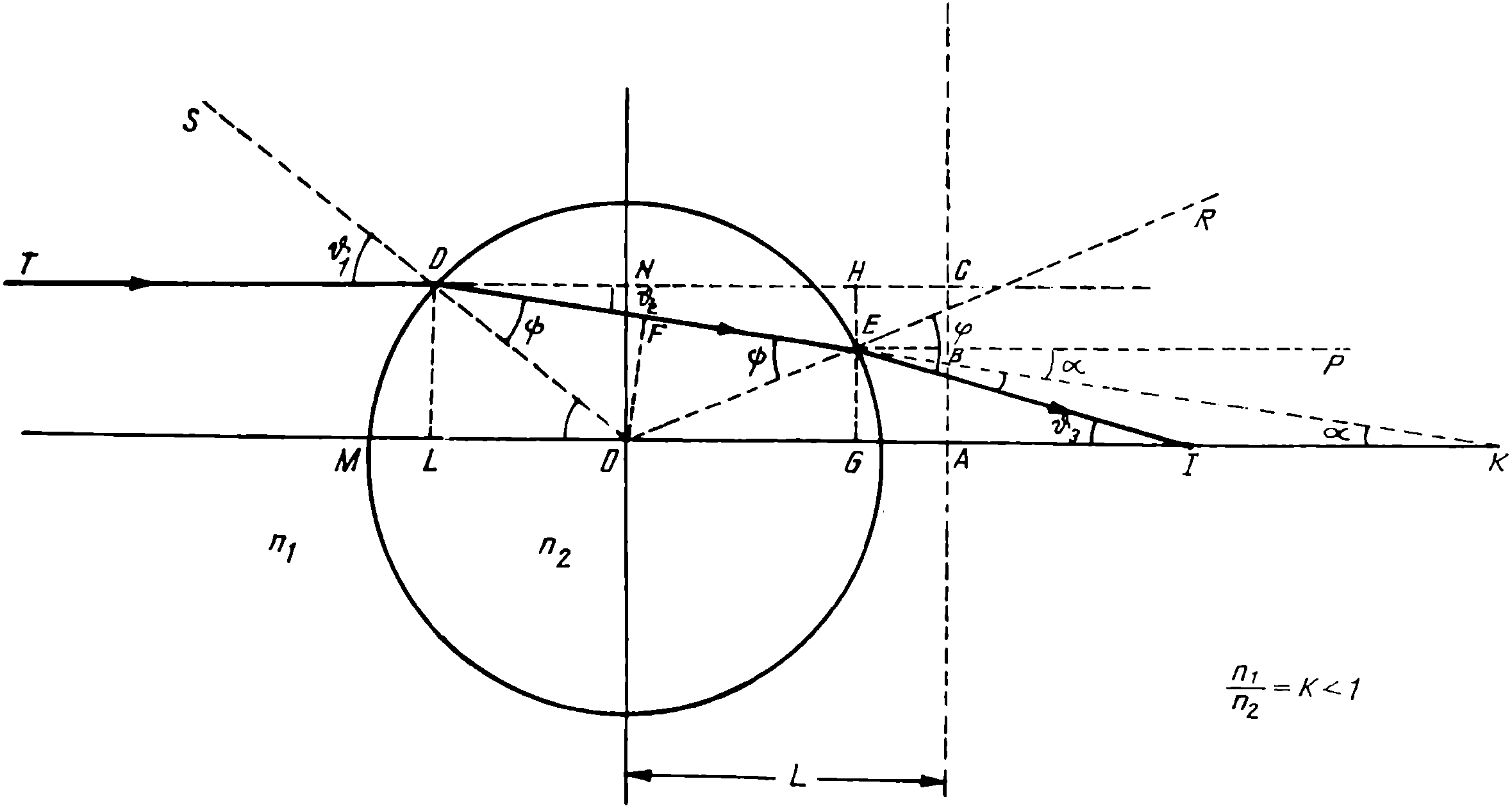
S
ϑ_1
T
D
N
ϑ_2
H
C
R
ϕ
F
ϕ
E
φ
B
α
P
ϑ_3
α
M
L
O
G
A
I
K
n_1
n_2
$\frac{n_1}{n_2} = K < 1$
L

Fig. 2 a

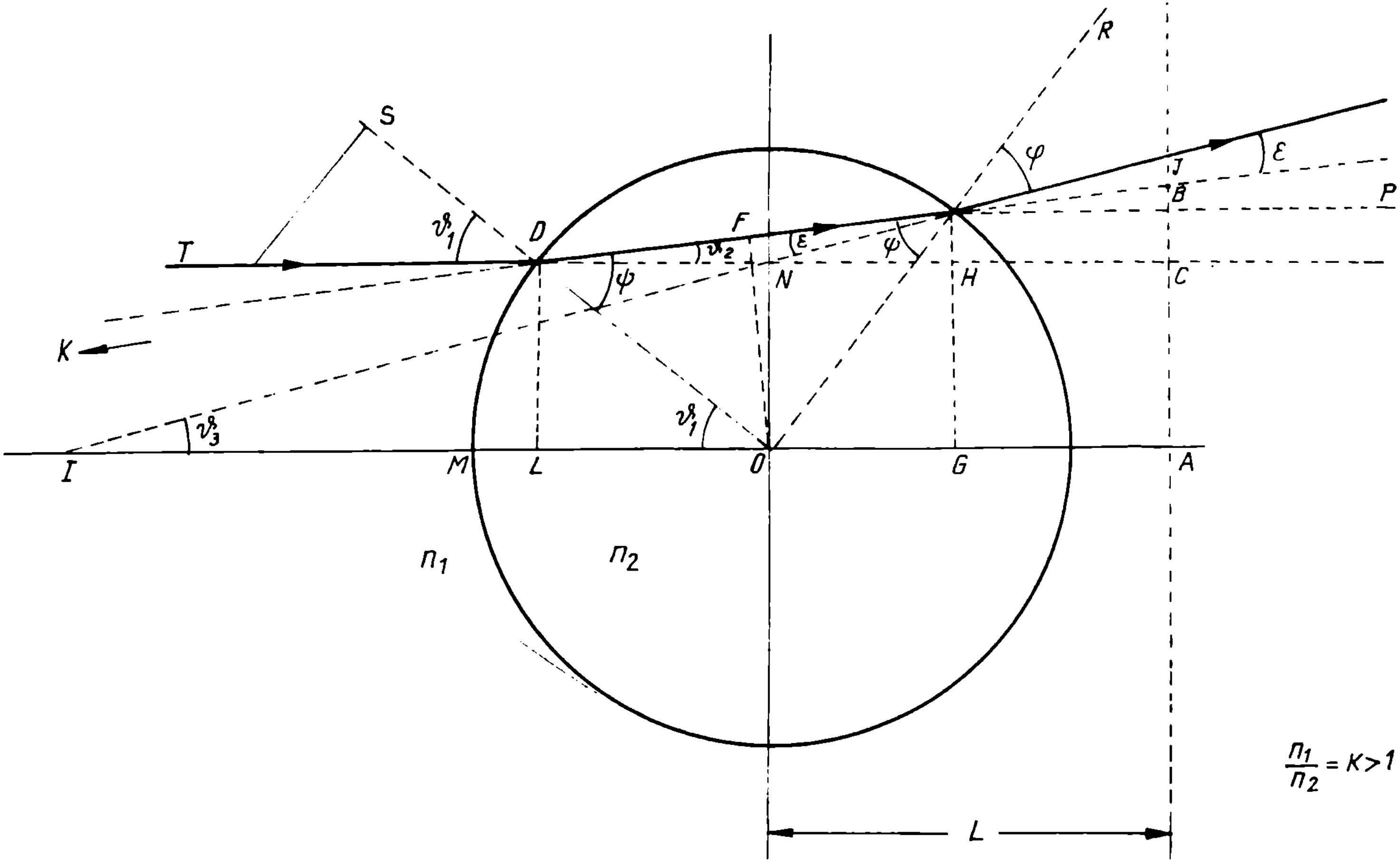
S
R
φ
ε
J
B
P
ϑ_1
D
F
T
ϑ_2
ε
φ
ψ
N
H
C
K
ϑ_1
ϑ_3
I
M
L
O
G
A
n_1
n_2
$\frac{n_1}{n_2} = K > 1$
L

Fig. 2 b

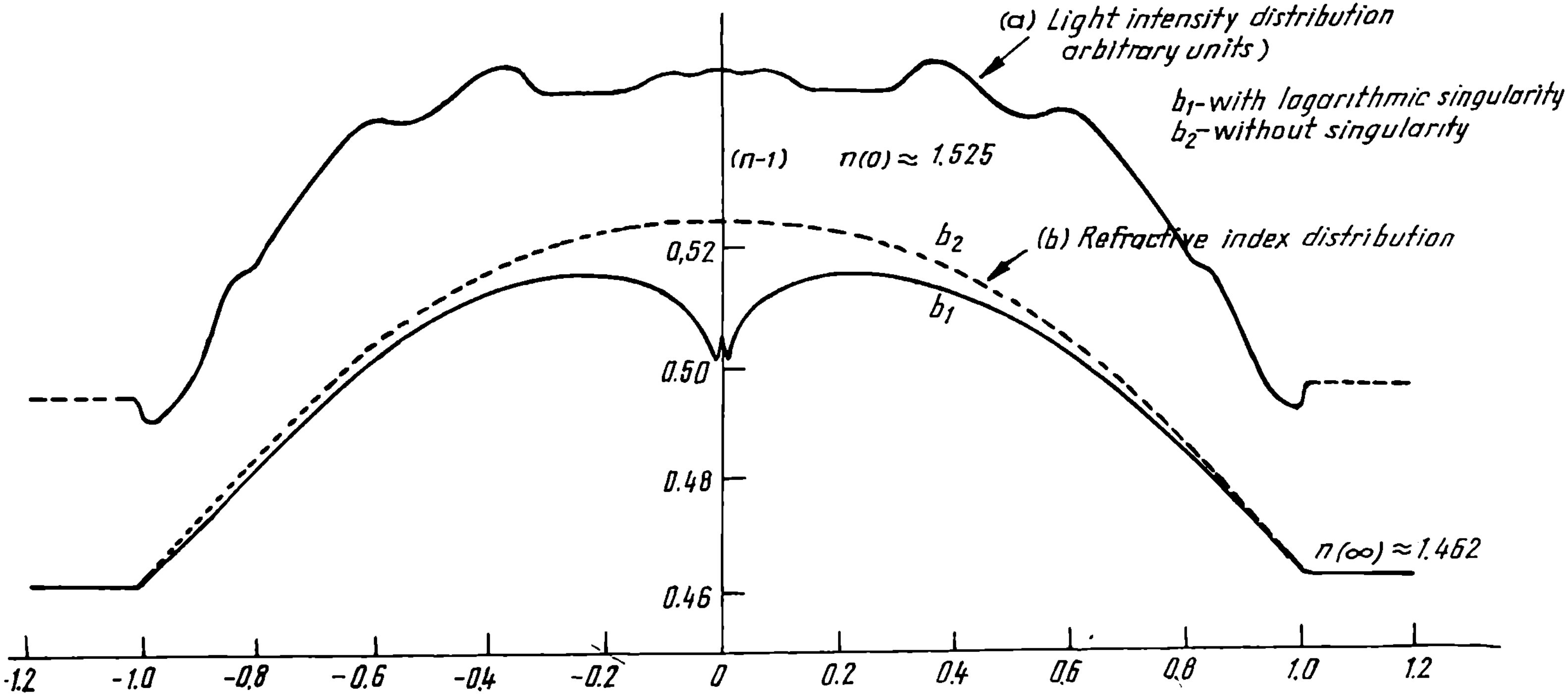
(a) Light intensity distribution
arbitrary units)
b1-with logarithmic singularity
b2-without singularity
(n-1)
n(0) ≈ 1.525
b2
b1
(b) Refractive index distribution
n(∞) ≈ 1.462
0,52
0.50
0.48
0.46
-1.2
-1.0
-0,8
-0.6
-0,4
-0.2
0
0.2
0.4
0,6
0,8
1.0
1.2

Fig.4

NEW APPLICATIONS OF THE He-Ne LASER INTERFEROMETERS

C.Blanaru, G.Popescu, D.Apostol, A.Ionescu, V.Vasiliu, V.Damian
Laser Dept., Central Institute of Physics, P.O.Box MG-6,
Bucharest, Romania

After a short review of the He-Ne laser measuring systems previously developed, the paper presents some new applications of the laser interferometry in the measurements technique. The applications include a Michelson-type He-Ne laser interferometer used to determine the thermal expansion coefficient of a body with variations in temperature; a length measuring interferometer used in a computer based system to metrologically characterize the length etalons; interferometric length measurement in order to determine the gravitational acceleration g; future projects connected to the development of a modular system to measure different geometrical quantities for industrial purposes and the interferometric measurements of very small amplitude vibrations in the sub-angstrom range. The operating principle of each of these applications is described and main technical characteristics are specified.

The laser interferometry has been successfully applied in laboratory and industrial measurements, to measure not only the length and the velocity of the displacement, but also many other geometrical quantities like angle, pitch, yaw, flatness, perpendicularity of the displacement, etc. High repeatability and resolution, high accuracy, long-range optical path, productivity and possibility of the automation of the measuring process are the main advantages of the laser interferometric system.

The use of the laser as a light source in the interferometers was a major step in man's ability to measure geometrical quantities easily and precisely. By coupling optical techniques with digital electronics, the laser interferometer became a highly accurate and versatile measuring system that can cope with industrial environments.

During last years, we developed several He-Ne laser interferometers for measuring different quantities both in laboratory and industrial conditions /1/.

IFLAS-1 /2/ is a He-Ne laser Fizeau interferometer, intended to be used as a checking device for the plane surface of the high quality optical components.

IFLAS-1 (Fig.1) interferometrically compares the wavefront reflected by the reference surface with the wavefront reflected by the surface under test.

The He-Ne laser beam, reflected by the plane mirrors M_1, M_2, is transformed in a plane wave by the collimator realized with a microscope objective (MO) 4oX, a 30 µm microdiaphragm (MD), placed in the focus of the microscope objective as a spatial filter, and a collimating lens (CL), which has the microdiaphragm in its focus.

The reference piece (RP) has the first surface polished at a certain angle to take out the reflection. The second surface is the reference surface, polished better than $\lambda/10$ for the 0.6328 μm wavelength.

The piece under test (TP) is placed on a table which can be manually adjusted to get the alignment.

The interference pattern is observed on a ground glass (G), placed behind a diaphragm (D) and a beam-splitter (BS).

The whole mechanical structure is supported by a vibration attenuator, with three independent isolators.

The IFLAS-1 Laser Fizeau Interferometer tests pieces with a maximum diameter up to 60 mm, with an accuracy better than $\lambda/10$. The maximum distance between the piece under test and the reference is 100 mm.

LINLAS-8 /3/ is a grating interferometer for measuring the straightness of large industrial machine parts. The sensor is a diffraction grating, which touches the surface under test. Any deviations from a straight line of the grating motion, except those parallel to the grating lines, come up as a movement of the fringe pattern in the interferometer.

LINLAS-8 (Fig.2) uses a He-Ne laser as a light source. The beam divergence is corrected by a collimator (C) of magnitude 10 X. The beam passes the beam-splitter (BS) and falls on the Ronchi type diffraction grating (G). The beams in the (+1) and (-1) diffraction orders are reflected back on the grating by the normally placed plane mirrors M_1 and M_2. They are diffracted again and two interfering waves are obtained along the incident beam. The interfering waves are separated from the incident beam by the beam-splitter and directed to two photodetectors (D_1, D_2), spatially placed as to obtain electric signals with a phase difference of $\pi/2$. The displacement of the grating in its plane and normally to its groves generates interference fringes with a period of p/4, where "p" is the pitch of the grating.

In this manner, by moving the grating along a line on the surface to be tested, the straightness can be measured by counting the interference fringes.

The electronic processing system (EPS) detects the fringes and electronically divides the period by 4, so a counting pulse has a weight of p/16, which becomes the resolution of the straightness measurement. The results of the measurement can be displayed or recorded.

Using a 48 μm pitch grating and plane mirrors of 120 mm in length, a resolution of 3 μm has been obtained for straightness measurements up to 8 m in length. The maximum straightness measuring range was ± 1 mm.

LASINTERF M-20 /4/ is a Michelson-type interferometer for measuring the length and velocity of the displacement. In order to perform measurements on long distances with high accuracy, it uses a Lamb-dip frequency stabilized He-Ne laser /5/.

LASINTERF M-20 (Fig. 5) measures the length of the displacement by counting the interference fringes obtained at the optical output of the interferometer when the moving retroreflector moves. The beam-splitter coatings are so that the signals detected by the two photodetectors have a relative phase shift of one quarter of a period, with the sign depending on the moving sense.

A period of the detected signal corresponds to a displacement of $\frac{\lambda}{2} \approx 0.3164$ µm, where λ is the He-Ne laser wavelength in air. This period has been electronically divided by 4, so the incremental resolution in the length measurement is $\frac{\lambda}{2} \approx 0.0791$ µm, which is converted to a metric resolution of 0.1 µm.

The influence of the atmospheric parameters on the laser wavelength is semiautomatically compensated in the range (8.5 - 35)°C for temperature variations and in the limits (674 - 788) torr for pressure variations.

Once the length information is available, it is easy to get the velocity of the displacement of the moving retroreflector by fixing a time base and counting the length pulses recorded in that time unit /6/. In the LASINTERF M-20 system, three time bases are available: 600; 60; 6 ms, generated by a quartz oscillator.

The experimental results obtained in laboratory and industrial measurements concluded that the following specifications are valid:

- * length mode:
    - - linear displacement up to 16 m
    - - resolution: 0.1 µm
    - - accuracy: $\pm 1.10^{-6}$ of the display ± 2 counts in the last digit
    - - velocity of the displacement: max. 12 m/min
- * velocity mode:
    - - measuring range: (1 - 10,000) mm/min
    - - resolution: 1 mm/min
    - - accuracy: $\pm 1.10^{-4}$ of the display ± 1 count in the last digit

LASINTERF T-20 /7/ is a measuring system for the length of the displacement, designed for permanent installation on a machine toll or measuring machine. With a single frequency stabilized He-Ne laser, two axes of motion may be simultaneously monitored. For this purpose, a two-ways remote interferometer, one for every axis, is used. The interferometers are completed with a 50% beam-splitter and additional optics to direct the beams. The electronic system displays the length measured on every axis.

The schematic structure of the system is presented in Fig. 4.

LASINTERF T-20 system measures the length of the displacement by counting the interference fringes obtained at the optical output of the interferometer when the moving retroreflector is displaced. An interference fringe is obtained for a displacement of λ /2 in the measuring arm of the interferometer. The $\frac{\lambda}{2} = 0.3164$ µm units are converted in metric units of 1 µm, and the influence of the atmospheric parameters on the laser wavelength is semiautomatically compensated in the range (8.5 - 35)°C for the temperature and (674 - 788) torr for the pressure.

The experimental results obtained in laboratory and industrial measurements concluded that the following specifications are valid:

- linear displacement up to 12 m on every axis
- resolution : 1 µm
- accuracy : $\pm 1.10^{-6}$ of the display ± 2 counts in last digit
- velocity of the displacement : max. 10 m/min

Based on the experience we have got during the development of these laser interferometers, some new applications became the subject of our interest.

LASINTERF D is a Michelson type He-Ne laser interferometer used to determine the thermal expansion coefficient of a body with variations in temperature. The expansion coefficient is given by the expression:

$$\alpha = \frac{1}{\Delta T} \cdot \frac{\Delta L}{L}$$

For a sample of a certain length L, to find out α means to measure the change in length L (expansion or contraction) with a variation ΔT in temperature.

Generally, the dilatometers are based on the same principle: the length change is mechanically sensed and converted to an electrical signal which is then amplified. The various dilatometers differ only in their technical data such as amplifier characteristics, stability, mechanical mounting, etc. They all are subject to an error, the expansion of the transducer system, which is difficult to calculate and becomes important in very accurate measurements. The laser dilatometers do not suffer from this limitation and represents a fundamental advance in dilatometry:

- the laser dilatometer readily determines the absolute expansion coefficient;

- the absolute accuracy is given by the laser wavelength stability, which is in the range of 10^{-6} for a frequency unstabilized laser;

- the length measurement accuracy could be 0.1 µm or even smaller.

LASINTERF-D is primarly intended to be used to determine the thermal expansion coefficient of different sorts of coal. According to the schematic diagram presented in Fig. 5, the test piece P is placed in a quartz tube, closed at one end. A plunger T, made from the same material as the tube, transmits the length changes of the test piece to the transducer, which is the moving cube corner prism PM from the measuring arm of the interferometer. By the action of a spring, the moving prism assembly pushes, through the plunger, the test piece with a certain force. The displacement of the moving prism is effectively frictionless guided and represents the expansion or contraction of the test piece with the temperature variations.

The moving prism, plunger and test piece are placed in a controlled atmosphere , realized by the vacuum pump PVP and a suitable inert gas, supplied by the reservoire RG.

The light source in the interferometer is a He-Ne laser model LG-5, with an output power of 3 mW. The beam divergence is corrected by the collimator L. The beam-splitter DFS is specially coated as to generate phase quadrature interferometer outputs, detected by two detector units CD. The electronic processing system BENA counts the interference fringes, converts the $\frac{\lambda}{8}$ pulses to metric units of 0.1 µm and displays the result.

The measuring range of the LASINTERF-D system is ± 10 mm at a resolution of 0.1 µm. The test piece length is about 10 mm, the thermal expansion coefficient is in the range (10^{-2} - 10^{-3}) grd^{-1}, the maximum temperature in the oven is 800°C, and the accuracy of the length measurement is ± 2.10^{-6} of the display ± 1 count in the last digit.

In order to easily plot the length-temperature diagram, BENA includes a time base, which synchronously commands the length and temperature readouts in decadic steps of 0.1; 1; 10 s resolution.

A particular application of the length measuring He-Ne laser interferometer is to metrologically characterize the length etalons.

The laser interferometer is a part of an elaborate system, which includes a microscope to read the markers on the length etalon and an electronic processing unit, which receives the length information from the laser interferometer when the microscope "reads" a marker and computes the data to completely characterize the etalon from a metrological point of view.

In order to reduce the errors to a minimum, the fixed part of the interferometer (see Fig. 6) is placed away from the heat source represented by the laser tube itself. The fixed cube corner prism from the reference arm of the interferometer is approximately placed at he halfway of the displacement interval of the moving prism. The moving prism is placed on the same carriage as the microscope objective which reads the markers on the length etalon.

The optical components are placed in a temperature controlled room, while all the electronics and controls are taken out, so there is no need for a human presence in the measuring room.

The optical scheme and the electronic system of the interferometer is basically the same as for LASINTERF M-20. The length information is transfered at the output to be processed by the main electronic unit when the microscope orders it.

The stringent demands of this particular application put to the laser interferometer are those of the noise immunity and high reliability in the operation.

Another application of the He-Ne laser interferometer is to measure the length of the displacement in order to determine the gravitational acceleration g. According to the operation principle, the moving cube corner prism PCCM (Fig. 7) in the measuring arm of the interferometer is thrown up by a mechanical arm. After reaching the maximum height point of the trajectory, where the speed equals zero, the prism begins to descend. During the descending trajectory, the fringes obtained at the optical output of the interferometer are detected and counted. The electronic processing unit determines the time moments when the moving prism reaches each of a great number of points placed at equal distances along the trajectory. These "equal distances" are determined by counting the same number of interference fringes detected at the optical output of the interferometer.

The electronic unit measures the time intervals with a resolution of 1 ns and statistically processes the data in order to determine the value of g in a certain point and the gradient of g along the trajectory.

The light source in the interferometer is a Lamb-dip frequency stabilized He-Ne laser LSF. The fixed cube corner prism PCCR in the reference arm of the interferometer is supported by a long period attenuator, while the whole interferometer structure is mechanically stabilized by a piezo-electric system.

The particular requirement of the interferometer in this application are connected to the maximum working frequency of the detecting,amplifying and signal conditioning circuits. For an useful measuring range of 1.5 m, a maximum working frequency of about 18 MHz is generated by the interference fringes of $\frac{\lambda}{2}$ period.

So far we presented some of the laser interferometry applications in the field of laboratory and industrial measurements. Of course, there are many other possible demands for measurements by the laser interferometry. Our future projects are connected to the development of a modular system to measure different geometrical quantities for industrial purposes. Using two types of He-Ne lasers (one frequency stabilized and the other one free running) and a certain number of opto-mechanical and electronic modules, the system will be able to perform such measurements as length and velocity of long range displacements, differential displacements, straightness, flatness, squareness, angular and non-contacting measurements.

The interferometric measurements of small mechanical displacements induced by some means will be further improved /8/. The limit of sub-angstrom measurements is no longer a limit in our experimental set-ups.

Our final aim is to develop a new interferometer using a He-Ne laser suited for the physics of the gravitational radiation. Two different ways we suppose to take on the way of reaching our goal (10^{-14} m as sensitivity of measurement): by using very stable resonators /9/ and then modulating their selective characteristics, and by using very long arm interferometers of some sorts /10/ (folded-path interferometers).

REFERENCES

/1/ C.Blanaru, "Interferometric applications of the He-Ne lasers", Proceedings of the International Conference and School, LAICS 1982, Bucharest, Part 1, 221

/2/ "IFLAS-1: Laser Fizeau Interferometer", Technical Manual, Central Institute of Physics, Bucharest (1979)

/3/ D.Apostol, P.Bachmann, C.Blanaru, St.Cazacu, V.Damian, A.Ionescu, V.Vasiliu, Stud.Cerc.Fiz., 33, 2, 203 (1981)

/4/ V.Vasiliu, C.Blanaru, "Laser interferometry for industrial applications", Prep. ICEFIZ, LOP-25-82 (Feb. 1982)

/5/ C.Blanaru, Gh.Popescu, A.Chetroiu, D.Apostol, A.Ionescu, Rev.Roum.Phys., 27, 2, 167 (1982)

/6/ C.Blanaru, A.Niculescu, Bul.Inf. CSEN, XI, 10-12, 10 (1975)

/7/ A.Brunfeld, C.Blanaru, Gh.Popescu, Constr. Mas., 31, 7, 391 (1979)

/8/ Gh.Popescu, D.Appstol, C.Blanaru, A.Ionescu, V.Damian, Stud.Cerc.Fiz., 36, 2, 125 (1984)

/9/ Gh.Popescu, to be published in Rev.Roum.Phys. (1985)

/10/ Gh.Popescu, D.Apostol, V.Damian, to be published in Rev.Roum.Phys. (1985)

FIGURE CAPTIONS

Fig. 1 IFLAS-1: Schematic diagram. M_1, M_2 - plane mirrors; MO - microscope objective; MD - microdiaphragm; BS - beam splitter; CL - collimating lens; RP - reference piece; TP - piece under test; D - diaphragm; G - ground glass

Fig. 2 LINLAS-8 : Schematic diagram. LG-5 - He-Ne laser; C - collimator; BS - beam splitter; G - diffraction grating; M_1, M_2 - plane mirrors; D_1, D_2 - photodetectors; L.- expanding lens; EPS - electronic processing system

Fig. 3 LASINTERF M-20 : Schematic diagram. M-20 L - laser and interferometer head; M-20 R -moving retroreflector; M-20 E - electronic unit; 1 - photodetector; 2 - piezoelectric transducer; 3 - laser mirror; 4 - laser tube; 5 - collimator; 6 - photodetector; 7 - beam splitter; 8 - fixed cube corner; 9 - moving cube corner

Fig. 4 LASINTERF T-20 : Schematic diagram. A - laser head; B - collimator; C - X axis interferometer head; D-X axis moving retroreflector; E - Y axis interferometer head; F - Y axis moving retroreflector; G - beam splitter; H - electronic unit; 1 - beam splitter; 2 -fixed cube corner; 3 - moving cube corner; 4 - detecting circuit

Fig. 5 LASINTERF D : Schematic diagram. BID - interferometer/detection block; LG-5 - He-Ne laser; L - collimator; DFS - beam splitter; CD - detector; PF - fixed prism; BTD - displacement transducer block; F - window; R - spring; G - bearing; PM - moving prism; P - sample; T - plunger; C - furnace; RG - gas supply; PVP - forevacuum pump; BENA - electronic block; SIT - laser power supply

Fig. 6 Schematic diagram of the interferometric measuring set-up. LSF - He-Ne frequency stabilized laser; C - collimator; DF - beam splitter; OP - plane mirror; PCCM - moving cube corner prism; PCCR - reference cube corner prism; D_1, D_2 - photodetectors

Fig. 7 Schematic diagram of the optical arrangement. LSF - He-Ne frequency stabilized laser; C - collimator; DF - beam splitter; PCCM - moving cube corner prism; PCCR -reference cube corner prism; D_1, D_2 - photodetectors

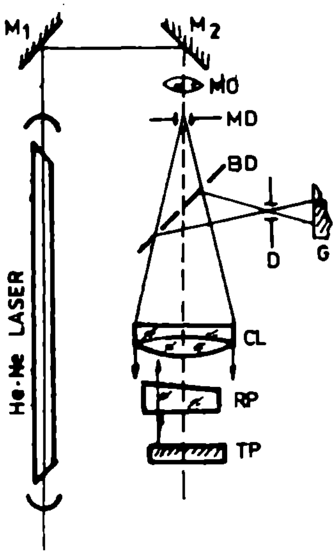

Fig. 1

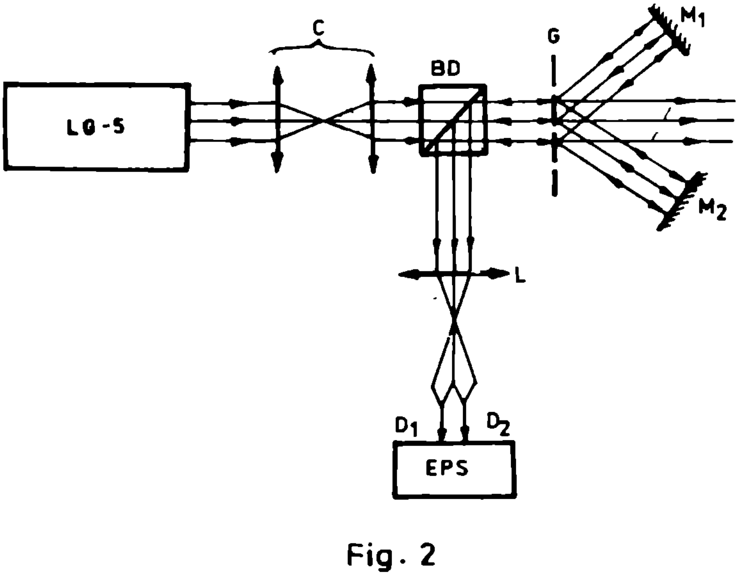

Fig. 2

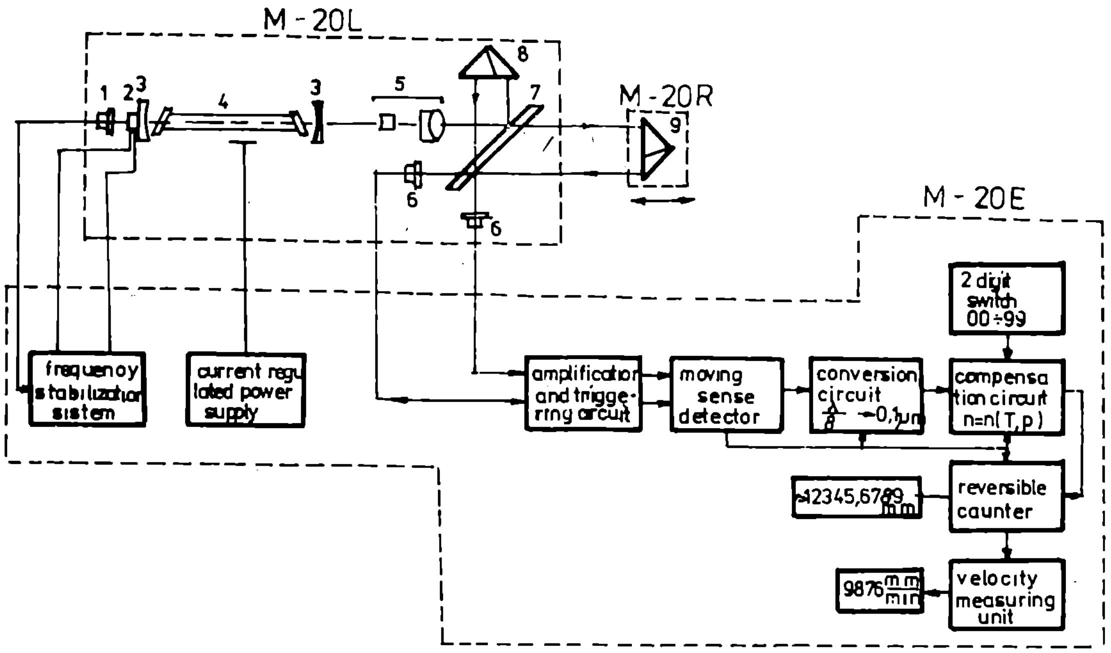
M - 20L
1
2
3
4
3
5
8
7
6
6
M - 20R
9
M - 20E
frequenoy stabilization sistem
current regu lated power supply
amplification and trigge-ring arcuit
moving sense detector
conversion circuit $\frac{\lambda}{8} \to 0,1\mu m$
2 digit switch 00÷99
compensa tion circuit n=n(T,p)
reversible caunter
≈12345,6789 mm
velocity measuring unit
9876 mm/min

Fig. 3

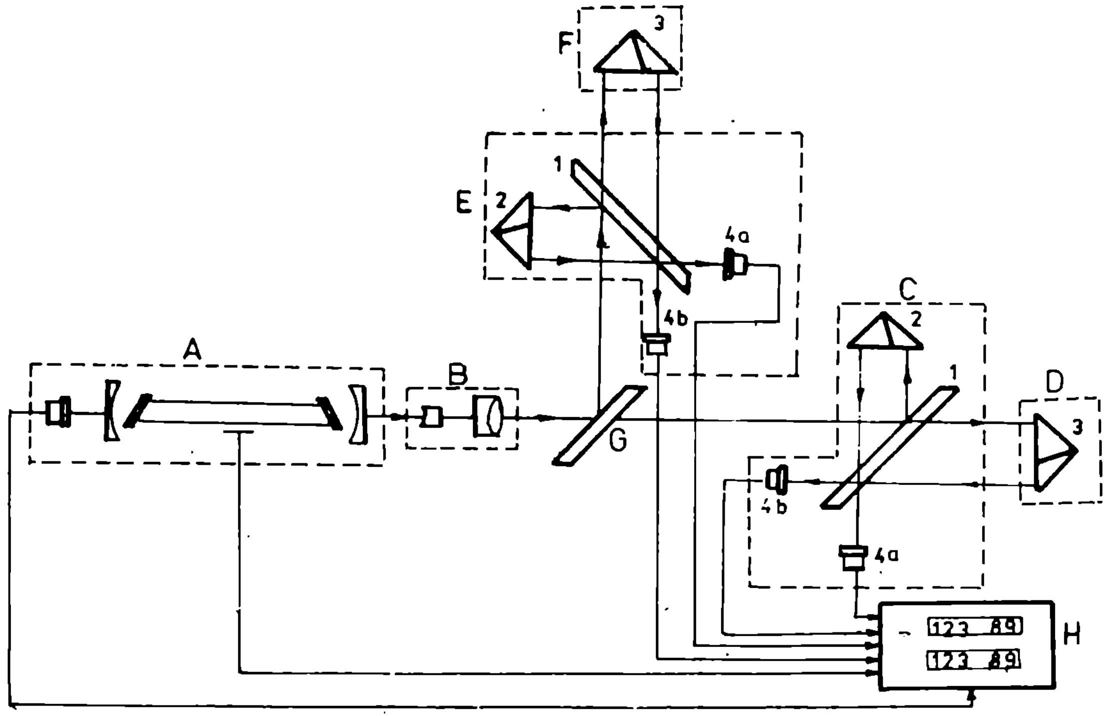

Fig. 4

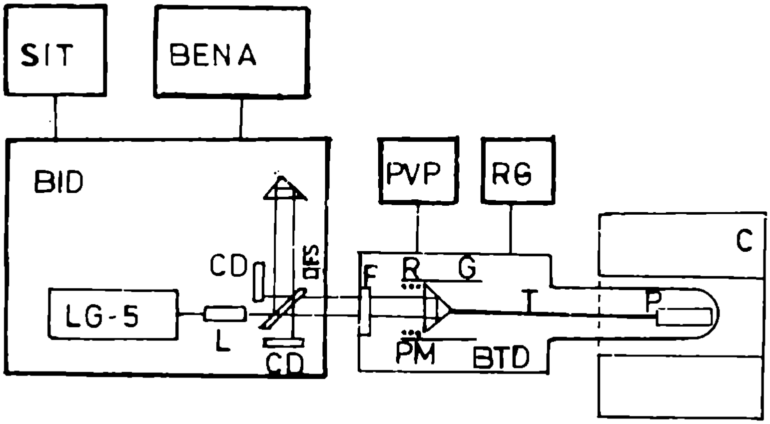

Fig. 5

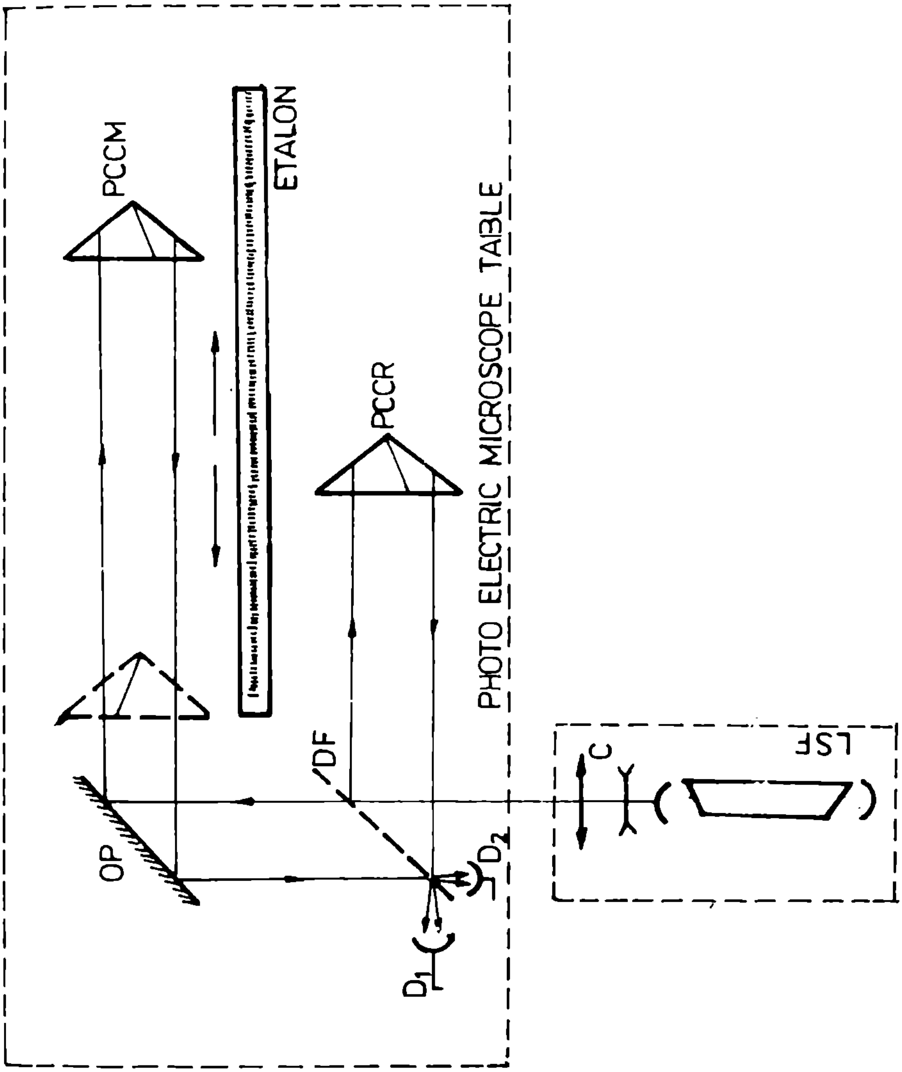
PCCM
ETALON
PCCR
PHOTO ELECTRIC MICROSCOPE TABLE
DF
OP
D2
D1
C
LSF

Fig. 6

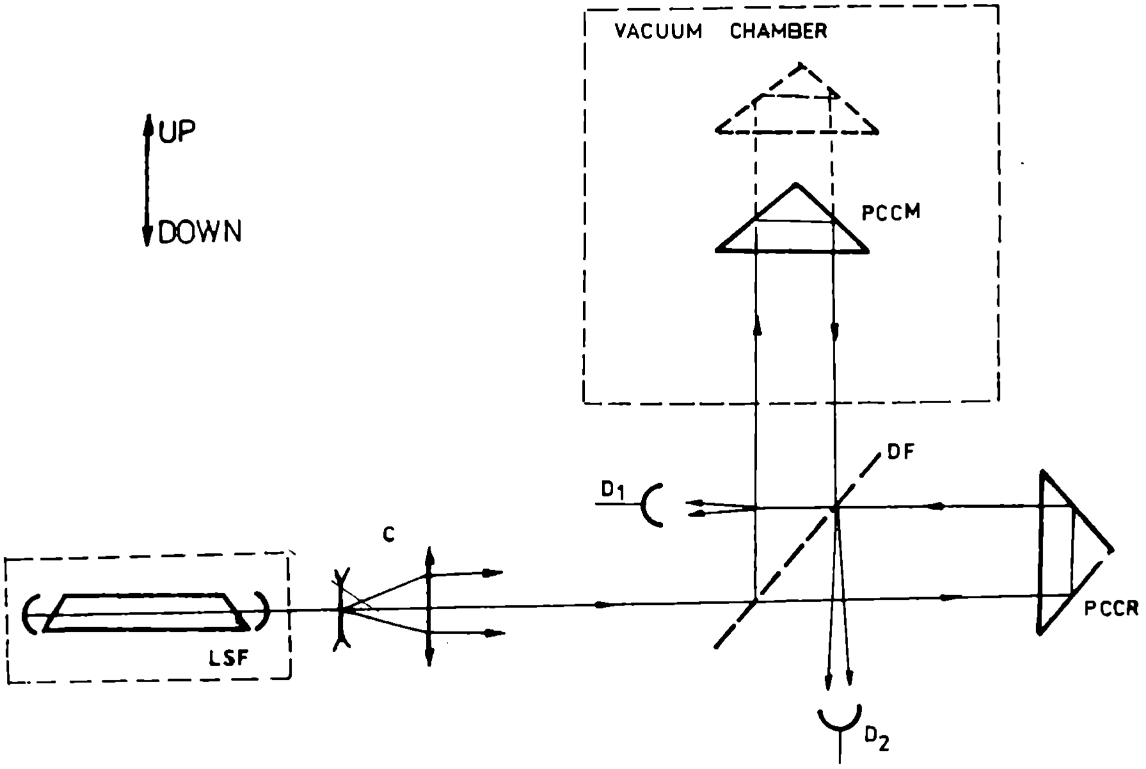

Fig. 7

CONJUGATE WAVEFRONT GENERATION IN SOME SEMICONDUCTOR MATERIALS AT THE WAVELENGTH 1.06 µm

V.I.Vlad, R.V.Dabu,
Central Institute of Physics, Bucharest, ROMANIA
G.V.Ostrovskaya, Y.V.Kovalchuk, E.L.Partnoy, O.V.Smolsky, I.A.Sokolov
Physics-Technical Institute, Leningrad, URSS

Conjugate wavefront generation (CWG) in GaP monocrystals using picosecond light pulses at the wavelength 1.06 µm, situated in the transparent range of the material, is demonstrated. The read-out beam was obtained from the black cleaved surface of the monocrystal as well as from an external mirror in DFWM configuration. We found the threshold of CWG at ~ 1 J/cm^2. The increase of signal energy with the laser energy is limited by the damage of the surface of the semiconductor material, at 2-3 J/cm^2. The recording mechanism is supposed to be thermal modulation of the refractive index. Furthermore CWG in a-Si on GaP monocrystals, at the same wavelength, is studied. The threshold of CWG was obtained at 0.1 J/cm^2, set by the detection noise. The range of CWG was up limited by the recording of stationary holograms, at 0.4 - 0.5 J/cm^2, due to the local polycrystallization of the amorphous material in solid phase. Thus, CWG can be used for the characterization of the early stages of crystallization of the amorphous layers.

Introduction

Since the first experiments of obtaining conjugate wavefront generation (CWG, dynamic hologram) in semiconductor materials carried out in silicon by Woerdman & Bolger (1),(2), a lot of work was done in this field. We mention the studies of Jarasiunas & Vaitkus(3) and Jain et al(4),(5) on silicon, Wiggings et al(6), Kennedy et al(7), Shank & Auston(8), Vaitkus et al(9), Linde et al(10), Hopf et al(11), Smirl et al(12), Moss et al(13) on germanium, and Hoffman et al(14), Jarasiunas et al(15) on GaAs and InP. Recent review papers by A.Miller et al(16) and Jain and Klein(17) give more information about this field.

Dynamic holography is powerful tool for the study of various short relaxation and diffusion processes by observing either the self-diffraction of the creating beams or the diffraction of a third, delayed (probing) beam. The use of short laser pulses for recording and read-out of dynamic holograms allows often the limitation of material heating and the reacording in principal by the spatial modulation of the refraction index. The application of such studies are found in real-time storage and processing of optical data, diagnostics of fast phenomena (in particular in semiconductor materials), construction of distributed feedback lasers, and integrated non-linear optics.

In this paper, is reported CWG in gallium phosphide (GaP) monocrystals using monocrystals using picosecond light pulses selected from a mode-locked Nd:YAG laser (λ =1.06 µm)(18). We have investigated GaP monocrystals due to their large bandgap (E_g = 2.24 eV) associated with interesting electro-optical properties and optical properties different from well-studied GaAs and InP. At λ = 1.06 µm, the refractive index in GaP is 3, so that the reflection coefficient at the cleaved surfaces is 0.25. The read-out beam was obtained from the back cleaved surface of the monocrystal (at ~ 3.5 mm from the front surface) as well as from an external mirror in the degenerate four-wave mixing (DFWM) configuration. We found the threshold of recording dynamic holograms in GaP is $E_{L\ th} \sim 1$ J/cm^2 for both orientations <111> and <100>, and for controlled quantities of impurities (n and p types). The increase of signal energy with the laser energy was limited to $E_{L\ max}$ = 2-3 J/cm^2 by the thermal damage of the surface of the semiconductor material.

Furthermore, we have studied CWG in amorphous layers of Si deposited on GaP monocrystals(19). The dynamic holograms were produced with light pulses from a Q-switched Nd: glass laser (oscillator and amplifier, τ ~ 20 nsec). For read-out, a pulse reflected by the last (free) cleaved surface of GaP substrate (~ 17% from the pump pulse energy) was used. The threshold of CWG in a-Si is $E_{L\ th} \sim 0.1$ J/cm^2 (limited by the photodetection noise). The energy density of S* beam increases with the increase of the energy density of the laser beam and is up limited by the recording of a stationary hologram due to the local polycrystallization of a-Si layer (in solid phase) at $E_{LS} \sim$ 0,5 J/cm^2. Thus, CWG can be used for the characterization (diagnostics) of the stages of crystallization of amorphous semiconductors.

Picosecond CWG in GaP at 1.06 µm. Experimental setup and results

The experimental setup used for the study of picosecond CWG in GaP monocrystals is shown in Fig.1. The passively mode-locked Nd:YAG laser oscillator was operated in a single transverse Gaussian mode. A single pulse (~60 psec) was switched off from the train of pulses produced by the laser and amplified in two stages. The energy of the laser pulse is measured through the beam-splitter (BS1), frequency doubler ($LiNbO_3$, FX2), green filter (GF), and large aperture photodiode (PD1) connected to an energy-motor (EM).

The laser beam was divided by the beam-splitter BS2 to form the pump (P) and signal (S) beams. These beams, after path equalization (by the combination of prisms PR1 and PR2), are superimposed on the GaP sample. The conjugated signal (S*) beam obtained by the read-out of the dynamic hologram is measured, after the reflection on the beam-splitter BS3, by the fast photodiode PD2 which is connected to a storage oscilloscope (OSC). For read-out, we have used the reflected P beam on the back cleaved surface of the monocrystal, which was perpendicular on the P beam and ~ 3.5 mm thick (near optimum for the pulse duration and material absorption). Due to the small width of the GaP sample (~ 0.3 mm), a cylindrical lens, L (focal length 1 m), is introduced in the laser beam. Alternatively, for the read-out, we have used a probing beam obtained from an external mirror M2 and aligned so that to be counterpropagating with P beam. In this alternative, the GaP sample was slightly misaligned from the former position.

The angle between S and P beams is $\theta = 30°$, yielding a dynamic hologram with the spatial carrier frequency $u_0 \sim \sin \alpha / \lambda = 1/2 = n/2 \lambda_0 \sim 1500$ mm^{-1}, i.e. the fringe period $\Lambda \sim 0.67$ µm. Thus, the fringe period exceeds the thermal and carrier diffusion lengths corresponding to laser pulse length and energy.

In the experiments with read-out beam yielded by the reflection of P beam on the back cleaved surface of GaP monocrystal, we obtained a conjugate signal beam (at PD2) only for the orientation <111> and normal polarization of the laser beam. The result from Fig.2 show a threshold for recording dynamic holograms in GaP situated at $E_{L\,th} \sim 1$ J/cm^2. The intensity of S* beam grows up non-linearly with the increase of the energy of the laser beam. Thermal damages of the surface of semiconductor material appeared at $E_{L\,max}$ = 2-3 J/cm^2 limiting seriously the dynamic range of this recording material to (2-3) $E_{L\,th}$. For proving the generation of the dynamic holograms inside th sample and elimination of any other parasitic effects, we frosted the back cleaved surface. No S* bam was recorded in this situation.

For investigation of the time evolution of the dynamic holograms, we have used a probing beam so aligned as to be identical with P*. In this alternative, the reflection from the back surface of the monocrystal was eliminated by a slight tilting of the sample. The mirror M2 was moved to delay the probing (read-out) pulse and to obtain a separation of the ultra-fast (electro-optical) and fast (thermal, electronic) effects. The experiments were carried out for the two orientations of the monocrystal <111> and <100> and for controlled quantities of n and p-types of impurities ($\sim 10^{17}$ cm^{-3}) as one can see from Fig.3.These results show that: (a) the threshold energy, $E_{L\,th}$, was the same for all situations; (b) $E_{L\,th}$ was not changed for the delays of the read-out beam in the range of τ = 0-160 psec; (c) the thermal damage of the material appeared at about the same level of the laser energy and limited the dynamic range of the recording material.

These experimental data lead us to assert that our dynamic holograms were produced by thermal effects with lifetimes longer than 160 psec in GaP monocrystals. The thermal effects mask any other non-linear effects which can contribute to the recording of the dynamic holograms.

Actually, one can estimate that ultra-fast non-resonant processes like those yielded by unharmonic motion of bounded electrons and nonlinear motion of free-carriers(17) are eliminated by the experimental results from Fig.3a, b. The fast (nanosecond) resonant processes produced by real transitions were not allowed by the large band gap of GaP, the excitation wavelength, and the other experimental condition (ambient temperature, different types of impurities lead to approximately same results). Thus, an attempt to explain CWG in GaP by thermal modulation of the refractive index(17),(20),(21) seems to be justified by all experimental facts (a,b,c). Above a certain threshold laser energy, free carriers created by ionization of localized surface impurities can acquire enough energy to create additional carriers by impact ionization. The results is avalanche multiplication of free carriers, abrupt growth of the absorption coefficient, and occurence of phenomenon of optical breakdown(22) which leads to the damage of the semiconductor surface and CWG range limitation.

CWG in aSi on GaP at 1.06 μm.

Experimental setup and results

The experimental setup for CWG in a-Si on GaP is shown in Fig. 4. The dynamic holograms were produced with light pulses ($E \rightarrow 1\ J/cm^2, \tau \sim 20$ ns) from Q-switched (QS):Nd glass (Laser OSC and AMPL) operated in single transverse gaussian mode. The laser beam passes through the variable attenuator (VA) and then is splitted by BS_2 to the energy monitor with the calibrated photodiode PD1 connected to a storage oscilloscope (OSC) and to the standard DFWM configuration for CWG (BS3, M9, M10, BS4) including the recording material (a-Si on GaP). The angle between the signal (S) and pump (P) beams was 5°-6°, yielding the spatial carrier frequency of the dynamic hologram

$$u_0 \sim \sin \alpha/\lambda \sim 1/10\lambda \sim n/10\lambda_0 = 370\ \mathrm{mm}^{-1},$$

i.e. the fringe period was $d_1 \sim 2.65$ μm. This period exceeds the thermal and carrier diffusion lengths, so that the dynamic holograms can build up in this configuration ($l_{th} \sim 1.2$ μm; $l_{h.c} = 0.2$ μm).

The recording (non-linear) material was a thin amorphous layer of Si (thickness 0.7 - 0.8 μm) deposited on GaP monocrystal (0.3 mm thick, orientation <100>). The surface of the recording materials is perpendicular on the P beam, so that its counterpropagating reflection from a certain interface parallel with the first surface (P^* beam) can be used for the read-out of the dynamic hologram. The absorption coefficients in crystalline (c) and amorphous (a) silicon are quite different at the probing wavelength ($\lambda = 1.06$ μm, $E_\lambda = 1.16$ ev), as can be seen from the next table.

Recording material	Absorption coefficient $\alpha(cm^{-1})$	Attenuation length α^{-1} (μm)	Refraction index, n
c-Si	4	$2.5 \cdot 10^3$	3.56
a-Si	$0.4 \cdot 10^4$	2.5	~4

Taking into account the reflection coefficients at the interfaces a-Si/GaP, $\rho_{12} \sim 0.02$, and GaP/Air, $\rho_{23} \sim 0.25$, and the reasonable absorption in aSi and GaP, one realizes that the read-out beam, P^*, can be obtained by the reflection of P beam on the last interface.

In our setup, the conjugated signal (S^*) beam obtained by the read-out of the dynamic hologram is measured, after the reflection on the beam-splitter BS4, by the calibrated photodiode PD2 which is connected to the dual channel storage oscilloscope (OSC).

The entire experimental setup was aligned with a He-Ne laser using additional mirrors (M5-8, BS1) and diaphragms (D2, D3).

Using the Q-switched Nd:glass laser, we selected from the beam a circular area with

2 mm diameter showing almost constant intensity. The threshold of CWG has appeared at $E_{L\ th} \sim 0.1\ J/cm^2$ and the energy density of S^* beam increases with the increase of the energy density of the laser beam as in Fig. 5. In the same diagram from Fig. 5 there are the values of the noise level measured in the absence of S^* beam at the corresponding values of the laser energy density. The noise could set the threshold CWG in our experiments. The increase of conjugated signals, S^*, was limited by the recording of a stationary (permanent) grating at E_{LS} = 0.4-0.5 J/cm^2. We have to remark that the threshold of CWG varied for different samples of recording material by a factor of 4-5, the range of CWG remaining almost constant. At this wavelength, the high absorption in the whole layer of a-Si yields the increase of temperature and the decrease of the band gap energy which increase again the degree of coupling of the laser beam to the amorphous layer. Moreover, the temperature dependent band narrowing provides barriers to spreading out the original electronic excitation(23),(24), so that CWG is the result of a transient thermal grating. The stationary grating appeared at the polycrystallization energy level observed in other experiments(25),(26). This crystallization stage occurred in solid state and probably did not reach the entire amorphous layer due to the low energy density involved in the recording of the stationary hologram.

These experiments have shown the usefulness of CWG methods in the characterization of some early stages of crystallization of amorphous layers. Moreover, we are working to extend the use of CWG in the characterization of crystallite and the phase transition to single crystal.

Conclusions

Picosecond CWG was obtained in GaP monocrystals with <111> and <100> orientations and controlled p- and n-type of impurities, at the wavelength 1.06 μm. The energy threshold for dynamic hologram recording was $E_{L\ th} \sim 1\ J/cm^2$ and the recording range was limited to (2-3) $E_{L\ th}$ by the surface damage of the semiconductor due to a phenomenon of optical breakdown. Infrared CWG in GaP are obtained by thermal effects (modulation the refractive index) which mask all other non-linear effects.

Furthermore, CWG in a-Si on GaP monocrystals was studied. The dynamic holograms were obtained at $\sim 0.1\ J/cm^2$ by thermal induced changes in the refractive index. The range of CWG was limited by the recording of stationary holograms by the local polycrystallization of the amorphous material. This transition occurs in solid phase at the energy density of $E_{LS} \sim 0.5\ J/cm^2$, consistent with the results of crystallization of a-Si with Q-switched lasers, at this wavelength, obtained with other methods. Therefore, CWG can be used for the characterization of the early stages of crystallization of amorphous materials.

Fig. 1 - The experimental setup for picosecond CWG in GaP monocrystals at 1.06 μm

Fig. 2 - Conjugated signal (S^*) intensity vs. the laser energy density for GaP <111> and normal polarization of laser beam. The read-out beam is obtained by reflection of P beam on the back cleaved surface of GaP monocrystal

Fig. 3 - Conjugated signal intensity vs. the laser energy density for doped GaP: (a) <111> orientation, n-doped ($\sim 10^{17}$ cm^{-3}), read-out beam obtained by reflection on the mirror M2 with different delays (0-160 psec); (b) <100> orientation, n- and p-doped samples ($\sim 10^{17}$ cm^{-3})

Fig. 4 - The experimental setup for CWG in a-Si on GaP, at 1.06 μm

Fig. 5 - The energy density of conjugated signal, S^*, vs. the laser energy density in a-Si on GaP <100>

REFERENCES

1. Woerdman J.P. and Bolger B., Phys.Lett. A, 30, 164 (1969)
2. Woerdman J.P., Optics Commun. 2, 212 (1970)
3. Jarasiunas K. and Vaitkus J., Phys.Stat.Sol., 44, 793 (1977)
4. Jain R.K. and Klein M.B., Appl.Phys.Lett., 35, 454 (1979)
5. Jain R.K., Klein M.B., and Lind R.C., Optics Lett., 4, 328 (1979)
6. Wiggins T.A., Bellay J.A. and Carrieri A.H., Appl.Optics, 17, 526 (1978); 18, 1921 (1979)
7. Kennedy C.J., Matter J.C., Smirl A.L., Weiche H., Hopf F.A., Pappu S.V. and Scully M.O., Phys.Rev.Lett., 32, 419 (1974)
8. Shank C.V. and Auston D.H., Phys.Rev.Lett., 34, 479 (1975)
9. Vaitkus J., Gaubas E. and Jarasiunas K., Soviet. Phys.Solid.St., 20, 1824 (1978)
10. Lindle J.K., Moss S.C. and Smirl A.L., Phys.Rev. B, 20, 2401 (1979)
11. Hopf F.A., Tomita A. and Liepmann T., Optics Commun., 37, 72 (1981)
12. Smirl A.L., Boggess I.F. and Hopf F.A., Optics Commun., 34, 463 (1980)
13. Moss S.C., Lindle J.R., Mackey H.J. and Smirl A.L., Appl.Phys.Lett., (1981)

14. Hoffman C.H., Jarasiunas K., Gerritsen H.J. and Nurmikko A.V., Appl.Phys.Lett., 33, 536 (1978)

15. Jarasiunas K., Hoffman C.H., Gerritsen H.J. and Nurmikko A.V., in Picosecond Phenomena, Ed. C.V.Shank et al., Springer Series in Chemical Physics, Vol.4, Berlin 1978, p. 327

16. Miller A., Miller D.A.B. and Smith S.D., Repts. on Progress in Physics, 44, 697 (1981)

17. Jain R.K., in Optical Phase Conjugation, R.A. Fisher Ed., Academic Press, N.Y., 1983, p.309

18. Kovalchuk Yu.V., Ostrovskaya G.V., Partnoy F.L., Smolsky O.V., Sokolov I.A., Dabu R.V. and Vlad V.I., Preprint LOP-38-1983, CIP Press, Bucharest, March 1983

19. Vlad V.I., Ostrovskaya G.V., Dabu R.V., Kovalchuk Yu.V., Sokolov I.A., Smolsky O.V., Preprint LOP-41-1983, CIP Press, Bucharest, September 1983

20. Tsay Y., Bendow B., Mitra S.S., Phys.Rev. B8, 2688 (1973)

21. Eichler H.J., Salje G. and Stahl H., J.Appl.Phys., 44, 5383 (1973)

22. Fradin D.W., Yablonowitch E., Bass M., Appl.Opt., 12, 700 (1973)

23. von Allmen M., in Laser and Electron-Beam Processing of Materials (LEBPM), Eds. C.W.White and P.S.Peercy, Academic Press, N.Y., 1980, p.6

24. Brown W.L., in LEBPM, p.20

25. Foti G., in LEBPM, p. 168

26. Baeri P., Foti G., Poate J.M. and Cullis A.G., in Laser and Electron-Beam Solid Interactions and Material Processing, Eds. J.F.Gibbons, L.D.Hess, T.W.Sigmon, North-Holland, N.Y., 1981, p. 39

27. Vlad V.I., Ostrovskaya G.V., Kovalchuk Y.V., Partnoy E.L., Dabu R.V., Smolsky O.V., Sokolov I.A., in Proc. CIRP-3, W.Ruërgsegger and F.K.Kneubühl Eds., Zürich, July 23-27, 1984, p. 518 and Infrared Physics, 25, 153 (1985)

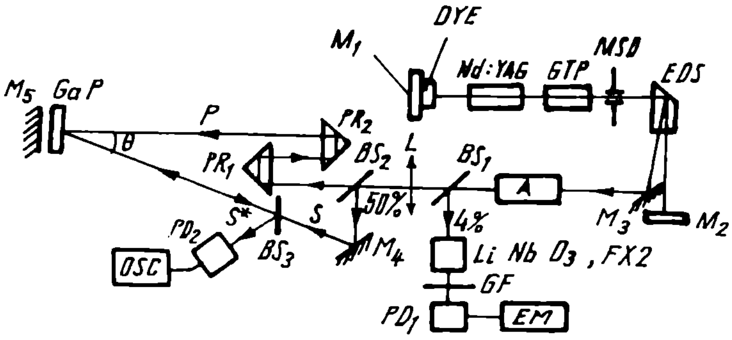
DYE
M1
Nd:YAG
GTP
MSD
EDS
M5
GaP
P
PR2
θ
L
BS2
BS1
PR1
A
50%
4%
S*
S
M3
M2
PD2
BS3
M4
Li Nb O3 , FX2
OSC
GF
PD1
EM

Fig. 1

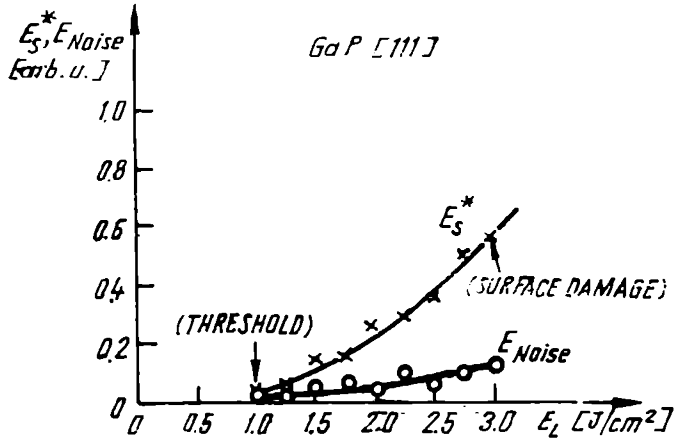
E_S*, E_Noise [arb.u.]
GaP [111]
1.0
0.8
0.6
0.4
0.2
0
(THRESHOLD)
E_S*
(SURFACE DAMAGE)
E_Noise
0
0.5
1.0
1.5
2.0
2.5
3.0
E_L [J/cm²]

Fig. 2

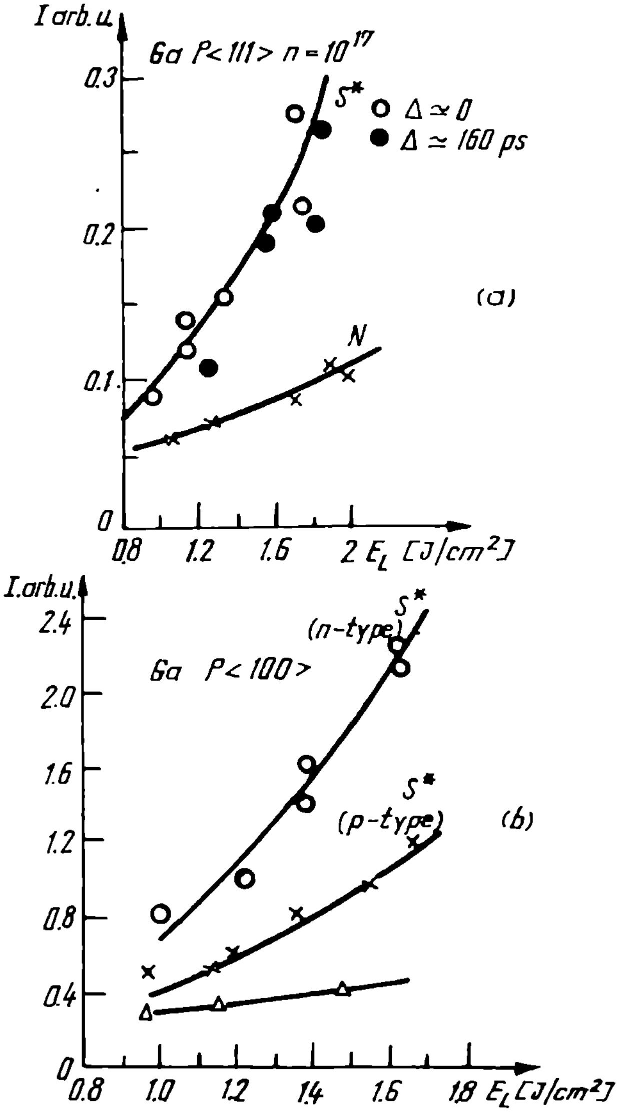
I arb.u.
Ga P<111> n=10^17
0.3
0.2
0.1
0
S*
○ Δ ≃ 0
● Δ ≃ 160 ps
(a)
N
0.8
1.2
1.6
2
E_L [J/cm²]
I.arb.u.
2.4
2.0
1.6
1.2
0.8
0.4
0
Ga P<100>
S*
(n-type)
S*
(p-type)
(b)
0.8
1.0
1.2
1.4
1.6
1.8
E_L [J/cm²]

Fig.3

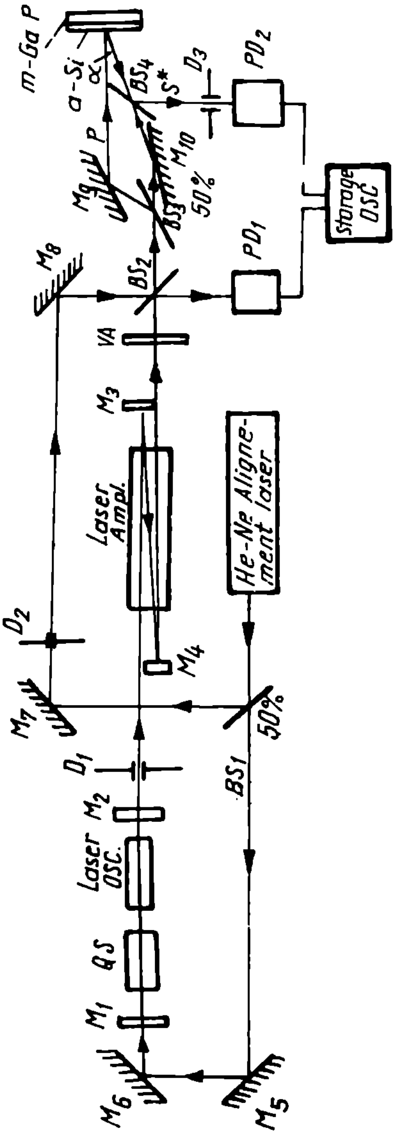
M6
M5
M1
Q.S
Laser OSC.
M2
D1
BS1
50%
M7
D2
M4
Laser Ampl.
He-Ne Alignement laser
M3
VA
M8
BS2
PD1
BS3
50%
M9
P
M10
Storage OSC
BS4
S*
α
a-Si
m-Ga P
D3
PD2

Fig.4

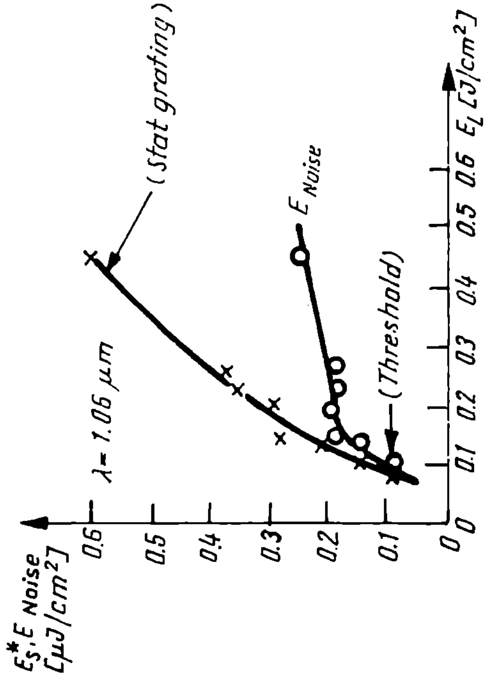
E*_S, E Noise [μJ/cm²]
0.6
0.5
0.4
0.3
0.2
0.1
0
0
0.1
0.2
0.3
0.4
0.5
0.6
E_L [J/cm²]
λ = 1.06 μm
(Stat grating)
E Noise
(Threshold)

Fig.5

ITERATIVE COHERENT OPTICAL PROCESSOR
IN A COMPACT MULTIPASS OFF-AXIS STRUCTURE

V.I.Vlad
Central Insitute of Physics, Bucharest, ROMANIA

This paper presents a new architecture for coherent optical processors which allows the iteration of Fourier transformation in a compact multipass structure. This architecture contains as principal elements two large coaxial spherical mirrors aligned under some special geometrical conditions, so that the off-axis laser beams reflected by the mirrors cover the surface of a rotational hyperboloid. We have theoretically and experimentally demonstrated the capability of its iterative coherent optical processor to perform as many as ∿ 30 iterative convolutions with a space-bandwidth product of 320. The synthesis equation of complex integral nuclei physically realizable in this processor is shown. Moreover, our iterative coherent optical processor can perform fast complex operations in images using only one type of optical filter: high order derivatives, high order moments, Hermite series coefficients, and generalized transverse filtering. The results of such optical preprocessing of images can be further used for pattern enhancement, analysis and recognition.

Introduction

The potential parameters of coherent optical processors have stimulated a broad scientific interest /1/ - /3/. However, a number of technical problems and a strong competition with the microelectronic processors are introducing obstacles in the way of a larger proliferation of the optical processors. The general problems which decrease the practical value of coherent optical processors enter in three classes:

(A) difficulties in the handling of input data, programs (filters), and output data with a speed comparable with the optical processing (light) speed;

(B) analog type of optical processing leading to lower precision than the precision of digital processing;

(C) inflexibility and limitation in changing the processing operations on the image data.

Each of these general problems has a different importance in the various operations performed by the coherent optical processors. Moreover, the recent research has shown that some limitations can be largely eliminated and one can find a number of areas in the field of information processing in which coherent optical technology is without competitors. Thus, the results which tend to remove the above mentioned limitations can be concentrated as follows:

(A') strong development of the spatial electro-optical modulators (with liquid crystals and acoustic waves), the electro-optical and opto-electronic arrays has demonstrated that, even at slower overall speed, the coherent optical processors have a useful processing capability (i.e., 1024x1024 pixels x 20 ms, at TV frame rate);

(B') defining a lot of information processing problems in which the high computational precision is not a serious limitation, for example the cases when the result is asked as an image to be examined by a human operator and when the input image must be preprocessed for a reduction/selection of the data supplied to the electronic processors;

(C') the development of the traditional and new architectures for the coherent optical processors have extended their classes of operations to nonlinear, inverse, logic operations involving difficulties in the interaction man-electronic machine.

In this paper, we introduce a new architecture for coherent optical processors which allows a large number of iterations of Fourier transform and convolution in a compact system. This architecture gives the possibility of practical implementation of the multiple plane, coherent optical processors proposed by Carlson and Francois /4/,/5/. We mention that multipass off-axis structures (resonators) were previously used for temporal processing and amplification of laser signals /6/, /7/. The Iterative Coherent Optical Processor with Multipass Off-axis Beams (ICOPMOB) designed and used in our work has the following capabilities /8/:

- executes N (∿ 30) convolutions in cascade in a compact structure (with the length d ∿ 1.5 m);
- yields all Fourier transforms with only two optical elements (mirrors) which are used for folding the processor;
- offers a convenient lateral access to the input, filtering, and output planes;
- allows the physical realizability of high complexity operations (integral nuclei) which means high flexibility;
- executes complex operations by iteration of some simple operations in real time.

These capabilities of ICOPMOB theoretically and experimentally demonstrated in this paper, tend to remove some limitations of the coherent optical processors, as are shown in (B') and (C') and to support the viability of coherent optical technology in the information (image) processing.

2. Design considerations for the iterative coherent optical processor with multipass off-axis beams

The theoretical description of a quite general, multiplane (iterative) coherent optical processor was recently given by Carlson and Francois /4/, /5/. The in-line (continuous optical axis) architecture imposes a very long spatial extent for such processors (each iteration is executed over a length equivalent to four focal lengths of the Fourier lenses). Moreover, the in-line architecture demands a large number of Fourier lenses, a condition which strongly diminishes its practical feasibility.

We have proposed the implementation of the iterative coherent optical processor in a multipass off-axis structure, which eliminates the above mentioned drawbacks /8/. The architecture of ICOPMOB has as principal components two coaxial spherical mirrors, 01 and 02, with large diameters, equal curvature radii, R = 2f, and a separation on Oz axis with the distance d (Fig.1). The collimated laser beam is introduced through an off-axis window (port) left transparent in the mirror 01. The geometric design allows the extraction of the output image through the same window (at a different angle). Using the same structure for temporal processing and amplification of uncollimated laser beams, Herriott et al /4/ have determined the coordinates of the successive reflection points on the mirrors

$$\begin{aligned} x_n &= x_0 \cos n\theta + \sqrt{d/(4f-d)}\,(x_0+2fx_0')\sin n\theta; \\ y_n &= y_0 \cos n\theta + \sqrt{d/(4f-d)}\,(y_0+2fy_0')\sin n\theta; \\ z_n &= \pm z_0 \quad ; \quad \cos\theta = 1-(d/2f) \quad ; \quad \frac{d}{f} \in (0,4) . \end{aligned} \tag{1}$$

These coordinates define in our processor the folding points of the processing axis. In eq. (1), (x_0,x')... are the coordinates and slopes of the uncollimated input beam (on the mirror 01).

Writing the equations of two laser rays, which are successively reflected onto the mirrors 01 and 02, as

$$\begin{aligned} (D_\lambda) \quad & \frac{x-x_n}{x_{n+1}-x_n} = \frac{y-y_x}{y_{n+1}-y_x} = \frac{z+z_0}{2z_0} \\ (D_\mu) \quad & \frac{x-x_{n+1}}{x_{n+2}-x_{n+1}} = \frac{y-y_{n+1}}{y_{n+2}-y_{n+1}} = \frac{z-z_0}{-2z_0} \quad , \end{aligned} \tag{2}$$

and imposing that $(x_N,y_N,z_N) = (x_0,y_0,z_0)$, we demonstrated that they are identical with the equations of the families of generatrices (D_λ) and (D_μ) of a rotational hyperboloid with one sheet, i.e.

$$(D_\lambda) \begin{cases} \frac{x}{a} + \frac{z}{c} = (1+\frac{y}{b}) \\ \frac{x}{a} - \frac{z}{c} = \frac{1}{\ }(1-\frac{y}{b}) \end{cases} \qquad (D_\mu) \begin{cases} \frac{x}{a} + \frac{z}{c} = \mu(1-\frac{y}{b}) \\ \frac{x}{a} - \frac{z}{c} = \frac{1}{\mu}(1+\frac{y}{b}) \end{cases} \tag{2'}$$

In this case, the equation of the hyperboloid generated by the multipass off-axis beams (more correct, their axes, Fig.2) takes the implicit form

$$\frac{x^2}{a^2} + \frac{y^2}{b^2} - \frac{z^2}{c^2} - 1 = 0 \tag{3}$$

or the parametric form

$$\frac{x}{a} = \frac{\lambda\mu+1}{\mu+\lambda} \quad , \quad \frac{y}{b} = \frac{\mu-\lambda}{\mu+\lambda} \qquad \frac{z}{c} = \frac{\lambda\mu-1}{\mu+\lambda} . \tag{3'}$$

In these equations, the parameters a and b are the half-axes of the directrix ellipse and $c^2 = f_1^2 - a^2 = a^2(e_1^2 - 1)$, with f_1 - the focal length and e_1 - the eccentricity of the generatrix hyperbole in xOy plane. Denoting by A and B the half-axes of ellipses yielding by the intersection of the hyperboloid with the mirrors 01 and 02 (on which lie all reflection points, at $z = \pm z_0$) we find the expression

$$c^2 = z_0 a/\sqrt{A^2 - a^2} , \tag{4}$$

which allows the calculation of the parameter c with easy measurable elements. In the following calculations, we shall consider for simplicity a circular directrix ($a = b$), the generalization of the results to elliptic directrix being straightforward.

Now, for the design of ICOPMOB, we must solve the following problems:

2.1. Given the input parameters of the laser beam into the structure 01-02, determine the hyperboloid parameters.

2.2. Calculation of the geodetic length between two successive reflection points on the mirrors 01 and 02.

2.3. Given a mirror configuration, determine the configuration and maximum number of reflections of the laser beam between the mirrors 01 and 02.

2.4. Calculation of the maximum numbers of convolvers which can be implemented in a given structure 01-02 together with the positions of input, filtering, and output planes.

2.5. Calculation of the space-bandwidth product.

2.1. The hyperboloid parameters

Considering that the input parameters of the laser beam (axis) are x_0, y_0, x_0' (and $y_0' = 0$), the condition to obtain a circular directrix implies the following relations

$$y_0^2 = x_0^2\left(\frac{4f}{d}-1\right) \qquad y_0 = \frac{A}{2}\sqrt{4-\frac{d}{f}} \tag{5}$$

$$x_0^2 + y_0^2 = A^2 \qquad x_0 = \frac{A}{2}\sqrt{\frac{d}{f}}\,, \tag{6}$$

and

$$x_0' = \frac{2x_0}{d} = \frac{A}{\sqrt{fd}}. \tag{7}$$

In this case, the coordinates of the successive reflection points become

$$x_n = A\sin(n\Theta+\alpha) \;;\; y_n = A\cos(n\Theta+\alpha) \;;\; z_n = \pm z_0 \;;\; \cos\Theta = 1-\frac{d}{2f} \tag{8}$$

odd reflections appearing on the mirror 01 and even reflections on 02. On every mirror, the neighbouring reflection points subtended the angle at the center 2Θ. A careful geometrical analysis leads us to the following results

$$a = \frac{2x_0}{d}\sqrt{d(4fx_0^2+dz_0^2)/(d^2+4x_0^2)}, \tag{9}$$

$$c = \frac{z_0}{d}\sqrt{d(4fx_0^2+dz_0^2)/(fd-z_0^2)}, \tag{10}$$

and

$$A = 2x_0\sqrt{f/d}. \tag{11}$$

One can remark that, given x_0 and f, the radii of the end (mirror) circles of the hyperboloid very as $d^{-\frac{1}{2}}$. In the relations (9) and (10), we can substitute

$$z_0 = \frac{d}{2} - 2f + \sqrt{4f^2-A^2} \sim \frac{d}{2} - \frac{A^2}{4f} = \frac{d}{2} - \frac{x_0^2}{d} = \frac{1}{2d}(d^2-2x_0^2) \tag{12}$$

so that the paraboloid parameters are obtained as functions of x_0, f and d only. Alternatively, taking into account the relations

$$d = \frac{2x_0}{x_0'} \quad ; \quad f = \frac{x_0^2+y_0^2}{2x_0'} \tag{13}$$

we can express the hyperboloid parameters as functions of the input beam parameters (which are not independent, as one can see in eqs. (5)-(7)).

For the concrete data of our structure : $x_0 = 0.05$ m, $f = 0.5$ m, and $d = 1.5$ m, we obtain:

$$a \sim x_0 = 0.05 \text{ m},$$

$$c \sim \frac{1}{2}\sqrt{d^2/(2-d)} = 0,65 \text{ m},$$

$$A \sim 0.07\, d^{-\frac{1}{2}} \sim 0.057 \text{ m},$$

and

$$z_0 \sim d/2 = 0.75 \text{ m}.$$

2.2. The geodetic length

We have shown that any laser generatrix ray is transformed after the reflection on a mirror, inside the structure 01-02, into a generatrix ray from the other family of the hyperboloid (eq. (2')). The reflection points at the mirrors 01 and 02 lie on end ellipses (circles or straight lines), which are contained in the plane $z = \pm z_0$. Calculating the length intercepted by these planes on a generatrix ray, one can obtain the geodetic length, S, between two successive reflection points on the hyperboloid surface. The result of this operation has the form:

$$S^2 = 4(A^2-a^2+z_0^2) \tag{13}$$

or

$$S^2 = \frac{4d(4fx_0^2+dz_0^2)}{d^2+4x_0^2} = a^2\frac{d^2}{x_0^2}\,. \tag{13'}$$

Therefore, in a given structure 01-02, the geodetic length has the same value for any generatrix ray. In practical cases, the geodetic length is approximately equal with the distance between the mirrors (eq. (13') and, using the actual data, we get

$$S \sim d = 1.5 \text{ m}.$$

2.3. The configuration and maximum number of reflections

Suppose that one asks to obtain N reflections on the mirrors and the superimposition of the (N+1)-th reflection onto the input spot, after q rotations of the successive reflections on the end circles (N = qk + p, where q, k and p are integers and p/q is a rational, irreducible, subunitary fraction). Then, the eq. (1''') yields the following expression for the mirror separation

$$d_{N,q} = 2f(1-\cos\frac{\pi q}{N})\,. \tag{14}$$

or, by using eq. (8),

$$2\theta N = 2\pi q, \tag{14'}$$

which leads to a supplementary connection between the parameters of the structure 01-02.

Let us see some simple combinations of these parameters(restricted by the stability condition $0 < (d/f) < 4$)

$q = 1$:

N	2	3	4	6	12
d/f	2.000	1.000	0.586	0.268	0.067

$q = 3$:

N	8	10	12	14	16	18	20	22	24
d/f	1.234	0.824	0.586	0.442	0.336	0.268	0.218	0.182	0.152

$q = 5$:

N	15	18	20	24	36
d/f	1.382	1.000	0.824	0.586	0.268

We observe that, imposing N and varying the q integer (by mirror titling), one can obtain sometimes the same values for the ratio d/f (or θ). Consequently, f given by construction, one can obtain a prescribed N with certain values for mirror separation (d) and titling (q). From eq. (14), we see that our conditions are fulfiled only when

$$\mathrm{arc\ cos}\left(1 - \frac{d}{2f}\right) = C\pi, \tag{14''}$$

with C a rational number. In this situation, the number of reflections could be very large ($N = q/C$), a first upper limit appearing only due to the strong decrease of the ratio d/f to unpractical values.

For our structure, giving f = 0.5 m and adjusting d = 1.5 m, eq. (14'') yields $C = \frac{2}{3}$ and, by eq. (14), one obtains $\frac{\pi q}{N} = \frac{2}{3}$. This means that, for different mirror tilt adjustments, it is possible to obtain the following (N,q) couples: (3,2), (6,4), (9,6), (12,8), (15,10), (18,12) etc.

Designing the coherent optical processor, we must take into consideration a second limitation of the maximum number of reflections due to the minimum aperture of the processed image, L_{min}, by the nonoverlapping condition for successive reflections

$$N_{max} \cdot L_{min} = 2\pi A, \tag{15}$$

or

$$N_{max} \cdot L_{min} = 2\pi x_o \sqrt{\frac{f}{d}} = \frac{2\pi x_o}{\sqrt{2(1 - \cos \pi q/N_{max})}} \tag{15'}$$

For our structure, imposing L_{min} = 10 mm (and x_o = 50 mm), one can find N_{max} = 18 and q = 12.

The third limitation comes from the mirror losses and from this restriction, N_{max} could reach ~ 100 reflections.

2.4. Maximum number of convolvers implemented in ICOPMOB

The maximum number of convolvers, K, which can be cascaded into the structure of ICOPMOB is given by dividing the total internal pathlength of the laser beams (2NS) by the length of a conventional convolver (4f):

$$K = \frac{2NS}{4f} = \frac{NS}{2f} = \frac{NS}{R} \tag{16}$$

Now, a practical question related to the convolver identification can be formulated: is there a structure 01-02 in which the total internal pathlength of the laser beams (geodetics) is integer multiple of the focal length of the mirrors, i.e.

$S = mf$ m natural number ? (17)

In our configuration, we have found $S \simeq d$, so that the discussion will be concentrated on the cases for which

$$d \sim mf \tag{18}$$

The cases: $m = 1$ (focal configuration) with $N = 2$

and $m = 2$ (confocal configuration) with $N = 3$

lead to a small number of reflections (and convolvers).

Due to the stability condition (see eqs. (1)), $0 < m < 4$, the case $m = 3$ remains the only interesting solution. We deduce that $d \sim 3f$ implies

$$\frac{\pi q}{N} = \frac{2\pi}{3} \text{ or } N = \frac{3}{2} q \tag{19}$$

This is exactly the case of our configuration 01-02.

In this interesting case, the maximum number of convolvers which can be cascaded inside ICOPMOB is

$$K \sim \frac{N \cdot 3f}{2f} = \frac{3}{2} N = \frac{9}{4} q. \tag{20}$$

With the above considered numerical data, $N_{max} = 18$ and $K_{max} = 27$ convolvers. The identification of the positions of the input, filtering, and output planes for each convolver can be done very convenient in this interesting configuration, by direct partition of the mirror distance in three equal (with f) segments and by ordered labeling of the resulted positions*).

2.5. The space-bandwidth product

Once establishing the minimum aperture of the processed image, we can calculate the resolution in the Fourier planes or the maximum spatial bandwidth of the processed image ($\lambda = 0{,}633\ \mu m$)

$$B \doteq \frac{L_{min}}{\lambda f} = 32\ mm^{-1} \tag{21}$$

Imposing these parameters for all processing planes, we can write the space-bandwidth of ICOPMOB

$$SBP = L_{min} \cdot B = 320. \tag{22}$$

We can also estimate the total number of pixels, which are simultaneously processed (in parallel), at $\sim 10^5$ pixels. These figures of merit are not high in coherent optics, but are very high for conventional image processors.

3. Optical realizability of the complex integral nuclei in ICOPMOB

Let us consider the integral equation

$$S_{out}(x_0, y_0) = \iint_{-\infty}^{+\infty} S_{in}(x, y) K(x_0, y_0; x, y)\, dx dy \tag{23}$$

relating the output, $S_{out}(x_0 y_0)$, and input, $S_{in}(x,y)$, to the transmittance (nucleus) of an arbitrary system. Now, we have to find the general form of the nucleus K which is optical realizable in

---

*) Actually, in this configuration, we have introduced some additional (secondary) lenses to preserve the conventional structure of the convolvers, which are not shown in the principial scheme from Fig.1.

the iterative coherent optical processor.

For a processor with p cascaded planes, which are separated by 2f and contain the transmittances $h_i(x_i,y_i)$, Francois and Carlson have demonstrated the following synthesis equation for the integral nucleus /5/

$$K_p(x_{p+1},y_{p+1};x_1,y_1) = h_1(x_1,y_1)\cdot h_{p+1}(x_{p+1},y_{p+1}) \int\!\!\int_{-\infty}^{+\infty}\!\!\dots\int e^{-i2\pi(x_1x_2+y_1y_2)} \prod_{i=1}^{p} h_i(x_i,y_i)\, e^{-i2\pi(x_ix_{i+1}+y_iy_{i+1})}\, dx_2dy_2dx_{2i}dy_{2i}\,. \tag{24}$$

Particularly, from eq. (24), one can find

$$K_1 = \exp[-i2\pi(x_1x_2+y_1y_2)]$$

$$K_2 = \tilde{h}_2(x_1+x_3,y_1+y_3) = F[h_2] \qquad \text{(Fourier analyzer)}$$

$$K_3 = F_2[h_2\cdot h_3] \qquad \text{(2-d order correlator)}$$

$$K_4 = F_{2,4}[h_2\cdot\tilde{h}_3\cdot h_4] \qquad (F_{2,4}=\text{Fourier transf.on variables } 2,4)$$

$$K_5 = F_2\int\!\!\int_{-\infty}^{+\infty}[h_2\cdot\tilde{h}_3\cdot h_4\cdot\tilde{h}_5]\,dx_4dy_4 \qquad \text{(4th order correlator)}$$

$$K_6 = F_{2,6}[h_2\cdot\tilde{h}_3\cdot h_4\cdot\tilde{h}_5\cdot h_6]$$

$$K_7 = F_2\int\!\!\int_{-\infty}^{+\infty}[h_2\cdot\tilde{h}_3\cdot h_4\cdot\tilde{h}_5\cdot h_6\cdot\tilde{h}_7]\,dx_6dy_6\,,$$

We remark that the synthesis rule is an iterative algorithm "correlation-filtering".

Using our iterative optical processor, ICOPMOB, we can give a simpler form to these results

$$\begin{aligned} S_{out} &\propto h_pF\dots Fh_5Fh_4Fh_3Fh_2F[h_1S_{in}] \\ &\propto h_pF\dots Fh_5Fh_4Fh_3(\tilde{h}_2\ast h_1S_{in}) \\ &\propto h_pF\dots Fh_5Fh_4F[h_3C_1] \propto h_pF\dots F[h_5\cdot C_2] \propto \dots \qquad (p = 2K)\,. \end{aligned} \tag{25}$$

The eq. (25) shows that the processed images, C_i, which are obtained in successive planes separated by 4f = 2R along the geodetics have the form

$$C_1 = \tilde{h}_2 \ast h_1S_{in}$$

and iteratively,

$$C_i = \tilde{h}_{2i} \ast h_{2i-1}\, C_{i-1}, \qquad (i = 1,\dots,K)\,. \tag{26}$$

From these equations, we have derived a simple synthesis equation for the integral nuclei, when the parameters of ICOPMOB and the transmittances h_i are known:

$$K = \tilde{h}_{2k} \ast h_{2k-1}\left\{\tilde{h}_{2k-2}\, h_{2k-3}\,\dots\,[\tilde{h}_4 \ast h_3(\tilde{h}_2\ast h_1)]\right\} \tag{27}$$

This expression is much more compact and significant than the eq. (24) and directly illustrates the iterative algorithm "correlation-filtering".

4. Complex processing of image data using the iteration of some simple operations in ICOPMOB

4.1. High order derivative calculation

The high order derivatives of an image were previously calculated by using complicate optical filters in the conventional optical convolver /9/-/11/. Our iterative optical processor yields the derivatives up to order K(= tens) rapidly and with a single elementary optical filter. The block diagram of these operations in ICOPMOB is shown in Fig.3. The image to be differentiated, f(x, .), is introduced in the input plane and the optical filters with the same transfer function H(u) = iu are introduced in the Fourier planes of the successive convolvers. In the output plane, some beam-splitters extract the successive derivatives (on x variable) of the input image. To obtain derivatives with respect to y, all filters are rotated with 90° and to obtain mixed derivatives, only the filters for derivatives on y are rotated with 90°.

The derivative filters are produced by electronic computation and plotting using the method of phase detour /9/ and optical methods using composite gratings (finite differences /10/) and Talbot effect /11/.

The derivatives can be sequentially obtained in a single output channel, at intervals of several nanoseconds (given by the propagation of a laser pulse through the successive convolvers) or continously in K parallel channels.

4.2. High order moment calculation

The calculation of high order moments for the automatic identification of the elements, dimensions and orientations in an image was proposed in the last years /12/-/15/. The low order moments of an image can be used for centroid location, size and orientation characterization. The high order moments of an image can be used in 2D and 3D pattern recognition. The interest for the processing methods which use moment calculation originates at least from two reasons:

- the moments possess very convenient transformation properties when the image is translated, rotated, reflected (in the plane), and scaled;
- any image has an unique approximand given by a finite set of its moments.

The moments of an image f(x,y) are defined as

$$M_{jk} \triangleq \iint_{-\infty}^{+\infty} x^j y^k f(x,y)\,dxdy \tag{28}$$

and can be also obtained from the Fourier transform of the image,

$$\tilde{f}(u,v) = \iint_{-\infty}^{-\infty} f(x,y) \exp[-i(ux+vy)]\,dxdy = \sum_{j=0}^{\infty} \sum_{k=0}^{\infty} \frac{(-i)^{j+k}}{j!k!} M_{jk} u^j v^k, \tag{29}$$

by a simple identification which yields

$$M_{jk} = \frac{1}{(-i)^{j+k}} \left[\left(\frac{\partial}{\partial u}\right)^j \left(\frac{\partial}{\partial v}\right)^k \tilde{f}(u,v) \right]_{u=v=0}. \tag{30}$$

Thus, two alternatives for moment calculation appear immediately: either the iterative differentiation of the image spectrum in the origin of Fourier plane (eq. 30), or the iterative integration (eq. 28). The first alternative can be implemented as in 4.1., so that here we shall take into consideration the second alternative only. We mention that other optical computing methods for the moments were proposed by Casasent and Psaltis /13/ and Teague /14/.

The moment computation by the iterative integration method can be done in ICOPMOB with the structure shown in Fig.6. In the input plane, we introduce the image spectrum, f(x,.), and in the filtering planes, optical filters with the transfer function, $H_i(u) = u-a$, $(i = 1,\ldots,K)$. In the output plane of each convolver i, there is a beam splitter which extracts the result and introduces it into a low-pass spatial filter, LPF. In the origin of LPF output plane, one can measure the moment of i-th order. Again, the moments can be obtained either sequentially in a single output channel (with very short laser pulses), or continuously in K parallel channels.

The filters $H_i(u)$ are achieved very convenient by the phase detour method using an electronic computer. From the usual moments, M_{ij}, one can also calculate other types of useful moments for image processing, i.e. Legendre (orthogonal) and Zernicke moments.

An important use of the moment computation appears in the case of a random image (2D signal), when the moment set characterizes completely the corresponding statistical distribution. Supposing the image described by a deterministic function g(x,y) with random variables $x = f(\xi)$ and $y = f(\eta)$, its moments have the form

$$M_{j\cdot} = \int_{-\infty}^{+\infty} g^j(u-a,\cdot)\, f(u)\,du. \tag{31}$$

These moments can be obtained in ICOPMOB with the same structure which was presented in Fig. 6, but introducing different filters with the transfer function $H_i(u) = g(u-a)$, (again yielded by digital computer). This use of moment computation is very interesting for laser imaging, which is always affected by speckle (noise).

4.3. The calculation of the Hermite series coefficients of an image

The calculation structure of ICOPMOB was designed using the definition formula of the Hermite (orthogonal) polynomials

$$H_n(x) = e^{x^2} \frac{d^n}{dx^n}\left(e^{-x^2}\right) \tag{32}$$

and the gaussian intensity distribution across the laser beam (TEM_{00n}). Thus, the Hermite polynomials can be iteratively generated by the differentiation of the collimated laser beam, (H_n^s), and multiplication by e^{x^2}. The last factor disappears in the calculation of the Hermite series coefficients of the function f(x,.),

$$\begin{aligned} a_n &= \frac{1}{2^n n! \sqrt{\pi}} \int_{-\infty}^{+\infty} e^{-x^2} f(x,\cdot) H_n(x)\,dx, \\ &= \frac{1}{2^n n! \sqrt{\pi}} \int_{-\infty}^{+\infty} f(x,\cdot) H_n^s(x)\,dx, \end{aligned} \tag{33}$$

with

$$f(x,\cdot) = \sum_{n=0}^{\infty} a_n H_n(x), \tag{34}$$

can be calculated either sequentially, in a single channel by filtering-integration-detection-multiplication (with very short laser pulses), or continuously in K parallel channels. The second alternative is shown in Fig. 7. The expansion on the variable y is independent and can be obtained by the rotation of the derivative filters with 90°, so that finally we can get

$$f(x,y) = \sum_{n=0}^{\infty} \sum_{m=0}^{\infty} a_n b_m H_n(x) H_m(y) . \tag{35}$$

4.4. Generalized transverse filtering

The transverse filtering is extensively used in the digital signal processing and recognition (by matched filtering). The structure of ICOPMOB have suggested the possibility of implementation of a generalized transverse filtering of images in the block diagram shown in Fig.8 with the result

$$S_{out} = \sum_{i=1}^{k} A_i S_{in} * (h_1 * h_2 \ldots * h_i) . \tag{36}$$

If we use very short laser pulses and the time delays between the successive convolvers as a sampling base, ICOPMOB can become a very fast 3D spatio-temporal processor.

5. Conclusions

In this paper, we have designed a new architecture for coherent optical processing, namely the iterative coherent optical processor with multipass off-axis beams (ICOPMOB). The structure of ICOPMOB was defined by the calculation of the principal parameters of the off-axis laser beams in function of the input parameters, mirror focal length and mirror separation. We have deduced the optimum conditions for convolver partition inside of ICOPMOB and the maximum number of convolvers defined by these conditions and the aperture of the processed images. Thus, in a small volume (approx. 2 x 0.5 x 1 m^3), ICOPMOB executes approximately 30 convolutions, performs all Fourier transformations with two optical elements (mirrors) only, and offers a convenient lateral access to the input, filtering and output planes. In our design, the dimensions of the processed images are 10x10 mm^2 and the resolution is 32 mm^{-1} (SPB = 320).

Concerning the physical realizability of mathematical operations in ICOPMOB, we have deduced the synthesis equation for quite complex (general) integral nuclei, which takes the form of a "correlation-filtering" algorithm. Our iterative architecture allows complex calculations in images, with high speed, by the use of only one type of elementary filter: high order derivatives, high order moments, Hermite series coefficients, generalized transverse filtering etc. These results can be further used for the analysis, description, and recognition of certain elements in an image.

By these features, ICOPMOB yields: pre-processing of the input images for a strong compression of the optical data which are introduced in the optoelectronic systems for image analysis; high flexibility in performing complex operations of optical information processing; and direct interaction between man and machine.

REFERENCES

/1/ J.W.Goodman, Proc.IEEE, 65, No.1, 29 (1977) and Optics News, 10, 25 (1984)

/2/ D.Casasent, Ed., Optical Data Processing, Springer Verlag, Berlin, 1978

/3/ V.I.Vlad et al., Prelucrarea optica a informatiei, Edit. Acad. R.S.R., Buc. 1976

/4/ F.P.Carlson and R.E.Francois, Proc.IEEE, 65, No.1 10 (1977)

/5/ R.E.Francois and F.P.Carlson, Appl.Optics, 18, No.16, 2775 (1979)

/6/ D.Herriott, H.Kogelnik, and R.Komfner, Appl.Optics, 3, No.4, 523 (1964)

/7/ L.Blanaru, A.Chetroiu, V.Vasiliu, St.Cerc.Fiz., 22, No.8, 831 (1970)

/8/ V.I.Vlad, Preprint LOP-26-1982, Central Institute of Physics, Bucharest, April 1982

/9/ A.W.Lohmann and D.P.Paris, Appl.Optics, 7, 651 (1968)

/10/ S.K.Yao and S.H.Lee, J.Opt.Soc.Am., 61, 474 (1971)

/11/ A.W.Lohmann and D.E.Silva, Opt.Commun. 2, 413 (1971)

/12/ M.K.Hu, IRE Trans. Inf.Theory IT-8, 179 (1962)

/13/ D.Casasent and D.Psaltis, in proc. SPIE, 201, 1979

/14/ M.R.Teague, Appl.Optics, 19, 1353 (1980) and J.Opt.Soc.Am., 70, 920 (1980)

/15/ R.Machuca and A.L.Gilbert, IEEE Trans.Pattern Analysis and Machine Intelligence, PAMI-3, 103 (1981)

FIGURE CAPTIONS

Fig. 1 The iterative coherent optical processor with multipass off-axis beams (ICOPMOB)

Fig. 2 The rotational hyperboloid defined by the off-axis reflected laser beams inside the mirror configuration 01-02

Fig. 3 Iterative calculation of the high order derivatives of an image by ICOPMOB

Fig. 4 Iterative calculation of the high order moments of an image by ICOPMOB

Fig. 5 Iterative calculation of Hermite series coefficients of an image by ICOPMOB

Fig. 6 Generalized transverse filtering of images using ICOPMOB.

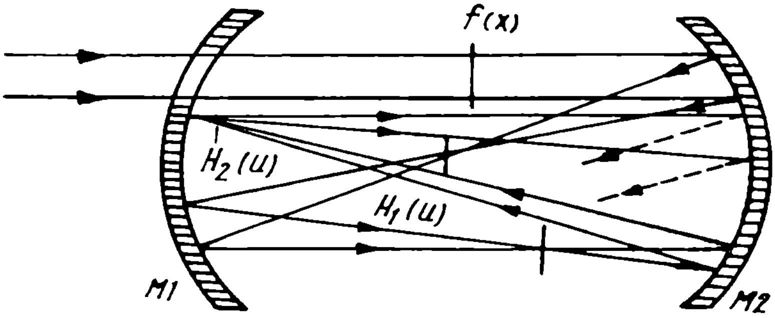

Fig. 1

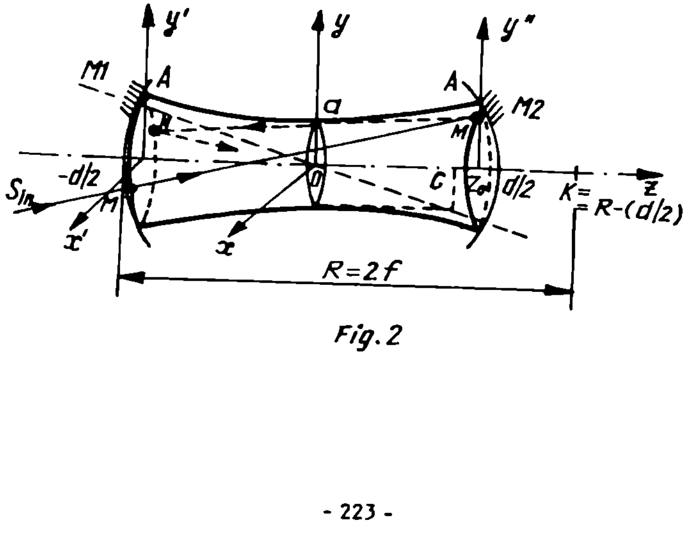

Fig. 2

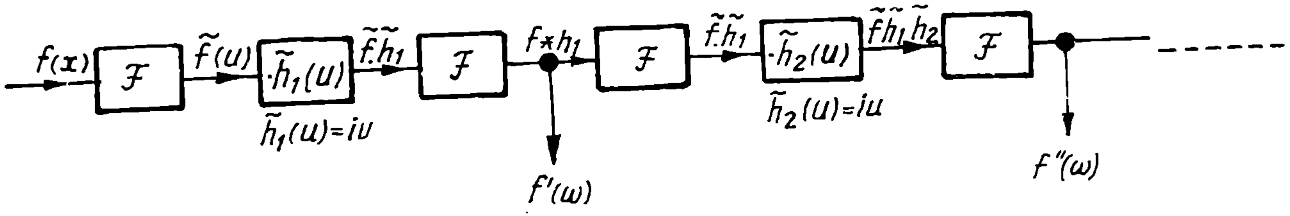

Fig. 3 High order derivative calculator

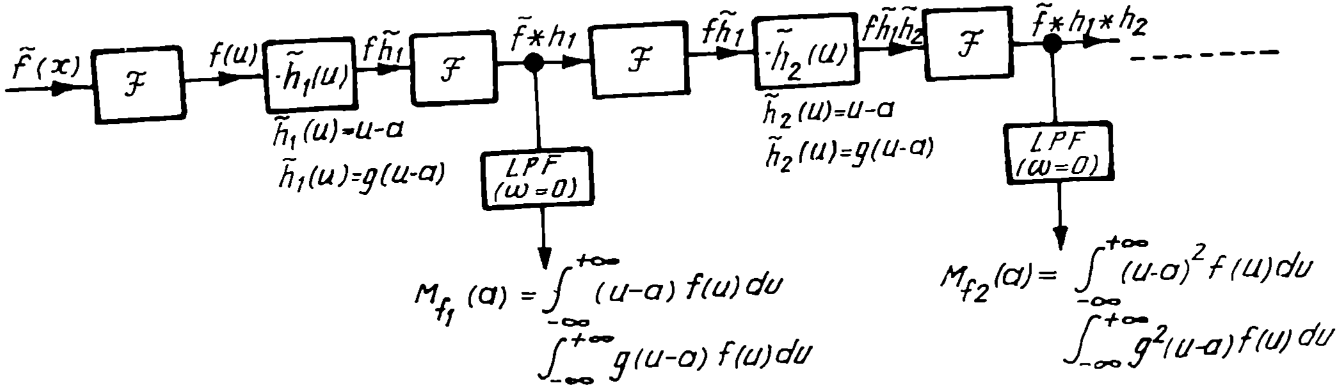

Fig. 4 High order moment calculator

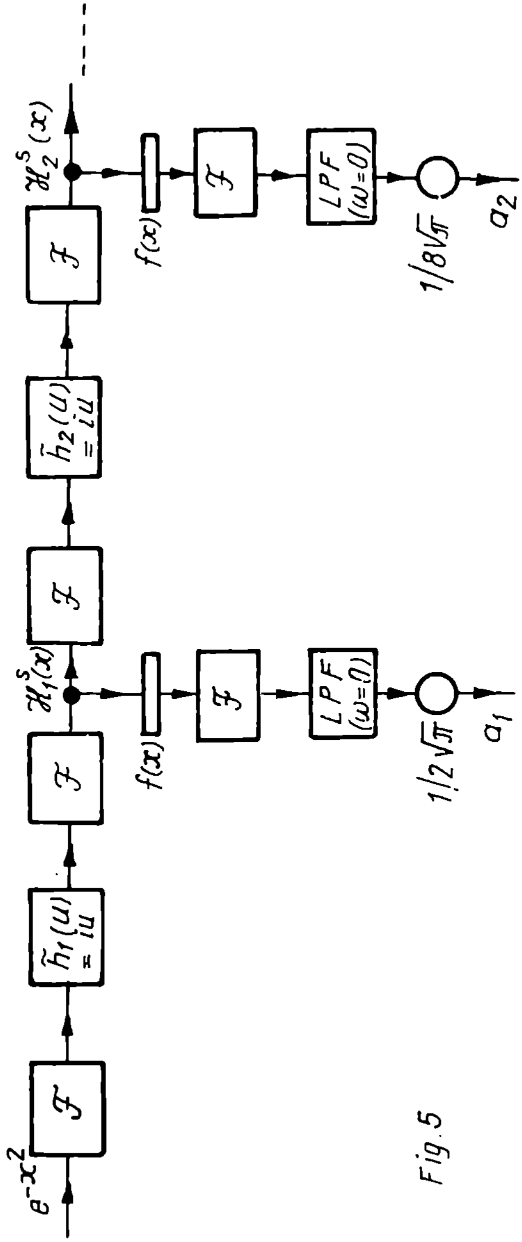
e^{-x^2}
$\mathcal{F}$
$\tilde{h}_1(u) = iu$
$\mathcal{F}$
$\mathcal{H}_1^s(x)$
$\mathcal{F}$
$\tilde{h}_2(u) = iu$
$\mathcal{F}$
$\mathcal{H}_2^s(x)$
f(x)
$\mathcal{F}$
LPF ($\omega=0$)
$1/2\sqrt{\pi}$
a_1
f(x)
$\mathcal{F}$
LPF ($\omega=0$)
$1/8\sqrt{\pi}$
a_2

Fig.5

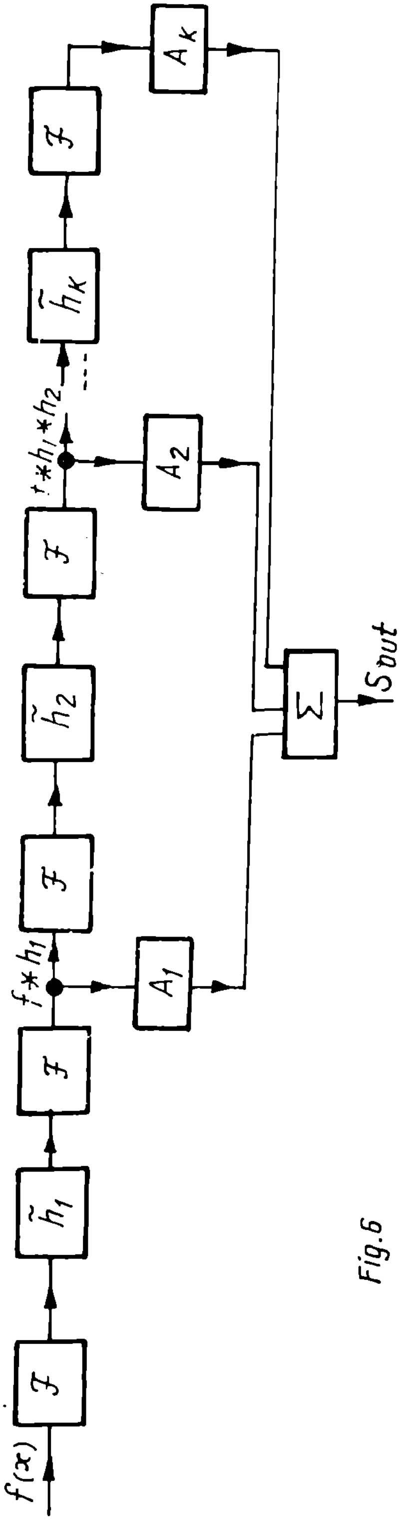
f(x)
$\mathcal{F}$
$\tilde{h}_1$
$\mathcal{F}$
$f*h_1$
A_1
$\mathcal{F}$
$\tilde{h}_2$
$\mathcal{F}$
$f*h_1*h_2$
A_2
$\tilde{h}_K$
$\mathcal{F}$
A_K
Σ
S_{out}

Fig.6

SPECTROSCOPIC CHARACTERISTICS OF Ti^{3+}:Al_2O_3 AS LASER MATERIAL

A.Lupei, V.Lupei, C.Ionescu
Central Institute of Physics, Bucharest, Romania
H.G.Tang, M.L.Chen
Anhui Institute of Optics and Fine Mechanics, China

Research in the field of solid state lasers in the recent years is especially connected to tunable generation of transition metal ions, phonon terminated lasers. Though the majority of the work has been connected with Cr^{3+} ions in different crystals, in the last years a particular interest has received Ti^{3+}in sapphire, due to its more allowed vibronic transitions. Room temperature tunable generation with maximum around 775 nm, using lamp or laser pumping has been obtained by several groups /1-4/. However, many technological as well as spectroscopic or laser characteristics are still under investigation.

This study is devoted to spectroscopic characteristics of α -Al_2O_3:Ti^{3+} system, by using absorption, luminescence and lifetime measurements at different temperatures.

Results and discussions

Single crystals of α -Al_2O_3 doped with titanium have been grown by Czochralski method. Titanium has been introduced as TiO_2 (3% weight). Atomic absorption measurements reveal a titanium concentration in the samples of ~ 0.2% by weight. It is difficult to say that all titanium has entered as +3 valency form, since it has the tendency to form +4 valency and one of the technological problems connected to this system is the stabilization of +3 valency.

As for other 3d ions in Al_2O_3, Ti^{3+} substitute Al^{3+} and the local symmetry is a slightly trigonally distorted octahedron.

Absorption spectra at room temperature consist of a broad band in visible, centered at ~ 490 nm and assigned to a transition ($^2T_{2g} \rightarrow {}^2E_g$) within $3d^1$ ground configuration of Ti^{3+} and a very intense band in u.v. (~ 220 nm) due probably to a charge transfer transition (Fig. 1). The shoulder observed around 520 nm has been explained by the splitting of ^2E_g level by trigonal crystal field, spin-orbit or Yahn-Teller effect /5/. Far infrared absorption has shown that ground term is split in three components with 37.8 and 107 cm^{-1} distance between them /6-7/. In order to explain these data as well as the EPR ones a dynamical Yahn-Teller distortion has been assumed /6,7/.

By working at low temperature with high resolution (and amplification) we have been able to observed a structure of the visible spectra (Fig. 2). The sharp line at 616.7 nm can be assigned to a zero-phonon transition between the lowest split $^2T_{2g}$ and ^2E_g levels. Other broader lines situated at 609.4, 601.7 nm could be connected to the resolved vibronic transitions. These lines are situated at ∿ 200 cm^{-1} one from the other; i.e. they form a vibrational series. It is a direct experimental data concerning the energy of the interacting phonon with the excited ^2E_g electronic level. It has a larger energy than that estimated from luminiscence data (∿ 160 cm^{-1}) /8/. A Cary 17 Spectrometer and Oxford Instruments cryogenic system have been used for these measurements.

Luminiscence spectra have been excited in two ways: (i) by using the second harmonic (λ_{exc} = 532 nm) and (ii) by using the fourth harmonic (λ_{exc} = 266 nm) of a YAG:Nd laser (Quantel III). Therefore, excitation in both absorption bands have been done. Besides the pumping laser, the experimental set-up consists of a GDM-1000 monochromator, S-20 photomultiplier and Boxcar integrator PARC-162.

When excited with 532 nm a red broad band luminscence is obtained (Fig. 3). Position of linewidth of this band are slightly temperature dependent. Two sharp zero-phonon lines are observed at 77 K (see Fig.3) at 16214 and 16180 cm^{-1} assigned to zero-phonon transitions $^2Eg \rightarrow {}^2T_{2g}$ (lower split levels) /8/. One of these lines is resonant with that observed by us in absorption spectra.

Luminescence spectra as well as absorption bands are polarized. The intensity of luminiscence for E ∥ C (C - optical axis) is twice as large as for E ⊥ C. Lifetime connected to this luminiscence line is also temperature dependent, ∿ 3.1 μsec at 300 K and 3.6 μsec at 77 K. A deviation from exponential decay has been noticed.

When pumping is performed with the fourth harmonic λ_{exc} = 266 nm, two luminiscent bands are excited: the red band discussed before and another strong blue-band emission, with a maximum at room temperature around 430 nm (Fig.4). This blue emission is also polarized. A lifetime of ∿ 32 μsec has been determined at room temperature. Again a deviation from the exponential decay is observed. This luminiscence band is very likely to be associated to Ti^{3+} charge transfer transition, but further investigation has to be done.

Work connected to the stability of +3 valency of Ti under green and u.v. pumping as well as an investigation of laser emission in these crystals is in progress.

REFERENCES

/1/ P.F.Moulton, Optics News, 6, 9 (1982)
/2/ B.K.Sevastianov et al., Kristallographia (sov.) 29, 5, 963 (1984)
/3/ G.S.Kruglik et al., J.Appl.Spetr. (sov.) XLII, 126 (1985)
/4/ G.F.Albrecht, Y.M.Eggleston, J.J.Ewing, Opt.Comm. 52, 6, 401 (1985)
/5/ D.S.McClure, J.Chem.Phys., 36, 2757 (1982)
/6/ E.D.Nelson, J.Y.Wong, A.L.Schawlow, Phys.Rev., 156, 298 (1967)
/7/ R.R.Joyce, P.L.Richards, Phys.Rev., 179, 375 (1969)
/8/ B.F.Gächter, J.A.Koningstein, J.Chem.Phys., 60, 2003 (1974)

Fig. 1

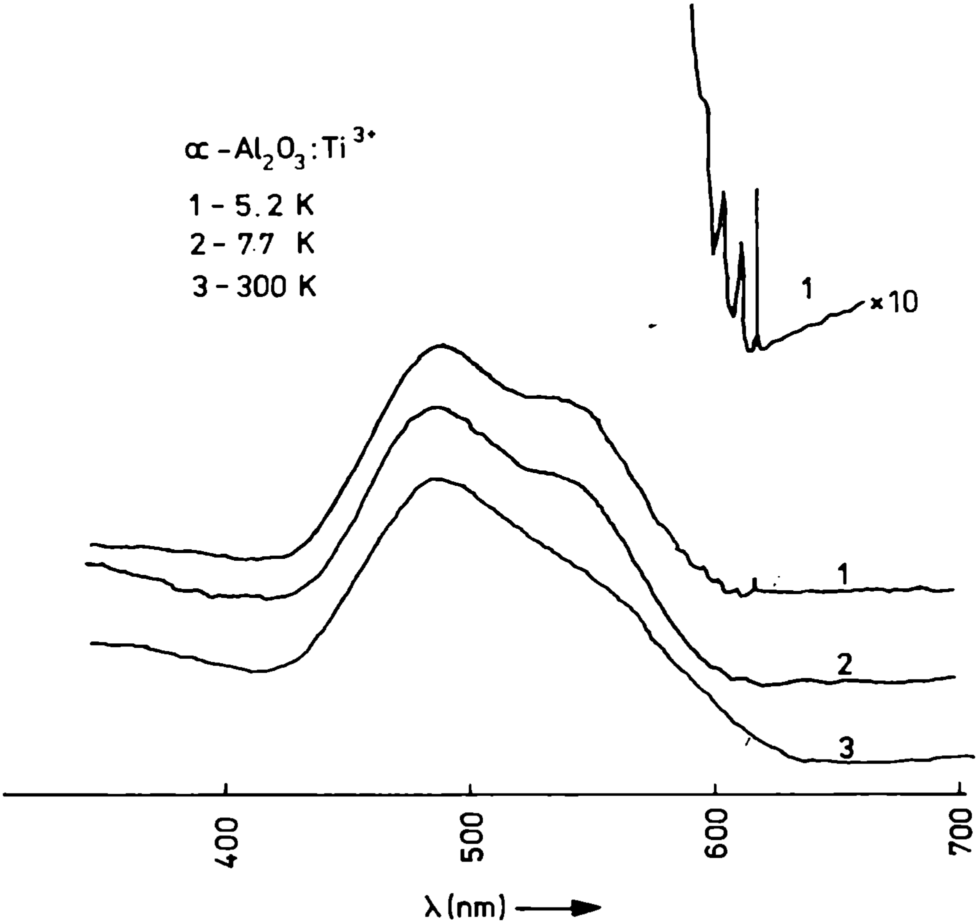

Fig. 2

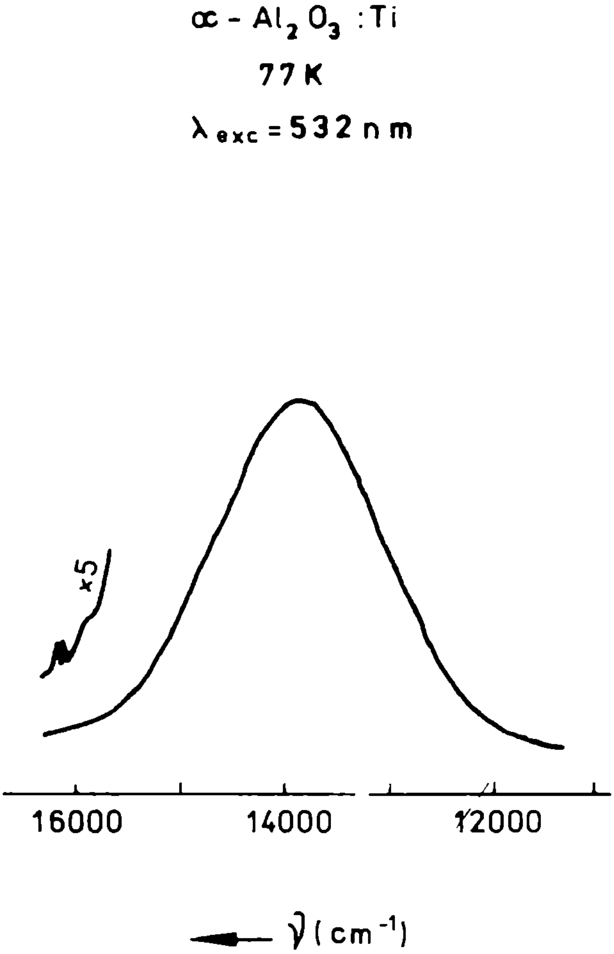
α - Al_2O_3 :Ti
77 K
λ_{exc} = 532 nm
x5
16000
14000
12000
$\leftarrow \tilde{\nu}$ (cm^{-1})

Fig. 3

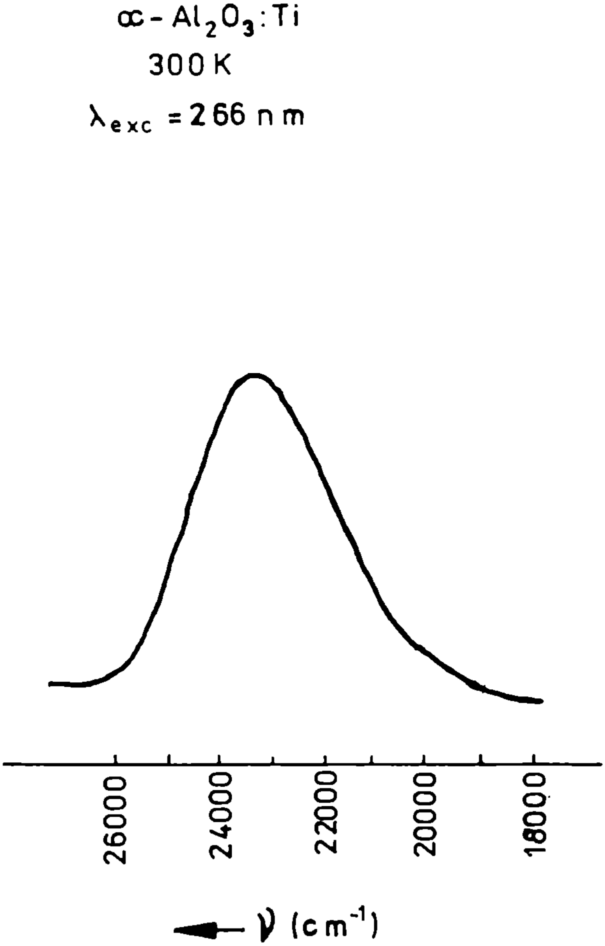
α-Al_2O_3:Ti
300 K
λ_{exc} = 266 nm
26000
24000
22000
20000
18000
← ν (cm^{-1})

Fig. 6

ON THE FACETTING IN YAG:Nd CRYSTALS

V.Lupei, E.Ristici, S.Georgescu, I.Voicu, O.Radulescu
Central Institute of Physics, Bucharest - Romania

1. Introduction

The YAG:Nd crystals are the most widely used active media in solid state lasers due to their good mechanical, thermal, optical and generation properties. However, growing YAG:Nd crystals of high optical quality is still a problem.

The Czochralski technique is the most usual method to obtain YAG:Nd single crystals. The YAG:Nd crystals pulled from the melt with a convex interface (to avoid high dislocation concentrations) exhibit a strained central core (of a few multimeters in diameter) due to the development of [211] and [110] type facets. This deffect occurs in these garnet crystals when the growing convex interface becomes tangent to these planes. Although present in the undoped crystals, these defects are enhanced when Nd substitutes occur in the crystals using the <111> growth direction that assure the minimum facet area. Basterfield et al. /1/ using X-ray topography revealed the nature of the optical inhomogeneities in the core of both undoped and Nd-doped YAG crystals. Only the [211] and [110] type facets have been observed.

The facet information is associated with strains, Cockayne /2/ reviewed the principal sources of the facet strain as, impurity segregation, changes in stoichiometry and oxygen vacancies.

Recently, Janusz et al /3/ have used the thermoluminiscence topography method to reveal the strained regions in YAG:Nd crystals.

Cockayne /4/ has shown the importance of the shape and stability of the growing interface in the presence of the dopant due to a small segregation coefficient (K < 1). A major defect, is the change of the growing interface from a smooth to a cellular morphology due to the constitutional supercooling /5/.

Besides the central core, the facets can appear in the annular region of the crystal, at well-defined values of the growing interface angles. These facets which have a deleterious effect similar to that encountered in the central core further reduce the volume of the crystal from which rods of high optical quality can be produced.

Growth striations are other defects present in all the crystals pulled from the melt. The striations represent the shape of the growing interface at any moment.

In the present work, the facets, striations and strains present in YAG:Nd crystals are evidence by the conventional optical methods. A correlation between the appearance and extension of the facets and the growing interface angle is made in order to find the best growing conditions to minimize the core area and to obtain high optical quality crystals.

2. Experimental

The YAG:Nd crystals with diameters up to 25 mm had been grown in our laboratory in iridium crucibles in a nitrogen atmosphere by the Czochralski method.

Various growing conditions to produce different interface angle were selected, and <111> oriented seeds were used (see Table I). Samples under study were cut parallel or perpendicular to the growth direction and optically polished.

The optical inhomogeneities were observed by shadow and photoelastic techniques using a spatially filtered He-Ne laser. To reduce the surface effects, the samples were immersed in an index-matching liquid.

3. Results and discussions

Samples selected from five crystals (A to E) presenting different interface angles in the range of 60° - 108° have been studied. The interface angles were measured from shadow patterns of the samples cut parallel to the <111> direction. Table I presents the interface angles and the observed facets for the studied crystals.

Table I.

The interface angle and the observed facets

for the YAG:Nd crystals

Crystal	A	B	C	D	E
interface	60°	74°	86°	100°	108°
observed facets	$[211], [2\bar{1}1]$	$[211], [2\bar{1}1]$	[211]	[211], [110]	[211], [110]

Fig. 1 presents the interface geometry. The shape was shown by the free growing interface obtained by decantation , and by the growth striations (Fig. 2). In the studied range of interface angles, the interface is generally conical, except for the central region where the "coring" takes place. We can assume that such interface corresponds to a freezing isotherm whose shape is conical with a small spherical bottom; the facets develop in this spherical region and their appearance is favoured by supercooling. The magnitude of supercooling determines which facets form preferentially in this spherical region. In our case all the crystals have [211] facets in the central region. In some cases weak [110] facets were also observed. Outside the core, the crystallization is determined by the angle of the conus; this is clearly seen in figure 2 where the angle of the striations changes sharply from the core to the bulk of the crystal.

In figure 1 we denote by α the growth interface angle and by φ the angle between the <111> direction and the normal to the generatrix of the conus. These two angles are connected by the obvious relation $\varphi = \pi/2 - \alpha/2$. If these normals are along low index crystallographic directions <ijk>, the corresponding planes (ijk) become tangent to the conus and facet formation in the conical part of the isotherm is favoured. The critical interface angle which favours the appearance of these facets tangent to the conus are $\alpha_{211} = 141.06°$, α_{110} $\alpha = 109.46°$ and $\alpha_{\bar{2}11} = 56.26°$.

The extention of these facets depends on the thermodynamics of crystallization; usually they are of tenths of a centimeter wide and are surrounded by a region of high strain. With the growing of the crystal, these narrow facets form inside the crystal "ghost" vertical collumns which can be clearly seen when the crystal immersed into an index-matching liquid is viewed through crossed polarizers.

Figures 3a to 3e present the shadow patterns of the sample A to E cut perpendicular to the <111> direction. As discussed above, the core [211] facets are present in all the crystals but the average diameter of this core varies from crystal to crystal and for our series of samples has a maximum value in the crystal E ($\alpha = 108°$).

In sample A, where α is close to α_{211}, six 211 facets are observed outside the core. At the same time, a strong development of the [211] facets on the outer surface of the crystal takes place and the transverse section of the crystal has the shape of a regular hexagon (Fig. 3a). When the interface angle is far from the critical values (samples B and C) only [211] facets occur (Figs. 3b and c), while in samples D and E, where α is close to α_{210}, three [110] facets develop (Figs. 3d and c) and the tendency to form external [110] facets becomes apparent. An enalrged view of the core of samples B and E is presented in Figs. 4 and 5 respectively. The facets were identified by comparing the shadow patterns with the stereographic projection (Fig. 6).

Photoelastic patterns revealing the strains in perpendicular cut samples are presented in Figs. 7a and 7e. The facets determine the strains in all the samples except for sample C which also presents an outer strained region. A minimum strained area is observed for sample B.

We also note that under some unfavourable growth conditions the conical interface can become concave toward the melt at the outer part of the crystal. This can lead to the appearance of [211] or [110] facets in the outer region of the crystal, thus reducing the part of high optical homogeneity of the crystal.

The data presented in this paper obtained by simple optical methods confirm the relation interface angles and the extent of the facets and evidence the useful parts of the YAG:Nd crystals. In the range of interface angles studied in this work, two regions around $\alpha_{211} = 56.26°$ and $\alpha_{110} = 109.46°$ lead to the development of facets along the conical generatrices dramatically reducing the useful part of the crystal. In these regions of angles the external facetting of the crystal in observed. A similar situation is expected for large interface angles, in the region around $\alpha_{211} = 141.06°$.

The change of the interface to concave in the outer region of the crystal leads to the development of additional low-index facets.

FIGURE CAPTIONS

Fig. 1 Interface geometry α -growth interface angle:
φ -angle between the <111> direction and the normal to the generatrix of the conus.

Fig. 2 Shadow pattern of a parallel sample from crystals E.

Fig.3a-e Shadow patterns of perpendicular sample cut from crystals A to E, respectively.

Fig. 4 Enlarged shadow pattern for the perpendiculart sample cut from crystal E(α =108°).

Fig. 5 Enlarged shadow pattern for the perpendicular sample cut from crystal B(α =74°).

Fig. 6 Stereographic projection of the facet planes in a cubic crystal as viewed along <111>.

Fig.7a-e Photoelastic patterns of the sample shown in 3a to 3e, respectively.

REFERENCES

/1/ J.Basterfield, M.J.Prescott, B.Cockayne, J.mat.Science 3 (1968) 33

/2/ B.Cockayne, J.Cryst. Growth, 42 (1977) 413

/3/ Cz.Janusz, W.Jelenski, A.Niklas, J.Cryst.Growth, 57 (1982) 593

/4/ B.Cockayne, M.Chesswas, D.B.Gasson, J.Mat.Science 4 (1969) 450

/5/ D.T.Hurle, Sol.State Electr. 3 (1961) 37

/6/ B.Cockayne, Phylosophical Magazine 12 (119) (1965) 943

/7/ W.Bardsley, B.Cockayne, Crystal Growth (Suppl.to J.Phys.Chem.Solids), B 14 (1967) 109

/8/ R.F.Belt, R.C.Puttbach, D.A.Lepore, J.Cryst.Growth 13/14 (1972) 268

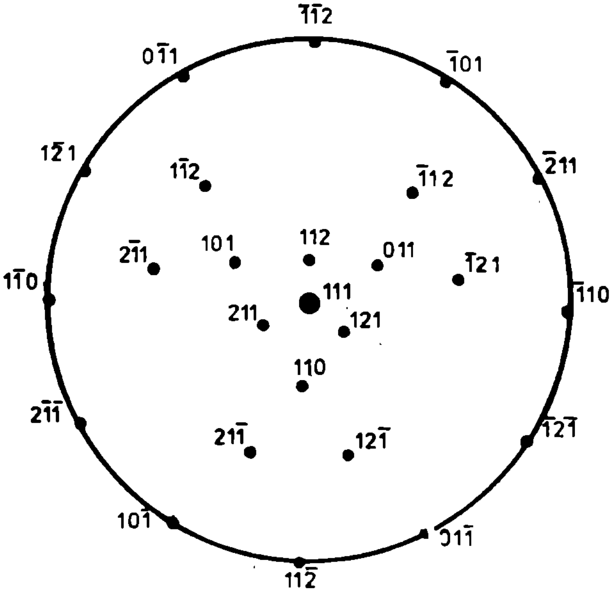

Fig. 6.

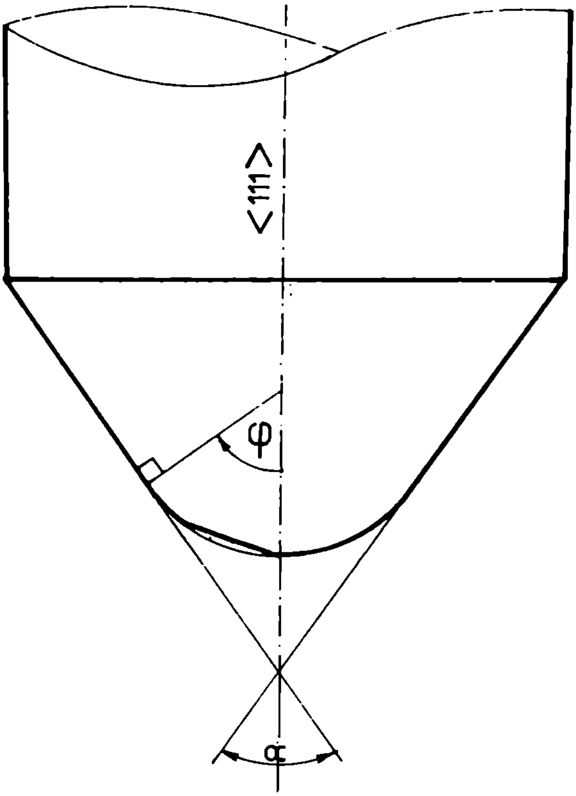

Fig. 1

Fig. 2


Fig.3.a

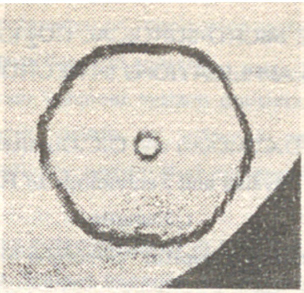
Fig.3.b

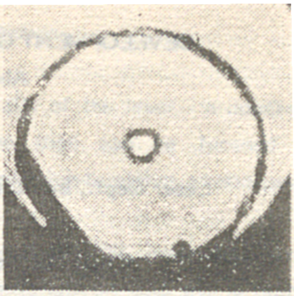
Fig.3.c

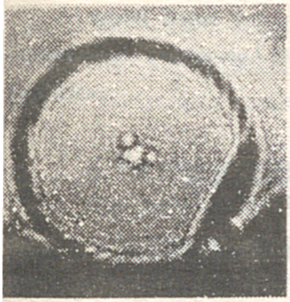
Fig.3.d


Fig.3.e.


Fig.4


Fig.5


Fig.7.a


Fig.7.b


Fig.7c.

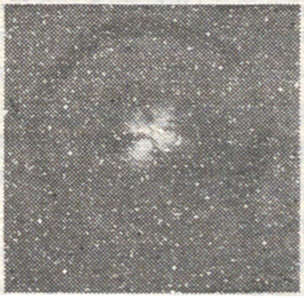
Fig.7.d

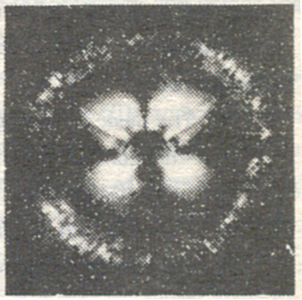

DEVELOPMENT OF THE MICRO-SURGICAL CO_2 LASER SCALPEL BILAS-10 AND ITS APPLICATIONS IN NEUROSURGERY

D.C.A.Dutu and D.C.Dumitras
Laser Dept., Institute for Physics and Technology of Radiation Devices, Bucharest
L.Danaila
Clinic for Neurosurgery, Hospital "Gheorghe Marinescu", Bucharest

1. Introduction

The carbon dioxide laser has been used to perform a wide variety of surgical procedures for many years. The first published surgical use of the CO_2 laser was by W.Z.Yahr and K.J.Strully /1/ in 1966.

The applications of the CO_2 laser in human experimental surgery began by S.Steller /2/with the palliative vaporization of malignant brain tumours in 1969.

Since that period the developing of the CO_2 laser surgical units has been progressed from year to year and laser scalpel has been used in virtually every surgical subspeciality.

With the development of suitable surgical instrumentation that fulfils the requirements of the clinical surgeon and designed to fit in with the physical conditions prevailing in the operating theatre, the present laser surgery shows signs of even more rapid progress and general acceptance as its applications and advantages in more and more fields of surgery are demonstrated.

The basic advantages can be summarized as follows:

- noncontact highly sterile surgery
- dry field, almost bloodless surgery
- easy access in confined areas
- a minimal marginal damage to tissues

- no electromagnetic interference on monitoring instrumentation
- minimal postoperative swelling and scarring.

As it is well known, a laser surgical system consists basically of the laser - a coherent source of intense monochromatic visible or infrared radiation that can be focused to submillimeter spot sizes, and a delivery system that conveys this radiation to either a hand-piece or a microscope attachment.

Out of the various systems currently used in medical practice, the CO_2 laser has proved itself as the most efficient laser scalpel because its infrared wavelength of 10.6 µm is highly absorbed in the living tissue (which includes between 75 to 95% water) and can produce the most effective tissue removal through evaporation.

Small tissue volumes are removed with single or multiple exposure pulses, while larger incisions are performed through progressive scans of the beam in the continuous mode of the operation.

2. The main specific features of a modern CO_2 laser scalpel

The main specific features of the modern CO_2 laser scalpels are as follows:

- the laser energy delivered in the operating area
- the power density in the focal spot
- the angular divergence and the transversal mode of the laser beam
- the efficiency of the interface between laser and patient
- the degree of safety ensured for surgeon and patient.

According to the definition in physics, the energy of a laser scalpel in the operating area is:

$$E = \int_0^t P dt \tag{1}$$

where P is the power in watts, t is the time in seconds and E is the energy in joules.

If the laser power is constant over the interaction time interval, the formula (1) will be more simple, namely

$$E = Pt. \tag{2}$$

Because the laser tissue incision and tissue removal is the result of tissue vaporization under the heat effect of the laser energy absorbed, the larger the output power or the longer the interaction time, the deeper will be the penetration into the irradiated tissue.

An illustration of the above observation can be obtained if we consider a 10 W CO_2 laser beam focused to 1 mm^2 impinging on the tissue. Since most tissues are about 80% water, we can assume in a first approximation that the irradiated system has the properties of water. Because the needed energy to transform 0.1 mm^3 of water initially at 37°C into steam at 100°C is about 0.25 joule, in the tissue exposed to vaporization a crater can be produced with 1 mm^2 cross-section and a depth of about 0.5 mm in approximately one tenth of a second.

The depth of penetration is proportional with the interaction time and the power density.

The power density is the power per unit area. For a uniform intensity distribution, it is calculated as P/A, where P is the power in Watt and A is the cross-section of the laser beam in cm^2. For the same output power, the power density is different for different beam sizes.

The smaller the focus spot, the higher the power density and the "sharper" the laser beam.

The size of the laser beam in the focal plane is directly dependent on the angular divergence and on the mode of the laser beam.

With respect to the optical laws, the size of the focal spot can be determined using the equation

$$D = F\theta \tag{3}$$

where D is the diameter of the spot, F is the focal length of the scalpel focusing lens and θ is the angular divergence (in radians) of the laser beam at the entrancy of the focusing lens.

As results from equation (3), there are two ways to increase the "sharpness" of the laser beam:

- to reduce the angular divergence of the laser beam
- and to use focusing lenses with shorter focal lengths in the "scalpel" (the endpiece of the radiation conveying system).

The mode of the laser beam is a parameter which describes the irradiance distribution in the laser beam cross-section.

The best beam mode is the fundamental mode, which has an irradiance distribution that decreases smoothly from the center to the edge of the beam, according to a Gaussian function.

This pattern which produces a single spot of light is also known under the name of TEMoo mode (Transverse Electric Magnetic).

The beam diameter in the laser operating in the TEMoo mode is defined as the diameter where the intensity decreases at 1/e of its maximum.

Because the TEMoo beam's angular divergence is the smallest possible, the output of the lasers used in surgical units is recommended to be in the fundamental mode TEMoo.

The use of the focused single mode laser beam as a surgical scalpel fulfils the general requirements of the noncontact surgery namely:

- a quick cut
- a fine cut line with sharp and clear edge.

For the application of laser beam in surgery, a special interface had to be developed between the laser and the patient, which was able to ensure the degrees of freedom required by the movement of the laser beam in the operating area.

This interface or the radiation conveying system have to be highly efficient in light transmission and at the same time with sufficient flexibility to various kinds of surgical operations.

Light conveying systems with efficiency higher than 70% are presently obtained using opto-mechanical articulated arms and optic fibers.

The main quality requirements for a light conveying system are:

- preservation of the laser beam's unique characteristics such as low angular divergence and fine coherence
- low transmission loss
- capability to transmit laser beams with high power density without damage to the system itself
- flexibility, adaptability and mobility
- handy appearance and size
- high quality focusing lens and availability of different focal lengths.

Another important feature of modern CO_2 laser scalpels refers to the degree of safety assured by the laser surgical unit for surgeon and patient.

A high degree of safety could be obtained if the laser surgical unit fulfils the safety requirements specified for electro-medical devices and laser apparata, and if the place where the laser beam will be applied in the operating area and the interaction time of the laser beam-living tissue is precisely controlled.

For many modern laser scalpels the positioning of the beam on the surgical area is accomplished by visible in-line laser beam (red or green) focused with the operating beam, with an accuracy better than ± 0.1 mm, while the interaction time is controlled by specialized electronic circuits with an accuracy better than 10%.

3. A technical review of the CO_2 laser scalpel BILAS 10

The CO_2 laser scalpel BILAS-10 was designed and built as an unitary (integrates) ensemble which consists of five main functionally modules, namely:

1 - the central laser unit

2 - the light conveying system

3 - the focusing head

4 - the electronic system for supplying, control and monitoring

5 - the mechanical structure which sustains the above mentioned four functional modules.

A block diagram of the CO_2 laser scalpel BILAS-10 is shown in Fig.1.

3.1. The central laser unit

The central laser unit includes a visualising low-power He-Ne laser and its high voltage power supply, a sealed-off medium power operating CO_2 laser, an electro-mechanical shutter which enables the emission control of the operating laser beam in the operating area, an opto-mechanical system for overlapping both laser beams on the same axis and a powermeter head for monitoring of the emitted operating beam.

The sealed-off CO_2 laser used in BILAS-10 has a maximum output power in the transverse mode TEMoo larger than 10 W and a lifetime which exceeds 2500 hours.

This CO_2 laser has an optimum design for single mode and long lifetime operation being the last type of medium power sealed-off CO_2 laser series LIR developed in the last fifteen years in the Laser Department of the Institute for Physics and Technology of Radiation Devices, Bucharest.

The CO_2 laser tube configuration is presented in Fig. 2 together with some dimensions in mm.

The bore diameter of the pyrex glass discharge tube is 7 mm and the total discharge length is 430 mm.

A water jacket for flowing tap water and a gas reservoir are both surrounding the plasma tube envelope.

To minimize gas clean-up by electrode sputtering and to shorten the discharge path, the electrodes were placed coaxially with the tube axis and were designed in the form of a hollow cylinder (anode) and hollow cone (cathode) with guard rings on the side of the discharge tube.

The conical shape of the cathode and the position along the tube axis prevent the mirror against the ionic bombardment.

The electrodes are made of nickel under a special technology of oxidation which has a direct contribution to the lifetime extension of the sealed-off CO_2 laser.

The laser tube is sealed by two internal mirrors that are attached to the tube terminals with epoxy. The tube is filled with an optimum mixture of CO_2, N_2, He, Xe and H_2 /3/, /4/ at a total pressure of about 32 torr.

The mirrors had a 19 mm diameter, one being spherical (1.5 m radius of curvature), totally reflecting (Cr + Au coating) made up of fused silica, and the other being dielectrically-coated flat germanium.

The transmission of the germanium mirror is about 20% and is near the optimum calculated value.

The optical configuration was chosen to ensure fundamental TEMoo mode operation, which is of primary importance for laser applications in surgery.

The mode selection criteria use the fact that by selecting appropriate values for the Fresnel number (that is for the tube bore diameter and for the cavity length) the diffraction loss for the TEM_{10} mode can be made great enough with respect to the available laser gain so as not to oscillate /5/.

In our case, the mirror spacing is 540 mm and the Fresnel number is 2. This involves a TEM_{10} loss to TEM_{00} loss ratio greater than 8.

The best optical configuration proved to be a half-symmetric cavity with g factors comprised in the (0.5 - 0.6) range which also ensures a minimum diffraction loss for the fundamental mode.

The divergence of the emitted laser beam is about 2.8 mrad and the spot waist on the output mirror is 4 mm.

The sealed-off CO_2 laser described above is used in the central laser unit to ensure the desired highly directionaly and intensive infrared operating beam, namely:

- output power in the transverse mode TEMoo ≥ 10 W $\pm$ 15%
- beam diameter at 1/e from the maximum power ≤ 4 mm
- divergence of the emitted beam 2.8 mrad

The second laser of the central laser unit is a small size 1 mW He-Ne laser whose red beam enable by coaxial and confocal processing with the infrared operating beam the accurate positioning on the surgical area.

The main technical parameters of the visualising He-Ne laser are:

- total length 310 mm
- external diameter 45 mm
- power ≥ 1 mW
- beam diameter at the output mirror of the laser approx. 2 mm
- beam divergence ∿ 2 mrad.

The coaxial overlapping of both laser beams is made with a two mirrors system which provide a double deflection with 90° of the He-Ne beam and the mixing of the beams.

Both mirrors are plane, one totally reflecting for $\lambda = 632.8$ nm made up of fused silica and the other one of germanium dielectrically antireflection coated for $\lambda = 10.6$ µm on both faces.

The adjustment of both mirrors is done by special three-axis adjustable aluminium holders.

Between the CO_2 laser and the mixing germanium mirror there is an electro-mechanical shutter which can control through a total reflecting movable copper mirror either the deflection of the infrared CO_2 laser beam on the radiometer head or to the exit of the central laser unit aperture.

When the shutter is off, the CO_2 laser beam is incident to the powermeter head and the power is monitored and when the shutter is on, the power is no more monitored and all the laser power becomes available to the entrancy aperture of the conveying system.

The operation of the electro-mechanical shutter is controlled in real time by an opto-electronic switch placed in the vecinity of the movable copper mirror.

To reduce the high voltage connections between the central laser unit and the electronic system for supplying, control and monitoring, the small size high voltage power supply of the He-Ne laser was also placed near the He-Ne laser in the central laser unit.

The central laser unit is placed horizontally on top of a foot-controlled hydraulic stack and can be translated 190 $\pm$ 5 mm in the vertical plane and rotated at an angle of 45° $\pm$ 3° in horizontal plane.

To control the operation of the laser devices from the central laser unit, its housing was equipped with two observation windows.

3.2. The light conveying system

Since in medical clinics it is not possible to move the patient in the laser beam like in many industrial laser applications it was necessary to develop a special interface between laser and patient - a light conveying system able to transmit the laser radiations with high efficiency and at the same time to have sufficient flexibility and facility to various kinds of surgical operations.

To fulfil these requirements, we have developed a very simple and efficient opto-mechanical articulated arm, which consists of special interchangeable mechanical mirror holders positioned at 45° on the beam direction and performing full rotations in a plane orthogonal to the beam direction.

The main features of the opto-mechanical articulated arm used in the construction of the CO_2 laser scalpel - BILAS 10, are:

- the efficiency at 10.6 μm > 75%
- six degrees of freedom
- very high adaptability, flexibility and mobility (through its modular structure)
- interchangeable endpiece attached to the articulated arm.

All the mirrors used in the opto-mechanical articulated arm are flat totally reflecting mirrors (Cr + Au coating) made up of fused silica.

3.3. The focusing head

The focusing head is a modular element placed at the end of the articulated arm which includes the laser beam focusing lens.

The scalpel is actually the endpiece attached to the articulated arm which includes either the focusing head and a hand-piece or the focusing head and a microscope attachement. The hand-piece is usually 10 - 20 mm shorter than the focal length of the lens.

The hand-piece is made up of stainless steel with a view to be suitable in the sterilization process.

Using focusing lenses of different focal lengths it is possible to control the size of the beam in the focal plane and the power density at the focal point.

Table 1 presents the dependence of the spot diameter and power density at the focal point of the CO_2 laser scalpel BILAS-10 (maximum output power 10 W, beam divergence 2.8 mrad) on the focal distance for three different focal lenses.

Table 1

F(mm)	150	200	250
$D = F\Theta$ (mm)	0.42	0.56	0.7
$P/A(KW/cm^2)$	7.2	4	2.6

Since the focusing lenses are made from single crystals of KCl or NaCl, a special care is necessary to protect them against the water vapours (special enclosure, special instructions for replacement a.s.o.).

3.4. The electronic system for supplying, control and monitoring

The electronic system for supplying, control and monitoring consists of all the electronic and electrical modules used to supply both laser devices and to control and monitor the main parameters of the laser scalpel, namely:

- the on/off control of the laser scalpel
- the output power of the operating laser beam
- the operation mode (CW-or pulsed with pulses of pre-established length)
- the presence of any failure (the absence of the electric energy, the absence of the tap water or a water flow rate lower than 1.5 l/min, the shutter blocked off or on, a wrong operation of the main timing circuit a.s.o) which stops the operation of the laser scalpel
- the emergency stop of the laser scalpel.

All the controls and monitoring elements are accessible from the front panel of the laser scalpel. A photograph of the BILAS-10 front panel is shown in Fig. 3.

The main part of the electronic system is the CO_2 laser high voltage, regulated current power supply which was specially designed to enable an efficient control of the emitted laser power, have a small volume and a very high efficiency.

To fulfil the above specified conditions we have developed a single transistor converter, which uses energy storage in the electric and magnetic field of an LC oscillating circuit.

The main ideas of this circuit and the detailed design considerations were described in a separate published paper /6/.

The current regulator stabilizes the laser emission against changes of gas mixture, pressure, coolant temperature, line voltage and power supply ripple.

The output power of the CO_2 laser can be controlled in a range which exceeds 60% of the maximum value by controlling the discharge current in the laser tube between 5 - 15 mA.

The installation has also special safety electronic circuits for control and opto-acoustic warning for the failure of the electronic system, against radiation hazard and faulty operating conditions.

3.5. The mechanical structure

The mechanical structure of the CO_2 laser scalpel BILAS-10 was designed with a view to fulfil the main ergonomic and functional conditions necessary for a portable and very versatile laser microsurgical system.

The direct access to every functional module and the modular structure ensure a very fast and easy service for the laser scalpel.

A photograph of the CO_2 laser scalpel BILAS-10 is shown in Fig. 4.

The laser scalpel can be transported by means of three all-direction wheels in the limits of the cooling and current supply system connections.

4. Experiments on the use of the CO_2 laser scalpel BILAS-10 in neurosurgery

At the 7-th Clinic for Neurosurgery of the Hospital "Gheorghe Marinescu" in Bucharest we have tested the CO_2 laser scalpel - BILAS 10 - developed in the Central Institute of Physics.

The laser scalpel was extensively used in a large number of cases and has clearly demonstrated its superiority as a cutting tool of the neural tissue.

During three months (from November 1st 1984 to January 31st 1985) we operated 21 patients. Six of them had hemispheric supratentorial tumours (2 temporal astrocytomas, 3 glioblastomas and 1 sarcom). After the extirpation of the tumours by classical methods, the focussed beam of the CO_2 laser at a power level of 4-10 W was used for the vaporization of the tumour fragments in the neighbourhood of the main arteries. To remove the tumour fragments from the remaining cavity walls and tumour portions situated near the critical areas (ventricles, basal ganglia) but far enough from the important arteries, the maximum laser power was used. The coagulation of the bleeding vessels was done by a defocused laser beam at a power level of 4-6 W.

At 2 patients with parasagittal meningiomas, the dissection of the tumour implantation basis on the upper longitudinal sinus was achieved in a mixed manner, both classically and with a focused or defocused laser beam at a power level which was varied between 4 and 10 W, function on the situation.

To achieve a complete obliteration of the lumen, the laser is used unfocused with the spot 2-4 times larger than the diameter of the vessel.

The small diameter arteries and the veins were coagulated by a defocused beam of 4-6 W, applied for 5-10 seconds by three, four times.

The removal of the tumour fragments which were infiltrating the bone was carried out at maximum focused output power.

In two cases of fusiform aneurysms of the median cerebral artery a pulsed defocused laser beam was used, with an irradiation of 3-6 seconds, to achieve a segmental constriction allowing a reduction in volume of the aneurysm and a good shrinking of the vessels. To minimize the tension of the aneurysm wall, distended by endoluminal pressure, intraoperative arterial hypotension was associated.

At a patient with cranial osteomyelitis and bone sechestrum and at another with encephalitis, the CO_2 laser was used at maximum power, with continuous irradiation, to obtain the sterilization of the operative field.

Another patient with chronic subdural hematome was irradiated at maximum laser power (10 W) for the section of dura mater and parietal capsule. The advantage of this procedure consists in the fact that both the section and the coagulation of the vessels at that level, were achieved at the same time.

At a patient with intraorbital tumour, the CO_2 laser was used at a power level of 3-5 W for the tumour vaporization near the optic nerve, and at a power level of 10 W for the sterilization of the frontal sinus opened during the operation.

In cerebellar tumours (1 meningioma of the cerebello-pontine angle, 2 acoustic neurinomas, 1 astrocytoma, 1 cerebellar metastasis, 1 vermis medulloblastoma) the laser was successfully used to remove the tumour fragments adherent to cranial nerves, to remaining cavity walls and near brain stem.

The laser was very useful in brain stem tumours (1 bulbopontine cystic astrocytoma) and in those which adhered to brain stem (1 ependimoma) or to the important vascular structures. The volume of these tumours was significantly reduced by a focused or defocused laser beam, with pulsed or continuous irradiation at a laser power level which varied between 4 and 10 W. After operation, none of these patients have passed away and the neurologic deficit was minimum.

Laser is definitely helpful in the operations where the tumours were situated deep and near critical areas requiring manipulation of the normal brain surrounding the tumour.

At these patients, the laser allows a more radical surgery than the traditional techniques and also a safer aggression on critical areas.

The use of CO_2 lasers is limited to such zones where the vascularization is quite poor. To obtain a complete effect (section, vaporization, coagulation and demolition of the tissue) it would be necessary to combine three different laser sources, that is a CO_2 laser, an ion argon laser and a Nd:YAG laser.

The main characteristics of the laser technique in neurosurgery are as follows:

1) the laser beam source is far enough from the operative field;

2) because there are no surgical instruments, the surgeon has a complete visual control on the operative field;

3) the energy is highly concentrated on the target, allowing a selective effect for the section, vaporization and coagulation of the tissue;

4) the thermal diffusion is very limited as compared with the monopolar or bipolar electrocoagulation, and consequently the side effects are considerably reduced;

5) experimentally, it was demonstrated that the laser produces a necrose 5 times more reduced than the electrocoagulation;

6) the mechanical manipulation of the surrounding healthy tissue is much reduced;

7) the hemostatic effect is often completely.

5. Conclusions

BILAS-10 is a portable CO_2 laser scalpel which has clearly demonstrated its superiority as a cutting tool of the biological tissues without physical contact and coincident mechanical trauma.

Through its carefully engineering, the CO_2 laser BILAS-10 fulfils all the safety conditions recommended for electro-medical devices and laser apparata.

The patient and the surgeon are protected against radiation hazard, including the case when the main timing circuit or/and the electro-mechanical shutter are out of operation.

Through its modular structure the CO_2 laser scalpel BILAS-10 can be quickly and easily modified and repaired.

The use of the CO_2 laser scalpel BILAS-10 in neurosurgery has demonstrated the following main advantages:

- there is no surgical instrument in the operative field to reduce the visual control in the operating area;

- the power control of the operating beam in the range 3 - 10 W and both modes of operation (cw and pulsed with pulses of pre-established length in the range 0.1 - 5 s) enable a selective effect for the section, vaporization and the coagulation of the neural tissue;

- the thermal diffusion is very limited compared with the monopolar or bipolar electrocoagulation and consequently the side effects are considerably reduced;

- as it was experimentally demonstrated the CO_2 laser produces a necrose 5 times more reduced than the electrocoagulation;

- the hemostatic effect is often completely.

REFERENCES

/1/ Yahr W.Z., Strully K.J., Blood vessel anastomosis by laser and other biomedical applications, J.Assoc.Adv.Med.Instrum. 1, 28-31 (1966)

/2/ Steller S., Experimental studies with the carbon dioxide laser as a neurosurgical instrument, Med.Biol.Eng., 8, 549-558 (1970)

/3/ D.C.Dumitras, D.C.Dutu, N.Comaniciu, V.Draganescu, Sealed-off CO_2 lasers, Rev.Roum.Phys., Tome 21, No.6, p.559-568 (1976)

/4/ D.C.Dumitras, D.C.Dutu, N.Comaniciu, V.Draganescu, The current dependence of the optimum hydrogen pressure in sealed-off CO_2 lasers, Rev.Roum.Phys., Tome 21, No.3, p.225-233 (1976)

/5/ T.S.Fahlen, Appl.Opt., 12, No. 10, 2381 (1973)

/6/ D.C.A.Dutu, D.C.Dumitras, High-speed regulated power supply for optovoltaic effect investigation in c.w. CO_2 lasers, Rev.Roum.Phys., Tome 27, No. 6-7, p.647-653 (1982)

FIGURE CAPTIONS

Fig. 1 The block diagram of the CO_2 laser scalpel BILAS-10

Fig. 2 The CO_2 laser tube configuration

Fig. 3 A photograph of the BILAS-10 front panel

Fig. 4 Photograph of the CO_2 laser scalpel BILAS-10

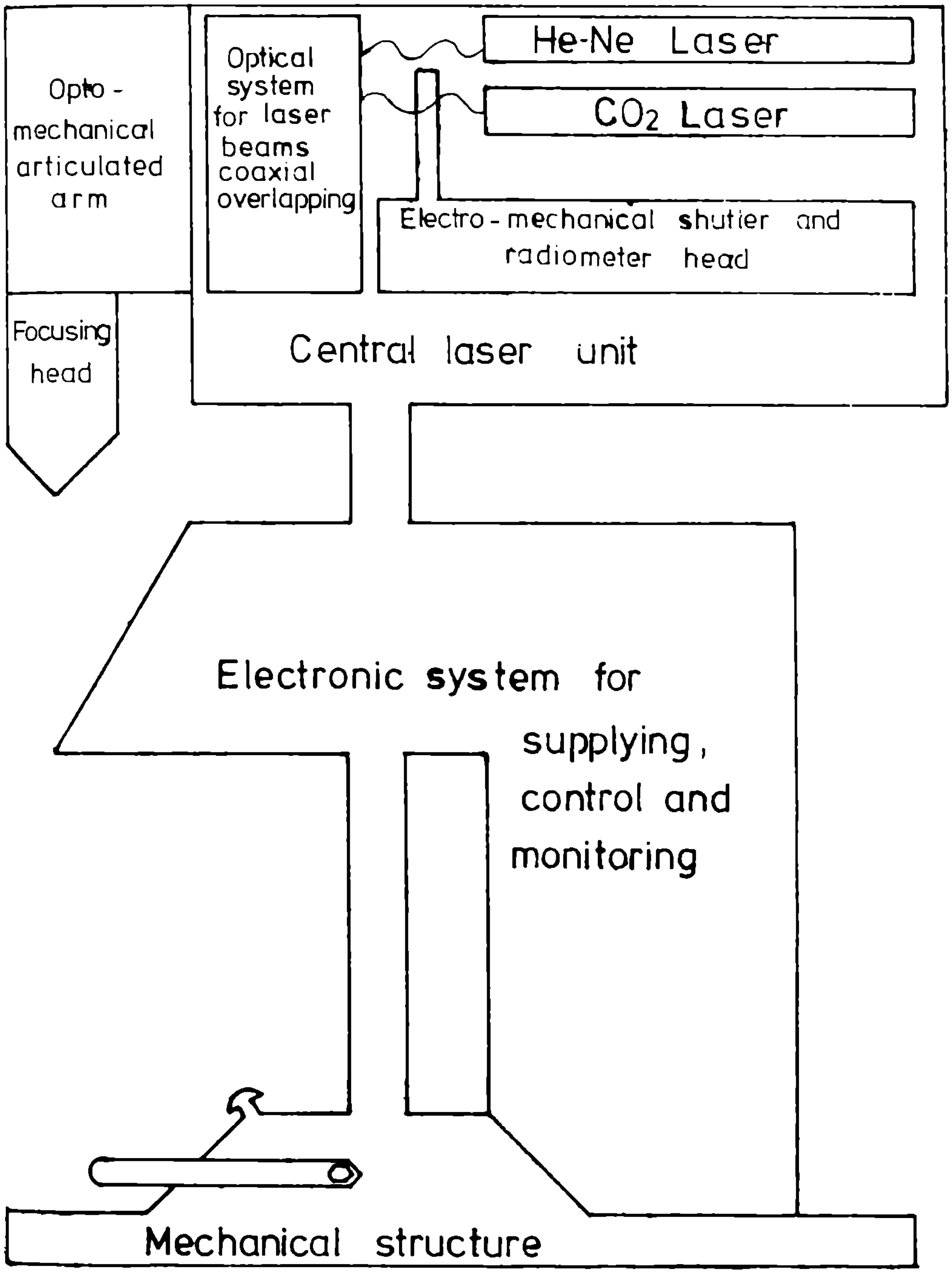
Opto-mechanical articulated arm
Optical system for laser beams coaxial overlapping
He-Ne Laser
CO_2 Laser
Electro-mechanical shutter and radiometer head
Focusing head
Central laser unit
Electronic system for supplying, control and monitoring
Mechanical structure

Fig. 1

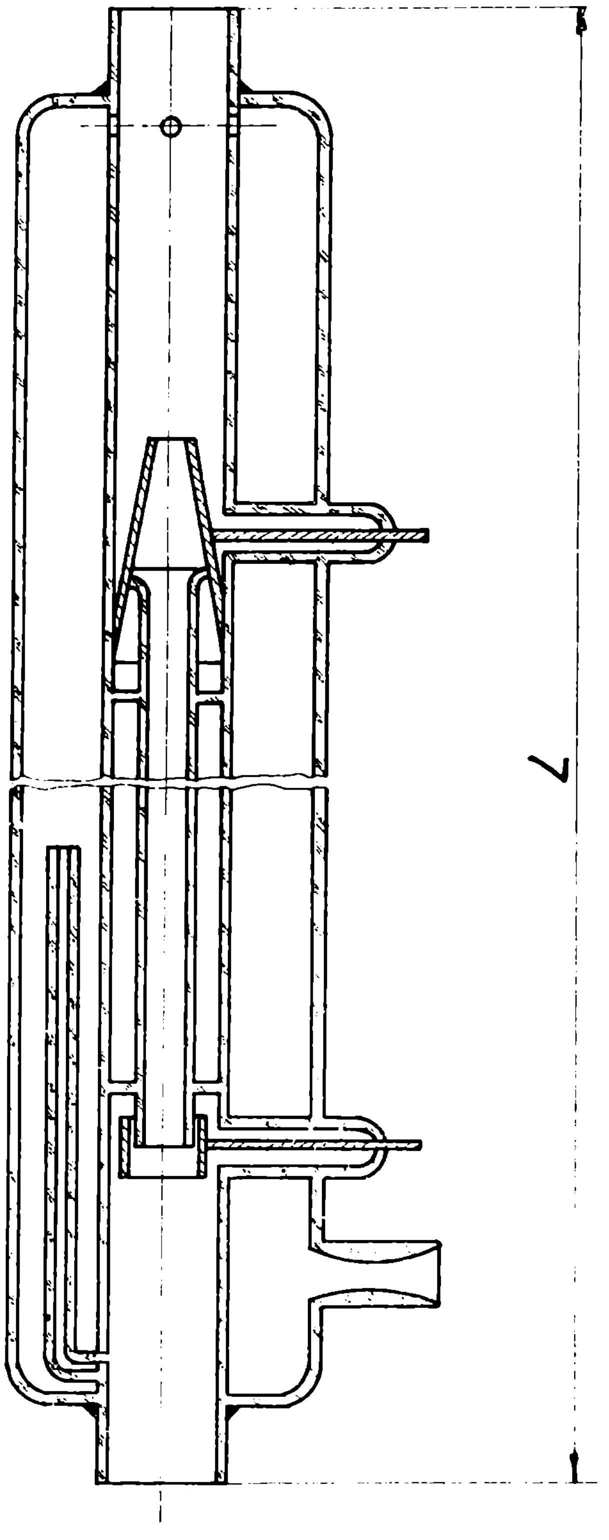

Fig. 2

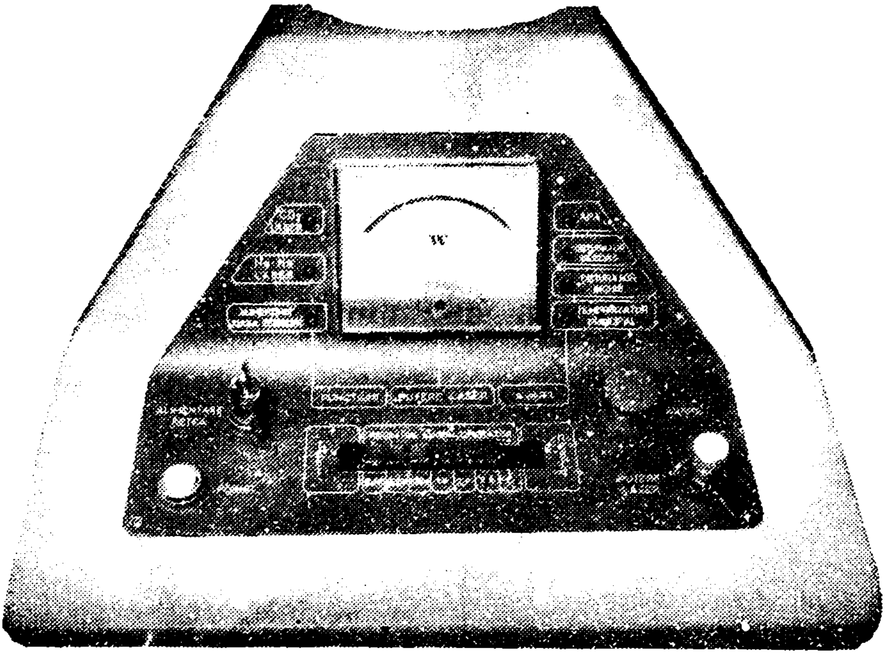

Fig.3

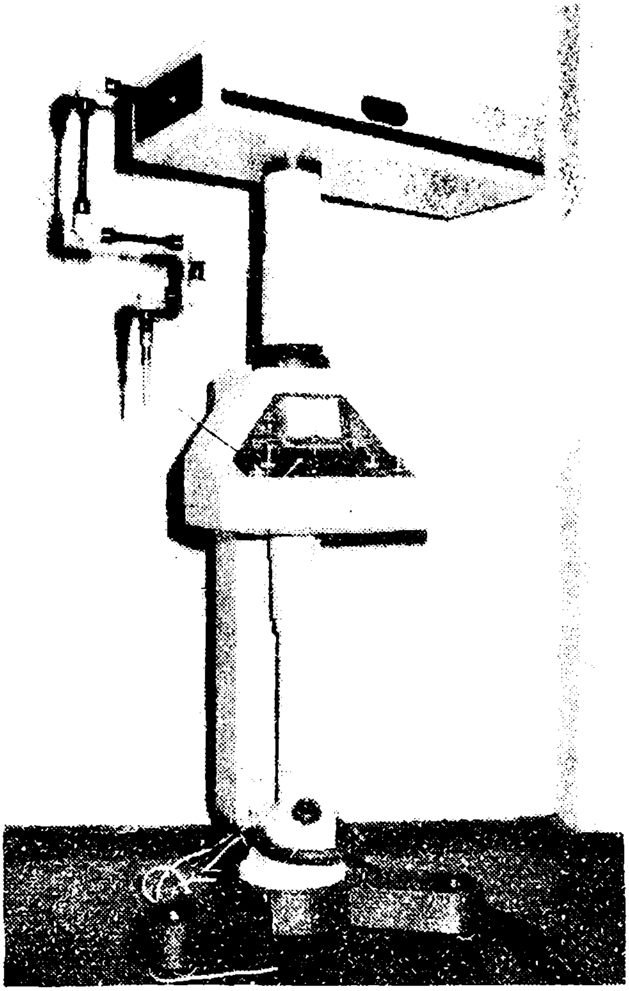

Fig.4

RESEARCH WORK IN HOLOGRAPHY AT THE PHYSICS DEPARTMENT OF THE POLYTECHNIC INSTITUTE OF BUCHAREST

I.Cucurezeanu, R.Chisleag, D.Popa, P.Suciu
Physics Department The Polytechnic Institute, Bucharest

The authors review some of their research in optical holography, started under the supervision of late professor Ion Agarbiceanu. The main contributions have been in the following areas: new hologram recording media, development of interferential hologram microscopes, new models for fringe interpretation in hologram interferometry, new applications of hologram interferometry, plasma diagnosis, holographic spectroscopy, manufacturing of holographic gratings and holographic optical processing.

The Physics Department at the Polytechnic Institute of Bucharest has an active research program in holography. The research activity has been directed to the following areas:

1) investigation of some crystalline substances to be used as recording materials in holography;

2) studies on the mechanical and thermal strains in some parts and devices;

3) studies of transparent objects by hologram interferometry;

4) vibration measurement;

5) investigations on the behaviour of photovoltaic solar cells;

6) manufacturing of holographic gratings;

7) development of techniques for the analysis of experimental data obtained by hologram interferometry.

Part of our activity was carried out in cooperation with the Laser and Holography Department of the Central Institute of Physics. The main areas of this work concern:

8) plasma diagnosis;

9) holographic spectroscopy;

10) optical data processing;

11) extension of sensitivity and spectral range in holographic interferometry and nondestructive testing.

1) Regarding the investigation of crystals used as recording materials in holography, we were interested in the silver chlorine doped with cooper ions /1-3/. It has been shown that this crystal can be used for recording holograms. A hologram is recorded in about 4 minutes using a 0.1 mW laser radiation. Thermal erasing of the hologram takes place after about 40 hours.

2) Measurements of mechanical and thermal strains in some machine parts by means of double-exposure hologram interferometry have been presented in papers /4,5/. Rotation angles of seconds and deflections of tenths of micrometer have been measured.

The temperature distribution in some electronic devices and semiconductors has been studied by various holographic methods. Paper /6/ presents the application of the double exposure hologram interferometry to the study of a transistor, type EFT 214 (fig.1), an integrated circuit, type µA 719 (fig.2) and a four-diode rectifying bridge, type RA 120 (fig.3). The suggested data analysis technique considers the fringes as isothermal curves. Under normal feeding conditions, the fringe spacing corresponds to a temperature difference of a few Kelvin (e.g. 3.6 K for the integrated circuit whose interferogram is given in fig.2). Moreover, the method permits the non-destructive identification of "hot-spots" developed in semiconductor devices during operation.

A new investigation technique called "the microscope hologram interferometry" has been introduced by the authors for the analysis of temperature distribution in some semiconductor structures having the size of the order of a millimetre or smaller. It allows an increase in the obtained quantity of information on a unit surface, and hence an increase in the accuracy of the obtained thermal maps of the investigated objects.

Indeed, according to /7/, the quantity of information I which can be obtained from an interferogram is given by:

$$I = f^2 m^2 \log_2 m \tag{1}$$

where f is the number of fringes considered on the visible object surface and m is the number of distinguishable zones on a fringe.

Using the microscope hologram interferometry technique, illustrated by the hologram recording (fig.4) and image reconstruction (fig.5) schemes, the quantity of information, I_M, will be /8/:

$$I_M = F^2 M^2 \log_2 M \cong \beta^2 I \cong \alpha^4 I \tag{2}$$

in which

$$F = \beta f \cong \alpha^2 f \tag{3}$$

where β is the axial magnification and α is the transverse magnification of the object.

Relevant experimental results /9-12/ are shown in fig. 6, 7 and 8.

Figure 6 shows the microscope hologram interferogram of a 2 N 3055 power transistor structure, generated by rest and normal feeding regimes. By examining this picture one can notice a normal operation of the structure (fringes appear on the feeding contacts and in their neighbourhood). The presence of the fringes and their distribution on the interferogram in fig.7 show an energy concentration in their particular place, hence a fault in the continuity of junction. The same interferogram shows no fringe parallel to this junction, meaning that the junction temperature is not significantly different from that of the neighbouring layers. Figure 8 shows the microscope hologram interferogram of a region belonging to the junction of a defect-free transistor of the same type, obtained at a much larger magnification. One can notice that the nonhomogeneities of the junction become visible. Instead of observing fringes parallel to the junction - as we should expect from the monotonous theoretical models - we notice many hot and cold spots on the junction.

The temperature gradient between two neigbouring isotherms (fringes) may be determined too. Let $\delta_1(\Delta t)$ be the temperature difference between two successive isotherms and $\delta_1(\Delta T)$ be the corresponding temperature difference on the magnified image of the object. Then the following equation holds:

$$\delta_1(\Delta T) \simeq \delta_1(\Delta t)/\beta \simeq \delta_1(\Delta)/\alpha^2 \tag{4}$$

Denoting by Δz the object surface displacement corresponding to the n-th fringe and by $\delta_1(\Delta z)$ - the displacement difference corresponding to two adjacent fringes, the hologram interferometry yields:

$$\delta_1(\Delta z) = d \cdot \xi \cdot z \cdot \delta_1(\Delta t) \tag{5}$$

and the microscope hologram interferometry yields

$$\delta_1(\Delta Z) \approx \beta \cdot d \cdot z \cdot \xi \cdot \delta_1(\Delta T) \tag{6}$$

where d is a constant ($d \leq 1$) dependent on the heat transfer in the sample, ξ is the coefficient of linear thermal expansion of the material, and z is the sample thickness.

In this case, for a silicon sample with thickness z = 0.2 mm and a linear expansion coefficient, $\xi = 7.6 \times 10^{-6} K^{-1}$, studied through hologram interferometry using a He-Ne laser with $\lambda = 632.8$ nm, placed normal to the illumination and observation wave vectors for $d = 1/2$, we obtain $\delta_1(\Delta t) \approx 400$ K. By means of microscope hologram interferometry, using a 20 x objective ($\alpha = 20$ and $\beta \approx 400$) we obtain $\delta_1(\Delta T) \simeq 1$ K.

This method may provide an experimental support for the statistical models of interpretation of thermal phenomena in the junctions of semiconductor devices besides its usefulness in nondestructive testing of semiconductor devices behaviour.

3) Studies of transparent objects by hologram interferometry have dealt with the determination of the variation $\Delta P(x,y)$ in a property of the object, e.g.: a) local change of the index of refraction, $\Delta n(x,y)$, for liquid crystal cell excited by currents with various frequencies (/13/ and fig.9a) or for a non-homogeneous optical glass (fig.9b); b) change of the molar concentration, $\Delta C(x,y)$ of a solved substance /15/; c) the molar concentration $C(x,y)$, of the new product formed in a mass transfer reactor /16/; d) local temperature difference, $\Delta T(x,y)$, during the thermal mixing in the storage tanks of solar power plants at different moments /17/or during the operation of air solar collectors as function of the profile of the absorbant surface

(/18/ and fig.10).

4) Time-average hologram interferometry techniques have been used in the study of vibration of various devices such as: a) telephone membranes /19/; b) membranes of pneumatic cells used in automatic control /20/; c) loudspeaker membranes /21/; d) delay relays; e) transformers; f) microdrivers etc. To give an example, we present the results of the study of a 9 cm diametre loudspeaker having a 3.5 ohm impedance. In order to determine the frequencies of interest, it was first studied by speckle interferometry. Then a steady excitation (of 35 mA (fig,11)) being applied it was studied by double exposure hologram interferometry in the second exposure.

The value of the set-up constant was C = 1.90 in the employed set-up, λ =0.633 µm, so that the bright fringe of p order apperared when the local deformation was L_p^b equal to:

$$L_p^b = p\,\frac{\lambda}{C} = p\ 0.333\ \mu\text{m}, \tag{5}$$

and the dark one where

$$L_p^d = (2p-1)\frac{\lambda}{2C} \tag{6}$$

The asymmetry of the membrane strain, as noticed from the photograph, even in the static regime shows a bad centering of the device. One can also notice undesired membrane local strains produced by the contacts of the coil connecting wires.

The membrane maximum deformation is ∿3.8 µm and the nonuniformity produced by the wire is ∿ 3 µm. Then the loudspeaker was studied by the time-average hologram interferometry, using the same value of the current and a frequency of 8.5 kHz (fig.12), getting deflections up to 0.5 µm. In the contrast to the circular fringes, which might be obtained under ideal conditions of membranes response, the study revealed a series of vibration modes characterized by patterns of axial symmetry and non-circular fringes. The role of wire insertions which has already been suggested by double exposure hologram interferometry, is obvious herein.

5) Simple or double exposure hologram interferometry has been succesfully used to study photovoltaic cells and modules /22-24/. Silicon photovoltaic cells, of 5 cm diameter, of V_1(p/n) and B_1(n/p) types were investigated, they were incapsulated or free and fed at U_{max} = 0.4 V and I_{max} = 0.25 A. These values are equivalents of those arising from normal illumination. Fig.13 shows a local deformation of the device surface (about 1/3 µm on a fringe spacing, normal on the surface) mainly due to the modification of the cell sandwich structure by defoliation (up to 3µm here) and less to the thermal expansion of the device.

Testing of different solar panels aimed at the identification of posible defect sources which might appear during operation. Panel quality and reliability depend on the correlation between thermal and mechanical properties of the materials used for window and support. Glass-aluminium panels proved to be more affected by the variation of environment parameters. The "hot spots" of the investigated modules (in fig.14, the small annular fringe on the right-down cell), the probable cause of major defects in operation have also been pointed out.

6) We mention the manufacture of holographic gratings /25/, under the provisions of a research contact between the Physics Department of the Polytechnical Institute of Bucharest and the Enterprise for Reserach Equipment and Devices in Bucharest. Grating of 40 x 40 mm^2 size and of 600, 1200 or 1800 lines/mm were manufactured.

To work by reflection, the grating surface was covered by an aluminium thin coating.

7) Important results have been achieved concerning some methods of fringe interpretation in hologram interferometry /17,26,27/. Among the authors' more important contributions we mention:

a) The unitary approach of the fringe interpretation problem, starting from a new equation for the phase difference:

$$d\varphi(\bar{r}) = d\left[\frac{n(\bar{r})\beta(\bar{r})\bar{K}(\bar{r})\bar{r}}{p}\right] \tag{7}$$

(see /17/, 4.6 where p is the shrinkage factor. This is a more general relationship than those known in the literature, which can be deduced from rel.7.

b) A new vector, the characteristic displacement vector L(r) is introduced by the equation:

$$\Omega(\bar{r}) = \bar{K}(\bar{r})\bar{L}(\bar{r}) \tag{8}$$

where Ω (r) is the fringe position function and K(r) is the sensitivity vector (see /17/, 5.1.2.), permitting the unitary interpretation of different kinds of movements (uniform, harmonically periodic, bistable).

c) The fringe function $\mathcal{M}$ (r, t), is better defined and a new notion is introduced (by relation (6.25) in /17/), the resolving power of hologram interferometry method. This makes possible to compare different holographic methods with one another and with other analyzing methods.

d) An original general model of fringe interpretation in hologram photoelasticity is presented in /17/, 6.9.

8) Concerning plasma diagnosis, a part of our work was related to the possibility of reconstruction of a three-dimensional refractive index field from multidirectional interferometric data /28/. That is why we have been interested to find some mew methods of inversion of the phase integral recorded by holographic interferometric methods /29/. The starting idea was to perform the analytic extension of the Radon transformation by help of an adequate constructed function

$$F(\alpha,\beta) = \sum_{n=0}^{\infty} \frac{1}{n!}(-1)^n \frac{d^n}{d\beta^n} (\beta)(\alpha-\beta)^n \tag{9}$$

where $\psi(\beta)$ represents an arbitrary function satisfying the following condition

$$\psi(\beta) \geq 0 \quad \int_{\alpha_1}^{\alpha_2} \psi(\beta)\,d\beta = 1 \quad \psi(\beta) \in \mathcal{C}^{\infty}(\alpha_1,\alpha_2) \quad n \leq N, \ \psi^{(n)}(\beta)=0, \alpha \in (\alpha_1,\alpha_2) \quad \beta = \alpha_1, \alpha_2$$

being the measuring interval, followed by a double Fourier transformation. Then we obtain for the refractive index field

$$f(x,y) = \iint_{-\infty}^{+\infty} \exp[2\pi i(x\xi+y\eta)] \int_{\alpha_1}^{\alpha_2} F(\alpha,\beta)\,G_s(\beta)\,d\beta\,d\xi\,d\eta \tag{10}$$

where

$$G_s(\beta) = \int_{-\infty}^{+\infty} \phi(r,\beta)\,e^{-ir\beta}\,dr \quad \phi(r,\alpha) = \int_{P_{r,\alpha}} f(x,y)\,dl \tag{11}$$

$\phi(r,\alpha)$ being the measured phase integral along the $P_{r,\alpha}$ direction. The whole calculation has to be performed separately for each z plane. The whole calculation can be performed in an optical set-up by an original method. So, it is possible to obtain the complete refractive index field from an interferometric recording of limited observing angle interval $(\alpha_1, \alpha_2) < \pi$ using only optical data processing.

In order to enhance the sensitivity for separate evaluations of electron and gas contributions we were also concerned with the spectral rage extension in the U.V. /30/ and I.R. /31/, as well as with reference wave modulation methods /32/.

An important effort for the theoretical systematization and experimental development of specific methods started by employing the spatial frequency multiplexing /33/ . One of the results obtained in this direction was phase object investigation by interferometric, schlieren and shadow methods using the same holographic plate /37/. The corroboration of the simultaneous measurements achieved by these three methods, with an adequate sensitivity which can be largely optimized by the reconstructing set-up, can be very useful in plasma and generally in phase object diagnosis.

9) Another research direction still related to plasma diagnosis is given by holographic spectroscopy. Our principal results refer to the investigation of the specific character of resolution power in holographic spectroscopy and the utillization of the redundant axis of the spectrogram /34/. Thus it might be possible to enhance the resolving power of the spectrogram by an order of magnitude or to record not only the holographic spectrogram of one same point but of a whole axis on one holographic plate.

10. Hologram interferometry in the Fourier plane has been one of our principal research direction in the last years. First of all, we had in view the development of the theoretical basis /35/, the diversification of the experimental methods and the further elaboration of the theory in order to apply it to phase objects of interest /36/, to the vibration analysis /37/ to enlarge the sensitivity and to take under control the measurement errors /38/, as well as to take advantage from previous results as with reference wave modulation /36/. One difficult problem was raised

by the inversion of the phase integral necessary for phase object investigation, solved under some restricting conditions /39/ by the extension of our previous results /28, 29, 36/.

One possibility for the experimental set-up is presented in fig.15. The local object deformation vector r_0 with components Δx, Δy, Δz is recorded by means of a reference wave R on the holographic plate H. Using the reconstructing wave C, each object point is selected and investigated in the Fourier plane, FP, where the fringe system is described by equation:

$$\frac{K\Delta_z}{2f'^2}(x_{nf}^2+y_{nf}^2) + \frac{K}{f}(x_{nf}\Delta x+y_{nf}\Delta y) = 2n\pi, \quad n \in N \tag{12}$$

which represents a set of concentric circles, centered in $y_{of} = f\frac{a}{c}$, where $a = \sqrt{\Delta x^2 + \Delta y^2}$ is the in-plane deformation and $c = \Delta z$ is the out-of-plane deformation. Measuring y_{of} and the diameter of one circle we obtain Δx, Δy, Δz for each object point.

For vibration analysis n has to be replaced by $\frac{p_n}{2\pi}$, p_n satisfying ec. $J_0(P_n) = 0$ where J_0 is the 0th order Bessel function.

For phase object of refractive index distribution f(x,y,z), the object plane will be like a diffusing surface, the local deformation vector, $r_0(\xi_i, \eta_i)$, describing the position of the image point (virtual object point for the second recording), (fig.16) being related to f(x,y,z) by eq.:

$$\eta_i = \int_0^\eta [f(\eta)-1]d\eta \qquad \xi_i = \int_0^{\eta_1}\left[\int_\eta^\eta \frac{1}{f}|\nabla f|\sin\beta d\eta\right]d\eta \tag{13}$$

Now r_0 being function of the observation direction, eq.12 does not represent any more a set of concentric circles and a phase difference $\Delta\phi = 2K\eta_i$ has to be added. Then η_1 and ξ_1 can be obtained from eq.:

$$\eta_i b_\eta + \xi_i b_\xi = m\lambda,$$

$$b_\eta = 2 + \frac{3}{2}\sin\alpha\ \mathrm{tg}\,\alpha, \quad b = \frac{\sin}{2}\left(3 - \frac{1}{\cos^2\alpha}\right) \tag{14}$$

by goniometric measurements of η for at least 2 different α values.

11) Nondestructive testing by holographic interferometry /40/ took our attention in order to eliminate parasite object displacement, to optimize the recording methods, to enable us to fulfil recordings under surrounding light and facilitate final data evaluation. Some of these methods took advantage of electronic data processing on TV recording systems /41/. All these results were partially stimulated and largely applied to solve several problems raised by our industry.

REFERENCES

/1/ I.Cucurezeanu, P.Suciu, P.Sterian, V.Ghiordanescu, Sesiunea IPB, 21-23 XII (1972)

/2/ I.Cucurezeanu, P.Suciu, P.Sterian, V.Ghiordanescu, Studii si cercetari de fizica, 25, 649 (1973)

/3/ P.Suciu, I.Cucurezeanu, P.Sterian, V.Ghiordanescu, Rev. Roum. Phys., 18, 685 (1973)

/4/ I.Cucurezeanu, P.Suciu, R.Chisleag, Volumul sesiunii stiintifice "Tehnologii si metode moderne de calcul in industria constructoare de masini", IPB, noiembrie 1974

/5/ I.Cucurezeanu, P.Suciu, R.Chisleag, St. si Cer. de Mec. Aplicata, 36, 593 (1977)

/6/ P.Suciu, R.Chisleag, I.Cucurezeanu, Bul. I.P.B., 39, 19(1977)

/7/ I.Cucurezeanu, R.Chisleag, P.Suciu, Feingerätetechnik (Berlin), 27, 537 (1978)

/8/ R.Chisleag, P.Suciu, I.Cucurezeanu, Optics Communications, 39, 351(1981)

/9/ P.Suciu, I.Cucurezeanu, R.Chisleag, Sesiunea St. ICEFIZ, Iunie 1976

/10/ R.Chisleag, I.Cucurezeanu, P.Suciu, Col.Nat.Opt., iunie 1978

/11/ I.Cucurezeanu, R.Chisleag, P.Suciu, A.Cicei, Rev.Roum.Phys., 27, 677(1982)

/12/ I.Cucurezeanu, R.Chisleag, P.Suciu, A XXVI-a Ses.Com.St.Univ. Galati, Oct. 1982

/13/ I.M.Popescu, I.Sofron, P.Sterian, R.Chisleag, Bul.I.P.B., 12, 23 (1979)

/14/ P.Suciu, J.Maurer, N.Luca, I.Cucurezeanu, Col.Nat. Opt., oct. 1980

/15/ R.Chisleag, R.Cicei, Ses.St., Inst.Petrol si Gaze Ploiesti, dec.1978

/16/ I.Cucurezeanu, I.Chisleag, J.Duta, "Internat.Conf.and School - Laser and Appl." - LAICS, Bucharest, 1982

/17/ I.Cucurezeanu, R.Chisleag, P.Suciu, D.Borza, "Aplicatii ale holografiei optice", Ed.Tehnica, 1984, p.204

/18/ V.Fara, R.Grigorescu, D.Cecan, V.Badescu, R.Chisleag, St.Cerc.Fiz., 33, 101 (1981)

/19/ R.Chisleag, A.Cicei, Metrologia aplicata, 23, 179 (1976)

/20/ R.Chisleag, Gh.Copot, A.Cicei, Colocviul National de Optica, iunie 1978

/21/ R.Chisleag, A.Cicei, Anal.St.Univ.Iasi, XXVI, 1980, Sectiunea Ib, Fizica, p.63-70

/22/ I.Cucurezeanu, R.Chisleag, N.Rosu, Ses.St. IPB, 1984

/23/ I.Cucurezeanu, R.Chisleag, N.Rosu, C.Popescu, Col.Nat.Optica, iunie 1984

/24/ I.Cucurezeanu, R.Chisleag, N.Rosu, R.Grigorescu, "Progrese in fizica", oct.1984, Sibiu

/25/ I.Cucurezeanu, R.Chisleag, N.Rosu, E.Carbunescu, Ses.Jubiliara Com.St. a IPB, dec. 1981

/26/ I.Cucurezeanu, R.Chisleag, P.Suciu, Ses.St. "Tehnologii si metode moderne de calcul in industria constructoare de masini", noiembrie 1974

/27/ I.Cucurezeanu, R.Chisleag, P.Suciu, St.si Cer.Mec.Apl., 36, 145(1977)

/28/ D.Popa, V.I.Vlad., J.Maurer, C.Popa, "A new method for the reconstruction of three - dimensional refractive index field from multidirectional interferometric data", LAICS 82, Bucharest

/29/ D.Popa, V.I.Vlad., J.Maurer, Noi metode de inversie a integralei de faza in interferometria holografica, Ses.St.Jubiliara IPB, 1981

/30/ V.I.Vlad, M.V.Udrea, D.Popa, U.V. pulsed interferometry and holography in nsec range using a N_2 laser, the X-th Conf. of High Speed Photography and Photonics, Moscow, 1924(1980); Rev.Roum,Phys., 26, nr.6, 565 (1981)

/31/ V.Vlad, D.Popa, Recent extension of holographic interferometry, Lecture LAICS'82, Bucharest

/32/ V.I.Vlad, D.Popa, General relativity and gravit. proceed., pag. 239 (1980)

/33/ D.Popa, V.I.Vlad, I.M.Popescu, P.Suciu, C.Popa, J.Maurer, Holographic interferometry fron the point of view of spatial frequency multiplexing, LAICS 82, Bucharest

/34/ D.Popa, V.I.Vlad, I.M.Popescu, C.Popa, J.Maurer, Some developments of holographic spectrscopy, LAICS 82, Bucharest

/35/ D.Popa, V.I.Vlad, I.M.Popescu, J.Maurer, C.Popa, Interferometria holografica in plan Fourier, Ses.St.Jub. IPB, (1981) Bucuresti

/36/ D.Popa, V.I.Vlad, I.M.Popescu, J.Maurer, C.Popa, "Phase onjects diagnosis by holographic interferometry in the Fourier plane", LAICS 82, Bucharest

/37/ V.I.Vlad, D.Popa, Rev.Roum.Phys. 27, nr.6-7, 685 (1982), Proceed.Int.Conf.on Holographic Nondestructive Testing, Dubrovnik (1982)

/38/ D.Popa, "Contributii la dezvoltarea unor metode optice noi de diagnosticare a plasmei", teza de doctorat, Institutul Central de Fizica, 1983

/39/ D.Popa, I.M.Popescu, J.Maurer, C.Popa, E.Hriatiuc, Inversia integralelor de faza in I.H.F., Conf.Nat.Fizica, Bucuresti 1982

/40/ V.I.Vlad, D.Popa, Interferometria holografica aplicata in controlul nedistructiv, Lucr.Simp.Nat. de Tensometrie, vol.2, p.407 (1977)

/41/ V.I.Vlad, D.Popa, R.Zaciu, C.Capatina, Al 2-lea Sim.Nat. de Tensiometrie, vol.A, p.101, Cluj, (1980); Raport 20-79-27, IFTAR.

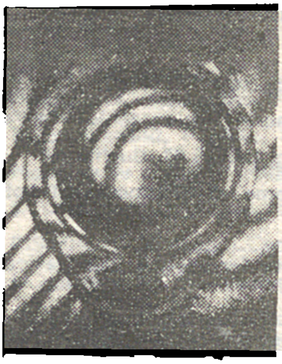

Fig.1

Fig.2

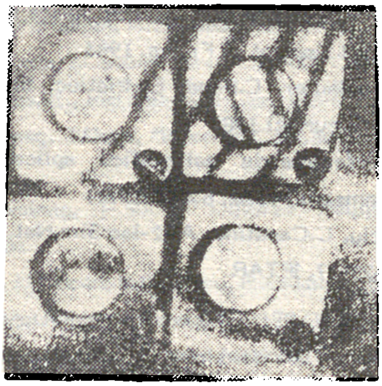

Fig. 3

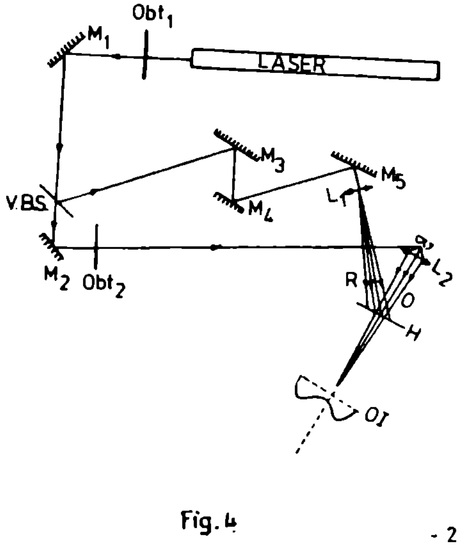

Fig. 4

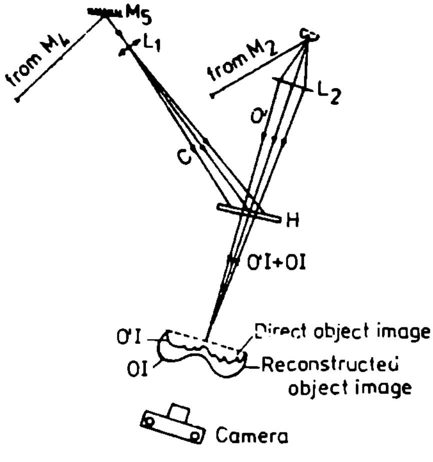

Fig.5

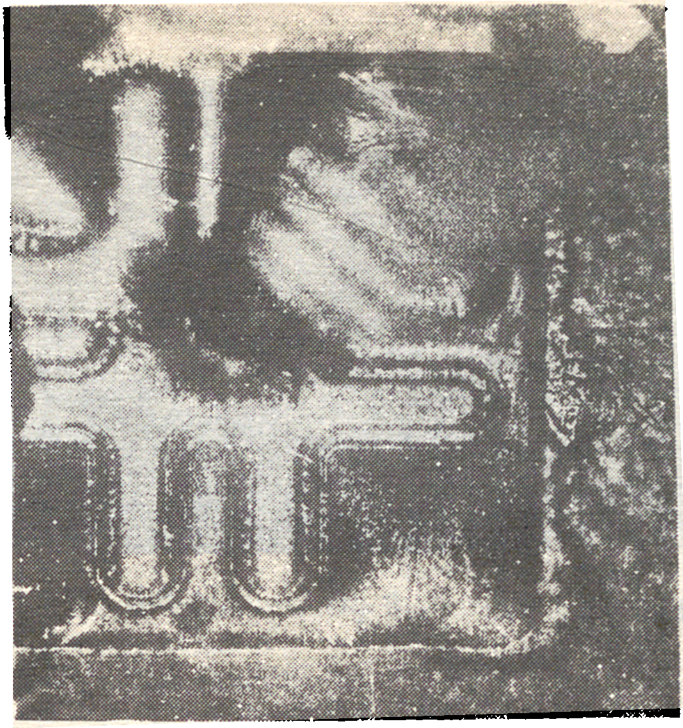

Fig. 6

Fig. 7

Fig. 8

Fig.9 a

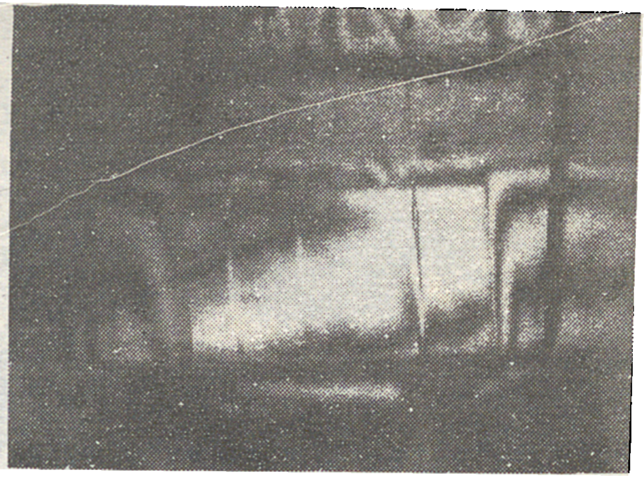

Fig 9 b

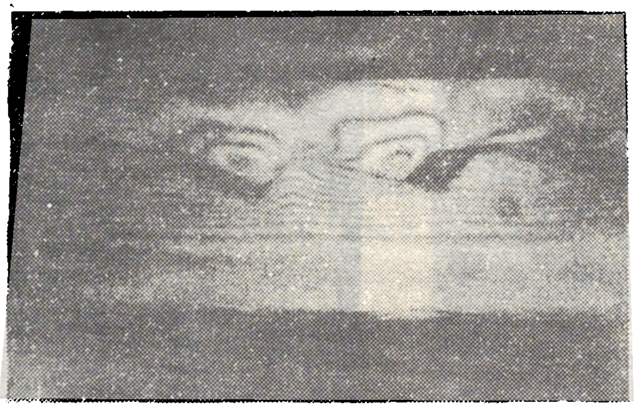

Fig. 10

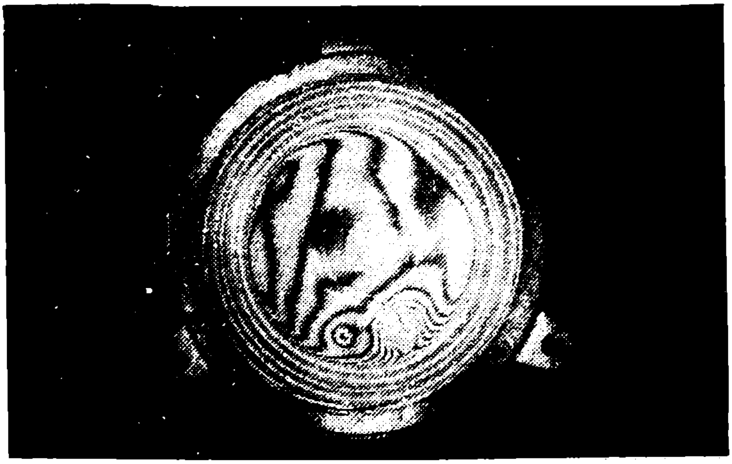

Fig. 11

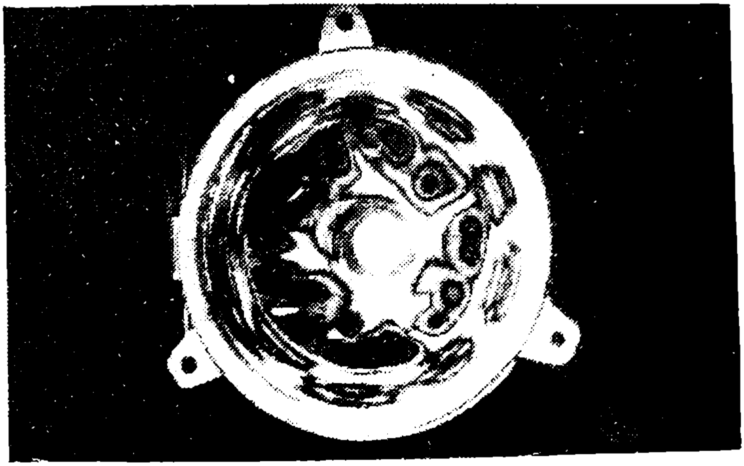

Fig. 12

Fig.13

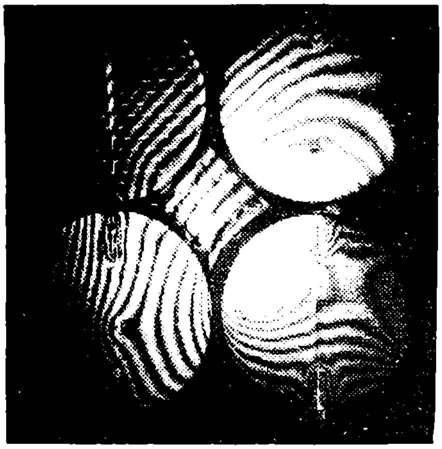

Fig.14

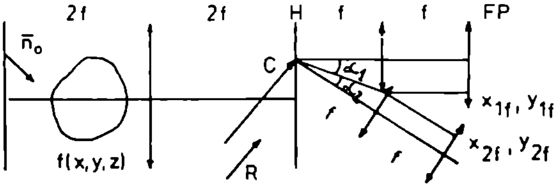

Fig. 15

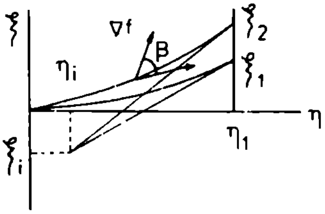

Fig.16

SINGLE MODE OPERATION OF A CO_2-HYBRID LASER

H.Albrecht*, R.Alexandrescu, I.Chis, D.Dragulinescu, C.Grigoriu,
Z.Morjan, W.Radloff*
Central Institute of Physics, Bucharest, ROMANIA
*Central Institute of Optics and Spectroscopy, Berlin, G.D.R.

The single mode performances of CO_2-hybrid laser are reported. Single longitudinal and single transverse mode have been achieved. Results on the output shape and delay time are presented.

1. Introduction

The spectral purity of a TEA-CO_2 laser is important feature in some applications like the multiphoton dissociation of molecules, where very good frequency selection must be achieved in order to obtain efficient processes /1/. Moreover, a well defined power in the laser pulse and the availability of smooth high power CO_2 laser pulses provide an easier interpretation of many nonlinear optical phenomena in gases.

As is already known the TEA-CO_2 laser pulse is usually far from monochromatic. Besides the possibility of operation on a number of rotation lines, there are many transverse and longitudinal modes in a given line which can oscillate as a result of the large gain width due to pressure broadening. The gain width in high-pressure discharge is very large (about 3GHz atmospheric pressure) in comparison to the mode spacing (the longitudinal modes are usually 50-150 MHz) apart, while the transverse modes are tipically separated by about 15 MHz). Therefore, the output pulse exhibits a strong modulation, resulting from beats between different cavity modes.

A technique often used to supress high-order transverse modes consists in introducing an aperture into the laser cavity, which allows for the operation in the lowest order transverse mode, the gaussian TEM_{00} mode.

The longitudinal mode selection is a more difficult problem /3,4/. The laser can not be made sufficiently short so that the longitudinal mode spacing $\nu_0 = \frac{c}{2L}$ becomes much greater than the gain-width. One approach is to introduce a frequency dependent loss into the cavity such as a grating; this method can be used to select the laser rotational lines does not provide sufficient dispersion to select the longitudinal mode.

Another approach is to insert a continous wave low-pressure CO_2 laser into the TEA-CO_2 laser cavity, known as the hybryd CO_2 laser technique. By inserting a low-pressure Doppler broadened gain tube (gain width about 60 MHz) a significant increase in gain for the one longitudinal mode inside the narrow gain profile of the low pressure section will result. The single longitudinal mode radiation already present in the cavity, generated by the low-pressure tube builds up when the electrical discharge in the high-pressure sections begins, so that the pulse will lack the characteristic gain-switched peak.

In the following section, the detailed description of our experimental arrangement for the hybrid laser will be given, together with the measurements concerning laser pulse characteristic parameters.

2. Experimental arrangement

The experimental configuration employed for measurements of the characteristic parameters of the hybrid laser is shown in fig.1.

The active medium consisted of high-pressure stage and a low-pressure one. The high pressure stage was a TEA CO_2 laser (Lamberton-Pearson) comprising matched uniform field profile electrodes defining an active volume of 8 x 10 x 200 mm^3.A 8.4 nF capacitor charged at 20÷30 kV was used for excitation. The TEA stage was separated from the low pressure stage by a NaCl Brewster angle window. The low-pressure discharge (40 cm length between electrodes) filled a glass tube with an internal diameter of 18 mm, operating with a CO_2-N_2-He mixture 1-1-4 at a total pressure of 18 torr and 15 mA current.

The resonator consisted of a 90% reflecting plane germanium output coupler a 4 m-radius of curvature gold mirror. The cavity length was fixed at 135 cm with a longitudinal mode separation of about 111 MHz. Single transverse mode operation (TEM_{00}) has been achieved by inserting an ajustable iris near the output coupler.

The output of TEA laser was measured simultaneously with a germanium photon-drag detector (rise time under 1 ns) giving the pulse shape and a pyroelectric joulemeter giving the laser energy. In order to measure the delay time between the TEA excitation current laser pulse a special coaxial current shunt with a rise time of 2 ns was used. The line emission of the laser was recorded by an IR grating monochromator D 330/D 331 - KM 11 together with a pyroelectric detector and a low-noise amplifier. The power of the CW laser was measured with a GR 201 powermeter.

3. Experimental results

The first part of the output pulse from multimode free-running TEA laser is illustrated in fig.2. One can see a modulated emission as a result of beating between longitudinal and transverse modes (TEM_{nmq}). The spacing between the modulation peaks, about 9 ns, agreed with the 2 L/c cavity transit time. The laser pulse displayed on 500 MHz oscilloscope shows that the modulation is produced by beating 4 longitudinal modes. The supplemental modulation of the envelope is produced by transverse modes beating.

Figure 3 shows the typical pulse shape of the TEA laser operating on TEM_{00} (unwanted transverse modes were supressed by decreasing the diameter of the aperture).

With the low-pressure CO_2 section delivering about 2.5 W (without any aperture in the resonator) a single longitudinal mode (SLM) operation, but still TEM_{nm}, was achieved, fig.4. One can observe a lower frequency modulation as a result of the transverse mode beating.

Finally, with a smaller aperture we achieved single transverse mode (SLSTM) operation of the hybrid laser, fig.5. It is to be noted that the operation of the hybrid laser was always on P20 of the 10.6 µm band. The peak power in SLSTM regime is 33% smaller then in the normal TEA laser operation. The output pulse energy was of a maximum 75 mJ in the multimode regime (mixture 1-1-4, voltage 30kV). in SLSTM regime the output energy descrease 26 mJ (aperture diameter 7 mm, placed at 10 cm from the output coupler).

The results concerning the delay time between the beginning of the current pulse and the beginning of the TEA laser output pulse, fig.6, are presented in table I.

TABLE I

		Delay time (ns)					
Mixture		1-1-8			1-1-4		
Operating regime		Multimode	SLM	SLSTM	Multimode	SLM	SLSTM
Charging	21	1460	560	700	-	-	-
voltage	24	1440	530	690	1080	510	610
(kV)	27	1340	480	670	990	440	550
	30	-	-	-	940	410	430

On can see that the delay was decreased by the CW laser operation. In SLSTM regim the delay is bigger than in SLM regime. In our experimental set-up we achieved SLSTM operation within a range of 10 mW - 2.5 W laser power.

REFERENCES

/1/ Letokhov, V.S., "Nonlinear laser chemistry", Springer Verlag, Berlin, Heidelberg, New York, (1983)

/2/ Crooker A. and Lamberton, H.M. "Electron.Lett., 7, 272 (1971)

/3/ Gondhalekar, A., Holtzhauser E.,Heckenberg, N.R.: Phys.Lett., 46A, 229 (1973)

/4/ Gondhalekar, A., Heckenberg, N.R., Holtzhauser E.,: J.Q.El., QE11, 103 (1975)

/5/ Girard A.: Opt.Comm., 11, 346 (1974)

/6/ Bruneau, J.L.:Opt.Comm., 41, 443 (1982)

FIGURE CAPTION

Fig. 1 The experimental set-up of configuration; the TEA-CO_2 laser: C = 8.4 nF, P = 1 atm.; the CW laser: 15 mA, CO_2-N_2-He/ 1-1-4, P = 18 torr; Photon - drag detector: Rofin 7415; Energymeter ED-200 Gen-Tek; Oscilloscope Tek 466; Monochromator D-330/331-KM 11; Powermeter CR 201; Pyroelectric detector 200 V/W; Low noise amplifier Brookdeal 450; Current shunt 2 mOhm

Fig. 2 The multimode output free running TEA-CO_2 laser pulse; 40 ns/div., 10 mV/div.

Fig. 3 The output TEA-CO_2 laser pulse in single transverse mode; 40 ns/div., 10 mV/div.

Fig. 4 The output hybrid laser pulse in single longitudinal mode; 40 ns/div., 10 mV/div.

Fig. 5 The laser pulse in single longitudinal and single transverse (TEM_{00}) mode; 40 ns/div., 10 mV/div.

Fig. 6 The discharge current pulse and output laser pulse sinumtaneously recorded for the delay time measurements; 200 A/div., 10 mV/div., 200 ns/div.

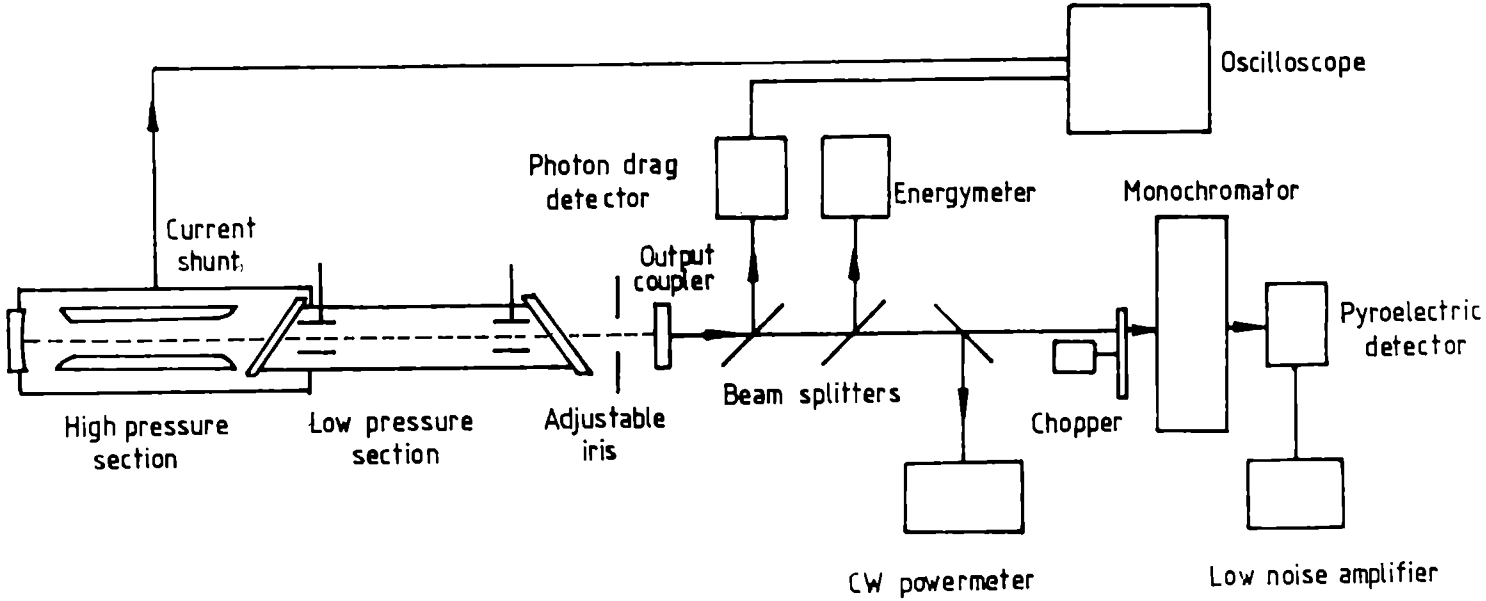
Oscilloscope
Photon drag detector
Energymeter
Monochromator
Current shunt
Output coupler
Pyroelectric detector
High pressure section
Low pressure section
Adjustable iris
Beam splitters
Chopper
CW powermeter
Low noise amplifier

fig. 1

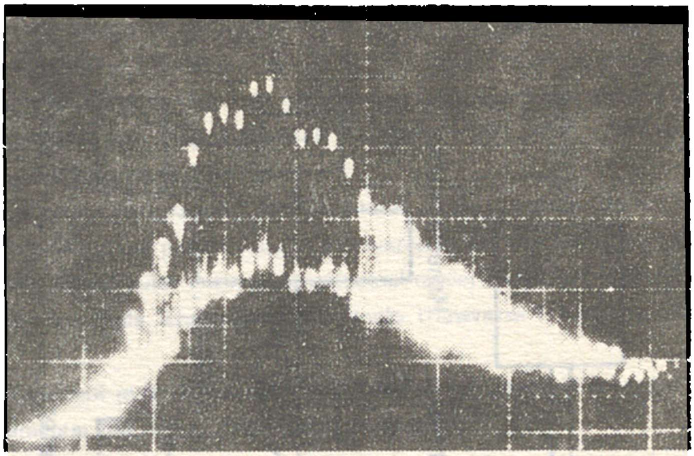

fig.2

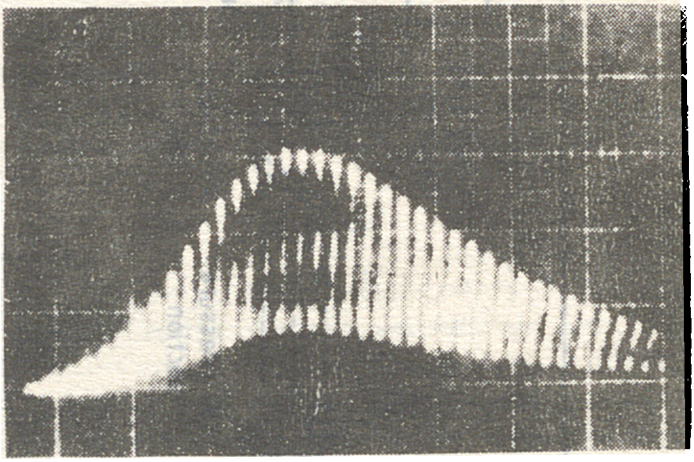

fig.3

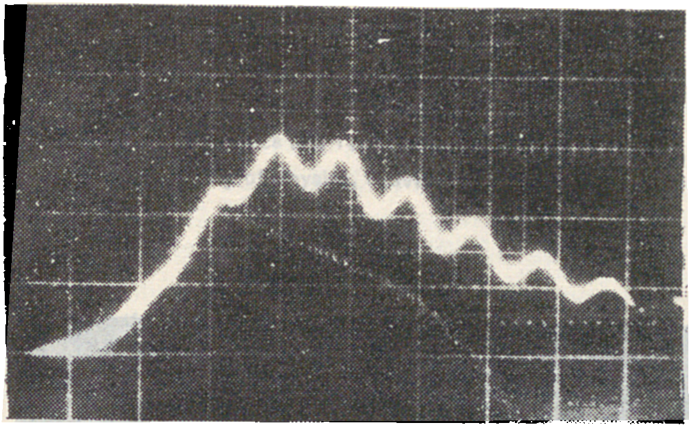

fig.4

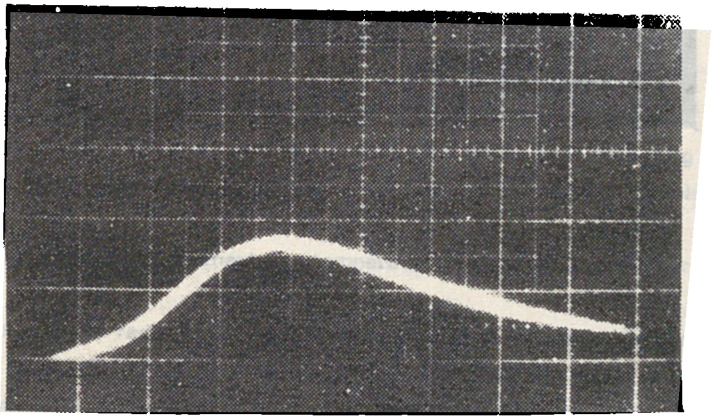

fig.5

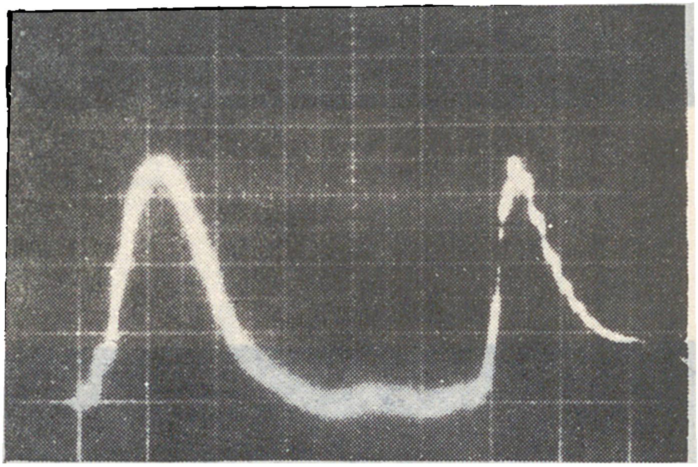

fig.6

ULTRAVIOLET TUNABLE LASER

M.L.Pascu*, A.Vasile*, M.Dumitras*, Peng Bai**, A.Pascu*,
G.Dumbraveanu*
* Institute of Physics and Technology of Radiation Devices
** Faculty of Physics, University of Bucharest

1. Introduction

The expansion of the laser radiation tunability towards wavelengths shorter than 350 nm, starting from visible tunable dye lasers, may be solved using nonlinear optical crystals.

In this case, the ultraviolet radiation is generated either by summing the frequencies of two distinct incident photons or by second harmonic generation (SHG).

The tunability range covered by SHG is extended to 230 nm, whereas by sum frequency mixing, the shortest generated wavelength is in the range of 185 nm.

In this paper is reported an experimental arrangement to obtain tunable ultraviolet laser radiation using SHG techniques, starting from the fundamental laser radiation emitted by a nitrogen laser pumped tunable dye laser which works in the visible spectral range.

The spectral range covered by the tunable ultraviolet laser radiation and the spectral characteristics of this light source are shown.

2. Experimental set-up

The tunable ultraviolet radiation was obtained by SHG effect, adjusting the temperature of an ADP nonlinear crystal in connection with the fundamental radiation wavelength emitted by a pulsed tunable laser.

The experimental arrangement for temperature tuning of the ADP crystal is shown in Fig.1.

The fundamental radiation is emitted by a dye laser which contains as pumping unit a nitrogen pulsed laser (NPL). The time width of the dye laser radiation pulse is 10 nsec /1/ (FWHM 5 nsec), the emission spectral range 400 nm- 700 nm /2/ and the peak power per pulse around 10 kW regardless the outputted wavelength /2/.

The dye laser radiation is focussed on the nonlinear crystal using a long focal length lens L_1; the crystal is introduced in a thermostated system which may be cooled using a REFRIGERATING UNIT down to -22°C and may be heated using a HEATING SUPPLY UNIT, up to 110°C.

The laser radiation which comes out of the nonlinear crystal contains the visible fundamental component incident on the crystal and the ultraviolet SHG radiation. They may be separated and spectrally analysed using a monochromator M and a photomultiplier PH mounted at the output of it, supplied by HVS. The photomultiplier's signal is processed (SIGNAL

PROCESSING) so that the resulting information may be recorded in real time.

The dye laser radiation wavelength was changed by a stepper motor SM properly supplied.

The nonlinear crystal was an ADP crystal of 30 mm length and 1 cm^2 section, cutted so that the propagation direction of the fundamental radiation along the crystal make 45° with the (100) direction and 90° with the (001) direction which is the optical axis of the crystal. The crystal was fixed in closed thermal contact with its mounting system for a good heat transfer and control of the temperature variations. Its temperature was measured using a thermocouple system which transmitted the temperature information to an electronic comparing circuit.

This circuit compared the instantaneous crystal temperature with the programmed temperature, allowing a temperature speed variation of not more than 3°C/min. Inside the thermostating system was introduced water vapour free nitrogen at atmospheric pressure.

The dyes used were: coumarine (5×10^{-3} M solution in ethyl alcohol/distilled water) and Na-fluoresceine (5×10^{-3} M basic solution).

3. Results

A first type of recording was done measuring the spectral distribution of the fundamental radiation, in the visible, which is shown in Fig.2, for coumarine and sodium fluoresceine. These two dyes are covering the spectral range within which the ADP crystal is doubling the fundamental frequency when its temperature is adjusted between -22°C and +95°C.

The experimental data are shown in Table 1.

TABLE 1

Crystal temperature (°C)	Fundamental wavelength (nm)	SHG radiation wavelength (nm)	Dye used
- 22	513.3	256.65	coumarine
- 18	514.3	257.15	coumarine
- 14	515.5	257.75	coumarine
- 12	516	258	coumarine
- 10	516.4	258.2	coumarine
- 8	517	258.5	coumarine
- 6	517.5	258.75	coumarine
- 4	518	259	coumarine
- 2	518.5	259.25	coumarine
0	518.7	259.35	coumarine
20	525	262.5	coumarine
25	527	263.5	coumarine
30	528	264	coumarine
35	529	264.5	coumarine

40	530.5	265.25	coumarine
50	535	267.5	coumarine
70	539.5	269.75	sodium fluoresceine
85	544.5	272.25	sodium fluoresceine
95	548	274	sodium fluoresceine

The spectral distribution of the ultraviolet laser radiation is shown in Fig.3, for the spectral range outlined in Table 1.

The conversion efficiency of the fundamental visible laser radiation into ultraviolet SHG laser radiation was greater than 10%.

The experimental data concerning the dependence of the wavelength of the fundamental laser radiation converted in ultraviolet radiation, function of the crystal temperature was compared with theoretical predictions.

The refractive indexes of the ADP crystal for the ordinary and extraordinary rays were computed starting from the Sellmeier equation /3/:

$$n^2(\lambda) = A + \frac{B_1}{\lambda^2 - B_2} - \frac{C_1\lambda^2}{C_2 - \lambda^2} \tag{3.1}$$

where λ is the laser radiation wavelength, and A, B_1, B_2, C_1, C_2 are constant. In the case of the ADP crystal, the values of the constants for the ordinary ray are: $A^o = 2.302842$, $B_1^o = 0.011125165$, $B_2^o = 0.013253659$, $C_1^o = 15.102464$, $C_2^o = 400$. The same constants for the extraordinary ray are: $A^e = 2.16351$, $B_1^e = 0.009616676$, $B_2^e = 0.01298912$, $C_1^e = 5.191896$, $C_2^e = 400$.

The computed values of the refractive indexes and the corresponding wavelengths are shown in Table 2.

TABLE 2

λ (nm)	n_o^{ω}	$n_e^{2\omega}$
500	1.529833	1.5351933
510	1.5290796	1.5324
515	1.5287164	1.5306521
520	1.5283618	1.5292494
525	1.5280154	1.5278975
530	1.5276765	1.5265
535	1.5273452	1.525336
540	1.527	1.5241218
550	1.5263927	1.5218

The refractive indexes dependence on temperature was computed using Phillips equation /4/:

$$n(T)=n(298^{o}K)+(n^{2}+an+b)c(298-T) \qquad (3.2)$$

where n is the refractive index, T the temperature in Kelvin degrees, and a, b, c are constants. For the ordinary ray, in ADP crystal case: $a_o = -3.0297$, $b_o = 2.3004$, $c_o = 0.713 \times 10^{-2}$. For the extraordinary ray at the same crystal: $a_e = 0$, $b_e = o$, $c_e = 0.675 \times 10^{-6}$.

In the case of the uncritical phase matching, the condition $n_o^{\omega}(T) = n_e^{2\omega}(T)$, leeds to a crystal temperature (Tm) dependence of the fundamental laser radiation, given in Table 3.

TABLE 3

λ (nm)	T_m(°K)	t_m(°C)
500	164.49	- 108.51
510	214.96	- 58.02
515	249.52	- 23.48
520	275.73	1.27
525	300.96	27.96
530	327.61	54.61
535	348.63	75.63
540	370.64	97.64
550	414.20	141.20

The curves showing the good enough agreement of the computed values in Table 3 and the experimental values are shown in Fig.4, where the experimental data are represented by crosses.

4. Conclusions

One of the ways of obtaining the ultraviolet tunable laser radiation is SHG either by temperature tuning or by angular tuning of a nonlinear crystal of the ADP type. The spectral range covered using temperature tuning and ADP crystals is hundreds of Angströms large at efficiencies greater than 10%. These facts make the ultraviolet laser radiation useful for laser spectroscopy experiments below 300 nm.

REFERENCES

/1/ M.L.Pascu, A.Pascu, A.Constantinescu, G.Dumbraveanu, Rev.Roum.Phys., 23, 10, 1121 (1978)

/2/ M.L.Pascu, A.Pascu, G.Dumbraveanu, D.Cristu, Proc.of the IVth Intern.Environment and Safety Conf., London, March 27-29 (1984)

/3/ S.K.Kurtz, Nonlinear Optical Material, in Laser Handbook, North-Holland, vol.1, 923 (1972)

/4/ R.Phillips, JOSA, 56, 629 (1966)

FIGURE CAPTIONS

Fig. 1 Experimental set-up

Fig. 2 Spectral distribution of the dye laser radiation in the visible

Fig. 3 Spectral distribution of the laser radiation in ultraviolet
(- 22 ÷ + 70)°C coumarine
(+ 85 ÷ +125)°C sodium fluoresceine

Fig. 4 Temperature dependence of the fundamental radiation wavelength
° theoretical data
x experimental data

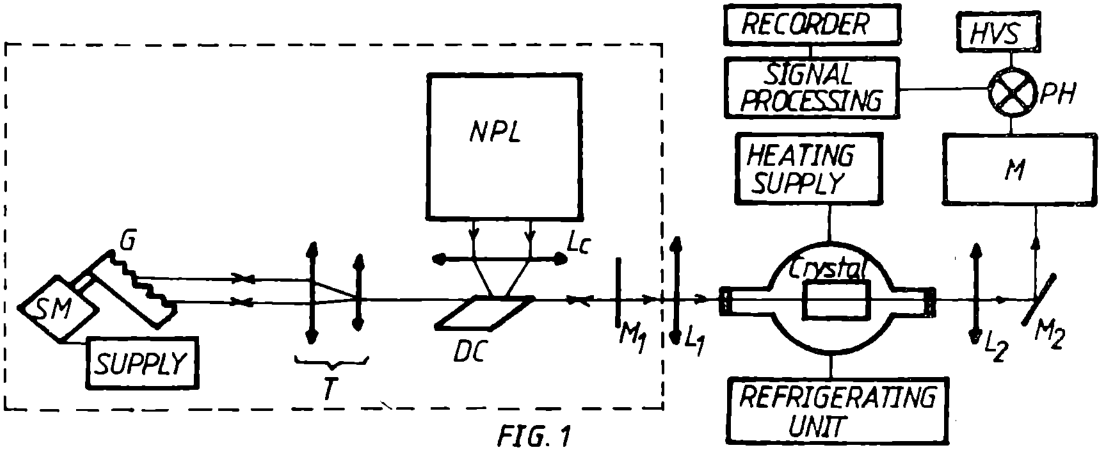
RECORDER
SIGNAL PROCESSING
HVS
PH
HEATING SUPPLY
M
NPL
G
Lc
Crystal
SM
SUPPLY
T
DC
M1
L1
L2
M2
REFRIGERATING UNIT

FIG. 1

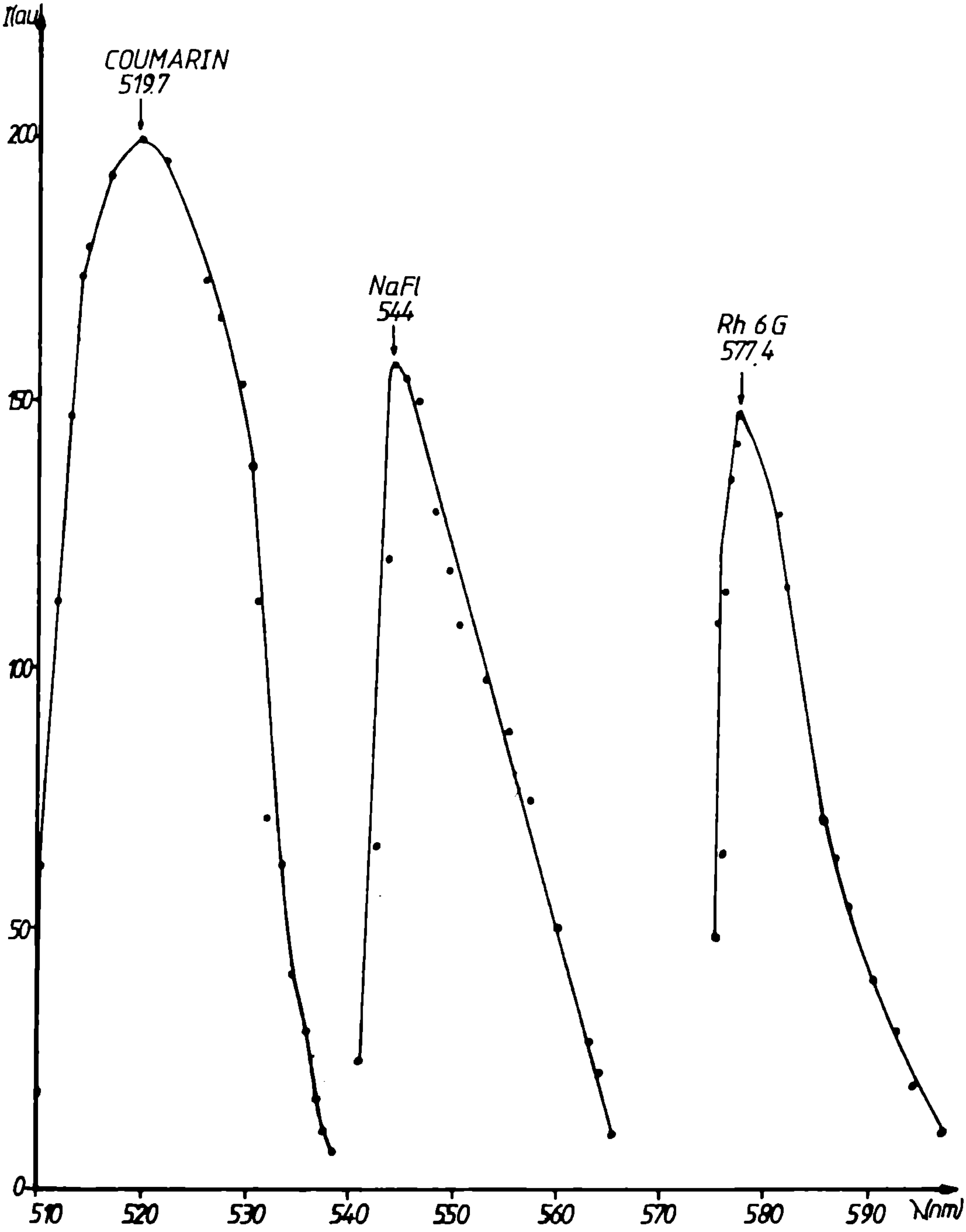
I(au)
COUMARIN
519.7
NaFl
544
Rh 6G
577.4
200
150
100
50
0
510
520
530
540
550
560
570
580
590
λ(nm)

FIG. 2

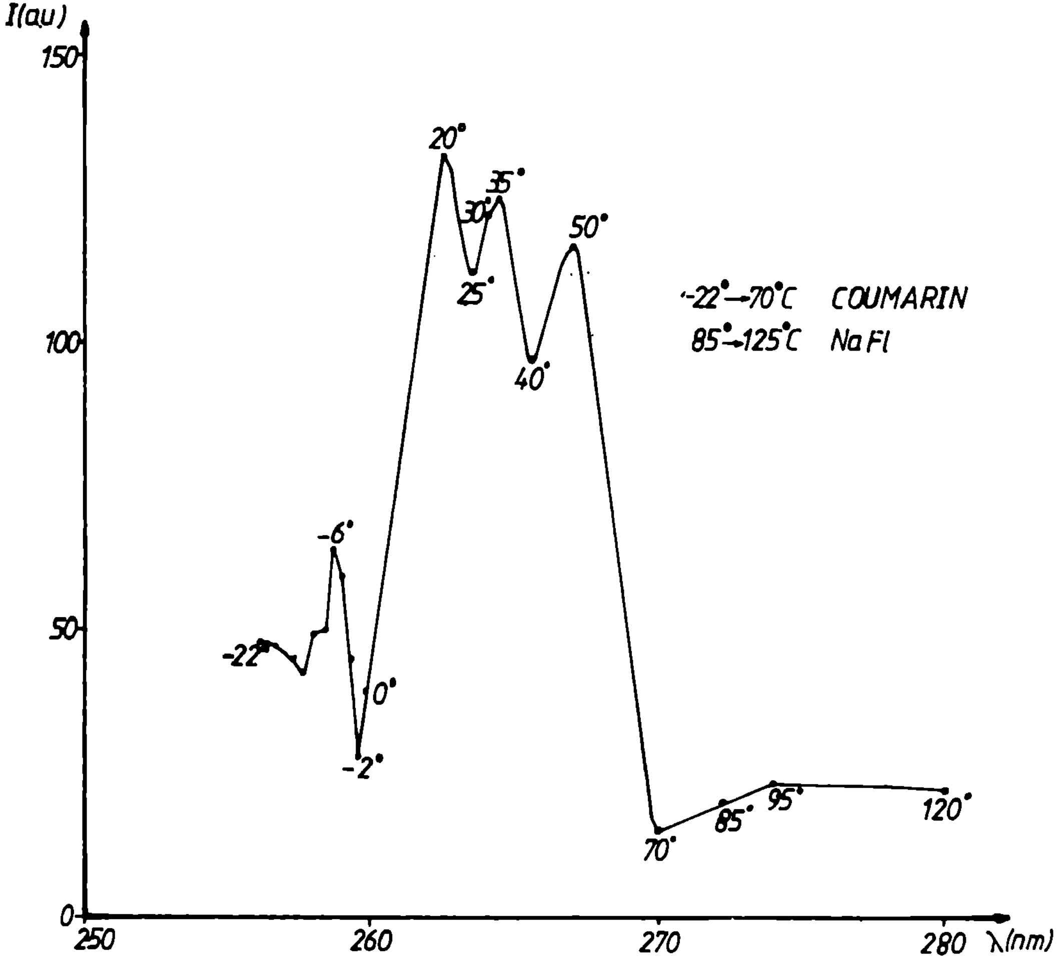
I(au)
150
100
50
0
250
260
270
280
λ(nm)
-22°→70°C COUMARIN
85°→125°C NaFl
-22°
-6°
-2°
0°
20°
25°
30°
35°
40°
50°
70°
85°
95°
120°

FIG. 3

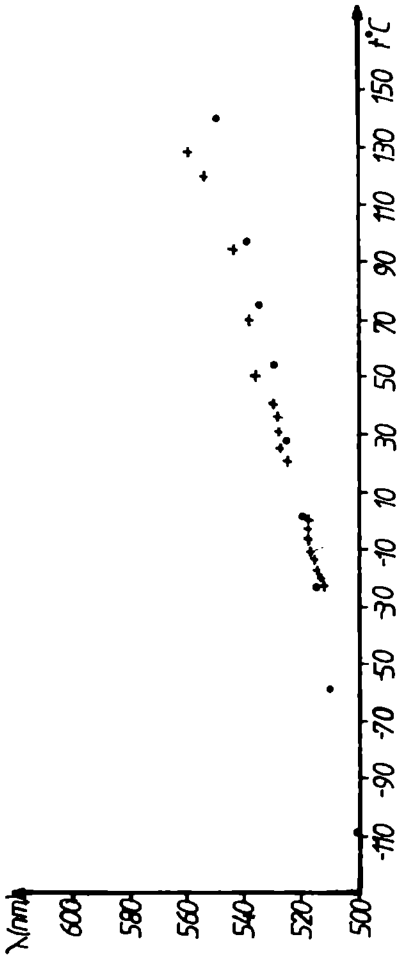
λ(nm)
600
580
560
540
520
500
t°C
-110
-90
-70
-50
-30
-10
10
30
50
70
90
110
130
150

FIG.4

HOLOGRAPHIC INTERFEROMETRY APPLIED TO IONIZING RADIATION DOSIMETRY

Silvia Nicolau
Laser Dept., Institute for Physics and Technology of Radiation Apparata, Bucharest

In this paper the applications of holographic interferometry to ionizing radiation dosimetry are presented. This paper shows that the integral absorbed dose and the spatial dose distribution in a volume can be holographically determined. Some advantages of the holographic method are outlined comparatively with conventional methods and the idea of developing a holographic ionizing radiation dosemeter, is suggested.

Studies of interaction of ionizing radiation with matter have become more and more frequent because of the spread of their applications in industry and science. The determination of the accurate value of dose delivered by an ionizing radiation source is a complex and very important problem which imposes different solutions depending on the experimental parameters. For this reason many experimental methods have been simultaneously developed, which permit proven solutions in radiation dosimetry. This paper presents a holographic method to determine the absorbed dose integrally as well as the three-dimensional distribution of the dose in a given volume /1,2,3/.

It is well known that radiation build up and attenuation on the path induce a variation of the energy deposition in the irradiation cell. Therefore, it is necessary to measure or to calculate the absorbed dose as determined by the energy deposition three-dimensionally. A good calculation of it implies a good knowledge of the field radiation spectrum in each point of the irradiated sample and of the chemical composition of the irradiated material. These requirements are not always easy to meet /4,5/.

The holographic interferometry permits the determination of the spatial dose distribution in transparent liquids at the laser wavelength used. The local variation of temperature without the use of sensors, which can distort the radiation field has been determined. Holographic interferometry with double exposure or in real time established the spatial distribution of the absorbed dose by the refractive index decrease of a transparent liquid with the temperature increase, dose distribution can be calculated from the interference pattern with the following assumptions:

1) the dose distribution must be symmetrical around the direction of radiation beam propagation

2) the dose is large enough and decreases monotonically with dose levels sufficiently small as a function of distance from the beam axis so as to provide a satisfactory number of

fringes in the irradiated volume.

3) the refractive index and the specific heat of the irradiated medium are known as a function of temperature.

4) the irradiation medium must be homogeneous.

These requirements can be easily reached experimentally /6,7/.

Holographic interferometry provides an interference pattern using the coherent light beam which passes through the medium before and after irradiation. In our case, the first exposure corresponds to the non-irradiated liquid and the second one to the irradiated liquid.

The principle is schematically shown in Fig. 1 (Holographic set-up).

The three-dimensional dose distribution can be evaluated from the interference pattern.

Determination of the integral absorbed dose by the calorimetric method

For this purpose, a special case is used i.e. a cubic quartz with double walls evacuated for the reason of thermal scattering during the long photographic exposure. For the determination of the integral absorbed dose this special case is recommended for it avoids thermal losses and, in this manner, the errors in appreciating the absorbed dose. The dose is:

$$D = \frac{m\ \lambda\ c}{x\ \frac{dn}{dT}} \tag{1}$$

where: m is the number of fringes

λ is the wavelength

c is the specific heat

x is the geometrical path

dn/dT is the temperature coefficient of the refractive index.

One can calculate the dose as depending on fringe number.

For example, in the case of water we have:

$$dn/dT = 8.10^{-5}\,{}^{\circ}C^{-1}$$

$c = 4.18\ J\ g^{-1}\ {}^{\circ}C^{-1} = 4.18\ .\ 10^{-1}$ Mrad/°C

$\lambda\ = 6328$ A.

The dose is measured in megarads and the pass length x in centimeters.

Since the light beam traverses the irradiated volume twice, this showed that, in order to obtain six fringes, a dose level of about 1 Mrad in 1 cm cell is required. We obtained different procedures to increase the holographic method sensitivity and to decrease the minimum dose level. The maximum level of the dose is practically unlimited.

Determination of the integral absorbed dose by chemical procedure

A chemical solution is used in which the reactant concentration is varied under irradiation. Analogously, we can write:

$$D = \frac{m \lambda k}{x \frac{dn}{dc}} \qquad (2)$$

wherer c is the reactant concentration

k is a proportionality factor, experimentally determined

m is the fringe number

λ is the wavelength

x is the path length

dn/dc is the concentration coefficient of the refractive index, experimentally determined. Relations (1) and (2) can be used to develop a holographic dosemeter for the ionizing radiation.

We worked to study a molecular process by holographic interferometry in irradiated organic liquids. We elucidated several fundamental mechanisms of interaction of radiation with matter and presented some "active media" for the ionizing radiation holographic dosemeter (especially for gamma and X radiation).

We applied the holographic dosimetry to clinical dosimetry and we used "tissue equivalent" materials and also biological products (blood plasma).

We can present (Fig.2) a gamma ray dose distribution in a polimer solution and a gamma ray dose distribution in a blood plasma (Fig.3).

The tretament planning in radiotherapy needs the knowledge of absorbed doses in the depth of irradiated tissue. We presented a simple and rapid method for the computation of absorbed doses as well as experimental determination by holographic interferometry as compared to conventional experimental methods. The results of the computation compared to experimental data obtained by a conventional method exhibit a good agreement, the maximum deviation being within 10%. The holographic method is more accurate, the maximum deviations being of about 4%, but the computation method is limited due to the dose range and to the geometry of the irradiated tissue. As experimental method, holographic interferometry (with double exposure or in real time) is the most indicated for the accurate determination of absorbed dose distribution used in Co^{60} Teletherapy /8,9,10,11,12,13,14/.

Conclusions

- Double exposure holographic interferometry can provide a permanent record of object variations between irradiated states.

- The information on "deformation" being recorded on a photographic plate, it is not necessary to have an exact position of the hologram after developing it.

- As a permanent record, holographic interferograms may be used many times without the risk of damage.

- An advantage of holographic interferometry is that holographic reconstruction uses the same optical components and the same geometry as those from the hologram recording and in this way, the interference fringes of local defects in the optical components and windows of irradiation cell are compensated in the registration-reconstruction process.

- The laser used can be of small power (3 mW).

- The method of holographic interferometry can determine the spatial distribution and the integral absorbed dose in transparent liquids.

- This method does not need temperature sensors which can disturb the radiation field.

- Any transparent medium can be used even in several layers with different atomic numbers, in which case we obtain information about dose distribution at interfaces.

- Ionizing radiation holographic dosemeters can be designed with much versatility and it is not necessary to have specific metrological devices.

- Being a permanent recording, the holographic interferogram can be used for fast checkings in standardization and calibration without any specific radiation metrological devices.

REFERENCES

/1/ S.Nicolau, D.Apostol, V.Vasiliu, St.Cerc.Fiz., 25, 855 (1973)

/2/ S.Nicolau-Rebigan, F.Rebigan, Commun.Session "Physics and Industry", Central Inst.of Physics, 5-6 Dec. 1977, Bucharest

/3/ S.Nicolau-Rebigan, Commun.Coll.Nat.Opt. Bucharest 29-30 June 1978

/4/ S.Nicolau-Rebigan, F.Rebigan, Commun.Session "Physics and Industry", Central Inst.of Physics, 16-17 Oct, 1978, Bucharest

/5/ S.Nicolau-Rebigan, F.Rebigan, Commun. U.S.S.M. Section Radiologie, Bucharest, 17 Oct. 1978

/6/ S.Nicolau-Rebigan, F.Rebigan, St.Cerc.Fiz., 31, 653 (1979)

/7/ S.Nicolau-Rebigan, Rev.Roum.Phys., 24, 6, 553 (1979)

/8/ S.Nicolau-Rebigan, F.Rebigan, Radiologia, 18, 1, 75 (1980)

/9/ F.Rebigan, S.Nicolau-Rebigan, A.Cavaleru, "Ensemble de Curie-therapie et nouveaux aspects de dosimetrie clinique" XVI Semaine Medicale Balkanique, Bucarest, Roumanie, sept.1980, Publ.Annal.Soc.Med.Balk. 1982 (French)

/10/ F.Rebigan, F.Scarlat, S.Nicolau-Rebigan, S.Cuzino, "Techniques de dose pour traitments des toumours malignes profondes" Congres XVII Semaine Medicale Balkanique, Sofia, Bulgaria, 29 VIII - 3 IX 1982 (French)

/11/ S.Nicolau-Rebigan, F.Rebigan, S.Cuzino, F.Scarlat, "Methode holographique avec lasers nouvelle application dans la radiotherapie", Congres XVII Semaine Medicale Balkanique, Sofia, Bulgaria, 29 VIII - 3 IX 1982 (French)

/12/ S.Nicolau-Rebigan, "Holographic interferometry applied to determine spatial dose distribution in-tissue equivalent - by ionizing radiation", Inter.Conf.and School "Lasers and Appl.", Bucharest 30 VIII - 11 IX 1982

/13/ S.Nicolau-Rebigan, "Determination of integral absorbed dose of ionizing radiation in materials-tissue equivalent - by holographic interferometry", Inter.Conf.and School "Lasers and Appl.", Bucharest 30 VIII - 11 IX 1982

/14/ S.Nicolau-Rebigan, S.Cuzino, "Computation and holographic determination of absorbed dose distribution in Co^{60} teletherapy", Inter.Conf.and School "Lasers and Appl.", Bucharest 30 VIII - 11 IX 1982

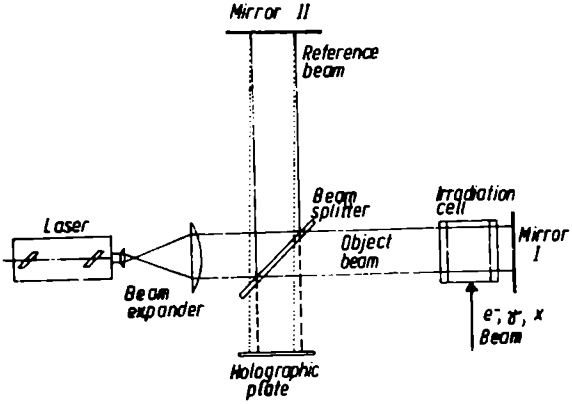

Fig. 1

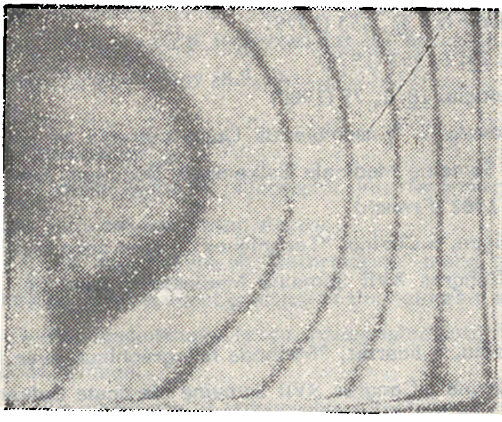

Fig.2

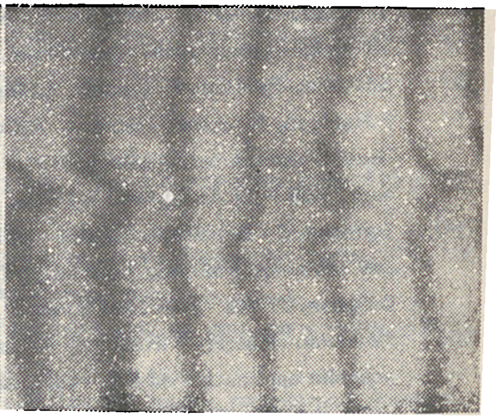

Fig.3

LASER GAUGING BY INTERFEROMETRY AND DIFFRACTION, UNDER MICROCOMPUTER CONTROL

N.Miron, D.Sporea
Laser Dept., Institute for Physics and Technology of Radiation Devices, Bucharest

The paper presents some industrial applications of interferometry and diffraction using visible He-Ne laser radiation. Interferometric methods were employed for dial indicators verification and outlines measurement in fine mechanics. Opaque thin fiber diameters are continuously measured during their manufacturing process by diffraction. A new approach in laser interferometry is pointed out using electro-optical phase-shift control. In all described applications, control and data processing are performed by computing systems built around microprocessors.

The modern technology used in some industrial fields like fine mechanics, machine building and electrical equipment building require high accuracy, non-contact and rapid measurements. Starting from these goals, some laser gauging equipments, based on interferometry and diffraction have been developed during the last four years, in the Institute for Physics and Technology of Radiation Devices. In spite of the different nature of the physical phenomena involved, a unique system for control and data processing built around an eight-bit microprocessor have been developed. Only the input peripherals are different from one kind of equipment to the other. The central unit and the output peripherals are the same for both equipments. The software was structured in a modular manner to achieve a great flexibility.

An innovative application of laser interferometry is an equipment for dial indicators verification. Dial indicators are high accuracy mechanical gauging devices used to measure the deviations from a given outline in precision machining. Their measuring accuracy is from 0.001 mm up to 0.010 mm in the range from 0.060 mm up to 30 mm, for most used devices. The rapid, complete and very accurate verification of dial indicators is the main requirement for each manufacturer of such devices. One of the major suppliers in this field needed an equipment like this, and it was the starting point for us to build it in close cooperation with the customer.

A method for the complex verification of the dial indicators was first devised. This method was basic for the laser equipment we have built. This equipment is able to verify practically all the types of the dial indicators, having a normal scale and also a zero-center scale. Both the method and the equipment represent innovations in the field, and are covered by some patents /1,2/.

The method for dial indicator verification which we have used, finds out the differences between the measured linear displacements of the dial rod and the nominal value of these displacements at certain verification points in the measuring range of the dial indicator to be verified. These differences are the measuring errors in the verification points and represent a set of data for the whole measuring range. Having these data for the direct and reverse displacement of the dial indicator rod, other important parameters are computed: the accuracy error for the whole range, the hysteresis error and the fidelity error.

The block-diagram of the equipment for dial indicators verification is shown in figure 1.

It consists of two main building blocks: the measuring block M, and the control and processing block CP.

The measuring block M has a He-Ne laser (1) as a coherent light source for the Michelson interferometer (2), a moving mechanism (3) to move forward/backward the dial indicator rod, a fixture (4) for the dial indicator to be verified (6) and a special non-constant angular transducer (5). For verification, the dial indicator is put in its fixture (4), having the angular transducer (5) over its face.

The rod (3.1) of the moving mechanism (3) moves forward and backward the dial indicator over its whole measuring range. One end of the moving mechanism rod (3.1) is always kept in contact with the dial indicator rod. The other end of this rod holds the mobile retroreflector of the Michelson interferometer (2). In this manner, the mobile retroreflector has exactly the same linear displacement as the dial indicator rod and produces to phase-shifted fringe patterns moving across two photodetector apertures. The electrical fringe signals arising at the two photodetectors load resistors are periodic, their periods corresponding to a $\lambda/2$ displacement of the dial indicator rod, and have a phase shift depending on the forward or backward movement of the dial indicator rod. Here, $\lambda = 0.6328$ µm is He-Ne laser wavelength, considered as a length standard.

The fringe signals from the two photodetectors are further amplified and fed to an up-down fringe counter, where they are accumulated. Hence, the content of this counter is red at the moments given by signals generated by the angular transducer. These signals correspond to the verification points in the measuring range of the dial indicator. The difference between the fringe counter content and the appropriate value stored in a ROM (Read Only Memory) represents the measuring error of the dial indicator at every verification point according to verification standards.

The amplification of the fringe signals, of the signals coming from the angular transducer, the fringe signals accumulation and the computation of the measuring errors are performed by the central unit (7) subassembly of the control and processing block CP. The central unit (7) also performs some other tasks. From the whole set of measuring errors depicted as described above, it computes the accuracy error for the whole range, the hysteresis error and the fidelity error of the dial indicator, and takes a go/no go decision. The central unit (7) also works as a controller for the whole equipment, managing the operation of the displacement mechanism (3), of the TV alphanumeric display (8), of the printer/plotter (9), of the magnetic cassette unit (10) and of the keyboard (11). It interpretes the flags set by laser power fail and/or abnormal behaviour of the dial indicator mechanism: out of operation during forward/backward movement. In all these situations, the verification is stopped and appropriate labels are displayed on the TV screen.

The work of the operator with this equipment is inter-active. The operator sends commands via the keyboard (11), and the equipment tells to the operator, via the TV display, the next step of operation and/or comments. At the completion of the verification procedure, the results are listed in an alphanumerical format and/or as an error diagram, at the operator's command. In certain cases, a data library containing verification results is useful for the customer. The equipment is able to get this, due to the magnetic cassette unit (10). The operator can also command data recording or reading via the keyboard (11).

The verification accuracy of this equipment is less than one third of the graduation for any type of dial indicator under verification, which is adequate. For a dial indicator 0.01 mm per graduation and a measuring range up to 10 mm, the verification time is of about 2 minutes (taking into account five verification cycles), so the equipment can be considered productive.

Another laser gauging equipment for on-line measurement during wire manufacturing process, based on diffraction, was also developed in the Lasers Department of the Institute for Physics and Technology of Radiation Devices.

Usually, the cylindrical enamelled copper wires are manufactured in the 0.01 mm up to 5 mm range, according to standards. Among the wires caracteristics, their nominal diameter is of major interest for the consumers in the electrical and electronic industries.

The laboratory instruments and methods used in enamelled wire meter measurements are specified by standards. For this purpose, samples of wires to be evaluated are colected from the final products and laboratory tested. The sampling procedure is distructive, and the lengths of the samples is up to five meters. This sampling process is thus material-consumming and is performed after fabrication.

For large volume production when samples are up to five million per year, the overall copper lost is significant (about six tones per year at a production rate of 10,000 tones).

In the range from 0.71 to 5 mm the diameter is measured by micrometers with 2 µm accuracy, having a measuring force in the range 0.75 N to 1.25 N.

For thin and very thin wires, 0.01 mm to 0.071 mm diameter, the micrometer can't be used due to the low mechanical resistance of the wire. In this case, indirect computing methods are employed, the wire diameter is derived from its measured resistance for a given conductor length.

Such measurements can be carried out for conductors up to one millimeter. New methods based on electrical micrometers have been introduced for laboratory use only, since 1980, and 1 µm accuracy can be achieved /3,4/. Like all above mentioned investigations, this one is also post-processing.

In the last years, active control of wire diameter during the manufacturing process has been facilitated by the use of laser transducers. In such a case, in situ, non-destructive and contactless measurement is carried out /5,6,7,8/. Two methods were mainly employed: the scanning of the wire to be measured by the laser beam, or the laser radiation diffraction.

An equipment for on-line wire diameter measurement during fabrication was developed at the Institute for Physics and Technology of Radiation Devices, in Bucharest (Fig.2).

A collimated He-Ne laser beam falls on the wire to be measured and the obtained diffraction pattern, detected by a closed circuit TV system, is evaluated by a microprocessor based unit. The laser, the optical and detection systems are mounted on a specially designed moving table so that up to 50 wires can be checked up one by one. The nominal wire diameters are in the range of 0.05 mm to 0.12 mm, having a measuring accuracy better than 2 µm. By using a keyboard, the operator can select the wire to be checked up, the upper and the lower limits allowed for the diameter and the operation modes of the equipment.

The diffraction patterns appear on a TV monitor and lases the optical alignment.

The whole equipment is controlled by a microprocessor system performing the following tasks: moving table displacement and its accurate positioning via an opto-electronic feedback, the keyboard control, diffraction pattern analysis, control of the display unit, generation of the acoustical and optical warnings, and display of the equipment status. For an easy debugging and in-field testing, an autodiagnosis facility was incorporated in the system software. Every time a measurement is carried out, all main modules are checked up: TV camera and monitor, laser output.

Three operating modes are available: a step by step wire measurement, the measurement of only one wire diameter selected by operator, and self-control.

In the first mode, up to 50 wires, enamelled simultaneously can be measured one by one using also statistics. The second mode is when the operator sets the process parameters for the first time. So that, only the selected wire is measured. From time to time, equipment control and calibration must be carried out, this is the control mode. In this case, the measurement of the standard wire is made.

In figure 3, the equipment for wire diameter measurement is presented, working in the enamelling line of the Enamelled Wire in Zalau.

• Besides the above described equipment, investigations are conducted to develop new measuring methods by laser interferometry. One of them, described below, is intended for accurate non-contact object size measurement /8/.

The intersection of two gaussian laser beams near their waists, produces a space domain with interference maxima discribed as parallel, equally spaced planes. If the beams cross into a vecinity of ± 45 W_0 near the waist (W_0 is waist radius), the derivation of the maxima planes from equidistance is less than 10^{-3}. Then, fringe distribution is this domain (measuring volume) can be used as a space lattice for one-dimensional measurements.

An appropriate projection of the measuring volume on a photodetector array will give an information about the size of an object located inside it (e.g. on a wire diameter). If a photodetector is located on each interference maximum image, and the maxima are parallel with the object edges, then the object dimension is given by the number of completely shaded photodetectors multiplied by the fringe spacing.

The accuracy can be improved by at least two orders of magnitude, if the fringe planes of the measuring volume make an angle with the boundaries of the object to be measured (Fig.3).

Fringes of the measuring volume are imaging on the $DM_1, \ldots, DM_q$ photodetector array. The shaded area with boundaries U_1U_2 and L_1L_2 represents the image of the object to be measured. Each boundary produces a partial illumination of a photodetector, hence being possible fringe interpolation. Refering to Fig.1, the object dimension D_o is given by:

$$D_o = (N_o + 1 - \frac{h_{cu} + h_{cl}}{h_i}) \frac{\lambda}{2 \sin \Theta}$$

where N_o is the number of totally shaded detectors, Θ is the half angle between beams, and λ is laser wavelength. By measuring the currents of partially illuminated photodetectors, the ratio $\frac{h_{cu}+h_{cl}}{h_i}$ can be computed with eight-bit resolution, resulting an accuracy of the method of 0.4% fringe spacing.

The spatial fringe position stabilization, essential for this measuring method is performed by a special electro-optical device, originally developed in our institute.

REFERENCES

/1/ Romanian Patent No. 71070; U.S.A. Patent No.4 732 160
/2/ Romanian Patent No. 79422
/3/ DIAEMAIL, Data Sheets, CCSITMS, Romania
/4/ Auto-Readout Laser Gauge, Data Sheets, Beta Instrument Company Ltd., U.K.
/5/ Non-Contact Optical Micrometer, Data Sheets, Addison Process Control Ltd., U.S.A.
/6/ Non-Contact Dimensional Measuring and Control Instruments, Data Sheets, Zumbeach Electronics Corp., U.S.A.
/7/ Romanian Patent No.
/8/ N.Miron, V.Draganescu, D.Sporea, Accuracy evaluation in Real Time Absolute Interferometric Measurements with Fringe Interpolation, Proceedings of the Fourth International School of Coherent Optics, Bechyne, Czchoslovakia, 1983

FIGURE CAPTIONS

Fig. 1 Block diagram of the dial indicators verification equipment

Fig.2a Photograph of the equipment for on-line wire diameter measurement

Fig.2b Detail on the control unit

Fig. 3 Image of the measuring volume fringes focused on the $DM_1, \ldots, DM_q$ photodetector array. The object to be measured had U_1, U_2, L_1, L_2 boundaries.

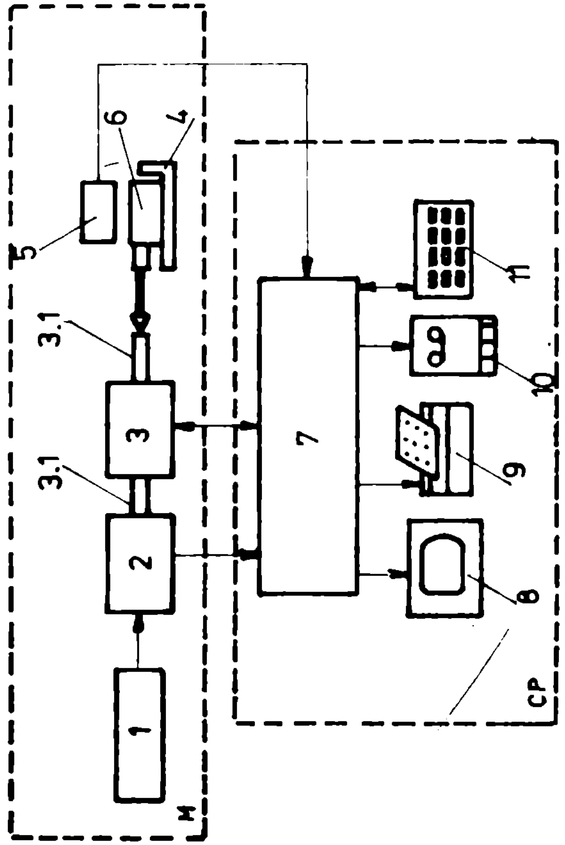

Fig. 1

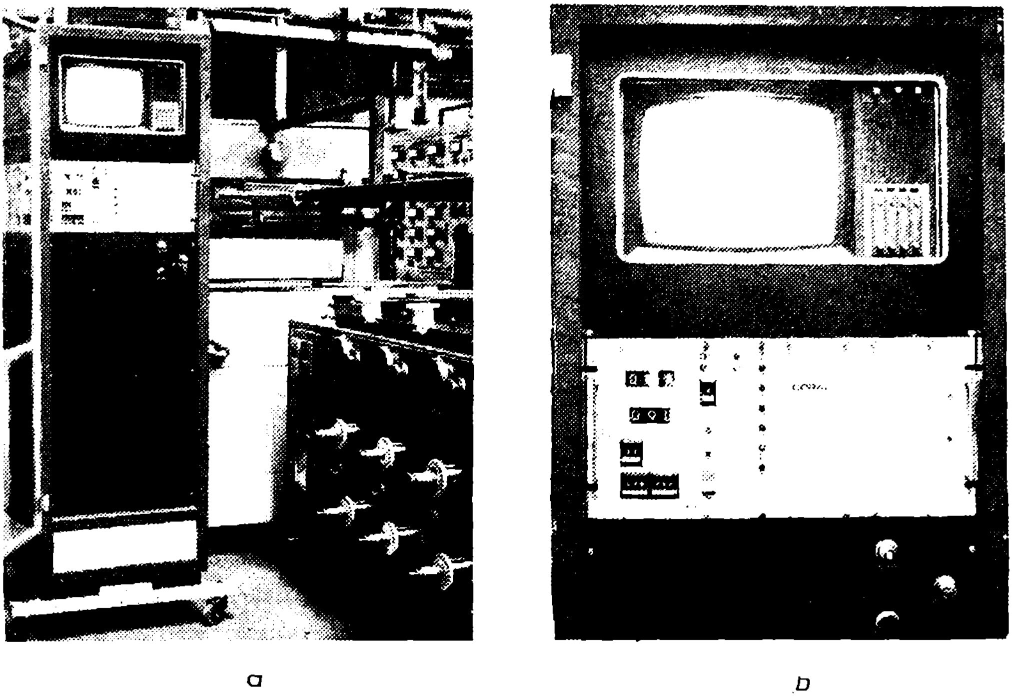

a

b

Fig. 2

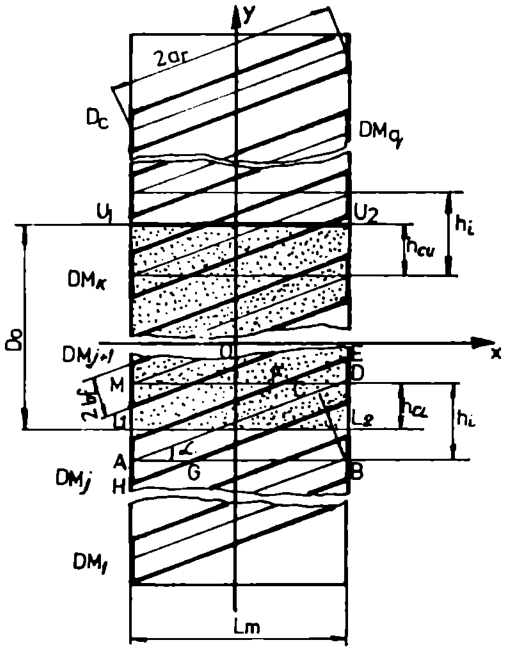
y
2ar
Dc
DMq
U1
U2
hi
hcu
DMk
Do
DMj+1
O
x
E
D
M
2bf
L1
hcl
hi
L2
α
A
G
B
DMj
H
DM1
Lm

Fig. 3

PLASMA REFRACTIVITY MEASUREMENT BY LASER TECHNIQUES

D.Apostol, Ileana Apostol, Doina Craciun, Maria Dinescu, A.Harsany,
A.Henning, I.N.Mihailescu, M.Sandu, Viorica Stancalie, Mihaela Stoica
Central Institute of Physics, Bucharest

This paper is a review of our contributions to plasma refractivity measurements using laser techniques. After a very short introduction to plasma refractivity and optical methods for measuring it - interferometry, shadow and schlieren, the helium-neon laser interferometer, the Mach-Zehuder Q-switch ruby laser interferometer, two infrared interferometers, a schlieren set-up using a free generation ruby laser and a shadow set-up - are described. The main results obtained with these experimental arrangements are also very shortly reviewed.

Introduction

Among the plasma defining parameters one of the most important is the particle density. As the particle density - electrons, ions, atoms - is directly connected with the plasma refractivity, the measurement methods have witnessed a particular development and any plasma facility has in its diagnostic equipment a method for plasma measurement.

In the last ten years we have developed many diagnostic equipments, their diversity being connected with their level of difficulty, because here, as in any other activity, the quantity and quality of information closely depend on the effort.

The laser-produced plasma studies were developed in the Laser Department at almost the same time as the development of the first high power laser (CO_2) and the diagnostic methods employed at the beginning, the existing techniques and apparata, as spectroscopic techniques. The first researches on laser diagnostic methods of plasma refractivity were developed only in 1974.

Laser radiation proved to have best qualities for refractivity measurements due to their monochromaticity, small divergence, high intensity, i.e. due to their coherence.

Most refractivity measurement methods are classical methods, as interferometry, schlieren, shadow, their new development being indebted to this ideal light source, which the laser is. For laser produced plasmas, as for all high speed developing plasmas, laser light has solved the problem of temporal and spatial resolution. Other more recent methods, such as holography, lateral shearing interferometry, infrared interferometry, Thomson scattering, optical heterodyning methods, cannot be imagined without the laser light source.

We shall describe the facilities for plasma refractivity investigation developed in the Laser Department of the Central Institute of Physics, and some of the results we have obtained.

Plasma refractivity

Plasma refractivity is known to be determined by the refractivities of its components i.e. electrons, atoms and all types of ions:

$$n-1 = \sum_{k} C_k N_k \tag{1}$$

where C_k is the refractivity of the particle of k type and N_k the number of particles for every type.

The electron refractivity is given by the well known relation /1/:

$$n_e - 1 = -4,49 \cdot 10^{-14} \cdot \lambda^2 \cdot N_e \tag{2}$$

For atoms and ions, whose resonances are not in the neighbourhoog of the investigated laser wavelength, the refractivity is given by:

$$n_a - 1 = \left\{ A + \frac{B}{\lambda^2} \right\} N_a \tag{3}$$

where A and B are practical constants for all gases.

So, for argon /2/:

$A = 1.039 \times 10^{-23}$ cm^{-3}

$B = 5.82 \times 10^{-34}$ cm^{5}

It can be seen that the term B/λ^2 can be neglected for the visible and infrared regions.

Optical methods for refractivity measurement

Optical interferometry is a well established technique for measuring the refractivity of transparent materials, by directly comparing the phase of a wavefront of interest with that of a reference wavefront. The method is extensively used and there are lots of well known reviews on this subject /3,4/.

Schlieren photography is used to obtain data on the shape and location of the plasma regions that exhibit a high gradient in the refraction index, that is to say, regions with high density gradients. The principle of schlieren photography is based on the deflection of a light beam as it passes through an optical inhomogeneous medium. The angle of deflection of a beam in a medium that exhibits a gradient in the refractive index is given by:

$$\theta = \int_0^l \frac{1}{n} \frac{\partial n}{\partial x} \, dz \tag{4}$$

where n is the refractive index and l is the path of the beam in the plasma; the original direction of the beam coincides with z axis, the x axis is the direction of the density gradient, and the Θ angles lies in the x-z plane /5,6/.

If the plasma under investigation is located in the path of the beam of parallel rays which illuminates a screen, a shadow image of the plasma is obtained on the scree. Since the optical length of the plasma is rather large for nonresonant radiation, the shadow image of the plasma will not be due to absorption effects, but rather to the change in the trajectory of the beam due to the inhomogeity in the refractive index. If the gradient is not constant, i.e. if the derivative $\frac{\partial^2 n}{\partial r^2}$ is nonvanishing, the illumination of the screen becomes nonuniform. In this case, the weakening of the illumination is proportional to the derivative of the density gradient

$$dI = -K\int_0^1 \left(\frac{\partial^2 n}{\partial x^2} + \frac{\partial^2 n}{\partial y^2}\right) dz \qquad (5)$$

Michelson interferometer with He-He laser

One of the first interferometers we have developed, for electronic density estimation of laser produced plasma, is schematically represented in Fig. 1.

The basic geometry /7/ is that of a conventional Michelson interferometer where the light source is an 18 mW/6328 A He-Ne gas laser (Model 124 A from Spectra Physics). A telescope reduced the laser beam divergence so that an emergent beam from the interferometer, which was almost uniform across its cross section, could be obtained only by adjusting the lengths of the two arms of the interferometer. A complete cycle of modulation of this unique fringe corresponds to a change in the optical length of one arm by $\lambda/2$. The diaphragm D (which is placed at the focus of the lens L_2) and the filter F eliminates the parasite reflections and the incoherent radiation from the plasma. Plasma production in one of the interferometer arms by a Lamberton-Pearson TEA-CO_2 laser, with xylene vapours addition to the $CO_2/N_2/He$ active mixture, focussed by an AR-coated germanium lens (L_1) in air at atmospheric pressure, induces a fast optical path change which is observed as an intensity variation of the emergent beam from the interferometer.

The intensity variation was detected with a BPY 13 photodiode (12 ns rise-time), displayed on a 7504 TEKTRONIX oscilloscope and photographed with a SHACKMAN INSTRUMENTS Inc. polaroid camera /8/.

The number N of fringes between two points of the interferometer output gives the corresponding change of the spatially averaged index μ in the interferometer arm containing the plasma:

$$N = \frac{2l\cdot\Delta\bar{\mu}}{\lambda} \qquad (6)$$

where λ is the laser wavelength l the plasma thickness. If non-electronic contributions to the index of refraction are negligible, μ can be related to the spatially averaged electron density n_e

$$n_e = 1{,}12\cdot 10^{13}\cdot\frac{N}{\lambda\cdot l}(\mathrm{cm}^{-3}) \qquad (7)$$

where l and λ are in cm. l was estimated photographically. Assuming a monotonical electron density decrease during the expansion, n_e was estimated by counting the corresponding fringe number. A value of:

$$n_e = (1 \pm 0.5) \times 10^{18}\ \mathrm{cm}^{-3} \qquad (8)$$

was obtained for a laser incident energy of 5 J. We used the same interferometer to study the blast wave expansion around the plasma produced in air /8/. A typical interferogram is given in Fig.2.

A "saddle point" was put sistematically into evidence after (20 ÷ 30) μs depending on the pressure in the irradiation room and the incident energy in the CO_2 laser pulse on the target. We suppose it is due to a change of the sign of the optical path variations appearing by the shock wave border breking and a subsequent turbulence density increase /9/.

Mach-Zehnder interferometer with ruby-laser

To obtain the spatial distribution of the plasma refractive index, we must "see" the plasma as a whole. For this purpose we used as an investigation beam the light emitted by a Q-switched ruby laser, with a pulse length of 30 ns. It is the light source for a Mach-Zehnder interferometer (Fig.3). Plasma was produced by focusing the TE-CO_2 laser beam on the surface of a solid target situated in air. In the focus of a germanium lens (f = 5 cm) a power density of 10^9 W/cm^2 was achieved.

The plasma initiation moment and its evolution was followed by viewing the plasma emitted light with a high speed photodiode.

The Mach-Zehnder interferometer /10/ consists of two beam splitters BS_2, BS_3 and to total reflecting prisms P_1 and P_2.

The ruby laser beam is expanded by the collimator C, such as to assure an interferometric field of 30 mm diameter. The plasma which is formed in the BS_2 - P_2 arm of the interferometer is expanding normally to the ruby beam propagation. To choose the proper investigation moment in the plasma evolution, the ruby laser was synchronized and reliably delayed as compared to the plasma initiation moment. This is achieved by high voltage switching of the ruby laser Pockels cell by means of a laser controlled spark-gap. The commutation of the pressurized spark-gap is done by focussing a part of the TE-CO_2 laser beam on one of its electrodes /11/.

The interference pattern was recorded on photographic film in the image plane of the lens L_4. To avoid the plasma emitted light we have introduced a diafragm in the focus of the lens L_4. At the same time, plasma evolution was monitored with a high speed SFR camera and plasma velocity was determined.

A great number of interferometric recordings of the gas plasma in the neighbourhood of solid targets, was performed for different laser energies (Fig.4) and different delays in respect to the plasma initiation moment.

For a 0.2 μs delay between the ruby laser pulse as against the plasma initiation moment, the radiation driven detonation wavefront could be observed to have a preferential propagation back along the laser beam axis. It was a radial propagation too, which is taking off the plasma from the action cone of the laser radiation.

On the front of the detonation wave a maximum shifting of the fringe is present. In the central part of the plasma the fringe shift sense is changed with a maximum on the axis.

For quantitative analysis we have considered the plasma as having a cylindrical symmetry.

For the conversion of the fringe shift data observed in the interferogram as a function of the radial distance to the refractive index, the Abel inversion method was used. The relationship between the fringe shift and an unknown function (the refractive index) is given by an integral equation of Abel type. Because of the cylindrical symmetry of the plasma, the refractive index is a function only of r. This function was approximated using a linear interpolation of finite domains: n = a + b.r, where the constants a, b are obtained from the following conditions:

$$\begin{aligned} n_i &= a + b\, r_i \\ n_{i+1} &= a + b\, r_{i+1} \end{aligned} \tag{9}$$

i = 1, N where N is the maximum number of domains into which the plasma radius was divided /12/. The discrete set of data representing the fringe shift was smoothed and regularized with a third degree polynomial.

The values obtained for the plasma refractivity are given in Fig.5 as a function of the plasma radial coordinate for different distances from the target surface (axial distances). On the front, a maximum positive variation of the refractive index can be seen. This is approximately constant for different axial distances, in the limit of experimental errors.

For air produced plasma the refractive index variations are dependent on both neutral species and electrons, as follows:

$$n-1 = 4{,}49\cdot 10^{-14}\cdot N_e\cdot\lambda^2 + (n_0-1)\frac{\rho_2}{\rho_0} \tag{10}$$

where $n_0 - 1 = 2.95 \times 10^{-4}$ for air at STP, ρ_2 is the neutral gas density and ρ_0 is the unperturbed gas density. The ratio ρ_2/ρ_0 is defined as gas compressibility. We can calculate the gas compressibility on the front from the measured velocity of plasma expansion. Using the standard equations for intense explosion in a gas /13/ for an investigation time of 0.2 μs as against the plasma initiation moment, we get a value of 5 for the compressibility. Taking into account this value for the compressibility and calculated values for the refractivity we have calculated the electron contribution to the refractive index. We obtained an electron density on the detonation front of the order of 10^{18} cm^{-3}.

The use of the interferometric method for the investigation of the gas produced plasma in the neighbourhood of solid targets investigation has revealed both the plasma structure and its expansion dynamics.

Infrared interferometry

Denoting by S_{min} the minimum measurable fringe shift, the minimum electron density that can be revealed is

$$(n_e)_{min} = \frac{S_{min}}{C \cdot l \cdot \lambda} \tag{11}$$

where l is the plasma length, $C = 4.49 \times 10^{-14}$ cm and λ is the wavelength of the investigation beam.

In spite of detection difficulties it is increasingly interesting to use IR light in plasma interferometry, as the revealable electron density is inversely proportional to the observing wavelength. For instance, using the 10.6 µm radiation the minimum electron density revealable is more than one order of magnitude lower than for visible wavelengths.

Unfortunately, classical interferometers such as Mach-Zehnder or Twyman-Green are rather difficult to operate in infrared, especially due to alignment complication and prices of infrared components.

So, we advanced up to now two very simple and unexpensive interferometers to be used in the infrared.

Infrared lateral shearing interferometer /14/

Bates first introduced in 1947 a lateral shearing interferometer for concave mirror testing with no use of any reference system. In such interferometer too superimposed, displaced images of the wavefront under testing are made to interfere with each other. Thus, they provide a comparison of a wavefront with a sheared image of itself. The necessity of a reference wave is then eliminated and testing of any form of wavefronts is made possible.

A simplest type of such interferometer was presented by Murty in 1964. In this case the interferometer was a simple glass plate. The small tilt between the two sheared beams in a direction perpendicular to the direction of the lateral shear was achieved by making the plate slightly wedge-shaped. The interference can be observed in either reflection or transmission.

The two wavefronts are laterally displaced even in reflection or in transmission by:

$$S = l \frac{\sin 2i}{\sqrt{n^2 - \sin^2 i}} \tag{12}$$

As the rezulting path difference is important, such an interferometer can be illuminated only with a laser source which has a coherence length larger than 2 ne and a lateral coherence of the order of the necessary S.

We obtained parallel and equidistant lateral shearing fringes in the infrared at 10.6 µm in both reflection and transmission (Fig.6).

To this end we used a germanium plate with a few-second wedge angle illuminated with a TE-CO_2 laser, and simply thermal printer paper as detector. This is a very simple and unexpensive interferometer without any alignement or stability difficulty.

A new infrared interferometer

Several attempts have been made during the last decade to overcome the main difficulty of infrared interferometry, i.e. to find appropriate recording techniques and materials.

In recent papers /15,16/, we have reported a complete set-up of IR interferometry and methods to record infrared interferograms. The optical system of the interferometer was designed with the aim of taking into account the following factors:

- the large coherence length of the CO_2 laser;
- the requirement to work at rather large angles between the interefering beams, as imposed by the large (10.6 µm) wavelength;
- the need for varying the incident energy density on the recording medium.

As a consequence, we chose the optical system outlined in Fig.7, including two spherical mirrors of 600 mm focal length, a ZnSe beam splitter and to flat Cr-Au mirrors on glass substrates. The set-up allows for chenging the path difference between the two arms of the interferometer and to modify the angles between the two interfering beams.

This interferometric arrangement provides an image of the object precisely on the surface of the recording material.

The first interferograms were recorded on plane samples of electrolytic graphite with dimensions of (100 x 100 x 10) mm^3. The pattern was clearly visible at small spatial frequencies (1-2 fringes/mm). The method appeared to be particularly useful when adjusting the interferometer. However, the graphite sample did not supply a resolution high enough to get good pictures for further processing and analysis.

That is why we further tested triacetate cellulose (TAC) as a recording material.

A third method we have developed allowed us to use common photographic film. The principle of the method consists in rising the sensitivity of ordinary film for about 1 ms by local heating using the incident 10.6 µm laser pulse. Thus, when subjected to the action of the interference pattern at 10.6 µm, the film becomes more sensitive to the subsequent visible light (delayed by about 1 ms as compared with the TEA CO_2 laser pulse) in the interference maxima than to that in the minima. A greater blackening is thus induced in the more sensitized zones, and one gets a recording of the interference pattern. For both methods we established the optimum recording conditions.

As for the light source of the interferometer we developed a TEA CO_2 laser source with appropriate temporal and spatial scheme, allowing us to obtain high quality interferograms. Specifically, the laser had a coherence length of about 50 cm and was able to generate pulses of about 1 J / 200 ns or about 8 J / 2 µm.

Figure 8 shows an interferogram of an arc discharge plasma impurified by Na, as recorded on triacetatecellulose.

An interferogram of a laser produced plasma in front of a graphite target is shown in Fig.9. The laser pulse was 200 ns long.

Schlieren set-up

A schlieren set-up with a ruby laser as a light source was devised for studying the laser beam-plasma-target interaction in ambient gas in front of a solid target /17/.

The schlieren method was developed in order to directly observe the laser plasma and shock wave expansion symmetry. Schlieren photographs of the laser plasma and associated shock waves, display the refractive index variations assuring the visualization of the plasma and shock wave boundary. From such records one may easily infer the symmetry and velocities of plasma and shock wave expansion.

A diagram of the experimental set up is shown in Fig.10.

An appropriate spatial and temporal resolution was achieved by using as a light source a home-made ruby laser, operated in relaxed regime, which emitted a train of pulses of about 400 µs duration and 1.5 J total energy. A better contrast of the individual pulses was obtained by introducing a thin layer of saturation absorber into the cavity. A singular pulse lasted for about 1 µs and the time lapse between pulses was of the order of 3 µs. Pulse shape and duration were detected by deflecting a small part of the laser beam to a first BPY 77 photodiode (PD 1) by a beam splitter (BS 1) and displaying it on a TEKTRONIX 519 oscilloscope. The ruby laser beam was enlarged by a 5 X beam-expander telescope.

The plasma was generated within a control pressure camera by focusing the TEA-CO_2 laser beam with a 2 inches focal length AR coated germanium lens (GL) onto a solid target.

The ruby laser beam also passed through the focal region of the germanium lens, in a direction perpendicular to the CO_2 laser beam. The Schlieren lens L (TESSAR 9/300) builds up the plasma image in the plane P of the camera (PENTACON SIX TL), the entire optical system having a three time magnification. The knife edge is cutting the focus of the schlieren lens. An interference filter was used to eliminate the light from the plasma. The alignment was carried out with a 50 mW He-Ne laser. Plasma initiation and its evolution were evidenced by visualizing the plasma emitted light with a rapid photodiode (PD_2). The plasma light total duration was of (10-15) µs, depending on the incident laser energy.

To assure plasma triggering during the ruby laser pulse train a special device for synchronization and adjustable delay was designed and constructed (Fig.11). The photodiode FD1 (rise time ∿ 0.5 ns) receives the light signal generated by the ruby laser and the resulting electric signal is amplified via an "optical signal amplifying stage".

The first amplified electric pulse related to the first laser spike drives on a (L → H) transition, the delay stage "pulse sweep" is activated. The delay stage allows to move the CO_2 driving moment to any chosen time.

The CO_2 laser driving pulse stage is triggered by the H → L transition of the output signal and generates the proper pulse to finally drive the CO_2 laser. The output of this stage consists in a positive signal of 5 µs. An automatic shut-off stage was also introduced to assure that the CO_2 driving pulse occurs only in a certain time window. The output pulse has the proper amplitude and width to secure and firmly command the CO_2 laser driver.

The ruby laser spikes subsequent to the plasma initiation moment as well as the plasma light signal were simultaneously visualized and recorded on the TEKTRONIX oscilloscope which was triggered by the PD2 photodiode signal (collecting plasma emitted light). An image of the plasma, shock wave boundary at a chosen moment of their evolution, is produced by every spike in the ruby pulse train subsequent to plasma production and recorded on a photographic film placed in the image plane of the schlieren lens.

By correlating the schlieren records with the ruby laser pulse shape, the plasma / shock wave expansion symmetry can be inferred and the corresponding boundary velocities can be computed. In Fig.12 typical schlieren images corresponding to different TEA-CO_2 laser incident intensities are given.

So, we have found that the shock wave front has at the beginning of its separation on the plasma boundary the same symmetry as the plasma (cylindrical or spherical symmetry depending on the value of the incident energy) while at later times in its expansion it has a spherical symmetry.

The shock wave velocity which was measured by schlieren methods was of the order of 10^5 cm/s at the beginning of its evolution, corresponding to the expansion velocity of the plasma source, followed by a lowering in the expansion time (Fig.13).

Shadowgraphy

To obtain a direct picture of the great density gradient zone, shadowgram pictures of the plasma were taken. The shadowgrams were obtained using the same interferometric set-up as earlier described with the reference arm of the interferometer obturated. A shadowgram of a laser produced plasma is presented in Fig.14. It can be seen that the region of higher density gradients is on the plasma front, and at later times in the plasma evolution, a turbulency appears in the region near the plasma front.

REFERENCES

/1/ A.H.Zaidel, G.V.Ostrovskaia, Laser method in plasma diagnosis, Nauka, Moscow, 1977 (in Russian)

/2/ P.W.Schreiber, A.M.Hunter, D.R.Smith Jr., Plasma Phys., vol.15, p.635 (1973)

/3/ R.A.Alpher, D.R.White, Phys.Fluids, 1 (1958) , Phys.Fluids 2 (1959) 153

/4/ Plasma diagnostics, ed. W.Lochte-Holtgaven (Amsterdam), North Holland Publ.Comp., 1968

/5/ I.M.Podgornii editor, Topics in plasma diagnostics, Plenum Press, New York, London, 1971

/6/ R.W.Ladenburg, ed. Physical Measurements in Gas Dynamics and Combustion, Oxford University Press, London (1955)

/7/ D.Apostol, I.Apostol, D.Dragulinescu, C.Grigoriu, I.N.Mihailescu, I.Morjan, Al.Nitoi, I.M.Popescu, Rev.ROum.Phys., 20, 2, 185 (1975)

/8/ D.Apostol, I.Apostol, E.Cojocaru, V.Draganescu, I.N.Mihailescu, I.Morjan, V.I.Konov, in Proceedings of the XII-th International Conference on Phenomena in Ionized Gases, Berlin, p.89 (1977)

/9/ D.Apostol, I.Apostol, E.Cojocaru, V.Draganescu, I.N.Mihailescu, I.Morjan, V.I.Konov, J.Appl.Phys., 51, 1238 (1980)

/10/ D.Apostol, I.Apostol, D.Barbulescu, M.Dinescu, A.Hening, I.N.Mihailescu, V.Stancalie, M.Stoica, Optics Commun., 44, 5, 333 (1983)

/11/ I.Apostol, R.Dabu, M.Ganciu-Petcu, A.Hening, Al.Harsany, I.N.Mihailescu, M.Sandu, Rev.Roum.Phys., 27, 733 (1982)

/12/ V.Stancalie, D.Apostol, internal report

/13/ L.I.Sedov, Similarity and dimensional methods in mechanics (Academic Press Inc., 1959)

/14/ D.Apostol, I.Apostol, I.N.Mihailescu, Infrared Physics, 16, 269 (1976)

/15/ I.Ursu, D.Apostol, I.Apostol, Al.Harsany, A.B.Berezin, I.I.Komissarova, G.V.Ostrovskaia, I.I.Ostrovsky, V.N.Filipov, E.N.Sedova, Sov.Phys.J.Tech.Phys., 52, N32 (1982) (in Russian)

/16/ M.Stoica, D.Apostol, I.Apostol, C.Craciun, Al.Hening, I.N.Mihailescu. Optics.Commun., 52, 1, 5 (1984)

/17/ D.Apostol, I.Apostol, R.Dabu, V.Draganescu, Al.Harsani, I.N.Mihailescu, M.Moldovan, M.Sandu, Rev.Roum.Phys., 6, 689 (1980)

FIGURE CAPTIONS

Fig. 1 Michelson interferometer with He-Ne laser

Fig. 2 Typical interferograms on the showave induced in air by laser produced plasma

Fig. 3 Mach-Zehnder interferometer with ruby laser

Fig. 4 Interferometeric recordings of the gas plasma in the neighbourhood of solid targets, for different laser energies and different delays in respect to plasma initiation moment

Fig. 5 The values obtained for the plasma refractivity as a function of plasma radial coordinate for different distances from the target surface (axial distances)

Fig. 6 Lateral shearing fringes in infrared at 10.6 μm

Fig. 7 A new infrared interferometer

Fig. 8 An interferogram of an arc-discharge plasma impurified by Na, registered on triacetatcelulose

Fig. An interferogram of a laser produced-plasma in front of a graphite target.

Fig. 10 A schematic diagram of the experimental schlieren set-up

Fig. 11 A special device for synchronization and adjustable delay to assure plasma triggering during the ruby laser pulse train

Fig. 12 A typical schlieren images corresponding to different TEA-CO_2 laser incident intensities

Fig. 13 The shock wave velocity measured by schlieren methods

Fig. 14 A shadowgram of a laser produced plasma

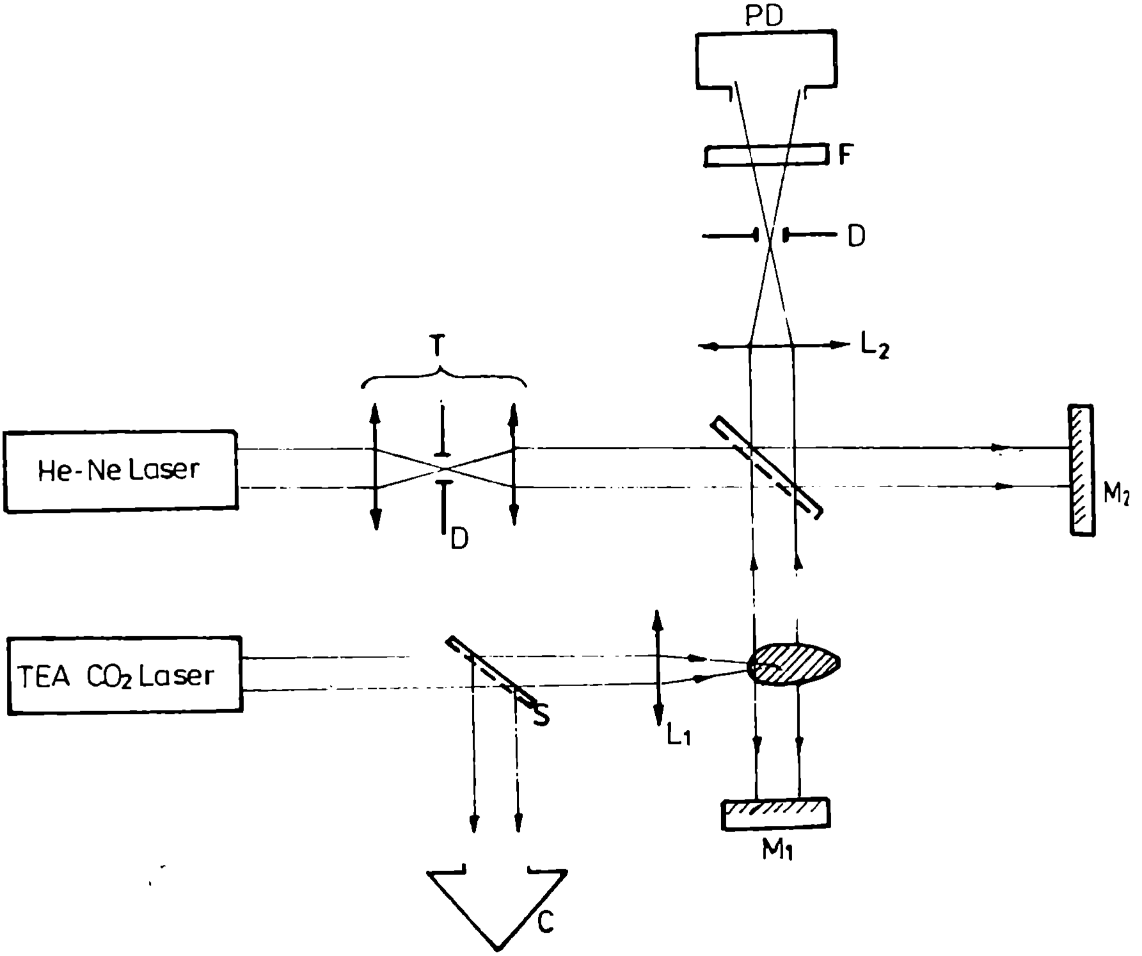

Fig. 1

P= 760 torr

E_p=28 10^5 erg

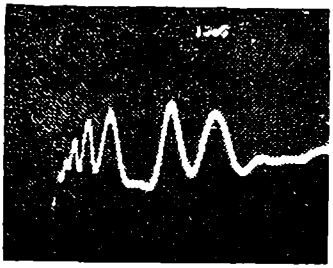

Fig. 2a

P= 456 torr

E_p=29 10^5 erg

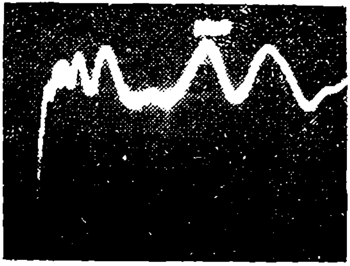

Fig. 2b

P= 290 torr

E_p=21 10^5 erg

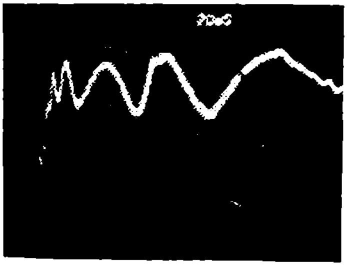

Fig. 2c

P= 152 torr

E_p= 37 10^5 erg

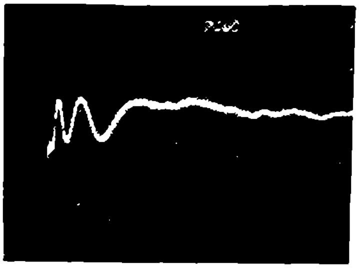

Fig. 2d

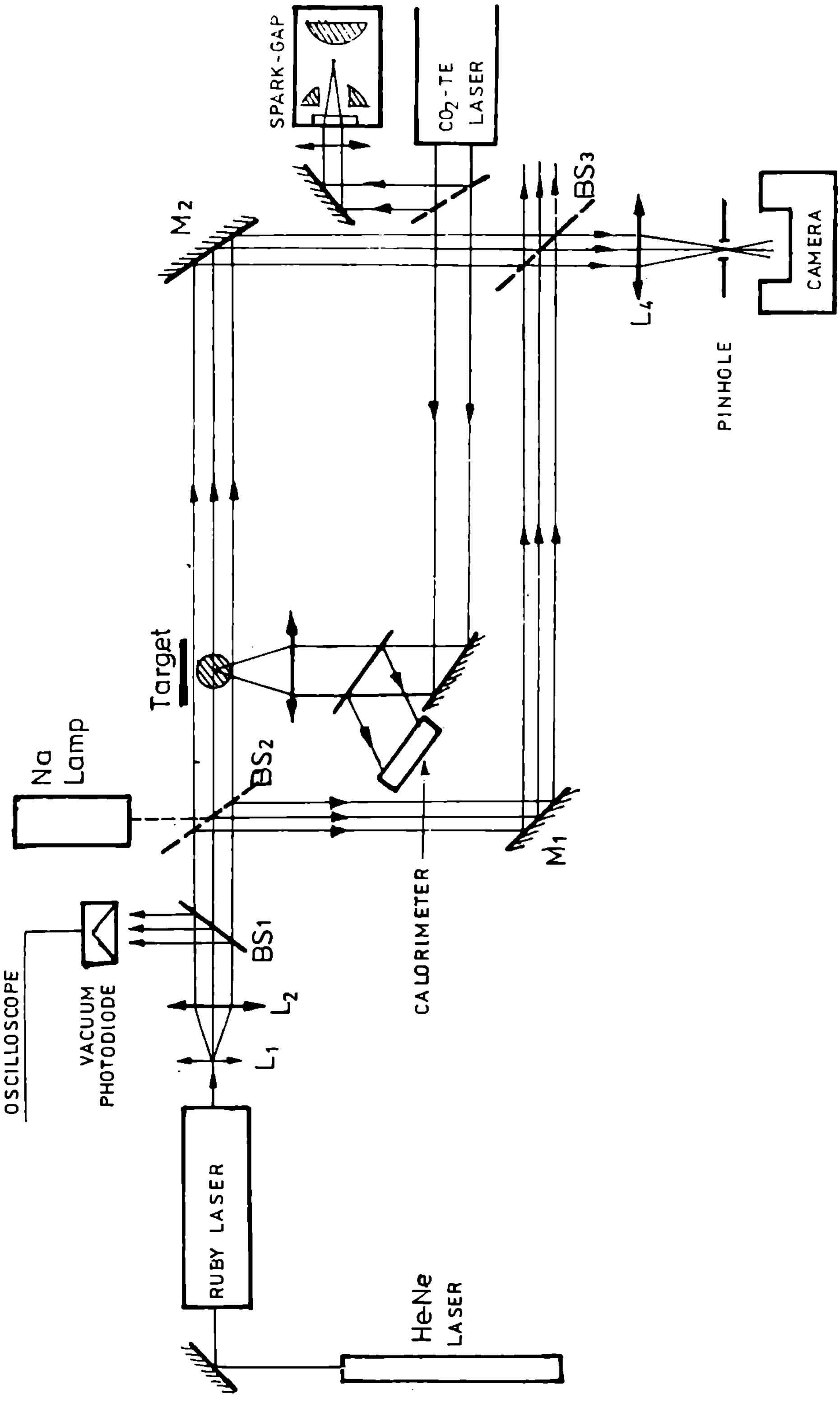
RUBY LASER
He-Ne LASER
L_1
L_2
VACUUM PHOTODIODE
OSCILLOSCOPE
BS_1
Na Lamp
BS_2
CALORIMETER
M_1
Target
M_2
SPARK-GAP
CO_2-TE LASER
BS_3
L_4
PINHOLE
CAMERA

Fig. 3

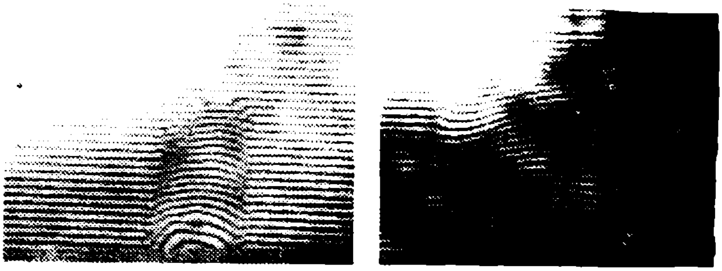

a b

Fig. 4

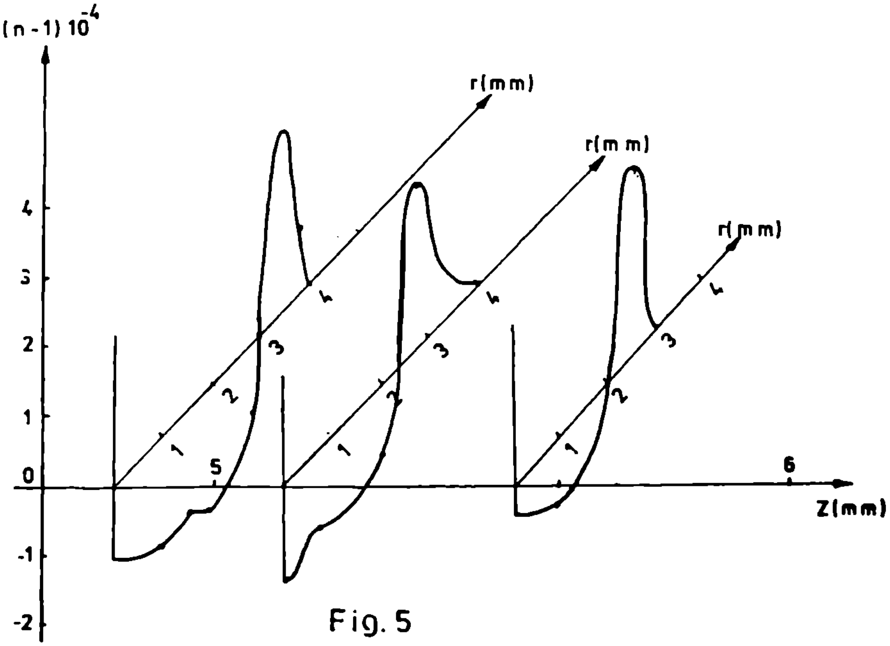

Fig. 5

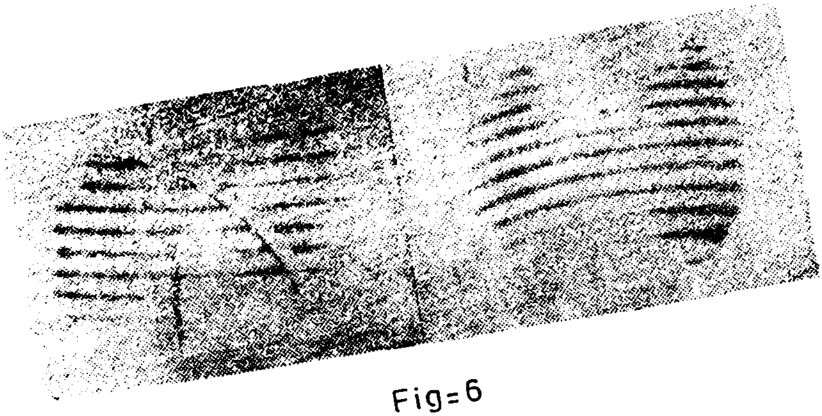

Fig=6

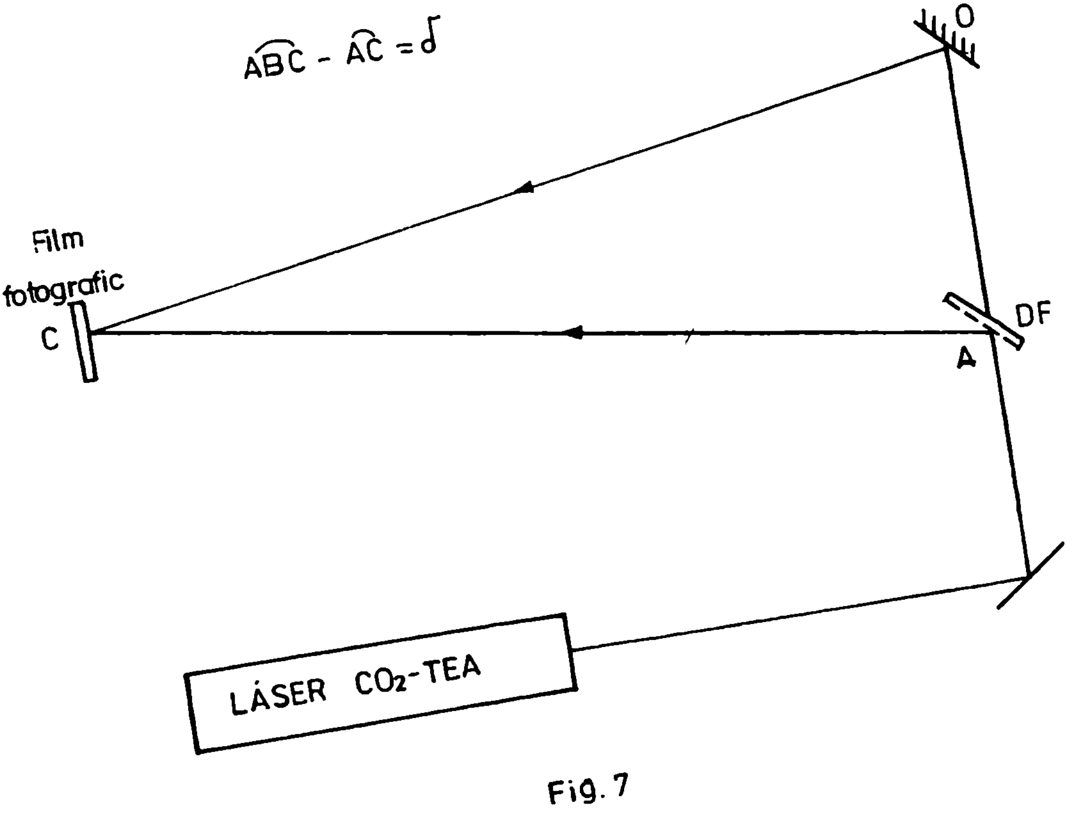
$\widehat{ABC} - \widehat{AC} = \delta$
O
Film fotografic
C
DF
A
LÁSER CO₂-TEA

Fig. 7

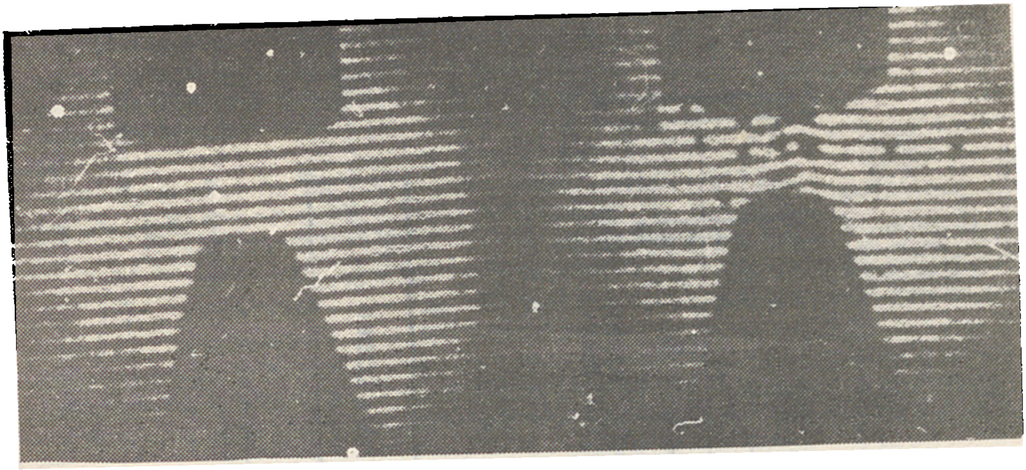

Fig. 8

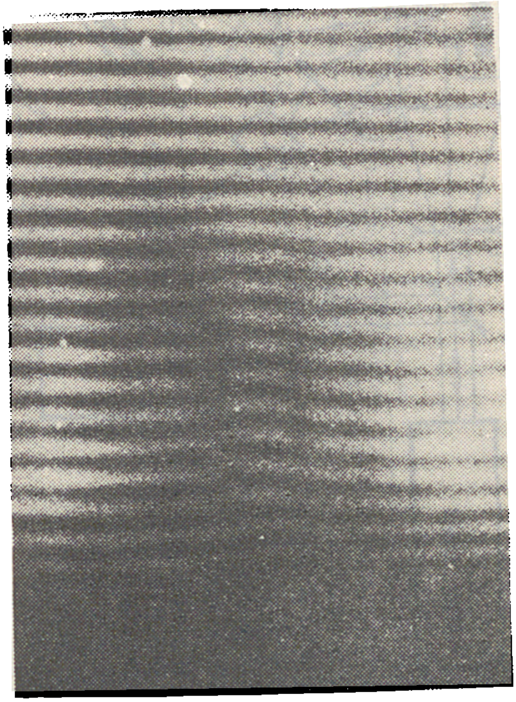

Fig. 9

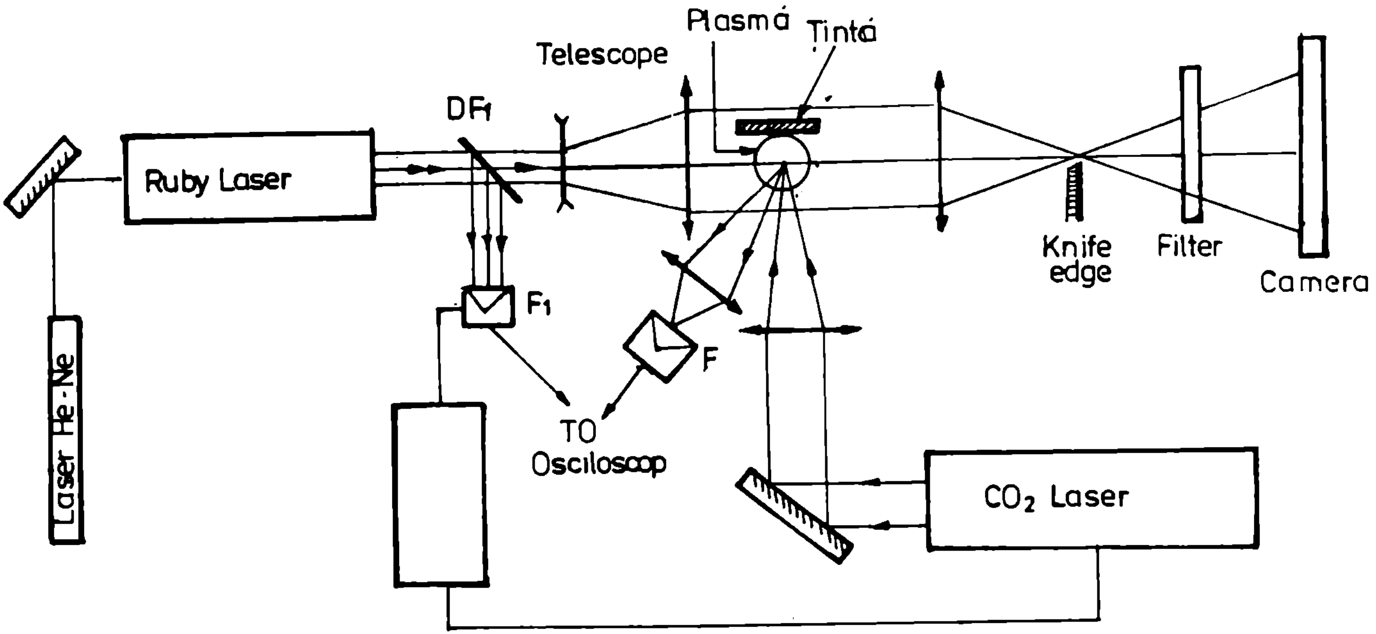
Plasmá
Tintá
Telescope
DF1
Ruby Laser
Laser He-Ne
F1
F
TO
Osciloscop
Knife
edge
Filter
Camera
CO2 Laser

Fig. 10

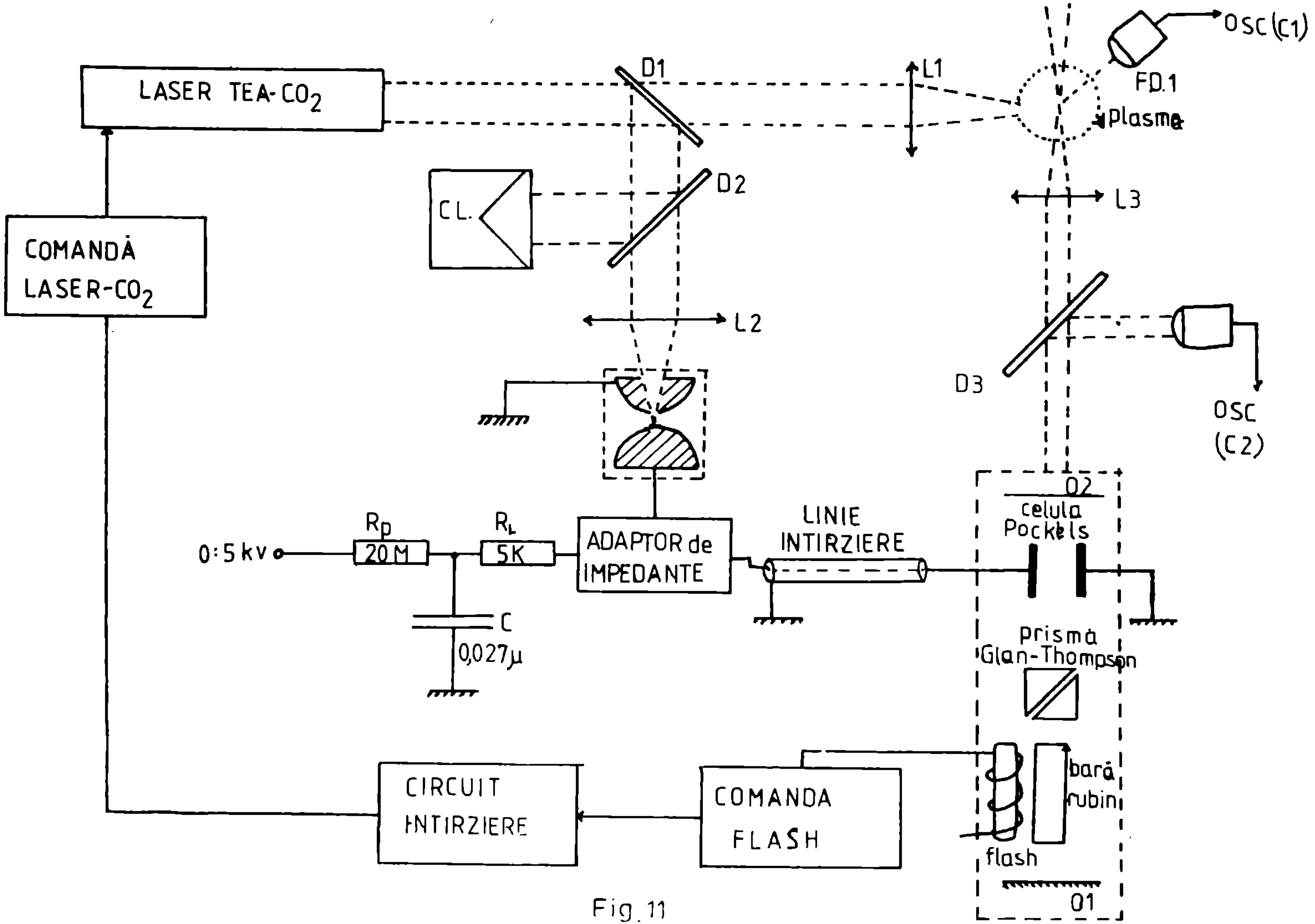
LASER TEA-CO$_2$
D1
L1
FD.1
OSC (C1)
plasme
D2
CL.
L3
COMANDĂ LASER-CO$_2$
L2
D3
OSC (C2)
O2
celula Pockels
R_p
20 M
R_L
5K
0:5 kv
ADAPTOR de IMPEDANTE
LINIE INTIRZIERE
C
0,027μ
prisma Glan-Thompson
bară rubin
flash
O1
CIRCUIT INTIRZIERE
COMANDA FLASH

Fig. 11

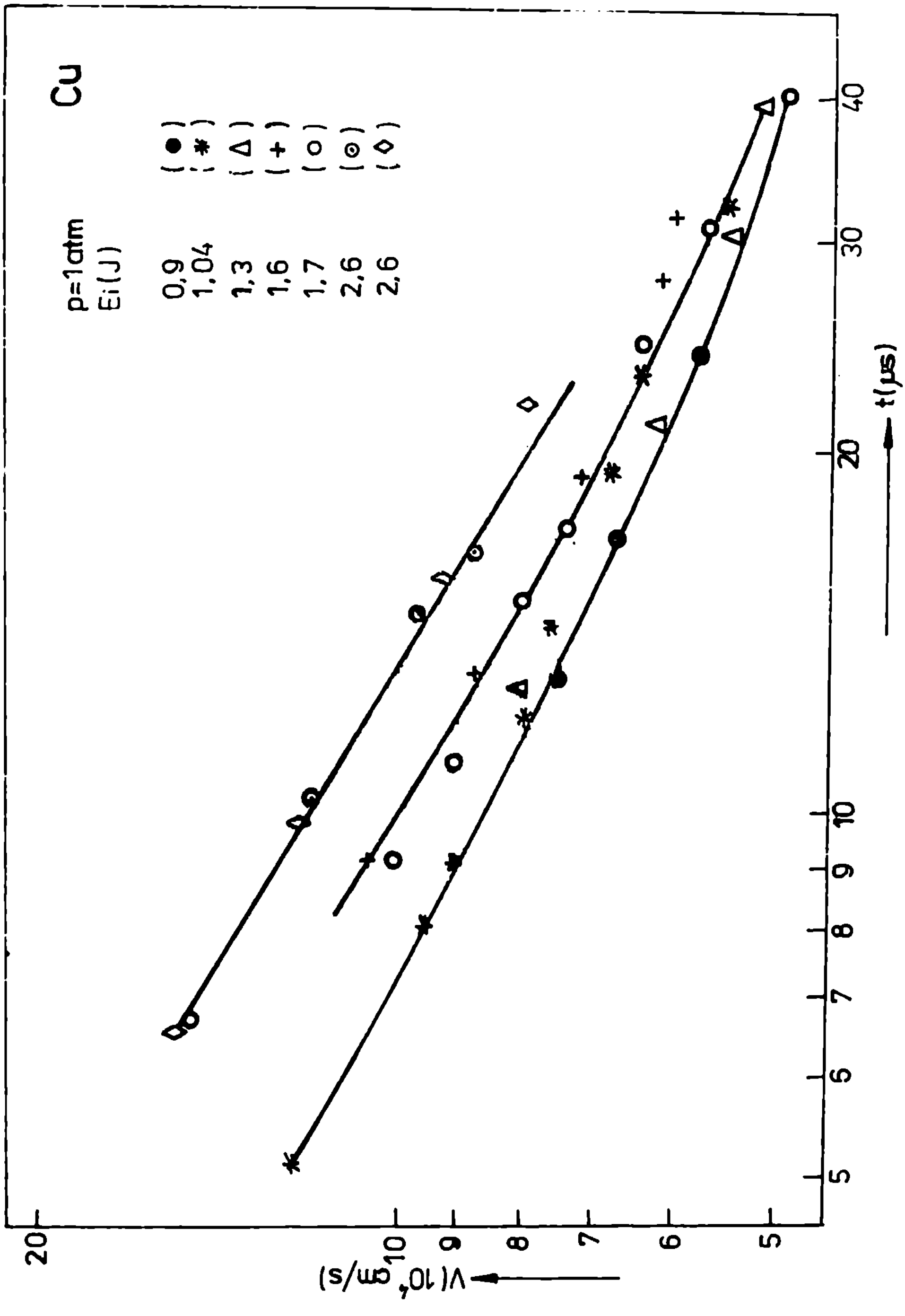
Cu
p=1atm
Ei(J)
0,9 (●)
1,04 (*)
1,3 (Δ)
1,6 (+)
1,7 (○)
2,6 (⊙)
2,6 (◇)
t(μs)
5
6
7
8
9
10
20
30
40
V(10⁴ cm/s)
5
6
7
8
9
10
20

Fig. 13

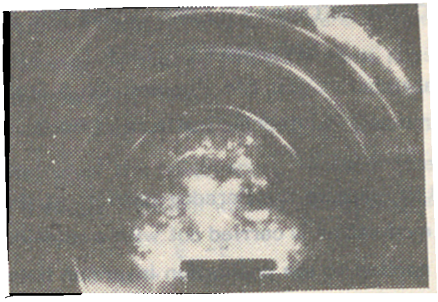

Fig. 12a

Fig. 12b

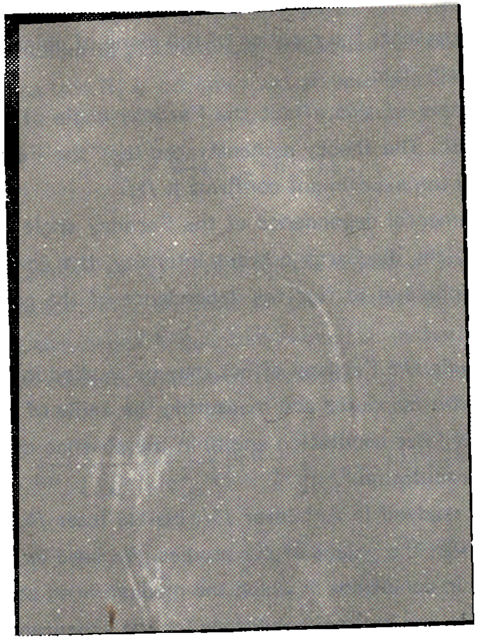

Fig. 14

LASER ACTIVE MEDIUM STUDIES USING THE RESONANT FARADAY EFFECT

Gabriela F. Cone, I.M. Popescu, Gh.A.Stanciu
Physics Department, Polytechnic Institute of Bucharest, ROMANIA

A method used to measure the Faraday rotation at the resonance is presented. The incident laser beam modulation is carried out with a rotating polarizer.

The method is applied to the population inversion between neon 3 s_2 and 2 p_4 level calculus. The dependence on gas mixture pressure and discharge current intensity of the population inversion is analog with the same dependance of the laser gain and power output /9, 10/. The method is applicable to any laser active medium to investigate the optimal condition for population inversion occurrence.

Introduction

In spite of the fact that 25 years have past since the first laser in the world was deviced, the problem of microscopic phenomena that contribute to or diminish population inversion in a laser active medium remains an important subject of investigation.

The optimal conditions for the population inversion to develop are still under study. In most cases, these conditions are known only empirically.

A physical phenomenon which makes it possible to study the optimal contidion for obtaining population inversion between the atomic level of a medium is the resonant Faraday effect. This phenomenon represents the rotation of the plane of polarization of the incident wave in a longitudinal d.c. magnetic field.

In the stimulated case of this effect the Faraday angle of the rotation is much bigger than in the nonresonant case. The theory demonstrated that the Faraday angle depends on the population inversion /1/ and the experiment confirms it /2/.

Studying the experimental dependence of the Faraday angle on various parameters such as the pressure of the gas, the discharge current intensity, the composition of the gas used as optic active medium, it is possible to find the dependence of the population inversion on these parameters.

In gaseous laser media the Faraday effect may be studied in two ways: a) by introducing the active medium in an optic resonator and measuring the angle of rotation of the polarization plane in the presence of the laser oscillation and b) in the absence of the optic resonator, that is in the absence of the laser oscillation.

The first case was studyed in Ar^+ laser /3/, He-Ne laser /4,5/, Xe laser /6/ and He-Cd laser /7/. The second case was the object of our studies. We used as optic medium gases such as Ne and the He-Ne mixture, in conditions in which the medium is an absorber or an amplifier.

Our results related to the optimal conditions for the appearance of the atomic population inversion are in good concordance with those established empirically for the He-Ne laser /8-10/. We consider that this method may be used to calculate some physical parameters of the atomic levels such as the atom's lifetime /11/.

Theory

In the resonant case, when the frequency ω of the incident radiation has a value closed to the transition frequency between a pair of atomic energy levels E_m and E_n, that is

$$\omega = \frac{E_m - E_n}{\hbar} + \Delta\omega \tag{1}$$

with $\Delta\omega << \omega$, the electric susceptibility for an isotropic medium containing weakly interacting atoms on the E_m and E_n atomic levels is /1/:

$$\chi_e = -\frac{1}{\hbar}\frac{n_n - n_m}{\Delta\omega - i\Gamma_{nm}}|<E_n|\sum_k \bar{p}_k|E_m>|^2 \tag{2}$$

where n_n and n_m are the population on the E_m and E_n atomic levels at equilibrium, Γ_{nm} are called the transverse relaxations rates of the off diagonal matrix elements of density matrix (related with the atom's lifetime), $\bar{p}_k$ are the electric - dipole moments.

We noted that at equilibrium, $n_n > n_m$ for $E_m > E_n$, and an electromagnetic wave is attenuated in the direction in which is propagates. But, in any circumstances if $n_m > n_n$ for $E_m > E_n$ (population inversion) the waves are amplified while propagation through this medium.

The index of refraction depends on the real part of the electric susceptibility.

If an isotropic medium is placed under the influence of the d.c. longitudinal magnetic field with magnetical induction B, it becomes anisotropic and the angle of Faraday rotation at the resonance, is:

$$\theta = \frac{\omega}{2c}(n_{\sigma^+} - n_{\sigma^-})L, \tag{3}$$

where n_{σ^+} and n_{σ^-} are the indices of refraction for the waves σ^+ and σ^- polarized circularly, left-hand and right-hand respectively, emitted in the atomic transitions in which $\Delta\mu = +1$ and $\Delta\mu = -1$ respectively, with μ the magnetic quantum number, L is the length of the medium.

The difference between the indices of refraction $n_{\sigma^+} - n_{\sigma^-}$ has the expression:

$$n_{\sigma^+} - n_{\sigma^-} = \frac{1}{n\hbar}\cdot\frac{n_n - n_m}{(\Delta\omega)^2 + \Gamma_{nm}^2}\Big\{|<E_{n}, J_n, \mu+1|\sum_k \bar{p}_k|E_m, J_m, \mu>|^2 - |<E_n, J_n, \mu-1|\sum_k \bar{p}_k|E_m, J_m, \mu>|^2\Big\} \tag{4}$$

where $\Delta\omega = \frac{eB}{m_e}$ is the Zeeman splitting, $n = \frac{1}{2}(n_{\sigma^+} - n_{\sigma^-})$ the index of refeaction when $B = 0$.

In an absorbing medium $n_n < n_m$ and $\theta < 0$, and an active (amplifying) medium $n_n > n_m$ and $\theta > 0$.

So, the apperance of the population inversion is indicated by the change of the Faraday angle sign measured in a laser active medium.

The imaginary part of the electric susceptibility appears in the gain coefficient wich has the expression /1/:

$$\alpha_{nm} = \frac{4\pi\omega}{\hbar c} \frac{(n_n - n_m)\Gamma_{nm}}{(\Delta\omega)^2 + \Gamma_{nm}^2} |\langle E_n | \sum_k \bar{p}_k | E_m \rangle|^2 . \tag{5}$$

We observe from eqs. (3)(5) that the Faraday angle θ and the gain coefficient α have the same dependance on the inversion of the population.

Experimental set-up

The Faraday rotation of the polarization plane of the incidenct laser beam was measured by modulation the incident laser beam with a rotating polarizer /12/. In this case, if the angle between transmission axis of the analyzer and polarizer is $\frac{\pi}{2}$, the intensity of the second armonics emerging from the analyzer vanishes. At a rotation $d\theta$ around the value $\theta = \frac{\pi}{2}$ the intensity of the second armonics emarging from the analyzer varies with:

$$(dI_{2\nu})_{\theta = \frac{\pi}{2}} = -\frac{1}{2} I_p \sin 2\pi\nu t \cdot d\theta , \tag{6}$$

where ν is the rotation frequency of the rotating polarizer and I_p is the laser intensity emerging from the polarizer (in our case the incident laser beam was linearly polarized). We can consider that $\frac{1}{2} I_p d\theta$ is the intensity of the second armonics for a Faraday rotation $d\theta$ around the value $\theta = \frac{\pi}{2}$.

This method has the following advantages: a) it is a method of null; b) the modulation is not dependent on the wavelength of the incident radiation; c) the polarizer conditions for the good quality are not severe because the continous component is very large; d) the signal / noise ratio depends on the intensity of the incident radiation.

In figure 1 the experimental set-up is shown. The optic active medium used was an atomic gas (helium-neon mixture and pure neon) to which we applied: a) an electric discharge which populated the excited levels; b) a laser beam linearly polarized in resonance with the atomic transition $E_m \rightarrow E_n$; c) a static magnetic field parallel to the propagation direction of the laser beam and to the discharge electric field.

The laser beam emerging from the glass tube with the gas mixture propagates through the rotating polarizer (R.P.) which is mounted in the center of the rotating diskus. An analyzer ssures the extinction of the laser beam. The signal from the photocell Ph_1 and the signal used for synchronization with the rotating polarizer enter a lock-in amplifier Ithaco Model 353. The magnetic fields is achieved in a coil wich assures 140 Gs/A with a precision of 3% at the ends in comparison with the middle. The rotating polarizer is of Leybold type and the frequency of its rotation is 98 Hz. The analyzer is a Nicol prism mounted on a goniometer devided into hundredths of a degree. The precision of the measurements depends on the mV - meter of the lock-in amplifier. The Ph_1 detector is a silicon photocell with 46% response at $\lambda = 632.8$ nm.

Experimental results

We used as parameters in the measurements the total pressure of the mixture of the gases and the discharge current intensity.

Figs.2-5 show the experimental dependances on these parameters of the Faraday rotation at the resonance. Comparing the curves in figs.2 and 3, we observe that the medium is amplifier if the ratio of the partial pressures of helium and neon has a value between 3($P_{total} < 1$ torr) and 14.5($P_{total} < 5$ torr). The role of helium in the appearance of the population inversion is evident. So, in the case of neon (fig.3) the Faraday rotation increases with the pressure to 5 torr and then becomes constant. Is is confirmed that the absorption probelibily increases with the collisions processes become important. In the case of the He-Ne mixture, at low pressure (~ 1 torr), the emission is dominant with respect to absorption, suggesting a selective population of the 3 s_2 neon level. The Faraday rotation has a maximum at the same radio of partial pressures and total pressure at that indicated in literature for the optimal conditions of laser oscillation /9,10/. So, at $P_{He}:P_{Ne} = 5$, θ has a maximum for P = 0.4 torr, that is p.d.= 3.6 torr. mm (the tube diameter d=9 mm), and for $p_{He}:p_{Ne}=10$, the maximum of θ appears at p = 0.65 torr, that is p.d.=5.85 torr.mm.

These conclusions on the absorbing or amplifying character of the medium agree with the results obtained by the method of perturbation spectroscopy /8/, and the dependence of the Faraday rotation θ on the total pressure is analog to the dependence of the He-Ne laser output on the gas mixture pressure /13/.

We have verified that if the helium neon mixture contains impurities such as O_2 or vapour, the Faraday rotation decreases below a value that we could measure with precision. This observation agrees with the hypothesis that the presence of impurities decreases the electronic temperature in the discharge reducing the number of high energy electrons that can excite the 3 s_2 neon level /14/. In fact, one of the difficulties in He-Ne lasers construction is the necessity to maintain the high purity of gas mixture.

As is seen in fig.4 and 5, the presence of He in the gas mixture modifies the electric discharge condition. This conclusion is confirmed in the literature /15/. In the case of a gas mixture the experimental dependence of the Faraday rotation at the resonance on the discharge current intensity is analog with the laser gain dependence on the same discharge current intensity /9,10/.

Population inversion calculation

We calculate the population inversion between the neon $3\ s_2$ and $2\ p_4$ levels using the eq.(4).

Fig.6 shows the dependence of the population inversion between these levels on the total pressure of a helium-neon mixture for the ratio of partial pressures $p_{He}:p_{Ne}=5$, and in fig.7 the dependence of the same population inversion on the discharge current intensity is plotted.

The dependence of the population inversion Δn on the angle θ and the magnetic induction $\bar{B}$ was calculated to be

$$\Delta n = 1.1344\times10^{27}\theta B + 1.92\times10^{27}\theta B\ tg^2 2\theta + 8.3842\times10^{23}\theta\ tg\ 2\theta + 9.1668\times10^{9}\ \frac{\theta}{B}(m^{-3}), \tag{7}$$

where θ is expresed in radian and B in tesla. The difference between the electric dipole matrix elements coresponding to the σ^+ and σ^- components has the value 16.905×10^{-58} (S.I.).

Dependences on the gas pressure and discharge current intensity are contained in the angle θ. In eq.(7) the first term is bigger than others at last hundredfold, so that, in first approximation, the dependence of the population inversion on the Faraday rotation is linear.

Conclusions

The method, advanced for the determination of the population inversion between two laser levels by measuring the Faraday rotation at the resonance, offers the posibility of studying the dependence of the population inversion on different parameters characteristic for electric discharge or for the gas mixture and the influence of diffusion on the tube walls on the population inversion.

The obtained results lead to useful conclusions regarding the optimal conditions for the appearence of population inversion and permit to study the collision processes between atoms, ions and electrons that are responsible for atomic excitation and dezexcitation on different energetic levels.

REFERENCES

/1/ W.S.C.Chang, "Princ. of Q.E.", 6.4. Addison Wesley Publ.Co., (1970)

/2/ Gabriela Cone et al., ICO-13 Conf. Digest, Sapporo 1984, p.492 (1984)

/3/ Douglas C. Sinclair, JOSA 56, 1727 (1966)

/4/ R.Rosemberg et al., Appl.Opt., 3, 1079 (1964)

/5/ W.C.West et al., Ninth Intern.Conf. on Phenom. in Ionized Gases, Bucharest, p.25 (1969)

/6/ R.L.Fork, C.K.Patel, Phys.Rev., 129, 2577 (1963)

/7/ Gabriela Cone et al., Rev.Roum.Phys., 25(6), 623 (1980)

/8/ A.I.Ciura et al., St.Cerc.Fiz., 29(8), 969 (1977)

/9/ A.D.White, E.I.Gordon, Appl.Phys.Lett., 3, 197 (1963)

/10/ A.D.White, E.I.Gordon, Appl.Phys.Lett., 3, 199 (1963)
/11/ Gabriela Cone et al., Bul.IPB, Seria Elth., XLV(1), 5 (1983)
/12/ Gh.Stanciu et al., Bul.IPB, Seria Elth., XLV(2), 5 (1982)
/13/ V.Vasiliu, St.Cerc.Fiz., 23(6), 637 (1971)
/14/ C.Berenyi et al., St.Cerc.Fiz., 22(3), 235 (1970)
/15/ V.P.Chebotayev, L.S.Vasilenko, Opt. i Spectr., 20, 505 (1966)

FIGURE CAPTIONS

Fig.1 Experimental set-up: LASER: He-Ne laser; PROBE: neon or helium-neon mixture: R.P. rotating polarizer; A-analyzer; Ph_1 and Ph_2-photocells; H.V.-high voltage supply; L.A.-look-in amplifier

Fig.2 Experimental dependence of the Faraday rotation θ on the total pressure of the He-Ne mixture for different ratios of partial pressures

Fig.3 Experimental dependence of the Faraday rotation θ on the pressure for pure Ne

Fig.4 Experimental dependence of the Faraday rotation θ on the electric discharge current intensity for pure neon

Fig.5 Experimental dependence of the Faraday rotation θ on the electric discharge current intensity for the He-Ne mixture

Fig.6 The dependence of the population inversion between the $3s_2$ and $2p_4$ neon levels on the total pressure of the gas mixture

Fig.7 The dependence of the population inversion between the $3s_2$ and $2p_4$ neon levels on the electric discharge current intensity for the gas mixture

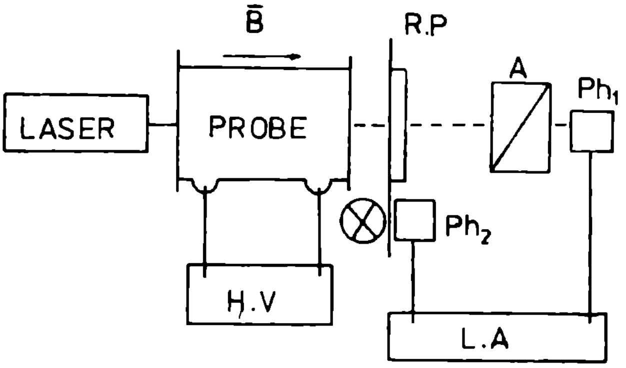

Fig 1

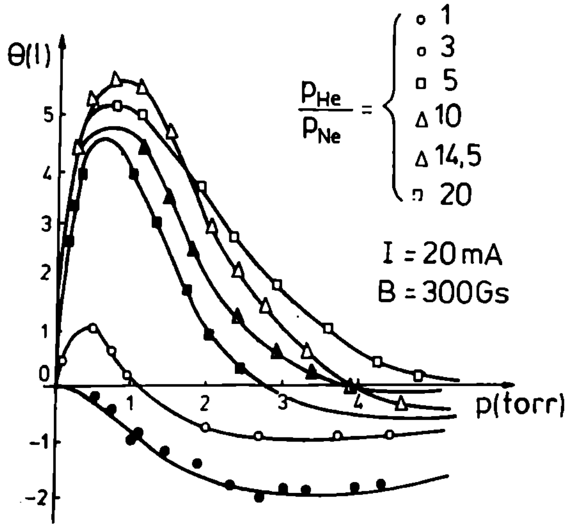

Fig. 2

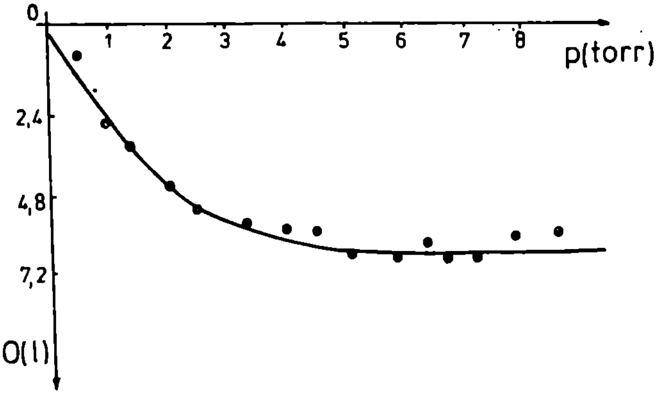

Fig. 3

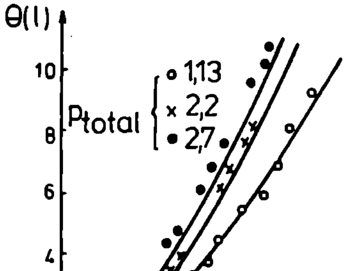

Fig. 4

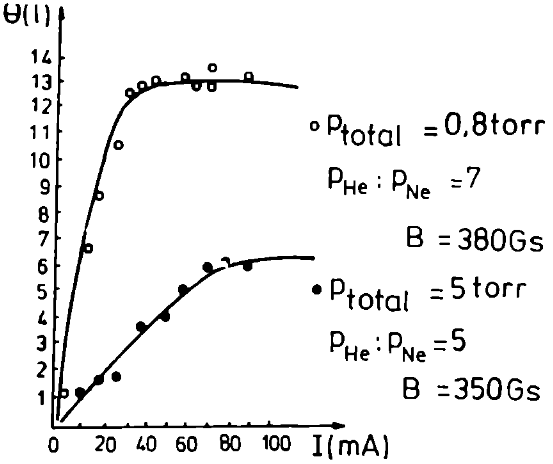

Fig. 5

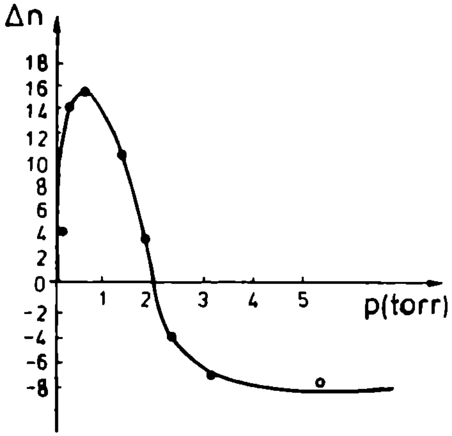

Fig. 6

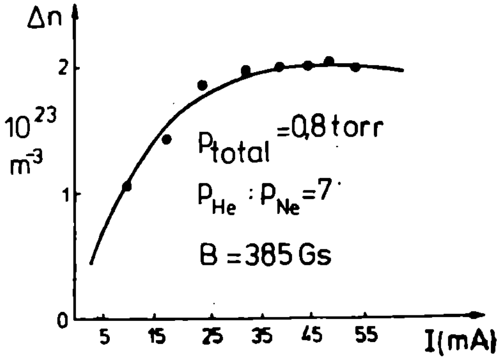

Fig. 7

LASER OPTICS

R.Medianu, C.Timus, C.Georgescu
Institute for Physics and Technology of Radiation Device, Bucharest

The paper deals with problems concerning resonators and optical components used in lasers and laser applications.

Different optical components - mirrors, filters, beam-splitters, polarizers a.s.o. - using the technology of high vacuum thermal deposition are presented.

There are two essential requirements for a laser: a cavity and an active medium within it; the purpose of the laser cavity is to direct the radiation back and forth many times through the medium, so that the gain by/stimulated emission exceeds the losses. So, in the optical cavity the amplifcation by the inverted population gives rise to a sustained oscillation as in a laser.

In the cavities constructed with plan parallel and spherical mirrors standing waves are established; corner-cube reflectors give rise to travelling wave systems in the cavity.

In standing waves there is a permanent phase and amplitude relationship between the waves travelling in opposite directions.

A mode is a pattern of field distribution that reproduces itself in spatial distribution and phase but not in amplitude, as the wave travels between the reflectors. The amplitude is not reproduced because of diffraction and reflection losses.

These unavoidable losses determine the lifetime of a mode: the time for its amplitude to decay to the fraction e^{-1} of its initial value.

While at microwave frequencies ($\lambda \approx 1$ cm) it is possible to construct cavities of the order of one wavelength at optical frequencies the cavities are necessarily multimode.

The system oscillates at frequencies which the resonator and active medium have in common.

Generally, the laser gain should be well above the threshold necessary for oscillation to obtain simultaneous oscillation of several modes.

Any highly reflecting enclosure will support resonances in the optical region. The mode density (i.e. the number of modes per unit volume of enclosure) is given by

$$P(\nu)d\nu = \frac{8\pi}{\lambda^3}\frac{\upsilon\nu}{\nu}$$

$d\nu$ is the frequency bandwidth of interest.

It depends on the laser application what kind of cavity will be chosen, but the different applications of lasers determined a large variety of optical resonators.

A resonator consists of two mirrors one totally reflecting (more than 99%), and the other one only partialy reflecting (depending on the laser).

Because of the variety of active media, that determine the spectral range of the emission, the resonators are correspondingly different for each type of laser.

Practically the laser mirrors are made by deposition of compact structures of reflectant layers on transmissible substrates in the laser spectral range. The laser mirrors must have a high reflectance at the laser wavelength and the same time small losses by absorption and diffusions.

The mirrors are the main components of a resonator, but there are also a lot of other optical components that achieve the optical processing of the laser beam in a laser application: windows, lens, filters, attenuators, beam splitters etc.

The first step in the technology of optical components is an adequate choice of materials, because the performance of the components depends on the quality of the materials. The optical finishing of the substrates is also of great importance as far as the lasers are concerned.

Generally, to achieve a performance of reflectance and transmittance in a spectral range the technology of thin dielectric films in single or multilayer structure is used.

There are different methods of thin film deposition; the most widely used are the method of thermal evaporation and electron beam evaporation. The degree of optical finishing depends on the laser wavelength so the less the wavelength is the finer the polishing. For visible lasers the optical finishing has to be within $\lambda/20$ - $\lambda/40$, while a smoothness of $\lambda/10$ - $\lambda/20$ is quite good in the infrared.

Substrates and dielectrics

Materials used as substrates must have a good transmission in the spectral range of interest and a low absorption.

For the visible range of 400 - 700 nm, the above conditions are successfully met by optical glass and quartz, as for the UV below 400 nm quartz optics is recommended, as well as crystals such as CaF_2, LiF etc.

The type of operation - either CW or pulsed - as well as the level of power or energy density determine the choice of the most suitable material.

In the infrared, II-VI compounds e.g. ZnSe, GaAs, Ge, ZnS, CdTe, are commonly used as substrates for mirrors and different other components, and crystal like NaCl, KCl, KBr, $CaBr_2$, CaF_2 etc are used for windows.

The dielectrics used for optical components in thin solid films have to meet several special requirements: purity more than 99.9, high transparency, constant index of refraction, low absorption, homogeneity, mechanical and chemical stability, good resistance to environmental conditions (humidity, temperature, radiations etc.).

Yet, the range of dielectrics is limited, so different experiments are made to extend the possible indexes. This is done by evaporation of mixtures of dielectrics with appropriate indexes.

Results

Metallic laser mirrors

The most common reflective coating is the first surface aluminium coated mirror. This mirror gives good reflectance from the UV through the infrared. A mirror with such a coating can withstand gentle handling and cleaning.

To protect the aluminium coating monolayers of silicon monoxide, silicon dioxide and magnesium fluoride are put on.

For higher reflectance the aluminium can be overcoated with two or more dielectric layers. This is the mirror commonly used for the UV. For even higher reflectance, silver is frequently used due to its reflectance greater than 96% and broad bandwidth of 0.4-10 µm.

The drawbacks of silver coatings are their quite bad adherence to substrate surface and tarnish at atmospheric exposure. The cost is higher than that of aluminium coatings.

Gold and copper are widely used as totally reflective mirrors in the infrared. The reflectance of these metals drops off rapidly in the visible spectrum.

Both coatings are soft and must be protected if the components are to be used in other environments than the laboratory.

It is possible to obtain reflective coatings using only dielectric materials. These reflectors approach 100% and are much more resistant than the metallic ones. High reflectance is available over a very limited wavelength interval that is just the case of laser mirrors.

All dielectric reflectors are more expensive than the metallic ones because the technology is more sophisticated and the fabrication time is longer.

Laser mirrors are generally made by deposition of compact structures of reflective multilayers on transparent substrates within a given spectral range.

To get reflector stacks alternating films of high and low refractive index are used

$$n_H > n_S \; ; \qquad n_L < n_S$$

n_H dielectric with high index

n_L dielectric with low index

n_S substrate index

Laser mirrors consisting of $\lambda/4$ stacks exhibit extremely low losses.

A compensation condition concerning the mechanical stresses has also to be met: one of the materials has to exhibit tensile stresses while the other compressive ones in order to avoid the cracking of the film.

For laser mirrors in the visible and near infrared spectral regions the following combinations of dielectrics are used:

$ZnS - MgF_2$	$CeO_2 - MgF_2$
$ZnS - ThF_4$	$ZnSe - ThF_4$
$ZnS - Na_3AlF_6$	$ZnSe - Na_3AlF_6$
	$TiO_2 - SiO_2$

For He-Ne lasers we commonly use $ZnS - MgF_2$ for both mirrors, only the number of stacks is different.

ThF_4 is very important as low index material for dielectric laser mirrors. The films are stable and very compatible with ZnS in multilayer coatings, but its " α " radioactivity is an obvious disadvantage.

In infrared the transparent substrates are germanium n = 4; GaAs n = 3.27; ZnSe n = 2.4; CdTe n = 2.67; ZnS n = 2.2.

For the 10.6 µm wavelength we frequently use germanium as substrate and the following combinations as reflector stacks

Ge - BaF_2	Ge - ZnSe
Ge - ThF_4	Ge - ZnS

We found the combination Ge / ThF_4 /ZnS to be the best mirror of high reliability, capable to withstand high density levels (Fig.1).

BaF_2 n = 1.4 is often used as low index material compatible with germanium. SrF_2 n = 1.35 is also recommended for IR, ZnSe is one of the best substrate materials for IR due to its high transparency (more than 70% in 2.5 - 25 µm) and low absorption (less than 10^{-3} cm^{-1}).

Due to its transparency even in the visible range, ZnSe is useful in the experimental setups as it facilitates alignmentThe reflection coatings for the ZnSe substrate consist of λ/4 alternating stacks of BaF_2 and ZnSe. GaAs is used at higher levels of operations (more than 500 W in cw operation at 10.6 µm) because the thermal runways and absorption are less then for germanium while the transparency if higher (about 55% and 10.6 µm).

Antireflection coatings

In order to avoid reflection losses on the first or on both faces most optical components are antireflection coated.

The greater index is the greater the reflection losses. A glass of index n = 1.5 gives rise to a reflection of 4.3 % in the visible, while germanium n = 4 reflects in the IR (λ = 2 µm) about 40 %.

The laser mirrors have a reflective coated face and a second antireflection coated one.

Even the rods of active media are antireflection coated.

The index of antireflection coating is the square root of the index of the substrate (so, to get a zero reflectance for a crown substrate of n_s = 1.51, it is necessry to use a dielectric of index n = 1.23).

Since optical materials with indexes in a continuum of values are unavailable as dielectrics a compound is used whose index is nearest to the recommended value.

Practically, it is not possible to achieve zero reflectance using an antireflection coating but an important decrease of the reflectance is obtained.

To decrease the reflectance as much as possible multilayer antireflection coatings are sometimes needed.

For the visible range of the spectrum we generally use a monolayer of MgF_2 n = 1.4, while for the IR for germanium ZnS n = 2.37 /1/.

The antireflection coatings of the ZnSe substrate consists of BaF_2 and ZnS. To get zero reflectance at 10.6 µm the thickness of the layers can be computed. Practically we have worked out for ZnSe the following combinations: a λ/8 BaF_2 as first layer and ZnS λ /16 as the second layer.

Filters

Filters are optical components which are useful in the optical processing of the laser beam; selection of a given spectral range with specific charateristics, the attenuation, the splitting of the beam a.s.o.

The method of classical alternating films in λ/4 structure doesn't provide any special spectral characteristics. Since this technology is not more valid only computers solve the problem by facilitating the computation of complex thin film systems.

In our laboratory some problems concerning filters have been solved: an antilaser filter, a filter at 2.8 µm, a gradual filter for the visible region.

For the antilaser filter a hybrid solution was adopted; the filter consists of two optical components - a large band wavelength neutral filter and the second optical components deposited with dielectric multilayers. Both components cemented achieve the necessary characteristics.

As had been resulted from the computation to get the filter for 2.6 - 2.8 µm a very laboriously technology was achieved. As substrate we used quartz, the cut and transmittance characteristics are achieved by depositing germanium and SiO in a complex structure of λ/8, λ /4 layers /2/.

When it is necessary to equalize the intensity of two beam attenuators must be used.

A variable attenuator for He-Ne wavelength was devised using metalic coatings. During the deposition, the obturator is gradually moved so the transmisions of the component decreases continuously, not in steps, allowing a very fine adjustment.

Beam-splitters

It is often necessary to have in an experimental set-up a reference beam to controle the different phenomena. This is achieved by a special optical component that splits the laser beam into two perpendicular beams a transmitted one and a reflected one.

These are applications that need more sophisticate beam spliters imposing some phase relation between the split beams. A type of such a beam splitter that accomplish a quadratic phase relation was obtained in our work group. The phase relation results from the differences in the optical ways imposed by the beam splitter /3/.

The technology of such component is not at all simple, the performance is achieved using metallic and also dielectric layers in a special geometrical configuration.

Polarizers

Brewster angle transmision polarizers were developed using optical glass BK 7 as substrate and depositing different thin dielectric films with indexes greater than the substrate index ZnS, ZrO_2, ZnSe, ZnTe, CeO_2.

These Brewster transmision polarizer are used instead of piles of glass plates, because of the greater degree of polarization.

Since the dielectric films are thin, in the computation of the degree of polarization we considered only the reflectance on a face, but if the film is thicker both reflectances must be taken into account.

These polarizers are used in infrared where prisms are not available. Only several plates achieved reasonable degree of polarization. The higher refractive index of the plates, the fewer is required. They are simple to produce and unexpensive.

The table below gives the parameters of the polarizers developed by us and verified in Infrared at 1.06 µm /4/.

THEORY	n	1,52	1,9	2,0	2,1	2,2	2,3	2,4	2,5	2,6	2,7	2,8
	p	0,10	0,19	0,22	0,25	0,28	0,31	0,33	0,36	0,38	0,4	0,43
	Θ_B	56°30'	62°10'	63°30'	64°30'	65°30'	66°30'	67°20'	68°10'	69°	69°40'	70°20'
EXPERIMENTAL	Film	BK7	CeO_2 ZrO_2			ZnS			ZnSe		ZnTe	
	Pexp	0,06	0,38 0,41			0,33			0,43		0,43	

Tests upon optical components

The first test, that must be carried out upon an optical component is the spectral characteristic that attest the special application of the component.

The spectral characteristic is very useful for improving the devised technology, according to the computing program, to fit the theoretical curve with the experimental one.

The climatic tests are recommended to establish the environmental conditions for an optical component. These tests are made just once for any type of optical components.

For these we use a Brabander Realtest - special climatic room.

The adhesion and damage tests are distructive, so they are not customary. The adherence is verified by the scoth test.

To establish the damage thresholds induced by a Q switch laser in a laboratory set-up a Nd:YAG laser operating in TEMoo mode was used and the power density of the laser beam was adjusted by moving the samples along the laser beam near the beam waist of a focusing lens /5/.

Different monolayers were tested.

The table presents the laser-induced damage threshold values under Q-switched conditions at 1.06 μm.

$\lambda/4$ film at 1.06 μm	Power density at threshold MW/cm^2
ZnS	200 - 300
CeO_2	300
SiO	400
MgF_2	500
$ZnS/ThF_4/ZnS$	250
BK 7	5×10^3

We soon hope to present our results referring to electron beam technology.

Acknowledgements

The authors are very much indebted to V.Vasile and M.Strachinaru for their helpful technical assistance.

REFERENCES

/1/ D.Dutu, C.Georgescu, R.Medianu, St.Cerc.Fiz., 24, 10, 1277-1284 (1972)

/2/ R.Medianu, C.Timus, C.Georgescu, T.Munteanu, "New optical components for IR", Nat.Coll.Opt., IIIrd Edition, June 14-15 (1984)

/3/ C.Blenaru, G.Popescu, C.Georgescu, A.Brumfeld, Patent 76929, Oct.20 (1979)

/4/ R.Medianu, G.Nemes, C.Timus, C.Fenic, Brewster angle transmission polarizers with thin films, Progress In Physics, IVth edition, Sibiu, Oct.4-6 (1984)

/5/ V.R.Medianu, C.Georgescu, A.Stratan, C.Timus, Rev.Roum.Phys., 26, 2, 109-113 (1981)

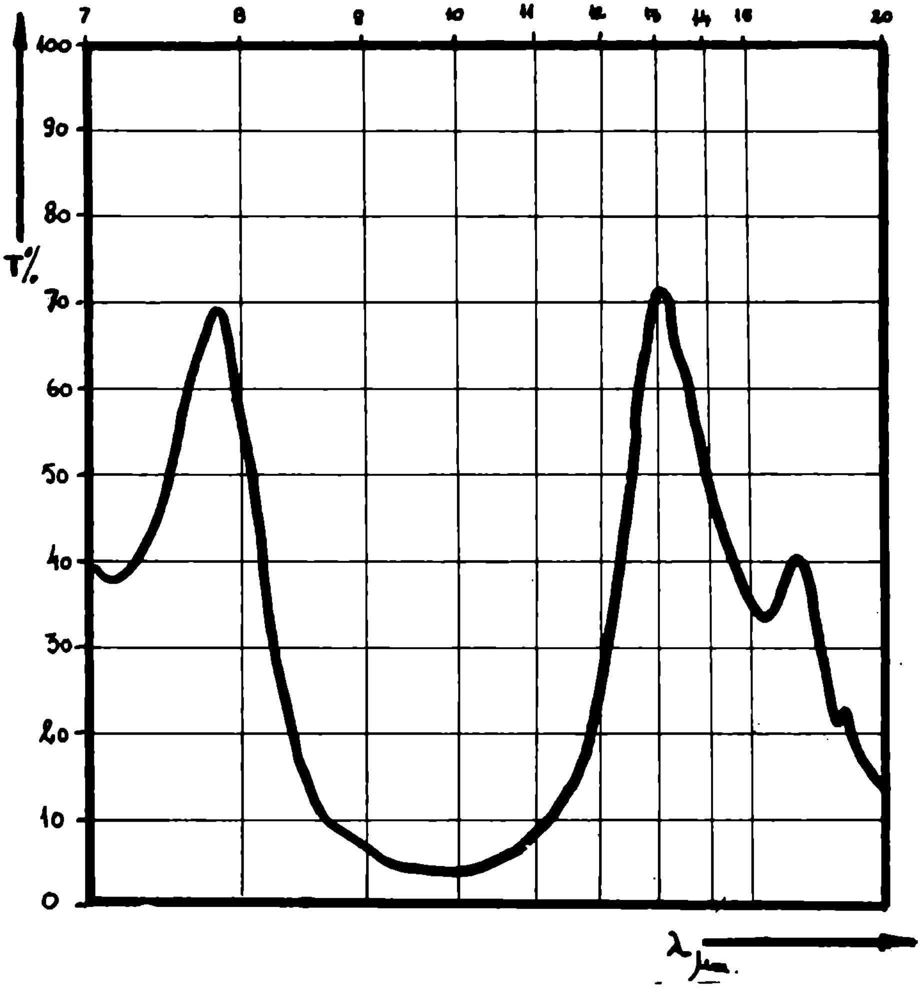

Fig. 1.

THE FREQUENCY STABILIZATION OF He-Ne LASERS

Gh.Popescu, C.Blanaru

Laser Dept., Institute for Physics and Technology of Radiation Devices

1. Introduction

A particular interest in the subject of He-Ne laser frequency stabilization has developed due to the possibility of applying such lasers in the fields of interferometry, metrology, geophysics. New stabilization methods have improved the stability of some lasers and promoted the idea of using an optical frequency standard superior to the existing krypton-86 standard.

From a historical point of view, the helium-neon laser was the earliest subject of study for frequency stabilization, so it is not surprising that the helium-neon laser - irrespective whether of visible or infrared wavelength - still maintains its place as the primary object of stabilization research /1/.

To suit either an optical standard or the above applications, a laser should possess some practical qualities. We are equally looking into the physics of the laser tube, the electrical parameters or the mechanical design. In a DC excited He-Ne laser the discharge is smooth, easy to maintain and does not require very high voltages or currents, this leading to a stable output power, low frequency shifts due to varying electric parameters or mixture pressure. The laser tube is easy to construct and does not require substantial cooling, which facilitates the construction of mechanically and thermally stable cavities. Depending on the actual applications, the output power could vary over two orders of magnitude which assures enough power from resonable long cavities.

The helium-neon laser is the most suitable laser to fulfil the conditions outlined earlier and particular interest will be paid to the red 633 nm line, which is dealt with in this paper.

The principle of all stabilization systems to be discussed is extremely simple. First of all, a single frequency laser is by some means constructed. Secondly, a stable frequency reference is to be found. As the laser frequency deviates from that of the reference, a third step has to be taken into account by developing an error-sensing mechanism or discriminant used to derive a signal proportional to the deviation. The laser frequency is controlled to that of the reference by a simple servo-loop. In doing that, the laser frequency is said to be locked to the frequency of the reference.

2. Factor to affect laser stability

A carefull choice of mirror radii and tube bare diameter could eliminate off-axis modes. The cavity resonances of TEM_{00q} mode are given by

$$\nu_q = q \cdot \frac{c}{2nL} \tag{1}$$

where q is the order of the mode (an integer) equal to the integral number of half-wavelength of the resonant radiation to fit exactly into the optical length of the cavity, c is the velocity of light, n - the refracting index of the medium between the laser mirrors, and L the cavity length. The changes in cavity length will affect the frequency of an oscillating mode and maintenance of a constant length is the prime objective in frequency stabilization schemes.

There are various possible perturabation on the cavity length arising either from external phenomena or from effects internal to the plasma tube. Among the external effects one should mention thermal variations occurring in the temperature of the spacers material between the endplates of the cavity which carry lasers mirrors. A fractional change $\Delta L/L$ as low as possible is first desired. A low coefficient of expansion of the spacer material may be found for Invar ($\alpha = 1.26 \times 10^{-6} {}^{\circ}C^{-1}$), fused quartz ($\alpha = 0.5 \times 10^{-6}$), zero-dur ($\alpha = 5 \times 10^{-8}$). Even with low-expansion materials thermal tunings of the cavity of 500 MHz/°C are tippically so that for good frequency stability (say 5 MHz) the cavity temperature must be constant to 0.01°C, a difficult-to-fit figure. Besides thermal variations, other external effects are atmospheric variations (altering the refracting index of the air n_{air}), mechnaical vibrations (mechnaical mouvements transmitted through working surfaces or airborne disturbances), variations in the position of optical components (external mirror lasers), magnetic fields (changes due to the magnetostrictive properties of the spacer material).

Internal effects are coming from considering discharge noise, given by fluctuation in the discharge current or plasma oscillations.

All the above perturbations have to be considered for improving the qualities of a free running laser in order to minimize frequency fluctuation in the laser to be stabilized. When the laser frequency has already been stabilized, the perturbations of importance are those which shift the frequency of the reference /2/.

3. Single frequency lasers and passive stabilization

Before any attempt is made to stabilize the frequency of a laser, a single frequency output must be ensured. A laser may normally operate simultaneously at several different frequencies which are the cavity resonant modes for which the laser gain exceeds any losses present within the laser cavity. The separation $\Delta\nu$ of longitudinal cavity modes is given from (1)

$$\Delta\nu = c/2nL \qquad (2)$$

Two techniques of selection of a single frequency have been used by authors as follows:

- if the length L of the laser is reduced, the mode separation $\Delta\nu$ is increased until only one mode is left within the gain bandwidth of the laser; a PZT traducer may then tune laser frequency throughout bandwidth by varying the cavity length /3/;

- if the optical length nL of a long laser includes an intracavity Fabry-Perrot type bandpass filter then only the wavelength radiation satisfying the resonance relationship $2\,n_e t \cos\phi = n_e \lambda_{laser}$ will get enough gain from the active laser medium to overcome losses and oscillate; changing either n_e, t or ϕ , one may tune the oscillation frequency of the laser within the gain bandwidth of the laser.

(In the above relation n_e - the refractive index of etalon, t - its thickness, ϕ - the angle between the incident light direction and the normal to the etalon surface, λ_{laser} - the wavelength of the laser light.)

One step further in the development of the frequency stable laser is to stabilize the single frequency laser output to some stable passive reference cavity. This cavity does not contain any discharge tube and no thermal effects proper to laser cavity are present.

We used this method of passive stabilization to limit the frequency shift of a free running single mode long He-Ne laser /6/. The intracavity etalon is a cylindrical bar of fused quartz the ends of which are polished flat and parallel at a high degree of precision (λ /10 flat over the active reqion and less then 2" parallel). The lenghth of the etalon (5 cm) is chosen so that its free spectral range (3000 MHz) exceeds the laser gain bandwidth (around 1200 MHz) thereby selecting only one laser mode. The finesse of the etalon is rather small (around 2.2 for uncoated ends). The width of the passband is correlated to the finesse of the etalon, but uncoated ends ensure a low insertion loss for such a low gain medium as that of the helium-neon laser. Using a careful, rigid mounting in an etalon oven and then temperature controlin the etalon length we manage to lock the laser frequency to a tunable frequency of the etalon which results in a passive stabilization of the laser frequency /8/.

4. Active stabilization

Following on from passive stabilization schemes, the next step is to search for reference frequencies which possess good long-term stability. The center frequency of the atomic lasing transitions was the first to be considered in avtive stabilization schemes. The power output curve is to be used as frequency discriminant. Using isotopes and an excitation above threshold, a dip could appear in the centre of this curve, known as the Lamb-dip /9/.

The width of the Lamb-dip in the visible helium-neon laser is some 200 MHz wide (between points considered at half its width) and is about 5-8% deep. The use of the helium-3 isotope may increase the laser power output by 20% as the coincidence of the metastable excited state with the upper laser level in neon-20 is closer than with helium-4 /10/. The maximum output power depends critically upon the quality of the optics used, and by using high quality optical components power closed to the 1 mW, enough power for a large field of applications becomes available from such a short laser /11/.

The gain bandwidth is about 1200 MHz wide at the half power points as to be compared to the width of the Lamb-dip. So the dip is narrower than the gain curve and the dip center represents a more clearly defined frequency than the peak of the gain curve.

To stabilize the frequency of a single frequency He-Ne laser we used a Lamb-dip method whose principle is easy to explain (see figure 1). The laser frequency is modulated over the narrow optical frequency range this modulation results in an intensity modulation of the laser power output whose phase depends on the actual laser oscillation frequency. So, the magnitude of the detected signal carries the information about the detuning from the dip center ν_0, while the phase relative to the applied modulation indicates on which side of the center the laser frequency lies. A phase sensitive detector output if smoothed properly by an integrator will give input signal for DC voltage amplifier which completes the servo-system. A PZT transducer having a modulation input and a high-voltage input translates electrical signals into laser frequency shifts.

The servo-system controls the laser cavity length so as to maintain PSD output voltage to zero and the laser frequency to be continually referred to the center frequency of the Lamb-dip.

Because such a simple electronic servomechanism forms the nodal point of any stabilization system it was for us a matter of choice to design and develop a modular electronic system capable to achieve frequency stabilization on different lasers /12/ (see figure 2).

The short-term and long-term frequency stability of our early developed single frequency He-Ne laser was measured by inter-comparison with a secondary standard in Brno, Czechoslovakia /3/. The frequency beats show a short-term frequency stability of 5×10^{-8} and long-term frequency stability of 10^{-8}, with a reproducibility laser wavelength of 6×10^{-9}.

In a similar manner, we worked out another experiment on the frequency - locked He-Ne laser by using the opto-galvanic effect /13/. The physics of the experiment is based on the self irradiation induced by the laser light upon the active laser discharge in laser tubes. The laser discharge conductivity variations show a profile similar to the power output curve, only the latter has a more marked Lamb-dip profile. Strong dependence of the amplitude of the self-irradiation opto-galvanic effect on the laser current was also noted.

Other possible stabilization schemes could be considered:

- using magnetic fields applied to the gain tube of an internal mirror single frequrency laser. The single laser frequency is split into two closely spaced frequency of opposite senses of circular polarization and the intensities are equal only when the tube frequencies are equally spaced from the central laser frequency.

- using staturated absorption involves placing an absorption cell (neon, iodine, methane) inside the laser cavity.

The homogeneous linewidth of the absorber is about two orders of magnitude narrower than He-Ne laser gain Doppler broadened curve. The strong standing-wave electric field inside the laser cavity gives rise to a saturation of the absorption and a Lorentzian shaped dip forms at the center of the absorption line.

Both mathods give more stable frequency references than that derived from features of the laser gain curve, allowing for a higher degree of frequency stability.

The above mentioned electronic system /13/ is provided with excelent parameters for the last two stabilization methods, and new results are expected to be reported in the near future.

REFERENCES

/1/ A.J.Wallard, J.of Physics E., Sci.Instrum., 6, 793 (1973)

/2/ E.Engelhard, J.Opt.Soc.Am., 61, 216 (1971)

/3/ C.Blanaru, Gh,Popescu, A.Chetroiu, D.Apostol, A.Ionescu, Rev.Roum.Phys., 27, 167 (1982)

/4/ Gh.Popescu, M.Ristici, A.Ionescu, V.Draganescu, V.Vasiliu, Rev.Roum.Phys., 27, 573 (1982)

/5/ Gh.Popescu, Rev.Roum.Phys., 26, 345 (1981)

/6/ Gh.Popescu Rev. Roum.Phys., 29, 341 (1984)

/7/ Gh.Popescu, Rev.Roum.Phys., 26, 719 (1981)

/8/ R.S.R.Patent no.79476

/9/ W.E.Lamb, Phys.Rev., 134A, 1429 (1964)

/10/ Gh.Popescu, C.Blanaru, St.Cerc.Fiz., 28, 95 (1976)

/11/ Gh.Popescu, Rev.Roum.Phys., to be published (1985)

/12/ Gh.Popescu Rev. Roum.Phys., 29, 431 (1984)

/13/ D.Apostol, C.Blanaru, A.Ionescu, Gh.Popescu, I.Iovit-Popescu, V.Vasiliu, Rev.Roum.Phys., 27, 581 (1982)

FIGURE CAPTIONS

Fig. 1 Block diagram for frequency stabilization using Lamb-dip method.

FD - photodetector; HQ-TA - high-Q tuned amplifier; PSD - phase sensitive detector; O - oscillator; PS - phase shifter; I - integrator; HVA - hogh voltage amplifier; MJ - mode-jump; PZT - piezoelectric transducer.

Fig. 2 Block diagram of the modular system for frequency stabilization of a single frequency laser with iodine cell within laser cavity. The same capital letters significance as in Fig.1 and more:

PA - preamplifier; NF - notch-filter; SD - switch driver; S - summator; RG - ramp generator; AQ-NF - adjustable Q notch filter; F - filter; VR - voltage regulator; QG - quartz generator; APS - analog phase-shifter; LPF - low pass filter; AG-BPF - adjustable gain band pass filter.

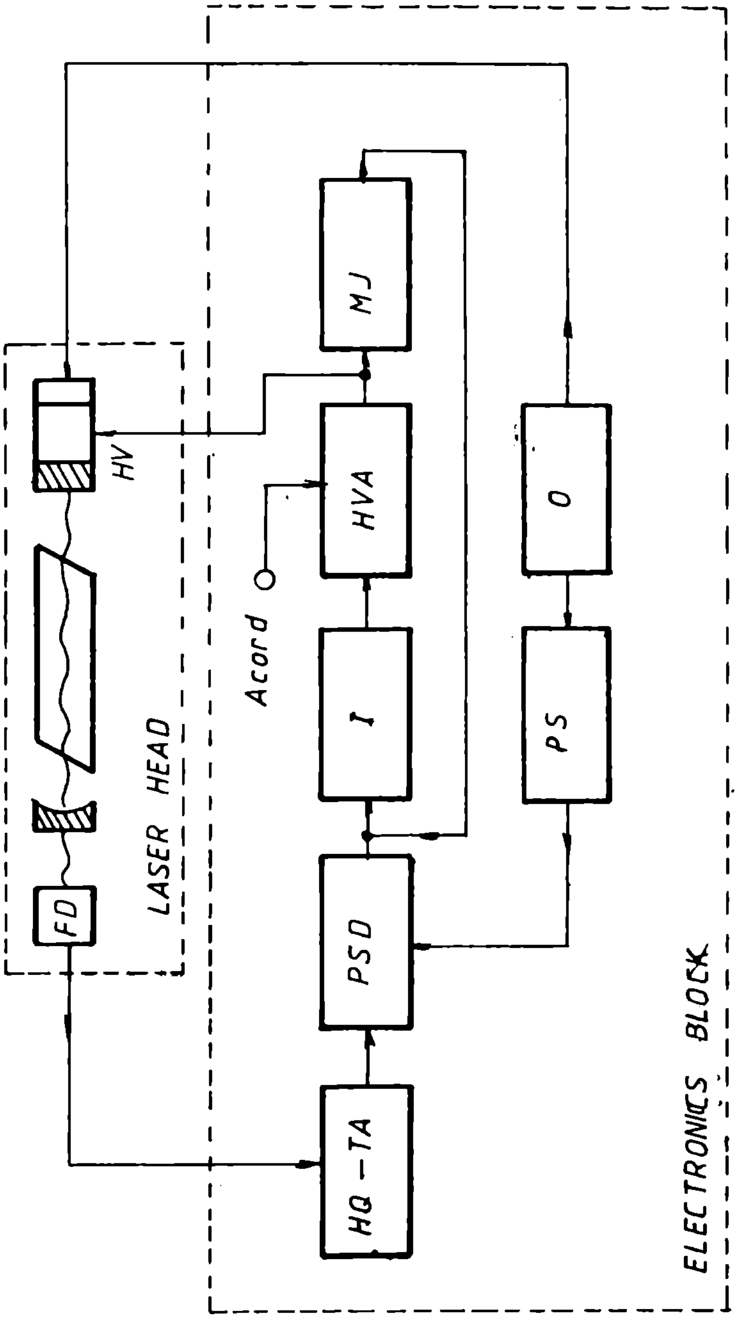
LASER HEAD
FD
HV
Acord
HQ – TA
PSD
I
HVA
MJ
PS
O
ELECTRONICS BLOCK

Fig. 1

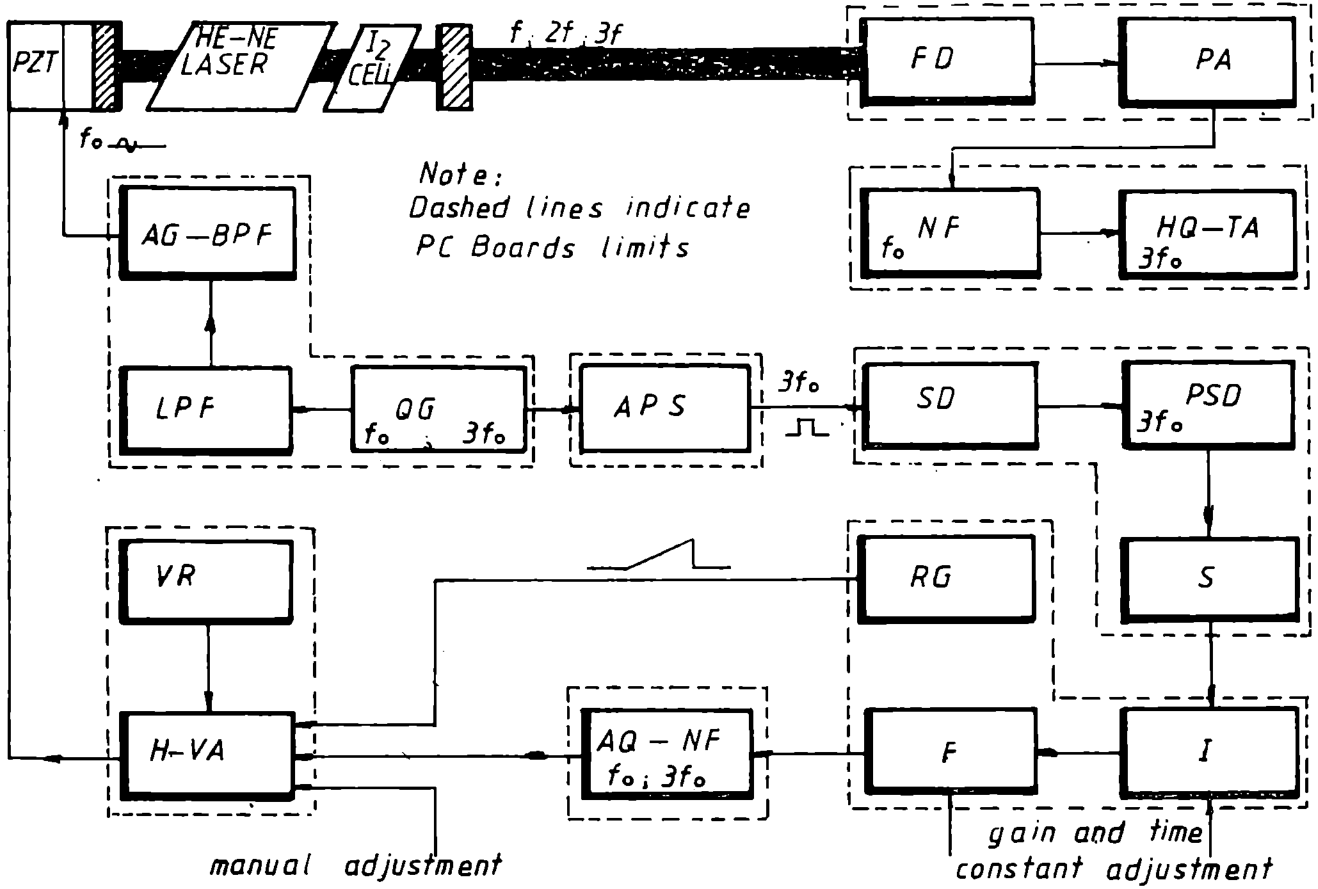
PZT
HE-NE LASER
I_2 CELL
f, 2f, 3f
FD
PA
f_0
Note:
Dashed lines indicate
PC Boards limits
AG—BPF
f_0 NF
HQ—TA $3f_0$
LPF
QG f_0 $3f_0$
APS
$3f_0$
SD
PSD $3f_0$
VR
RG
S
H-VA
AQ – NF f_0; $3f_0$
F
I
manual adjustment
gain and time constant adjustment

Fig 2

STUDY OF THE SEMICONDUCTOR DEVICES USING A LASER SCANNING DIGITAL SYSTEM

G.A.Stanciu, I.M.Popescu, Gabriele F.Cone
Department of Physics, Polytechnical Institute of Bucharest

In this paper the laser scanning digital system is presented. Some results obtained using this system are also shown.

Introduction

Contactless measurement methods are classified into two kinds from the point of principle as follows:

(1) scanning techniques with an electron beam;

(2) scanning techniques with laser beam.

With regard to (1), the scanning electron microscope (SEM) has been the most versatile instrument for the study of surfaces of the semiconductor materials or devices because of its high resolution. However, this method is more ore less destructive due to collison of the charged electrons with a surface, and its application requires a lot of time.

On the other hand, with regard to (2), laser scanning techniques are completely nondestructive and permit to study of devices in the working conditions.

The photoresponse properties of semiconductor devices have been investigated for possible use in detecting and locating various semiconductor devices. With a light beam detailed information can be obtained about the structure and operating behaviour of the devices.

In this paper we report some results obtained by investigations on power and commutation transistor, photodiodes and integrated circuits.

2. Description of the scanning laser digital system

The scanning system used in our experiments has been described in detail in /1-3/. A schematic digital scanner is shown in fig.1. A helium-neon laser, oscillating at 632.8 nm is utilized. The laser beam is scanned with orthogonal mirrors O and O_1. The raster is projected onto the tube ocular of a standard metalurgical microscope and, in this way is focused on the surface of the sample. High resolution is achieved by focusing the light onto a spot of 2 µm diameter with typical objective lenses (40 X). The beam power was varied by means of two polarizers placed in front of the laser and saturation of the examined devices in certain regions was avoided. The two scanners were galvanometer movements which were driven in present applications by a digital current obtained from digital voltages by using correction circuits. Typically, maximum y rates (O_1) were 10 Hz, whereas x scanners could be driven to 500 Hz.

The laser beam - generated photocurrent modulates lead to an ac voltage on a series resistance. This ac signal is amplified with a video amplifier and applied to a memory oscilloscope OG 2-31 RFT.

The spot position on the sample surface is displayed by means of a digital display system in cartesian coordinates. Depending on the way which the current was fed into oscillosocope, a display "map" or a graphical representation were possible. In the latter case, the signal controlling the vertical deflections consists of some photoresponse devices and the signal proportional to the signal driving the vertical deflector.

3. Results and typical applications

3.1. Light sensitity of p-n junctions

A brief qualitative description of p-n junction behaviour in the presence of light will be given. Laser beam striking the surfaces of a semiconductor device in the vecinity of a p-n junction causes a voltage to be generated. The magnitude of this photogenerated voltage is dependent on the intensity, wavelength, and area of incident light, as well as on several characteristics of the semiconductor material itself and the external load.

The energy of the photon creates electron-hole pairs which separate in presence of the electric field in the junction depletion region, cross the junction, and produce a current flow in an external circuit (Fig.2).

From energy level consideration, a certain minimum energy of the incident photon is necessary to excite the electrons from the valence band into conduction band producing a nonequilibrium photocurrent. This minimum energy corresponds to wavelength of about 1.1. μm for silicon. It should be noted, however, that the acceptor and doner impurities whose energies lie in forbidden gap are completely ionized at normal temperature and therefore do not generate photocurrent at low energy photon excitation.

The wavelength of the light also determines the penetartion of the light through the sample. For the case of the helium-neon laser oscillating at 632.8 nm, most of the photogenerated electron-hole pairs are produced within about 1 micron of the surface of the sample.

Referring to fig.2, the magnitude of the photoresponse as a function of the laser spot distance from the junction is shown. This diagram represents an ideal description of a photoscan across a p^+n diode.

As the light spot traverses the sample from left to right, there is a length out to x_{ln}, where no photocurrent is generated. As the spot reaches x_{ln}, which is about a diffusion length from the depletion region a small photocurrent is produced as some of the generated electrons are able to reach the depletion region before recombining. Once these electrons reach the depletion, they are swept across by the field and become majority carriers on the "n" side of the junction and flow through the external circuit. When the spot gets closer to w_p, which is the edge of the depletion region of the "p" side of the junction, the fraction of the photogenerated electrons which reach the junction increases, causing an increase in photocurrent. As the spot passes W_p and crosses into the depletion region of the "p" type material nearly all of the photogenerated electron-hole pairs are immediately separated by the field and flow through the external circuit. The photovoltage decreases after the light spot crosses W_n which is the edge of the depletion region. As the light spot moves out to W_n, the number of generated holes reaching the space charge field decreases causing a decrease in a photocurrent.

3.2. Photoscan of HF pnp transistor

We have investigated the pnp silicon switching transistors whose superficial geometry is shown in fig.3.

The base region of the transistor was scanned with Oy axis along emitter stripes. Figure 4 shows a system of graphs obtained on the unbiased transistor. The central graphs represent the photocurrent if the laser "linie" crossing the base and emitter contacts. The minima in the photoresponse represent the emitter and base contacts. The two lateral maxima are due to the depletion region of the collector-base junction.

The base-collector junction of the transistors is at 1.9 µm from the surface and this location makes carrier generation possible in the emitter, base and collector regions. The transistor has two emitters which have the same metal contact.

a) Location of diffusion pipes

One of the most important mechanisms of the laser in the bipolar trnasistors is the formation of diffusion channels or localized emitter-to-collector leakage paths. The methods used in the localization of the diffusion channels are based on the electrochemical decoration technique correlated with microscopic observation. But, this method proved to be destructive because of the number of defects which appeared on the wafer surface.

Using a laser scanning digital system we developed nondestructive and extremely rapid technique for the location of diffusion channels /4/.

Figure 5 a shows the "map" of the transistors as obtained by laser scanning. The light zone represents the base region an portion of the unplated emitter regions. The central dark band stands for the base contact, while the two dark side-bands represent the metal coatings of the emitters. One can notice the position of the two channels on a 11.5 V reverse biased transistor. The variation of the photocurrent with the reverse voltage for the channel from the left emitter region is shown in Fig.5b. The base-collector junction was 10.5, 10.25 and 10.3 V reversely biased.

b) Identification of regions with microplasma

A typical photoresponse patterm of a transistor with microplasma is shown in fig.6. At 11 V, a localized increase in photocurrent occurs. This appears just near the base stripe. This can be caused by microplasma at the collector-base junction which produces a significant decrease of breakdown voltage /5/.

3.3. Photoscan of p^+n Si photodiodes

Photocurrents generated by laser beam on a photodiode p^+n with inversion channel are illustrated in fig.7 for simplicity six graphs are given. In the right region of the guard-ring photodiode an intense photocurrent is observed that represents the channeled collector area. The photocurrent increase with increasing voltage V_{BC} until reaching the vecinity of the breakdown voltage, where the increase is unessential as in the fig.7.

Evolution of the photocurrent in a region with inversiun layer was presented in detail in /6,7/.

3.4. Photoscan of a power transistor

Figure 8a is "the map" of the region of the silicon npn transistor type 2W 3055. The light zones represent the base and emitter contacts. Figure 8b shows the photocurrent at the junction emitter - base of the transistor at OV bias using six graphs. Uniformity of the multiplication is observed.

3.5. Photoscan of the integrated circuits

Testing integrated circuits is often more of a problem than making-them. Pressure of mechanical probes on chip pads can if too heavy, cause a damage n, if too light; results in poor electrical contact and unwarranted rejections. Electrical tests are complex.

Using the laser scanning system testing IC are non-destructive.

Photoscan with laser system gives an instantaneous display of an IC's surface, revealing flows and anonedies.

Figure 9 is a laser-scan picture of the IC-s TAA5 50. Semiconductor material is white and metal black. The most intense responses indicate where the junction comes vertically to the surface and outline the different components.

Conclusion

Using a laser scanning digital system it is possible to see such potential reliability problems as masking defects, metallization disturbance, large conductivity variations, diffusion pipes, microplasma region and many other light sensitive anomalies. This non-destructive technique is applicable to both discrete circuits and integrated circuit. The combination of the laser scanning with a computer is possible. Thus, interpretation of the results could be simplified.

REFERENCES

/1/ I.M.Popescu, G.A.Stanciu, C.M.Stoichita, Bul.I.P.B., Seria Electrotehnica, XXXIX (4), 11 (1977)

/2/ G.A.Stanciu, I.M.Popescu, C.M.Stoichita, Rev.Phys.Appl., 15, 55 (1980)

/3/ G.A.Stanciu, I.M.Popescu, C.M.Stoichita, St.Cerc.Fiz., 33, 259 (1981)

/4/ G.A.Stanciu, I.M.Popescu, C.M.Stoichita, Rev.Roum.Phys., 25, 1119 (1980)

/5/ G.A.Stanciu, D.T.Sachelarie, Rev.Roum.Phys., 24, 683 (1979)

/6/ G.A.Stanciu, I.M.Popescu, C.M.Stoichita, Phys.Stat.Sol.a 71, K17 (1982)

/7/ G.A.Stanciu, I.M.Popescu, Gabriela F.Cone, The 13th Congres of the International Commission for Optics, August 20-24 (1984), Sapporo, Japan, p.544

FIGURE CAPTIONS

Fig. 1 Block diagram of the scanning laser digital system

Fig. 2 Photocurrent generation at a p-n junction

Fig. 3 Micrograph of the pnp transistor surface

Fig. 4 Photocurrent profiles on a pnp transistor with base-collector junction unbiased

Fig. 5 Transistor with two diffusion pipes

a) the scanned / "micrograph";

b) the photoresponse VS reverse bias the pipe from the left emitter

Fig. 6 a) The "micrograph" of the transistor with microplasma

b) Photocurrent profiles on the same transistor (V_{BC} = 11 V)

Fig. 7 Photocurrent profiles on a p^+n silicon photodiode exhibiting inversion layers:

a) $V_R = 0$; b) V_R = 7 V; c) V_R = 14 V; d) V_R = 30 V

Fig. 8 a) The "Map" of a region of the power npn transistor

b) photocurrent of the transistor at OV bias using six graphs

Fig. 9 The laser-scan picture of the surface of the IC-s TAA-550

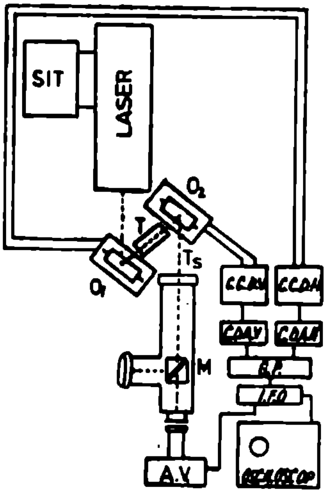

Fig.1

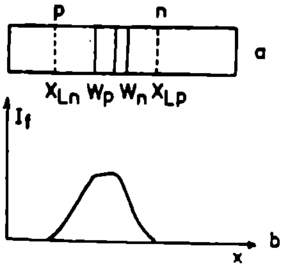

Fig.2

Fig.3

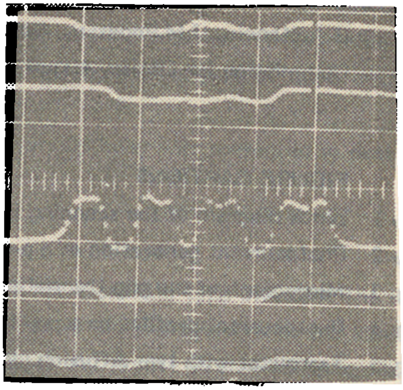

Fig.4

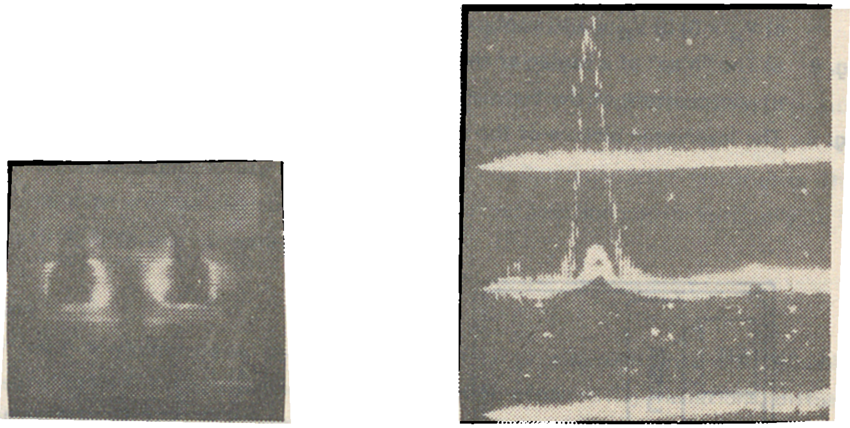

a.

b.

Fig.5

Fig.6

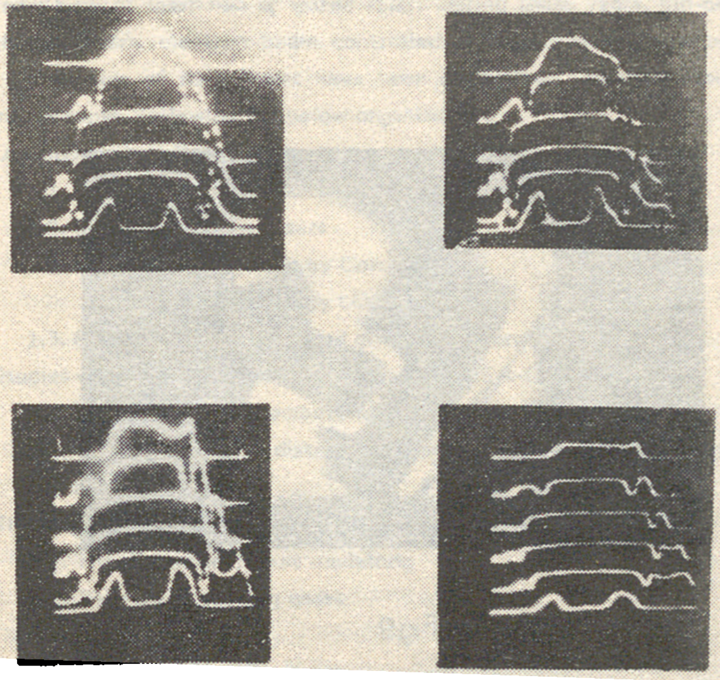

Fig 7

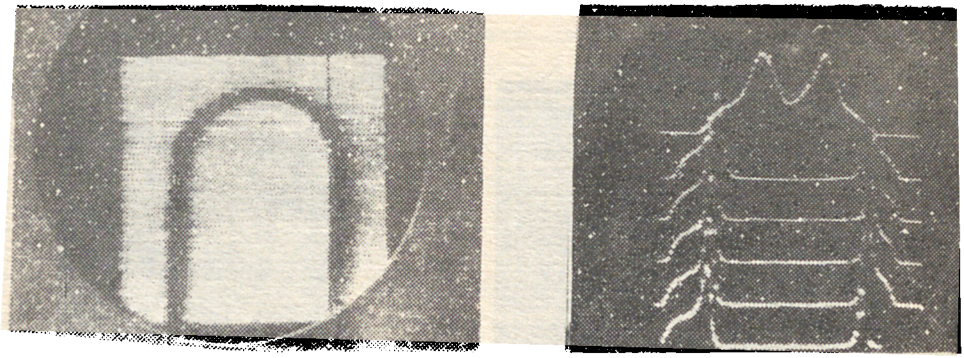

a. b.

Fig.8

Fig.9

PULSED TEA-CO_2 LASERS

A.I.Ciura, C.Grigoriu, M.V.Udrea
Laser Dept., Central Institute of Physics, Bucharest, ROMANIA

A review of the research in the field of TEA-CO_2 lasers at the National Centre of Physics is presented. The most significant results in the two main research directions - the development of the typical TEA-CO_2 lasers and the active medium study - are shortly discussed.

The research on the field of atmospheric pressure, pulsed CO_2 laser excited by transverse discharge started at the National Centre of Physics soon after the first publications about this new type of laser had appeared /1.2/. During these years, pin-pin discharge lasers, double discharge lasers, electron beam controlled discharge lasers have been developed and studies on the physics of such lasers have been conducted. The main results will be briefly presented in this paper, following the below organisation:

1. Development of TEA-CO_2 lasers
    1.1. Pin-pin discharge lasers
    1.2. Double discharge lasers
        1.2.1. Preionization by Corona effect
        1.2.3. Preionization by U.V. radiation
    1.3. Electron beam controlled discharge lasers
2. Studies on the active medium of the seeded TEA-CO_2 lasers
    2.1. Ionization and recombination coefficients
    2.2. Electron energy distribution function in typical mixtures of the TEA-CO_2 lasers
3. The modelling of TEA-CO_2 lasers
    3.1. The discharge circuit modelling
    3.2. The role of seeding gases

1. Development of TEA-CO_2 lasers

1.1. Pin-pin discharge lasers /4,5/

Among pin-pin discharges, the helical electrode configuration has been studied due to some advantage relying mainly on its possibility for obtaining oscillation in the lowest order transverse mode.

One of the lasers that were built /5/, consisted of four identical sections with 909 electrodes pairs, and the spacing between pins was of 24 mm. The cavity length was of 515 cm, the active volume of about 100 cm and the total gas volume of 13 l. The optical cavity consisted of a plane Ge mirror, 50% reflectivity and a gold coated mirror with a 20 m curvature radius.

The excitation electric pulse was obtained from a Marx Generator with a capacity of 100 nF, having values between 24 and 57 kV, a rise time of 50 ns and 1 µs full width at half maximum (FWFM). The stability of the discharge was assured by balast resistors.

For all the studied mixtures, the pulse shape obtained was that typical for TEA-CO_2 lasers with a CO_2:N_2:He active gas: a peak with FWHM smaller than 100 ns and tail lasting for several µs. The pulse energy shows a strong dependence on the composition and total pressure.

Figure 1 presents the output energy as a function of the applied voltage for a 1:1:8 CO_2:N_2:He mixture at several total pressures. For each voltage, there is an optimum pressure, as shown in figure 2.

It was also observed, that for a given pressure of the active mixture, the output energy depends rather critically on the ratio of the CO_2 and N_2 partial pressures. When the ratio P_{CO_2}/P_{N_2} is greater than unity, the optimum pressure is in the range of 400 - 450 Torr, and for P_{CO_2}/P_{N_2} smaller than unity, the optimum pressure is between 150 and 300 Torr.

The maximum output energy was of 1.6 J, obtained from a 2:3:10, CO_2:N_2:He mixture, at 300 Torr total pressure and for 57 kV excitation pulse voltage. So, the efficiency is of about 1%, and output density energy 15 J/e, which are quite good figures for such lasers.

1.2. Double discharge lasers

The Lamberton-Pearson model /6/, and the laser with preionization by U.V. radiation produced by sparks between pins /7/, have been the most studied double-discharge lasers in our department.

1.2.1. Preionization by Corona effect /2,8-16/

Using preionization by an auxiliary discharge between wires and the main electrode, some lasers with high energy per pulse, with medium repetition rate or sealed-off were built.

The maximum energy per pulse (23 J), was obtained from an oscillator with a discharge cross-section of 4.5 x 3.5 cm^2 and the active length of 80 cm. The optical cavity is closed by a plane Ge mirror (50% reflectivity) and a gold coated mirror with a 6 m radius of curvature.

Maximum energy was obtained with a 20:20:60 CO_2:N_2:He mixture. The efficiency did not saturate up to the maximum available input energy (250 J/l).

The work /10/ describes an oscillator with two identical sections. The essential problem of this oscillator, the minimum jitter in the triggering of the two spark-gaps, were solved by carefully chosing their working regime. So, working with a voltage 20% lower than breakdown potential of the spark-gaps and at a pressure of 3-4 atmospheres, the delay between the firing of the two spark-gaps was less than 25 ns. Figure 3 shows the output energy as a function of the CO_2 partial pressure for several supply voltages. The efficiency of the laser, shown in fig.4, presents an optimum, after which it decreases rapidly with the input energy.

The two con tructions employed small quantities of xylene vapours added to the basic mixture, to improve the stability and efficiency of the laser /17/.

A tunable CO_2-TEA laser was built using a diffraction grating /13/. The active volume of 2 x 2 x 75 cm^3 excited by the discharge of a 100 nF capacitor charged at 22 kV was able to give 1.5 J in a cavity formed by an uncoated Ge mirror and a 12 m radius of curvature gold coated mirror. Replacing the gold coated mirror by 135 lines/mm grating (type ML 304-04, PTR Optics), more than 70 emission lines in the P and R branches of the 9.4 and 10.4 µm bands were observed. The maximum energy, obtained on the P (18) or P(20) lines, was of about 0.5 J.

The same oscillator allowed us to sutdy the possibility of shortening the emission pulses by working in mixtures without N_2 and by absorption in the breakdown plasma /12/. When the laser works with a free N_2 mixture, the pulse tail completely disappeared, FWHM being of 60 ns. The energy was of 0.5 J and the pulses showed a good reproductibility. When the pulses were absorbed by the breakdown plasma it has produced in air, the FWHM was of 20-30 ns, the pulses energy of 0.1 - 0.2 J, but the reproductibility was evidently not so good as in the first case.

Some researches were aimed at the development of a small-size, sealed-off TEA-CO_2 laser /15/. A Lamberton-Pearson structure was chosen because the dissociation is lower in this case as compared with the U.V. preionized laser by sparks.

The active volume was of 22 x 1 x 1 cm^3. The cavity consists of a gold coated mirror (3 m radius of curvature) and a plane, coated Ge mirror, with 85% reflectivity.

The main capacitor was of 6.5 nF, where as the auxiliary ones of 150 pF. With a 1:1:5 CO_2:N_2:He mixture, without any additives, the discharge begins to degenerate after about 100 pulses. By the addition of small quantities of CO (4-5 %) and N_2 (2-3%) the lifetime of the laser greatly increased.

The maximum energy was of 350 mJ, but in order to obtain a longer lifetime, the working voltage was reduced so that the pulse energy was of 150 mJ. Figure 5 shows the output energy as a function of the pulse number. One can see that after 1.2 million pulses the pulse energy is still about 100 mJ. The arcing number was less than 0.6%. Many materials were tested as electrodes and the best results from the lifetime point of view were obtained with brass electrodes.

1.2.2. Lasers with preionization by U.V. ionization /18/

For some photochemistry researches, a laser able to work at 5 pps with an energy up to several joules was developed. A construction with preionization by U.V. radiation produced by pin-pin auxiliary discharges was adopted for this purpose.

The main discharge is produced between Chang profiled electrodes /19/, 70 cm length and spaced at 22 mm. The main capacitor (100 nF) can be charged up to 40 kV. The U.V. radiation is produced by two rows of pin-pin sparks each of which is supplied by a 1 nF capacitor. Eight fans were employed to circulate the active mixture. The output energy was extracted by a plane Ge mirror, with about 65% reflectivity.

The main results are shown in Figs. 6 and 7. One can see a rather strong decrease of the output energy with the repetition rate, due to the reduced flowing capacity of the fans. The maximum output energy density was about 33 J/l, with an efficiency of 8%.

1.3. Electron beam controlled discharge lasers /20-23,25/

The electron beam controlled discharge laser (EBCDL) /24/, proved to be the most appropriate means to obtain high pulse energies in the medium infrared.

Our electron beam-controlled discharge laser had a 900 mm active length /20/. Figure 8 shows a schematic cross-section through the device.

There are two main parts: the laser (1) and the gas chamber (2). The laser cavity consists of a concave gold mirror with a 5 m curvature radius and a plane KRS-5 mirror with 25% reflectivity. The 90x900 mm^2 main discharge anode is plane with rounded edges and is connected to the main capacitor battery.

The electron gain had a 900 mm length and 50 mm width copper cold cathode. The surface of the copper cathode foil was pinched out to enhance the emissivity. The cathode is placed at 65 mm from a 50 μm titanium foil which separates the gas chamber from the laser chamber. The foil is sustained by a set of 1.5 mm diameter steel wires placed transversally from 20 to 20 mm. The high voltage pulse from a Marx generator is applied by a ceramic insulator.

Figure 9 shows the output energy as a function of the input energy of several mixtures. The maximum energy was obtained for a 3:7:10 mixture. At a total pressure of 1 atm. and an initial electric field of 4.5 kV/cm, the output energy density was of 15 J/l with 17% efficiency.

For this laser, the small signal gain coefficient at low pumping levels was measured /21/. The probe signal is supplied by a CW laser placed in a screened room. The continuous beam is led by means of a mirror system through the discharge cavity of the EBCDL and is reflected back by a mirror in a similar way towards a liquid nitrogen cooled Ge:Au detector. The gain coefficient as a function of the input energy is shown in Fig.10 for three working mixtures.

The electron beam intensity and uniformity were also measured /23/. This was performed by a Faraday cup, moved over the titanium foil surface.

The peak value of the signal detected by the Farady cup at different points on the width of the titanium foil is shown in Fig.11. One can see a good symmetry around the centre.

The penetration depth was also measured. The beam intensity decrease practically linearily with the distance from the titanium foil.

For a 3:7:10 CO_2:N_2:He mixture attenuation was 70% at 9 cm.

From the measured electron beam intensity one can calculate the secondary electron density produced by the fast electrons which enter the laser cavity. If no main discharge is produced, the number of secondary electrons decrease by recombination and attachement. Assuming that the recombination process prevails over the attachment one, the equation governing the electron density, Ne, can be written:

$$\frac{dN_e}{dt} = S(t) - \alpha N_e^2 \qquad (1)$$

where S(t) is the source term and α the recombination coefficient. We have used for S(t) a shape similar to the total Marx generator current shape with a peak value of 4×10^{19} $cm^{-3}s^{-1}$, and for α value of 1.7×10^{-6}. The result of the numerical calculation for Ne is shown in fig.12. The microsecond tail of the electron density is suitable to sustain an uniform discharge in the gas.

A microscopic study on the cathode damage after several hundreds of pulses was also carried out /25/. The amount of evaporated cathode material was estimated and it was emphasized that the plasma which was created during the pulse by ohmic heating was the electron source. The propagation time of this plasma from the cathode to the foil is in agreement with the electron beam pulse duration.

2. Studies about the active medium of the seeded TEA CO_2 lasers /27-30/

Besides the development of some types of lasers, many researches have been conducted on the active medium characteristics, especially for seeded lasers, /27-30/. Among these works, we shall review the measurements of the ionization and recombination coefficients, the determination of the elctron energy distribution function and the theoretical modelling of the additives' role.

The experimental basis for some studies were the voltage and current measurements on a Lamberton-Pearson type laser. The active mixture can be doped with TPA or xylene in a controlled manner. Special precautions were taken to assure the measurements accuracy. The voltage was measured with the special designed resistive high voltage divider (10 ns rise time) and as current probe we used a fast current shunt with 2 ns rise time and 2 mOhm resistance. To remove the RF noise generated by the pulsed discharge we employed double shielded cables and a Faraday cage equipped with special filters.

2.1. The apparent ionization and recombination coefficients /27,28,30/

These coefficients can be calculated from current measurements performed at several voltages, following the procedure of Ernst and Boer /31/. So, the temporal evolution of the electric density, Ne, can be deduced from the relations:

$$\frac{1}{N_e}\,\frac{dN_e}{dt} = v_d\,(\alpha - \eta) - \gamma N_e \qquad (2)$$

$$N_e(t) = \frac{I(t)}{eAv_d} \qquad (3)$$

Here, v_d is the electron drift velocity, α is the first Townsend coefficient, η the elctron attachment coefficient, γ the recombination coefficient; I(t) is the current intensity and A the discharge area on the electrodes.

The left-side of the equation (2) is evaluated by numerical derivation of the Ne obtained from equation (3). From this purpose, the experimental curves were smoothed by properly chosen Chebyshev polinomials.

As electron drift velocity v_d, the values computed by Judd /32/ for a 1-1-8 mixture we used. The approximation is rather good, because v_d depends weakly on the active mixture. The values $\frac{1}{N_e}\frac{dN_e}{dt}$ depend linearily on Ne and, therefore, they define a family of straight lines depending parametrically on E/p and on the dopant partial pressure. The intersection of each line with the ordinate and its slope give both $v_d(\alpha-\eta)$ and γ respectively, for a given E/p and dopant level.The calculations were done on the basis of the current measurements at 20, 24, 28 and 32 kV supplying voltage in a 1-1-10 mixture at several dopant partial pressures.

Figures 13 and 14 show the calculated recombination coefficient and the apparent ionization coefficient as functions of E/p. The recombination coefficient has a shape similar to that reported by Ernst and Boer /31/ and does not depend on the dopant pressure. One can see an unexpected increase for a reduced electric field greater than 8 V/cm torr.

The apparent ionization coefficient increases with reducing the electric field. The TPA has a more important effect on the ionization coefficient and this can be explained by the lower ionization potential of the TPA (7.2 eV) as compared to that of xylene (8.5 eV).

2.2 Electron energy distribution function in mixtures typical for TEA-CO_2 lasers /28,29/

The influence of the additives on the electron energy distribution function allows us to obtain qualitative and quantitative information about the processes inside the laser.

The direct measurement of the EED in a TEA-CO_2 laser discharge id difficult due to the fast discharge at high current and voltage. That is why we performed EED measurements in a similar plasma, i.e. in a DC glow discharge with typical characteristics (reduced electric field, ratio of partial presseures, flow velocity, ratio of electron density versus neutrals), like in a TEA laser.

In order to determine the EEDF we used the asymmetrical double probe method /33/. It is well known thet the EEDF, f(v), can be obtained from the second derivative of a simple probe characteristic

$$f(v) = \frac{2}{eA_p} \left(\frac{2\ m_eV}{e}\right) \frac{d^2I}{dV^2} \tag{4}$$

where V is the retarding potential, A_p the probe area, m_e and e the mass and electron charge respectively.

The main problem is to have an asymmetrical double probe system which approximate well the simple probe as a condition for applying the relation (4).

In our case, the probe is a cylindrical tungsten wire (0.05 mm in diameter, 1.5 mm in length) placed at 10 mm from the reference electrode and 5 mm aside the axis of the discharge tube (20 mm in diameter, 500 mm in length). The reference electrode is a nickel cylinder (16 mm in diameter and 7 mm long), placed axially at 200 mm from the tube anode. So, the areas ratio of the reference electrode to probe is 1470. Some authors /34,35/ show that in order to obtain correct results, this ratio must be greater than 10^4. But Kawashima and Yamori /36/ showed that when the area ratio is unsufficient, the experimental probe characteristic gives results which are greater by a factor G than the "true" values and this factor is constant over a rather large range of plasma parameters. To obtain the G factor we performed a measurement in pure helium and compared the EEDF with already known results.

The EEDF was obtained from the recorded probe characteristics by numerical derivations, employing suitable methods for such problems.

Figures 15 an 16 show the EEDF function for CO_2-N_2-He mixtures, 1-1-1 and 1-1-10, at 20 V/cm torr.

In pure CO_2-N_2-He mixtures, in the flowing regime the EEDF typically presents two peaks. If the discharge tube is sealed-off, the second peak decreases and a concentration of the slow electrons increases. This effect, also observed by Bourquard et al. /37/ can be qualitatively explained by the disociation of the CO_2 molecules.

In the pure 1-1-1 mixture, the second peak is by far more important than in the 1-1-10 mixture and is shifted towards smaller energy values.

The effect of the seeding gases (TPA or X) on the EEDF consists in reduction of the high energy electron density, due to the low ionization potential of the two gases. As a consequence, the electron density increases, as was already observed in our measurements of the current and voltage /27/. The shift towards smaller energies has a favourable effect on the laser efficiency because the maximum cross sections by electronic collisions for CO_2 and N_2 are in the range 0.3 -3 eV. So, the change of the EEDF, when small quantities of TPA or X are added, can explain the observed increase by 10-20% in the laser efficiency at the optimum dopant pressure.

3. Modelling the TEA-CO_2 lasers /26-28/

The modelling of the TEA-CO_2 lasers involves a wide area of problems: plasma pheomena, pulse dynamics, discharge circuit, influence of the additives etc.

A simple, three-level model, to study the dynamics of the TEA-CO_2 lasers was proposed /26/. The model is described by a set of non-linear differential equations which take into account the partial pressures, pumping power, electric pulse length.

In the following, we shall discuss two aspects of the TEA-CO_2 lasers modelling: the discharge circuit and the additives influence on the laser.

3.1. Discharge circuit - modelling /27-28/

The basis for the circuit modelling consisted in the current and voltage measurements. These curves clearly show the important role of the preionization circuit, which must be taken into acount for correct modelling. It is also important to consider the nonlinear discharge resistivity in the first discharge stages. This resistance becomes nearly constant 200 ns after triggering.

Based on the experimental results, the circuits shown in fig.17 was advanced. C_m is the main capacitor, Ca the preionization capacitor and R the nonlinear discharge resistance. The preionization circuit resistance is considered proprotional to R. From the fitting of the experimental data with the theoretical ones, the proportionality factor was deduced to be 0.5.

To calculate the current and voltage waveshape, we used the equations:

$$\frac{Q}{C_m} + L\frac{d^2Q}{dt^2} + R(t)\ \left[\frac{dQ}{dt} - I_2 \right] = 0 \tag{5}$$

$$\frac{1}{C_a} \int_0^\infty I_2 dt + \frac{R}{2}(t + \Delta t) I_2 + R(t)\ \left[I_2 - \frac{dQ}{dt} \right] = 0 \tag{6}$$

with the initial conditions

$$Q = C_m U_o\ , \qquad (dQ/dt)_{t=o} = 0\ , \qquad I_2(0) = 0$$

$Q = C_m U_o$ is the electric charge of the main capacitor, $I_1 = \frac{dQ}{dt}$, $I = I_1 - I_2$ is the main current and I_2 is the preionization current and Δt is the delay time between preionization and the main discharge.

Figure 18 shows the calculated and experimental waveshapes of the discharge current, voltage and resistance. A good fit is to be noted between the theoretical and experimental curves.

3.2. Modelling the additives role in the TEA-CO_2 lasers /28/

Some experimental results clearly show the existence of the optimum dopant level for the laser working regime. So, by performing some measurements on the laser as used for these studies in chapter 2, we have obtained the dependence of the output energy v_s xylene pressure, shown in fig.19. We worked under atmospheric pressures to have a homogeneous discharge even without any additive. The optimum dopant pressure increases with the active medium total pressure.

We consider the effect of the additives on the electron energy distribution function as the favourable factor in increasing tne laser energy. The process which leads to the energy decrease is the radiation absorption by the dopant molecules. The absorption coefficient at 10.6 μm is in the range of 10^{-4}/cm torr for the most widely used dopants, but has a rather strong influence on the laser kinetics.

The proposed model, based on Lyon's equations /38/, takes into account the rotational relaxation and the absorption by the dopant molecules. Without a detailed discussion about the model, we present in fig.20 the pulse-shape for three values of the absorption coefficient. One can see the strong influence of the lasers, even in the range 10^{-4} cm^{-1} torr^{-1}.

In conclusion, we consider that the charge of the EEDF under the influence of the additives and the absorption of the laser radiation by the dopant molecules can explain the behaviour of the doped TEA-CO_2 lasers.

REFERENCES

/1/ A.J.Beaulieu, Appl.Phys.Lett., 16, 504 (1970)

/2/ R.Dumanchin, J.C.Farcy, M.Michon, J.Rocca Serra, Proceedings of the Intern.Quantum Electr.Conf., 1970, Kyoto, Japan

/3/ A.I.Ciura, E.Cojocaru, C.Grigoriu, I.M.Popescu, V.G.Velculescu, Rev.Roum.Phys., 17, 399 (1972)

/4/ I.N.Mihailescu, I.Neda Apostol, I.M.Popescu, V.S.Tatu, Rev.Roum.Phys., 18, 137 (1973)

/5/ I.Apostol, Gh.Dragulescu, D.Dragulinescu, C.Grigoriu, I.N.Mihailescu, I.Morjan, A.Nitoi, I.M.Popescu, V.S.Tatu, Stud.Cerc.Fiz., 28, 3 (1976)

/6/ H.M.Lamberton, P.R.Pearson, Electr.Letters, 7, 141 (1971)

/7/ O.P.Judd, Appl.Phys.Lett., 22, 95 (1973)

/8/ I.Chis, A.I.Ciura, E.Cojocaru, C.Grigoriu, T.Julea, I.M.Popescu, V.G.Velculescu, Stud.Cerc.Fiz., 25, 875 (1973)

/9/ I.Apostol, D.Dragulinescu, C.Grigoriu, I.N.Mihailescu, Al.Nitoi, I.M.Popescu, Rev.Roum.Phys., 18, 1185 (1973)

/10/ I.Apostol, D.Dragulinescu, C.Grigoriu, I.N.Mihailescu, Al.Nitoi, Stud.Cerc.Fiz., 28, 181 (1976)

/11/ D.Dragulinescu, C.Grigoriu, Al.Nitoi, I.M.Popescu, Rev.Roum.Phys., 21, 665 (1976)

/12/ St.Badescu, I.Chis, A.I.Ciura, V.Dinu, D.Dragulinescu, C.Grigoriu, T.Julea, Al.Nitoi, St.Cerc.Fiz., 31, 279 (1979)

/13/ C.Grigoriu, D.Dragulinescu, I.Morjan, R.Alexandrescu, N.Comaniciu, D.Dumitras, R.Medianu, D.Dutu, Rev.Roum.Phys., 26, 569 (1981)

/14/ I.Chis, A.I.Ciura, V.Draganescu, D.Dragulinescu, K.N.Firsov, C.Grigoriu, T.Julea, Al.Nitoi, V.G.Velculescu, Rev.Roum.Phys., 27, 267 (1982)

/15/ I.Chis, A.I.Ciura, D.Dragulinescu, C.Grigoriu, A.Nitoiu, Stud.Cerc.Fiz., 34, 417 (1982)

/16/ I.Chis, A.I.Ciura, D.Dragulinescu, C.Grigoriu, T.Julea, A.Nitoiu, Rev.Roum.Phys., 27, 595 (1982)

/17/ C.Grigoriu, H.Brinkschulte, Phys.Letters, 42A, 347 (1973)

/18/ I.Chis, A.I.Ciura, D.Dragulinescu, C.Grigoriu, T.Julea, A.Nitoiu, Rev.Roum.Phys., 27, 595 (1982)

/19/ T.Y.Chang, Rev.Sci.Instr., 44, 405 (1973)

/20/ I.Chis, A.I.Ciura, V.Draganescu, Gh.Dragulescu, C.Grigoriu, E.Udrea, V.G.Velculescu, Rev.Roum.Phys., 26, 115 (1981)

/21/ I.Chis, A.I.Ciura, Gh.Dragulescu, M.V.Udrea, V.G.Velculescu, Rev.Roum.Phys., 26, 561 (1981)

/22/ V.Draganescu, M.V.Udrea, Stud.Cerc.Fiz., 33, 673 (1981)

/23/ A.I.Ciura, V.Draganescu, C.Grigoriu, E.Udrea, M.V.Udrea, V.G.Velculescu, G.P.Kuzmin, Rev.Roum.Phys., 27, 599 (1982)

/24/ C.A.Fenstermacher, M.J.Notter, W.T.Leland, K.Boyer, Appl.Phys.Lett., 20, 56 (1972)

/25/ M.V.Udrea, C.Timus, Rev.Roum.Phys., 28, 591 (1983)

/26/ V.G.Velculescu, M.V.Udrea, Rev.Roum.Phys., 18, 1177 (1973)

/27/ I.Chis, A.I.Ciura, V.Draganescu, D.Dragulinescu, K.N.Firsov, C.Grigoriu, T.Julea, Al.Nitoi, V.G.Velculescu, Rev.Roum.Phys., 27, 267 (1982)

/28/ C.Grigoriu, Ph.D.Thesis, Bucharest 1982

/29/ A.I.Ciura, C.Grigoriu, V.G.Velculescu, unpublished results

/30/ I.Chis, A.I.Ciura, D.Dragulinescu, K.N.Firsov, C.Grigoriu, T.Julea, Al.Nitoi, V.G.Velculescu, work presented at the Symposium on Plasma Physics, Bucharest, 1981, p.91

/31/ G.J.Ernst, A.G.Boer, Opt.Commun, 34, 235 (1980)

/32/ O.P.Judd, J.Appl.Phys., 45, 4572 (1974)

/33/ T.Okuda, K.Yamamoto, J.Phys.Soc.Japan, 11, 57 (1956)

/34/ E.P.Szuszczewicz, J.Appl.Phys., 43, 874 (1972)

/35/ Jen-Shih Chang, J.Phys. D: Appl.Phys., 6, 1674 (1973)

/36/ N.Kawashima, A.Yamori, Jap.J.Appl.Phys., 12, 1227 (1973)

/37/ S.Bourquard, J.M.Mayor, P.Kocian, Journ.de Physique, C7, 385 (1979)

/38/ D.L.Lyon, IEEE Journ.QE, QE-9, 139 (1973)

FIGURE CAPTIONS

Fig. 1 Output energy as a function of excitation voltage for a 1:1:8 mixture /5/

Fig. 2 Output energy as a function of total pressure for U = 51 kV, and for several active mixtures /5/

Fig. 3 Output energy as a function of CO_2 partial pressure at several working voltages /10/

Fig. 4 Laser efficiency as a function of the input energy /10/

Fig. 5 Output energy as a function of the pulse number for a sealed-off laser /15/

Fig. 6 Pulse energy as a function of the capacitor charging voltage at a repetition rate of 1 pps /18/

Fig. 7 Pulse energy as a function of the repetition rate /18/

Fig. 8 Cross-section of the EBCDL /20/

Fig. 9 Output energy as a function of the input energy for several active mixtures /20/

Fig. 10 Gain coefficient as a function of the input energy for the EBCDL /21/

Fig. 11 Electron beam intensity distribution on the width of the foil; a continuous line shows the foil shape /23/

Fig. 12 Secondary electron density as a function of time /23/

Fig. 13 Recombination coefficient as a function of a reduced electric field for a CO_2-N_2-He 1:1:10 mixture /27/

Fig. 14 Apparent ionization coefficient v_s reduced electric field for a TPA and xylene doped mixture /27/

Fig. 15 Electron energy distribution function for a 1:1:10 mixture /29/

Fig. 16 EEDF for a 1:1:1: mixture /29/

Fig. 17 Discharge circuit for the TEA-CO_2 laser /27/

Fig. 18 Comparison between calculated and experimental discharge current, voltage and resistance /27/

Fig. 19 Output energy vs. xylene dopant pressure /28/

Fig. 20 Pulse shape as a function of the absorption coefficient /28/

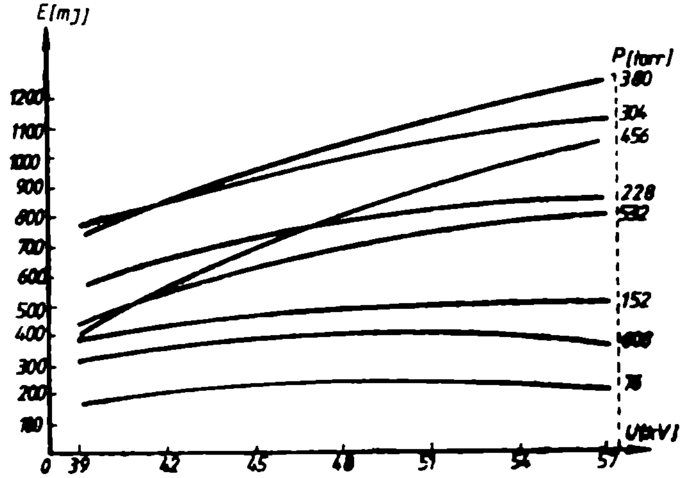

fig. 1

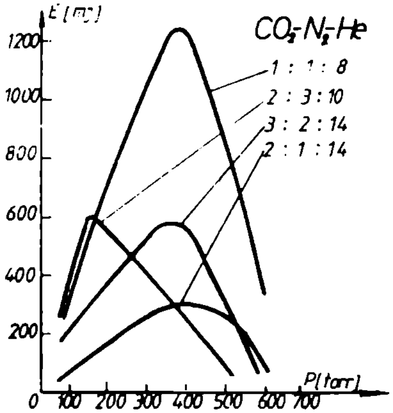
E (mJ)
1200
1000
800
600
400
200
0
CO_2-N_2-He
1 : 1 : 8
2 : 3 : 10
3 : 2 : 14
2 : 1 : 14
P(torr)
100
200
300
400
500
600
700

fig. 2

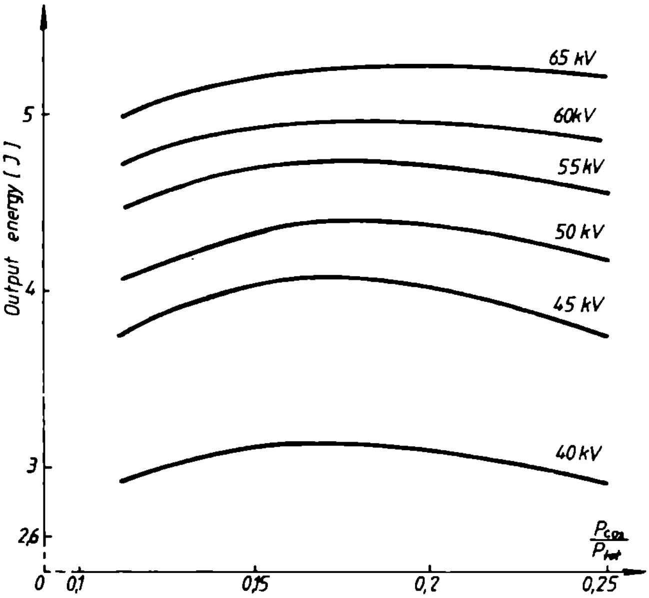
Output energy (J)
5
4
3
2,6
0
0,1
0,15
0,2
0,25
$\frac{P_{CO_2}}{P_{tot}}$
65 kV
60kV
55kV
50 kV
45 kV
40kV

fig.3

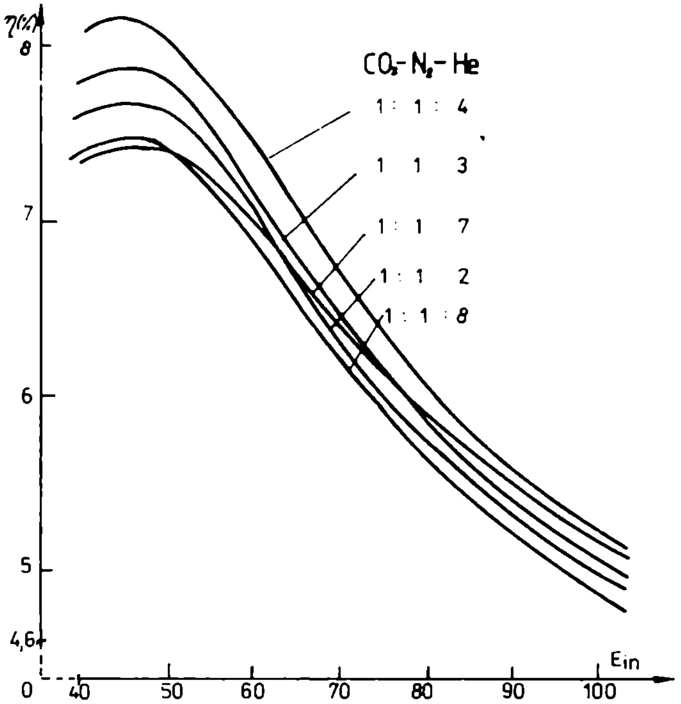

η(%)
8
7
6
5
4,6
0
40
50
60
70
80
90
100
E_{in}
CO_2-N_2-He
1 : 1 : 4
1 1 3
1 : 1 7
1 : 1 2
1 : 1 : 8

fig. 4

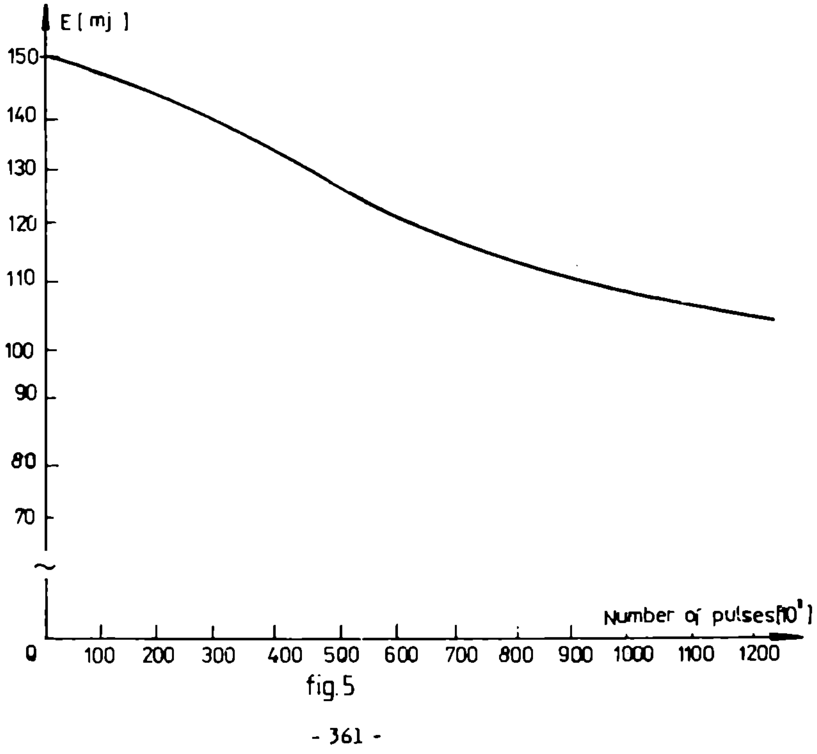

E [mj]
150
140
130
120
110
100
90
80
70
0
100
200
300
400
500
600
700
800
900
1000
1100
1200
Number of pulses[10³]

fig. 5

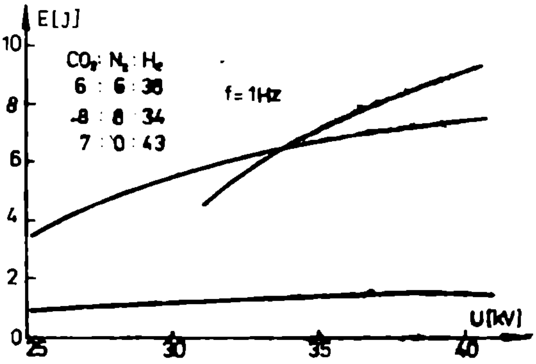
E[J]
10
8
6
4
2
0
CO2 : N2 : He
6 : 6 : 38
8 : 8 : 34
7 : 0 : 43
f = 1Hz
U[kV]
25
30
35
40

fig. 6

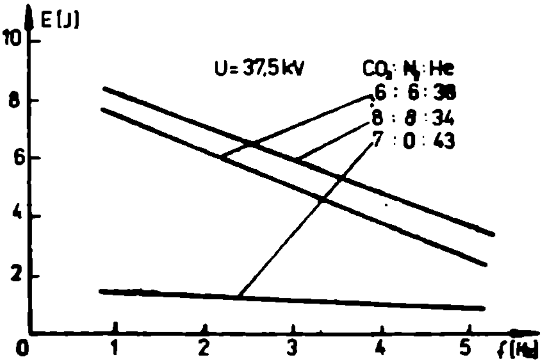
E[J]
10
8
6
4
2
0
U = 37,5 kV
CO2 : N2 : He
6 : 6 : 38
8 : 8 : 34
7 : 0 : 43
1
2
3
4
5
f [Hz]

fig. 7

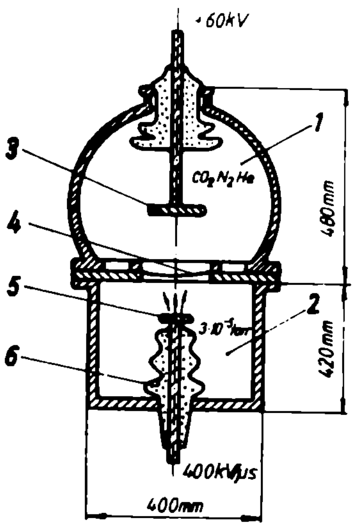

fig. 8

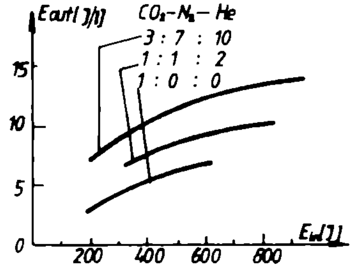

fig. 9

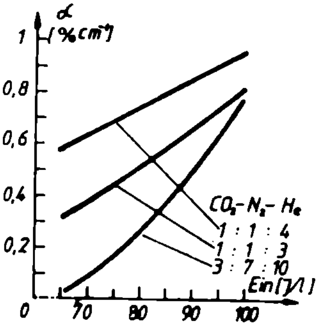

fig. 10

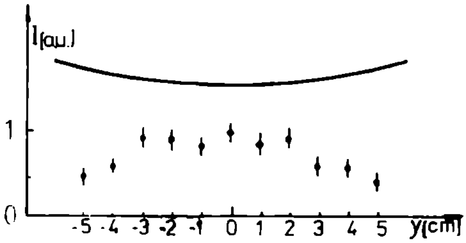

fig. 11

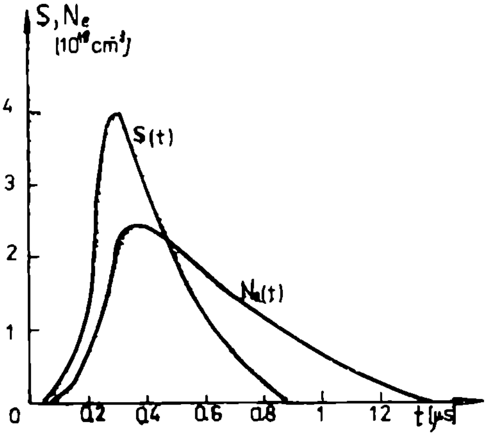

fig. 12

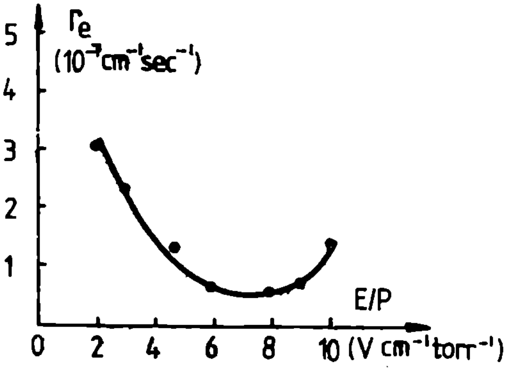

fig. 13

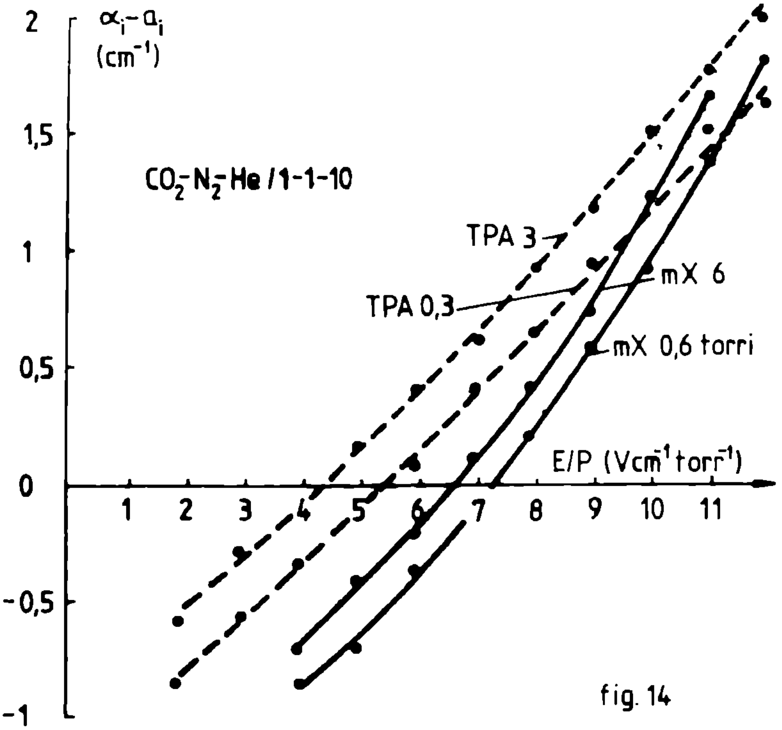
$\alpha_i - a_i$ (cm^{-1})
2
1,5
1
0,5
0
-0,5
-1
CO_2-N_2-He /1-1-10
TPA 3
TPA 0,3
mX 6
mX 0,6 torri
E/P (Vcm^{-1}torr^{-1})
1
2
3
4
5
6
7
8
9
10
11

fig. 14

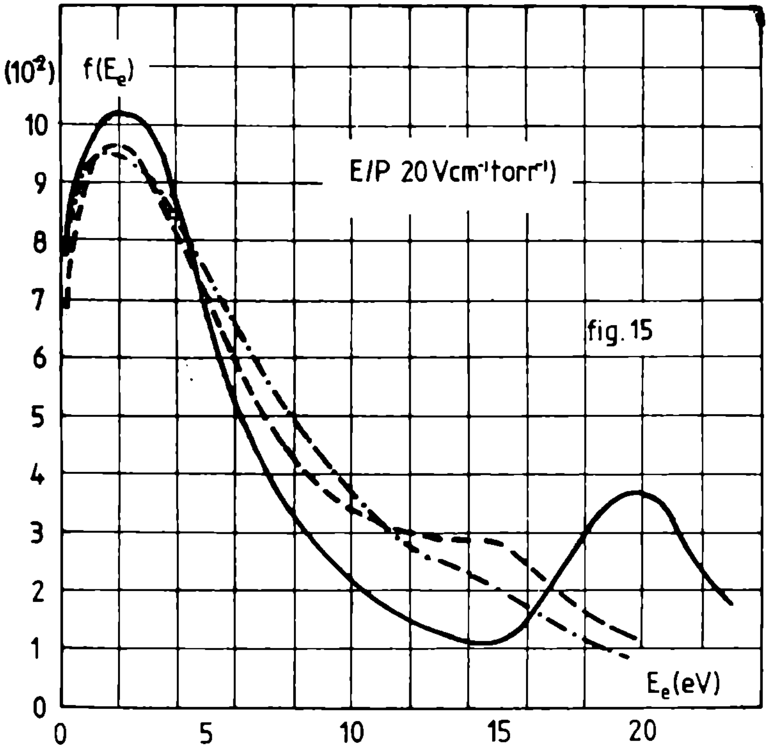
(10^{-2})
f(E_e)
10
9
8
7
6
5
4
3
2
1
0
E/P 20 Vcm^{-1}torr^{-1})
E_e(eV)
0
5
10
15
20

fig. 15

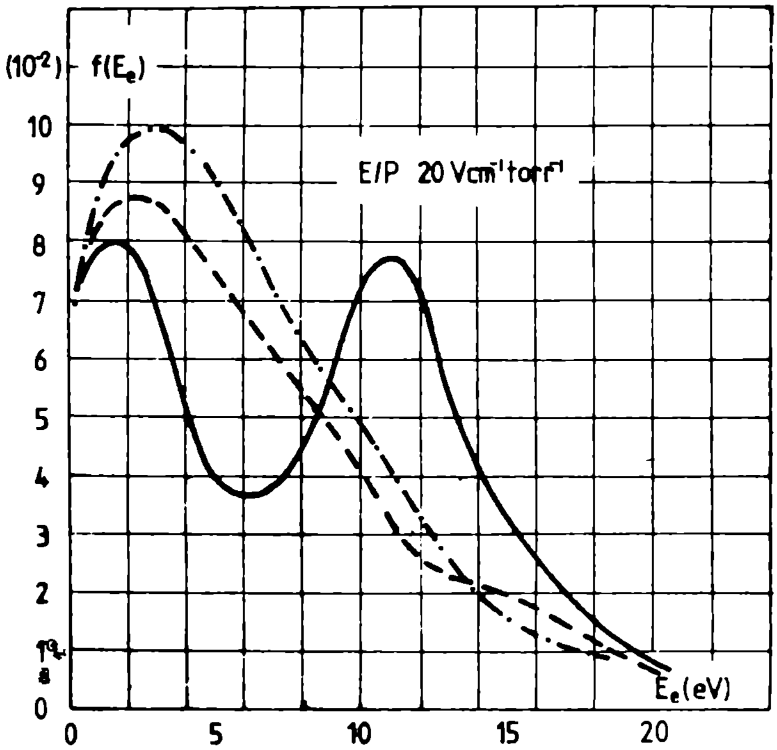
(10⁻²) f(Eₑ)
10
9
8
7
6
5
4
3
2
1
0
E/P 20 Vcm⁻¹torr⁻¹
Eₑ(eV)
0
5
10
15
20

fig, 16

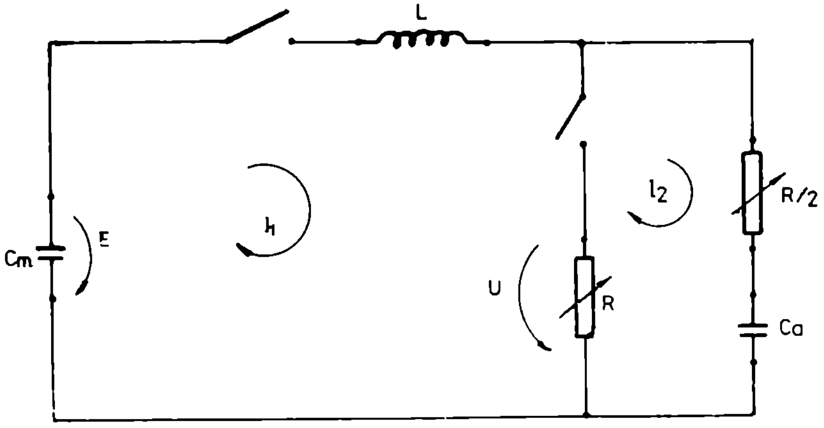
L
Cm
E
I1
U
R
I2
R/2
Ca

fig. 17

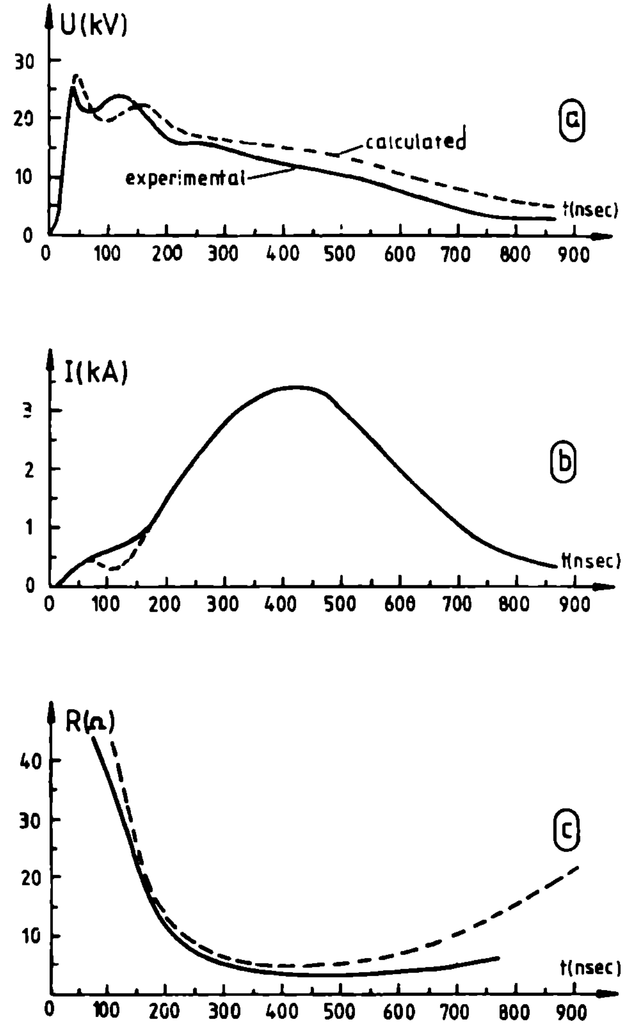

CO_2-N_2-He / 8,3-8,3-83 ; 100nF/ 24kV; Δt=30nsec.

fig 18

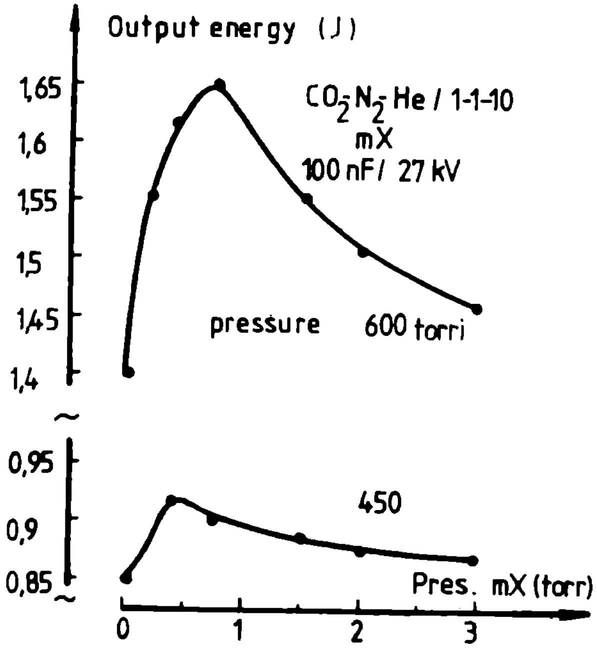
Output energy (J)
1,65
1,6
1,55
1,5
1,45
1,4
0,95
0,9
0,85
CO_2-N_2-He / 1-1-10
mX
100 nF / 27 kV
pressure
600 torri
450
Pres. mX (torr)
0
1
2
3

fig. 19

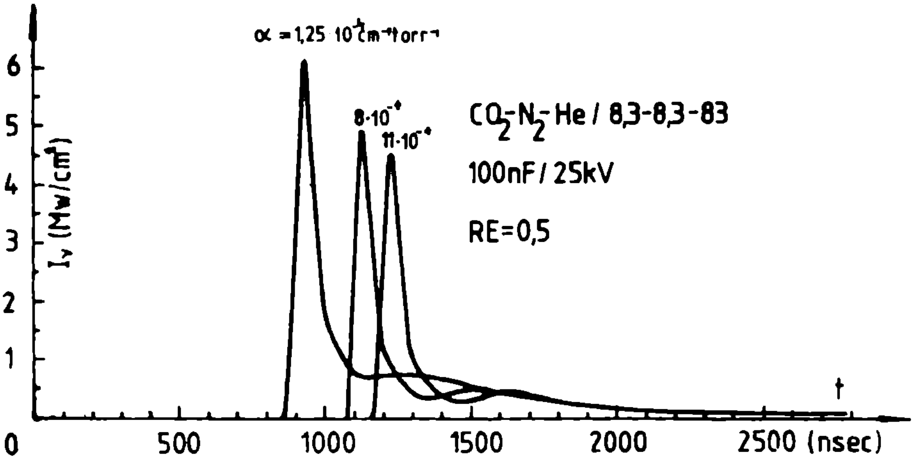
$\alpha = 1,25 \cdot 10^{-4}\ cm^{-1} torr^{-1}$
$8 \cdot 10^{-4}$
$11 \cdot 10^{-4}$
CO_2-N_2-He / 8,3-8,3-83
100nF / 25kV
RE=0,5
I_v (Mw/cm²)
6
5
4
3
2
1
0
500
1000
1500
2000
2500 (nsec)
t

fig. 20

LASER "LIGHTMOTIVES"

I. A. DOROBANTU

Institute of Physics and Nuclear Engineering, Bucharest, ROMANIA

Immediately after the birth of the laser, twentyfive years ago, it became clear to everybody that the new device was to bring about a revolution in all fields of optics with a previsible extension to all domains of contemporary experimental physics and technology.

Fewer were however those who would have thought of it as a fundamental tool in theoretical research. The situation did not change considerably for the following years, until the early seventies when Hermann Haken published an impressive monograph entirely devoted to the theory of the laser /1/ and a triplet of papers appeared describing lasing as a second order phase transition /2/. At about the same time, H.Haken introduced a new model, which he called Synergetics, and which has grown since into a true scientific field of interdisciplinary research. The underlying philosophy of this new branch of science was the laser, and thus the famous first book on synergetics /3/ was also the first writing in which "laser" was more than a word, or a concept, or a device: it was a "leitmotive".

So, today, some seven hundred years since Robert Grosseteste tried to deduce the whole Universe from one simple element - light - this same element ranges among the leitmotives of theoretical physics, by means of a "something" made up of, possibly, a glass tube, a pair of mirrors and a flash and which we now call by the name of " LASER "..

As a hommage to the laser, I shall try in the following to review some of its theoretical impacts or as stated in the title, some of the laser "lightmotives".

What should one include in the list ? There are first the **coherent states** /4/ of the electromagnetic field and all the related theoretical achievements : expressing other states and operators of the e.m. field in terms of them, the so called P-representation etc. Then, **superradiance** /5/, a possibility of coherently emmitting radiation first described by R.H.Dicke and then developed by many others - H.Eberly and R.Bonifacio being among the first and most important; a related and even more interesting concept, also due to R.Bonifacio, is **superfluorescence**. **Bistability** - a hot topic of today, of much theoretical interest, but also of very wide experimental application. Also with fascinating practical applications there are the theoretical developments the laser has made possible in the fields of **nonlinear optics** and **holography**. One can also add the **laser turbulence** (or **laser chaos**), a rather new issue which now focuses the interest of more and more people. There is not the right place here (and not space enough) to review all of them and I am not qualified to do it. I shall only elaborate a bit on the laser - phase transition analogy, which is one of the most meaningful concepts of physics and, is also related to practically all the topics in this list.

Let us thus start with the coherent states, the Dicke Hamiltonian and the Laser Phase Transition .

Coherent states , $|\alpha\rangle$, have been introduced in physics, in the form they are used today, by Roy J.Glauber /4/ in 1963 as eigenstates of the photon annihilation operator

$$|\alpha\rangle = \alpha|\alpha\rangle \qquad (1)$$

Their definition is of course not related to the laser, but it is there that they find their full use (among other things, the squared modulus of the coherent state eigenvalue, α , is related to the average density of coherent photons in the cavity). A very important, however simple, example is the obtaining of the expression of a (generalized) free energy which allows the investigation of the laser phase transition. (It is worthwhile stressing at this point that, as it will become more clear from the following, the importance of the laser as a theoretical model comes mainly from the fact that it is THE soluble model of nonequilibrium systems, enjoying in a way the same importance as does the Ising model for equilibrium systems)

Now, since the laser system consists of an electromagnetic field coupled to a system of (two-level) atoms, we need a Hamiltonian to describe this. For this purpose we can use the Dicke Hamiltonian /5,6,7/ which can be written in a simplified form as:

$$H = a^+a + \varepsilon/2\ S + \lambda/2\sqrt{N} \qquad (a^+s^- + as^+) \qquad (2)$$

where h = c = 1 and the rotating wave approximation and the so-called spin representation of atomic operators* have been used. This Hamiltonian describes the interaction between an one-mode radiation field and the system of two-level atoms described by the operators a, a^+ and S, $S^{\pm}$, respectively. It formed the object of investigation of a beautiful paper by Hepp and Lieb /6/, a treatment which was simplified in the work of Wang and Hioe /7/.

The critical temperature - the threshold inversion - can be obtained by calculating in turn the partition function $Z(N,T) = \mathrm{Tr}\ \exp\{-\beta H_N(T)\}$, where β is the inverse of the temperature and the free energy $f(T) = -\lim(\beta N)^{-1} \cdot \log Z_N(T)$ which we can then expand into a series of even powers of the modulus of the coherent state eigenvalue, α . The result will be obtained after straight forward, though rather intricate calculations /8/, so that, putting here temperature as equivalent to the unsaturated inversion (S_o), we get

$$f(S_o) = f_o - \frac{g}{2\varkappa\gamma^2}(S_o - S_c)|\alpha|^2 + \frac{\tau g^4}{\gamma^2}|\alpha|^4 + \ldots \qquad (3)$$

where g is proportional to the coupling constant λ and $\varkappa, \gamma$, τ are specific laser constants.

---

* In this representation, the spin operators S, $S^{\pm}$ stand as a shorthand for:

$$S^+ = \sum_i (a_2^+ a)_i \quad , \quad S^- = (S^+)^+ \quad , \quad S = \sum_i (a_2^+ a_2 - a_1^+ a_1)_i$$

with i denoting the position of atoms and 1 and 2 referring to the two relevant atomic levels.

At the laser threshold (i.e. at the critical temperature), the electromagnetic radiation is no longer incohererent. A symmetry is broken in this way (order is gained), which fully justifies treating the lasing as a second order phase transition.

The laser phase transition is now an extensively discussed subject. Among other things, lasing has been investigated in the frame of Catastrophe Theory (a rather recent mathematical theory on which a few words will be said at the end of this paper) /9,10/. This has supplemented the physical frame of the discussion with welcome mathematical rigor. Moreover, it has helped turn the laser into a most reliable concept/instrument to be used in approaching questions from other domains where the laser finds its place as an instrument or would have a meaning as a concept.

Since the very first papers on the laser phase transition, attempts have been made to put it in relation to two other apparently different phenomena - superconductivity and superfluidity. Playing on words, I termed them all, years ago, as "superbehaviours" /11/. And then, why not ! Similarly to the vanishing of electrical resistance or of a fluid's viscosity, the light generated or amplified in a laser "loses" its natural incoherence, and acquires instead the property of coherence which makes it so special.

The laser thus joins the family of "super" systems, enjoying however one extra quality - its being a nonequilibrium or to be more precise, a far from equilibrium system. This feature is due to the fact that the true laser system is not only the electromagnetic field-plus-atoms system described by the Dicke Hamiltonian. One has to include as well the coupling to reservoirs accounting for the different losses in the laser cavity. At this point, let me clarify a possible misunderstanding: the Dicke Hamiltonian describes in fact a superradiant system. Here the coherence of the emitted radiation is due to the high degree of cooperativity among the atoms (see the papers of R.Bonifacio et al. /12/ for a very intuitive presentation). To use the same Hamiltonian for describing a real laser, one has to resort to an artificial intoduction of the loss terms for the field and atoms. This has been done and explained in /9/, and is one of the main reasons why I have stressed the importance of the catastrophe theory approach to the laser for clarifying to some extent the mathematics of the model.

The laser thus belongs to those systems exhibiting striking analogies in their behaviour, even though they are in most cases of an extremely different nature: liquids, metals, magnets, nuclei, biological and ecological systems. What makes the laser so special however is that it could be made to provide a good pattern for thinking in relation to these systems, due in part to its very simple mathematical structure, and also to the fact that, while a nonequilibrium system, it is amenable to a remarkably clear physical presentation.

It is possible that in a not so distant future the laser will help us make considerable headway in understanding not only the analogies I refer to, but the very reason for their existence. Why should in fact a fluid go into a superfluid, a paramagnet into a ferromagnet a.s.o., in practically the same way ? Or why is the mode selection in the laser so similar to the species selection in ecology ? We might gain a lot in clarifying this by pushing the investigation of the laser a bit further.

A first step in this direction is, undoubtedly, the setting of synergetics as an increasingly self consistent domain of science.

So, let us stop at Synergetics as the most important lightmotive in our list. In many ways, this is something of an Urmotif, since though some ten years younger than laser itself, it is now becoming an all-embracing philosophy based on the laser concept.

I will not attempt a definition of Synergetics. Its name was meant by Hermann Haken, the founder of the domain, to denote a "science of cooperation". (The first paper to coin the name was called "Synergetik-die Lehre vom Zusammenwirken" and it appeared in Umschau, 6 (1971), 191.) It would be perhaps even better to place it in the frame of a general natural philosophy, since it transcends the borders of pure physics and sheds a new light on some fundamental problems raised by chemistry, as well as by biology and sociology.

To get a picture of what Synergetics intends to do - and can do - we shall elaborate a bit on two parallel schemes meant to be used in the investigation of natural systems made up of large numbers of subsystems (components). The presentation of these two schemes is largely taken from one of H. Haken's papers and it refers to two possible alternatives which could be roughly classified as mathematical and physical, respectively: the first derives from Rene Thom's theory of structural stability, while the second can be taken as expressing the point of view of Synergetics itself.

But first a few words about Thom's theory, better known as Catastrophe Theory, a model which can also be considered to feature laser as a lightmotive. A catastrophe, as its name suggests, is a sudden change in the state of a system, brought about by a smooth modification of some external parameters, called control parameters or variables. Phase transitions are one such example, with temperature as one of the control parameters.

Thom's "tour de force" was to prove, based on some very fine mathematical developments due to a pleiade of mathematicians, from Poincare and Lyapounov to Andronov, Smale and Arnold, that in the case of gradient systems, there exists a finite number of catastrophes which can be exhibited in the system if the number of control parameters does not exceed **four**. We have seven catastrophes in this case, which Thom called **elementary**; we also have a finite number of elementary catastrophes for five and six control parameters (11 and 14, respectively), but beyond that - their number becomes infinite. Some kind of a catalogue is thus made available, which we can use whenever we have to investigate phenomena taking place in such systems. Besides the already mentioned phase transitions, other well studied catastrophes relate to caustics, to the buckling of a rod, morphogenesis, the shape of rotating stars, certain malfunctions of the central nervous system etc. I shall insist no more on this, since details can be found in the many books and scientific papers written on the subject (see for instance /9/which also includes a very interesting bibliography).

Let us proceed now to the Haken schemes. They start, as I already said. with two different (and one could say opposite) points of view : one of them is that of the matematician who tries to make the best of the available mathematical apparatus and, in a way, to adapt reality to it. The other one is perhaps more realistic and is specific of physics : it takes reality as it is and tries to find the proper mathematical reasoning that would solve the problem. The schemes run as follows :

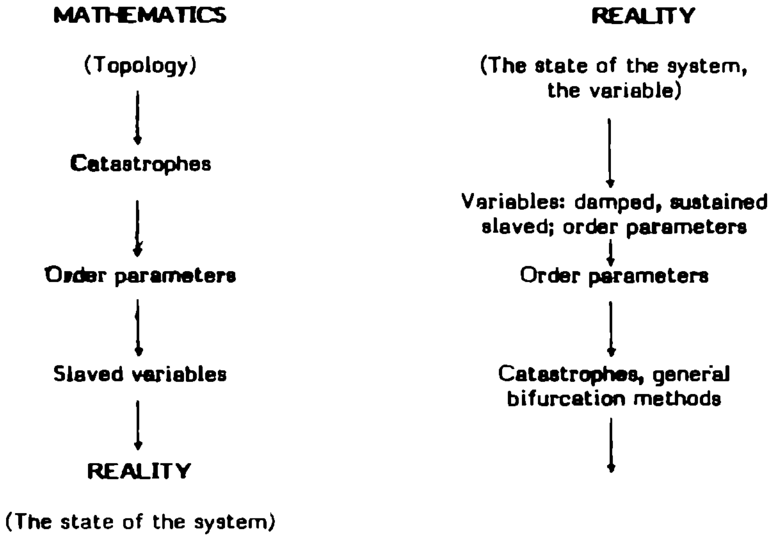

Two points are of particular importance here : there is first the sequence **slaved variables - order parameters** and, second, the apparent impression that one can get at a superficial impression, that the two schemes are merely the reverse of each other. Now, splitting the variables into the slaved ones and those slaving them, is the consequence of one of the most fundamental principles of Synergetics : the slaving principle. According to it, one can establish that in every system the symmetry , in fact the whole behaviour, is governed by the variation of a few (most often one) of the variables. These are therefore the only ones worth retaining for further study. The other variables are simply **slaved** by them and should thus be disregarded. The name "order parameters" is used in analogy to the theory of phase transitions, where it appears for example in the famous Landau series expansion of the free energy in even powers of the order parameter.

As to the second observation, this is of a more general (and even methodological) relevance : let us stress from the very beginning that by no means would one be able to get one of the schemes by simply reading the other one from bottom to top. This is especially true for the physical scheme which includes as an essential step the elimination of the slaved variables in favour of the order parameters, which is something far from being easy to perform !

The mathematical scheme has the advantage of being simple and straightforward, except for the fact that it is not very clear beforehand how to get the right (and all of them!)slaved variables when knowing the order paramter(s), these being, in turn, quite readily detectable when using the right catastrophe, which is also not very difficult to do ...if one is familiar enough with some domains of mathematics, topology in particular, which ...

And, there remains of course the big problem : is the final stage reached in the mathematical scheme the same as the first (starting) stage in the physical one ? Since, as a great Romanian philosopher, Lucian Blaga, once said, in interrogating Nature we might quite obtain the answer we would like to obtain and not the true one !

All this let aside, these two schemes are to much profit for the scientist, especially when one is skillful enough to combine them and balance mathematical rigor with the delicate and intricate requirements of physics.

I should of course have better said physics **or** chemistry, **or** biology, **or** any other domain under the focus of Synergetics. For, reaching soon its 15th anniversary (another round figure!), Synergetics is only at the beginning of its way through science. Built up around the laser as not merely its central device, but also as its central concept, Synergetics is still awaiting its full utilization in getting a deeper understanding of natural systems. One can however notice that, in spite of its young age (or, maybe, just because of it !) one common feature of every progress of this truly interdisciplinary field of science, is bold reasoning -among the boldest in contemporary science, where such reasonings, let me call them " extreme reasonings " , are not rare at all. Just a few examples I have tried to gather in this short presentation. Others are obvious from all the papers in the volume. Much more of these, based as the other ones on this unique invention of physical thinking -the laser, are still to come. I feel thus tempted, after reading this volume which is equally a hommage to those who have invented the laser and to the laser itself, to propose one more alternative for this now famous acronym, which also expresses our hope for the fulfillment of a wish :

L ong A ttempted S olutions to E xtreme R easonings

* * *

Almost exactly twenty years ago I stepped for the first time into the office of Professor Agarbiceanu, who was heading the lasers department of the then Institute of Atomic Physics, in Bucharest. I did not know very much at the time of all he had done for physics in our country, but anybody would have been impressed by the light in his eyes, by his natural kindness, by his profound understanding of Physics. He was loved and admired by his coworkers and his personality helped in no small degree to shaping the personality of the lasers department itself.

He would have been proud to see this volume and the big family of physicists, chemists, engineers and so on, who in today's Romania devote their life and work to developping the laser and turning it into a more useful and used device, to the full benefit of science, of national economy, of social life.

And there are still many of us for whom, at the beginning of our life with physics, the name of Professor Agarbiceanu would almost spell as " Laser ".

Or was it the reverse ?

REFERENCES

/1/ H. Haken, Laser Theory, in Handbuch der Physik, Band XXV/2C, Springer Verlag, 1970

/2/ R. Graham, H. Haken, Z.Physik, 237, 31 (1970)
V. de Giorgio, M.O. Scully, Phys.Rev., A2, 1170 (1970)
S. Grossmann, P.H.Richter, Z.Physik, 242, 458 (1971)

/3/ H. Haken, Synergetics: an Introduction, Springer Verlag, 1977

/4/ R.J. Glauber, Phys.Rev., 130, 2529; 131, 2766 (1963)

/5/ R.H. Dicke, Phys.Rev., 93, 99 (1954)

/6/ K. Hepp, E.H.Lieb, Helv.Physica Acta 46, 573 (1973)

/7/ Y.K. Wang, F.T. Hioe, Phys.Rev. A7, 831 (1973)

/8/ G. Costache, I.A. Dorobantu, Rev.Roum.Phys., 21, 795 (1976)

/9/ T. Poston, I. Stewart, Catastrophe Theory and its Applications, Pitman Publ.Ltd.,1978

/10/ I.A. Dorobantu, "Lasers and Catastrophes", in "Lasers and Applications" p.641, Eds.I.Ursu, A.M. Prokhorov, CIP Press, 1983

/11/ I.A. Dorobantu, St.Cerc.Fiz., 24 (1972) 627

/12/ R. Bonifacio, P.Schwendimann, F. Haake, Phys.Rev., A4 302, 854 (1971)

DIO Printed at
Central Institute of Physics
Institutul Central de Fizica
Information and Documentation
Office
Bucharest POB 5206 ROMANIA

LASERS AND APPLICATIONS

A VOLUME DEDICATED TO ALL THOSE WHO INVENTED THE LASER AND MADE POSSIBLE ITS APPLICATION IN SCIENCE AND TECHNOLOGY

EDITORS I. URSU V. VASILIU
I.A. DOROBANȚU, V. DRĂGĂNESCU

CIP PRESS BUCHAREST, 1985